AD

ARCCB-SP-99015

PROCEEDINGS OF THE NINTH U.S. ARMY SYMPOSIUM ON GUN DYNAMICS

MC LEAN, VIRGINIA

17-19 NOVEMBER 1998

ERIC L. KATHE, EDITOR

US ARMY ARMAMENT RESEARCH,
DEVELOPMENT AND ENGINEERING CENTER
CLOSE COMBAT ARMAMENTS CENTER
BENÉT LABORATORIES
WATERVLIET, N.Y. 12189-4050

DISCLAIMER

The findings in this report are not to be construed as an official Department of the Army position unless so designated by other authorized documents.

The use of trade name(s) and/or manufacturer(s) does not constitute an official endorsement or approval.

DESTRUCTION NOTICE

For classified documents, follow the procedures in DoD 5200.22-M, Industrial Security Manual, Section II-19, or DoD 5200.1-R, Information Security Program Regulation, Chapter IX.

For unclassified, limited documents, destroy by any method that will prevent disclosure of contents or reconstruction of the document.

For unclassified, unlimited documents, destroy when the report is no longer needed. Do not return it to the originator.

REPORT DOCUMENTATION PAGE

Form Approved
OMB No. 0704-0188

1. AGENCY USE ONLY *(Leave blank)*	2. REPORT DATE	3. REPORT TYPE AND DATES COVERED
	March 2000	Final

4. TITLE AND SUBTITLE

PROCEEDINGS OF THE NINTH U.S. ARMY SYMPOSIUM ON GUN DYNAMICS

5. FUNDING NUMBERS

AMCMS No. 6226.24.H191.1

6. AUTHOR(S)

Eric L. Kathe, Editor

7. PERFORMING ORGANIZATION NAME(S) AND ADDRESS(ES)

U.S. Army ARDEC
Benet Laboratories, AMSTA-AR-CCB-O
Watervliet, NY 12189-4050

8. PERFORMING ORGANIZATION REPORT NUMBER

ARCCB-SP-99015

9. SPONSORING / MONITORING AGENCY NAME(S) AND ADDRESS(ES)

U.S. Army ARDEC
Close Combat Armaments Center
Picatinny Arsenal, NJ 07806-5000

10. SPONSORING / MONITORING AGENCY REPORT NUMBER

11. SUPPLEMENTARY NOTES

Presented at the Ninth U.S. Army Symposium on Gun Dynamics, McLean, VA, 17-19 November 1998.
This symposium was sponsored by Benet Laboratories and the U.S. Army Research Office.
Note the report number was assigned in advance of report publication. The final copy of this publication was approved in March 2000.

12a. DISTRIBUTION / AVAILABILITY STATEMENT

Approved for public release; distribution unlimited.

12b. DISTRIBUTION CODE

13. ABSTRACT *(Maximum 200 words)*

This publication represents a compilation of the technical papers concerning modeling, analyses, design, measurements, and instrumentation of gun dynamics. The authors represent a cross section of the scientific and technical community, including universities, industrial, and government research laboratories.

14. SUBJECT TERMS

Ballistics, Barrel Vibration, Dynamics, Precision, Controls, Target Acquisition, Accuracy, Heating, Erosion

15. NUMBER OF PAGES

519

16. PRICE CODE

17. SECURITY CLASSIFICATION OF REPORT	18. SECURITY CLASSIFICATION OF THIS PAGE	19. SECURITY CLASSIFICATION OF ABSTRACT	20. LIMITATION OF ABSTRACT
UNCLASSIFIED	UNCLASSIFIED	UNCLASSIFIED	UL

TABLE OF CONTENTS

SESSION III – SPECIAL APPLICATIONS

SESSION IV – THERMAL CONSIDERATIONS

SESSTION V – FUTURE CONSIDERATIONS

SESSION VI – LIGHTWEIGHT SYSTEMS

SESSION VII – DYNAMICAL ANALYSIS OF SYSTEMS

LUNCHTIME PRESENTATIONS

NINTH U.S. ARMY SYMPOSIUM ON GUN DYNAMICS

17-19 NOVEMBER 1998
MC LEAN, VIRGINIA

SYMPOSIUM MANAGEMENT

Symposium Manager, Joel Leifer
Proceedings Publication, Jeff McQuilkin
Technical Coordination, Chris Tomko

PROGRAM COMMITTEE MEMBERS

General Chair: Eric Kathe, Benet Laboratories

Technical Chair: Tom Simkins, Consultant

Bruce P. Burns, ARL/WMRD

Giuliano D'Andrea, Benet Laboratories

Bob Dillon, RHIT

Ron Gast, Benet Laboratories

Gregg T. Geiger, UDLP

Richard Hasenbein, Benet Laboratories

G. Albert Pflegl, Benet Laboratories

Henry J. Sneck, Benet Laboratories

John D. Vasilakis, Benet Laboratories

Stephen Wilkerson, ARL/WMRD

ALPHABETICAL INDEX OF AUTHORS

A CHRONOLOGY OF GUN DYNAMICS SYMPOSIA

In-Bore Dynamics Symposium
Naval Postgraduate School, Monterey, CA, 8-9 July 1976.
Thomas N. Tschirn, Chariman.

First Conference of the Dynamics of Precision Gun Weapons
Rock Island, IL, 26-27 January 1977.
Proceedings: R-TR-77-008, E.J. Haug, Editor.

Second U.S. Army Symposium on Gun Dynamics
The Institute on Man & Science, Rensselaerville, NY, 19-22 September 1978.
Thomas E. Simkins, General Chairman.
Proceedings: ARLCB-SP-78013.

Third U.S. Army Symposium on Gun Dynamics
The Institute on Man & Science, Rensselaerville, NY, 11-14 May 1982.
Thomas E. Simkins, General Chairman.
Proceedings: ARLCB-SP-82005.

Fourth U.S. Army Symposium on Gun Dynamics
Riviera Beach, FL, 7-9 May 1985.
Thomas E. Simkins, General Chairman.
Proceedings: ARLCB-SP-85009.

Fifth U.S. Army Symposium on Gun Dynamics
The Institute on Man & Science, Rensselaerville, NY, 23-25 September 1987.
Thomas E. Simkins, General Chairman.
Proceedings: ARCCB-SP-98023.

Sixth U.S. Army Symposium on Gun Dynamics
Tamiment, PA, 15-17 May 1990.
Thomas E. Simkins, General Chairman.
Proceedings: ARCCB-SP-90015.

Seventh U.S. Army Symposium on Gun Dynamics
Newport, RI, 11-13 May 1993.
Thomas E. Simkins, General Chairman.
Proceedings: ARCCB-SP-93034.

Eighth U.S. Army Symposium on Gun Dynamics
Newport, RI, 14-16 May 1996.
Proceedings: ARCCB-SP-96032, G. Albert Pflegl, Editor.

Gun Tube Wear/Erosion Prevention Using Combustion-Synthesized, Functionally-Graded Materials

Gary J. Hanus, Rod E. Reeve, Kevin T. Uznanski
PHOENIX Solutions Co.
5900 Olson Memorial Hwy
Minneapolis, MN 55422-4999

Emil Shtessel
Exotherm Corp.
1035 Line St.
Camden, NJ 08103

R. Nathan Katz
Worcester Polytechnic Institute
100 Institute Road
Worcester, MA 01609-2280

Substantial operational savings, cost reduction and performance enhancement (i.e. ability to use more energetic propellants) can be met with development of materials, processes and/or components/equipment for gun barrels that exhibit wear and erosion protection characteristics greatly improved over current materials and methods. Development of tube liners with functionally-graded material (FGM) properties may eliminated current ceramic/refractory metal liner interfacial, thermal/mechanical failure mechanisms. Utilizing self-propagating, high-temperature synthesis (SHS) techniques, SHS gun barrel/liner production methods have been identified and tube samples fabricated which exhibit FGM characteristics. An SHS processing unit has been designed, fabricated and tested, producing 150 mm diameter, 6 inch long ring segment samples. Functionally-graded material coatings from 1 to 3 mm thick were synthesized on the inside surface of 150 mm tubes. The demonstration coatings showed excellent welding/bonding to the parent steel tube substrate/interface. An increase in hardness of over 4X from the substrate to the coated tube ID was verified, with much of the change attributed to formation of compounds such as titanium carbo-nitride with the SHS process. Coatings were shown to have both axial and circumferential uniformity for the segments processed.

INTRODUCTION

The Army must maintain battlefield dominance well into the next century. This commitment is being carried out via two major initiatives to guide mid and long range thinking: **"Force XXI"** and the **"Army After Next (AAN)"** [1]. **Force XXI** will prepare forces for facing challenges up to the year 2010. The **AAN** looks at concepts and enabling technologies that will shape the Army beyond 2010. Rapid deployment is a technology-dependent doctrine that will help win the wars of the future. Certainly a key element of this doctrine is developing hardware which is lightweight and transportable **and** sufficiently lethal and survivable (i.e. battlefield life-cycle). With such functional and performance characteristics in hand, rapid deployment of "energy on target" hardware for a sufficient period of time makes it possible to establish a survivable and credible position against entrenched, heavy domestic firepower. Energy on target advancements for artillery and tanks are proceeding with advanced propellants, allowing scaling down of size and weight of delivery systems. However, these improvements drive acceptable hardware survivability and battlefield life-cycle past current design and materials limits. New materials and component design capabilities are emerging which may provide the opportunities to meet the challenges of **AAN.**

Much of the improvement in the range and energy on target has come from advancement in propellants, providing greater impetus through lowering the average molecular weight of the products of combustion as well as increasing the adiabatic, isochoric flame temperature. The increase in combustion temperature and associated gas pressure loading and corrosives have put a severe strain on the thermal-mechanical design of gun barrels. Large caliber guns have generally been mechanical fatigue limited in their lifecycle, while smaller, rapid-fire guns experience erosion-related problems. With the push for higher muzzle velocity designs in the larger guns, ever-greater proportions of condemnation are occurring due to both erosion and mechanical fatigue [2]. Erosion is enhanced at elevated operating temperatures and pressures, pushing the local metal surface temperatures above the melting point. Localized melting and re-solidification changes the surface properties of the parent barrel material and may mask development of micro-cracks that ultimately reduce fatigue life. Non-thermal erosion is also introduced through both combustion gas/surface chemical interaction as well as mechanical interaction of the projectile with the bore (engraving stresses). Effective, yet difficult to implement, protection concepts such as external barrel cooling and projectile ablatives have been investigated for gun barrel protection. However, other erosion-reduction approaches have evolved to the forefront of gun protection technology: propellant additives; thin, abrasion-resistant, high-melting-temperature metallic coatings; and expendable liners.

Combinations of high melting temperature, high thermal conductivity and specific heat, low thermal expansion and high modulus of elasticity are required of coatings/liners to insure proper functional barrel performance. For many years, the cobalt-based material, Stellite 21, served as an excellent small caliber liner. Other refractory metals such as molybdenum, tungsten, tantalum and columbium have been investigated more recently, with hope for future potential through greater design knowledge of the interplay between material properties and mechanical assembly/shot dynamics (i.e. liner compressive stresses to counteract barrel pressure loads in order to avoid liner cracking). Chromium plating, via electro-deposition, has long been a mainstay for barrel bore protection and research continues for improved application, bonding and cost-effective processing techniques [3,4]. Between the late 1970's and the early '90's, ceramic gun barrel liners were investigated for their high-temperature, high strength and erosion resistance characteristics. Support for these efforts came from the Army's Advanced Concepts and Technology Program as well as the Army Materials Technology Laboratory. ARPA also contributed to work in the late 1980's. A number of programs using SiC and/or Si_3N_4 demonstrated that ceramic liners could work in the smaller caliber range (up to 25 mm) with over 200 high-energy rounds completed with little erosion damage. The programs provided clear evidence of the benefits of ceramic liners while laying the groundwork for proper material selection, failure mode identification and future design approaches. Extension of this technology to larger bores will pay significant performance and life-cycle costs benefits if successfully implemented.

Having recognized the long-range potential of incorporating combustion-synthesized (Self-propagating High-temperature Synthesis, SHS) processing techniques for gun barrel wear and erosion prevention, the US Army Research Laboratory, Aberdeen, Maryland, awarded Phoenix Solutions Co. in November, 1997, a Phase I SBIR contract to investigate the development of 150 mm diameter-class, functionally-graded material gun barrel liner processing techniques via combustion synthesis. This document represents a work-in-progress of this SBIR program. The following introductory sections briefly review the background and significance of the gun barrel life-cycle problem and describe the SHS process and the opportunities it presents for advanced gun barrel protection. The Phase I program objectives and results will then be presented.

DESCRIPTION OF THE PROBLEM AND THE SOLUTION STRATEGY

The fundamental problem facing successful implementation of protective gun barrel liners, whether refractory metal, cermet or ceramic, is cracking. The cracking results from the mismatch of the coefficient of thermal expansion and the elastic modulus between the liner and the jacket. The phenomenon of axially spaced, circumferential cracks in ceramic liners has been well documented in the Advanced Materials Gun System Program [5]. Typically, the ceramic liner is fit within a heated, thermally-expanded, containment jacket. Upon cool-down the ceramic liner is loaded in both radial as well as axial compression, due to the larger coefficient of thermal expansion (CTE) of the jacket. With cooling, there is some axial slippage between the liner and the jacket at the ends, reducing somewhat the axial compression at these boundaries. During rapid firing, the liner and jacket come to pseudo-local, thermal equilibrium. Since the CTE for the jacket is greater than the liner, the jacket expansion imposes an axial tensile load on the liner, reducing its precompression. Near the center portion of the liner, the axial compression is maintained; however, near the ends, the imposed tensile stresses of the jacket off-set

the already lowered (at ambient conditions) axial compression, so as to give a net tensile stress. This net tensile condition causes a circumferential crack to form. Repeated heat-up and cool-down cycles form new cracks which appear regularly down the axis of the tube. Each new crack effectively shortens the length of the liner. Spalling appears to occur near the barrel ends and is attributed to the crack formation. The hoop compression, however, is maintained during this failure mechanism.

The loss of axial compression causes ceramic liners to fail. The problem is caused by the CTE mismatch between the liner and the jacket. Equalizing the CTE's between the liner and the jacket would eliminate interfacial stress mismatch and alleviate the cracking. However, matched CTE's would mean that the liner would be constructed of a material which would be incapable of withstanding both the thermal and erosive environment at the liner inside diameter (the hard, high-temperature materials needed in the bore have low CTE's but the tough, high-strength gun barrel steels have low temperature capability and high CTE's). Based on ceramic and ceramic matrix composite behavior [6,7,8] and, specific to gun barrel applications [9], Katz et al suggest that a liner design is needed which **transitions** from the properties needed at the bore to those required for crack-free performance at the liner-jacket interface. Such a transitioning, or "**functionally-graded material**" **(FGM)** might have a monolithic ceramic or cermet at the bore and transition to a complete metallic at the jacket. A process whereby this might be accomplished would greatly benefit advancements in the Army Product Improvement Process (PIP) for such equipment as smooth bore guns.

The opportunity exists to demonstrate fabrication of a functionally-graded gun tube liner using recent advancements and processing experience in combustion synthesis techniques. Recent meetings of civilian and Army panels, assessing the improved mission capabilities and increasing durability needs of the Army, indicate a near/short term potential (5 to 10 years) for applying combustion-synthesis to gun tube manufacturing at medium to high rates [10]. Over the last four years combustion synthesis manufacturing processes have been developed by the authors for advanced ceramic filter tube elements for hot-gas clean-up technology in the coal-fired, power industry. Thin-walled, tubular components, not unlike potential gun barrel liner configurations have been fabricated. Over 150 composite ceramic material combinations have been processed and show superior high-temperature strength, corrosion and thermal shock resistance and cost-effective fabrication potential [11]. The tube processing relies on a versatile combustion synthesis technique called self-propagating, high-temperature synthesis (SHS), also referred to as combustion synthesis of inorganic materials (CSIM).

The self-propagating high-temperature synthesis (SHS) method is a combustion-driven, material synthesis technique that offers many advantages over traditional methods of producing metallic, ceramic and composite phase materials. SHS reaction processes are energy-efficient, simple, adaptive to complex shape development, controllable and adaptive to selective material properties variations (i.e. porosity, thermal conductivity, density, etc.) and are suitable for development of solid solutions and a wide variety of composite matrix formations. Self-Propagating High-Temperature Synthesis (SHS) is a material processing method that uses energy from highly exothermic reactions to sustain the chemical reaction in a combustion wave [12,13]. Heat is applied locally to ignite a powder mixture, which produces a chemical reaction that is sufficiently exothermic to be self-sustaining. A high temperature thermal wave then propagates through the powder mixture, converting the selected reactants into the desired product. Depending upon the composition and structure of the initial powder mixture, the speed of the combustion wave may vary from about 0.1 to 10 cm/sec. Maximum temperatures reached in the combustion process fall in the range from 1200 to 4000 C. After the wave passes through the powder mixture, a partially sintered material structure is formed. SHS has been used to synthesize a broad range of materials [14,15]. The spectrum of materials synthesized include: borides, carbides, carbonitrides, chalcogenides, composites, hydrides, intermetallics, nitrides, cermeted nitrides, and silicides. SHS has also been used as a novel method for the production and application of tightly-bonded coatings.

SHS processing techniques can be effectively utilized to develop next-generation, ceramic gun barrel liners. Combustion synthesis techniques may provide an excellent opportunity for the Army to realize a functionally-graded, ceramic/metallic liner design that can meet the thermal/mechanical challenges of future, large-diameter-bore gun barrels. The following sections will describe the implementation of an SHS experience base to develop functionally-graded material tube liners for gun tube protection. Program tasks and significant milestones on work-in-progress with a US Army SBIR Phase I contract will be now reviewed.

RESEARCH PROGRAM AND PRELIMINARY RESULTS

Overall Program Objectives

The primary objective of the Phase I effort was the demonstration of a SHS fabrication technique to produce a preliminary, functionally-graded material suitable for incorporating in large bore gun assemblies. As such, a preliminary processing model was developed which served as the basis for demonstration. The SHS tube-processing model was developed by starting with a tube liner of similar material as a typical parent gun barrel material. This would insure that mismatches in thermal expansion during repeated firings will not arise and create a ratcheting effect that will lead to circumferential cracks. The objective was to create an alloy with carbide reinforcement that is integral to the tube liner material. A preliminary screening of SHS material requirements and gun barrel liner performance needs suggested that nickel, cobalt, chromium and/or tungsten-based alloys with carbide reinforcement may be good candidates.

The Processing Concept

The SHS processing model and procedure take advantage of expected SHS reactant and product properties when exposed to a centrifugal load. Starting with a 150 mm ID liner tube of material similar to the parent gun barrel a thin-walled, porous graphite or SiC tube or fabric is inserted. The assembly is spun and a layer of SHS precursor powder mixture is built up on the rotating liner/porous sleeve assembly. This SHS mixture might include CoO, Al, CrO_2, CrO_3, WO_3, NiO and Si. The centrifugal forces keep the powder mixture in place. The system is taken to a high rotational rate and ignited. During reaction, liquid metals of Co, Cr, W, Ni etc and oxides (Al_2O_3, etc.) form quickly. The density differences between the liquid metals and the oxides allow the metal to settle to the porous carbon insert interface. The liquid metals infiltrate the pore structure of the porous inner liner and react to form precipitated carbides for reinforcement. In the meantime, some liquid metal continues to migrate to the outer radius of the porous sleeve, having reached the interface with the metal liner. The outside metal liner tube in the meantime may be externally heated which allows its temperature to be brought closer to the liquid metal temperature in the vicinity of the metal liner/ porous liner interface, thus affecting a melted sublayer, fusing the outer metal liner with the complex metal-based alloy and carbide reinforced structure. Upon cooling, the ID of the final product contains a layer of alumina and/or other high temperature ceramics. This layer can be left in place and evaluated as a high-temperature bore erosion/wear inhibitor or removed to expose the carbide reinforced structure which might stand on its own merits as a survivable interface. This process model is illustrated in Figure 1.

The process model requires very exothermic reactions. This develops the high adiabatic temperatures necessary for releasing the metals from their initial metal oxide, powdered form and also allow sufficient thermal energy for the metals to melt a thin layer (about 1 mm) of the parent tube or liner to insure proper fusion. Preliminary calculations indicate that mixtures of aluminum and silicon with oxides of cobalt, chromium, tungsten, nickel and aluminum will produce individual reaction temperatures from 2200 K to nearly 4000 K. Success of the process depends on selection of proper initial powder constituents, amounts of the constituents and characteristic times associated with the various process regimes. Five characteristic times must be carefully considered: combustion/reaction rate time scale, characteristic sedimentation time, characteristic infiltration time, melt temperature time and the characteristic cool-down time.

Maintaining the proper relationship among the various time scales is important to affect the required end-product characteristics. The time scales can be varied by control of the reactive constituents, the imposed centrifugal loads through rotation rate, the pore size and fiber dimensions of the porous sleeve and the amount of external pre-heat of the outer metal liner. As an example, if the combustion time frame is of the order of the sedimentation time scale, a cermet may be created instead of a distinctively separate monolithic inner oxide layer. Additionally, the degree of carbide precipitated can be controlled depending on the selection of the porous sleeve characteristics (i.e. flow resistance encountered by the flowing metal droplets) and/or the degree of system rotation.

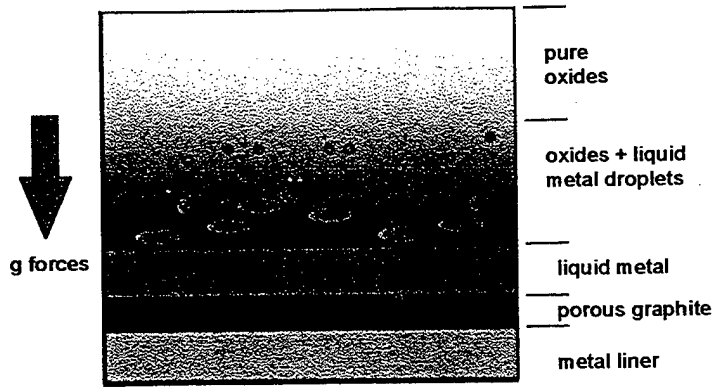

Figure 1. Process Model to Produce Functionally-Graded Properties in Gun Tube Liners

Test Hardware Description

The SHS Centrifugal Processing Unit (CPU) unit is a versatile processing fixture designed to accept primarily 150mm diameter tube segments (although it can be used for other diameter tubes) for the purpose of depositing SHS synthesized, functionally-graded materials on the inside diameter of the pipe/gun barrel liner simulator. The unit, as depicted in Figure 2, consists of a welded structure that supports a drive motor and a set of three high temperature bearings so that an 22 inch long test pipe segment can be rotated about the pipe axis at sufficient speed to assist in SHS reaction dynamics. The entire test unit is approximately 4 feet high by 4 feet wide by 6 feet long and is designed to be transported via forklift for easy insertion and removal from the process chamber. The process chamber is a 12 foot long by 12 foot diameter chamber capable of handling process gases, temperatures and pressures over a wide range of operating conditions.

The CPU processor can operate over a wide range of rotational rates and test tube pre-heat temperatures. As noted earlier it is important for creating the correct SHS material processing characteristic time scales that the combustion synthesis process be controllable under specific centrifugal loads. Up to 200 g's may be useful for processing and to date over 100 g's have been demonstrated in an actual SHS combustion synthesis test. The ultimate g-factor achievable will be limited to the dynamic stability of the rotating assembly, with careful balancing and component alignment critical to reaching a 100+ g condition. The CPU fixture is equipped with externally-opposed, radiant quartz heaters capable of raising the rotating tube test assembly to preheat conditions sufficiently high to off-set the heat sinking capacity of the liner tube during attempted welding of the SHS material to the tube wall. Preliminary calculations indicate that preheating the liner tube to near 200 to 250 deg F will be sufficiently beneficial to the SHS synthesis/welding process.

Test Procedure and Processing Description

Various techniques were investigated for loading the SHS powder into the test tube. These included the injecting the powder into the rotating liner using a powder feeder, pouring the powder into a rotating pipe using a trough or ladle, or "cartridge loading" the test liner remote from the spinning apparatus. The cartridge method allowed the most flexibility, uniformity and processing control and was used for all test setups. The test liner tube was cleaned to remove any oxide layers and residual machining oil prior to loading. In addition, the inner surface was prepared to increase surface roughness and enhance welding during the firing. A means of safely and efficiently igniting the

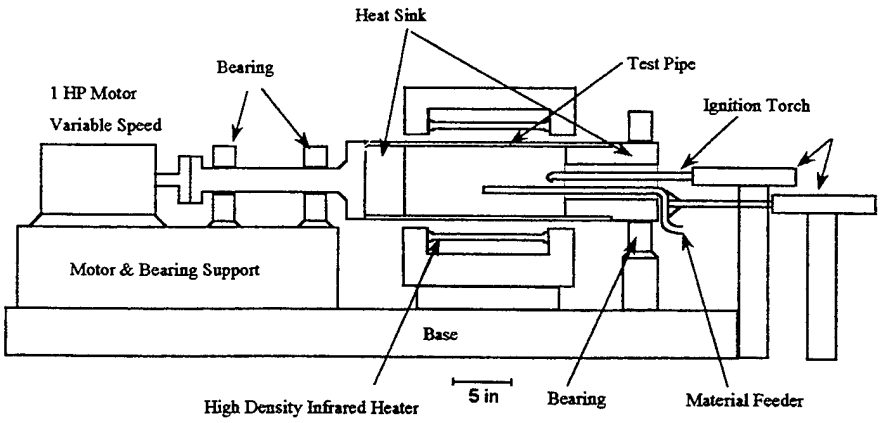

Figure 2. Sketch of SHS Centrifugal Processing Unit (CPU)

rotating powder mixture was devised. Concepts investigated included the use of spark ignition, acetylene/propane torches, direct ignition (ignitor stick), and lacquered cannon fuse. The cannon fuse proved to be most effective and safe ignition source. It could be inserted and lit without the test article rotating. By varying fuse length, one could control the delay between fuse ignition and SHS mixture ignition. This allowed personnel and equipment to be moved a safe distance from the test article.

The firing sequence for the SHS processing begins by lighting the fuse. The CPU is energized to rotate the tube liner segment. When the fuse reaches the entrance to the rotating tube all monitoring and data acquisition systems are turned on. The SHS reaction begins approximately 1 second after the SHS ignition precursor powder ignites and completes the reaction process about 35 seconds after lighting the fuse. Gas evolves out the front end of the test liner and lasts for about 3 seconds before gas is expelled out the back end of the test liner through the vent holes. The test tube maximum outside metal temperature occurs about 12 seconds after ignition. The test liner remains glowing at this intensity for approximately 120 seconds and then starts to cool. The test liner remains spinning for approximately 10 minutes to provide further cooling.

Summary of Test Matrix and Results

Six spinning tests have been completed to date. Spin tests 1 and 2 were used to develop procedures and checkout the hardware. The high exothermic SHS powder for these tests was a commercially available powdered iron oxide - aluminum material. The low melting/ low exothermic powder was a Ni-Mn-Si-Cu mixture. Acceleration attained during the tests was 75 and 55 g respectively. Spin test 3 was conducted using black nickel oxide mixed with aluminum as the high exothermic powder. Although this mixture provided sufficient energy to melt and weld the low exothermic material to the parent steel pipe, it contained a high percentage of impurities which caused substantial gas evolution. As the gas escaped from the test pipe, it entrained much of the low exothermic powder and little welding occurred. Spin test 4 used a pure form of nickel oxide (green nickel oxide) mixed with aluminum powder in an attempt to reduce gas evolution by an order of magnitude. In addition, the low exothermic powder (Ni-Mn-Si-Cu) was mixed (10% mass basis) with the high exothermic powder. This reduced the reaction rate and lowered the adiabatic reaction temperature by approximately 10%. Acceleration was increased to 105 g to enhance metal – glass separation and increase welding efficiency. Spin test 5 was a repeat of test 4 except the low exothermic powder made up 20% of the total SHS powder. An additional 10% (mass) of SiO_2 was added to produce a low viscosity glass during the SHS reaction and further enhance metal-glass separation and while reducing the reaction rate. Spin test 6 used the same high exothermic mixture with 20% low exothermic powder (Ni-Mn-Si-Cu) and 10% silica, as in test 5. A Ti-Ni-Cu mixture was used for the low exothermic powder. In addition, carbon cloth was attached to the inner surface of the test pipe in an attempt to produce titanium carbide and increase the hardness of the resulting coating.

Visually all test firings produced a functionally graded material. Good separation occurred between the molten metallic and liquid ceramic reaction products, with the metal being driven to the pipe wall. Post-test inspection revealed a porous, weakly bonded interface between the two layers, although both the ceramic and metal layers were often quite dense. It is believed that better attachment of the layers can be attained, if desired, by reducing the radial acceleration. All test liners were water-jet cut, polished, and prepared for evaluation. Figures 3 and 4 are typical cut samples from Spin tests 4 and 6, respectively. Figure 3 shows the uniform weld interface between the test pipe and the SHS material. The glass-ceramic material on the inner surface of the SHS coating was removed during the cutting process and left a slightly buffed surface. Figure 4 shows a 1-inch wide sample from Spin test 6. Two distinct layers are visible, with the bottom layer welded to the steel test pipe and the top layer having a rough surface due to the removal of ceramic material during sample preparation.

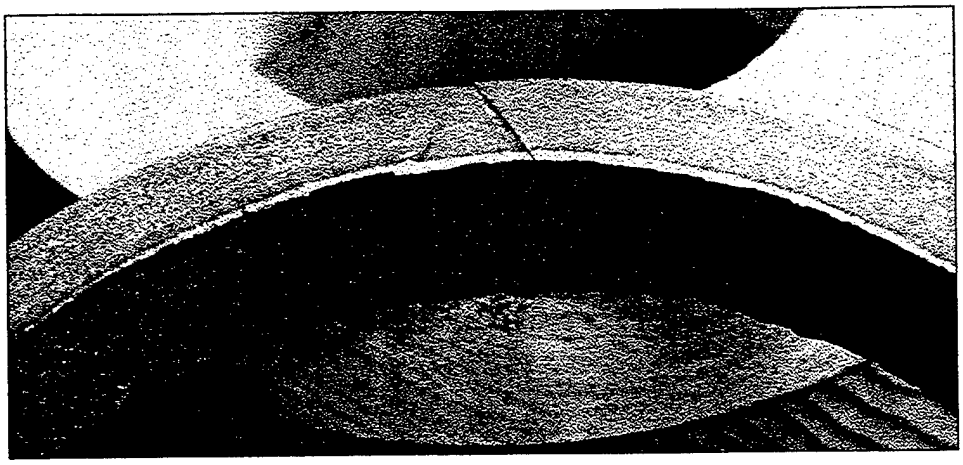

Figure 3. Test Liner 4 Ring Segment – SHS Inner Coating and Liner Tube Cross-section

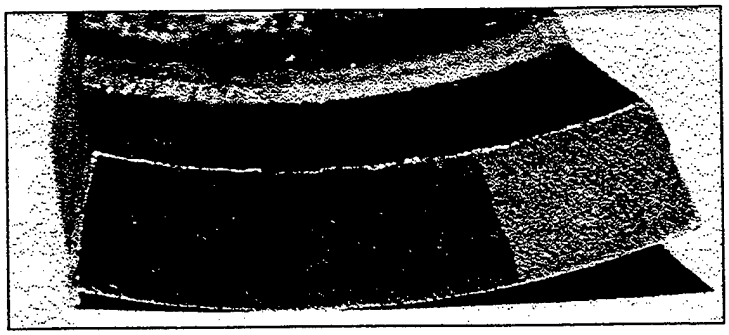

Figure 4. Test Liner 6 Close Up of SHS Coating Bonded to Liner (2.5 mm Coating Thickness)

Scanning electron microscopy (SEM) and energy dispersive analysis by X-ray (EDAX) were routine procedures used to document the details of the SHS coating/liner system. Figure 5 shows a typical SEM photograph from spin test 4 and illustrates a rather unique grain structure which developed as a result of the SHS/centrifugal processing. The figure shows a columnar grain structure at 75x magnification. Going from right to left in the figure is the steel pipe, a zone of "small" elongated grains, and a transition elongated columnar grains. These elongated columnar grains develop as the result of the steep, essentially unidirectional, radial thermal gradient from the steel pipe to the liquid inside diameter of the SHS material. Of all the grains of the SHS alloy which nucleate at the steel/liquid interface, only those nuclei with the fastest crystallographic growth direction aligned parallel to the thermal gradient will be able to maintain their growth beyond the immediate interface zone. Thus, even though the resulting microstructure is polycrystalline, one would anticipate a high degree of crystallographic alignment.

Indeed, a careful look at Figure 5 reveals a substructure within each grain, and these sub-grain boundaries shift by only a few degrees from grain to grain. This is evidence of the anticipated crystallographic alignment. Such highly oriented, elongated columnar microstructures are used in high-temperature alloy gas turbine blades to minimize creep and fatigue problems. Since the columnar grains are oriented with their long axis in the radial direction (the principal stress axis during firing) it is possible that SHS coatings with such a microstructure may be beneficial in gun tubes as well. The figure also shows the excellent interfacial bond between the coating and the base steel. Another important observation from Figure 5 is that there is very little solidification porosity (less than 2%) and the porosity that is present is typically less than 5 microns.

Micro-hardness tests were performed to evaluate the SHS coating and verify the functionally-graded properties aspect of the SHS processing technique. The hardness scale used was the Knoop 500 (HK_{500}). Figure 6 shows the variation in hardness through the coating and into the parent liner metal. With the exception of test liner 4, all coatings showed an increased hardness compared to the parent metal. Test liner 6 had the highest Knoop hardness at 828 (64 HRC). Using both SEM and elemental comparative EDAX techniques, the presence of a titanium-carbo-nitride compound within a nickel-based metal was verified and is thought to be the basis for the favorably high hardness levels for test liner 6. Recall, typical gun steel has a hardness of approximately 380 Knoop (38 HRC). There was some annealing of the liner parent material with about a 15% hardness drop (200 Knoop) in the interface relative to the unaffected region of the outside diameter (230 Knoop UNS G10260 cold drawn seamless tubing). The hardness summary results, showing steady improvement over the course of Phase I, illustrate the progress made in understanding how to control the process and to affect properties improvements. Combining SHS powder constituents with various woven carbon mesh fiber mats proved useful in creating various carbides (in-situ), most notably the titanium-carbo-nitride as well as titanium carbide throughout the functionally-graded layers. This is one of the more exciting developments in the proof-of-concept Phase I study as it offers a wide range of synthesis possibilities for creating unique materials to coat the interior of the liner. The hardness levels demonstrated for test liners 5 and 6 may lead to significant improvement over typical levels found in advanced liner designs using stellite, CrMoV and Ta-10W compositions.

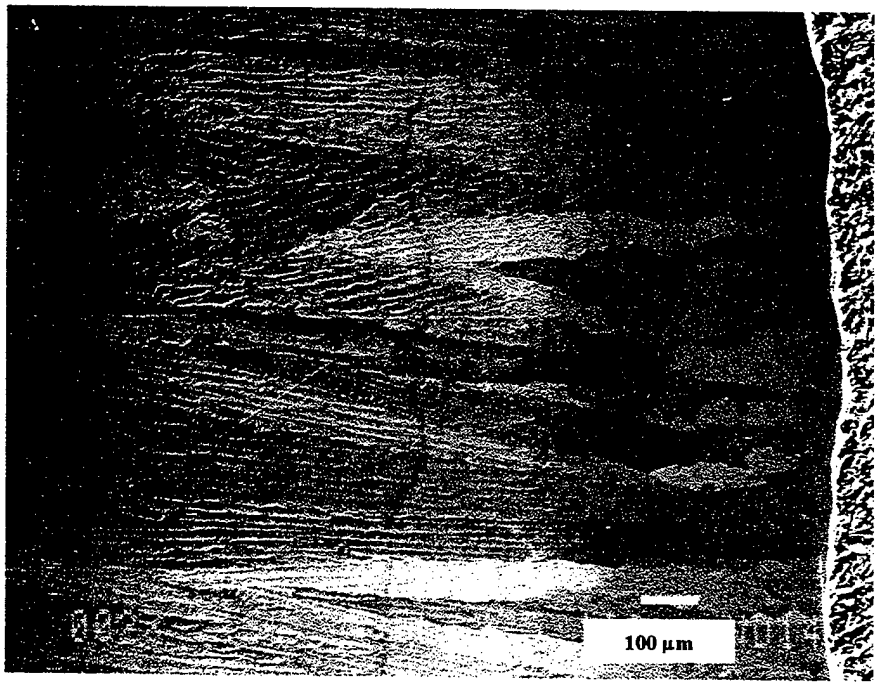

Figure 5. Columnar Grain Structure in SHS Coating of Test Liner 4

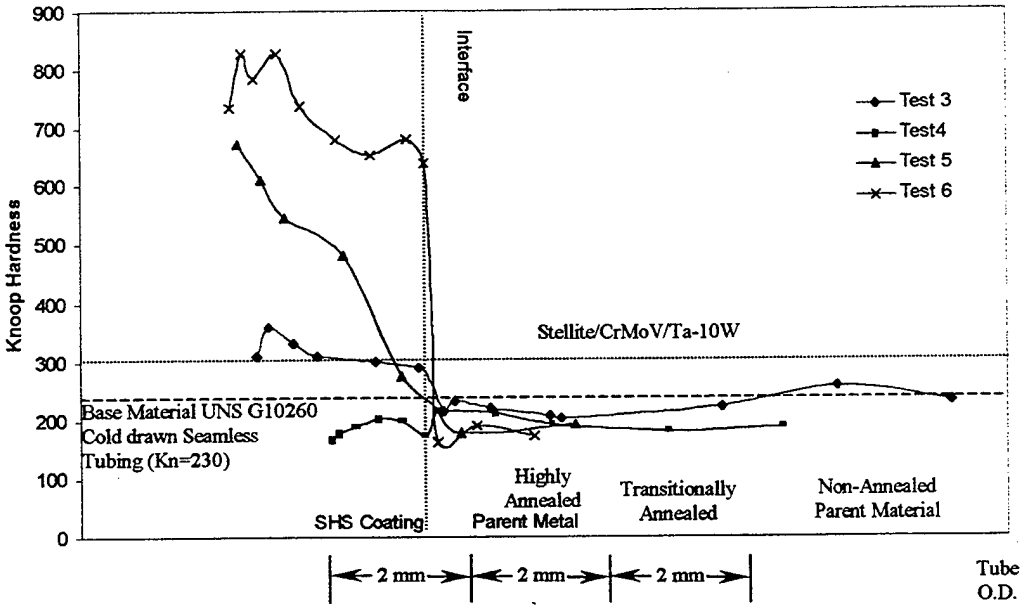

Figure 6. Functionally-Graded Material Property Demonstration – Hardness Summary

CONCLUSIONS AND RECOMMENDATIONS

The major research tasks and objectives of Phase I were successfully completed. The significant Phase I accomplishments generally group into three key areas: 1) unique SHS processing hardware/techniques, 2) demonstration of application of SHS synthesized materials as internal layers to the inner diameter of a 150mm liner tube and 3) documentation of unique SHS liner material characteristics and structure beneficial to future liner development. The details of these accomplishments are summarized as follows:

- SHS has been shown to be a viable processing candidate for creating functionally-graded gun tube liners
- Selection of SHS precursor constituents was shown to be appropriate for synthesis of a final product that demonstrated mechanical properties consistent with internal gun tube functional requirements
- For 150 mm class of tubes, the SHS process proved successful in synthesizing a functionally-graded, 1 to 2 mm layer of hard, potentially erosion-resistant material on the inside diameter of the tube
- The SHS process under a rotational, high radial g-loading environment proved controllable and selective to affect various final internal liner coatings
- The internal coatings created by SHS centrifugal processing proved that functionally-graded layers of up to 2mm thickness could be deposited with hardness levels at the inner bore of up to 2 ½ to 3 times the hardness of typical liner materials such as stellite, CrMoV or Ta-10W.
- The degree of interfacial bonding between the created SHS inner layer and the parent tube material was shown to be excellent and revealed a unique columnar (in the radial direction) microscopic grain structure that may be structurally beneficial.
- Combining SHS powder constituents with various woven carbon mesh fiber mats proved useful in creating various carbides (in-situ). Most notable was the identification of a titanium-carbo-nitride as well as titanium carbide in various analyses of the functionally-graded layer. This is one of the more exciting

developments in the proof of concept Phase I study as it offers a wide range of synthesis possibilities for creating unique materials to coat the interior of the liner.

- The demonstrated Phase I process was for tube segments of 18 inches in length (6 inch SHS coated region) and results indicate that scaling the process to lengths appropriate for full-scale development is achievable for the next Phase of investigation

This Phase I effort demonstrated a highly versatile SHS processing unit capable of lining a 150 mm class gun barrel liner segment with synthesized SHS materials. This technique may lead the way for future SHS materials development suitable for protection and performance enhancements of advanced guns using higher energy propellants. The process concept, procedure and processing unit were instrumental in demonstrating the proof-of-concept whereby SHS processing techniques could lead to advanced, functionally-graded gun tube liners.

ACKNOWLEDGEMENT

This work was supported by the US Army Research Laboratory with the Phase I Small Business Innovation Research (SBIR) DOD Contract No. DAAL01-98-C-0023. The technical assistance and support of Mr. Robert Dowding of the US Army Research Laboratory, Aberdeen Proving Ground, Maryland, is greatly appreciated.

REFERENCES

1. Killebrew, Col. R.B., " The Army After Next—TRADOC's Crystal Ball Eyes the Service's Shape Beyond Force XXI", Armed Forces Journal International, October, 1996, pp.36-45.
2. Ahmad, I., "The Problem of Gun Barrel Erosion: An Overview", Gun Propulsion Technology, Vol. 109 of Progress in Astronautics and Aeronautics, AIAA, 1988, pp.316-317.
3. National Materials Advisory Board, " Application of Non-conventional Materials to Guns and Gun Tubes", NMAB-423, National Academy Press, 1986.
4. Mawella, K.J.A., " Research on Coatings for the Protection of Gun Barrels From Wear and Erosion", Proceedings of the Sagamore Workshop in Gun Barrel Wear and Erosion, Wilmington, DE, July, 1996, pp 667-684.
5. Advanced Materials Gun System Program, Phase II Final Report, Contract DAA A21-88-C-0037, August 1992.
6. Katz, R. N. and Bowman, K. J., " Introduction and Overview, Chapter 1", Handbook on Discontinuously Reinforced Ceramic Matrix Composites, Purdue University Press and the American Ceramic Society, 1996, pp. 1-29.
7. Katz, R. N., "Applications of Silicon Nitride Based Ceramics", Ceramics: Charting the Future, ed. P. Vincenzini, Techna, 1995, pp 2299 -2310.
8. Cho, K., Katz, R. N. and Bar-On, I., " Strength and Fracture Toughness of Hot Pressed SiC Materials", Proceedings of Ceramics Science and Engineering, vol. 16, No. 4, 1995, pp. 105-112.
9. Katz, R. N., " Ceramic Gun Barrel Liners: Retrospect and Prospect", Proceedings of the Sagamore Workshop on Gun Barrel Wear and Erosion, Wilmington, DE, July, 1996, pp.67-84.
10. Panel Report / Short Term Needs and Issues for Enhanced Materials Performance, " Hot Gas Erosion and Wear of Materials", University of Michigan Workshop, September, 1996, pp.2-5.
11. Hanus, G. J., DeCoursin, D. G., Uznanski, K. T. and Shtessel, E., " New Materials and Manufacturing Options for Low-Cost Candle Filter Production", Proceedings of the 22nd International Technical Conference on Coal Utilization and Fuel Systems, March, 1997, pp. 691-700.
12. Merzhanov, A. G. and Borovinskaya, I. P., "Self-Propagating High-Temperature Synthesis of Inorganic Compounds", Dokl. Akad. Nauk. SSSR (Chem), Vol. 204, pp. 429-432, 1972.
13. Crider, J. F., "Self-Propagating High Temperature Synthesis - A Soviet Method for Producing Ceramic Materials", Ceram. Eng. Sci. Proc., Vol. 3, pp 519-528, 1982.
14. Shtessel, E. A., Kuravlev, M. V., Merzhanov, A. G., "The Peculiarities of Self-Propagating Processes at the Interaction of Aluminum With Iodine", Dokl. Akad. Nauk. SSSR, Vol. 238, No. 5, pp 1168-1177, 1986.
15. Shvestov, Y. A., Kovalev, D. Y., Kostogorov, P. and Shtessel, E. A., "Gas Transport SHS Reaction Efficient Method of Obtaining Metals of Carbides", 1st Intl. Symp. Self-Propagating High-Temp. Synthesis, Alma-Ata, 1991.

ANALYSIS OF ENGRAVING AND WEAR IN A PROJECTILE ROTATING BAND

Peter C.T. Chen
U.S. Army ARDEC, Close Combat Armament Center
Benet Laboratories, Watervliet, NY 12189-4050

A large deformation analysis of the engraving process and wear in a projectile rotating band is considered by using the finite element program – ABAQUS. The tube and the projectile are assumed to be rigid and the bore of the tube is assumed to be smooth and axisymmetric. An elastic-plastic material model is chosen for the copper band which remains attached to the projectile and an appropriate coefficient of sliding friction is chosen. The magnitude and distribution of the contact pressure between the band and the tube are obtained during engraving . The band pressure is large and severe plastic deformation occurs in the band.

INTRODUCTION

It has been postulated that due to today's higher energy propellants and heavier projectiles the rotating band deforms so severely that it loses the ability to properly support the projectile resulting in unanticipated wear at the muzzle end. Earlier research has indicated it is probable that all cases of rotating band failure can be attributed to excessive wear in the initial portion of the projectile's travel even when the failure does not occur until well down the tube [1,2]. When the projectile enters the barrel of the gun, the rotating band passes through a forcing cone which places it under compressive interference stresses and large plastic deformation occurs along the driving edges of the forcing cone. The radial pressure between the projectile band and bore produces friction and an abrasive action on the bore surface. Approximate theoretical estimates of radial band pressure have been obtained by using the rigid-plastic flow theory and assuming uniform distribution [3,4]. A satisfactory stress analysis of the engraving process and wear has never been reported.

In this paper, a large deformation analysis of the engraving process in a projectile rotating band is considered by using the finite element program – ABAQUS [5]. The calculations are obtained by assuming the bore of the tube as smooth and axially symmetric. Furthermore the tube and the projectile are assumed to be rigid and the copper band is considered as elastic-plastic. The copper band, which remains attached to the projectile, will slide against the bore when the projectile enters the barrel of the gun. Appropriate coefficient of sliding friction is also chosen. The magnitude and distribution of the contact pressure between the band and the tube are obtained during different stages of engraving . The deformations, strains and stresses are also obtained. The magnitude of the band pressure is large and severe plastic deformation occurs in the band. Wear in the band will be discussed.

MODELING

Geometry : The rotating band chosen in this study is of axial length Lo =37.084 mm and radial thickness Bo =2.3114 mm. A simple mesh of the band is constructed of 281 nodes and 250 4-node bilinear elements. The radius of the projectile is Rp =76.581 mm and the band is attached to the projectile. The radius of the bore behind the forcing cone is Ro =79.38 mm and the length of the forcing cone is Lc = 40.54 mm. The radii of the bore after the forcing cone through the groove and land are Rg =78.74 mm and Rl =77.485 mm, respectively. Therefore the reduction in thickness through the groove and land are 6.6% and 60.9%, respectively.

Material : The tube and projectile are assumed to be rigid and the copper band is considered as elastic-plastic. The values of Young's modulus and Poisson's ratio for the copper are 110 GPa and 0.33, respectively [6]. The initial yield stresses in compression and shear are 314 Mpa and 181 Mpa, respectively. The dependence of the yield stress upon the plastic strain in the plastic range are piece-wisely defined by the data points (314MPa, 0.0), (620MPa, 0.126) and (620MPa, 10.0).

Boundary Conditions : There is no separation between the band and the projectile because the band was welded to the projectile. In addition to sliding contact between the band and the tube in the forcing cone, the band may be deformed to slide axially in either direction against the projectile faces. Therefore there are four contact pairs and the coefficients of sliding friction are assumed to be 0.01 for the band/tube pair and 0.10 for the band/projectile pairs.

Force/Displacement : Initially the back face of the band is only 40.0mm behind the entrance of the forcing cone whose length is 40.54mm. Therefore when the projectile travels 80.54mm, the band will have passed the forcing cone and the engraving process is considered as completed. The prescribed displacement used in this nonlinear analysis is 100mm.

ENGRAVING THROUGH GROOVE

The initial thickness of the band is Bo=2.3114mm and the final thickness of band after passing through the groove will be Bg=Rg-Rp=78.74mm-76.581mm=2.159mm. Therefore the reduction in thickness through the groove is (1- Bg/Bo)x100%= 6.6%. It takes 49 increments to complete the analysis. Figure 1 shows the initial and final position of the band after traveling 100mm through the groove. Figure 2 shows the enlarged original and deformed mesh after traveling 100mm. Larger plastic deformation occurs at the front and back ends near the band/projectile interface. The contour plots of the Mises stress and equivalent plastic strain in the final stage are shown in Figures 3 and 4, respectively. The size of the plastic zone can be seen in Figure 3 and the maximum equivalent plastic strain is 2.233 at the back end close to the band/projectile interface. The distributions of the contact pressure between the tube and the band at different stages of traveling through the groove are shown in Figures 5 to 8. The maximum value of contact pressure is 3548 MPa as shown in Figure 5. If the coefficient of sliding friction is less than 5 %, then this value of contact pressure would generate a maximum shear stress of 177 MPa which is smaller than the shear yield stress of 181 MPa of the copper band. Therefore it seems engraving through the groove can be completed without causing damage to the band or tube.

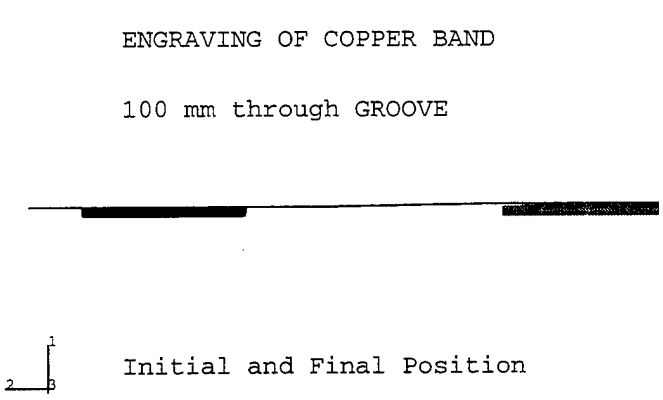

Figure 1 Initial and final position of band after traveling 100 mm through groove

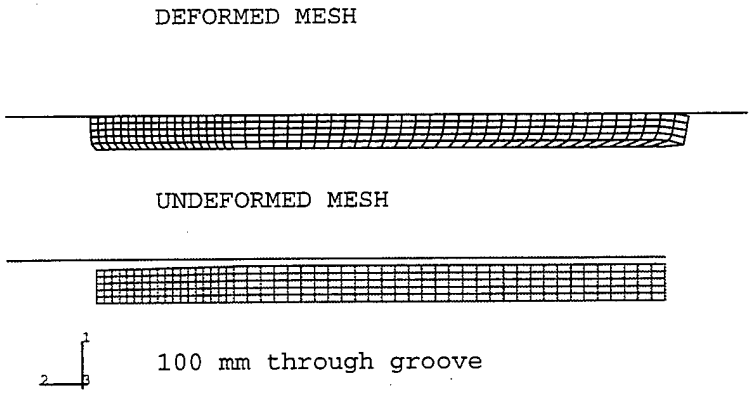

Figure 2 Original and deformed mesh after traveling 100 mm through groove

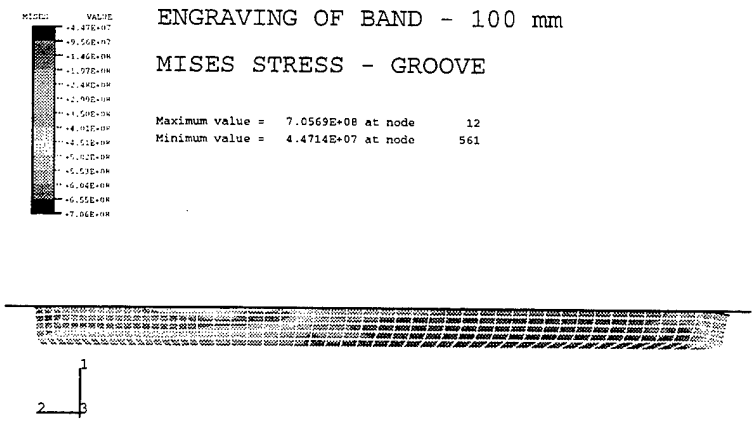

Figure 3 Contour of Mises stress in band after traveling 100 mm through groove

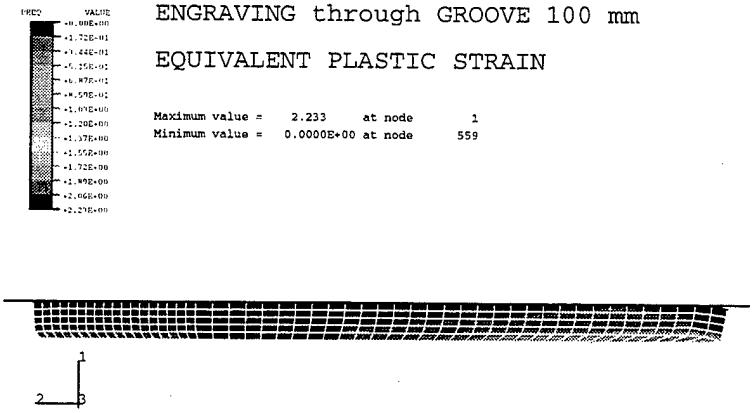

Figure 4 Contour of equivalent plastic strain after traveling 100 mm through groove

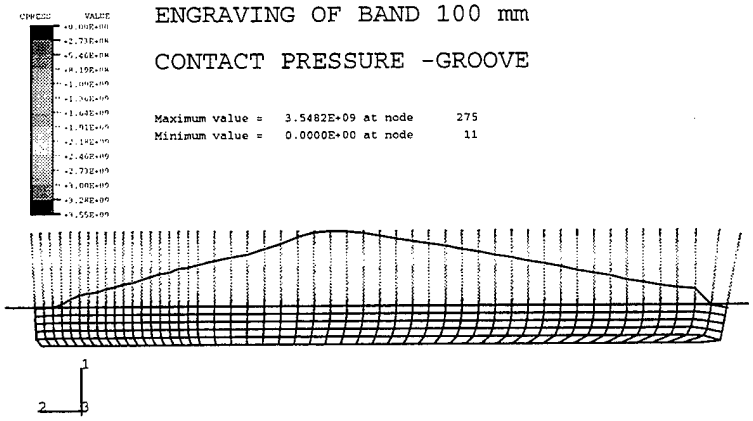

Figure 5 Contact pressure between band and tube after traveling 100 mm through groove

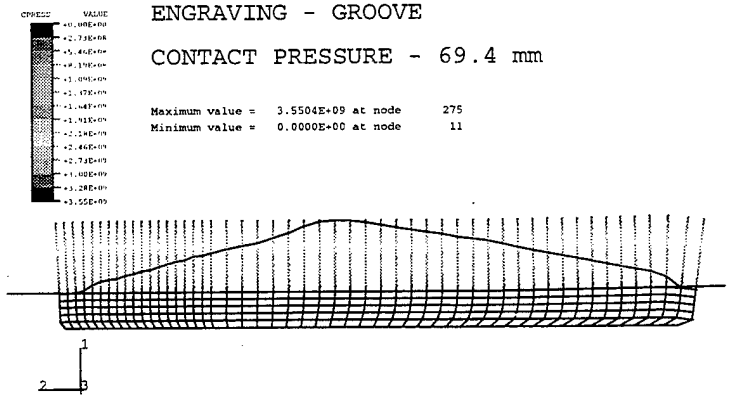

Figure 6 Contact pressure between band and tube after traveling 69.4 mm through groove

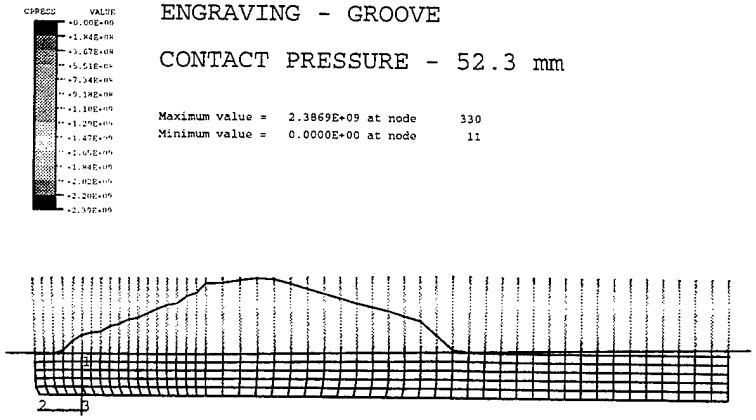

Figure 7 Contact pressure between band and tube after traveling 52.3 mm through groove

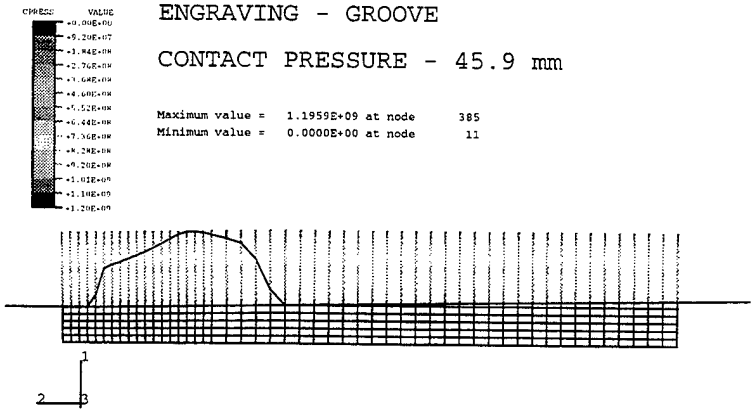

Figure 8 Contact pressure between band and tube after traveling 45.9 mm through groove

ENGRAVING THROUGH LAND

The initial thickness of the band is Bo =2.3114 mm and the final thickness of band after passing through the land will be Bl =Rl – Rp =(77.485 - 76.581) mm= 0.904 mm. Therefore the reduction in thickness through the land is (1- Bl/Bo)x100% = 60.9%. It takes 227 increments to travel 49.7mm and the analysis ends because the time increment required is less than the minimum (0.001mm) specified. Figure 9 shows the initial and final position of the band after traveling 48.4mm through the land. Figures 10a-c show the enlarged deformed meshes at the front, middle and back of the band. Plastic deformations are very large and severe distortions have occurred especially at the front and back ends near the band/projectile interface. The distortions are so severe that computation stops. The contour plots of the Mises stress and equivalent plastic strain in the final stage are shown in Figures 11 and 12, respectively. The size of the plastic zone can be seen in Figure 11 and the maximum equivalent plastic strain is 57.58 at the front end. This value of plastic strain is so large that some failure criterion has to be introduced. The distributions of the contact pressure between the tube and the band at different stages of traveling through groove are shown in Figures 13 to 16. The maximum value of contact pressure is 6991 MPa as shown in Figure 13. If the coefficient of sliding friction is large than 2.59 %, then this value of contact pressure would generate a shear stress larger than the shear yield stress of 181 MPa of the copper band. Therefore it seems engraving through the land cannot be completed without causing damage to the band. The contact pressure between the band and tube is so large that it together with friction would be likely to cause an abrasive action on the bore surface.

DISCUSSION

This paper based on a simple band is the first report on the subject. We have tried different types of elements and different boundary conditions. The constraints on the band by the projectile play an important role in the computation. If the band were allowed to slide between the tube and projectile, then the computation through the land could be completed without difficulty as an extrusion process. The requirement of no separation at the band/projectile interface causes the computation to stop earlier because more severe distortions have occurred at the front and back ends.

We have also completed the computation for a two dimensional model of the refined band including the cannalure. These results will be reported later. In addition we have generated a two-dimensional rigid surface model of the tube and a three-dimensional solid model of the rotating band, but the 3-D simulations are computationally expensive and the results are not accurate.

REFERENCES

1. Summerfield, Martin et al (editors), 1988, "Gun Propulsion Technology," AIAA, Inc, Washington, DC
2. Montgomery, R.S., 1985, "Wear of Projectile Rotating Bands," ARLCB-TR-85008, US Army Benet Lab, Watervliet, NY.
3. DARCOM, "Design for Projection," Engineering Design Handbook, AMC Pamphlet No. 706-247, July 1964.
4. Tirosh, J..and Dayan, A., "On the Impact Engraving of Metal Bands," Proceedings of the 15th NAMRC, Vol 2, pp.358-363, May 1987.
5. Hibbitt,Karlsson & Sorensen,Inc, "ABAQUS/Standard User's Manual," version 5.7, 1998.
6. Boyer, H.E.(editor), "Atlas of Stress-Strain Curves," 1987 ASM International, Metals Park, Ohio.

ACKNOWLEDGMENTS

The author appreciates the valuable assistance provided by my collegues, Dr. J.M. Coyle, J. Higgins and M. Leach.

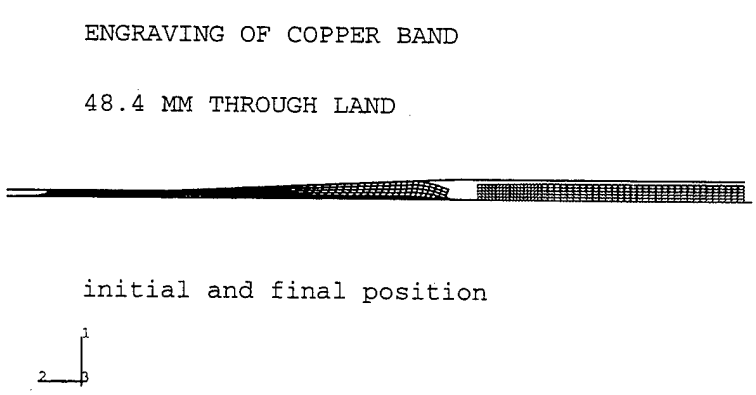

Figure 9 Initial and final position of band after traveling 48.4 mm through land

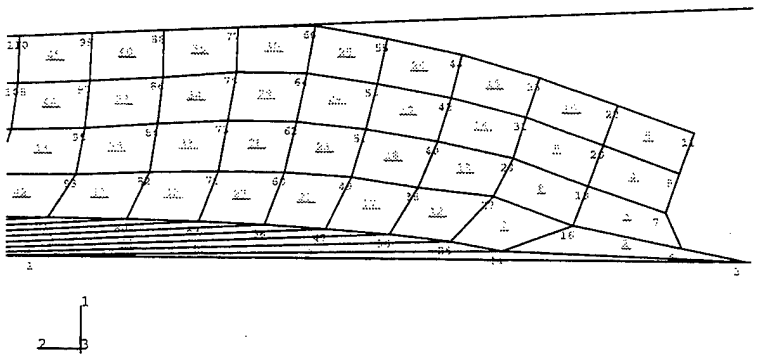

Figure 10a Deformed mesh at the back end of band after traveling 48.4 mm through land

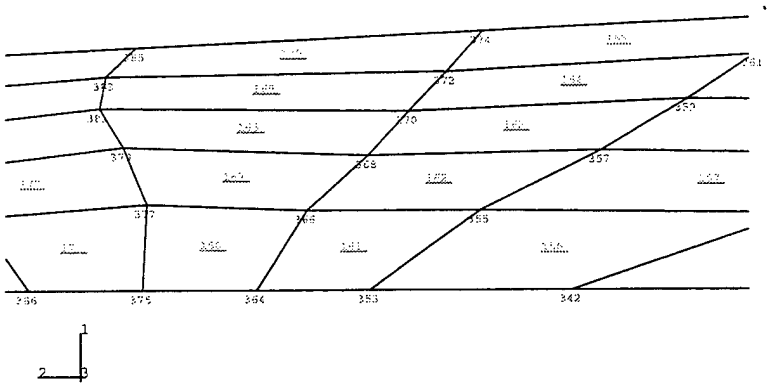

Figure 10b Deformed mesh near the middle of band after traveling 48.4 mm through land

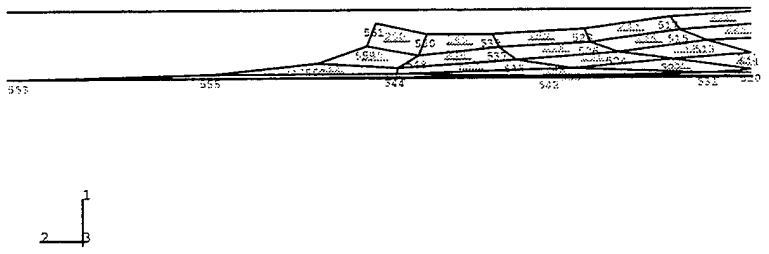

Figure 10c Deformed mesh at the front end of band after traveling 48.4 mm through land

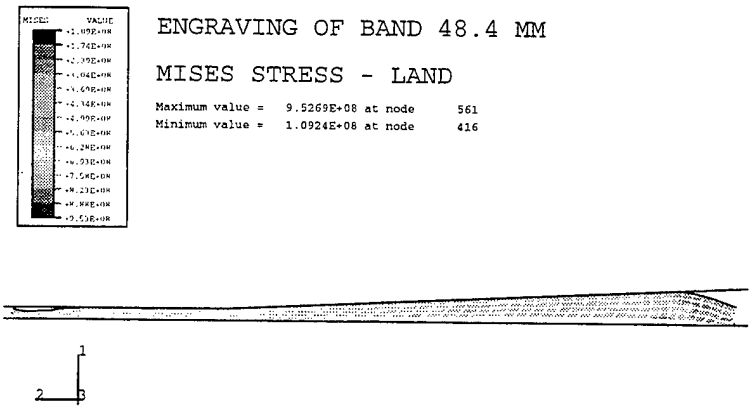

Figure 11 Mises stress contour after traveling 48.4mm through the land

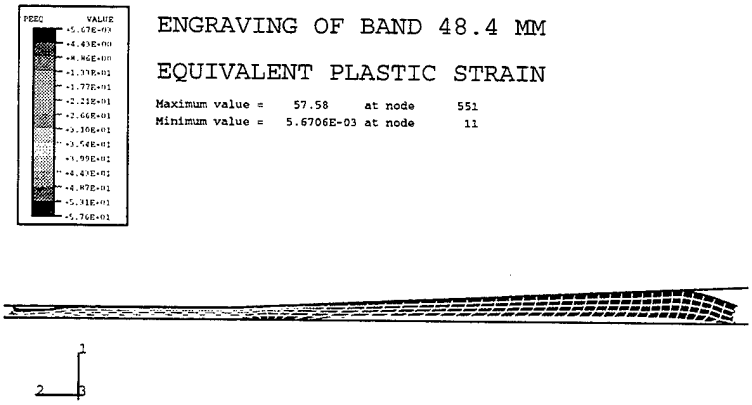

Figure 12 Equivalent plastic strain contour after traveling 48.4mm through the land

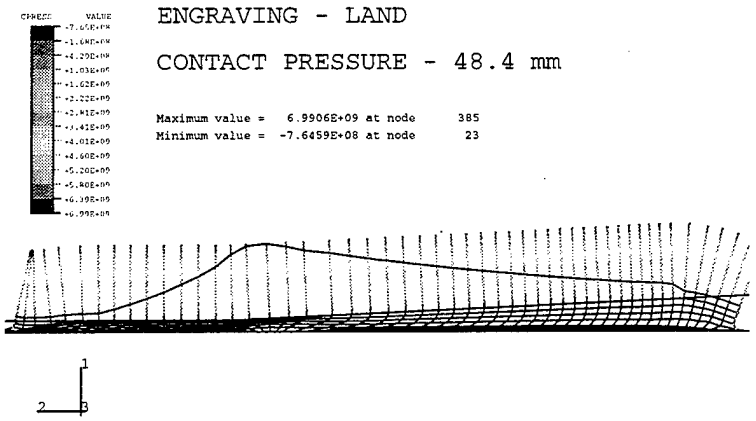

Figure 13 Contact pressure between band and tube after traveling 48.4mm through the land

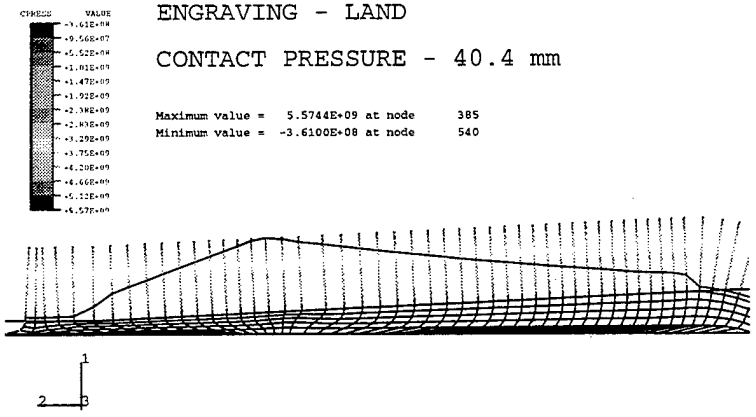

Figure 14 Contact pressure between band and tube after traveling 40.4mm through the land

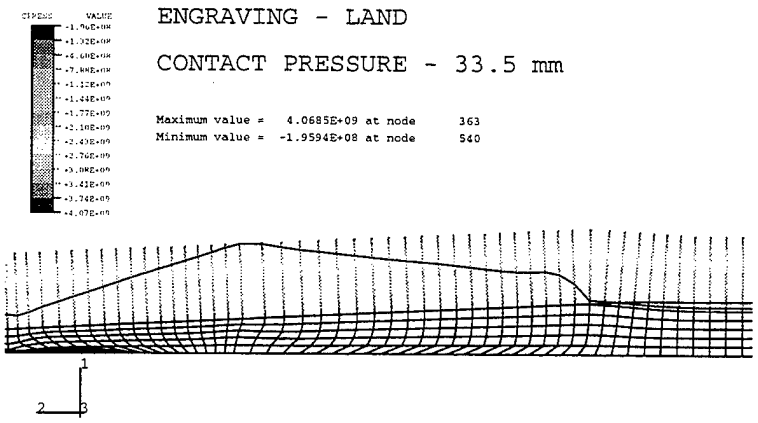

Figure 15 Contact pressure between band and tube after traveling 33.5mm through the land

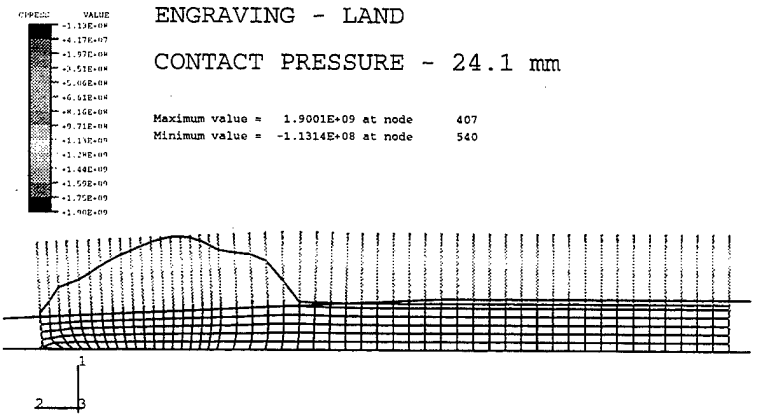

Figure 16 Contact pressure between band and tube after traveling 24.1mm through the land

Improved 155MM Rotating Band for Extended Range

Kok Chung, Robert Lee, Andrew Readdy

US Army ARDEC

ABSTRACT

The higher level of muzzle energy and longer tube travel has resulted in large down bore cannon wear with 52+ caliber 155mm weapons. The down bore wear is primarily due to projectile body engraving which occurred after the copper rotating band has worn out. Inadequate obturation, lubrication, bore surface contamination, poor barrel plating and other factors all contributed to accelerate rotating band wear. The large down bore cannon wear will adversely impact accuracy; munitions performance and cannon wear life.

The ARDEC Cannon Projectile Compatibility Program addresses the problem by updating rotating band and obturator designs for the extended range environment. This tech base program investigates the use of alternate rotating band materials with high melting temperatures and improved wear characteristics. One dimensional finite element wear models and body engraving models have been developed to aid in the design of new bands. Welding techniques and parameters for soft iron, nickel, MONEL and stainless steel were developed to assure band integrity at all launch conditions. Preliminary test results for a new rotating band design with alternate band materials have been extremely encouraging.

INTRODUCTION

The primary function of the rotating band and obturator is to impart spin to the projectile and maintain a positive gas seal, the failure of which will adversely impact projectile and weapon performance. During the development of 155mm extended range weapon systems in the early 80's excessive wear of the rotating band, projectile body engraving and origin/muzzle wear are often the cause for cannon condemnation. The ARDEC Tech Base "Cannon Projectile Compatibility (CPC) Program" objective is to develop a rotating band/obturator combination that will perform satisfactorily in extended range weapon systems.

BACKGROUND

To achieve higher muzzle velocities and longer ranges, weapon designers rely on larger quantities of high energetic propellant and longer cannons with larger chambers. During the ERO (extended range ordnance) developmental program in the 1980's the increased range came at the expense of rapid origin wear of steel cannons and worn projectile rotating bands with severe body engraving on projectiles. The steel 52 caliber cannons were often condemned in less than a 100 round high zone firings. From the test results, the need for improved bore protection and an improvement in rotating band performance is evident.

The larger volume of propellant used for extended range and the increased combustion activities is responsible for the accelerated origin wear of steel cannons. High refractory metal coatings such as chrome plating has slowed the erosion at the origin but has not prevented down bore wear. Down bore wear is due primarily to projectile body engraving after the rotating band has worn out. Many factors contributed to the rapid band wear. A combination of higher muzzle velocity (increased spin and frictional heating), poor obturation and bore surface effects caused rapid heating and melting of the copper band. The severely worn

band and gas blowby will result in projectile body engraving, which will accelerate chrome chipping and stripping and finally unacceptable muzzle wear. The enlarged bore diameter will result in poor precision and higher balloting forces on the ammunition. The reliability of the fuze could also be affected because of the higher pitch and yaw motions at muzzle exit.

The ARDEC tech base Cannon Projectile Compatibility Program Goal is to develop the next generation rotating band and obturator for future projectiles.

PROGRAM OBJECTIVE

The objective of the CPC Program is to provide an improved rotating band and obturator combination for future projectiles that will be compatible with the next generation extended range weapons. The band and obturator will function at a velocity of greater than 1000 meter per second and at a pressure of 60,000 PSI. The band will have no low zone sticker or projectile fallback problems. The requirement for the rotating band to perform at very high muzzle velocity and not have a sticker problem is contradictory. For high zone firings a strong band is desired, but a small band is desired for the low zone to minimize sticker problems. For the CPC program, selecting a suitable band material will insure adequate high zone performance and designing the proper band configuration will eliminate any sticker problem.

CURRENT ROTATING BAND DESIGN

There are three common band configurations used in the current projectile inventory, the M107, M864/M549A1 and the M483A1 types (Fig. 1). The band material is either copper or a copper/zinc alloy. The swaged M107 band is compatible up to the M119A2 charge velocity (684 MPS) while the welded overlay bands such as the M864/M549A1 types are compatible up to the M203/M203A1 charge level (826 MPS). At the 950 MPS velocity range, all band designs performed poorly with 52+ caliber cannons.

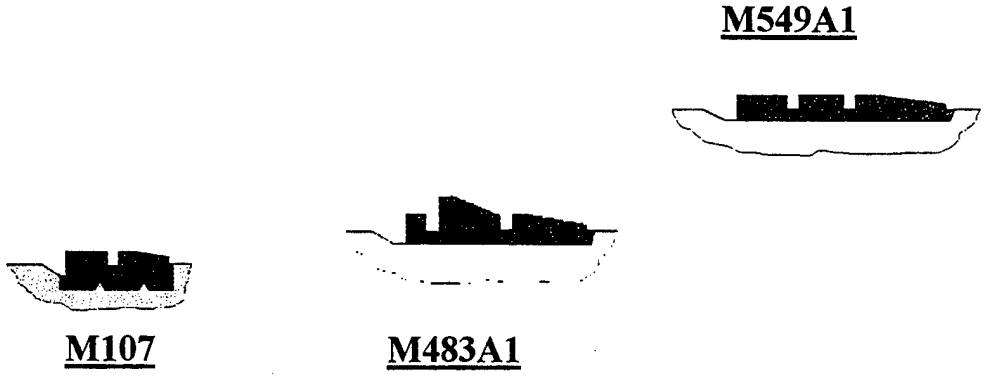

Figure 1
Existing Rotating Band Design Shapes

ROTATING BAND DESIGN CRITERIA

The main requirements of rotating bands include that they be compatible with higher velocity limits, have improved performance with 4th Qtr (worn) cannons, utilize existing manufacturing techniques, minimize torsional impulse, provide no increase in projectile drag, produce no projectile fallbacks, and no stickers. In general, the rotating band must not wear out completely otherwise it will result in projectile body engraving and down bore wear. Historically, in 39 caliber systems existing copper bands did a very good job of satisfying all of these requirements depending on the rotating band shape or configuration used. In recent years however, results of 155mm 54 caliber test firings have shown that many of the existing copper rotating bands wear excessively and can not survive the longer tube travel. Because rotating band

wear is one measure of a rotating band's performance, members of the Cannon Projectile Compatibility Program developed a criteria for inspecting and evaluating fired and recovered rotating band hardware. This inspection criterion is related to the observations made upon examining hundreds of recovered projectiles during the course of the Cannon Projectile Compatibility Program. Some of the characteristics that are on recovered rotating bands are shown on Figure 2.

RECOVERED ROTATING BAND OBSERVATIONS

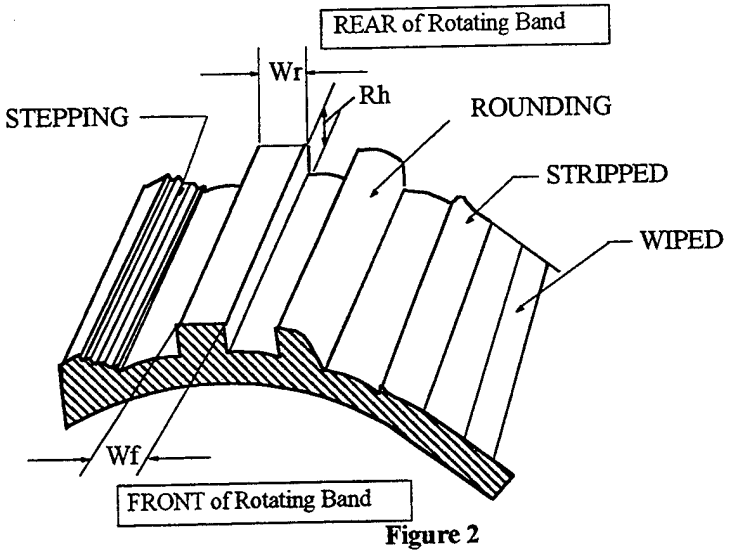

Figure 2

Recovered Rotating Band Characteristics

These characteristics were used to describe and evaluate various rotating band and obturator performance tests conducted under the Cannon Projectile Compatibility Program as well as on other programs such as the Crusader Program where tube wear and rotating band performance is a concern. For an ideal rotating band Wf and Wr would be equal to .25 and Rh would be equal to .05. There should always be some detectable remaining driving edge width. When there is none the projectile may not be sufficiently spin-stabilized resulting in a loss of accuracy or component malfunctions.

ROTATING BAND MATERIAL SELECTION

In order to determine which viable alternate rotating band materials were good candidates in evaluating through testing, an extensive historical search and review of material data properties was conducted by ARL, ARDEC and ArrowTech Associates. Desirable material properties were defined and compared to the current 155MM rotating band material (Copper/Gliding Metal). All aspects of the materials were evaluated including their feasibility in welding, machining, tensile strength properties, melting point characteristics, their availability, and cost. Most importantly the material properties were reviewed in order to determine their ability to readily form to the contour of the gun tube while maintaining its engraved shape and integrity during launch. Basically the rotating band material must have sufficient ductility and sufficient tensile (shear) strength in order to engrave and survive 300 inches of tube travel. In materials' these properties are mutually exclusive, as the higher a material's tensile strength, the less its ductility. Thus, some materials, which had no favorable data, or any data at all to indicate that it could be used as a rotating band material were eliminated from being a candidate rotating band material. A list of the candidate materials that were selected for further evaluations and how their basic properties compare to the current copper/gliding metal material is shown on Table I.

Table I

Candidate Materials for Rotating Bands

	Cu-Zn Gliding Metal	Cu-655 UNS 65500 (High Si-Bronze)	Monel 400 (Ni-Cu)	Soft Iron	Nickel	Stainless Steel
Melting Point (C)	1021	971	1343	1536	1453	1454
Thermal Cond. (W/m/C)	189	36	22	78	89	16
0.5% Yield Strength (ksi)	10	21	30	30	20	58
Tensile Strength (ksi)	37	56	68	45	52	88
2" Elongation (%)	45	60	40	22	40	35

The five alternate materials that were chosen for further evaluations were Silicone-Bronze, Monel, Soft Iron, Nickel and Stainless Steel. Each of these materials had their advantages and disadvantages as a rotating band material either in cost, producibility, availability or operationability. Silicone-Bronze was selected because of the fact that it is a copper alloy with a high tensile strength and excellent work hardening properties. Since existing rotating bands are copper based, an attempt to adopt a higher strength copper alloy as a new rotating band material is prudent. Monel and Nickel were selected for their high melting point as well as their high tensile strengths. Soft Iron was selected from historical studies of medium caliber systems (20mm-40mm, and 80mm Anti-Aircraft Gun) and the fact that welded rotating bands in the past were made from ARMCO Iron. Stainless Steel was selected because like Iron and Nickel, it has exceptional wear characteristics, but unlike Iron it does not corrode during long term storage. Stainless Steel is also readily available, unlike ARMCO Iron that is no longer commercially available.

MODELING

As a member of the Cannon Projectile Compatibility Program, ArrowTech Associates was able to develop a rotating band wear program in which the wear function was determined by experimental data. This program, which is part of their PRODAS (Projectile Design and Analysis System) software, used an empirically determined wear constant for each band material. This constant which is an exponent was determined for iron and copper. Their values are 17 and 16.7 respectively. Because no experimental data had been obtained in the past for nickel and stainless steel, ArrowTech Associates interpolated a wear function by comparing the melt temperatures of iron, stainless steel and pure copper. Upon determining the constants for stainless steel and nickel, a predicted band wear for the M549A1 projectile fired in a 48 land & groove Crusader Tube with an 8.927 degree exit angle (20 cal/rev), using a MACS zone 6 Propelling Charge was plotted. The results are shown on Figure 3.

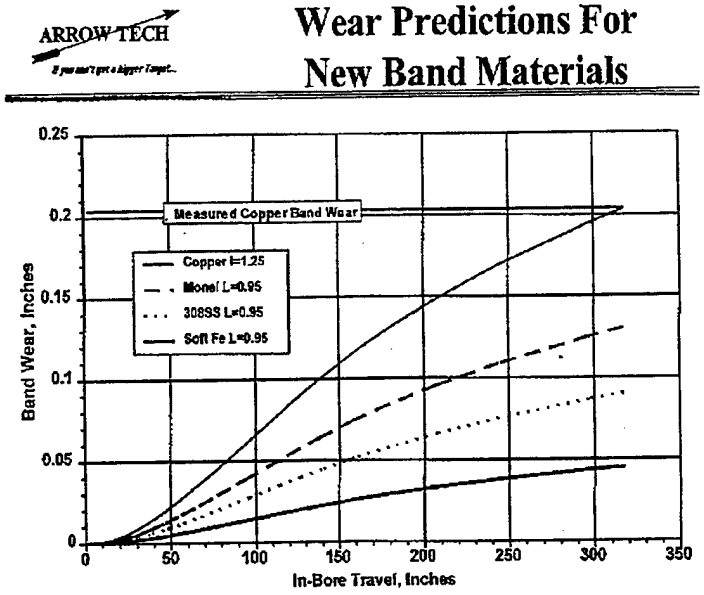

Figure 3

Wear Predictions For New Rotating Band Materials

The projected wear plot shown in Figure 3 was used as an initial indicator of how well the alternate rotating band materials would perform as the length of the gun tube exceeds 39 caliber. In addition to the Arrow Tech wear model, the Structural and Solid Mechanics Department at Sandia National Laboratories in Livermore, CA. (SNLL) had conducted a Rotating Band Study as part of the Cannon Projectile Compatibility Program. The objective of the Sandia study was to generate a simplified structural, heat transfer, and wear analysis model that could be used to estimate projectile rotating band capabilities for existing and new in-bore loading environments. As a result of the Sandia study, a one-dimensional model that estimates temperature distributions and wear in rotating bands taking in account parameters such as axial acceleration-time histories, projectile masses, and rifling twist rates was developed. This model was used to estimate the test results of down selected rotating band designs.

TEST FIRINGS

Upon completion of the first lot of Ballistic Test Projectiles, ARDEC conducted a structural integrity test to confirm the results of the ANSYS stress analysis. This test also provided some preliminary data on the effectiveness of the candidate rotating band materials. A completed CPC Ballistic Test Projectile welded with a nickel rotating band material is shown on Figure 4.

Figure 4

CPC (XM982) Ballistic
Test Projectile Simulator

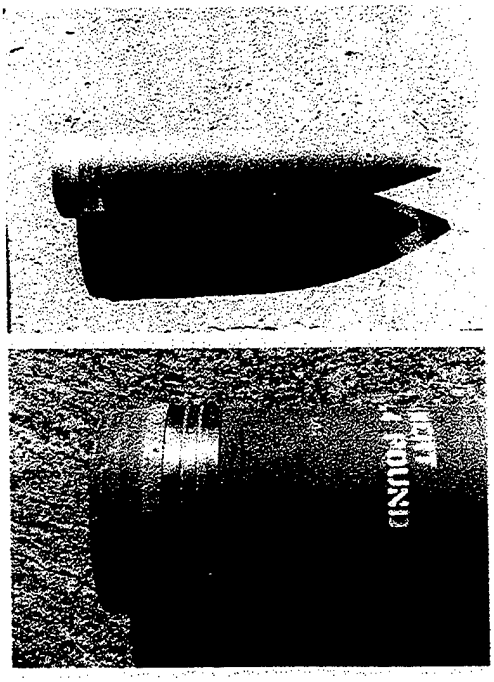

Nickel Rotating Band
M864 Obturator

The structural test was conducted on July 30 and 31st of 1997. The test consisted of sixteen rounds fired out of an M199 tube using M203A1 zone 8 propelling charges conditioned hot (+145 degrees F). Eight CPC Ballistic Test Projectiles were fired. Four of the eight CPC Ballistic Test Projectiles that were fired had copper rotating bands. The copper rotating bands were used as a direct comparison to the two silicon-bronze, one soft iron and nickel band. M864 projectiles and M483 projectiles were also fired as comparison rounds and warmer rounds. Hadlin camera data showed that the projectiles were structurally qualified to survive a pressure of at least 56 KPSI. Upon recovery of the fired rounds, rotating band inspections and measurements were performed and results were excellent.

Based on the ARDEC structural test results, a firing at Yuma Proving Ground was conducted in order to evaluate the rotating band materials in a 58 Caliber gun. This firing was completed in November of 1997. It consisted of using an XM282, 58 Caliber, HC Chrome cannon with a 1700 cubic inch chamber. The rifling twist was 1 in 22.5 and the propelling charge used was an XM230 zone 6 conditioned at ambient temperature. Along with three M864 projectiles used as comparison rounds, a total of fourteen CPC Ballistic Test Projectiles were also fired. The fourteen CPC Ballistic Test Projectiles consisted of rotating bands manufactured out of copper, Silicon-bronze, soft iron, nickel, Monel and Stainless Steel. All of the test projectiles were fitted with standard M864 obturators. The results of this test are summarized on Table II and some of the recovered hardware is shown on Figure 5.

Table II
Yuma Rotating Band Test Results

58 Caliber, Avg.. Pressure= 41,700 psi, Avg. MV=874.6 m/s

Projectile	# Fired	Rotating Band	RB Left (Thousands)	% Worn
BTP	1	[illegible]	Sawtooth	NA
BTP	2	Silicone Bronze	Disbonded	NA
M864	3	[illegible]	107	[illegible]
BTP	2	Monel	190	24
BTP	3	Nickel	204	18.4
BTP	3	Iron	217	13.2
BTP	3	Stainless Steel	215	14

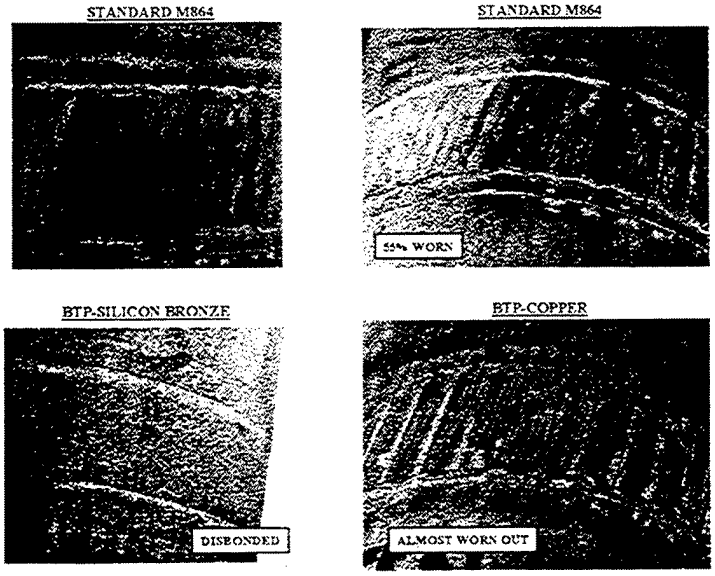

Figure 5
Recovered Ballistic Test Projectile Rotating Bands

Upon completing a Low-Zone Sticker test at ARDEC on the same rotating band designs used in the above Yuma Rotating Band Test, a redesigned the Nickel and Stainless Steel rotating band configuration was initiated. Based on the results of the ARDEC Low Zone Sticker Test, the effective rotating band lengths were reduced to satisfy Low Zone applications. The Cannon Projectile Compatibility Program then conducted a follow on high zone test at Yuma during August of 1998, using the redesigned Nickel and Stainless Steel rotating band designs. Six SS and Nickel bands were fired with the XM224 charge. An average velocity of 970 MPS and pressure of 54,000 PSI was obtained. The result as determined by the amount of band worn was similar to the Nov 97 test. The nickel band slightly

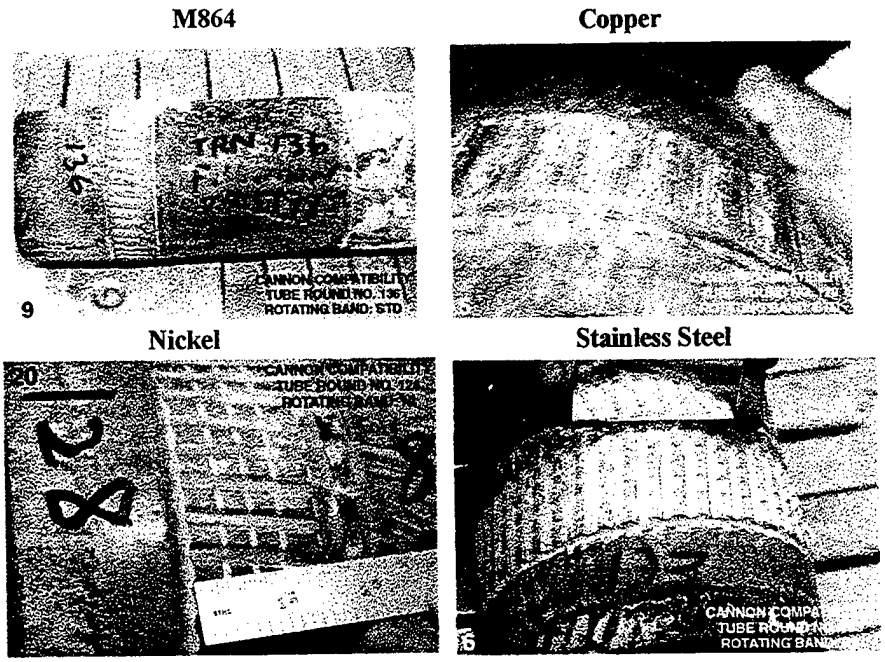

Figure 6
Recovered Nickel and Stainless Steel Rotating Bands

Out performed SS. The recovered projectile hardware shown in Figure 6 and the tabulated average wear measurements shown on Table III summarizes the results of this test.

Since the predicted wear measurements shown in Table III were generated based on pressure

Table III
Yuma Rotating Band Test Results with Re-Designed NI &SS

58 Caliber, Avg.. Pressure= 54,000 psi, Avg. MV=967.2 m/s

Projectile	# Fired	Rotating Band	RB Left (Thousands)	% Worn	
BTP	7	Nickel	206	18	24▲
BTP	6	Stainless Steel	195	22	23▲
M864	3		87		40▲

▲ Predicted wear based on SNLL 1-D Model.

profiles not used in the actual gun firing, the correlation of predicted versus actual rotating band wear is noted to be slightly skewed. Additional factors affecting the percentage differences in the predicted data versus the actual data is due to the fact that wear is three dimensional and contingent upon surface conditions of the gun tube. Never the less, the generated data can still be correlated to expected wear values. In any case, the reduced effective length of the rotating bands using Nickel and Stainless Steel did not affect the performance of the projectile at high zone firings. Based on these results another Low Zone Sticker test was conducted to verify that the new design would be adequate in satisfying the Low Zone application. This Low Zone Sticker Test was conducted on October 21, 1998 at ARDEC. The results for the Low Zone Sticker were successful having none of the Nickel or Stainless Steel rotating bands causing the projectile to get stuck in the tube.

CONCLUSION

In the Cannon projectile Compatibility Program, alternate rotating band materials were demonstrated to be superior to copper alloy bands for high velocity application. The higher melt temperature and tensile strength properties of Nickel and stainless steel are capable of outstanding performance in extended range weapon systems. The test results validated the design objectives established for the CPC program. Models developed under this program will be useful tools for evaluating band material and cannon parameters on band wear. The combination of a projectile rotating band with alternate band material and an improved obturator will meet the requirements of next generation artillery systems.

REFERENCES

Siewert, Jeff., January 1998, "Rotating Band Wear, Body Engraving, Sticker and Aerodynamic Performance Assessment of 155MM Projectiles", Arrow Tech Associates, So. Burlington, Vermont.

Projectile Rotating Band Wear Model

Arlene M. Schauer
Sandia National Laboratories
P.O. Box 969
Livermore CA 94551-0969

Today's challenge is to redesign rotating bands in order to deliver projectiles to longer distance targets. This projectile rotating band wear model is a tool to provide simplified structural, heat transfer, and wear analysis to estimating a rotating band's capability. A one dimensional heat transfer equation is solved in the rotating band. The estimation of the band wear has correlated well with experiments. The model predicts the effect of different band materials, projectile mass properties, and gun twist angles on band performance.

INTRODUCTION

New rotating bands are needed to withstand the challenging situations of firing projectiles from the gun barrel to high zone targets. These projectiles require a rotating band which withstands higher pressures for longer periods of time. Due to the considerable expense of experimentation during development, band wear characterization must be understood analytically. The one dimensional temperature profile provides two indicators of wear in the rotating band. First, material is removed from the band when it reaches melting temperature. The second indicator is the reduction in material strength which occurs with increasing temperature. The model was calibrated using experimental results for Oxygen-Free High Conductivity (OFHC) copper. Thereafter other materials were used, and the results compared favorably with experiment.

To better understand the rotating band environment, the gun barrel (gun tube) - projectile system will be briefly discussed. A projectile with rotating band is shown in Fig. 1. To provide stability to projectile flight, the inside of the gun barrel is grooved, with corresponding lands, which twist at a slight angle (Fig. 2). Before using the projectile, the rotating band is solid as shown in Fig. 3a. The projectile is then rammed into the rear of the gun barrel, also called the forcing cone. The rotating band becomes slightly grooved because of contact with the barrel lands. Once the propellant is ignited, the band becomes fully engraved (Fig. 3b) and the projectile accelerates down the tube. After exiting the tube, the band will resemble Fig. 3c. As seen in this picture, the wear in the rotating band, as represented by the grey shaded region, occurs circumferentially, not radially. Moreover, the heat from the friction at the sliding interface between band and barrel drives the wear of the band.

GOVERNING EQUATIONS AND BOUNDARY CONDITIONS

The temperature response of the rotating band was modeled as a one dimensional problem. Since the rotating band contacts the gun barrel at n surfaces, i.e. as many as the number of gun barrel grooves/lands, the heat transfer problem can be solved over one of these segments. This geometry is represented in Fig. 4, where the temperature field is calculated in the x direction.

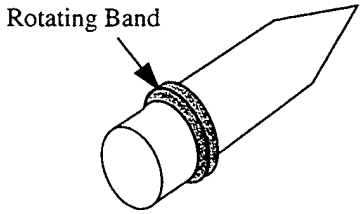

Figure 1. Projectile with Rotating Band

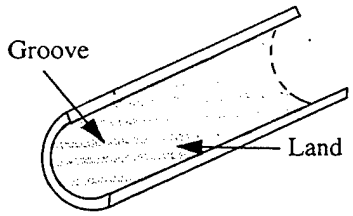

Figure 2. Gun Barrel Section

Solid Band

Band is gouged by lands in the gun barrel

Band is worn from heat input

(a) (b) (c)

Figure 3. Schematic of Band Wear

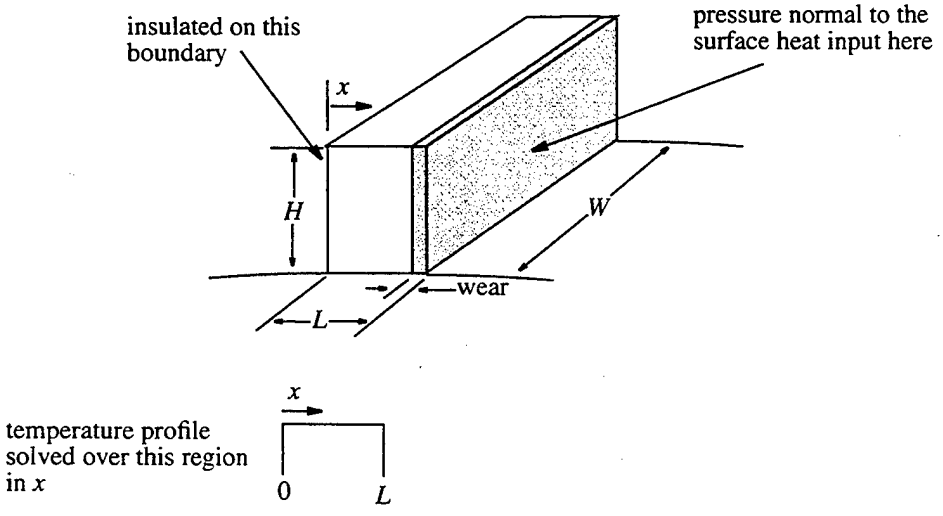

Figure 4. One of n teeth of the band

The partial differential equation describing the heat conduction problem over one of the n segments is shown in Eq (1).

$$\frac{\partial^2 T}{\partial x^2} = \frac{\rho c_p(T)}{k(T)} \frac{\partial T}{\partial t} \tag{1}$$

where T is the temperature in the rotating band. The material properties in the equation, density (ρ), specific heat (c_p), and thermal conductivity (k) can be functions of temperature. For the temperature ranges of the problem, however, density shall be considered a constant.

Two boundary conditions define the solution of Eq (1). The surface with no contact with the gun tube is adiabatic (Fig. 4). For this situation, Eq. (2) is applied:

$$-k(T)\frac{\partial}{\partial x}(T(0, t)) = 0 \tag{2}$$

The other surface of the rotating band is in constant contact with the gun tube, creating a heat source. The following equation quantifies this heat flux:

$$-k(T)\frac{\partial}{\partial x}(T(L, t)) = q(t), \tag{3}$$

where $q(t)$ is the heat input.

The initial temperature profile is specified in Eq. (4), and is a function of position along the rotating band only.

$$T(x, 0) = T_0(x) \tag{4}$$

The heat input created from the rotating band - gun barrel interaction, $q(t)$, drives the wear of the rotating band. This heat flux is expressed as the product of four parameters calculated at the contact surface:

$$q(t) = C\mu v_{rel}(t) p_b(t) \tag{5}$$

where the coefficient of friction (μ), the relative velocity (v_{rel}), and the bearing pressure (p_b) are determined at the rotating band-gun barrel interface. The parameter C can have a value between 0 and 1 to vary the percentage of heat transferred into the band. The following sections discuss how to obtain the three later parameters.

Bearing Pressure on Rotating Band, $p_b(t)$

The bearing pressure on the rotating band, a force per unit area, normal to the band surface (see Fig. 4) is calculated through kinematics given a base pressure time history. This base pressure is due to the explosives at the rear of the projectile, propelling it through the gun barrel. The base pressure, $p(t)$, imparts a force onto the projectile, causing the projectile to accelerate:

$$\Sigma F_z = m\ddot{z} = p(t)A \tag{6}$$

$$\ddot{z} = \frac{p(t)A}{m} \tag{7}$$

where m is the mass of the projectile and A is the area of the rear of the projectile. The force from the contact between rotating band and projectile is not included since it is small compared to the base pressure force. Note that $A = \pi r^2$, r being the radius of the projectile.

The angular acceleration is determined from the relationship between the angle through which the projectile has rotated, θ, and the distance z travelled along the length of the gun tube:

$$\theta = \frac{\pi z}{Rr} \tag{8}$$

where θ is in radians and R is a constant representing the rate of twist of the gun barrel lands. A "1 in R" twist rate means that a gun barrel land will make one circumferential revolution around the gun barrel in a distance of R diameters in the axial direction (z) of the tube (see Fig. 5). Differentiating Eq. (8) twice with respect to time, the angular acceleration, $\ddot{\theta}$, is:

$$\ddot{\theta} = \frac{\pi \ddot{z}}{Rr} \tag{9}$$

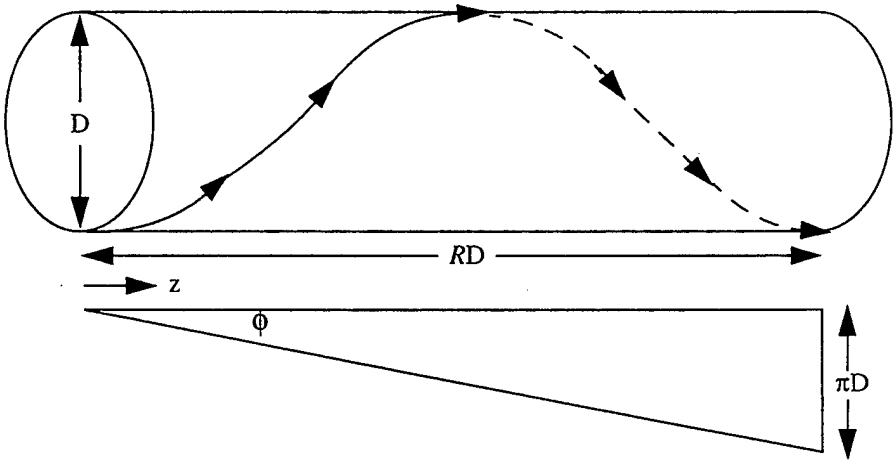

Figure 5. Twist Angle ϕ and "1 in R" Twist Rate

Once knowing the angular acceleration, the torque (T_F) can be calculated at the surface where the rotating band is in contact with the gun barrel. Since the band is in contact with the gun barrel at n surfaces, the torque imparts an equal force on each of these surfaces (Eq. (10) and (11)):

$$\Sigma T_F = J\ddot{\theta} = nF_b r \tag{10}$$

$$F_b = \frac{J\ddot{\theta}}{nr} \tag{11}$$

where J is the polar moment of inertia of the projectile, n is the number of lands of the gun tube, and F_b is the force imparted on each contact surface. The bearing pressure on each of these n surfaces is:

$$p_b = \frac{F_b}{wh} \tag{12}$$

where w and h are the linear dimensions of the band surface (see Fig. 4). After substituting Eq. (11), (9), and (7) into Eq. (12) and simplifying, we obtain:

$$p_b(t) = \frac{\pi^2}{nRwhm} J p(t) \tag{13}$$

The final expression, Eq. (13), for the bearing pressure on the rotating band contains the mass properties of the projectile, J and m, the dimensions of the gun tube, the width and height of the lands, plus the twist rate.

Relative Velocity at Contact Surface

The relative velocity, v_{rel}, at the rotating band - gun barrel surface determines the heat input into the band. The velocity of the projectile itself can be calculated by integrating the acceleration:

$$v = \int \ddot{z} dt \tag{14}$$

Here the velocity in the θ direction is neglected because it is small compared to the axial velocity. The relative velocity on the band surface is simply $v_{rel} = v/(\cos\phi)$ where ϕ is the angle of twist of the gun barrel lands. After substituting Eq. (7) for the acceleration into Eq. (14) and solving for the relative velocity, the relative velocity is:

$$v_{rel} = \frac{1}{\cos\phi}\frac{A}{m}\int p(t)dt \tag{15}$$

Coefficient of Friction

The coefficient of friction is needed to calculate the heat input into the rotating band. A melt lubrication model for two rubbing solids is taken from Stiffer [1]:

$$\mu = \frac{2k_s(T_m - T_s)}{p_b\sqrt{\pi\alpha_s w v_{rel}}} \tag{16}$$

This theoretically derived expression takes into account a thin film of melted band material in-between the band and gun barrel surface. Here k_s and α_s are respectively, the thermal conductivity and diffusivity of the steel gun tube, while T_s is the temperature of the gun tube far away from the contact surface. T_m is the melting temperature of the band material and w is the dimension of the rotating band in the direction of sliding. The bearing pressure and relative velocity are as calculated in Eq. (13) and (15), respectively.

SOLVING THE EQUATIONS

The governing equation and boundary conditions (Eq. (1)-(3)) are solved using a modified version of ONEDIM[2], a code created at Sandia National Laboratories to solve one dimensional heat transfer problems. The ONEDIM code has been validated against analytical solutions for many different types of problems. For the rotating band model, the code solved for the temperature field using a Crank-Nicolson finite-difference technique. When a portion of the rotating band reached a temperature equal or greater than the melt temperature of the material, this portion was removed from the band. A modification was needed to model this removal of band material, where instead of completely restarting the problem and solving the equations over a smaller domain, the removed material was given a thermal conductivity equal to air. Since the conductivity of air is six orders of magnitude less than the conductivity of the band material, all heat is effectively moved into the band once the heat source is translated to the melting surface. This translation maintains the heat flux at the eroding surface. This solution method was validated by comparison of the results to closed form solution[3].

CALIBRATING THE MODEL

After the validation of the code, the results were compared to experimental data of copper rotating bands from projectiles fired at ARDEC in July 1997 [4]. The recovery of these used projectiles showed how much of the rotating band remained. The heat input was calibrated to match the results from the copper band data.

Friction Coefficient Modification

The equation for the friction coefficient at the slide interface was modified to match experimental pin on disk data found[5], especially in the lower velocity/pressure region. Recall that (from Eq. (16)) that:

$$\mu \propto \frac{1}{p_b \sqrt{v_{rel}}} \tag{17}$$

The curve fit for Montgomery's [5] friction coefficient behaves like the following (see Fig. 6):

$$\mu \propto \frac{1}{p_b^{(0.4)} \sqrt{v_{rel}}} \tag{18}$$

Moreover, the expression in Eq. (18) allows a contribution from the twist rate of the gun barrel. As the angle of twist of the gun barrel increases, so should the wear on the rotating band because the bearing pressure increases. Recall Eq. (5), the expression for the heat input into the band. If Eq. (17) is substituted into Eq. (5), the following relationship is obtained:

$$q(t) \propto \frac{\sqrt{v_{rel}(t)}}{\cos\phi} \tag{19}$$

Here the effect of a slight change in ϕ (twist angle) on the heat input is negligible as the cosine of small angles, e.g. 6 and 8 degrees, hardly differ. Also, the contribution from the bearing pressure is lost. The relationship in Eq. (19) will not produce a realistic band wear because of that loss. On the other hand, by using Eq. (18) in Eq. (5) we obtain:

$$q(t) \propto \frac{\sqrt{v_{rel}(t)}}{\cos\phi} \cdot p_b^{(0.6)} \tag{20}$$

This relation preserves the relationship between pressure and heat input. That is, an increase in bearing pressure increases wear. In addition, the dependence on twist rate is retained in the bearing pressure, p_b. Before melt occurs, i.e. at low pressures and velocities, the friction coefficient, μ, is capped at 0.5.

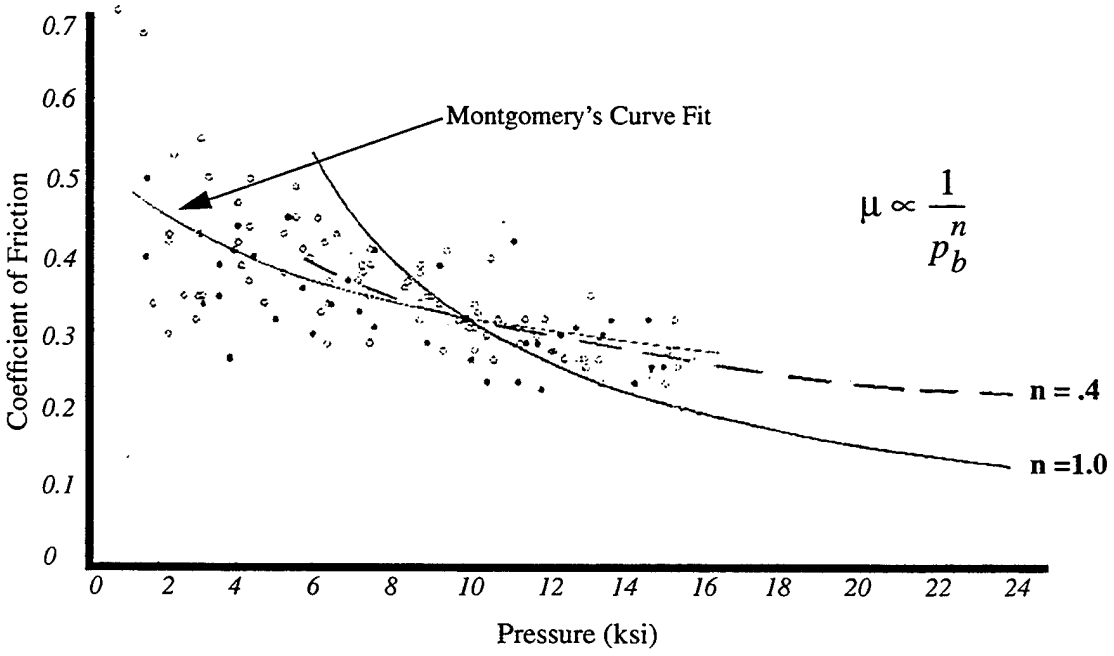

Figure 6: Friction Coefficient vs. Pressure for Gilding Metal

At high pressures near the yield strength of the band material, layers of the copper rotating band will be sheared off. This material removal causes the friction to increase because the material is being removed before being fully melted. To quantify this increase in friction the results from the code were compared with copper band experimental results. It was concluded to increase the coefficient of friction by a factor of $(Y_s/p_b)^{1.2}$ when the bearing pressure, p_b, was greater than the yield strength of the band material, Y_s.

Modifying the Heat Input

After making changes to the friction coefficient, the solution removed much more material than was observed in the experimental data. Therefore, the amount of heat entering the rotating band was too large. Recall that Eq. (5) states that $q(t) = C\mu v_{rel}(t)p_b(t)$, where C is a constant whose value can lie between 0 and 1. The first step was to determine the distribution of heat to the band and to the barrel. An assumption was made that the thermal gradients in both materials near the contact surface were equal. This reasoning results in the following proportion of the heat transferred to the rotating band.

$$C_1 = \frac{k_{RB}}{k_{RB} + k_{barrel}} \tag{21}$$

The amount is proportional to the thermal conductivities of the rotating band (k_{RB}) and gun barrel (k_{barrel}) materials.

In reality heat conduction occurs in three dimensions, but the governing equations are limited to one dimension. The heat input must be modified to reflect this simplification. Heat is conducted radially into a portion of the rotating band which will never be eroded away (see Fig. 7). This heat is also conducted into the projectile itself. To account for this loss, the amount of heat entering the band was reduced by 25%, i.e.

$$C = 0.75C_1 \tag{22}$$

These assumptions about the heat transferred into the rotating band model produced results for copper rotating band wear which matched the experimental results from copper rotating bands on fired projectiles.

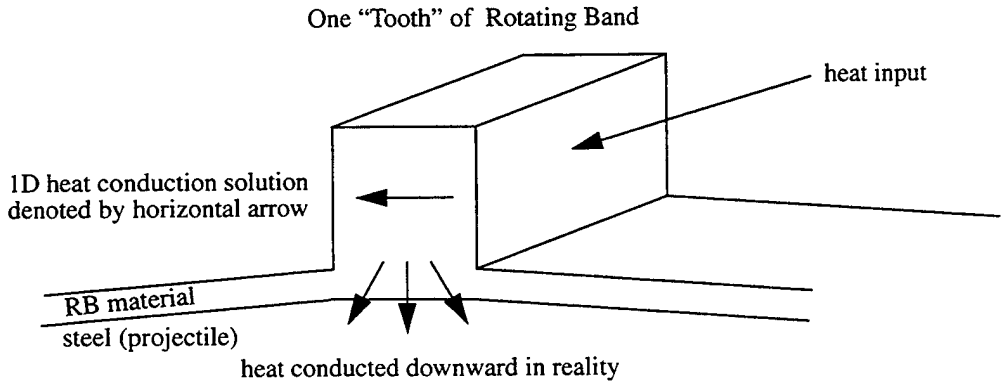

Figure 7. Direction of Heat Flow

RESULTS

As seen in the previous section, the model was calibrated for copper rotating band materials. The results from two different sets of experiments are compared to model prediction. Both sets were completed at the U.S. Army Yuma Proving Ground in Arizona [4] with a 58 caliber gun. This gun had a 155 mm diameter and a 1 in 22.5 twist rate.

The first set of calculations was completed using the configuration from the November 1997 tests at the U.S. Army Yuma Proving Ground [4]. For that setup Figure 8 shows the base pressure loading. Rotating bands made of copper, monel, stainless steel, soft iron and nickel were tested and their predictions were calculated by the model. The band wear results are summarized in Table I. The wear percentages state the percentage of material which has been removed from the band. For a copper band with a tube twist rate of 1 in 22.5, the wear was 33%. This number is far smaller than the wear, 57%, as seen in the experiment. This discrepancy could be due to lubrication effects from residue from other rotating bands. For the nickel band the model predicts 20% wear which is higher than the experimental value of 18%. Also, for stainless steel, the model prediction is 17% compared to 14% for the experiment. For the soft iron bands in the experiment, the average wear was 12%, very close to the value calculated by the model, 13%. For the monel band, the experimental wear is 24% slightly higher than the predicted wear, 22%. For this series of rotating band experiments the model might not predict the wear exactly, but the wear trends are valid.

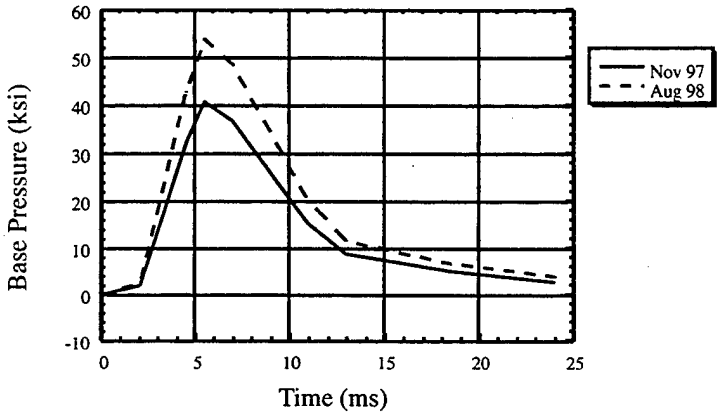

Figure 8: Base Pressure Time Histories

TABLE I. Summary for November 1997 Experimental Configuration

band material	model prediction	experimental results	rate of twist
OFHC Copper	33%	57%	1 in 22.5
Monel	22%	24%	1 in 22.5
Nickel	20%	18%	1 in 22.5
Stainless Steel	17%	14%	1 in 22.5
Soft Iron	12%	13%	1 in 22.5
OFHC Copper	39%	NA	1 in 20
Nickel	22%	NA	1 in 20

For sake of argument, if a gun with a 1 in 20 twist rate is used in the model with everything else held constant, the wear in the copper band is 39%. For a nickel band the calculated wear is 22%. The higher amount of wear agrees with theory due to larger twist angle ϕ (from the 1 in 20 twist rate) which increases the amount of pressure (Eq. (13)), thus increasing the heat input (Eq. (5)).

For the set of experiments completed in August 1998, a new rotating band was used. For this series of tests, the base pressure profile is shown in Fig. 8. A summary of the results and model predictions is in Table II. For the copper rotating band the model under-predicted the wear, 52%, compared to 65% wear seen in experiment. The model over-

predicts the wear for the nickel band. However, unlike the November 1997 case, the model under-predicts the wear value for the stainless steel band. This occurs because the newer band has a slightly different shape.

TABLE II. Summary for August 1998 Experimental Configuration

band material	model prediction	experimental results	rate of twist
OFHC Copper	52%	66%	1 in 22.5
Stainless Steel	26%	28%	1 in 22.5
Nickel	27%	24%	1 in 22.5

An increase in wear from using a 1 in 22.5 twist rate to a 1 in 20 twist rate was demonstrated, consistent with theory. For the cases where the model calculated the nickel and soft iron band wear, the model overpredicted the values. For these two cases the assumptions made on the variable C from Eq. (5), the parameter that varies the amount of the created heat for the input heat flux, are not conservative enough. However, for the copper bands the model underpredicted the wear. A solution to this problem would be to use a different value of C for each material since each material has different thermal properties. Moreover, the code is limited to heat flow in one dimension. The amount of heat lost to flow in the other dimensions cannot be determined using this model. In addition, the phenomenon occurring at the interface between barrel and band is not entirely understood. Even though the program overpredicts the wear of the rotating bands for nickel and soft iron, the trends in band performance are valid and can be used as an aid in design.

SUMMARY

To enable projectiles to hit farther targets, rotating bands must withstand higher pressures for longer periods of time. Since repeated testing is expensive to design new rotating bands, computer simulation is a more effective means of development. Using a one dimensional heat transfer equation solved over one of n teeth in the rotating band, an estimate of band wear is provided. The results of the simulations when compared to experimental data show that the program can be used by a designer to predict trends of band wear.

ACKNOWLEDGMENT

This work was supported by the US Army Research Development and Engineering Center (ARDEC) at Picatinny Arsenal under proposal 087960402. The author thanks Gabe Gabrielson for his help in modifying the code ONEDIM.

REFERENCES

1. Stiffler, A.K., "Friction and Wear With a Fully Melting Surface," *ASME Journal of Tribology*, 1984, Vol 106, pp. 416-419.

2. Gabrielson, V.K., Grange, B.W., and Christian, K.D., 1970, "ONEDIM - A Computer Code for Solving One-Dimensional Nonlinear Heat Transfer Problems," SCL-DR-69-99, Sandia National Laboratories, California

3. VanSant, J.H., 1983, "Conduction Heat Transfer Solutions", UCRL--52863-Rev., DE87 012387, Lawrence Livermore National Laboratory, California

4. Chung, K., 1999, "Final Technical Report of the Cannon Projectile Compatibility (CPC) Program", (to be completed), US Army Research Development and Engineering Center (ARDEC), Picatinny Arsenal, NJ

5. Montgomery, R.S., "Friction of Gilding Metal Sliding on Chromium-Plated Steel," 1978, Vol 50, No. 2, pp. 387-392

VISUALIZATION OF CANNON WEAR USING ULTRASONIC MEASUREMENTS AND MATLAB®

J. Michael Coyle
Benet Laboratories - U.S. Army
AMSTA-AR-CCB-TA
Watervliet Arsenal
Watervliet, NY 12189-4050

ABSTRACT

CUGS (Computerized Ultrasonic Gauging System), the synergistic use of ultrasonic and computer technology, is used to obtain measurements of a gun tube's bore surface. The bore surface is displayed as a "topographical map" whose colors are related to the physical dimensions of lands and grooves. In this manner, bore wear and erosion can be detected as differences in colors. Visualization software is written in the MATLAB® programming language/environment. All aspects of the process are described with special emphasis on the visualization algorithms and techniques. Examples of typical results obtained from CUGS and the visualization software are presented and discussed.

INTRODUCTION

The wear and erosion of a cannon tube's bore surface, i.e. inner diameter, has always been of great concern. The wearing away of material anywhere on or along this surface can detrimentally affect the fatigue life of a tube and/or the accuracy of the associated weapon system. Methods of detecting, predicting, and/or alleviating wear and erosion are of great import to the cannon designer, tester, and user.

Ultrasonic measurement techniques [1] have recently been applied to the wear detection problem. In particular, a system denoted as CUGS (Computerized Ultrasonic Gauging System) [2, 3] has been used to detect wear in rifled cannon tubes. This is a significantly more difficult task than detecting wear in smooth bore tubes since the difference in dimension between the lands and grooves can cause sound waves to reflect and interfere in unpredictable ways. CUGS uses an on-board computer and specially written software to control all aspects of its operation and is able to scan an entire tube in a remarkably short amount of time. CUGS is also able to display a representation of the bore surface by associating the land and groove dimensions with a particular color spectrum. Differences in dimension on the bore surface are then represented as differences in color on the display.

In an attempt to enhance graphical capabilities and increase portability, a method to display CUGS results outside of the CUGS environment was developed. This new display method was developed in the MATLAB® [4] programming language/environment and relies on the same technique of associating different dimensions with different colors. The purpose of this paper is to detail how the visualization of the CUGS data is achieved in MATLAB®. A certain familiarity with MATLAB® is assumed for the purposes of this paper and references are included for the unfamiliar [4, 5].

The next section entitled, "Computerized Ultrasonic Gauging System," contains a brief description of the CUGS system. It is not the intention of this paper to describe CUGS in detail but CUGS is not as well known as MATLAB® and some familiarity is necessary. References that do describe CUGS in detail have been included.

The third section entitled, "Visualization in MATLAB®," is where the description of how the data is displayed outside of CUGS is found. Special emphasis is placed on two algorithms. The first algorithm determines the center

of the tube from the CUGS data. The location of this center is necessary in order to display the dimensions as colors properly. The second algorithm is a color-matching algorithm. The CUGS data is obtained in tube sections. The colors between sections don't always match due to different calibrations for the different sections. An iterative procedure is described which attempts to match the end of one section with the beginning of the next by using one of the calibration parameters.

The final two sections are entitled, "Results" and "Discussion." In the first, typical results from this visualization process are presented. In the later, conclusions are drawn and future plans are discussed.

COMPUTERIZED ULTRASONIC GAUGING SYSTEM

CUGS represents a synergism of (a) software controlled electronics, data gathering, calculation, storage, and real-time display, (b) squirter technology, and (c) pulse sensing. It was conceptualized and developed by Reed [2]. A lathe supports the tube and allows it to turn as a carriage supporting what's called the tool holder moves past. The latter holds the squirter, which in turn contains the 10 MHz transducer where the ultrasonic pulses are generated. The acoustic wave travels along a liquid stream produced by the squirter to enter and return from the outer and inner diameters (OD and ID) of the tube. This arrangement allows the tube surface to travel past the transducer at a rapid rate.

A Matec ultrasonic system containing computer-controlled electronics, with pulser and receiving circuits, is connected to the transducer. The echoes are received and processed by the receiving circuits. An encoder that is mounted on the lathe controls the pulse repetition frequency of the ultrasonic transmitter. As data is taken, the ultrasonic signal generator pulses at the same position around the tube at each rotation, so that the mapping scheme for the tube remains consistent. This is accomplished by means of the encoder, which measures the angular position of the tube as it rotates in the lathe.

The output of the encoder is a digital signal that is used for triggering the pulsing circuitry and as a count for the position. A high resolution Hewlett Packard counter measures the time interval between the firing of the initial pulse and the interface echo (OD) and the interval between the interface (OD) and the first back echo (ID). This information is fed into the computer which controls the operation of the system, records, analyzes, displays, and stores the data in real time.

Since the time measurements are made with excellent resolution (within 1 nanosecond), knowledge of the tube dimensions is limited by the accuracy with which the sound velocity of the particular medium (water and steel) is known (between 0.1 and 0.01%). The three dimensional bore is then represented in two dimensions, in the manner of a topographical map, where the radius dimensions are mapped to a scale using color.

Sometimes due to storage requirements and sometimes due to OD dimensional changes, the tube is divided into sections. Each section is then measured independently. This requires a new calibration to be performed for each section since CUGS requires a calibration before each new measurement. One of the calibration parameters to be determined at this stage is the distance from the transducer to the center of the lathe. This parameter becomes important in the next section.

VISUALIZATION IN MATLAB®

Although CUGS has the ability to display its own measurements, a requirement developed to display results off-line, i.e. outside of CUGS. The MATLAB® programming environment (Ref.) was chosen for this task. Besides MATLAB's® well known ability to perform computations quickly and efficiently, especially matrix computations, it also has a large collection of graphical and imaging functions which greatly simplifies the coding of the visualization techniques [5]. Essentially, after the data has been properly processed, one call to the MATLAB® image function displays the data as desired.

The need to perform a large amount of calculations was also necessary. Each individual circumferential scan has two values per measurement associated with it, a thickness value and an outer diameter value. Each scan can be composed of as many as two thousand measurements and hundreds of scans are performed on each section depending on its length. For each measurement, an inner radius value is calculated from the other two values. These values are measured from the center of the lathe however. A transformation must be performed to get the proper values relative to the center of the tube. Finally, the inner radius dimension values must be transformed into a MATLAB® color map and displayed using the image function. Treating all the values obtained in a scan of an entire section as one matrix allows all these calculations to be performed for the entire section at once in MATLAB®.

The center of the tube is not known a priori and must be calculated from the accumulated data for each scan individually. The centroid formula is used with numerical integration used to determine the integrals. Using all the data turned out to give inaccurate results and so only groove data is used to determine the center of each scan.

Distinguishing between land and groove data was a computational challenge due to the effect of the measurements being relative to the center of the lathe and so off center with respect to the tube. The data was grouped into ten sectors in order to compensate for this effect. Within each sector an average value is found and values on one side of this average are obviously land data and ignored. The remaining data is not obviously only groove data and so another average is found. Values close to this second average are good candidates for groove data and so the standard deviation is found. Only values within two standard deviations of this second average are used to determine the centroid. This procedure is not rigorous in many ways, but there were time constraints when it was developed and has performed quite adequately since.

Since an entire tube can not be measured at once and is done in sections, slight differences between sections develop. This is because the system must be calibrated each time a new section is measured. This difference between sections is seen as a difference in color when two adjoining sections are displayed in unison.

A Newton iteration scheme [6] was developed in order to match the colors between sections. The average inner radius groove dimension, r, of the last ten circumferential scans of a section is determined. A calibration parameter , normally determined by CUGS, is then found by iteration so that the average inner radius groove dimension of the first ten circumferential scans of the next section is identical to r.

The calibration parameter used is the distance from the transducer to the center of the lathe. The functional relationship is complicated involving reciprocals of square roots of sums of squares. It was not clear that the iteration procedure would necessarily converge for such a complicated function. However, the iteration has never failed to converge to date and the blending of colors from section to section has greatly improved as a result.

RESULTS

In Fig. 1 is presented the inner radius data resulting from one complete scan of a tube's circumference. This figure clearly displays the two main problems associated with visualizing the bore surface of the entire tube. First the data is noisy, typical of most experimental data collecting techniques. Second the underlying radius function of the data is not flat but curved due to the fact that the measurements are being taken relative to the center of the lathe not the center of the tube.

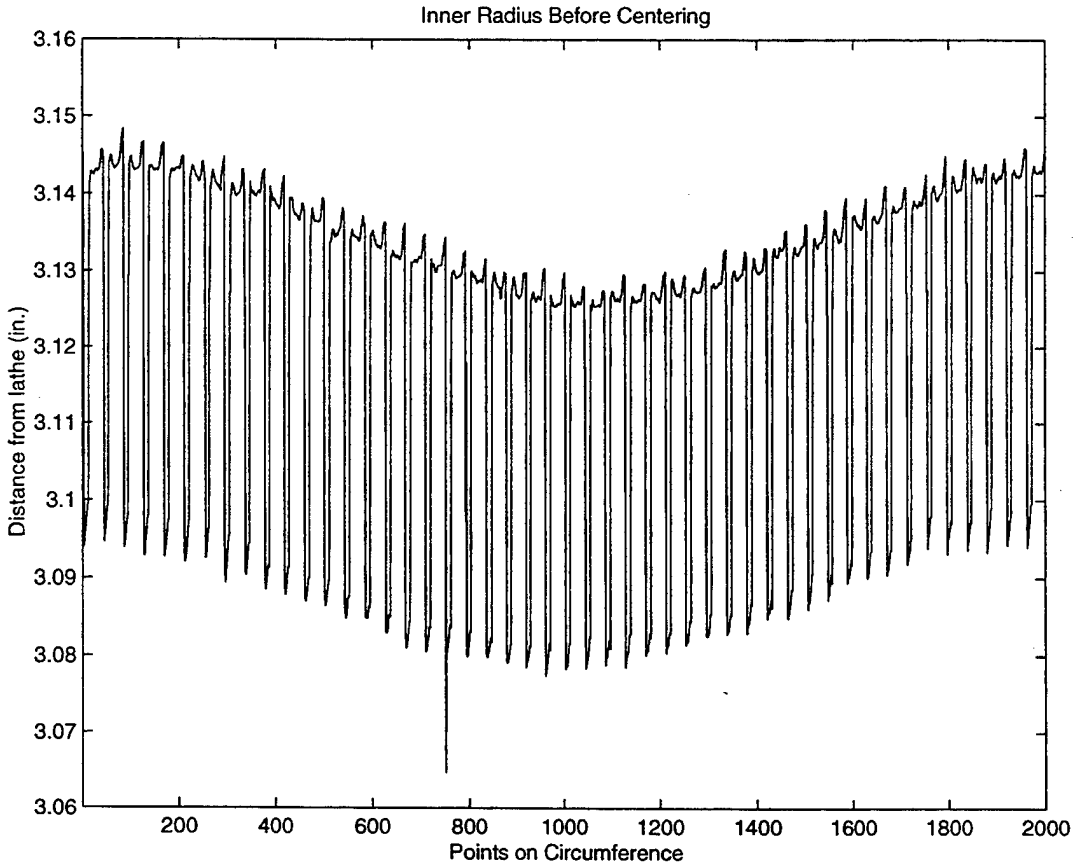

Figure 1 Example of one scan of CUGS data before centering

In Fig. 2 is presented the representation of the bore surface of an entire tube section. Notice the difference in colors from the left side of the figure to the right. This due to the curved radius function, not due to any wearing away of the tube. This figure illustrates why it was necessary to find the center of the tube and display the data relative to this point and not the center of the lathe.

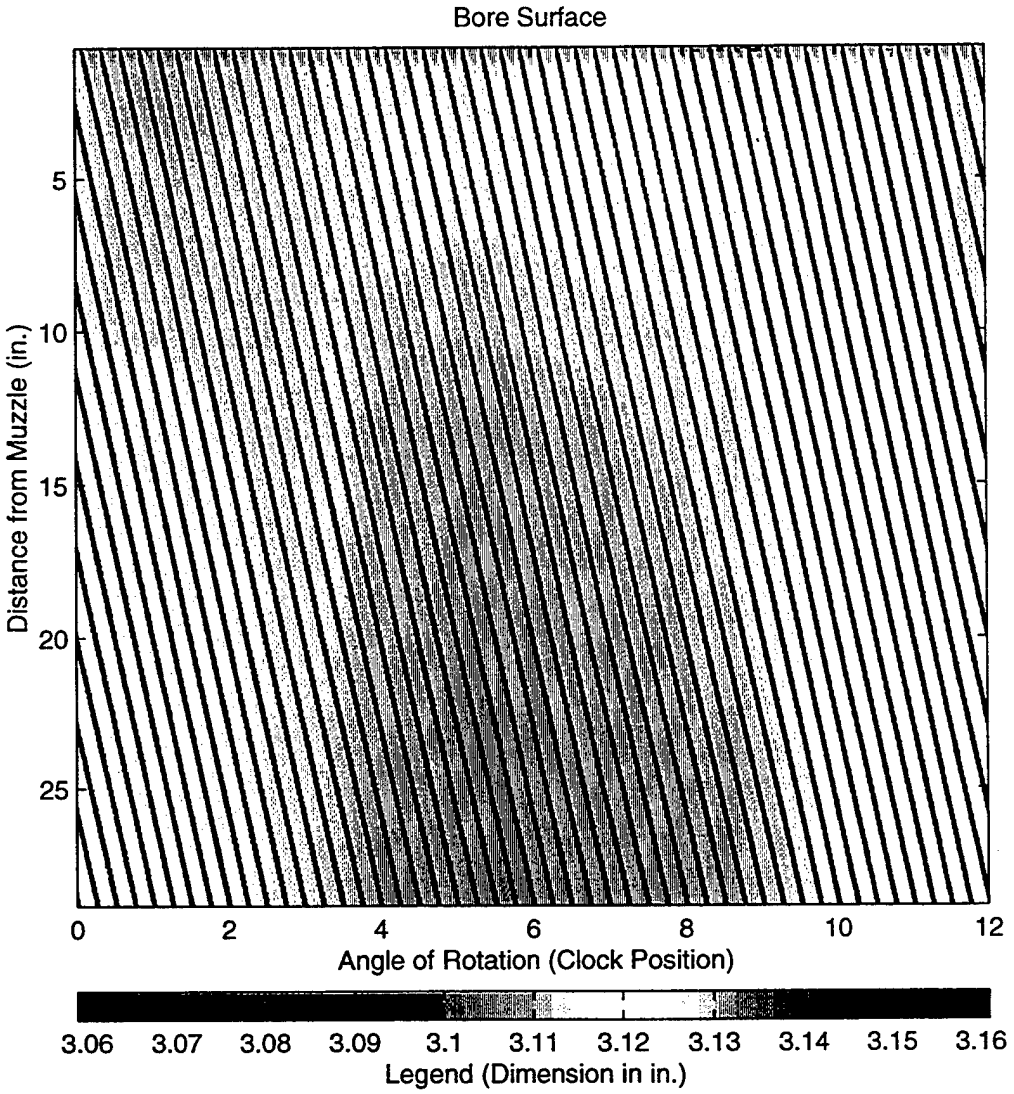

Figure 2 Example of one section of CUGS data before centering

In Fig. 3 is shown the inner radius data resulting from one complete scan of a tube's circumference after centering. This figure shows how well a job the centering algorithm is doing as the underlying radius function is now almost flat. Although it's not clear from Fig. 3 that the exact center of the tube has been found, perhaps such preciseness is not possible given the data and perhaps not necessary. In Fig. 4 is presented the representation of the bore surface of an entire tube section after centering. Notice there is now no obvious difference in colors from the one side of the figure to the other. The precise center of each circumference may or may not have been discovered but the process has performed well enough so that an observer is no longer deceived.

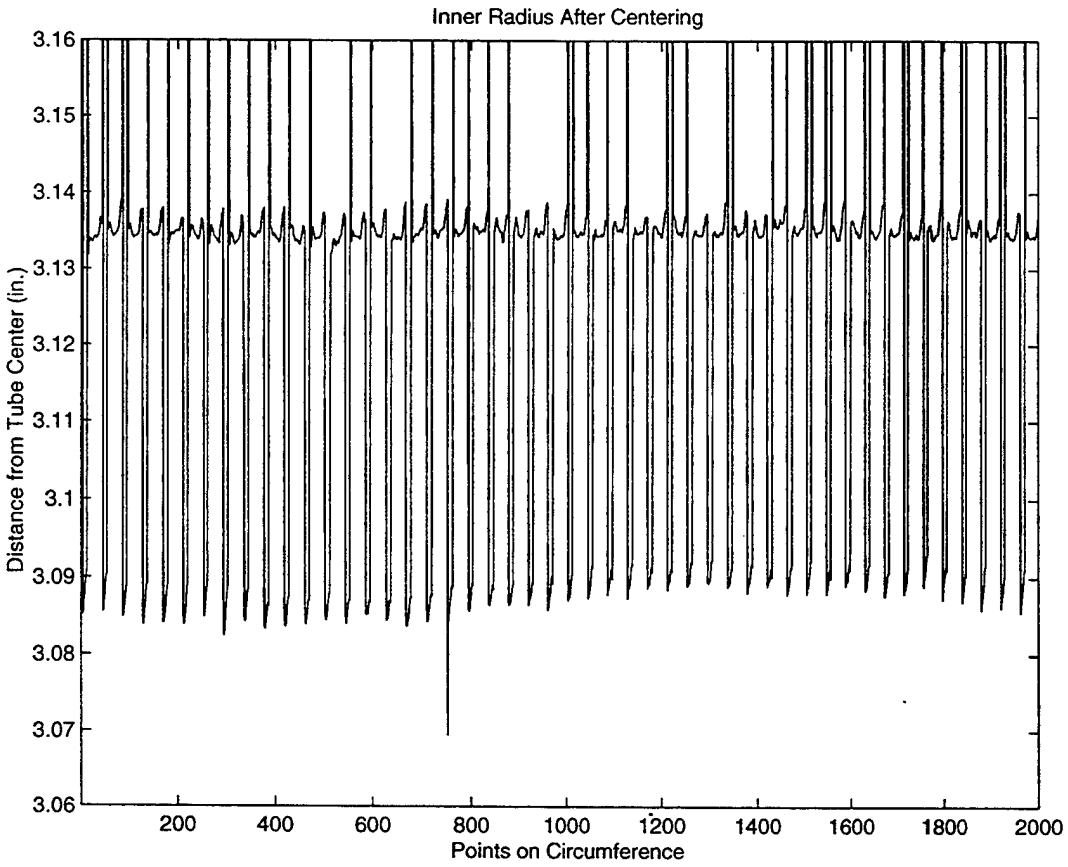

Figure 3 Example of one scan of CUGS data after centering

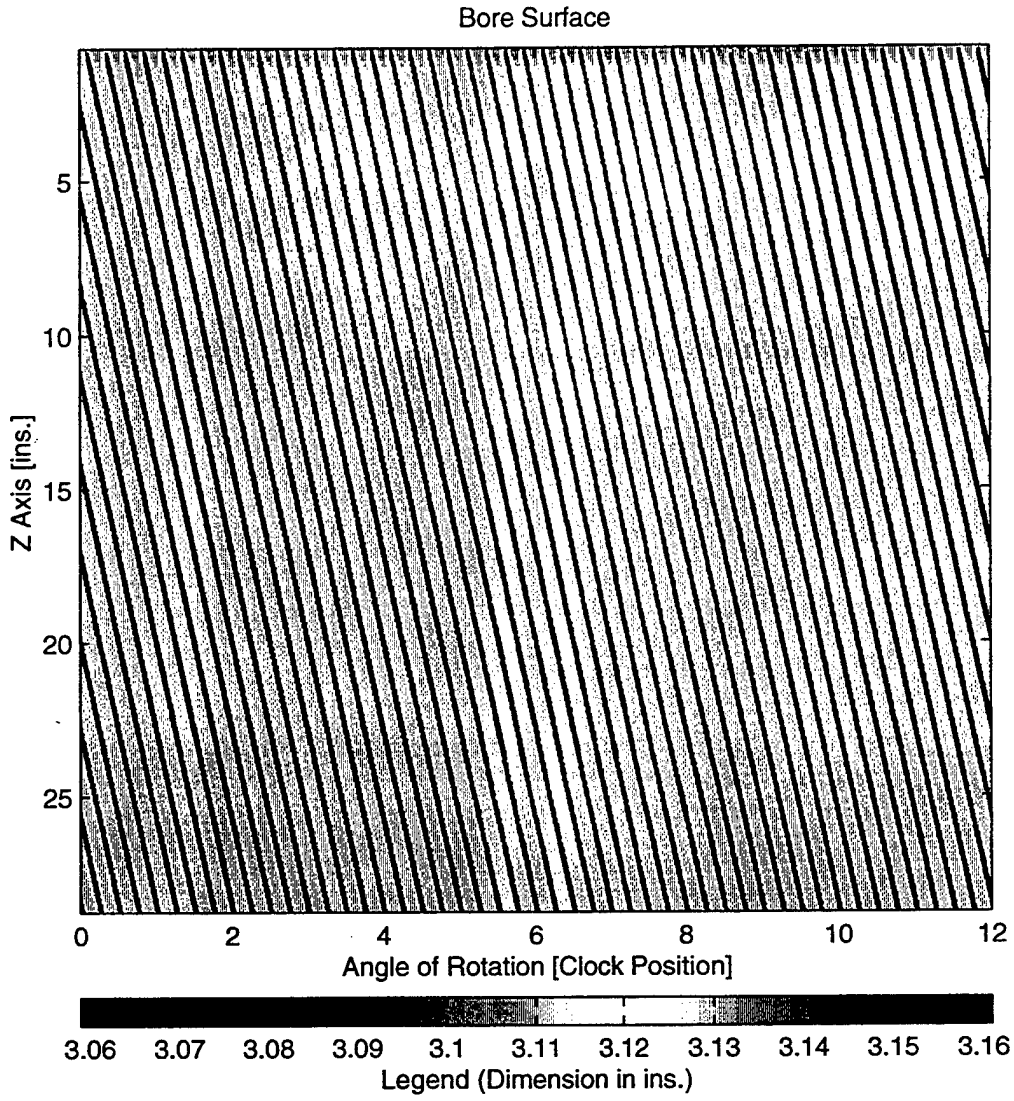

Figure 4 Example of one section of CUGS data after centering

In Fig. 5 is presented the representation of the bore surface of an entire tube after centering but before matching the colors from section to section. Notice the difference in colors from the top of the figure to the bottom resulting mainly from the different calibrations performed on the individual sections since the sections were measured independently. Fig. 6 displays the representation of the bore surface of the entire tube after centering and after matching. The colors from section to section blend together better in this figure. An exact match of colors was perhaps not achieved however. The iteration did converge for each matched section so it is felt at this time that the noisiness of the data prevents an exact matching. Better data should result in better bore representations.

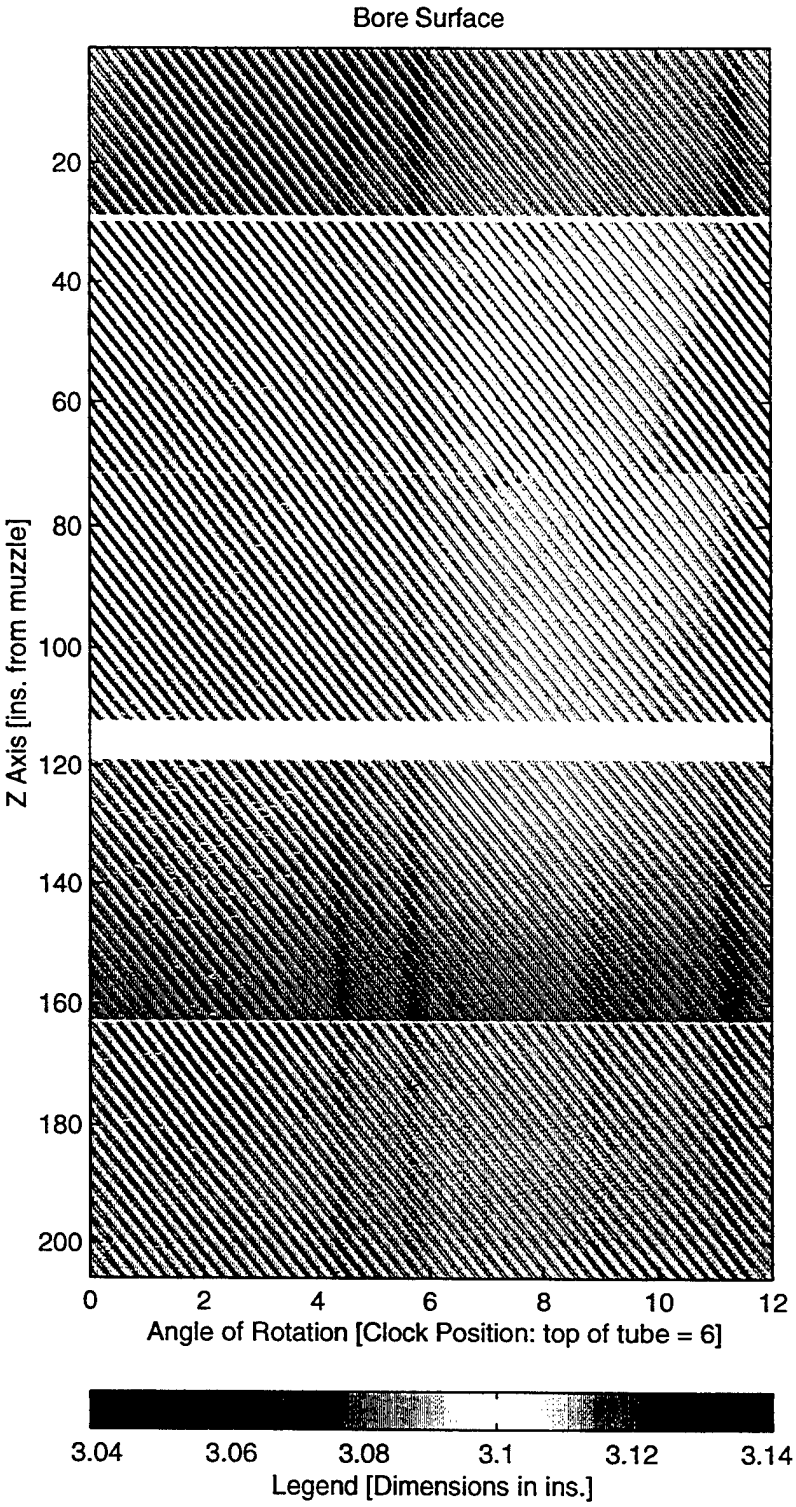

Figure 5 Example of 5 sections of CUGS data before matching

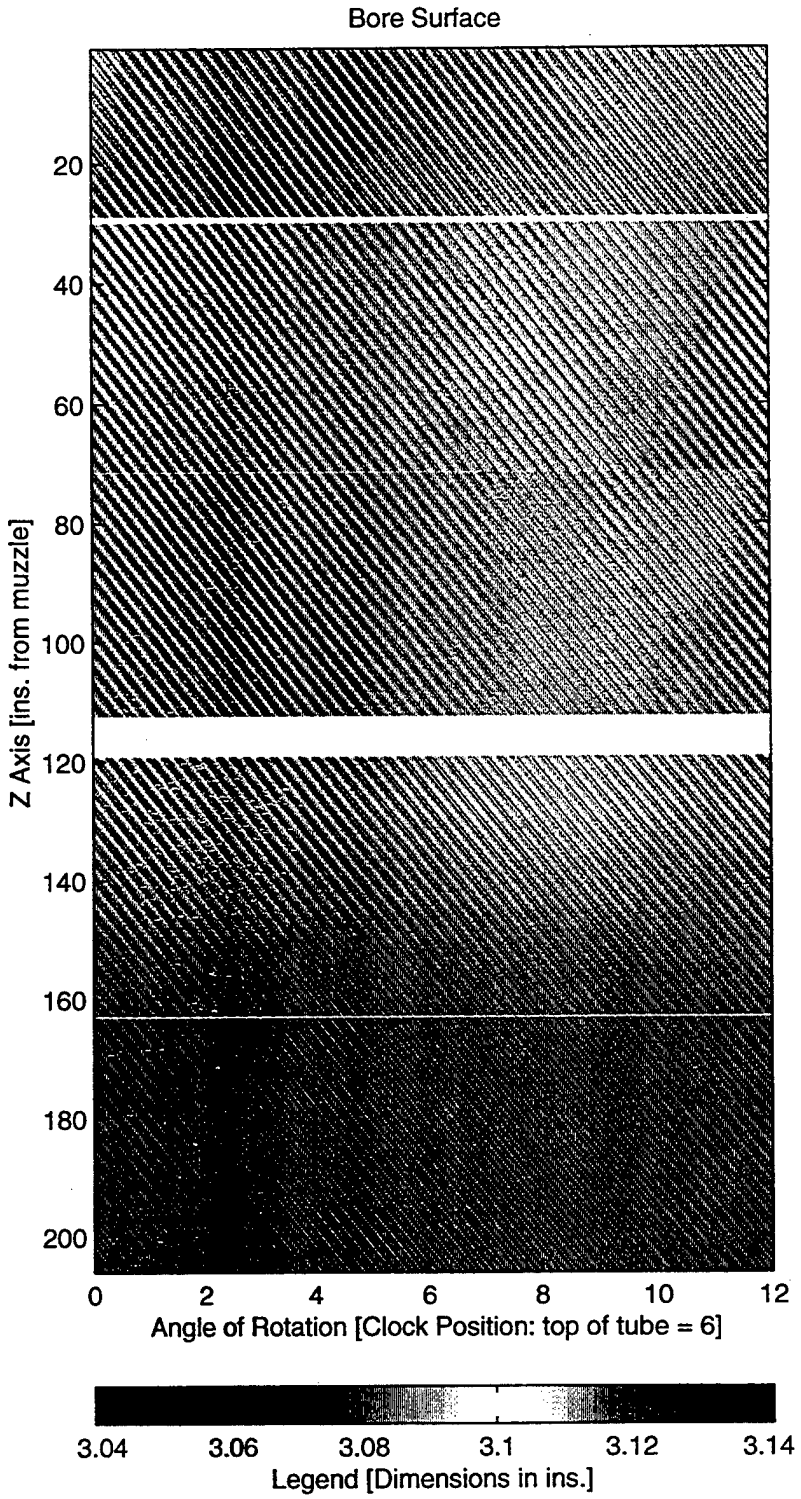

Figure 6 Example of 5 sections of CUGS data after matching

In order to indicate the usefulness of this method, in Fig. 7 is presented the representation of the bore surface of an entire tube section with only land data displayed. A wear spot is clearly made visible by this figure. The location of this wear spot has been corroborated by another measuring technique.

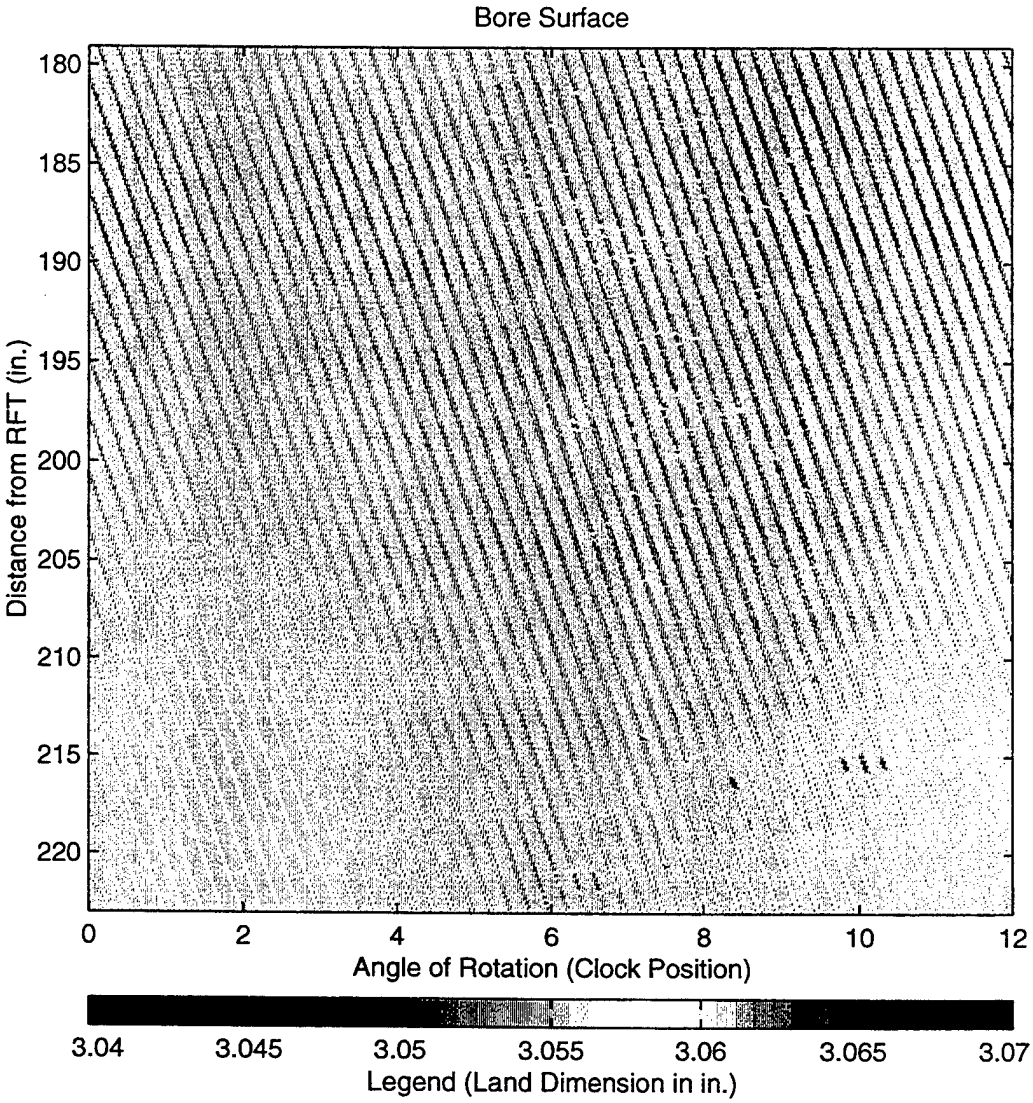

Figure 7 Example of land data alone indicating a wear spot

DISCUSSION

In many ways the results are better than expected. The centering procedure seems to be performing well with no significant change in color from one side of a tube to the other (cf., Figs. 2, 4). This is despite the ad hoc manner in which the algorithm was developed and no analysis being performed to guarantee or predict the quality of the results.

Differences between section colors have definitely been reduced after the application of the color-matching scheme (cf., Figs. 5-6). The matching could, perhaps, be better. However, given the noise in the data and the complicated dependence on the iteration parameter the degree of success achieved surpassed expectations.

In the future, other centering algorithms will be considered. This is due to the lack of any proof that the centering presented here will work for all data sets. Fortunately, this scheme has performed more than adequately to date. On the other hand, there are no plans to develop any other color matching procedures. The dependence of the matching on parameters such as the noisiness of the data and the number of scans being matched does need to be investigated further.

In general, it seems remarkable that such clear pictures of a tube's bore surface can be obtained in this manner. The minuteness of the dimensions involved coupled with the dependence on timing and distinguishing between reflected sound waves seems prohibitive at first. Yet the theory is sound and well understood and the equipment is sensitive enough to produce the pictures presented in this report. Perhaps Figs. demonstrates the most encouraging result of all - . These pictures are clear evidence that bore wear can indeed be detected and displayed by this method.

REFERENCES

1. Blessing, G. V,. et. al., "Precision Ultrasonic Thickness Measurements on Thin Steel Parts., *Materials Evaluation*, 1991, Vol. 49, pp. 982-986

2. Reed, R. W., "On-Machine Ultrasonic Gauging and Flaw Detection," *Review of Progress in Nondestructive Evaluation*, 1990, Vol. 9, pp. 1949-1956

3. Reed, R. W., Abbate, A., and Frankel, J., "Computerized Ultrasonic Gauging," submitted for publication to *Research in Nondestructive Evaluation*

4. "Using MATLAB," 1996, The MathWorks Inc., Natick, Mass.

5. "Using MATLAB Graphics," 1996, The MathWorks Inc., Natick, Mass.

6. Burden, R. L., Faires, J. D., and Reynolds, A. C., 1978, *Numerical Analysis*, Prindle, Weber, and Schmidt, Boston, Mass.

Comparison of Balanced and Out Of Balance Main Battle Tank Armaments

David J Purdy
Royal Military College of Science
Shrivenham Swindon
England, SN6 8LA

It has been commonly thought that stabilising an out of balance gun on a moving platform (tank or ship) is very difficult or impossible to achieve. Using models of a balanced and out of balance gun on a main battle tank this is shown not to be the case. The models of the guns used, include the effect of non-linear friction and out of balance. To improve the stabilisation of the out of balance gun, trunnion vertical acceleration feedforward is used.

INTRODUCTION

The primary objective of the Weapon Control System (WCS) on a Main Battle Tank (MBT) is to maximise the probability of hitting a stationary or moving target with the first round, in the shortest possible time, from a stationary or moving vehicle. The current practice for tank designers is to place the centre of gravity at the trunnions. This is because of the widely held belief that if the centre of gravity is not aligned with the trunnion the stabilisation of the gun will be significantly reduced. Two quotes from the literature relating to this are;

> *"With this equilibrating system a complete equilibrium can only be achieved for a stationary gun on a horizontal base. If the gun is tipped on its trunnion axis on sloping ground, or, as with tank and naval guns, rocked while travelling, than additional mass forces on the center of gravity of the elevating part cause the compensation to be disrupted.*
>
> *For this reason, the naval guns* [and presumably tank guns] *can not use an equilibrator and must place the center of gravity of the elevating part in the trunnion axis."* [1],
>
> and
>
> *"An equilibrator can only balance an otherwise unbalanced system statically. It will be apparent that, in the dynamic state, acceleration forces act at the centre of gravity of the elevating mass, giving rise to varying moments that cannot be counteracted by a conventional equilibrator. It is for this reason that equilibrators cannot be used in stabilised systems."* [2].

Using simulation techniques, this paper, compares the quality of stabilisation of the elevation axis for two WCS, one having a balanced gun and the other an Out Of Balance (OOB) gun. The elevation model and closed-loop controller used in this study have been taken from [3,4]. The elevation model can be either linear or non-linear, with the principal non-linearities in the non-linear model being the OOB, and static and kinetic friction. The elevation model allows the MBT motions to be coupled into the gun via the hull pitch rate and vertical acceleration at the trunnions. The gun barrel is modelled as two rigid sections and is referred to in the paper as a Lumped Parameter Flexible Beam Model (LPFBM). To improve the stabilisation of the OOB gun, trunnion vertical acceleration feedforward is incorporated into the controller.

WEAPON CONTROL SYSTEM MODELS

A brief description of the models used is given in this section, the interested reader is referred to [3,5] for a more detailed description of the models. This section is broken down into three subsections, the first two subsections examine the elevation models for the balanced and OOB guns respectively and the third subsection shows the simulated results of the two elevation models.

BALANCED GUN

A diagram of the elevation channel is shown in Figure 1. The input to the elevation drive is a voltage to the servo-amplifier. The servo-amplifier produces a current, proportional to its input voltage. The prime mover is a d.c. servo-motor and in conjunction with the amplifier, can be considered as producing torque proportional to its input current [6]. The remainder of the drive-line consists of a gearbox, and rack and pinion. The servo-amplifier, motor and gearbox are represented by a single drive torque constant K_t. Sensors are used to measure the angular rate of the motor, and angular rate and position of the cradle.

The drive inertia I_d represents the motor inertia referred to the output of the gearbox. The drive torque is given by;

$$T_d = K_t v_i \tag{1}$$

where v_i is the input to the servo-amplifier. The viscous friction at the drive is c_d. The radius of the pinion is R_p. The drive-line stiffness k_d has been lumped between the rack and the cradle, which is equivalent to the model in [5,6]. The cradle, breech and gun barrel in this model are represented by two rigid sections, of length l_1 and l_2, mass m_1 and m_2, and moment of inertia about the centre of gravity I_1 and I_2. The distance to the centres of gravity are η_1 and η_2, the pin-joint linking the two sections has a torsional stiffness of k_{12} and viscous friction c_{12}. This type of flexible beam model has been used to simulate and control flexible space-borne manipulators [7] and to investigate the design of WCSs [3,4,5]. The method used to select the lengths of the rigid sections is given in [3,5,7], in which the muzzle displacement and rotation for the first cantilever mode are matched to a finite element model. The torsional spring rate is calculated to make the first cantilever mode frequencies of the LPFBM and finite element models equal.

The inputs to the model are the voltage to the servo-amplifier v_i, the trunnion vertical acceleration $\ddot{y}_t$ and the MBT hull pitch rate $\dot{\theta}_p$. The outputs from the model are the drive angular velocity $\dot{\theta}_d$, the breech angle θ_1 and velocity $\dot{\theta}_1$ and the muzzle angle θ_2. The equations of motion for small motions are;

$$\mathbf{M}_1\{\ddot{\theta}\} + \mathbf{C}_1\{\dot{\theta}\} + \mathbf{K}_1\{\theta\} = \mathbf{I}_1\{u\} \tag{2}$$

where the mass $\mathbf{M}_1$, damping $\mathbf{C}_1$, stiffness $\mathbf{K}_1$, and input $\mathbf{I}_1$ matrices are give by;

$$\mathbf{M}_1 = \begin{bmatrix} I_d & 0 & 0 \\ 0 & I_1 + m_1\eta_1^2 + m_2 l_1^2 & m_2 l_1 \eta_2 \\ 0 & m_2 l_1 \eta_2 & I_2 + m_2\eta_2^2 \end{bmatrix}$$

$$\mathbf{C}_1 = \begin{bmatrix} c_d & 0 & 0 \\ 0 & c_{12} + c_{1p} & -c_{12} \\ 0 & -c_{12} & c_{12} \end{bmatrix}$$

$$\mathbf{K}_1 = \begin{bmatrix} k_d R_p^2 & 0 & -k_d R_p X_{tp} \\ 0 & k_{12} + k_d X_{tp}^2 & -k_{12} \\ -k_d R_p X_{tp} & -k_{12} & k_{12} \end{bmatrix}$$

$$\mathbf{I}_1 = \begin{bmatrix} 1 & 0 & 0 & -k_d X_{tp} R_p \\ 0 & -(m_1\eta_1 + m_2 l_1) & c_{1p} & k_d X_{tp}^2 \\ 0 & -m_2\eta_2 & 0 & 0 \end{bmatrix} \tag{3}$$

The vector of inputs and outputs are;

$$\{\mathbf{u}\}^T = \{T_m \quad \ddot{y}_t \quad \dot{\theta}_p \quad \theta_p\}$$

$$\{\theta\}^T = \{\dot{\theta}_d \quad \theta_1 \quad \dot{\theta}_1 \quad \theta_2\} \tag{4}$$

In state space form the equations for the model are given by;

$$\begin{aligned} \dot{\mathbf{x}} &= \mathbf{A}\mathbf{x} + \mathbf{B}\mathbf{u} \\ \mathbf{y} &= \mathbf{C}\mathbf{x} + \mathbf{D}\mathbf{u} \end{aligned} \tag{5}$$

where;

$$\mathbf{A} = \begin{bmatrix} \mathbf{0} & \mathbf{I} \\ -\mathbf{M}_1^{-1}\mathbf{K}_1 & -\mathbf{M}_1^{-1}\mathbf{C}_1 \end{bmatrix}$$

$$\mathbf{B} = \begin{bmatrix} \mathbf{0} \\ \mathbf{M}_1^{-1}\mathbf{I}_1 \end{bmatrix} \quad \mathbf{C} = \mathbf{I} \quad \mathbf{D} = [\mathbf{0}]$$

$$\{\mathbf{x}\}^T = \{\theta_d \quad \theta_1 \quad \theta_2 \quad \dot{\theta}_d \quad \dot{\theta}_1 \quad \dot{\theta}_2\} \tag{6}$$

and **I** is a unit matrix of appropriate dimensions.

The non-linear elevation model has been formed by incorporating non-linear friction into the drive and trunnions, and the out-of-balance of the gun. The out-of-balance torque being caused by the centre of gravity of the elevating mass being 8.0 mm in front of the trunnions. The non-linear friction model used is a modified reset-integrator representation [8]. The modification to this model includes a random component of friction added into its output. This is generated by integrating white noise and adding it into the friction force, the mean level being zero and the standard deviation being approximately 1% of the kinetic friction. The static friction provides an additional 25% of the kinetic friction level. The drive friction was taken as 1% of the trunnion friction. For the elevation system under investigation the trunnion kinetic friction has been set to 1 kNm. A full set of data for the linear and non-linear models and their derivation can be found in [3].

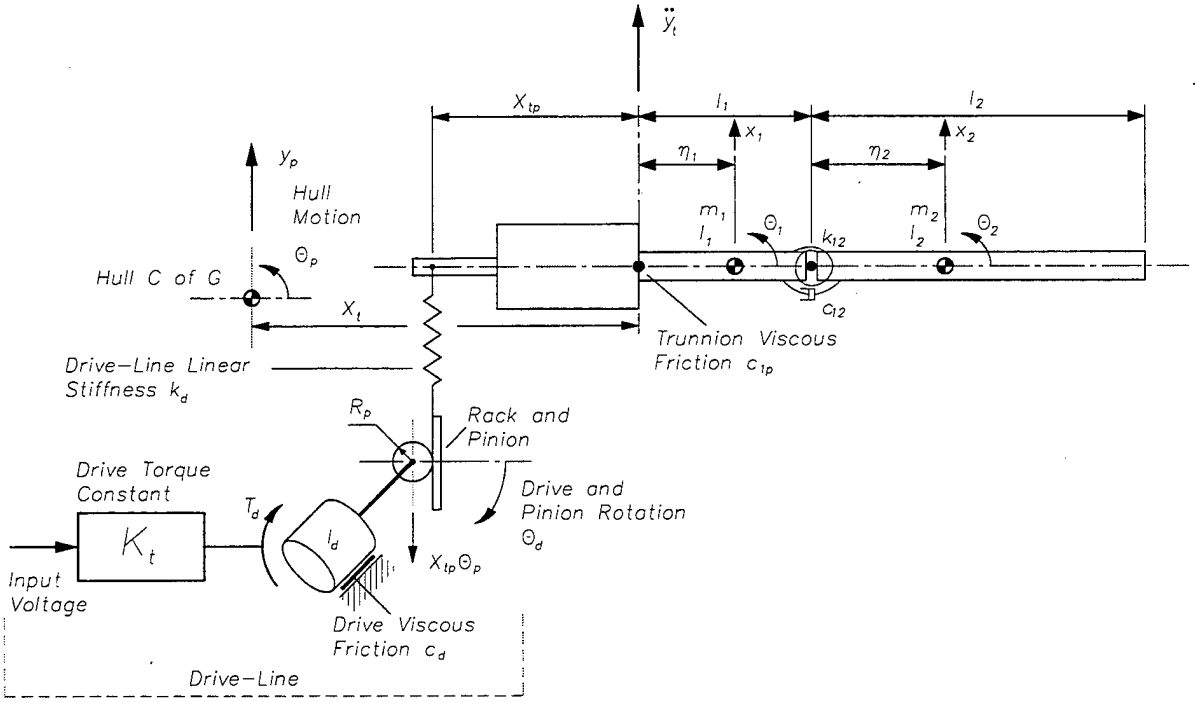

Figure 1 Elevation model with two section LPFBM.

OUT OF BALANCE GUN

The only parameter that has been altered for the OOB gun is the distance from the trunnions to the centre of gravity of the total elevating mass. This has been increased from 0.008 to 0.515m. The equation for the out of balance moment as a function of breech rotation (θ_1) is given by;

$$M_{ob} = m_t g \eta_t \cos\theta_1 \tag{7}$$

where M_{ob} is the out of balance moment, m_t, g and η_t are the total elevating mass (2500 kg), gravity (9.81 m/s^2) and the distance from the trunnions to the centre of gravity (0.515m). The maximum static OOB moment for the gun is 12.63 kNm.

It has been assumed that the static OOB has been totally removed from the gun, by the use of a suitable equilibrator. For a real situation there will still be some residual OOB, which will have a small effect but this has been ignored because it is primarily the stabilisation that is being considered.

SIMULATED MODEL RESPONSES

To compare the models of the balanced and OOB gun cases, the responses have been plotted in Figures 2 and 3. These plots are for the linear components of the models only. The non-linear elements having been removed.

The responses shown in Figure 2, are the open-loop frequency responses between the drive torque and breech angle. Below 18 Hz the response of the OOB gun, Figure 2a, has a lower gain than the balanced, above 18 Hz this changes over. This reduction in gain at low frequency is expected because of the increase in inertia. The two resonances (poles) at approximately 18 and 23 Hz, for the balanced gun, have increased in frequency by about 1 Hz for the OOB case. The anti-resonance (zero) at about 11 Hz has remained the same, this is to be expected because it represents the first cantilever mode of the barrel [9]. There is very little difference between the phase, Figure 2b, for the balanced and OOB situations. The slight differences are due to the changes in the resonances.

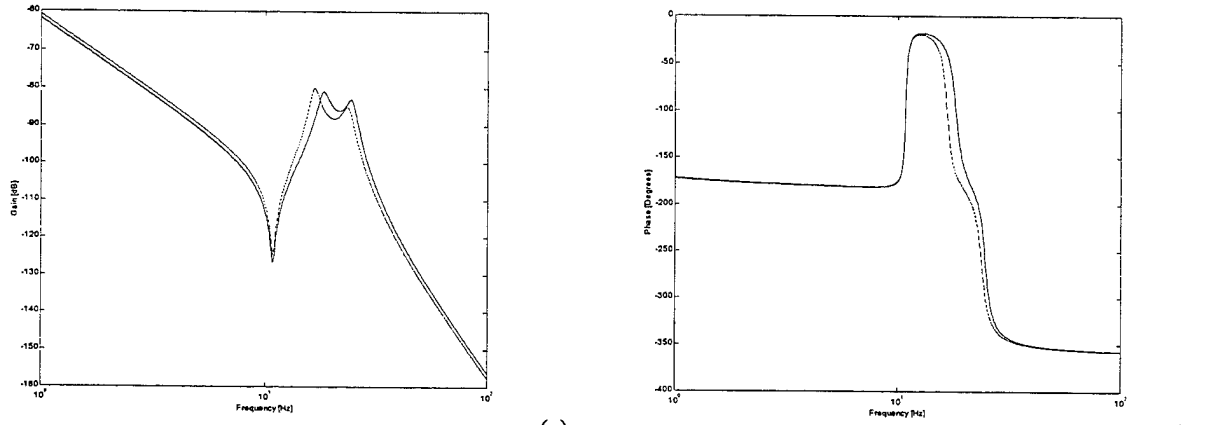

(a) (b)

Figure 2 Plot of the open-loop frequency responses, between the drive torque and breech angle for the gain (a) and phase (b), with the OOB [solid] and balanced [dash] gun.

The response of the two gun cases to the disturbance inputs are shown in Figure 3. The response to trunnion vertical acceleration, Figure 3a, shows that below 10 Hz the OOB gun has a greater gain than the balanced. Above 10 Hz this changes and the balanced has a greater gain. At 1 Hz the OOB gun has over 30 dB greater gain than the balanced. This again is expected, because it is this effect that the authors are referring to in the quotations in the introduction. The point of interest is that at some frequencies the balanced gun is worse than the OOB. The OOB has an isolation ratio of approximately -45 dB at 1 Hz, reducing to about -85 dB at 10 Hz. Thus, the static view does not give the complete picture of the gun's motion due to the vertical acceleration at the trunnions. The effect of the hull pitch rate disturbance, Figure 3b, for the OOB gun is very similar to the balanced, except that it is about 1 dB better up to 18 Hz. This is because the inertia of the OOB gun is greater than the balanced and thus resists the frictional and drive disturbance torques better.

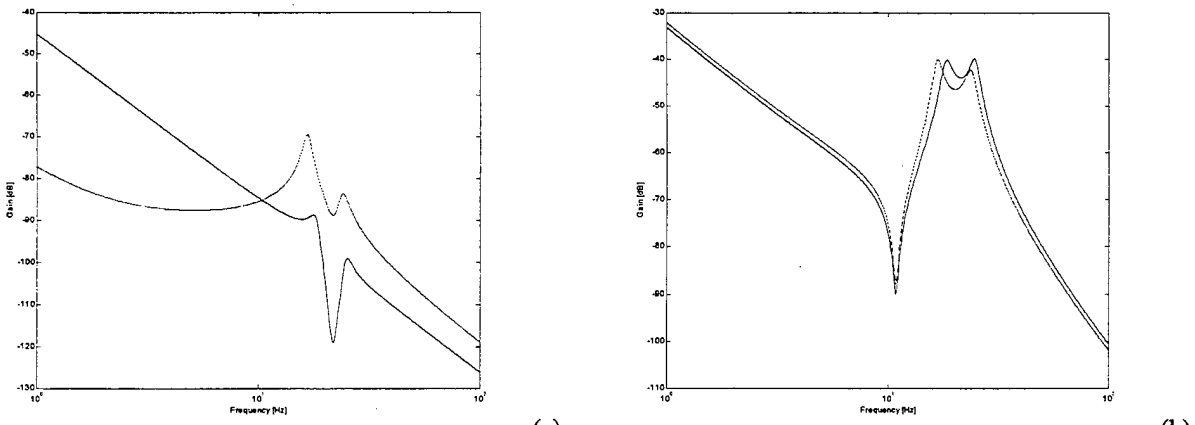

(a) (b)

Figure 3 Plot of the disturbance response of the elevation model to the trunnion vertical acceleration (a) and hull pitch rate (b), with the OOB [solid] and balanced [dash] gun.

WEAPON CONTROLLER DESIGN

This section examines the design of the closed-loop and disturbance feedforward controllers for the balanced and OOB weapon control systems. Only a brief discussion of the controller for the balanced gun is given here, a more detailed description is given in [3,4,5].

BALANCED GUN

To investigate the performance of the elevation model, a classical closed-loop controller was designed, which was based on the open-loop frequency responses. The form of the closed-loop controller is shown in the lower part of Figure 4, and consists of an inner-loop breech rate controller and outer-loop breech position controller. The outer-loop controller is based on a traditional proportional plus integral structure, while the inner-loop has a proportional controller augmented with a notch and low pass filter. No attempt has been made to optimise the response of the closed-loop weapon control system. In addition to the closed-loop part, the controller is augmented with hull rate feedforward and non-linear friction compensation, this is to enhance the isolation of the gun from the hull [4].

OUT OF BALANCE GUN

The controller structure for the OOB gun is shown in Figure 4. The controller has the same closed-loop and hull pitch rate feedforward components as the balanced. The proportional gain of the OOB case has been increased over the balanced by 8.3 %, so that they both have the same closed-loop bandwidths. In addition to this, the OOB controller has trunnion vertical acceleration feedforward. This is to help reduce the effect of the disturbance caused by the coupling between the vertical trunnion acceleration into the breech rotation.

FEEDFORWARD CONTROLLER DESIGN

It can be shown [10] that for the trunnion vertical acceleration disturbance to have no effect on the gun, the ideal feedforward controller $F_a(s)$ is given by;

$$F_a(s) = \frac{D_a(s)}{G(s)} \tag{8}$$

where $D_a(s)$ and $G(S)$ are the disturbance and forward path transfer functions, see Figure 4.

Thus, if the feedforward controller is the ratio of the disturbance and system transfer functions, then the effect of the disturbance will be cancelled out. To simplify the transfer function for this feedforward controller design, the elevation model has been reduced to a single degree of freedom. This has been accomplished by removing the flexibility in the barrel and drive-line. The transfer function for this system, ignoring the hull pitch rate, is then given by;

$$\Theta_g(s) = G(s)M(s) + D_a(s)A_t(s) \tag{9}$$

where $M(s)$ and $A_t(s)$ are the command input and vertical trunnion acceleration respectively.

In this case;

$$G(s) = \frac{K_t X_{tp}/R_p}{I_e s^2 + c_e s} \tag{10}$$

$$D_a = \frac{-\eta_t m_g}{I_e s^2 + c_e s} \tag{11}$$

where;

$$I_e = I_g + \left(X_{tp}/R_p\right)^2 I_d$$

$$c_e = c_g + \left(X_{tp}/R_p\right)^2 c_d$$

The ideal feedforward transfer function is thus given by;

$$F_a(s) = \frac{-\eta_t m_g}{K_t X_{tp}/R_p} \tag{12}$$

For the trunnion vertical acceleration the ideal feedforward transfer function is a gain and can be implemented directly.

SIMULATED CLOSED-LOOP RESPONSES

The closed-loop step and frequency responses for the balanced and OOB WCSs (linear models only) are shown in Figure 5. The bandwidth, Figure 5b, for both cases are the same at approximately 2 Hz, though the OOB case has a higher peak gain. The step responses, Figure 5a, show that the damping for the OOB situation is less than the balanced because of the greater overshoot.

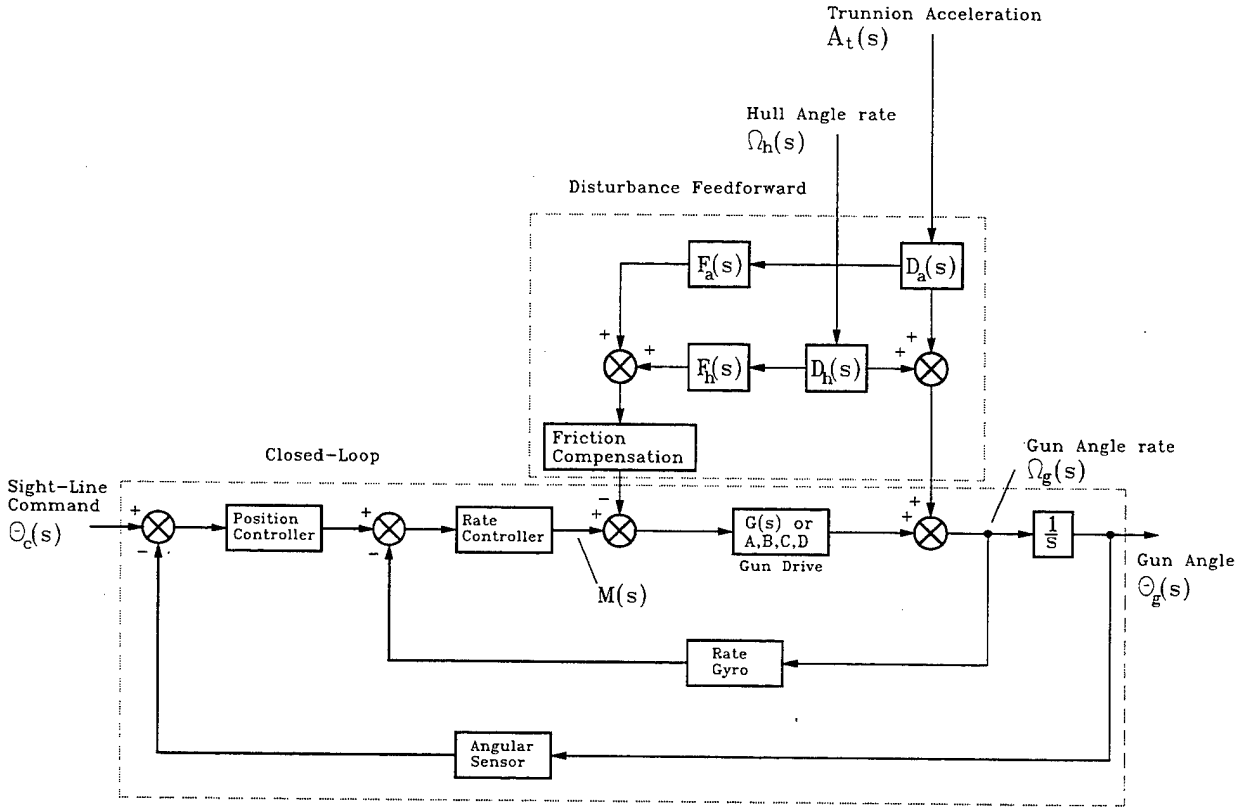

Figure 4 Controller structure for the OOB and balanced weapon control systems.

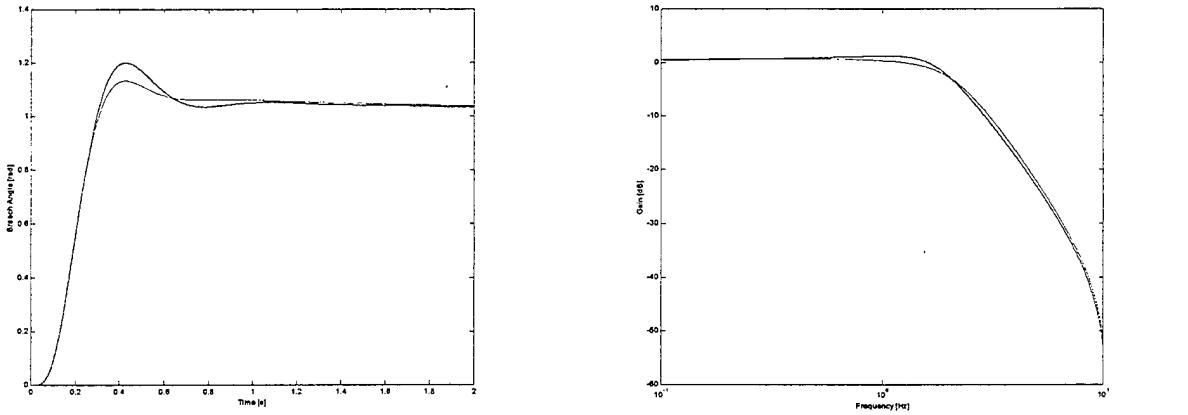

(a) (b)

Figure 5 Plot of closed-loop step (a) and frequency responses (b), with the OOB [solid] and balanced [dash] gun.

SIMULATION RESULTS AND DISCUSSION

In this investigation, simulation results have been obtained for the balanced and OOB weapon control systems on a MBT model crossing random terrain. The MBT vehicle model and terrain data have been taken from [3,5]. The simulation of the vehicle and WCSs was for 40 seconds.

A plot of the breech angle against time for the balanced and OOB gun, is shown in Figure 6. From examining this plot, it is not immediately obvious which of the weapon control systems is performing the best. The rms values for the balanced and OOB system are 1.14 and 1.27 mrad respectively. Thus the OOB situation is 11.4 % worse. The drive torque, Figure 7, shows that the OOB case has a greater amplitude and more higher frequency activity. There is an increase of 33.5 % in the drive torque for the OOB over the balanced case. The rms power required by the OOB gun is 51.0 W and the balanced 44.0 W, which is an increase of 15.9 %.

The largest increase in the OOB case is the rms drive torque demand at 33.5 %, while the rms breech angle and power have only small increases of 11.4 % and 15.9 % respectively. The results for the two cases are summarised in Table 1.

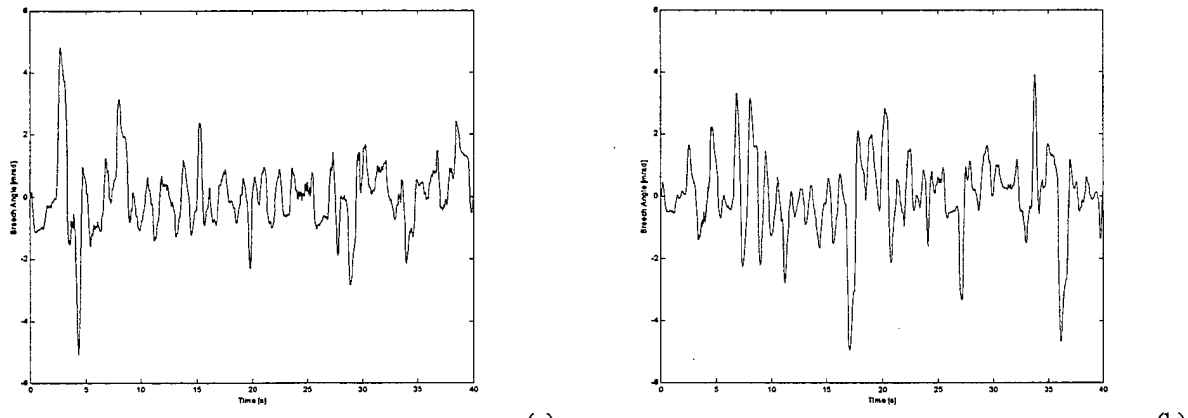

(a) (b)

Figure 6 Plot of the breech angle, with the balanced (a) and OOB (b) gun.

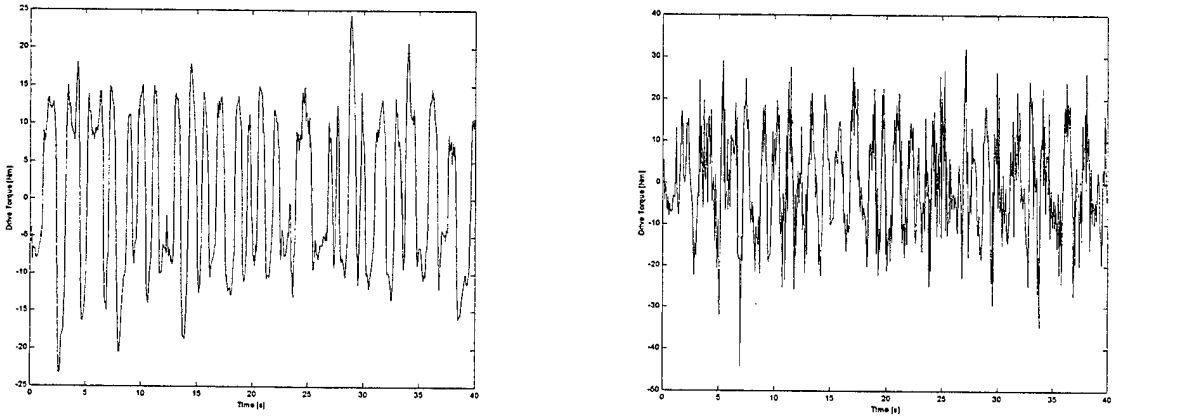

(a) (b)

Figure 7 Plot of the drive torque, balanced (a) and OOB (b).

Parameter	rms		% Increase
	Balanced	OOB	
Breech Angle [mrad]	1.14	1.27	11.4
Command Signal [v]	1.94	2.59	33.5
Drive Torque [Nm]	10.55	14.09	33.5
Power [W]	44.0	51.0	15.9

Table 1 Comparison of balanced and OOB performance.

CONCLUSION

A comparison of an OOB and balanced gun in a MBT crossing random terrain has been presented. The controller for the OOB case has included a feedforward term derived from the vertical acceleration of the trunnions.

The results have shown conclusively that it is possible to stabilise an OOB gun on a moving platform, with only a small reduction in performance, an increase of 11.4 % rms breech angle motion and 15.9 % rms power.

REFERENCES

[1] Rheinmetall Handbook on Weaponry, second English edition, Rheinmetal GmbH, 1992, pp. 385 & 386.

[2] Warwick, H. D., A guide to the design of main armament gun mountings for armoured fighting vehicles (U), DERA Chobham Lane Chertsey UK, Report No. 82019, pp 61-66.

[3] Purdy, D. J., Modelling And Simulation Of A Weapon Control System For A Main Battle Tank, Proceedings Of The Eighth US Army Symposium On Gun Dynamics, 14-16 May 1996.

[4] Purdy, D. J., Main battle bank stabilisation ratio enhancement using hull rate feedforward, Journal of Battlefield Technology, Vol. 1, No. 2, July 1998.

[5] Purdy, D. J. "An Investigation Into The Modelling And Control Of Flexible Bodies", PhD. Thesis, Cranfield University (RMCS), England, 1994.

[6] Dholiwar, D. K., Development Of A Hybrid Distributed-Lumped Parameter Open Loop Model Of Elevation Axis For A Gun System, Proceedings Of The Seventh US Army Symposium On Gun Dynamics, 11-13 May 1993.

[7] Woerkom, P.Th.L.M., On Fictitious Joints Modelling Of Manipulator Link Flexibility For The HERA Simulation Facility Pilot, National Aerospace Laboratory NLR The Netherlands, Report No. NLR TR 88086 U, 1988.

[8] Haessig, D. A. and Friedland, B., On The Modeling And Simulation Of Friction, Transactions Of The ASME Journal Of Dynamic Systems, Measurement And Control, Vol. 113, pp. 354-362, Sept 1991.

[9] Miu, D. K., Physical interpretation of transfer function zeros for simple control systems with mechanical flexibilities, Journal of Dynamic Systems, Measurement and Control, Vol. 113, 9/1991.

[10] Maciejowski, J. M., Multivariable Feedback Design, Addison-Wesley, pp. 10-13, 1989.

Measurements of Gun Tube Motion and Muzzle Pointing Error of Main Battle Tanks

Peter L. McCall
U.S. Army Aberdeen Test Center
Aberdeen Proving Ground, MD 21005-5059

ABSTRACT

Beginning in 1990, the U.S. Army Aberdeen Test Center (ATC) began testing a prototype cannon mounted in a nonarmored turret fitted to an M1A1 Abrams tank chassis. The cannon design incorporated a longer gun tube as a means to increase projectile velocity. A significant vertical dispersion problem was measured early in the test program. Through investigative efforts, the cause of the error was linked to the increased dynamic bending or flexure of the longer tube. Research and investigative work was conducted through a collaborative effort with the U.S. Army Research Laboratory, Benet Laboratory, Project Manager - Tank Main Armament Systems, U.S. Army Research and Engineering Center, and Cadillac Gage Textron Inc.. New test methods, instrumentation, data analysis procedures, and stabilization control design resulted through this series of investigations into the dynamic flexure error source. Through this joint research, improvements in tank fire control design have been developed to improve delivery accuracy. This paper discusses the instrumentation implemented, methods applied, and analysis procedures used to characterize the tube flexure during dynamic tests of a main battle tank and the relationship between gun pointing error and muzzle pointing error.

INTRODUCTION

Consider for the moment that you are on a test range firing the main gun from a prototype main battle tank moving over rough terrain. You just missed the target. Why? There are many factors that govern the probability of a projectile hitting an intended target. The projectile's trajectory, prevailing winds, aiming error, target motion, the motion of the firing platform, and propellant temperature are just some of the many variables which influence where the projectile will impact. The flight of the projectile after it leaves the muzzle and how the environment interacts with its trajectory has been the subject of extensive research. Today, if we were to launch a projectile from point 'A', wish it to impact point 'B', and know what the environment is between points 'A' and 'B', we can predict with a high degree of accuracy where we need to point the gun. Referring back to our original question and knowing that the projectile is flying as it should, we make the obvious conclusion that the gun is not pointed correctly. Yet the tank system outputs and on-board instrumentation are telling us that the gun is indeed pointed where it should be. Why did the projectile miss? This is where the story begins...

HISTORY OF FIRE CONTROL DESIGN AND TEST METHODS

The M60 and M1 series tanks have, for all intents and purposes, treated the gun tube as a rigid beam. The centerline of the tube bore is aligned with the gunner's sight. This boresight alignment is then periodically realigned using a Muzzle Reference System (MRS) to compensate for static deflections caused by uneven cooling or heating of the tube. The gun is offset relative to the line-of-sight so that the projectile will impact the target at some given range. The gun pointing direction consists of an offset to account for the ballistics involved to hit the target (called ballistic offset), a correction for parallax between sight and gun, and an additional offset for ballistic jump (called 'zero correction'). The ballistic jump is a correction from the boresight alignment to compensate for launch characteristics of a projectile type. The error or deviation of the total gun pointing direction from the line-of-sight is measured relative to the trunnion in the elevation axis and the turret structure for the azimuth axis. The gun control system attempts to drive these two errors to zero. The stabilization system does an efficient job of correcting for the pitch and yaw of the tank as it negotiates the terrain. Translation of the vehicle in the vertical and horizontal axis, referred to as heave and slip, respectively, is corrected by the gunner by his re-laying of the reticle on the target.

The disturbance imparted to the tube by the motion of the vehicle chassis and the gun drives causes flexing in the tube. With this control design, the flexing of the tube is not part of the feedback to the stabilization control.

The delivery accuracy of these systems is measured by the use of video cameras. One camera is used to capture the image the gunner sees in his primary sight, called the 'through-sight image'. This is done by the use of a beam splitter in the optical chain. The commander's extension, which already incorporates a beam splitter, is replaced with a camera for the M1 series tank. A second camera is mounted on the gun mantlet above the trunnion and aligned parallel to the bore centerline. This video signal is called the 'gun tube image'. These images are processed through contrast trackers to provide three digitized outputs: Gun Tube (GT), which is the gun pointing direction from the initial boresight alignment; Through-Sight (TS), which is the position of the aimpoint within the field-of-view relative to the initial boresight position; and Reticle (RT), which is the reticle position in the field-of-view of the through-sight video relative to the boresight position. The gunner's Lay Error (LE) or aim error can be determined from equation (1).

$$LE = TS - RT \qquad \text{Eq.(1)}$$

The Absolute Required Lead (ARL) is determined by measuring the change in position of the target relative to the tank from time = t to time = t + time of flight (tof) of the projectile in the future. The Total Gun Pointing Error (TGPE) or theoretical miss distance is computed using equation (2).

$$TGPE = GT - ARL - BO - Z \qquad \text{Eq.(2)}$$

Where 'BO' is the required Ballistic Offset, which includes the superelevation for the trajectory of the projectile and corrections for the environment (wind, barometric pressure, air temperature, and propellant temperature) and 'Z' is the zero correction factor.

Target Induced Error (TIE) is that portion of the TGPE resulting from relative target motion between time = t and time = t + tof that cannot be accounted for by the system equation (3).

$$TIE = ARL - dX(t)/dt * tof \qquad \text{Eq.(3)}$$

Tracking Rate Error (TRE) is the difference between the actual target rate and the gunner's tracking rate at time = t (see Eq.(4)).

$$TRE = dLE(t)/dt \qquad \text{Eq.(4)}$$

The System Required Lead (SRL) is the amount of lead that should be computed by the system. This is based on the actual traverse rate of the turret determined by the actual target rate plus the tracking rate error at time = t (see Eq.(5)).

$$SRL = (dX/dt + TRE(t)) * tof \qquad \text{Eq.(5)}$$

In addition to the parameters measured using the video system and vehicle/target locations, the system errors are also recorded. As discussed, these errors are measures between the sight reticle, trunnion, and turret structure. These errors are known as the System Implementation Errors (SIEs) and are the total gun pointing errors less the gunner's aiming error (see Eq. (6)).

$$SIE = TGPE + ARL - LE - SRL \qquad \text{Eq.(6)}$$

Beginning in the early 1990's, the U.S. and several foreign countries began gun development programs where the gun tube is 4 to 5 feet longer than the current fielded gun systems. Testing of a longer gun system was conducted at ATC in a similar fashion as thus far described and parallel tests were conducted on the M1A1 tank. During nonfiring tests, the SIEs were nominal and the tank appeared to be functioning efficiently. When firing actual ammunition, hit probability results were poor and did not reflect the nonfiring test results. Therefore, why were the projectiles missing the target?

AUTOMATIC/CONTINUOUS MUZZLE REFERENCE SENSOR DEVELOPMENT

During the same period of time, ATC was assisting the Army Research Laboratory in testing a Continuous Muzzle Reference System (CMRS) built by Princeton Scientific Instruments under a Small Business Innovative Research (SBIR) contract [2]. The instrument that was developed is capable of continuous measurement of muzzle motion with a dynamic range of ± 5 milliradians and a precision of 5 microradians at a bandwidth of 1000 Hz. Testing had begun in November 1989 using an M1A1 tank with the M256 gun. A second series of tests was conducted in March 1990. In 1993, ATC purchased two units for gun dynamics measurements. One of these units was put to use on the prototype long gun program to help characterize the gun tube flexure and control problem.

The CMRS is an autocollimator-type instrument with a point light source (Light-Emitting Diode (LED)) originating at the focus of a small diameter telescope and a position detector also located in the focal plane. The LED source is collimated to form a parallel beam aimed to strike a mirror mounted to the muzzle. The light is reflected back to the telescope and is re-imaged on the position detector located in the focal plane (see Figure 1). Figure 2 shows the circuit diagram for the unit.

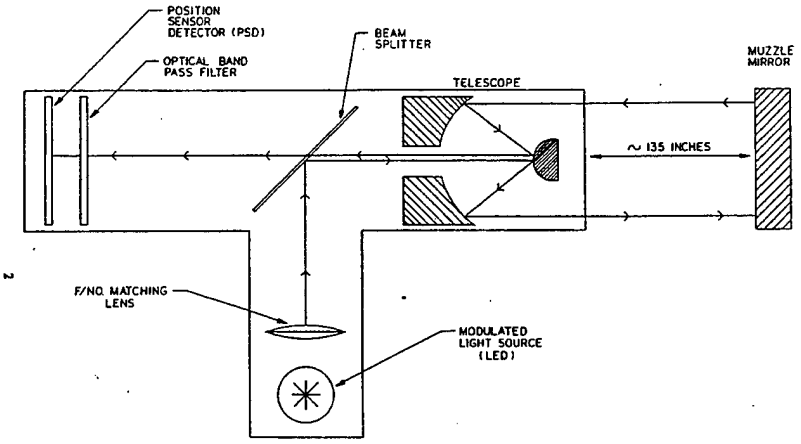

Figure 1. Schematic diagram of CMRS optics assembly

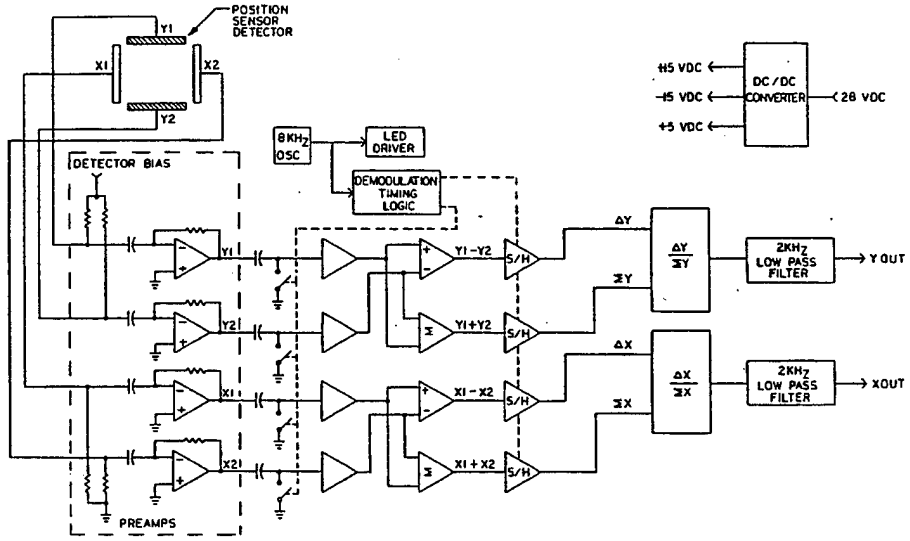

Figure 2. Circuit diagram of CMRS

Figures 3 and 4 show the transform functions of the detector in the elevation (y) and azimuth (x) axes, respectively.

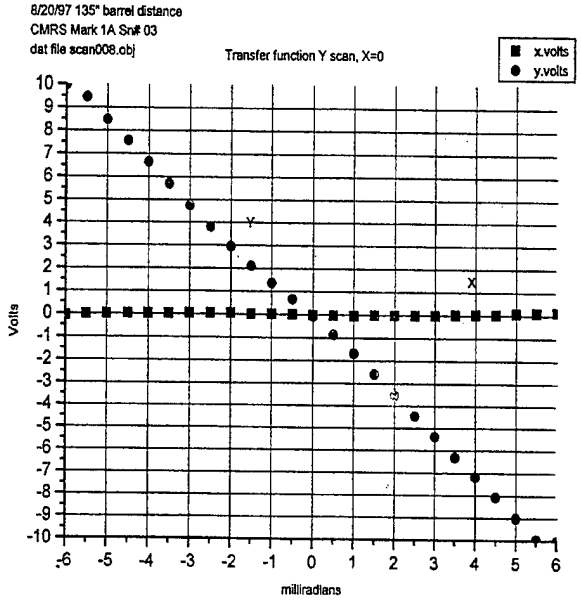

FIGURE 3. Transfer function 'Y' scan

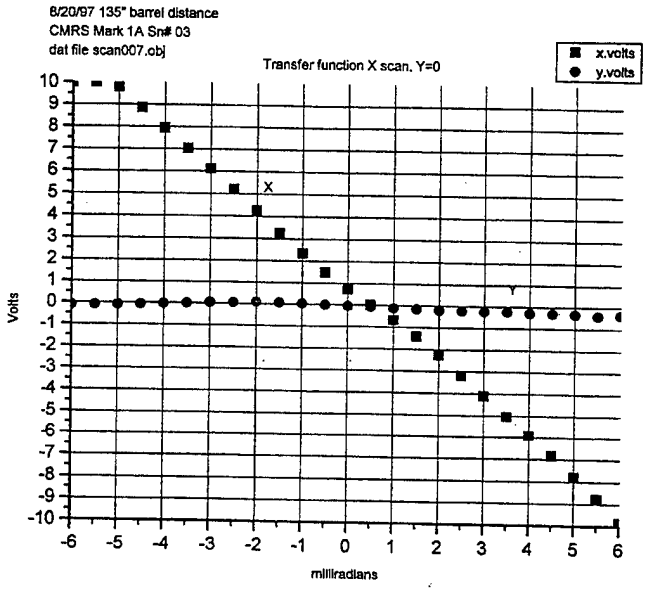

Figure 4. Transfer function 'X' scan

Using the CMRS unit allowed ATC to acquire gun flexure information on the gun and relate the muzzle pointing angle to the projectile miss distance. A sample of the data collected is presented in Figures 5 through 8 for 15mph and 20 mph over a bump course. Figures 6 and 8 show a detailed view of the section of time the tube goes into a resonance. From this information, the influence of the tube flexure becomes evident. But how does this compare to the M1A1 and the way delivery accuracy is measured?

DELIVERY ACCURACY CHARACTERIZATION WITH RESPECT TO THE MUZZLE

As discussed earlier in this paper, characterization of the delivery accuracy of a system was with respect to the trunnion and relative to the line-of-sight. This also reflects the way the stabilization and gun control had historically been implemented. As system specifications become more stringent, requiring higher hit probabilities at extended ranges, greater terminal effects, faster firing platforms, etc., the influence of the dynamics of the tube becomes more critical. An increased tube length simply amplifies the effect. To characterize the influence of the tube flexure in delivery accuracy, information was collected for various control systems and tube lengths for the prototype gun and also for two M1A1 production tanks. The standard deviations of the gun tube flexure and system errors measured in milliradians for complete test runs over the bump course at specified speeds are presented in Figures 9 through 12. A description of the configurations depicted on the graphs is as follows:

W/O – Denotes a control system that does not utilize the CMRS signal or any improved stabilization control design.

SHORT – Refers to a prototype gun tube that was manufactured to M256 length.

M1A1#1 and #2 – Two M1A1 production tanks with instrumentation added to collect the same parameters as measured on the prototype gun system.

To obtain a true gun pointing error, which reflects the delivery accuracy of the weapon system, gun pointing errors need to be relative to the muzzle pointing direction. In this light, we need to define some additional terms. The Muzzle Pointing Angle (MPA) is defined as the angle of the muzzle from the boresight alignment. The Total Muzzle Pointing Error (TMPE) would then be defined as:

$$TMPE = TGPE + MPA \qquad \text{Eq.(7)}$$

Particular attention must be paid to the sign convention of the MPA and must be the same as TGPE.

The System Implementation Error with respect to the Muzzle (SIE_m) would then be as follows:

$$SIE_m = TMPE + ARL - LE - SRL \qquad \text{Eq.(8)}$$

CONCLUSIONS

Fire control design is now taking into account the tube dynamics to improve delivery accuracy. To measure system accuracy in a non-firing environment, errors must be referenced to the muzzle to determine the performance of these designs. Determining pointing errors with respect to the muzzle rather than the trunnion is only the beginning in relating impacts to where the muzzle of the gun is pointing. Testing has shown that the shape of the tube as the projectile travels down the bore influences the jump of the projectile. The velocity component of the tube as it is flexing imparts an additional vector to the equation. Additional research needs to be done in these areas as well as in the cross-coupling effect that is seen when you reduce the flexure in one axis only to have the flexure in the other axis increase. I guess it is safe to say that the story does not end here....

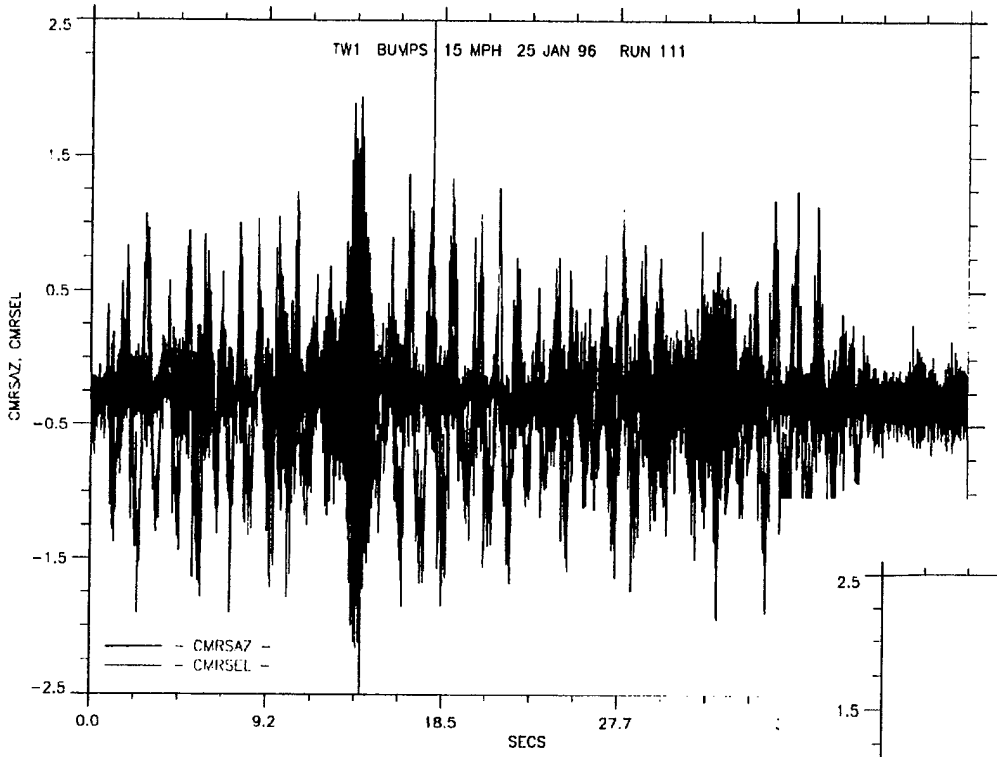

Figure 5. CMRS azimuth and elevation time history over RRC-9 bump course at 15 mph

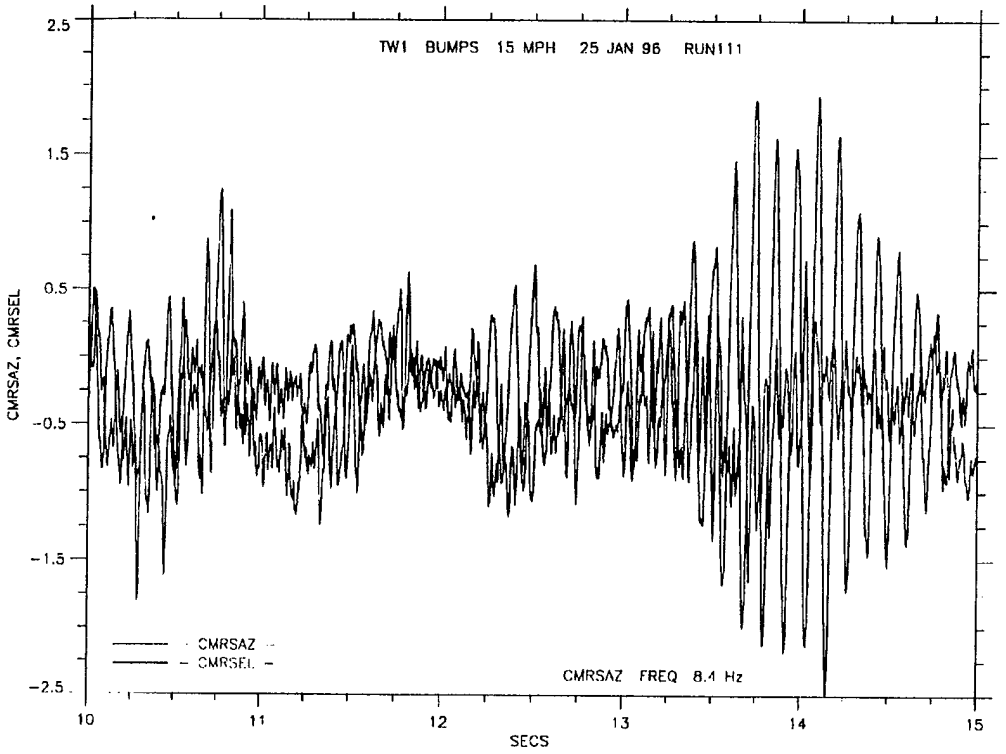

Figure 6. CMRS azimuth and elevation time history, detail view

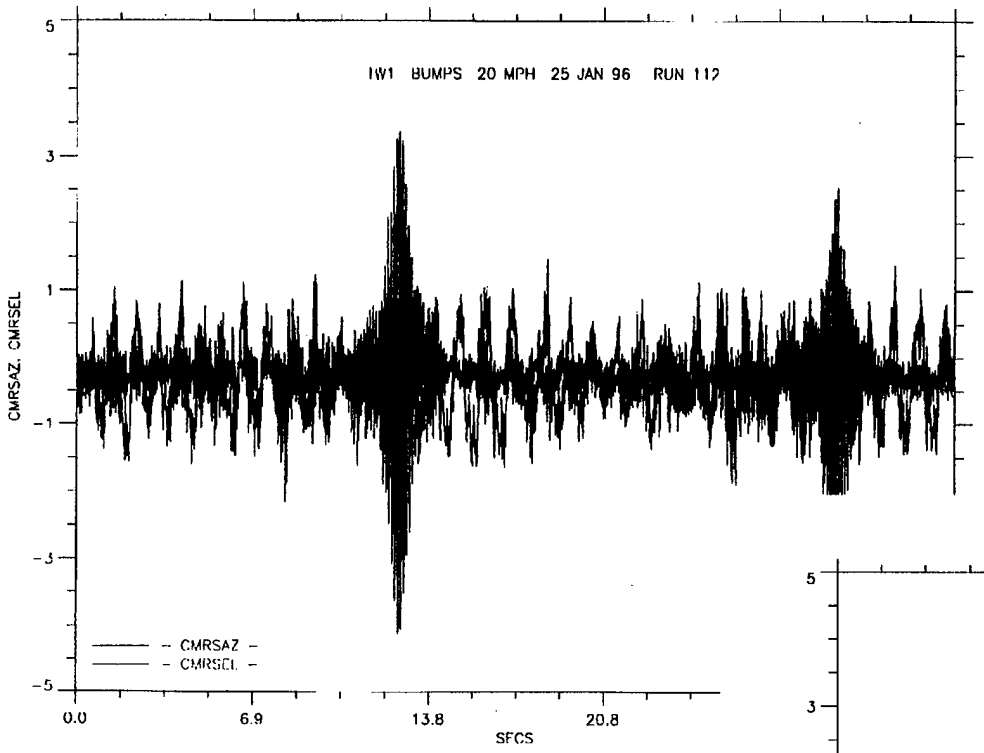

Figure 7. CMRS azimuth and elevation time history over RRC-9 bump course at 20 mph

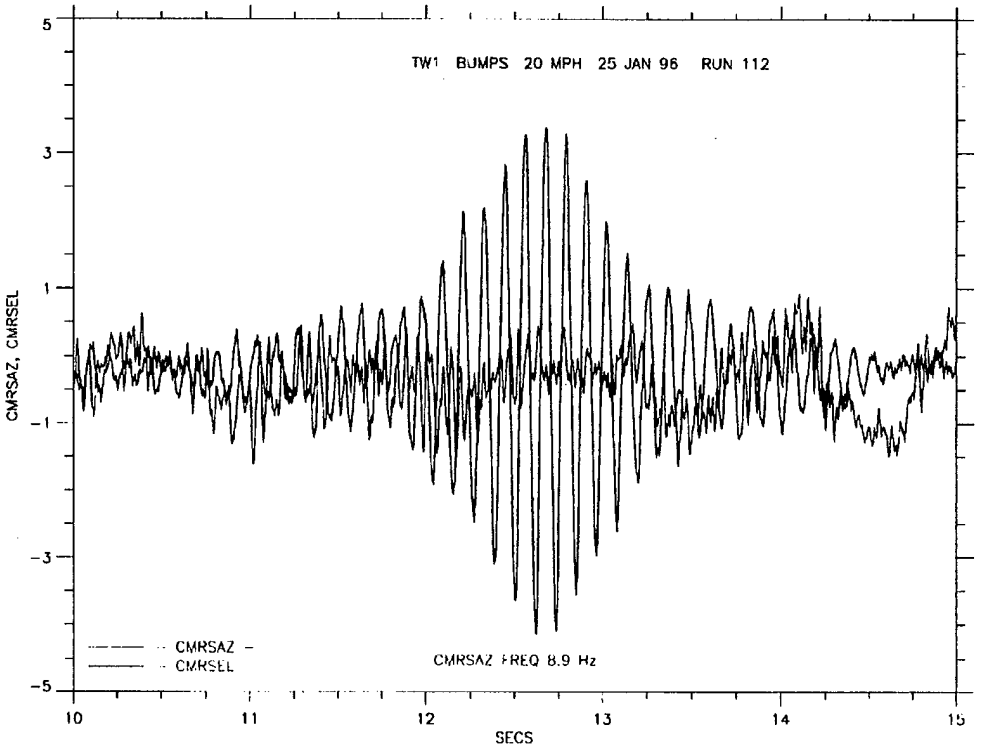

Figure 8. CMRS azimuth and elevation time history, detail view

Figure 9. CMRS azimuth average standard deviations

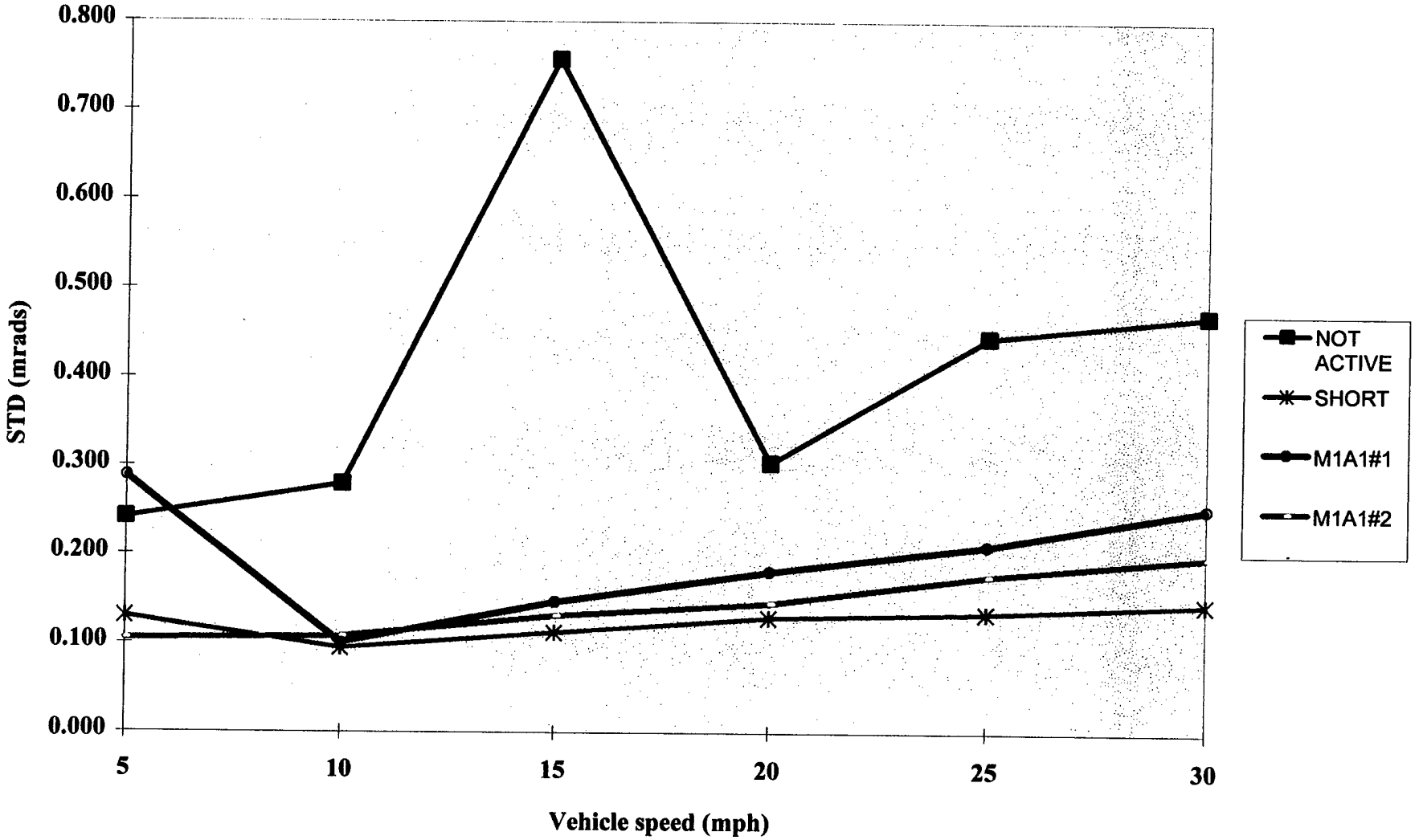

Figure 10. CMRS elevation average standard deviations

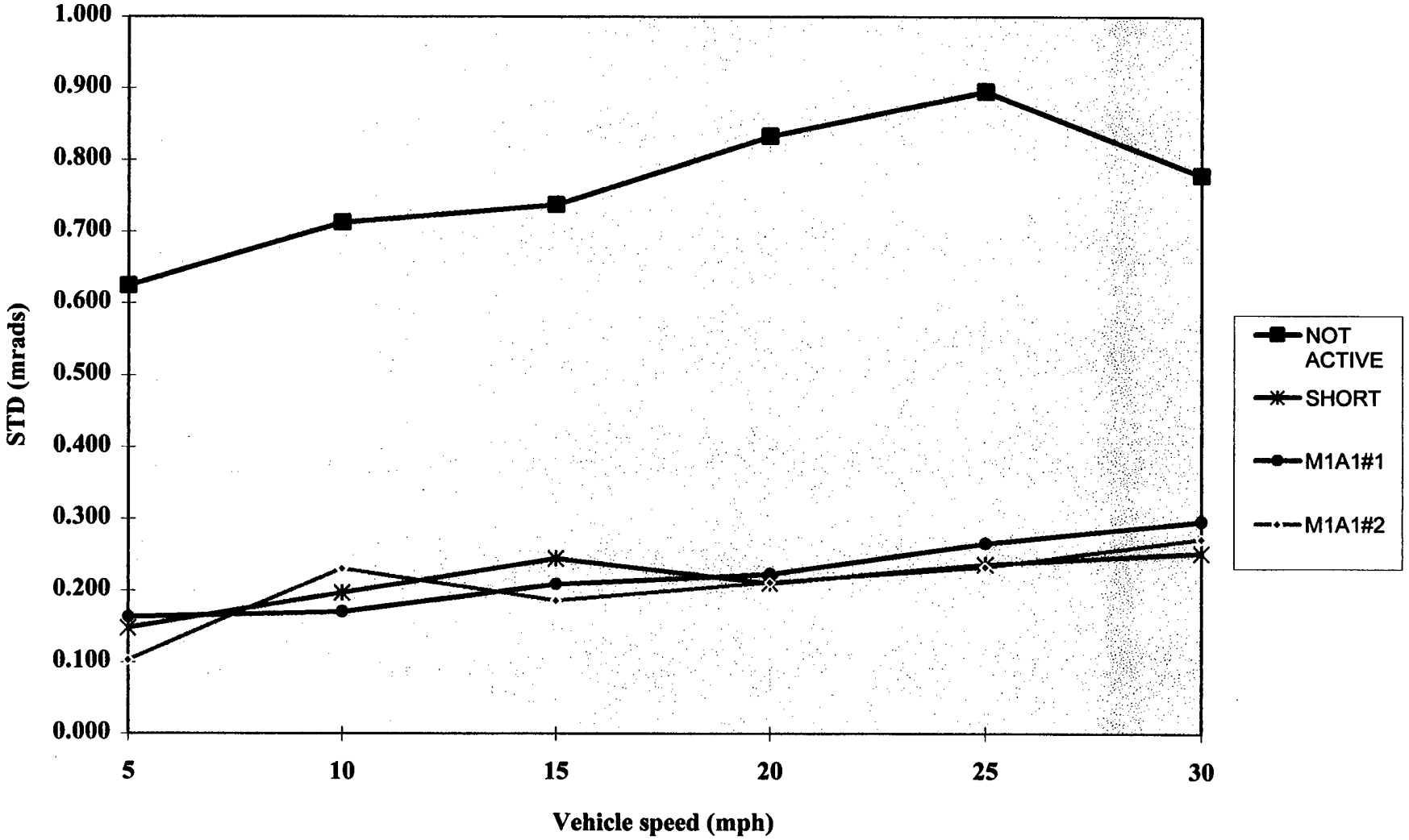

Figure 11. Azimuth error standard deviation

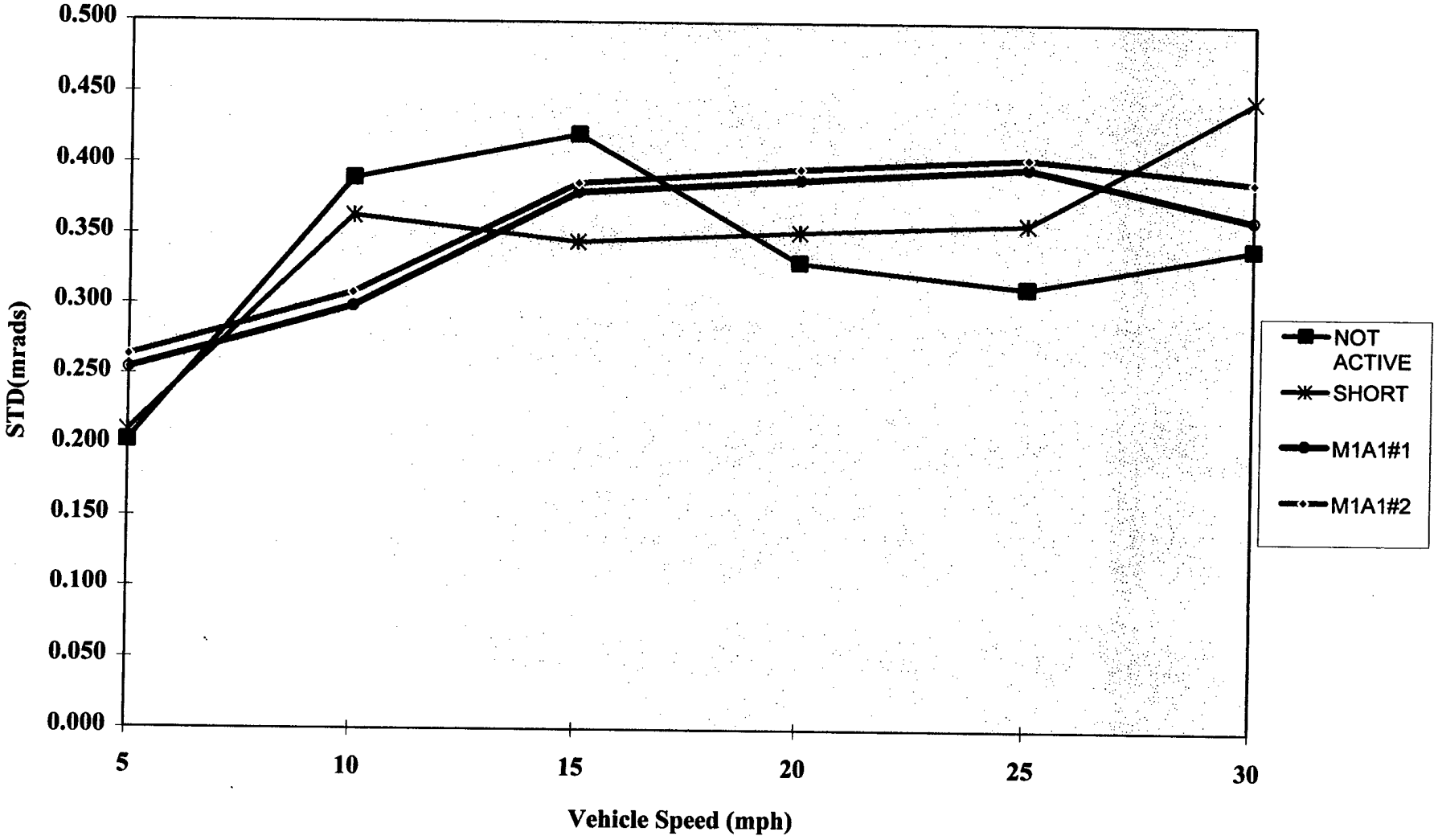

Figure 12. Elevation error standard deviation

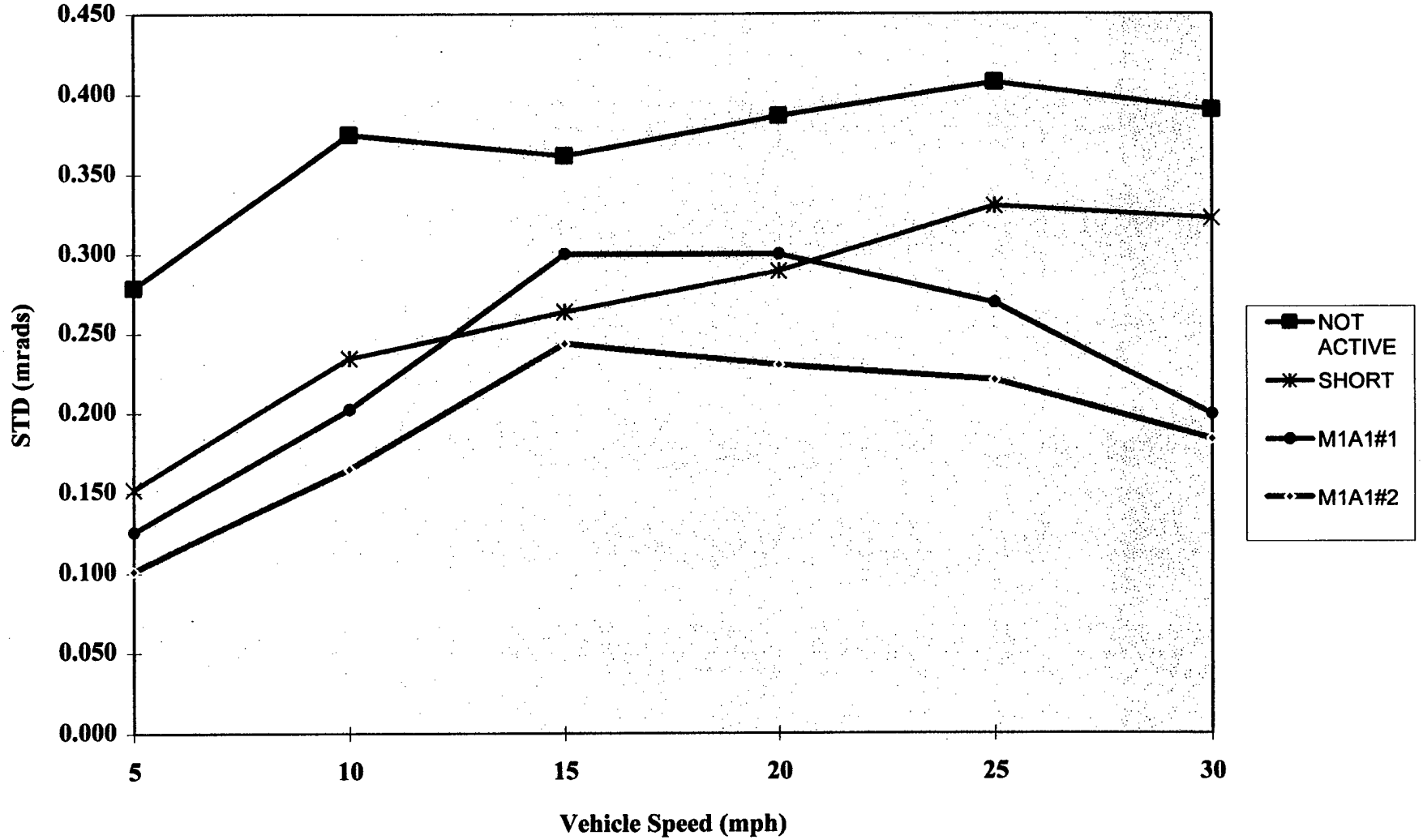

REFERENCES

[1] McCall, P.L., 1997, "Proof Of Principle Demonstration of the Advanced Tank Cannon System," ATC-7994, Aberdeen Test Center, Aberdeen Proving Ground, MD.

[2] Karcher, P.B. & Cope, A.D., 1990, "Continuous Muzzle Reference System (CMRS)," BRL-CR-643, Army Research Lab, Aberdeen Proving Ground, MD.

AN ASSESSMENT OF MAIN BATTLE TANK FLEXIBLE GUN TUBE DISTRUBANCE REJECTION

Dr. Henry J. Sneck
Benet Laboratories
Close Combat Armaments Center
Watervliet, NY 12189-4050

ABSTRACT

A rational approach to disturbance rejection is proposed and applied to a simple two degree-of-freedom model of a flexible gun tube using feedforward and feedback compensation. It is shown that ideally the effect of the disturbance can be removed from the actuated DOF, but not entirely from the free DOF. The analysis of a two degree-of-freedom flexible tube model serves to illustrate the inherent disturbance rejection limitations of existing actuation systems.

INTRODUCTION

Present day tank gun fire control systems are based on the assumption that the tube behaves as a rigid body. The vibrational characteristics of the gun are not directly factored into the control strategy. Purdy (1) has developed a simple model that incorporates the basic features of a flexible tube gun control system powered by a D.C. electric motor drive. This model offers the analyst an opportunity to investigate the affects of vehicular motion on a simple flexible tube model, as well as, the methods for mitigating its affects. The objective of this study is to assess the opportunities for improving shot accuracy of a flexible gun tube.

PURDY MODEL

A block diagram of the Purdy model is shown in Figure 1 along with some relevant dimensions and variable names.

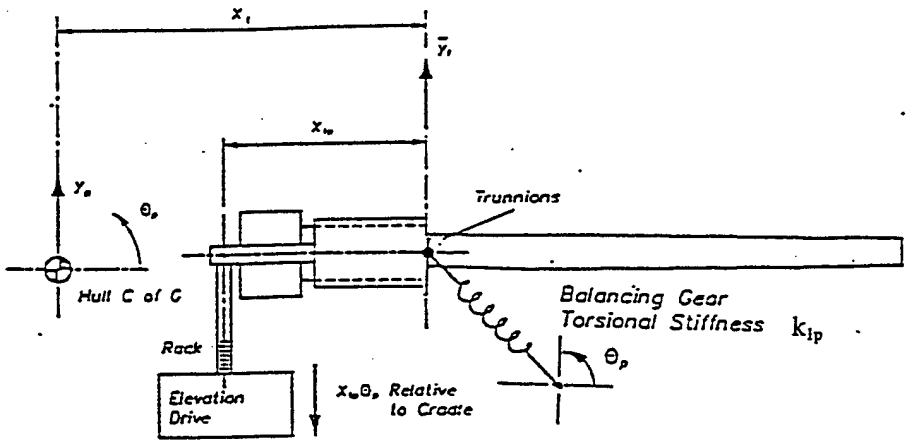

FIGURE 1–COUPLING OF THE HULL MOTION INTO THE ELEVATION MODEL

Figure 2, taken from Purdy [1], is a more detailed drawing of this model that shows the tube segmented into two rigid sections joined by a torsional spring and dashpot.

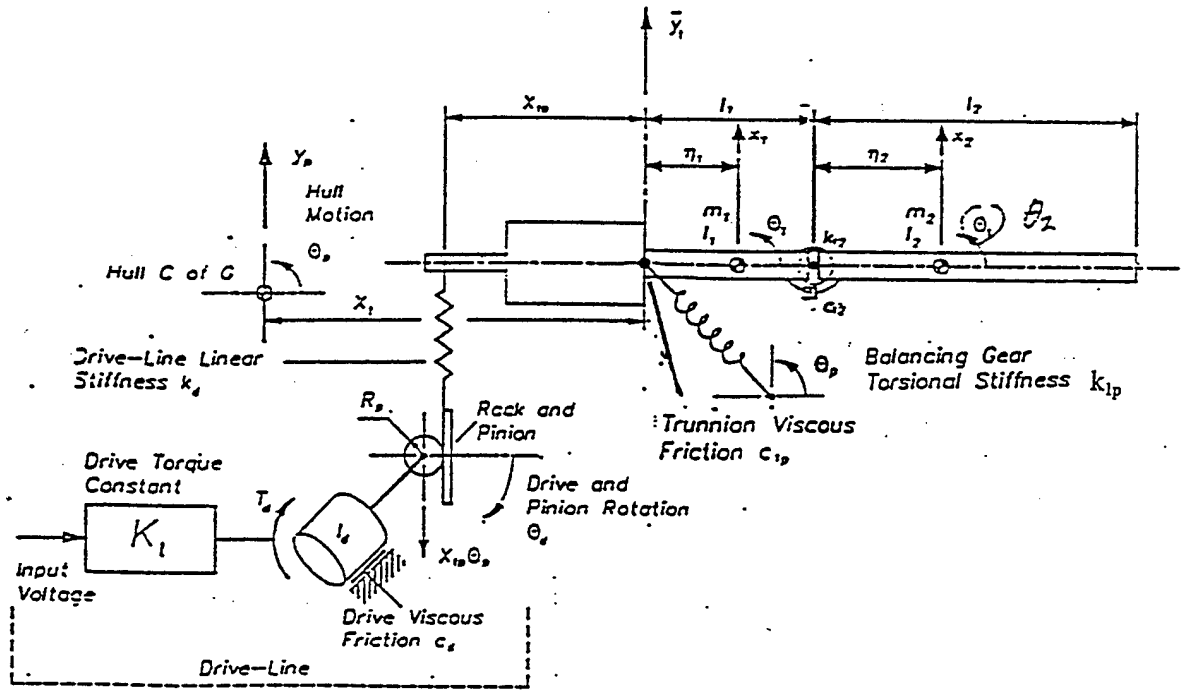

FIGURE 2–MBT ELEVATION MODEL WITH TWO SECTION BARREL

This model is at best, a crude representation of the first flexible mode of a gun tube. Despite this Purdy was able to obtain quite good matching of this simple model to a FEM model of the tube and drive system. The comparison is best at the lower frequencies (<40H_z). The model equations taken form Purdy [1][2] are reproduced below.

A free body diagram for the system, assuming small motions, is shown in Figure 3. The lateral force between sections is f_{12} and the vertical force at the trunnions is f_y.

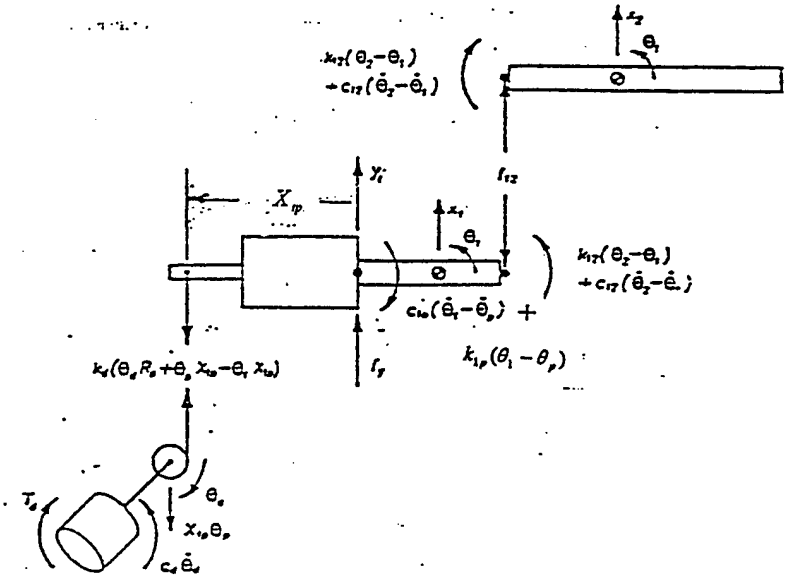

FIGURE 3–FREE BODY DIAGRAM OF THE ELEVATION MODEL FOR SMALL ROTATIONS (PURDY [1])

The equations of motion for the components of the system are:

drive;

$$I_d\ddot{\theta}_d = T_d - c_d\dot{\theta}_d - k_d(\theta_d R_p + \theta_p X_{tp} - \theta_1 X_{tp})R_p \tag{1}$$

breech section;

$$\begin{aligned} m_1\ddot{x}_1 &= f_y - k_{d1}(\theta_d R_p + \theta_p X_{tp} - \theta_1 X_{tp}) - f_{12} \\ I_1\ddot{\theta}_1 &= k_d(\theta_d R_p + \theta_p X_{tp} - \theta_1 X_{tp})(X_{tp} + \eta_1) - c_{1p}(\dot{\theta}_1 - \dot{\theta}_p) - k_{1p}(\theta_1 - \theta_p) \\ &- f_y\eta_1 - f_{12}(l_1 - \eta_1) + k_{12}(\theta_2 - \theta_1) + c_{12}(\dot{\theta}_2 - \dot{\theta}_1) \end{aligned} \tag{2}$$

muzzle section;

$$\begin{aligned} m_2\ddot{x}_2 &= f_{12} \\ I_2\ddot{\theta}_2 &= f_{12}\eta_2 - k_{12}(\theta_2 - \theta_1) - c_{12}(\dot{\theta}_2 - \dot{\theta}_1) \end{aligned} \tag{3}$$

The equations of constraint for the breech and muzzle sections are;

$$\begin{aligned} y_t &= x_1 - \theta_1\eta_1 \\ y_t + l_1\theta_1 &= x_2 - \eta_2\theta_2 \end{aligned} \tag{4}$$

The equations of motion for the system are obtained by eliminating the linear coordinates x_1 and x_2 to give;

$$M_1\{\ddot{\theta}\} + C_1\{\dot{\theta}\} + K_1\{\theta\} = I_1\{u\} \tag{5}$$

where the mass M_1, damping C_1, stiffness K_1, and input I_1 matrices are given by;

$$M_1 = \begin{bmatrix} I_d & 0 & 0 \\ 0 & I_1 + m_1\eta_1^2 + m_2 l_1^2 & m_2 l_1\eta_2 \\ 0 & m_2 l_1\eta_2 & I_2 + m_2\eta_2^2 \end{bmatrix} \quad C_1 = \begin{bmatrix} c_d & 0 & 0 \\ 0 & c_{12} + c_{1p} & -c_{12} \\ 0 & -c_{12} & c_{12} \end{bmatrix} \tag{6}$$

$$K_1 = \begin{bmatrix} k_d R_p^2 & -k_d R_p X_{tp} & 0 \\ -k_d R_p X_{tp} & k_{12} + k_d X_{tp}^2 + k_{1p} & -k_{12} \\ 0 & -k_{12} & k_{12} \end{bmatrix} \quad I_1 = \begin{bmatrix} 1 & 0 & 0 & -k_d X_{tp} R_p \\ 0 & -(m_1\eta_1 + m_2 l_1) & c_{1p} & k_d X_{tp}^2 + k_{1p} \\ 0 & -m_2\eta_2 & 0 & 0 \end{bmatrix}$$

and the vector of output rotations and inputs are given by

$$\{\theta(t)\} = \begin{Bmatrix} \theta_d(t) \\ \theta_1(t) \\ \theta_2(t) \end{Bmatrix} \quad \{u(t)\} = \begin{Bmatrix} T_d(t) \\ \ddot{y}_t(t) \\ \dot{\theta}_p(t) \\ \theta_p(t) \end{Bmatrix} \tag{7}$$

The elements of these vectors are:

$\theta_d(t)$ = drive motor armature displacement .

$\theta_1(t)$ = tube angular displacement at the trunnion.

$\theta_2(t)$ = tube angular displacement at muzzle (MRS).

$T_d(t)$ = drive motor armature torque.

$\ddot{y}_t(t)$ = trunnion vertical acceleration.

$\dot{\theta}_p(t)$ == turret pitch rate.

$\theta_p(t)$ = turret pitch angle.

The left side of the matrix equation can be represented in the frequency domain by

$$\begin{bmatrix} a_{11} & a_{12} & 0 \\ a_{21} & a_{22} & a_{23} \\ 0 & a_{32} & a_{33} \end{bmatrix} \begin{Bmatrix} \theta_d \\ \theta_1 \\ \theta_2 \end{Bmatrix} = [a]\{\theta\} \tag{8}$$

The elements of the symmetric [a] matrix are

$$\begin{aligned} a_{11} &= I_d s^2 + c_d s + k_d R_p^2 \\ a_{12} &= a_{21} = -k_d R_p X_{tp} \\ a_{13} &= a_{31} = o \\ a_{22} &= (I_1 + m_1\eta_1^2 + m_2 l_1^2)s^2 + (C_{12} + C_{1p})s + k_{12} + k_d X_{tp}^2 + k_{1p} \\ a_{23} &= a_{32} = m_2 l_1 \eta_2 s^2 - C_{12} s - k_{12} \\ a_{33} &= (I_2 + m_2\eta_2^2)s^2 + C_{12} s + k_{12} \end{aligned} \tag{9}$$

The right hand side of the matrix equation can be represented in the frequency domain by

$$\begin{bmatrix} I_{11} & 0 & 0 & I_{14} \\ 0 & I_{22} & I_{23} & I_{24} \\ 0 & I_{32} & 0 & 0 \end{bmatrix} \begin{Bmatrix} T_d \\ s^2 Y_t \\ s\theta_p \\ \theta_p \end{Bmatrix} = [I_i]\{U\} \tag{10}$$

The elements of the $[I_i]$ matrix are:

$$
\begin{aligned}
I_{11} &= 1 \\
I_{14} &= k_d X_{tp} R_p = a_{12} = a_{21} \\
I_{22} &= -(m_1 \eta_1 + m_2 l_1) \\
I_{23} &= C_{1p} \\
I_{24} &= k_d X_{tp}^2 + k_{1p} \\
I_{32} &= -m_2 \eta_2
\end{aligned}
\tag{11}
$$

MODEL RESPONSE WITHOUT THE DISTURBANCE

In the absence of the disturbances the response is determined by the equations:

$$
\begin{aligned}
& k_d R_p^2 \theta_d - k_d R_p X_{tp} \theta_1 = T_d \\
& -k_d R_p X_{tp} \theta_d + (k_{1p} + k_{12} + k_d X_{tp}^2)\theta_1 - k_{12}\theta_2 = 0 \\
& -k_{12}\theta_1 + k_{12}\theta_2 = 0
\end{aligned}
\tag{12}
$$

At static equilibrium, when the balance spring k_{1p} causes $\theta_1 = \theta_2 = 0$, both θ_d and T_d are also zero. The tube is then straight, horizontal and aimed at a target at trunnion level. Hence, T_d in the dynamic equations represents the dynamic portion of the motor armature torque, while θ_1, θ_2 and θ_d are measured from their static equilibrium references as shown in Figure 2.

SOLUTION FOR THE DYNAMIC RESPONSE OF THE GUN SYSTEM

The steady state response of the system is

$$
\begin{Bmatrix} \theta_d \\ \theta_1 \\ \theta_2 \end{Bmatrix} = [a]^{-1} [I_i] \begin{Bmatrix} T_d \\ s^2 Y_t \\ s\theta_p \\ \theta_p \end{Bmatrix}
\tag{13}
$$

$$
or \quad \{\theta\} = [a]^{-1} [I_i] \{U\}
\tag{14}
$$

The cofactors of the matrix [a] are

$$
\begin{aligned}
C_{11} &= a_{22}a_{33} - a_{23}a_{32} & C_{22} &= a_{11}a_{33} \\
C_{12} &= C_{21} = -a_{12}a_{33} & C_{23} &= C_{32} = -a_{11}a_{32} \\
C_{13} &= C_{31} = a_{21}a_{32} & C_{33} &= a_{11}a_{22} - a_{12}a_{21}
\end{aligned}
\tag{15}
$$

The determinant of [a] is

$$
\det[a] = a_{11}(a_{22}a_{33} - a_{23}a_{32}) - a_{12}a_{21}a_{53}
\tag{16}
$$

In matrix form the solution or the total response is, symbolically

$$\begin{Bmatrix}\theta_d\\ \theta_1\\ \theta_2\end{Bmatrix} = \frac{1}{\det[a]}\begin{bmatrix}C_{11} & C_{21} & C_{31}\\ C_{12} & C_{22} & C_{32}\\ C_{13} & C_{23} & C_{33}\end{bmatrix}\begin{bmatrix} I_{11} & 0 & 0 & I_{14}\\ 0 & I_{22} & I_{23} & I_{24}\\ 0 & I_{32} & 0 & 0\end{bmatrix}\begin{Bmatrix}T_d\\ s^2Y_t\\ s\theta_p\\ \theta_p\end{Bmatrix}$$

$$= \begin{bmatrix}B_{11} & B_{12} & B_{13} & B_{14}\\ B_{21} & B_{22} & B_{23} & B_{24}\\ B_{31} & B_{32} & B_{33} & B_{34}\end{bmatrix}\begin{Bmatrix}T_d\\ s^2Y_t\\ s\theta_p\\ \theta_p\end{Bmatrix} \qquad (17)$$

or

$$\{\theta\} = [B]\{U\}$$

The elements of the matrix [B] are listed in Appendix A.

PLANT AND DISTURBANCE TRANSFER FUNCTIONS

The portion of the response due to the torque is

$$\{\theta_T\} = \begin{bmatrix}B_{11}\\ B_{21}\\ B_{31}\end{bmatrix}T_d = [G_p]T_d \qquad (18)$$

The portion of the response due to the disturbance is

$$\{\theta_D\} = \begin{bmatrix}B_{12} & B_{13} & B_{14}\\ B_{22} & B_{23} & B_{24}\\ B_{32} & B_{33} & B_{34}\end{bmatrix}\begin{Bmatrix}s^2Y_t\\ s\theta_p\\ \theta_p\end{Bmatrix} = [G_D]\{D\} \qquad (19)$$

CONTROL OBJECTIVE

The objective of the aiming control strategy is to maintain $\theta_1 = \theta_2 = 0$ in the presence of the disturbance {D} with the appropriately applied dynamic motor displacement θ_d and armature torque T_d.

FEEDBACK AND FEEDFORWARD CONTROL

The block diagram below incorporates two commonly used control strategies, i.e. feedback and feedforward.

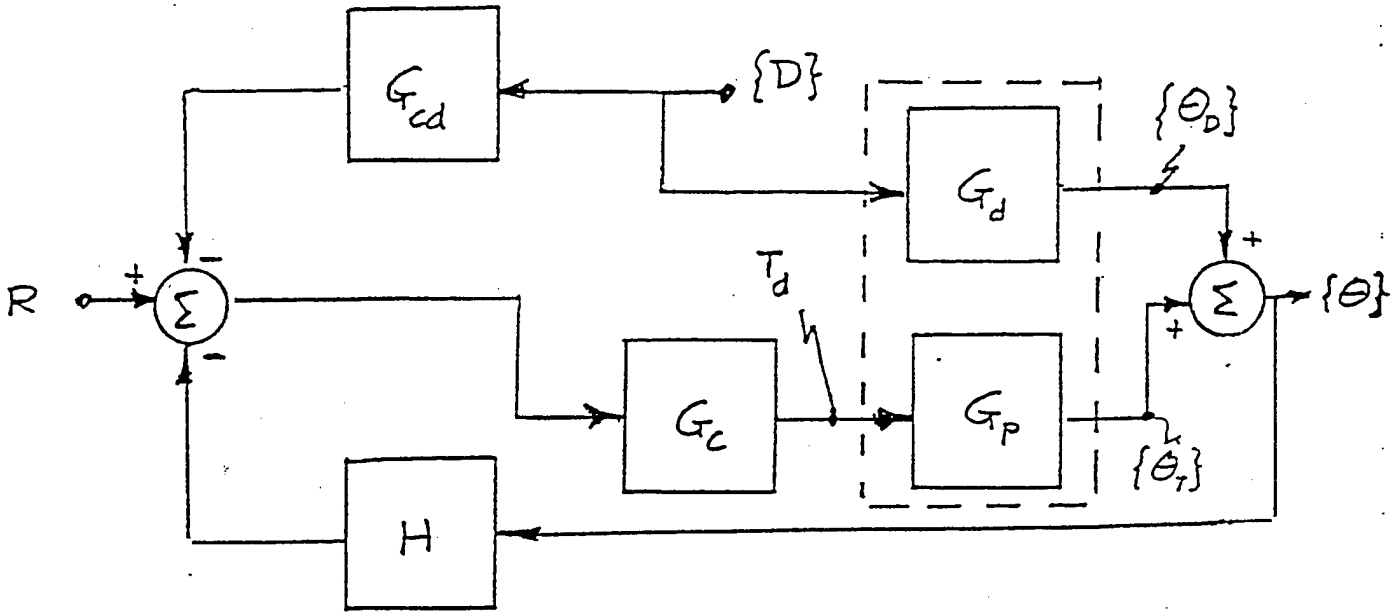

Figure 4 – Block Diagram of Gun System with Controllers.

The control references for feedback are $\theta_1 = \theta_2 = 0$. If either or both of these are not zero a torque must be applied to the plant. Since the torque is a scalar the feedback transfer function is chosen to be:

$$[H] = [0\ G_{22}\ G_{23}] \tag{20}$$

where G_{22} and G_{23} are, as yet, undetermined transfer functions.

Since the reference and torque are scalars let the feedforward transfer functions be:

$$[G_{cd}] = [G_{11}\ G_{12}\ G_{13}] \tag{21}$$

where G_{11}, G_{12}, and G_{13} are also undetermined transfer functions.

The response to the disturbance for the controlled system is

$$\left[[G_d] - [G_p][G_c][G_{cd}]\right]\{D\} = \left[[I] + [G_p][G_c][H]\right]\{\theta_D\} \tag{22}$$

In this equation $[G_c]$ is a scalar and [I] is the identity matrix. The left side of the equation is

$$\begin{bmatrix} B_{12}-B_{11}G_cG_{11} & B_{13}-B_{11}G_cG_{12} & B_{14}-B_{11}G_cG_{13} \\ B_{22}-B_{21}G_cG_{11} & B_{23}-B_{21}G_cG_{12} & B_{24}-B_{21}G_cG_{13} \\ B_{32}-B_{31}G_cG_{11} & B_{33}-B_{31}G_cG_{12} & B_{34}-B_{31}G_cG_{13} \end{bmatrix}\{D\}$$

$$or \qquad (23)$$

$$=[d]\{D\}$$

The matrix on the right side of the equation reduces to

$$[q]=\begin{bmatrix} 1 & B_{11}G_cG_{22} & B_{11}G_cG_{23} \\ 0 & 1+B_{21}G_cG_{22} & B_{21}G_cG_{23} \\ 0 & B_{31}G_cG_{22} & 1+B_{31}G_cG_{23} \end{bmatrix} \qquad (24)$$

The solution for the response to the disturbance is

$$\{\theta_D\}=[q]^{-1}[d]\{D\} \qquad (25)$$

The cofactors of [q] are

$$\begin{aligned} r_{11} &= 1+B_{31}G_cG_{23}+B_{21}G_cG_{22} \\ r_{12} &= r_{13}=0 \\ r_{21} &= -B_{11}G_cG_{22} \\ r_{22} &= 1+B_{31}G_cG_{23} \\ r_{23} &= -B_{31}G_cG_{22} \\ r_{31} &= -B_{11}G_cG_{23} \\ r_{32} &= -B_{21}G_cG_{23} \\ r_{33} &= 1+B_{21}G_cG_{22} \end{aligned} \qquad (26)$$

In terms of the cofactors the disturbance response is, symbolically

$$\{\theta_D\}=\frac{1}{\det[q]}\begin{bmatrix} r_{11} & r_{21} & r_{31} \\ 0 & r_{22} & r_{32} \\ 0 & r_{23} & r_{33} \end{bmatrix}\begin{bmatrix} d_{11} & d_{12} & d_{13} \\ d_{21} & d_{22} & d_{23} \\ d_{31} & d_{32} & d_{33} \end{bmatrix}\{D\} \qquad (27)$$

$$where\ \det[q]=1+B_{31}G_cG_{23}+B_{21}G_cG_{22}=r_{11} \qquad (28)$$

DISTURBANCE REJECTION CRITERIA

To reject the influence of the disturbance on θ_1 each of the following sums must equal zero, i.e., $R_{11}=R_{12}=R_{13}=0$

$$\frac{1}{\det[q]}(r_{22}d_{21} + r_{32}d_{31}) = R_{11}$$

$$\frac{1}{\det[q]}(r_{22}d_{22} + r_{32}d_{32}) = R_{12} \qquad (29)$$

$$\frac{1}{\det[q]}(r_{22}d_{23} + r_{32}d_{33}) = R_{13}$$

To reject the influence of the disturbance on θ_2 each of the following sums must equal zero, i.e., $R_{21} = R_{22} = R_{23} = 0$

$$\frac{1}{\det[q]}(r_{23}d_{21} + r_{33}d_{31}) = R_{21}$$

$$\frac{1}{\det[q]}(r_{23}d_{22} + r_{33}d_{32}) = R_{22} \qquad (30)$$

$$\frac{1}{\det[q]}(r_{23}d_{23} + r_{33}d_{33}) = R_{23}$$

To make the rejection equations consistent requires that the following expression be true

$$\frac{r_{22}}{r_{23}} = \frac{r_{32}}{r_{33}} \qquad (31)$$

or

$$(1 + B_{31}G_cG_{23})(1 + B_{21}G_cG_{22}) = (B_{31} + G_cG_{22})(B_{21}G_cG_{23})$$

or

$$1 + B_{31}G_cG_{23} + B_{21}G_cG_{22} = 0 = \det[q]$$

Since we cannot permit determinate [q] to be zero it will not be possible to completely reject the affect of the disturbance on both θ_1 and θ_2.

DISTURBANCES $\dot{\theta}_p$ *and* θ_p

The equation that is related to $\dot{\theta}_p$ can be reduced to

$$\frac{a_{33}}{\det[a]}\ (a_{11}\,I_{23} + a_{12}I_{11}G_cG_{12}) = -R_{12} \qquad (32)$$

and

$$\frac{a_{32}}{\det[a]}(a_{11}I_{23} + a_{12}I_{11}G_cG_{12}) = R_{22} \qquad (33)$$

Hence, the affect of $\dot{\theta}_p$ on θ_1 and θ_2 can be eliminated by choosing

$$G_c G_{12} = -\frac{a_{11} I_{23}}{a_{12} I_{11}} \tag{34}$$

The equations related to θ_p can be reduced to

$$\frac{a_{33}}{\det[a]}(-a_{12} I_{14} + a_{11} I_{24} + a_{12} I_{11} G_c G_{13}) = -R_{13} \tag{35}$$

and

$$\frac{a_{32}}{\det[a]}(-a_{12} I_{14} + a_{11} I_{24} + a_{21} I_{11} G_c G_{13}) = R_{23} \tag{36}$$

The affect of θ_p on θ_1 and θ_2 can be eliminated if

$$G_c G_{13} = \frac{a_{12} I_{14} - a_{11} I_{24}}{a_{12} I_{11}} \tag{37}$$

Bode plots of G_cG_{12} and and G_cG_{13} for the Purdy model are shown in Appendix B.

DISTURBANCE $\ddot{y}_t$

The determinant det [q] as note earlier is

$$\det[q] = 1 + B_{31} G_c G_{23} + B_{21} G_c G_{22} \tag{38}$$

When the θ_1 and θ_2 equations for the response to $\ddot{y}_t$ are substituted into this expression the results is

$$B_{21} R_{21} - B_{31} R_{11} = B_{31} B_{22} - B_{21} B_{32} \tag{39}$$

There are three possible solutions of this equation.

1. If $R_{21} = 0$, then

$$R_{11} = \frac{B_{21} B_{32} - B_{31} B_{22}}{B_{31}} = \frac{I_{11} I_{32}}{a_{32}} \tag{40}$$

where

$$a_{32} = m_2 l_1 \eta_2 s^2 - c_{12} s - k_{12} \tag{41}$$

Since a_{32} has a change of sign the response θ_1 is unstable, as expected.

2. If, on the other hands, $R_{11} = 0$, then

$$R_{21} = \frac{B_{31}B_{22} - B_{21}B_{23}}{B_{21}} = -\frac{I_{32}}{a_{33}} \tag{42}$$

which is stable. The feed forward transfer function G_cG_{11} becomes

$$G_cG_{11} = \frac{1}{B_{21}}(B_{22} + K_{11}G_cG_{23}) \tag{43}$$

where

$$K_{11} = B_{31}B_{22} - B_{21}B_{32} = \frac{I_{11}I_{32}a_{12}}{\det[a]} \tag{44}$$

A Bode plot of B_{22}/B_{21} is shown on Appendix C. The bode plot of R_{21} in Appendix C shows that the affect of the trunnion acceleration on θ_2 is substantially attenuated by this choice of G_cG_{11}.

3. The third possible solution is

$$R_{11} = -B_{22} = -\frac{C_{22}I_{22} + C_{32}I_{32}}{\det[a]} \tag{45}$$

$$R_{21} = -B_{32} = -\frac{C_{23}I_{22} + C_{33}I_{32}}{\det[a]} \tag{46}$$

which yields the feed forward transfer function

$$G_cG_{11} = -B_{22}G_{22} - B_{32}G_{23} \tag{47}$$

Bode plots of R_{11} and R_{21} for this case are shown in Appendix D using Purdy's data and $k_{1p} = 2.1(10^5)\ Nm/rad$. The magnitude of the low frequency asymptote is determined by the value of k_{1p}.

RESPONSE OF θ_d TO THE DISTURBANCE

The drive motor displacement is given by

$$\theta_d = \left(\frac{r_{11}d_{11} + r_{21}d_{21} + r_{31}d_{31}}{\det[q]}\right)s^2Y_t + \left(\frac{r_{11}d_{21} + r_{21}d_{22} + r_{31}d_{32}}{\det[q]}\right)s\theta_p + \left(\frac{r_{11}d_{13} + r_{21}d_{23} + r_{31}d_{33}}{\det[q]}\right)\theta_p \tag{48}$$

However, $d_{22} = d_{32} = d_{23} = d_{33} = 0$. Evaluation of the remaining terms yields

$$\theta_d = \left(\frac{I_{22}a_{33} - I_{32}a_{32}}{a_{12}a_{33}}\right)s^2 Y_t - \left(\frac{I_{23}}{a_{12}}\right)s\theta_p + \left(\frac{I_{24}}{a_{12}}\right)\theta_p \quad (49)$$

The second and third coefficients are constants. The first coefficient is a proper transfer function, i.e. the order of the numerator and denominator are equal (See Appendix E).

REQUIRED MOTOR RESPONSE TO THE DISTURBANCE

The mortar armature torque T_d, current I_d, and voltage E_2 are determined by

$$T_d = K_t I_d = a_{11}\theta_d + a_{12}(\theta_1 - \theta_p)$$
$$K_t E_d = s\theta_d \quad (50)$$

In steady state $\theta_1 = 0$. Because θ_d is uncontrollable the current and voltage required to drive the gun are also uncontrollable and dependent only upon the system parameters.

CONCLUSIONS

1. The affects of the *pitch and pitch rate* can be eliminated form the model by the appropriate choice of the feed forward transfer functions G_cG_{12} and G_cG_{13}, which depend only on the mechanical properties of the tube

2. The affect of the *trunnion acceleration* cannot be eliminated from the muzzle segment of the model because of a tube-induced instability.

3. The affect of the *trunnion acceleration* can be eliminated from the trunnion segment of the model by the appropriate choice of the feed forward transfer function G_cG_{11} which depends on the tube mechanical properties and the feedback transfer function G_cG_{23}.

4. Since the *feed forward transfer functions* are improper their realization will require filtering at higher frequencies.

5. The affects of the *trunnion acceleration* can be distributed over both segments by the proper selection of G_cG_{11} which depends on the tube mechanical properties and the feedback transfer functions G_cG_{22} and G_cG_{23}

6. The ability of the D.C. motor to respond to the required torque and angle demands is crucial to the successful implementation of any control system. That problem is not addressed here.

7. The results of this analysis identify the inherent limitations imposed by the model on attempts to reject the disturbances, and provide a rational basis for choosing the feed forward transfer functions subject to these limitation.

8. The results of this analysis suggest the difficulties that maybe encountered designing actual tube disturbance rejection systems.

REFERENCES

1. Purdy, D.J., Modeling and Simulation of a Weapon Control System for a Main Battle Tank, Proc. 8th U.S. Army Symposium on Gun Dynamics, ARCCB-SP-96032, pgs. 20-1 to 20-19, May 1996.

2. Purdy, D.J., An Investigation into the Modeling and Control of Flexible Bodies, PhD Thesis, Cranfield University, England, 1994.

APPENDIX A. Matrix [B]

The elements of Matrix [B] are

$$B_{11} = \frac{C_{11}I_{11}}{\det[a]} \quad B_{21} = \frac{C_{12}I_{11}}{\det[a]} \quad B_{31} = \frac{C_{13}I_{11}}{\det[a]}$$

$$B_{12} = \frac{C_{21}I_{22} + C_{13}I_{32}}{\det[a]}$$

$$B_{22} = \frac{C_{22}I_{22} + C_{32}I_{32}}{\det[a]}$$

$$B_{32} = \frac{C_{23}I_{22} + C_{33}I_{32}}{\det[a]}$$

$$B_{13} = \frac{C_{21}I_{23}}{\det[a]}$$

$$B_{23} = \frac{C_{22}I_{23}}{\det[a]}$$

$$B_{33} = \frac{C_{23}I_{23}}{\det[a]}$$

$$B_{14} = \frac{C_{11}I_{14} + C_{21}I_{24}}{\det[a]}$$

$$B_{24} = \frac{C_{12}I_{14} + C_{22}I_{24}}{\det[a]}$$

$$B_{34} = \frac{C_{13}I_{14} + C_{23}I_{24}}{\det[a]}$$

APPENDIX B TRANSFER FUNCTION $G_c G_{12}$ FOR THE PURDY MODEL

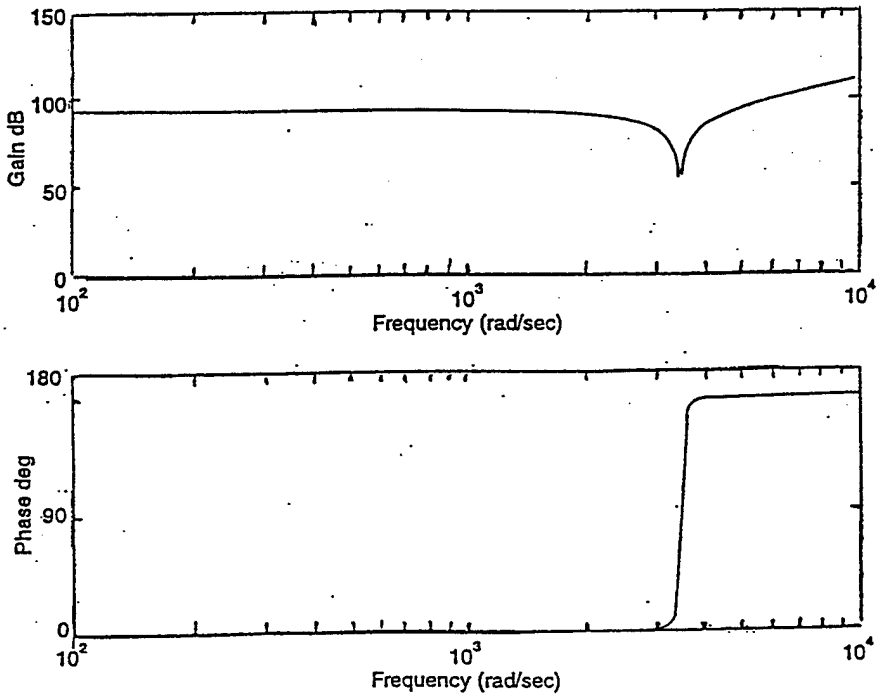

TRANSFER FUNCTION $G_c G_{13}$ FOR THE PURDY MODEL

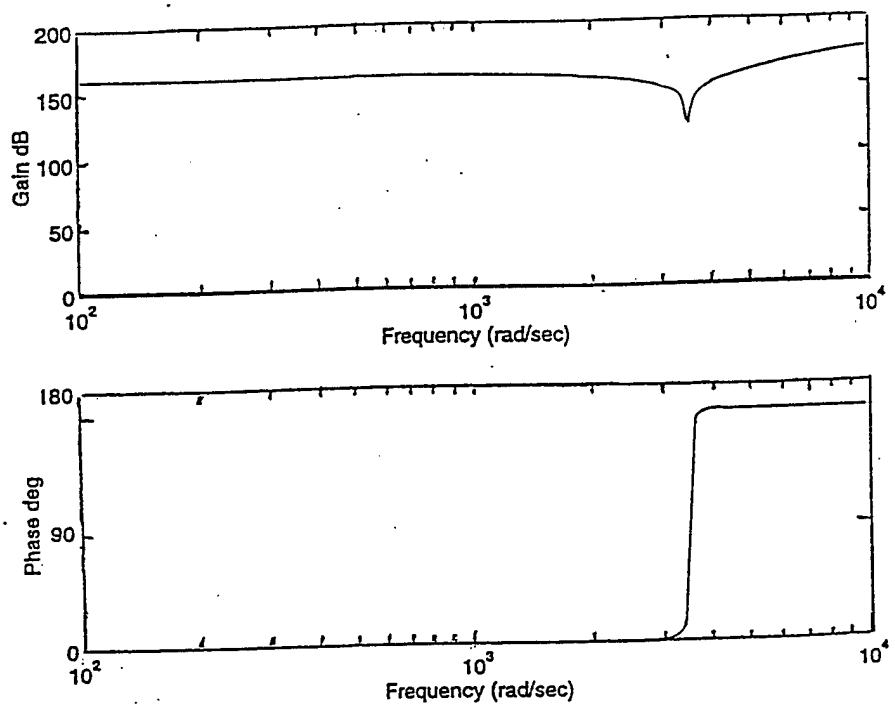

APPENDIX C TRANSFER FUNCTION B_{22}/B_{21} FOR THE PURDY MODEL

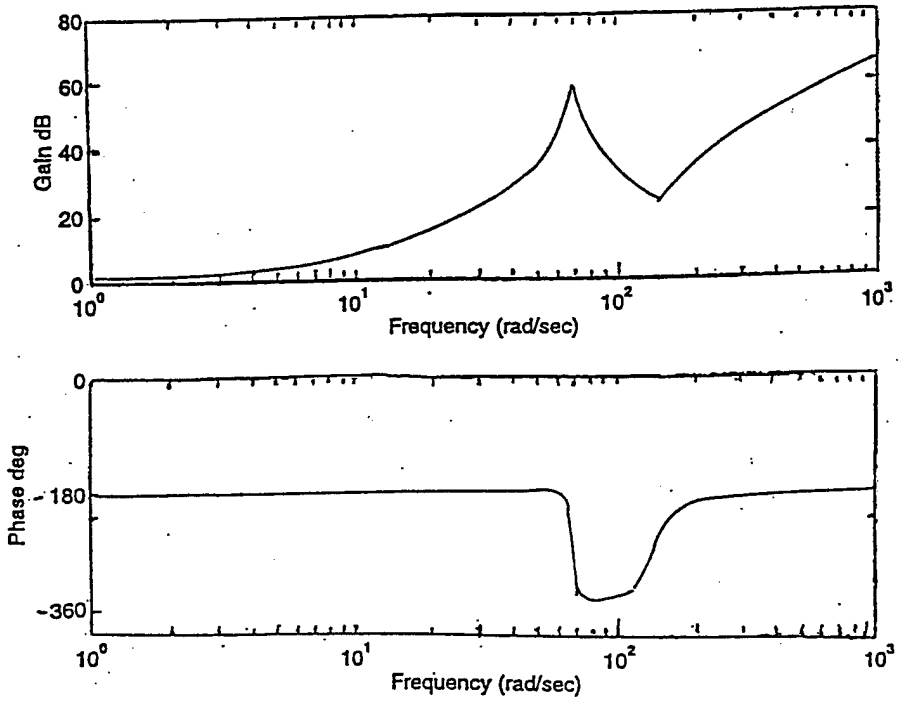

RESIDUAL R_{z1} CALCULATED FOR THE PURDY MODEL

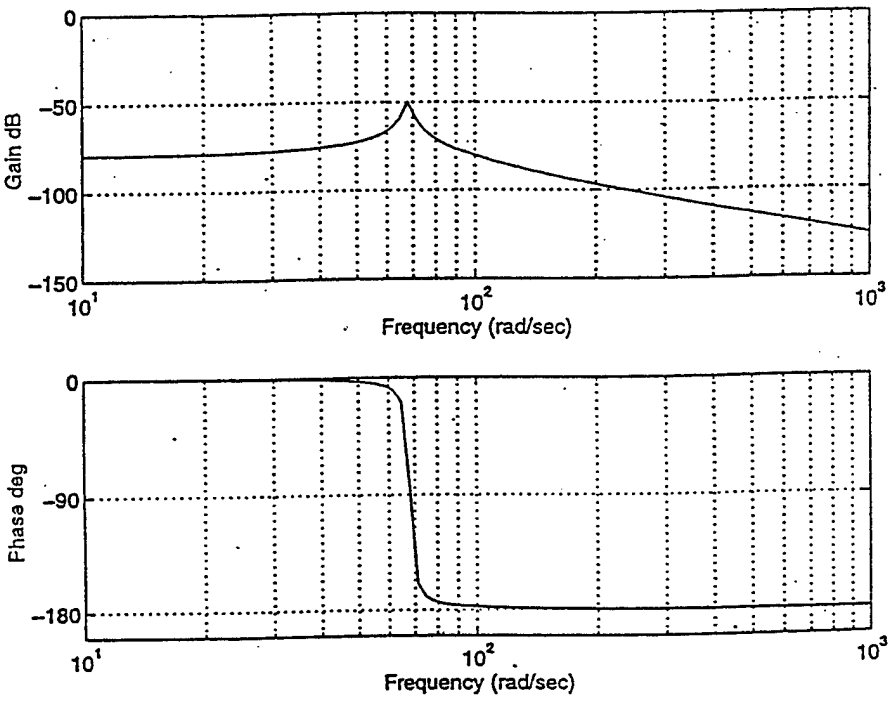

APPENDIX D

RESIDUAL $R_{11} = -B_{22}$ CALCULATED FOR THE PURDY MODEL

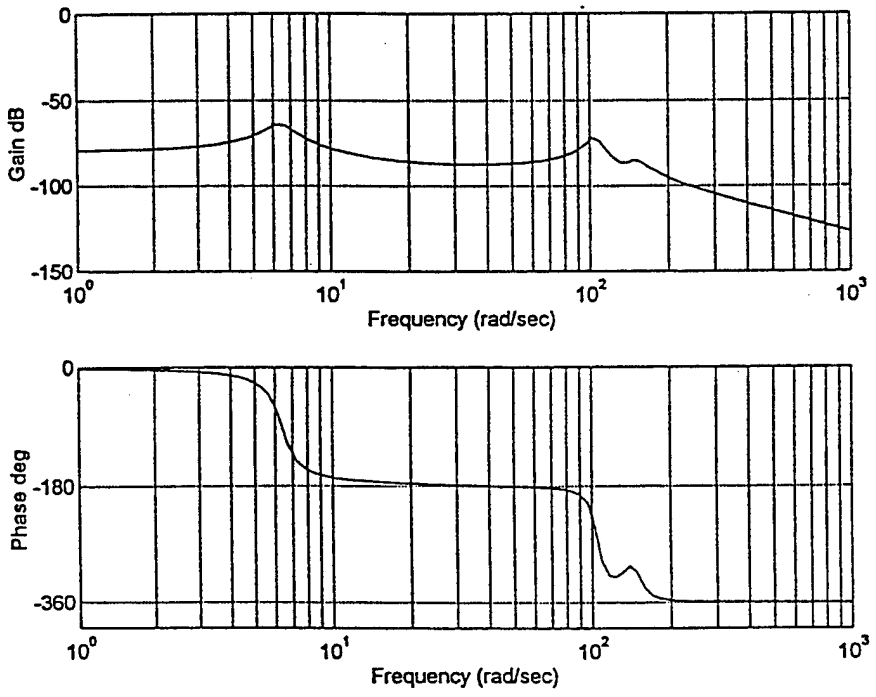

RESIDUAL $R_{21} = -B_{32}$ CALCULATED FOR THE PURDY MODEL

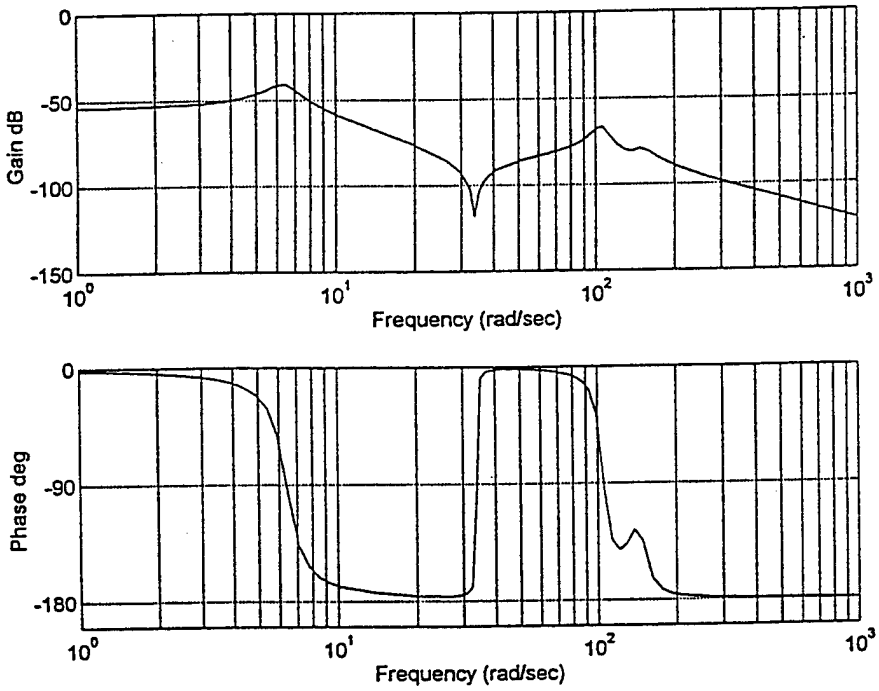

APPENDIX E DISTURBANCE TRANSFER FUNCTIONS FOR θ_d (PURDY MODEL)

$s^3Y_i: \quad \frac{I_{22}a_{33} - I_{32}a_{32}}{a_{12}a_{33}}$

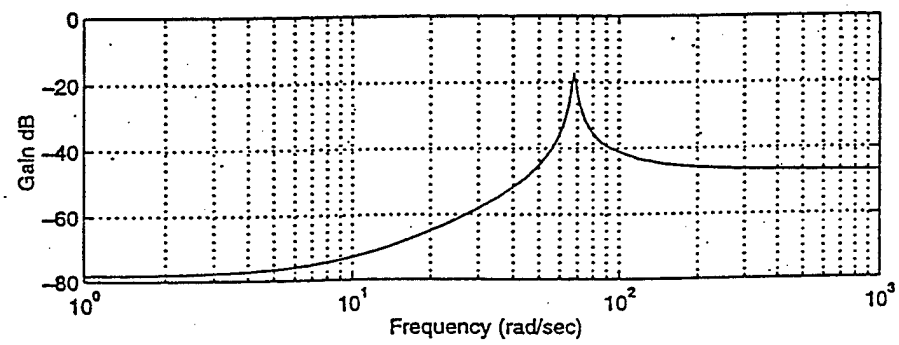

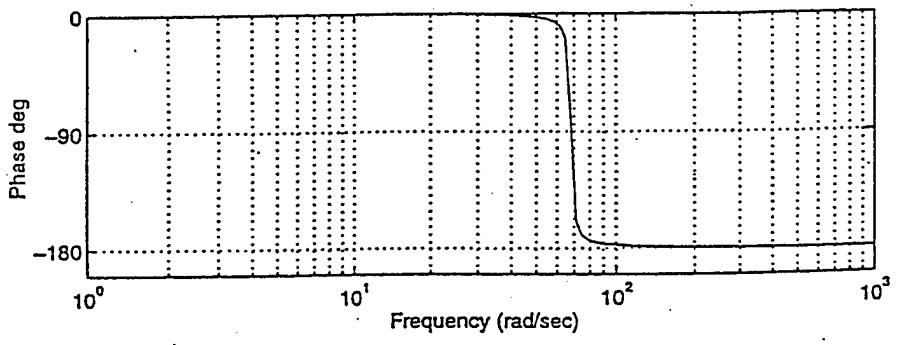

$$s\theta_p: \quad \frac{I_{22}}{a_{12}} = \frac{C_{1p}}{k_d R_p X_{ip}} = 0.00833$$

$$\theta_p: \quad \frac{I_{24}}{a_{12}} = \frac{k_d X_{ip}^2 + k_{1p}}{k_d R_p X_{ip}} = -18.8$$

Modeling of passive constrained layer damping as applied to a gun tube

Dr. Margaret Z. Kiehl and CPT Wayne Jerzak

We study the damping effects of a cantilever beam system consisting of a gun tube wrapped with a constrained viscoelastic polymer on terrain induced vibrations. A time domain solution to the forced motion of this system to forced motion is developed using the GHM (Golla-Hughes-McTavish) method to incorporate the viscoelastic properties of the polymer. An impulse load is applied at the free end and the tip deflection of the cantilevered beam system is determined. The resulting GHM equations are then solved in MATLAB by transformation to the state-space domain.

INTRODUCTION

The production of long slender gun systems to meet increased exit velocity requirements of rounds has subsequently increased the effect of terrain induced vibrations. The increased susceptibility of long gun tubes to environmentally induced vibrations effects precision and accuracy of firing as well as barrel/round interactions during firing. A lightweight, low cost method is desired to dampen terrain-induced vibrations thereby increasing performance of the gun system. A relatively inexpensive and lightweight method of dampening vibrations in some structures is to apply a surface treatment of a viscoelastic material and a constraining layer. The viscoelastic material is bonded to the base material, a gun tube in our case, and to the constraining layer. Transverse vibrations in the system result in shear deformation of the viscoelastic material, which in turn dissipates the energy.

The integration of viscoelastic damping materials into various structures has been widely studied and various methods of modeling viscoelastic damping can be seen in the literature. Euler-Bernoulli beam theory has been used to model viscoelastic materials using the Rayleigh Ritz approximation to damping. Timoshenko beam theory incorporates both shear deformation and rotational deformation in the formulation. The modal strain energy method [1] makes use of the relationship between damping factors and modal loss factors in order to assign damping factors to real elastic modes as an approximation to light damping. The Ross-Kerwin-Ungar (RKU) theory uses continuum mechanics to derive a sixth order PDE for a three layer beam which incorporates damping using a complex shear modulus. The Golla-Hughes-McTavish (GHM) method [2],[3],[4] uses a finite element approach where viscoelastic damping in introduced as a series of mini-oscillator terms and auxiliary dissipation coordinates.

DiTaranto and Blasingame [5] and Mead and Markus [6] derived a sixth order PDE to model the transverse vibrations of a three layer beam system based on the RKU equations developed for flexural vibrations of layered plates. In this approach damping of the viscoelastic layer is incorporated through the use of a complex shear modulus. Solutions of this equation in the frequency domain have lead successful predictions of loss factors and modal frequencies of a damped sandwich beam. Many investigators have used this approach in the study of sandwiched beams. Notably Miles and Reinhall [7] extended the theory to include thickness deformations, which allows for compression of the viscoelastic layer to contribute to the damping of the system. While this approach is stable in the frequency domain, the complex coefficients cause instability in the time domain.

Golla, Hughes, and McTavish [3] developed a finite element method approach to model constrained layer damping which is referred to as the GHM method. GHM starts from the framework of finite element analysis where the mass and stiffness matrixes are determined. Viscoelastic damping is incorporated into the model by replacing the constant material modulus with a stress-strain history law. Dissipation coordinates, which track the dissipation of energy, are then coupled with the physical coordinates of the model through a system of equations. Ro, El-Din and Baz [8] used this modeling technique in a layered system to model active constrained layer damping of a gun tube with a moving load.

Given the need for a time domain solution, this study investigates the implementation of the GHM method in formulating a FEM model of a constrained layer gun tube.

VISCOELASTIC CONSTRAINED LAYER MODEL

A mathematical model of the system is determined by considering the equations of motion. We treat the gun tube as a long steel rod, coated with a layer of viscoelastic material and a thin constraining layer, Figure 1. Assumptions are made that a perfect bond between the layers and that the sandwiched rod is much longer than it is thick. A cross section of the system consists of five layers, however, making full use of symmetry, the constrained rod can be modeled as a three-layer system.

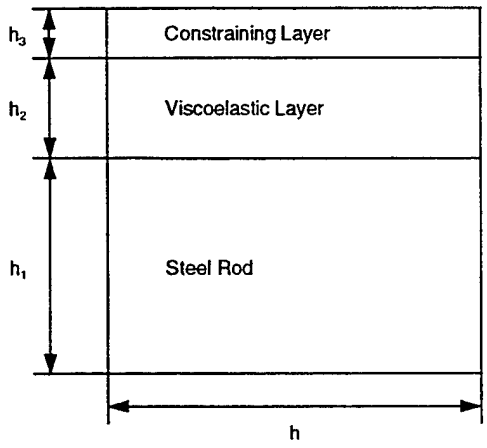

Figure 1. Unbent Three Layer Sandwich Bar

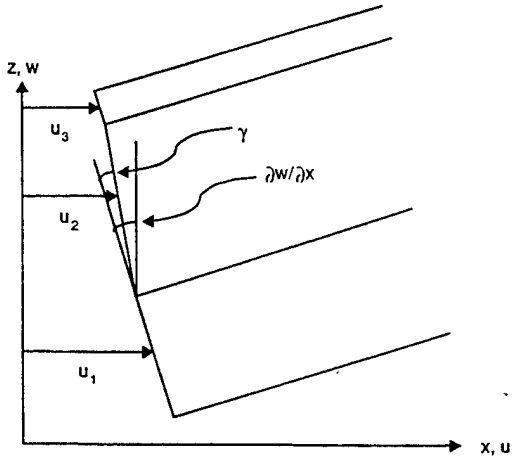

Figure 2. Deflected Bar

As a transverse vibration passes along the rod, the layers of the system undergo varied deformation. Figure 2 depicts the deformation of the sandwich rod resulting from vibration. Due to the relative stiffness of the rod and constraining layer, the viscoelastic polymer undergoes shear deformation. The material properties of the constraining layer under shear deformation provide for dissipation of energy and thus a damping of the vibration.

In order to incorporate viscoelastic properties into FEM, the GHM method uses a strain history constitutive relationship to develop the **M** and **K** matrices for the system. Viscoelastic material properties are incorporated directly into the mass and stiffness matrices, eliminating the need for complex coefficients which result in instability in the time domain. The viscoelastic properties are incorporated in the frequency domain through the use of 'mini-oscillators' [mh] to represent the material modulus of each layer. Transformation back into the time domain gives rise to the introduction of dissipation coordinates. The dissipation coordinates have no realization, but they are coupled to the real coordinates to account for the dissipation of energy from the system and are treated as additional degrees of freedom in the finite element formulation. This approach is stable in the time domain and is shown to give plausible results for a single finite element of a three-layer rod.

FINITE ELEMENT MODELING

The configuration of the sandwiched rod considered is that of a cantilevered beam, thus a finite element formulation for the time domain solution to the forced motion of a cantilever beam system is developed. The GHM method is employed to numerically compute the tip deflection of the cantilevered constrained layered rod for an impulse load applied at the free end. Assumptions made in using the GHM method are that 1) the core damping is linearly viscoelastic; 2) shear strains in the constraining layer and rod are negligible; 3) transverse displacements w of each layer are equal; and 4) the constraining layer is to have no dissipative energy.

The sandwich rod is formulated into a finite element method (FEM) using one-dimensional beam elements with two nodal points, one at each end of the element. Four degrees of freedom are associated with each node. These are used to describe the longitudinal displacement u_3 of the constraining layer, the longitudinal displacement u_1 of the

central rod, the transverse displacement w, and the slope of the displacement line $\partial w/\partial x$ (Recall Figure 1). The basis vectors used to describe the longitudinal displacements are assumed to be linear polynomials, b_i for u_3 and β_i for u_1, and the basis vectors used for the transverse deflection are cubic Hermite polynomials, ϕ_i. The resulting overall basis for a single beam element of length h are given by:

$$\begin{aligned} b_1 &= \beta_1 = 1 - x/h, \\ b_2 &= \beta_2 = x/h, \\ \phi_1 &= 1 - 3(x/h)^2 + 2(x/h)^3, \\ \phi_2 &= x - 2h(x/h)^2 + h(x/h)^3, \\ \phi_3 &= 3(x/h)^2 - 2(x/h)^3, \\ \phi_4 &= -h(x/h)^2 + h(x/h)^3. \end{aligned} \tag{1}$$

The generalized coordinate vector for a single beam element with initial starting value x_o is

$$\mathbf{q} = [u_1(x_o,t) \;\; u_3(x_o,t) \;\; w(x_o,t) \;\; w_x(x_o,t) \;\; u_1(x_o+h,t) \;\; u_3(x_o+h,t) \;\; w(x_o+h,t) \;\; w_x(x_o+h,t)]^{\mathrm{T}}. \tag{2}$$

The use of the above basis and generalized coordinate vector for several beam elements comprising the system allows for the continuity of lateral displacements and transverse displacements and slopes across the elements.

The mass matrix $\mathbf{M}_i$ and the stiffness matrix $\mathbf{K}_i$ for the i$^{\text{th}}$ element of the sandwich rod are obtained from the kinetic and potential energy, respectively. The kinetic and potential energies are determined by considering the contribution of each layer. By summing the contributions of each layer, the kinetic energy T and corresponding mass matrix for the ith element become

$$T = \frac{1}{2}\sum_{j=1}^{3} p_j A_j \int_{L_i} \left(\dot{w}^2 + \dot{u}_j^2\right) dx = \frac{1}{2}\mathbf{q}_i^{\mathrm{T}} \mathbf{M}_i \mathbf{q}_i \tag{3}$$

where the j index indicates the jth layer, L_i is the length of the ith element, and the dot indicates a time derivative. In a similar fashion, the potential energy V and associated stiffness matrix become

$$V = \sum_{j=1}^{3} \frac{E_j A_j}{2} \int_{L_i} \left(\frac{\partial u_j}{\partial x}\right)^2 dx + \sum_{j=1}^{3} \frac{E_j I_j}{2} \int_{L_i} \left(\frac{\partial^2 w}{\partial x^2}\right) dx + \frac{G_2 A_2}{2} \int_{L_i} \gamma^2 \, dx = \frac{1}{2}\mathbf{q}_i^{\mathrm{T}} \mathbf{K}_i \mathbf{q}_i \tag{4}$$

where G_2 is the viscoelastic shear modulus and γ is the shear strain. When the system is modeled using on beam element, the equation of motion for the system, analogous to the FEM formulation of an Euler-Bernoulli beam, is given by

$$\mathbf{M}\ddot{\mathbf{q}} + \mathbf{K}\mathbf{q} = \mathbf{f} \tag{5}$$

where $\mathbf{f}$ is a vector containing the forcing terms.

GHM Method Implementation

Incorporation of the viscoelastic damping is implemented by first expressing the stiffness matrix as a sum of stiffness matrices each of which depend upon an individual layer:

$$\mathbf{K} = \sum_j \mathbf{K}_j = \sum_j G_j \overline{\mathbf{K}}_j . \tag{6}$$

For each layer, the long-term behavior of the material modulus is then factored out of the corresponding stiffness matrix as G_j. A hereditary stress-strain law is then used to incorporate the viscoelastic damping. For illustration purposes, the development of the GHM viscoelastic element will first be presented for a one-element/one layer beam. The general finite element equations of motion are of the same form as found in Equation 5 with the appropriate mass and stiffness matrix for a viscoelastic layer and the material modulus factored out. The stress-strain law results in the following equations of motion

$$\mathbf{M}\ddot{\mathbf{q}}(t) + \int_o^t G(t-\tau)\mathbf{K}\dot{\mathbf{q}}(\tau)d\tau = \mathbf{f}(t). \tag{7}$$

This becomes

$$s^2\mathbf{M}\tilde{\mathbf{q}}(s) + s\tilde{G}(s)\overline{\mathbf{K}}\tilde{\mathbf{q}}(s) = \tilde{\mathbf{f}}(s) \tag{8}$$

when transformed into the Laplace domain.

GHM uses a sum of a finite number of mini-oscillators terms to incorporate viscoelastic damping. Let us first consider the case of one mini-oscillator to define the material modulus. In the Laplace domain, this is represented as

$$s\tilde{G}(s) = G^{\infty}\left[1 + \alpha\frac{s^2 + 2\xi\omega s}{s^2 + 2\xi\omega s + \omega^2}\right] \tag{9}$$

where α, ξ, ω are positive constants. In particular, ω represents a model frequency while α and ξ determine the shape of the material modulus function in the Laplace domain. A column vector of dissipation coordinates is introduced with the following behavior:

$$\tilde{\hat{\mathbf{z}}}(s) = \frac{\omega^2}{s^2 + 2\xi\omega s + \omega^2}\tilde{\mathbf{q}}(s). \tag{10}$$

Coupling the dissipation coordinates with Laplace domain equations of motions and converting to a second-order time domain realization, our resulting system of equations become

$$\begin{bmatrix} \mathbf{M} & \mathbf{0} \\ \mathbf{0} & \alpha\frac{1}{\omega^2}\mathbf{K} \end{bmatrix}\begin{bmatrix} \ddot{\mathbf{q}} \\ \ddot{\hat{\mathbf{z}}} \end{bmatrix} + \begin{bmatrix} \mathbf{0} & \mathbf{0} \\ \mathbf{0} & \alpha\frac{2\xi}{\omega} \end{bmatrix}\begin{bmatrix} \dot{\mathbf{q}} \\ \dot{\hat{\mathbf{z}}} \end{bmatrix} + \begin{bmatrix} \mathbf{K}(1+\alpha) & -\alpha\mathbf{K} \\ -\alpha\mathbf{K} & \alpha\mathbf{K} \end{bmatrix}\begin{bmatrix} \mathbf{q} \\ \hat{\mathbf{z}} \end{bmatrix} = \begin{bmatrix} \mathbf{f} \\ \mathbf{0} \end{bmatrix}. \tag{11}$$

In order to eliminate the rigid body modes from the stiffness matrix, spectral decomposition is used resulting in

$$\mathbf{K} = G^{\infty}\overline{\mathbf{K}} = G^{\infty}\overline{\mathbf{R}}\,\overline{\Lambda}\,\overline{\mathbf{R}}^T \tag{12}$$

where $\overline{\Lambda}$ is a diagonal matrix of nonzero eigenvalues of $\overline{\mathbf{K}}$ and the columns of $\overline{\mathbf{R}}$ are the corresponding orthonormalized eigenvectors. G^{∞} is then multiplied back into the diagonal matrix and the following substitutions, Equations 13, are made into Equation 11.

$$\mathbf{z} = \overline{\mathbf{R}}^{\mathrm{T}}\hat{\mathbf{z}} \qquad \mathbf{R} = \overline{\mathbf{R}}\Lambda \tag{13}$$

Pre-multiplying the bottom row by $\mathbf{R}^{\mathrm{T}}$, the equations of motion are of the form:

$$\mathbf{M}_{v}\begin{bmatrix}\ddot{\mathbf{q}}\\ \ddot{\mathbf{z}}\end{bmatrix} + \mathbf{D}_{v}\begin{bmatrix}\dot{\mathbf{q}}\\ \dot{\mathbf{z}}\end{bmatrix} + \mathbf{K}_{v}\begin{bmatrix}\mathbf{q}\\ \mathbf{z}\end{bmatrix} = \begin{bmatrix}\mathbf{f}\\ \mathbf{0}\end{bmatrix} \tag{14}$$

where the GHM matrices are

$$\mathbf{M}_{v} = \begin{bmatrix}\mathbf{M} & \mathbf{0}\\ \mathbf{0} & \alpha\dfrac{1}{\omega^{2}}\Lambda\end{bmatrix} \qquad \mathbf{D}_{v} = \begin{bmatrix}\mathbf{0} & \mathbf{0}\\ \mathbf{0} & \alpha\dfrac{2\xi}{\omega}\Lambda\end{bmatrix} \qquad \mathbf{K}_{v} = \begin{bmatrix}\mathbf{K}(1+\alpha) & -\alpha\mathbf{R}\\ -\alpha\mathbf{R}^{\mathrm{T}} & \alpha\Lambda\end{bmatrix}. \tag{15}$$

The GHM method can be extended to three layers with individual material properties. The mass and stiffness matrices for each individual layer are formulated as discussed above. Once the mass and stiffness matrices are then combined, the resulting equations of motion for the system once stress-strain history is applied become

$$\mathbf{M}\ddot{\mathbf{q}}(t) + \int_{o}^{t}\left[\sum_{j} G_{j}(t-\tau)\mathbf{K}_{j}\right]\dot{\mathbf{q}}(\tau)d\tau = \mathbf{f}(t). \tag{16}$$

Note that j indexes the layer. Each of the material moduli, G_j, for which GHM is used to incorporate viscoelastic damping is written as a sum of a finite number of mini-oscillators terms. Using three mini-oscillator terms, the damping is represented in the Laplace domain as

$$s\tilde{G}_{j}(s) = G_{j}^{\infty}\left[1 + \sum_{k=1}^{3}\alpha_{jk}\frac{s^{2} + 2\xi_{jk}\omega_{jk}s}{s^{2} + 2\xi_{jk}\omega_{jk}s + \omega_{jk}^{2}}\right] \tag{17}$$

where $\alpha_{jk}, \xi_{jk}, \omega_{jk}$ are positive constants associated with the kth mini-oscillator for the jth layer. For each mini-oscillator within a layer, a column vector of dissipation coordinates is introduced with the following behavior:

$$\tilde{\hat{\mathbf{z}}}(s) = \frac{\omega_{jk}^{2}}{s^{2} + 2\xi_{jk}\omega_{jk}s + \omega_{jk}^{2}}\tilde{\mathbf{q}}(s). \tag{18}$$

Coupling the dissipation coordinates with Laplace domain equations of motions and converting to a second-order time domain realization in a way analogous to the presentation described above, our resulting system of equations become

$$\mathbf{M}_{v}\begin{bmatrix}\ddot{\mathbf{q}}\\ \ddot{\mathbf{z}}\end{bmatrix} + \mathbf{D}_{v}\begin{bmatrix}\dot{\mathbf{q}}\\ \dot{\mathbf{z}}\end{bmatrix} + \mathbf{K}_{v}\begin{bmatrix}\mathbf{q}\\ \mathbf{z}\end{bmatrix} = \begin{bmatrix}\mathbf{f}\\ \mathbf{0}\end{bmatrix}. \tag{19}$$

Now the GHM viscoelastic matrices are of the form

$$\mathbf{M}_v = \begin{bmatrix} \mathbf{M} & \mathbf{0} & \cdots & \cdots & \cdots & \mathbf{0} \\ \mathbf{0} & \alpha_{11}\dfrac{1}{\omega_{11}^2}\Lambda_1 & \mathbf{0} & \cdots & \cdots & \mathbf{0} \\ \vdots & \mathbf{0} & \ddots & \mathbf{0} & \cdots & \mathbf{0} \\ \vdots & \vdots & \mathbf{0} & \alpha_{jk}\dfrac{1}{\omega_{jk}^2}\Lambda_j & \mathbf{0} & \mathbf{0} \\ \vdots & \vdots & \vdots & \mathbf{0} & \ddots & \mathbf{0} \\ \mathbf{0} & \mathbf{0} & \mathbf{0} & \mathbf{0} & \mathbf{0} & \alpha_{33}\dfrac{1}{\omega_{33}^2}\Lambda_3 \end{bmatrix}$$

$$\mathbf{D}_v = \begin{bmatrix} \mathbf{0} & \mathbf{0} & \cdots & \cdots & \cdots & \mathbf{0} \\ \mathbf{0} & \alpha_{11}\dfrac{2\xi_{11}}{\omega_{11}}\Lambda_1 & \mathbf{0} & \cdots & \cdots & \mathbf{0} \\ \vdots & \mathbf{0} & \ddots & \mathbf{0} & \cdots & \mathbf{0} \\ \vdots & \vdots & \mathbf{0} & \alpha_{jk}\dfrac{2\xi_{jk}}{\omega_{jk}}\Lambda_j & \mathbf{0} & \mathbf{0} \\ \vdots & \vdots & \vdots & \mathbf{0} & \ddots & \mathbf{0} \\ \mathbf{0} & \mathbf{0} & \mathbf{0} & \mathbf{0} & \mathbf{0} & \alpha_{33}\dfrac{2\xi_{33}}{\omega_{33}}\Lambda_3 \end{bmatrix}$$

$$\mathbf{K}_v = \begin{bmatrix} \mathbf{K} + \sum_{j,k}\alpha_{jk}\mathbf{K}_j & -\alpha_{11}\mathbf{R}_1 & \cdots & -\alpha_{jk}\mathbf{R}_j & \cdots & -\alpha_{33}\mathbf{R}_3 \\ -\alpha_{11}\mathbf{R}_1^{\mathrm{T}} & \alpha_{11}\Lambda_1 & \mathbf{0} & \cdots & \cdots & \mathbf{0} \\ \vdots & \mathbf{0} & \ddots & \mathbf{0} & \cdots & \mathbf{0} \\ -\alpha_{jk}\mathbf{R}_j^{\mathrm{T}} & \vdots & \mathbf{0} & \alpha_{jk}\Lambda_j & \mathbf{0} & \mathbf{0} \\ \vdots & \vdots & \vdots & \mathbf{0} & \ddots & \mathbf{0} \\ -\alpha_{33}\mathbf{R}_3^{\mathrm{T}} & \mathbf{0} & \mathbf{0} & \mathbf{0} & \mathbf{0} & \alpha_{33}\Lambda_3 \end{bmatrix}$$

where the *j* indexes the layer and the *k* indexes the mini-oscillator.

Space-State Formulation

Once these matrices have been formulated, the system can be transformed into a space-state formulation [9]. This is done by first defining the state-vector as follows:

$$\mathbf{x} = \begin{bmatrix} \mathbf{r} \\ \dot{\mathbf{r}} \end{bmatrix} \quad \text{where} \quad \mathbf{r} = \begin{bmatrix} \mathbf{q} \\ \mathbf{z} \end{bmatrix}. \tag{20}$$

Equation 19 can then be posed in terms of $\mathbf{r}$ and $\dot{\mathbf{r}}$ as

$$\dot{\mathbf{r}} = \mathbf{I}\dot{\mathbf{r}}$$
$$\ddot{\mathbf{r}} = -\mathbf{M}_v^{-1}\mathbf{K}_v\,\mathbf{r} - \mathbf{M}_v^{-1}\mathbf{D}_v\,\dot{\mathbf{r}} + \mathbf{M}_v^{-1}\mathbf{f} \tag{21}$$

This can then be transformed into a format that is compatible with the capabilities of MATLAB by expressing the system as

$$\dot{\mathbf{x}} = \mathbf{A}\mathbf{x} + \mathbf{B}\mathbf{u}$$
$$\mathbf{y} = \mathbf{C}\mathbf{x} + \mathbf{D}\mathbf{u} \tag{22}$$

where the matrices **A, B, C,** and **D** are constructed as prescribed by the equations given below.

$$\mathbf{A} = \begin{bmatrix} \mathbf{0} & \mathbf{I} \\ \mathbf{M}_v^{-1}\mathbf{K}_v & \mathbf{M}_v^{-1}\mathbf{D}_v \end{bmatrix} \quad \mathbf{B} = \begin{bmatrix} \mathbf{0} \\ \mathbf{M}_v^{-1} \end{bmatrix}$$
$$\mathbf{C} = \begin{bmatrix} \mathbf{I} & \mathbf{0} \end{bmatrix} \quad \mathbf{D} = [\mathbf{0}] \tag{23}$$
$$\mathbf{y} = \mathbf{q} \quad \mathbf{u} = \mathbf{f}$$

This representation of the time domain problem can then be solved using the ***impulse*** command in MATLAB.

MODEL RESULTS

The specifications for the sandwich rod modeled using a finite element formulation and GHM method are given here. The steel rod used to simulate the gun tube has an inner radius of $0.0222\ m$ and an outer radius of $0.0445\ m$. The density and Young's modulus are given by $7832\ {}^{kg}/_{m^3}$ and $207\times10^9\ Pa$ respectively. The constraining layer has the following properties: $\rho = 1993\ {}^{kg}/_{m^3}$, $E = 24.1\times10^9\ Pa$, and thickness of $0.0005\ m$. Sorbithane, the viscoelastic polymer, is characterized by a thickness of $0.003175\ m$, density of $1281\ {}^{kg}/_{m^3}$, Poisson's ratio $\nu = 0.49$, and bulk shear modulus and elastic modulus given by $G = 0.3356\times10^6\ Pa$ and $E = 1\times10^6\ Pa$. The moment of inertia, I, and cross sectional area, A, are calculated using the standard formulas $I = {}^1/_4\pi r^4$ $A = \pi r^2$. The material parameters for the sandwich rod are taken from tables and manufacturer provided specifications.

In incorporating the GHM model, it is assumed that the shear strain the constraining layer is negligible. This results in modeling the steel rod and constraining layer as elastic medium while the polymer is considered to be linearly viscoelastic. Additionally, it is assumed that transverse displacements for any given cross section are uniformly constant for the entire system. As a first approximation, the values for the material modulus shape functions $\alpha_{jk}, \xi_{jk}, \omega_{jk}$ reported by Ro, etal [8] are implemented. Curve fitting of experimental data will provide more accurate values for these parameters.

DISCUSSION AND CONCLUSION

Our initial modeling of the time domain was done as a one element – three layer beam. This solution to the cantilever beam with impulse shock applied to the free end is given in Figure 3. An implementation was also attempted for a three element – three layer beam model. The details of this model are still under investigation to obtain a converging finite element solution. The primary goal of any further research will be to successfully implement the three element – three layer beam model. This is key to the capability to model the gun tube using n elements.

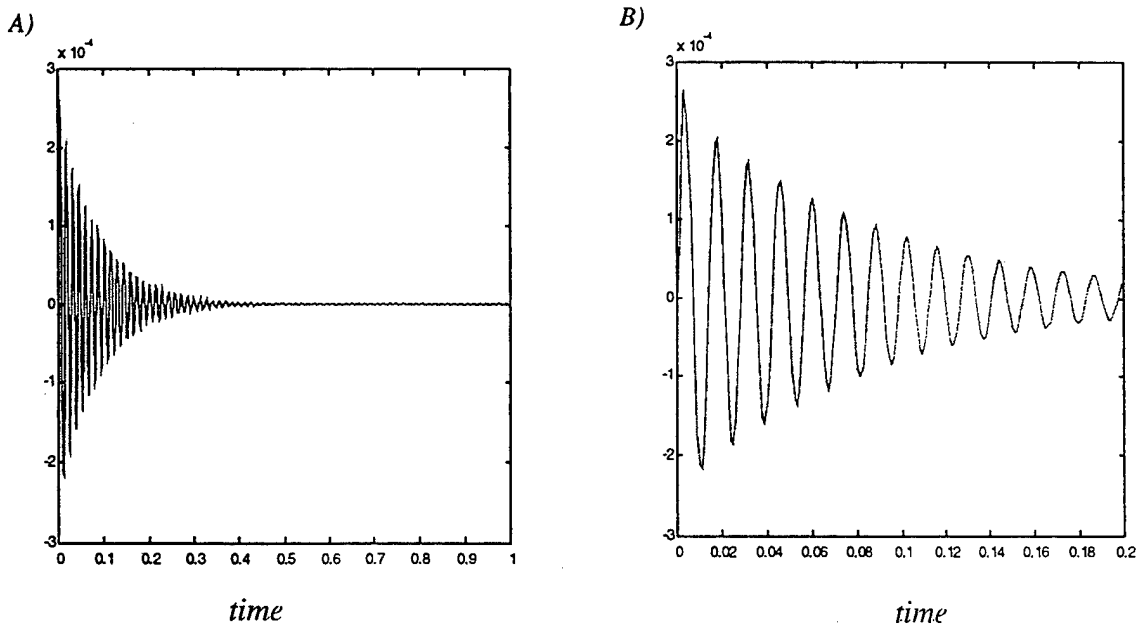

Figure 3 Damping of cantilever beam subject to an impulse at the free end, where A) depicts long time behavior and B) depicts short time damped oscillations.

There are other things that need to be considered for future work in order to validate the model. There is a need to run frequency test on the viscoelastic polymer and gun tube in order to determine the appropriate values for $\omega_j, \xi_j,$ and α_j for the j modal frequencies we wish to use in this model. Data obtained from the frequency tests can then be curve fit using modal circles. Further steps towards verification of the model include construction of a constrained layer damped rod. Impulses from a hammer could then be applied to this mechanical model and experimental results could be gathered. This would allow for the comparison of the FEM model to the experimental results.

The initial findings of the model are very encouraging. The implementation of GHM in order to incorporate viscoelastic damping allows for a stable time domain solution in the simplified case of a single finite element. Initial results indicate that a time domain solution for multiple finite elements will follow accordingly. Also, significant damping of the impulse applied to the tip of the sandwiched rod is seen using the model. This result is consistent with the application of a constrained viscoelastic layer.

REFERENCES

1. Johnson, C.D. and Kienholz, D.A., "Finite element prediction of Damping in Structures with Constrained Viscoelastic Layers," *AIAA Journal*, 1982, Vol 20 No 9, pp. 1284-1290.

2. McTavish, D.J. and Hughes, P.C., "Modeling of Linear Viscoelastic Space Structures," *Journal of Vibration and Acoustics*, 1993, Vol 105, pp. 103-110.

3. D.H. Golla and P.C. Hughes., "Dynamics of Viscoelastic Structures - A Time-Domain, Finite Element Formulation," *Journal of Applied Mechanics*, 1985, Vol 52, pp. 897-906.

4. Gibson, W.C. and McTavish, D.J., "Implementation of the GHM Method for Viscoelastic Materials using MATLAB and NASTRAN," *SPIE Proceedings*, 1995, Vol 2445, pp. 312-323.

5. DiTaranto, R.A. and Blasingame, W., "Composite damping of vibrating sandwich beams," *Journal of Engineering for Industry*, 1967, Vol 89, pp. 633-638.

6. Mead, D.J. and Markus, S., "The Forced Vibration of a Three-layer, Damped Sandwich Beam with Arbitrary Boundary Conditions," *Journal of Sound and Vibrations*, 1969, Vol 10(2), pp. 163-175.

7. Miles, R.N. and Reinhall, P.G., "An Analytical Model for the Vibration of Laminated Beams Including the Effects of both shear and thickness deformation in the adhesive layer," *Journal of Vibration, Acoustics, Stress, and Reliability in Design*, 1986, Vol 108, pp. 56-64.

8. Ro, J., El-Din, K. S. and Baz, A., "Vibration Control of Tubes With Internally Moving Loads Using Active Constrained Layer Damping ," W. Clark, *Active/passive vibration control and nonlinear dynamics of structures: presented at the 1997 ASME International Mechanical Engineering Conference and Exposition, November 16-21, 1997. Dallas, Texas*, 1997, American Society of Mechanical Engineering, New York, pp. 1-12.

9. Kathe, E.L., "MATLAB Modeling of Non-Uniform Beams Using the Finite Element Method for Dynamic Design and Analysis." ARCCB-TR-96010, U.S. Army Armaments Research, Development and Engineering Center; Close Combat Armaments Center, Benèt Laboratories, Watervliet, NY.

LESSONS LEARNED ON THE APPLICATION OF VIBRATION ABSORBERS FOR ENHANCED CANNON STABILIZATION

Eric Kathe
U.S. Army Tank-automotive and Armaments Command
Armament Research, Development, and Engineering Center
Benét Laboratories
Watervliet, NY 12189-4050
ekathe@PICA.ARMY.MIL

ABSTRACT

This paper will summarize the successful application of muzzle-end vibration absorbers to reduce cannon vibration. This technology constitutes a weapon stabilization approach that focuses on passive mechanical structural modification of the cannon, rather than relying upon an external control law to actively cancel vibrations. Challenges encountered during field testing, non-ideal behavior, and performance evaluation using digital signal processing will be highlighted.

INTRODUCTION

Structural vibrations of gun systems is becoming an increasingly important issue in the tank community due to increased exit velocity requirements of rounds to defeat anticipated and current threat reactive armor. Increased velocity demands longer gun barrels and subsequently increased receptance to enviromentally induced vibration. Considering the strong desire to minimize weight, and increase performance while the weapon platform is outmaneuvering its target, the need to introduce methods to attenuate the receptance of the gun system to environmental vibration becomes clear.

The increased system receptance has manifest itself in decreased weapon accuracy during live-fire bump-course testing of a developmental extended length 120mm tank cannon (the XM291) conducted at Aberdeen Proving Grounds, Maryland. The decreased accuracy is particularly sensitive to the traverse speed of the tank over the bump-course, and decreases significantly for system configurations that have utilized a shorter barrel[1]. This degradation of accuracy is wholly absent for live-fire testing of the same gun system from a stationary mount[2] where the developmental system outperforms its shorter in-field counterpart, the M256.

It is also very likely that the discharge conditions of long rod penetrators are introducing an increased yaw state. (The angel between the momentum vector and the axial center-line of the projectile.) Increased yaw at impact decreases penetrator performance. This projectile condition is damped out during flight by the fins of the round, and their associated drag and range limitations. Thus, the effectiveness of the weapon for near-targets may be impaired, even though precision accuracy may not be a consideration under such circumstances.

For these reasons, the current focus of engineering efforts to enhance the accuracy and performance of extended length launchers is focused upon attenuation of the receptance of gun systems to enviromentally induced barrel vibrations, while maintaining the length at levels that enable muzzle velocity capable of defeating anticipated target armor. It is believed that this approach will achieve enhanced accuracy by reducing dispersion caused by variation in the initial conditions of the gun structure at the commencement of launch; i.e., shoot-out of a straighter barrel.

Structural control of the barrel during the launch dynamics would prove a daunting task due to the particularly narrow time window during which corrective action must be taken —typically less than eight milliseconds. Coupled with the need for significant sensor information, high actuation power levels (due to the brief time window), and a

severe operating environment; the application of smart structure technology to control launch dynamics is not viable for a developmental system that is targeted for near term applications such as a potential M1 tank series up-gun. Such technology may however find application for next generation systems.

For these reasons, intermediate technology solutions that are essentially compatible with the current M1 weapon platform and its subsystems have been sought.

TRADITIONAL ENGINEERING SOLUTIONS

Several engineering approaches to reduce vibration receptance of gun systems have been applied, with differing advantages.

1) Stiffening the gun via thicker barrels raises density nearly in proportion to stiffness, especially near the muzzle end, where the cylinder is not too far from a thin-wall approximation.

2) Cradle/mount extension effectively decreases the cantilevered length of the gun, and has successfully increased modal frequencies[3]. However, extended cradles present significant weapon platform integration issues; i.e., they don't fit in the allotted space for a retrofit that does not require a new turret.

3) Application of composite over-wraps to enhance the stiffness to density ratio have encountered challenges during firing, manifest as delamination of the composite from the gun steel. This is not to rule out the future of composite applications.

4) Active vibration suppression via the fire-control and weapon stabilization system has been considered. (This is the system that points the gun on target.) Although a promising candidate to enhance the performance, active control approaches are hampered by the performance of the hydraulic elevation and azmuthal actuators, limited sensory information, and integration with the existing control hardware and software.

A MUZZLE END VIBRATION ABSORBER

A muzzle end vibration absorber has been proposed as an intermediate technology enhancement that suffers virtually no integration issues with the current weapon platform. Both a conceptual schematic and an image of the system utilized in the testing are shown in Fig. (1). Such an absorber concept was numerically modeled[4] and subsequently

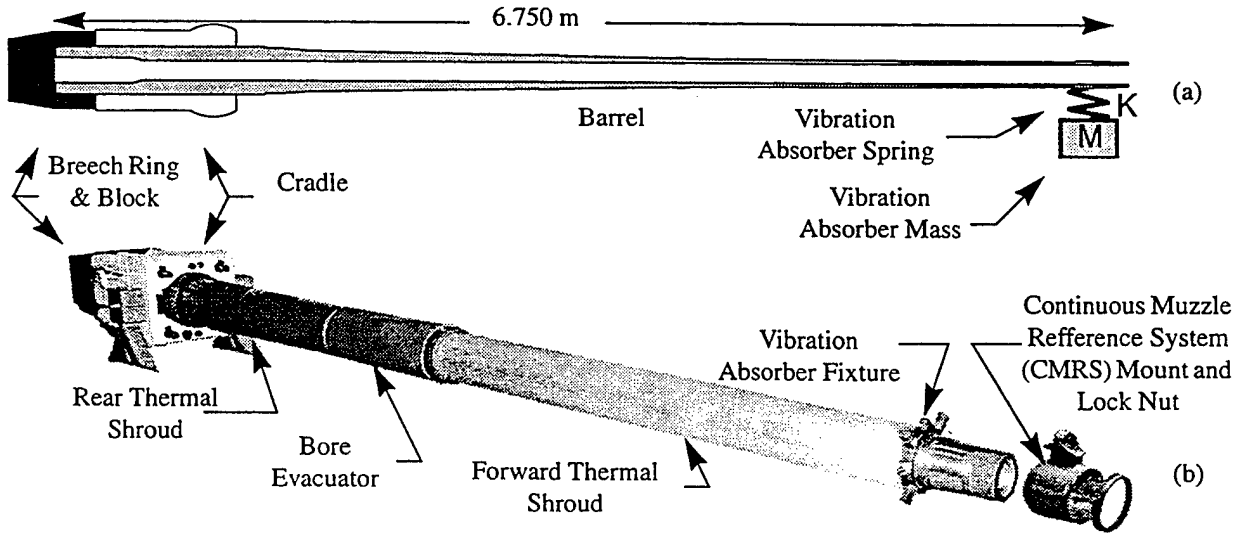

Fig. (1) Schematic depiction of a muzzle-end vibration absorber (a) and an image of the gun system tested (b).

Fig. (2) Image of "Thumper" Returning from a Test.

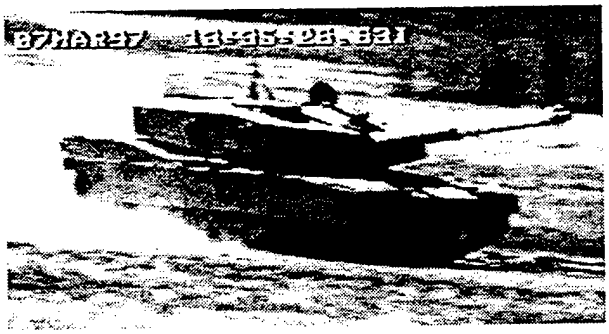

experimentally validated in a laboratory setting[5], prior to construction of the test fixture.

Details of the absorber integration with the gun system to enable function in a severe operating environment are not yet approved for public release. Specifically, information on the constraint of the vibration absorber fixture to endure high recoil acceleration (as high as 500 g's) is only available via a limited distribution report[6].

For pragmatic reasons, the free amplitude of the absorber relative to the barrel was severely restricted to a nominal value of plus or minus three millimeters. An enegy absorbing rubber material was applied to the inner surface of the vibration absorber fixture to act as a snubber and prevent metal to metal impact.

The "proof-of-principle" fixture depicted utilized off-the-shelf helical springs to provide the elastic restoring force of the absorber. The springs were interchangeable with springs of differing stiffness to enable testing of various absorber parameters to optimize overall system performance. Although shock absorbers could be integrated with the design to control damping levels, significant friction inherent in the mechanism prevented full control of this parameter. Thus the mechanism constituted a damped vibration absorber. Provisions were also included to add weights (not shown) to adjust the mass of the absorber.

A vibration absorber offers several clear advantages. The additional weight of the absorber (nominally twenty pounds for the best performer) poses little integration challenge. The absorber constitutes a purely passive approach, and thus no sensor, actuator, or fire-control integration is required. The absorber is fully compatible with all other engineering solutions. Further, the absorber does not interfere with the optical path used by the continuous muzzle reference sensor. The principle disadvantage of a vibration absorber is that a moving part is applied to a particularly harsh dynamic environment; albeit a simple moving part.

THE TESTS

The vibration absorber was mounted to a modified M1A1 tank nicknamed "Thumper" depicted in Fig. (2). The tank modifications were extensive and include an XM291 120-mm gun system, and XM91 bustle autoloader, enhanced feed-forward and feedback stabilization systems, a continuous muzzle reference system, extensive data collection, and telemetric data relay.

The XM291 gun system is just under five feet longer than the current M256. Simply put, this additional length provides greater working volume for launch. This results in greater muzzle velocities with lower propellent temperatures and pressures than would be required by an M256. Because the XM291 is longer, it is more susceptible to flexural vibrations.

Testing was conducted on the RRC-9 stabilization course at Aberdeen Proving Grounds, Maryland. The course consists of a gravel road with several dozen steel ramp bumps spaced along its length. The bumps are all introduced in pairs, one for each track of the tank, such that only pitch and heave (not roll) is introduced by the bumps.

Two types of bumps were used. Type A bumps consist of a six inch rise over a six foot span, and type B consist of

a three inch rise over a two feet. The geometry of the bumps and the time sequence at which they are encountered at fifteen miles per hour is shown in Fig. (3).

The gun stabilization system was maintained in the active mode during the testing. This control system maintains the gun pointing angel (as seen at the turret and trunnions) fixed relative to earth in both elevation and azimuth. Aside from live-fire testing, this is the most realistic test available to asses the performance of the gun barrel vibration absorber.

Three runs were made down the bump-course for both the base-line and absorber modified gun systems. A total of three absorber configurations (spring stiffness and mass) were tested. For the base-line testing the vibration absorber mechanism was removed and the remainder of the system was restored to its original condition.

THE ANALYSIS

Data Collected

Data recorded during the testing included a measure of vertical barrel flexure, horizontal barrel flexure, vertical pointing error, and horizontal pointing error.

The flexure is a measure of the difference between the pointing angel of the gun at the cradle and the pointing angle of the gun at the muzzle. The vertical and azimuthal mount angles are measured via resolvers at the trunnions and turret ring respectively, while the muzzle angels are measure optically by a system (the CMRS) that bounces a source beam from the turret off of a mirror mounted to the muzzle of the barrel and measures the deflection.

The pointing error is a measure of the difference between the command pointing direction and the direction measured by the aforementioned resolvers at the cradle. With the stabilization in the active mode, the command pointing direction is fixed relative to earth. The semantics are a bit awkward as the pointing direction of a non-straight barrel is somewhat of a misnomer and is not likely best represented by the direction measured at the cradle alone.

The data was recorded above 2kHz, and subsequently reduced to 463Hz for file transfer, well above twice the fundamental bending modes of the barrel.

To ensure that only consistent data was used in the analysis, a method identifying the bump-course —in the measurement data— had to be developed. This need was caused by a lack of consistency in the start and end times of the data records.

The series of thirteen type B bumps encountered at 275 feet (12 1/2 seconds bump-course time) were found to provide a distinct signature in the horizontal bending data near the ten second location in the data files, indicating truncation of the first seconds of the data. This signature point was quantitatively identified using a narrow band-pass filter constructed and implemented in MATLAB (The Mathworks, Natick, MA) to identify the peak that is asserted to occur at 12 1/2 seconds bump-course time. The data sets were then truncated to begin at three seconds and end at twenty-two seconds bump-course time to provide a consistent data set for further analysis.

This approach does not make-up for uncontrollable variation in speed and an occasionally straddled bump while

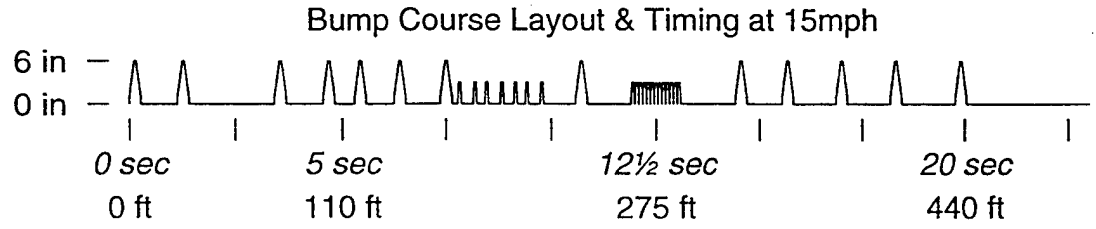

Fig. (3) Exaggerated Plot of Bump-Course Profile and Corresponding Time Axis for a Fifteen MPH Course Run.

traversing the course. This testing is particularly challenging to the driver when the bumps are encountered in a series; the reaction of turbine power-plant is not instantaneous and the drag of the bumps is significant. Therefore direct correlation analysis, bump-for-bump is hampered.

Root-Mean-Square (RMS) Amplitude

Table (1) Normalized RMS Performance of the Configurations Tested.

Configuration	Vertical Bending	Horizontal Bending	Vertical Pointing Error	Horizontal Pointing Error
A	94.3%	61.4%	44.3%	36.5%
B	82.8%	52.2%	43.7%	41.2%
C	76.2%	43.4%	39.3%	35.9%
Base-Line	100%	47.8%	41.0%	37.6%

All of the data has been normalized by the RMS amplitude of the vertical bending angle. This value would provide specific accuracy information on the gun system. This RMS flexure is on the order of one milliradian, representing an error magnitude that correlates to a target with a radius of one meter at a distance of one kilometer.

The normalized RMS values are listed in Table (1).

Clearly, the configuration of vibration absorber C, was the best overall performer. Configurations A and B appear to have shifted some energy from vertical bending into horizontal bending, although all three reduced vertical bending. The absorber's had little affect on the pointing error RMS values.

Fig. (4) Juxtaposed Power Spectra.

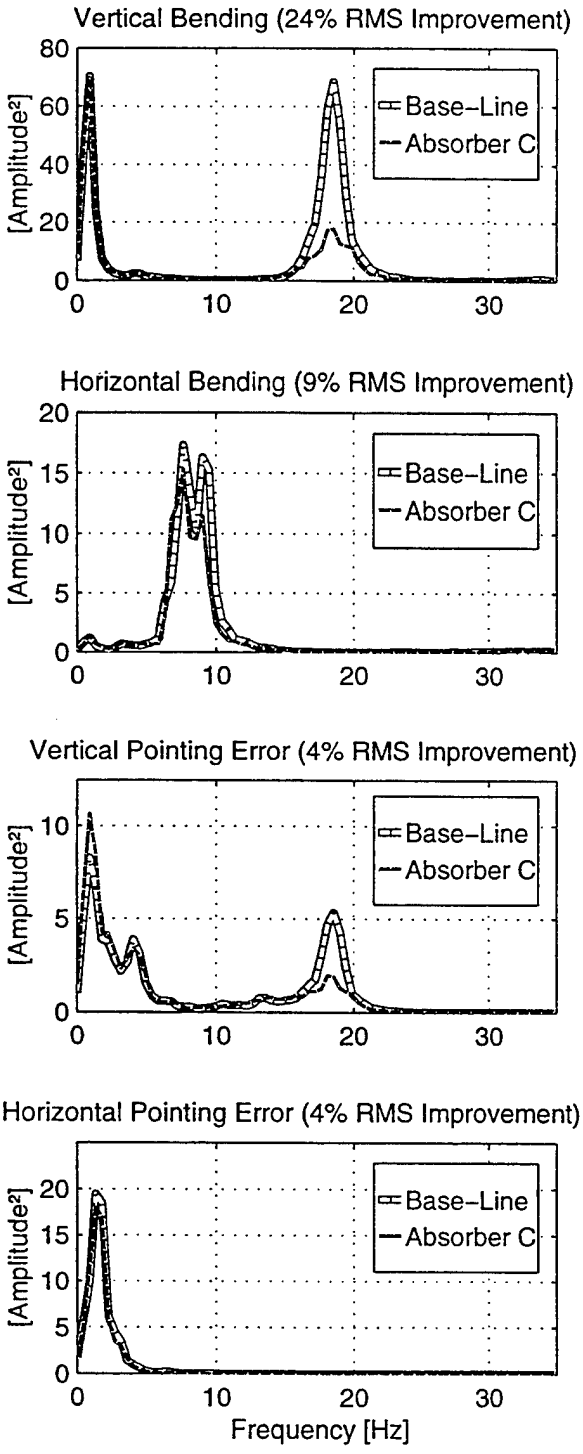

Power Spectra

The power spectra for the base-line and vibration absorber C were computed using a 1024 element Hanning window (2.2 seconds at the data sampling frequency of 463 Hz). An overlap of half the window size was used to reduce leakage effects from the non-stationary behavior of the bump-course. The power spectra for each of the three runs were subsequently averaged to reduced sensitivity to variation in traversing the bump-course. The results are displayed in Fig. (4).

DISCUSSION

The vibrations of the gun system can roughly be broken down into three frequency regimes.

Forced Vibration Near 2 Hz

Although the entire tank is one structure, the hull upon its suspension may be considered a forced excitation platform that provides force input into the gun and mount structure. Due to its vastly smaller mass, the gun structure does not sensibly affect the hull vibrations in this frequency range. The fundamental modes of the tank are low, due to its great mass —over sixty ton— which is supported by a compliant suspension. Thus, the fundamental modes of the tank impose a forced response upon the gun structure. This results in a particular solution to the differential equations of the gun system, with response frequency identical to the input force frequency, the fundamental modes of the hull suspension system.

Fundamental Horizontal Mode Near 7 Hz

In the horizontal orientation, the barrel is coupled to the relatively massive turret by the two horizontally opposed trunnion pins. These pins may be considered to mimic a very stiff torsional spring that couples the azimuthal angle of the barrel —at the trunnions— to the turret. In addition, the trunnions prevent linear deflection relative to the turret in the horizontal plane. Thus the trunnions provide two nearly rigid constraints to the barrel. Since the mass and rotational inertia of the turret is much higher than that of the gun system, the boundary condition may be expected to approach that of a cantilevered barrel in flexure, with a rigid body mode that is not discernible in the flexure data.

The first two fundamental modes of a nearly rigid boundary condition have been approximated for the gun system without the thermal shrouds, bore evacuator, and CMRS mount. Using beam finite elements, the modes have been computed to be 7.24 Hz and 25.0 Hz[7]. Instrumented impact testing of the structure in a controlled laboratory setting has demonstrated the modes to be 7.25 Hz and 25.4 Hz[5]. The principle effect of the missing components on the test and the model was a slight reduction in inertia from the fully configured case, and thus somewhat lower frequencies

should be expected from the field data.

The cause of the notch in the center of the power spectra for this mode is unknown. Its existence for both the absorber and base-line cases precludes it from being a consequence of the absorber itself. (This notch was absent for absorber configurations A and B and was replaced with a peak at the notch with a power spectrum amplitude nearly three times higher[6]. This is where the horizontal RMS energy in Table (1) is located.)

Fig. (5) Image of the Coupled Barrel and Turret Structure that Vibrates Horizontally with an Open-Loop Rotational Rigid Body Mode About the Turret Ring.

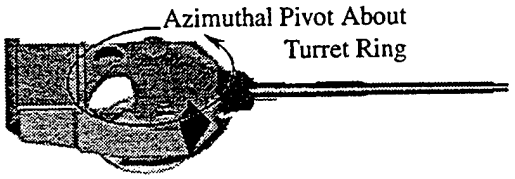

To better illustrate the disparity in size between the gun system and turret, a computer aided design image of the turret-barrel structure is depicted in Fig. (5).

Fundamental Vertical Mode Near 19 Hz

In the vertical orientation, the barrel is coupled to the turret by the two trunnion bearings, that provide for pivoting action. In addition, the elevation mechanism provides control actuation some distance behind the trunnions (about a half of a meter). The trunnions prevent vertical translation of the gun system relative to the turret and hull with a nearly rigid constraint, and little torsional resistance. The cantilevered configuration of the barrel is maintained by the vertical force input of the elevation system. Operated by hydraulics, and implemented with a control scheme, the constraint of the elevation system is not nearly rigid, but rather much softer.

This forgiving servo compliance is essential to prevent the force input from the suspension from reeking havoc with the stabilization and gun systems; it is desirable to decouple the gun system from the pitch and heave of the tank.

The center of mass of the gun system is not coincident with the trunnions but rather over hangs them by some distance. An open-loop control term, based upon a vertically oriented accelerometer fixed to the turret near the trunnions is used to compensate in real-time for the moment created by the weight of the gun at the center of mass and the acceleration at the trunnions. This enables the soft feedback servo-control parameters for the imbalanced system.

The first two flexible modes of a pinned free boundary condition have been evaluated using beam finite elements for the gun system without the thermal shrouds, bore evacuator, and CMRS mount. The resulting modes were computed to be 19.1 Hz and 32.4 Hz[7]. As in the horizontal case, the principle effect of the missing components on the model was a slight reduction in inertia from the fully configured case. This would tend to lower the fundamental modes.

Fig. (6) Image of the Barrel Structure that Vibrates Vertically with an Open-Loop Rotational Rigid Body Mode About the Trunnions.

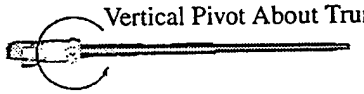

An illustration of the vertical system is depicted in analogy with Fig. (5) in Fig. (6).

The cause of the large amount of high frequency vibrational energy that is exciting the first vertical mode of the gun system is not clear. The second horizontal mode of the gun system is near in frequency, yet nearly no discernible energy is in its power spectrum above twelve Hz. At well over sixty tons in mass, the tank is a very effective low-pass filter and should drop off nominally at twenty decibels per decade from its two Hz fundamental as would any other second order damped system.

It has been suggested by Dr. Mark Kriegal, ARL, that the turret vibrates with a rigid body mode relative to the hull that is orthogonal to the azimuthal pivot in this frequency range. Such a structural coupling could cause a migration of this vibrational energy to the gun system.[8]

Another candidate for the high frequency source would be the open-loop control term used to counter the over-

hanging center of mass of the gun system. This term, although effective at maintaining the rigid body mode on target, applies a predictable disturbance bending moment to the gun system and vertical load to the turret and hull through the non-compliant trunnion bearings. Thus there is the potential for an undesirable feed-back loop, although the disparity in mass between the tank and gun system should lessen this type of effect.

Regardless, a higher order open-loop control term could counter any negative affects on performance by leveraging the inverse dynamics of a gun system model to compensate for the predictable disturbance applied by the current open-loop term. This would also provide enhancement to the low frequency disturbance, regardless of its validity as a cause for the high frequency disturbance.

Performance in Vertical Bending

The absorber performance was most pronounced in vertical bending; currently believed to be the largest contributor to degraded performance. The attenuation of the vertical bending was achieved without the migration of energy to other portions of the vertical bending spectrum. However, the absorber had little affect on the low frequency response that is asserted to be a direct result of the tank suspension.

This lack of low frequency performance is to be expected. A low frequency absorber would either require excessive mass to bring down its natural frequency, or an excessive amplitude envelope to store the potential energy of much softer springs.

Performance in Horizontal Bending

Of the three absorber configurations analyzed, two made horizontal bending significantly worse. The cause of the increase in horizontal bending for these two cases has been postulated to be the migration of vertical mode energy into the horizontal mode. The reason for the absence of this effect for absorber configuration C is not clear.

The shifting of this energy may be due to the severe amplitude restrictions placed upon the vibration absorber. Snubber engagement is a common event, and although it is likely to occur with the most momentum in the vertical orientation. The momentum transfer is likely to occur off the vertical axis, with a significant vector component delivered into the horizontal mode. For example, the vibration absorber ring, may impact the muzzle with vertical momentum, but strike the muzzle at a two O'clock position and thus rebound up and right, while forcing the barrel down and to the left.

To attempt to counter the migration of energy into the horizontal mode, future efforts will tune the horizontal and vertical mode absorbers separately via orientation dependent spring constants. An alternative would be to constrain the absorber from relative motion in the horizontal mode.

Regardless, modest increases in horizontal bending energy is likely worth significant reductions in vertical bending energy.

Performance in Vertical Pointing Error

The affect of the vibration absorber on vertical pointing error was a zero-sum-gain in the time domain. As can be seen in Fig. (4), the energy was shifted from the 19 Hz mode to much lower frequencies, a trait shared by the two other absorbers configurations[6]. This provides significant advantage for any active control scheme using the existing hardware.

Performance in Horizontal Pointing Error

The affect of the absorber on horizontal error was negligible. This lack of horizontal pointing sensitivity is likely caused by the large inertia of the turret structure that must be over come. (Recall that in the vertical mode, only the gun is pointed. In the horizontal mode, the entire turret is pointed.) This error signal is not likely to be reduced by a simple light-weight passive device, but neither is it greatly exacerbated by longer barrels.

Future Work / Preliminary Results

Although the most concentration has been applied to the design of a vibration absorber to external excitation; the concept may also be applied to attenuation of barrel flexure caused by successive fire. The preliminary test results of such a test firing are depicted below in Fig. (7).

The tests demonstrated that the vibration amplitude could be essentially cut in half using a simple vibration absorber. Evaluation of the effect on accuracy was not possible due to the short trajectory of the projectile flight within Benét gun dynamics laboratory. Further evaluation of the concept will be conducted later this fiscal year at the Advanced Testing Facility at ARDEC in Picatinny Arsenal, NJ.

CONCLUSIONS

This testing set out to demonstrate the proof-of-principle that a simple muzzle end vibration absorber could significantly enhance the structural dynamics of a tank cannon. This has been aptly demonstrated for absorber configuration C, as shown in Table (1) and Fig. (4). Therefore, investment in a ruggedized fixture to endure a firing environment is warranted.

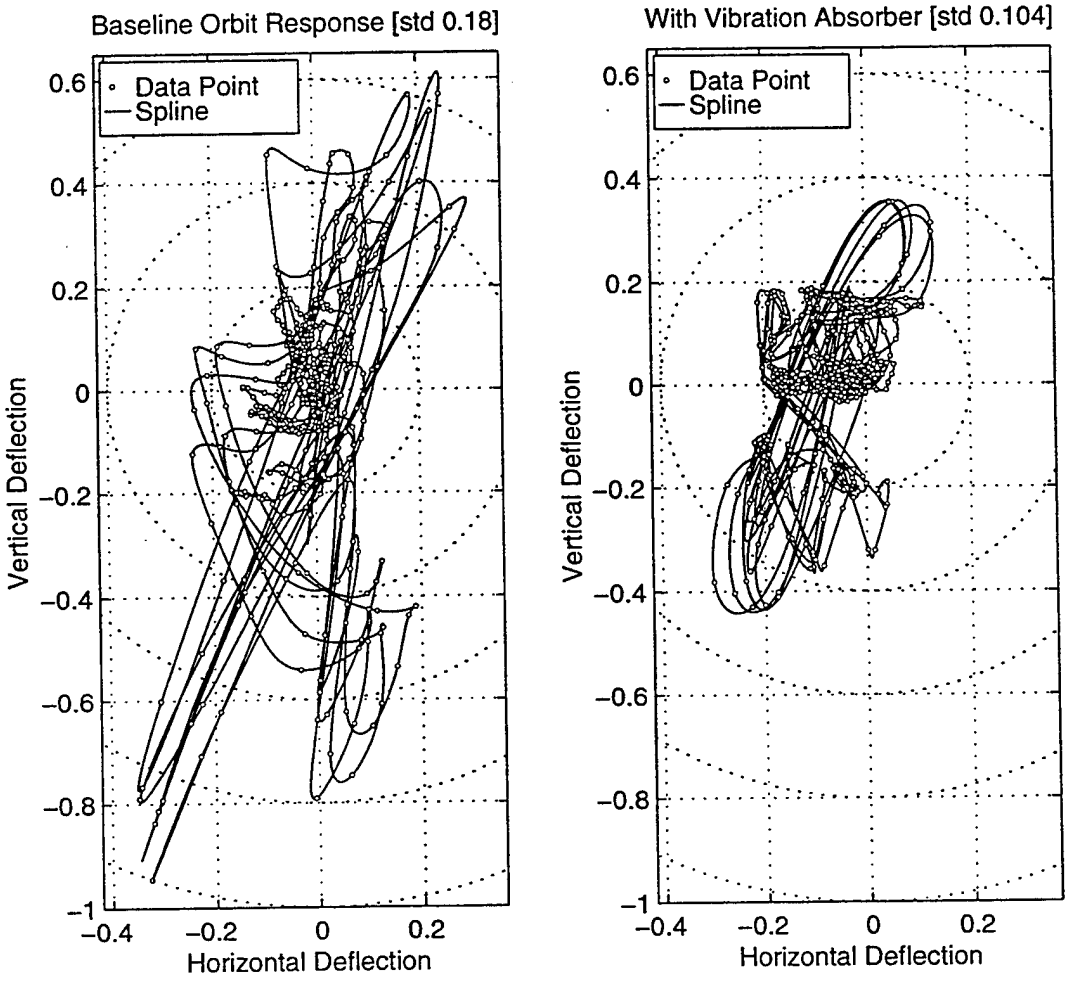

Fig. (7) Normalized Orbit Plots from Five Round Fire of Test Gun at Benét.

It must be emphasized that the performance gain demonstrated was achieved with virtually no impact on any other portion of the weapons system and no restrictions placed upon other future enhancement options.

Little direct correlation between the flexural state of the barrel and the ultimate impact on accuracy and performance is available. However, much indirect evidence indicates that shooting out of a vibrating barrel is not as effective as shooting out of a quiet barrel. Strong evidence for static curvature affects (manufacturing tolerance, thermal gradients, and gravity droop) on accuracy has been published. (See for example Wilkerson[9], Bundy[10], and Kathe et al[11].)

ACKNOWLEDGMENTS

The author would like to acknowledge the support of Rodger Billington and Charles Cording of the Program Manager - Tank Main Armament Systems, (PM-TMAS), Picatinny Arsenal, New Jersey; technical collaboration with Drs. Steven Wilkerson and Mark Kriegal, Army Research Lab, (ARL) and Peter McCall, Army Test Center, (ATC), Aberdeen Proving Grounds, Maryland, and Professor Andrew Lemnios, Rensselaer Polytechnic Institute, Troy, NY; and the assistance of Michael Soja, Albert Pflegl, and dedication of Edmund Vanderwerken, of Benét Laboratories.

BIBLIOGRAPHY

1. McCall, P., "ATAC TEST RESULTS: Summary of Test Configurations and Test Results from 1993 to Present," Presented at a Meeting of the Program Manager - Tank Main Armament Systems, (PM-TMAS), Picatinny Arsenal, NJ, 22 March 1996.
2. Soja, M., "XM291 Hardstand Fire Testing Results," presented at Join Meeting of PM-ABRAMS, PM-TMAS, and Benét Laboratories, Watervliet Arsenal, NY, 06 December 1995.
3. Gast, R. G. et al, "Accuracy Enhancement of the 120-mm XM291 Gun," Proceedings of the Eighth U.S. Army Symposium on Gun Dynamics, G. Albert Pflegl, Ed., ARDEC Technical Report ARCCB-SP-96032, Benét Laboratories, Watervliet, NY, May 1996, pp. 22.1-28.
4. Kathe, E. L., "Design of Passive Vibration Absorber to Reduce Terrain-Induced Gun Barrel Vibration in the Frequency Domain," Proceedings of the Eighth U.S. Army Symposium on Gun Dynamics, G. Albert Pflegl, Ed., ARDEC Technical Report ARCCB-SP-96032, Benét Laboratories, Watervliet, NY, May 1996, pp. 28.1-17.
5. Kathe, E. L., "Design and Validation of a Gun Barrel Vibration Absorber," Proceedings of the 67th Shock and Vibration Symposium: Volume 1, Published by the Shock and Vibration Information Analysis Center (SAVIAC), Monterey, CA, 18-22 November 1996, pp. 447-456.
6. Kathe, E. L., "Performance Assessment of a Synergistic Gun Barrel Vibration Absorber During Bump-Course Testing," ARDEC Technical Report ARCCB-TR-97022, Benét Laboratories, Watervliet, NY, September 1997.
7. Kathe, E. L., "MATLAB Modeling of Non-Uniform Beams Using the Finite Element Method for Dynamics Design and Analysis," ARDEC Technical Report ARCCB-TR-96010, Benét Laboratories, Watervliet, NY, April 1996.
8. Kriegal, M., "Private Communication," July 1997.
9. Wilkerson, S., "The Effect of Initial and Gun Mount Conditions on the Accuracy of Kinetic Energy (KE) Projectiles," U.S. Army Research Laboratory Technical Report ARL-TR-895, Aberdeen Proving Ground, MD, November 1995.
10. Bundy, M. L., "Thermally Controlled Bore Straightness During Firing," Proceedings of the Eighth U.S. Army Symposium on Gun Dynamics, G. Albert Pflegl, Ed., ARDEC Technical Report ARCCB-SP-96032, Benét Laboratories, Watervliet, NY, May 1996, pp. 6.1-12.
11. Kathe E., Wilkerson S., Zielinski, A., and Baz, A., "Gun Structural Dynamics Considerations for Near-Target Performance of Hyper-Velocity Launchers," IEEE Transactions on Magnetics, *to appear*, January 1999.

APPENDIX

The data for the median vertical bending RMS base-line test and absorber configuration C test are included for completeness. The plots include time response, frequency response (square-root of the power spectrum magnitude), and hybrid time-frequency response. The time axes are keyed to a depiction of the bump-course, as in Fig. (3), below at the base of the plots to facilitate reading cause and effect in the temporal data. To ease the computational burden, all of the data was decimated by a factor of five prior to analysis after appropriate low-pass filtering.

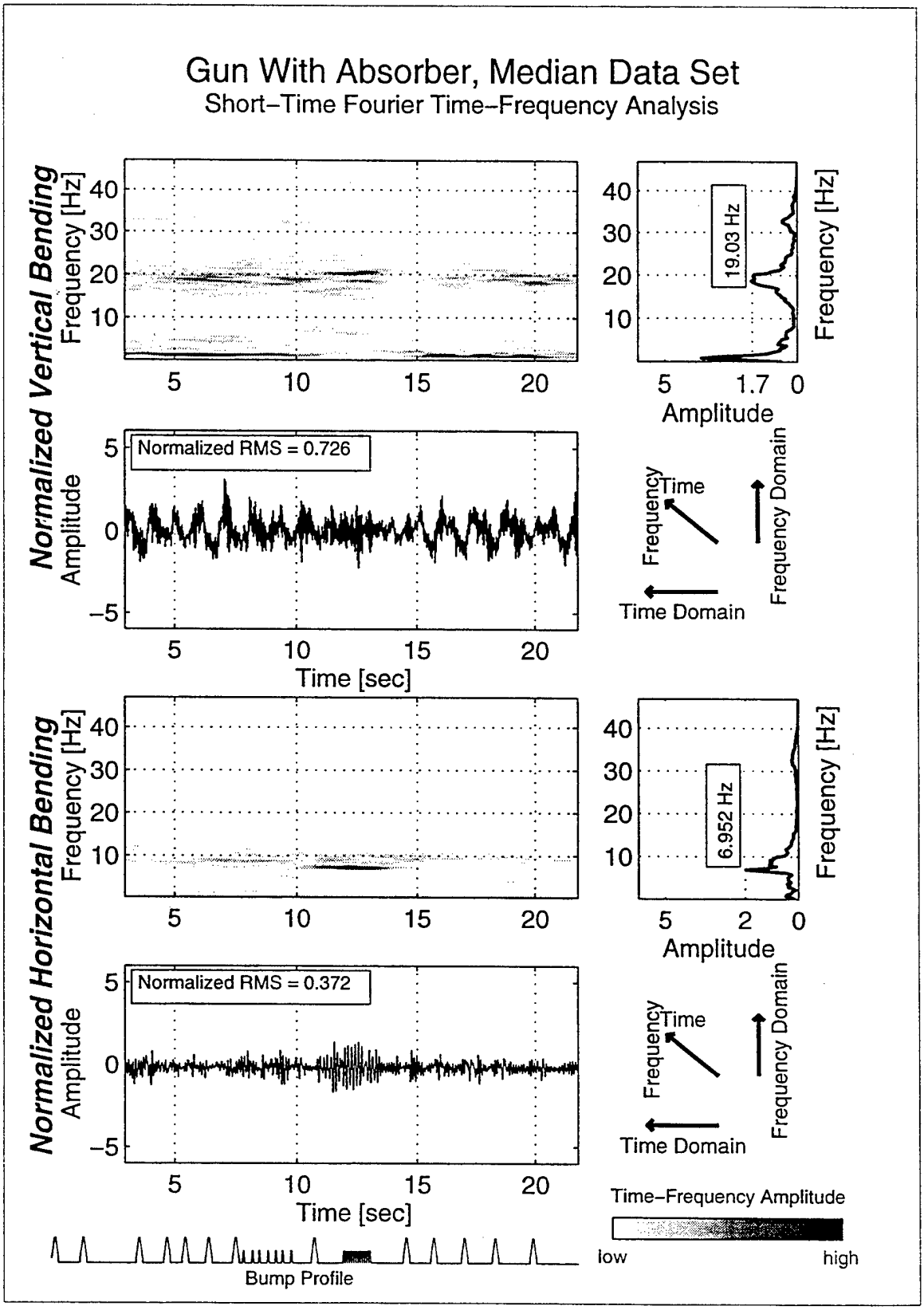
Gun With Absorber, Median Data Set
Short–Time Fourier Time–Frequency Analysis
Normalized Vertical Bending
Frequency [Hz]
40
30
20
10
5
10
15
20
19.03 Hz
5
1.7
0
Amplitude
Frequency [Hz]
Normalized RMS = 0.726
Amplitude
5
0
−5
Time [sec]
Frequency
Time
Frequency Domain
Time Domain
Normalized Horizontal Bending
6.952 Hz
Normalized RMS = 0.372
Time–Frequency Amplitude
low
high
Bump Profile

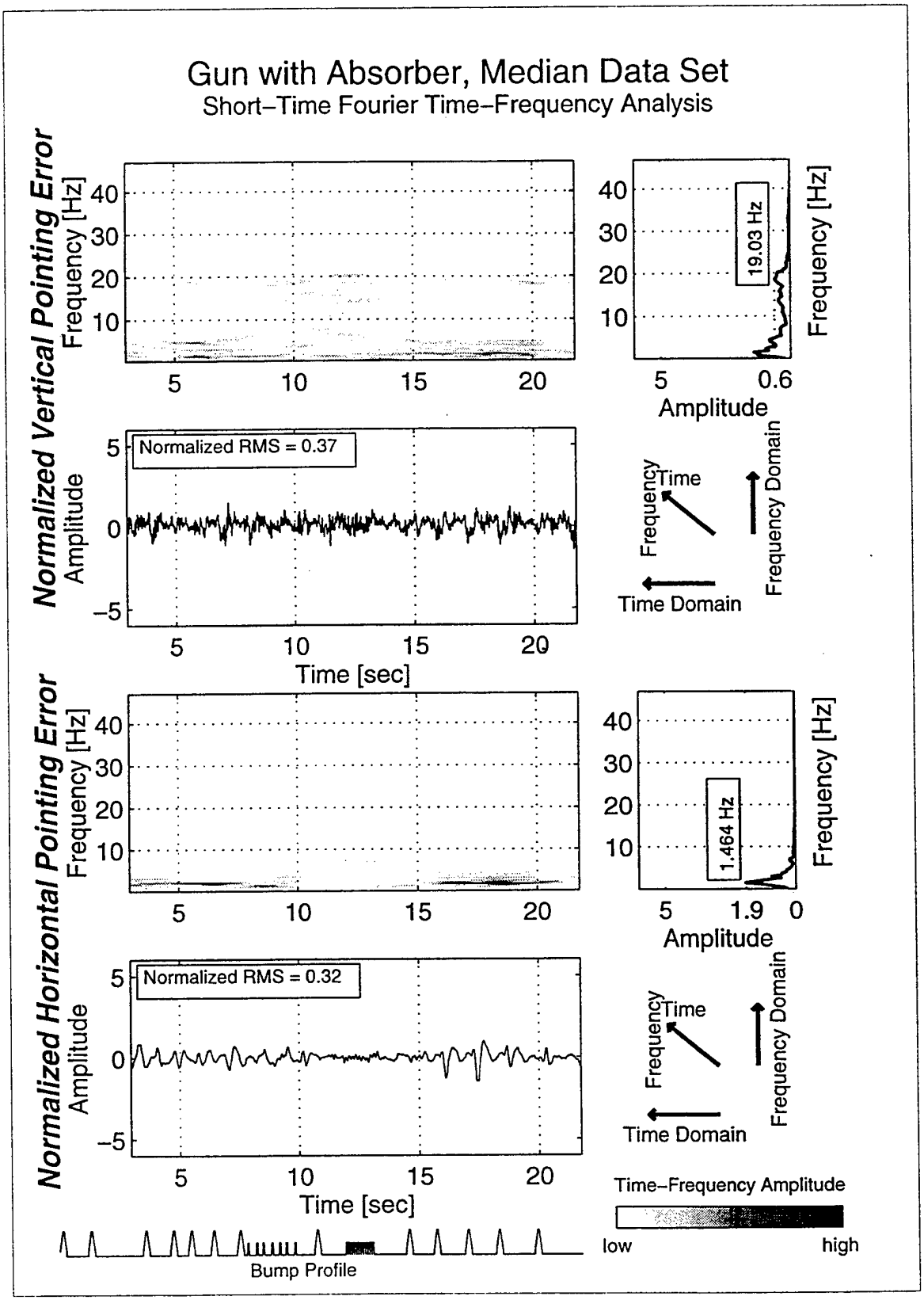
Gun with Absorber, Median Data Set
Short–Time Fourier Time–Frequency Analysis
Normalized Vertical Pointing Error
Frequency [Hz]
40
30
20
10
5
10
15
20
19.03 Hz
5
0.6
Amplitude
Frequency [Hz]
Normalized RMS = 0.37
Amplitude
5
0
−5
5
10
15
20
Time [sec]
Frequency
Time
Frequency Domain
Time Domain
Normalized Horizontal Pointing Error
Frequency [Hz]
40
30
20
10
5
10
15
20
1.464 Hz
5
1.9
0
Amplitude
Frequency [Hz]
Normalized RMS = 0.32
Amplitude
5
0
−5
5
10
15
20
Time [sec]
Frequency
Time
Frequency Domain
Time Domain
Time–Frequency Amplitude
low
high
Bump Profile

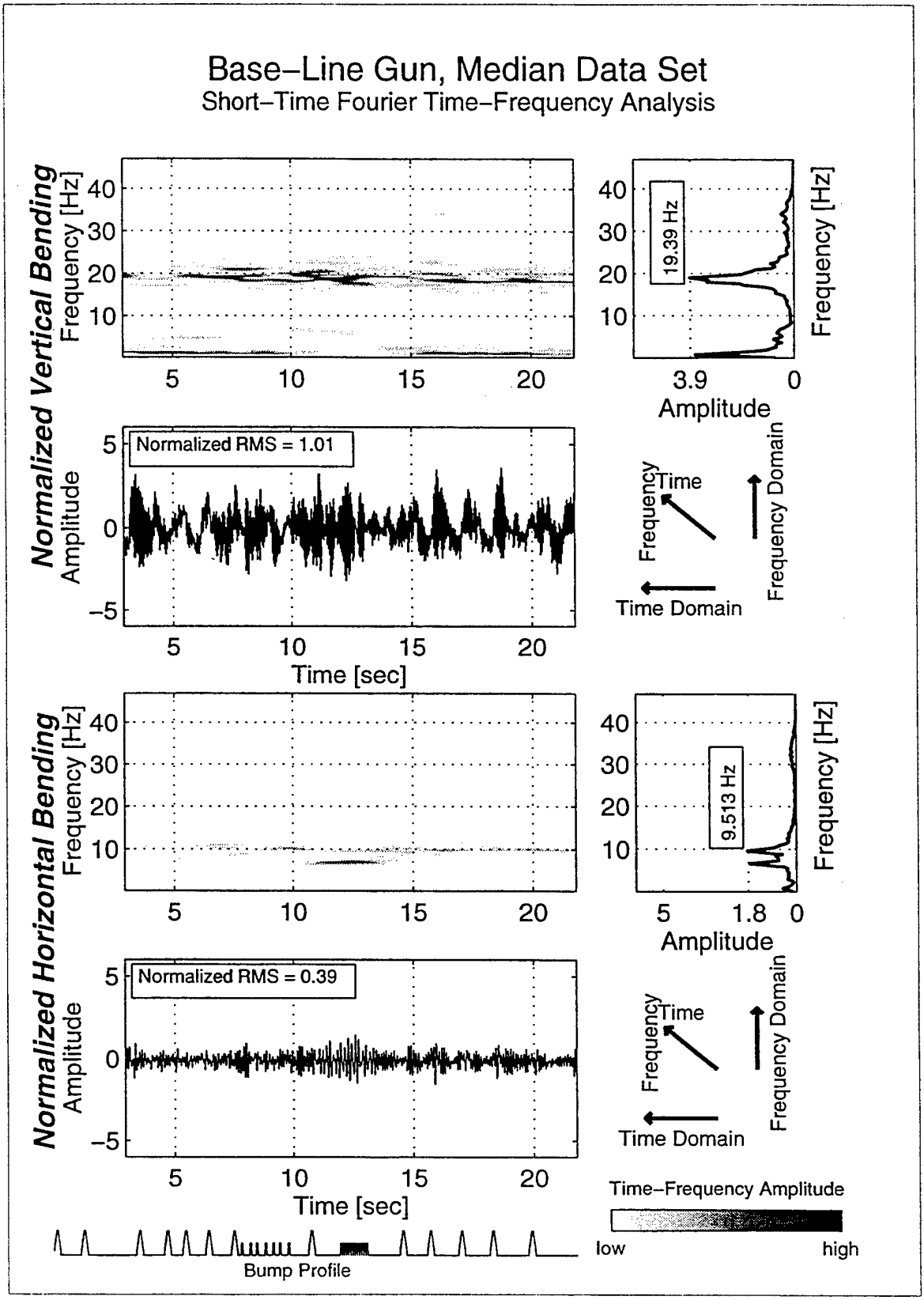
Base–Line Gun, Median Data Set
Short–Time Fourier Time–Frequency Analysis
Normalized Vertical Bending
Frequency [Hz]
40
30
20
10
5
10
15
20
19.39 Hz
3.9
0
Amplitude
Frequency [Hz]
Normalized RMS = 1.01
Amplitude
5
0
−5
Time [sec]
Frequency
Time
Frequency Domain
Time Domain
Normalized Horizontal Bending
9.513 Hz
1.8
Normalized RMS = 0.39
Time–Frequency Amplitude
low
high
Bump Profile

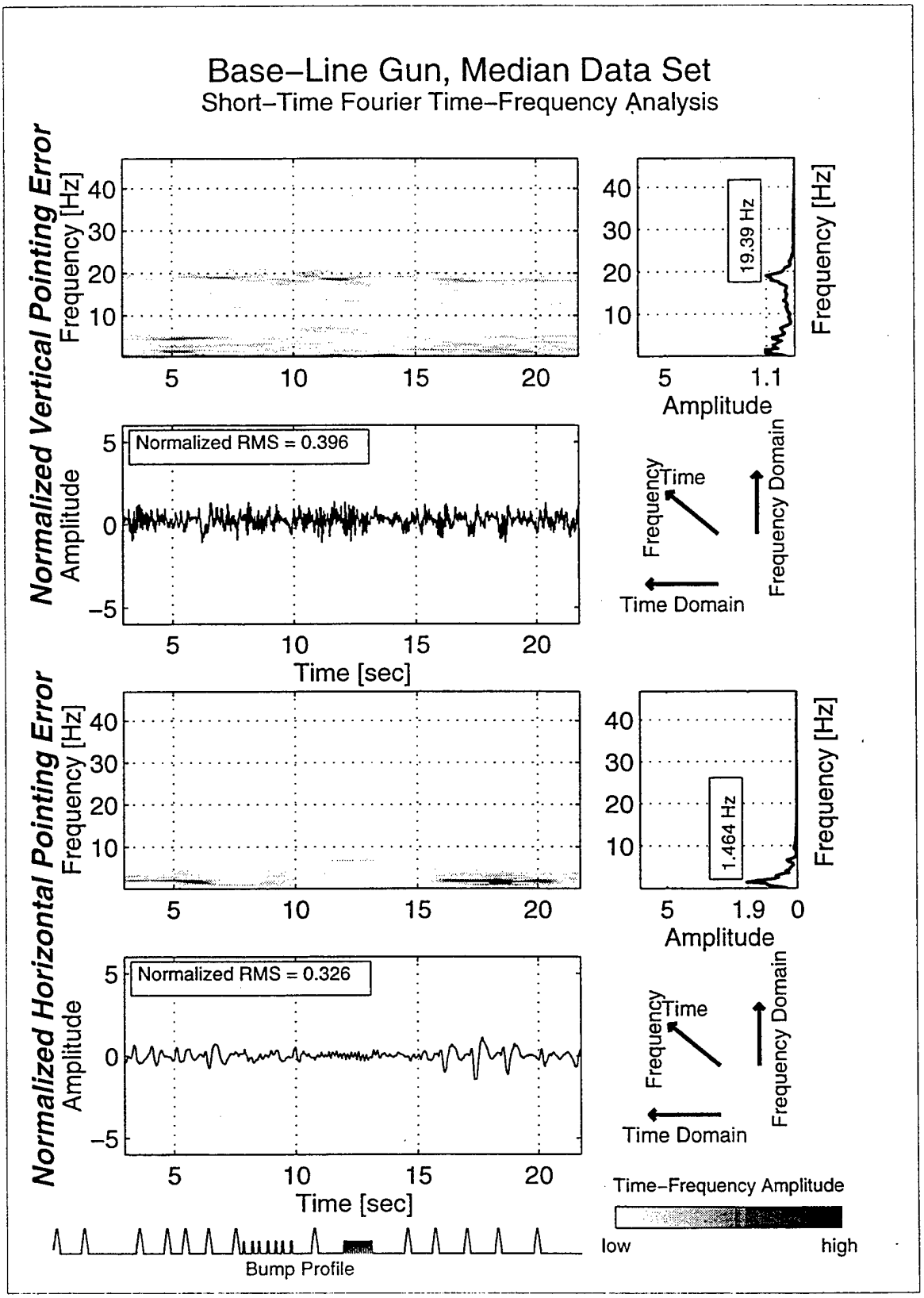
Base–Line Gun, Median Data Set
Short–Time Fourier Time–Frequency Analysis
Normalized Vertical Pointing Error
Frequency [Hz]
40
30
20
10
5
10
15
20
19.39 Hz
5
1.1
Amplitude
Frequency [Hz]
Normalized RMS = 0.396
Amplitude
5
0
−5
Time [sec]
Frequency
Time
Frequency Domain
Time Domain
Normalized Horizontal Pointing Error
1.464 Hz
1.9
0
Normalized RMS = 0.326
Time–Frequency Amplitude
low
high
Bump Profile

Launch Dynamic Calculations in DADS for Calibre 155 mm (L/52)

Christer Larsson
Bofors Weapon Systems
SE-691 80 KARLSKOGA
SWEDEN

Tests have shown in later generations of howitzers some problems regarding launching disturbances at the projectile exit and barrel wear. A mechanical model of the gun and projectile has been developed in the program DADS in order to simulate in-bore dynamics. The barrel is divided into a number of rigid bodies which are connected to each other via elastic beam elements. The model can handle drooped barrel forms due to gravity as well as bent forms due to manufacturing. An investigation using this model shows that there are some important parameters inducing these problems. These are:

- the center of gravity in the radial direction of the projectile
- the barrel straightness especially in a small distance from the muzzle

INTRODUCTION

Later generations of howitzers have improved their range of fire quite dramatically. This is due to, among other things, longer (L/52) barrels. Tests have pointed out some problems regarding launching disturbances at the muzzle exit. The projectile leaves the muzzle in a direction that diverts from the barrel attitude. If the initial difference in attitude becomes to large, a major barrel wear and a reduction in range and accuracy will occur.

This report is a summary of [1] Bofors Weapon System's document No 2744705 edition No 1, Studie av utskjutningsstörningar i L/52 kaliber 155 mm (Investigation of launching disturbances in L/52 calibre 155 mm).

THE MECHANICAL MODEL

The simulation is based on a mechanical model consisting of barrel, projectile, muzzle brake, breech, cradle, etc.

The barrel is divided into rigid bodies which are connected to each other via elastic (Euler-Bernoulli) beam elements. The rigid bodies represent the barrel mass and mass moment of inertia. Transparent cylinders are plotted by the program for visual checking. Elastic beams represent the stiffness of the barrel. Mass points such as breech and muzzle brake can be connected to the barrel. The model can handle drooped barrel forms due to gravity as well as bent forms due to manufacturing. The barrel is connected to the cradle via bearings. The connection is represented by a contact algorithm. The algorithm uses the bearing gap and the bearing stiffness. It is also possible to couple a recuperator and a recoil buffer between the barrel and the cradle.

The projectile can be modelled rigid or elastic. In the elastic case this is done by means of rigid bodies connected by elastic beam elements. The projectile is visualized as a solid cone (see fig 1). The projectile center of gravity and the position/orientation at start are examples of input data. The projectile interacts with the barrel via the rear and the front centering bands. This connection to the barrel is represented by a Bofors developed contact algorithm, using a gap function (includes wear) and linear/non linear stiffness. The influence of the rifling is controlled by constraint equations which transform the projectile translation to rotation. In the simulation the

projectile is accelerated by the pressure of the propellant combustion gases which act at the rear face of the projectile.

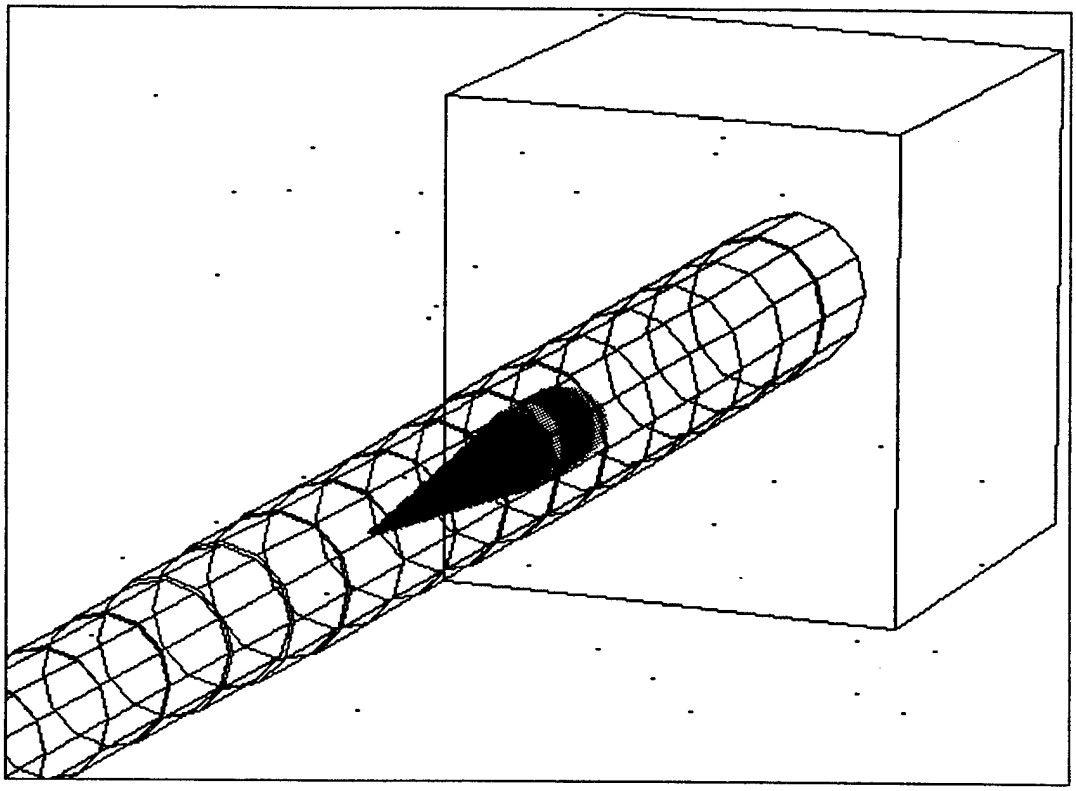

Fig 1. Some parts of the model.

The model is simulated in the program DADS [2] (Dynamic Analysis and Design System) which consists of a preprocessor, a solver and a postprocessor. The solver forms the mathematical equations and can solve nonlinear differential algebraic equations. Position, velocity, acceleration and reaction forces are predicted for all parts in the model. Finally, the analysis results can be studied in the postprocessor. Animation of the results to visualize the total system behavior is fairly straight forward.

One of the reasons for making the model in DADS is that the user quite easily can make changes and implement other options. Some examples of these options are:

- counter mass gun
- firing in a recoil swing mounting
- elastic mount coupled to the elevating system
- connections to control systems

In many cases it is also important to simulate a total gun system since different technical areas are depending on each other. For example, when firing multiple shots (repeated fire), the mounting has a big influence on the motion of the projectile. The recoil forces will exite constraint modes and after the first shot also normal modes (structural vibration modes) of the elevating system, the mount and the weapon carrier. These modes are possible to get through structural analysis of a finite element model (FEM).

An other technical area is the influence of the control system when firing. When the recoil forces act at the trunnions the transmission will be forced to move because of the elastic behaviour of the mount.

The problem is to integrate these different analyses into a single program to be able to simulate a total gun system. The way Bofors has made this is presented in figure 2.

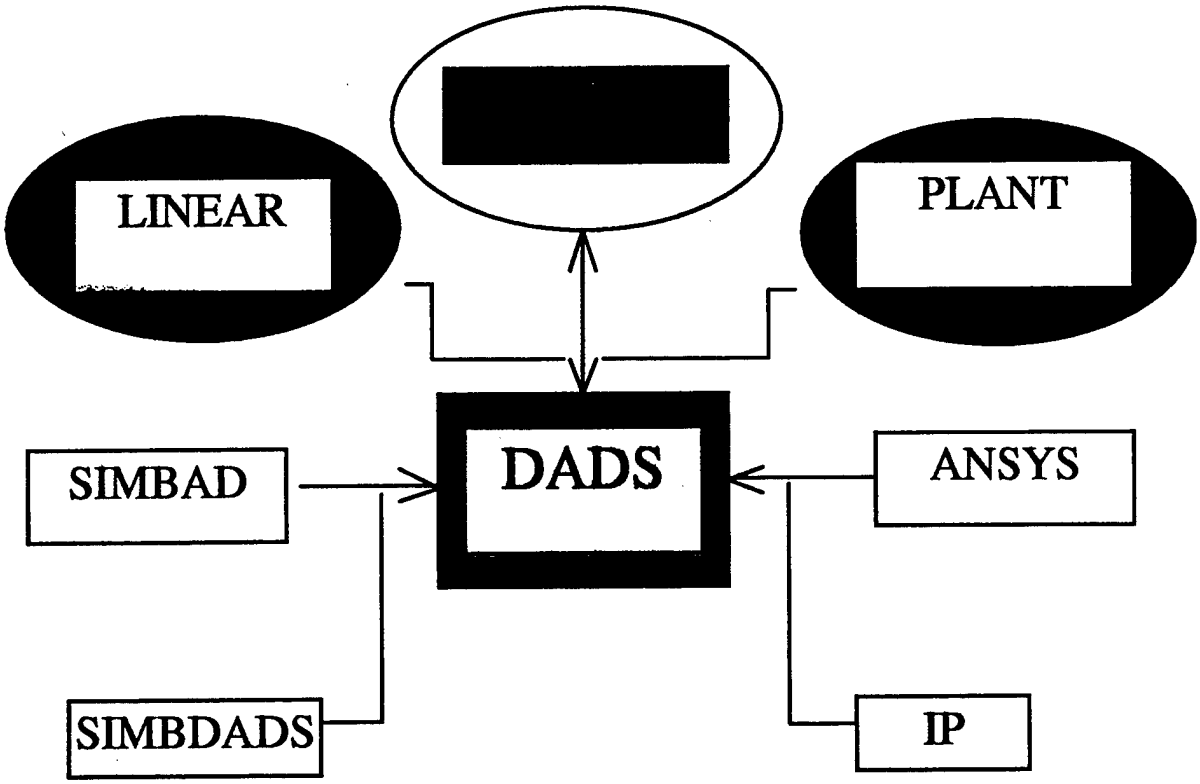

Figure 2. Simulation of a total gun system.

The main program to do these analyses is DADS. The constraint and normal modes are calculated in the FE program ANSYS [3] and are incorporated to the bodies in DADS via an interface called IP (Intermediate Processing).

To speed up the development process the launch dynamic model is built in SIMBAD [4] (SIMulation of BArrel Dynamics) and transfered to DADS via a Bofors developed interface called SIMBDADS. Thereby data such as barrel profile and wear are quite easily put into the program interactively. This enables the user to make parametrical studies in order to find sensitive parameters.

The control system is built in $MATRIX_X$ [5]. DADS and $MATRIX_X$ then simulate the dynamics of the total gun system together. At the same time step in the analysis $MATRIX_X$ sends forces and torques to the bodies which are controlled and DADS sends the motions of the bodies as an input to the control system.

After the projectile exit it is also possible to make exterior ballistics calculations into DADS.

BARREL STRAIGHTNESS

The barrel straightness due to manufacturing is measured and figure 3 shows an example of the barrel center line in a bad case. This example has been used in some of the calculations.

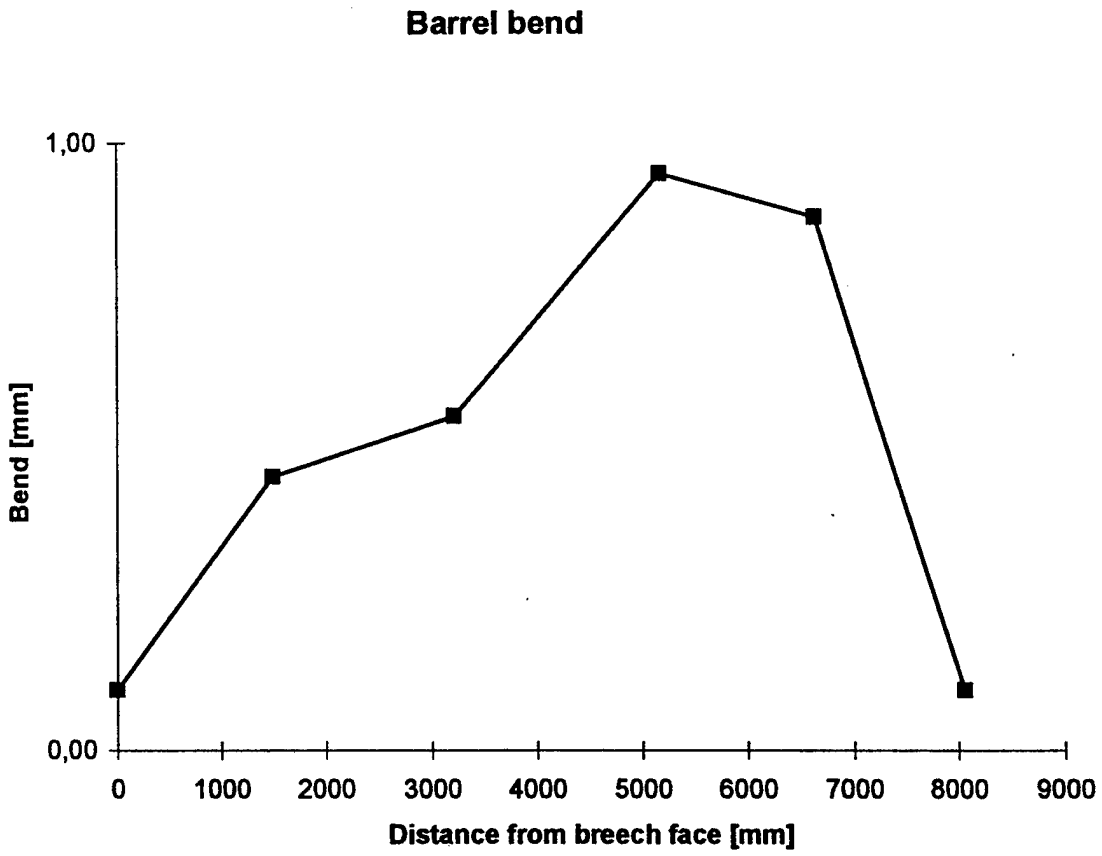

Fig 3. Example of barrel bending due to manufacturing.

PROJECTILE DATA

Some projectile data were measured on the configuration below (see fig 4). In this setup an adapter replaced the proximity fuze. This was done in order to rotate the projectile on two supports with a proper distance between them because the position of the center of gravity is close to the front centering band.

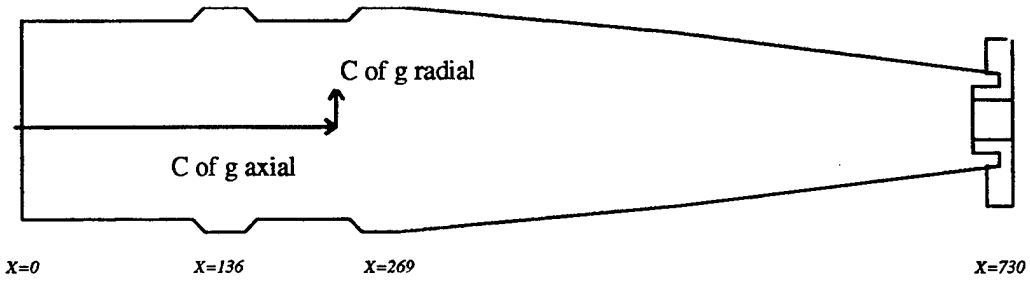

Fig 4. Projectile configuration for measurement.

Mass and center of gravity

The projectile mass was found by putting the projectile on a balance. The center of gravity in the axial direction was measured by a balance. The center of gravity offset in the radial direction was calculated from measurements in a balancing machine on the rotating projectile. The rear face of the projectile equals origo, see fig 4. For results see fig 5.

Mass moments of inertia

The mass moments of inertia in the pitch, yaw and roll directions were measured in a rotation machine. The results were adjusted according to the difference in mass moment of inertia between the dummy and the proximity fuze. Each projectile was measured five times to achieve good accuracy. The output given in fig 5 is a result from measurements on the rotating projectile as in fig 4.

Geometric difference of attitude

The geometric difference of attitude is in this case defined as the angle between the axes of the "perfect" projectile and the balanced axes of the test projectile. This is done by measuring the radial deflection during rotation (see fig 4, 5).

Inclination of the principal axis of inertia

The inclination of the principal axis of inertia is in this case defined as the angle between the principal axes of inertia of the "perfect" projectile and the principal axes of inertia of the test projectile. These values were calculated from measurements in a balancing machine (see fig 4, 5).

Properties		Mean
Weight	(kg)	41.7
Center of gravity		
Axial direction	(mm)	326
Offset in the radial direction	(mm)	0.15
Mass moments of inertia		
Pitch	(kgm^2)	1.78
Yaw	(kgm^2)	1.78
Roll	(kgm^2)	0.141
Geometric difference of attitude		
Yaw	(mrad)	0.008
Pitch	(mrad)	-0.026
Dynamic inclination of principal axis of inertia		
Yaw	(mrad)	0.003
Pitch	(mrad)	0.369

Fig 5. Data for HEER (BB).

FE CALCULATION OF CONTACT INTERFACE BARREL/SHELL

The shell and a piece of the barrel were modelled in the finite element code ANSYS (see fig 6). The purpose was to analyze the behaviour of the deformation during contact to obtain input data for the simulations.

The calculation was done statically in an acceleration field in the transverse direction. The barrel was given a zero density in order to put the load only on the shell. This means that the shell was accelerated by x m/s^2 relative to the barrel according to the load case in fig 7.

The contact stresses, resulting in forces, transmitted via the centering bands can be studied in fig 8. The displacement together with the nodal forces gave the contact stiffness. These stiffnesses are nonlinear and vary along the barrel. Some results are presented in fig 7.

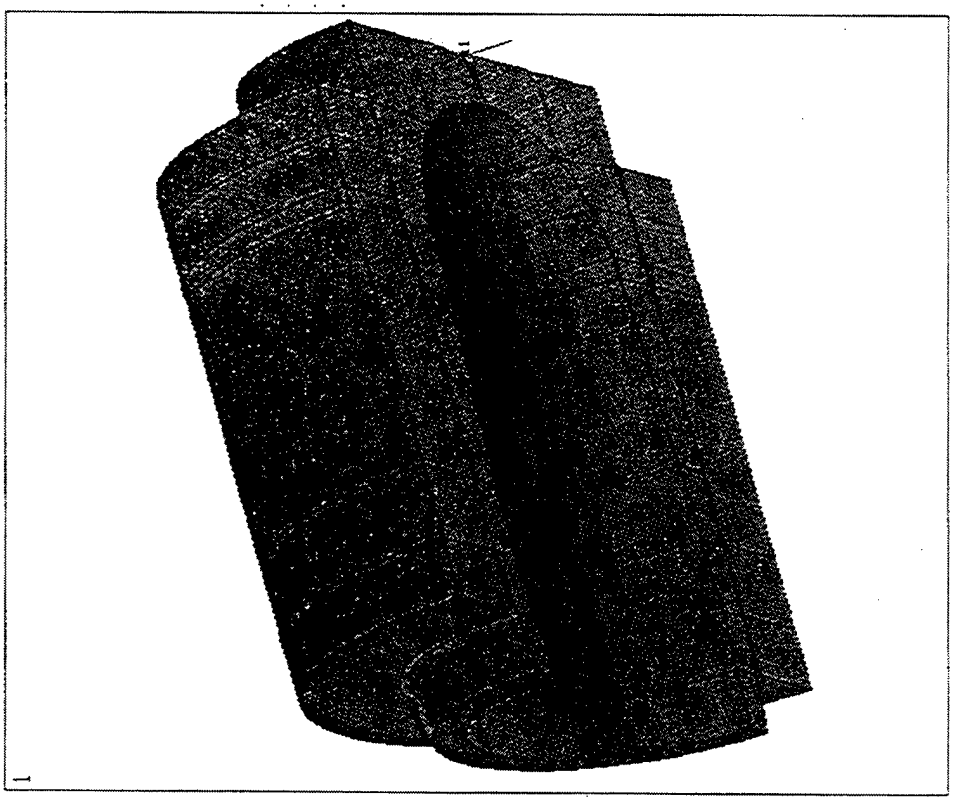

Fig 6. FE-model of HEER (BB) inside the barrel.

Load case (m/s^2)	Contact stiffness front centering band (N/m)	Contact stiffness rear centering band (N/m)
10000	$1.20*10^8$	$3.19*10^8$
30000	$1.37*10^8$	$3.41*10^8$
100000	$1.47*10^8$	$3.52*10^8$

Fig 7. Contact stiffness between barrel and shell.

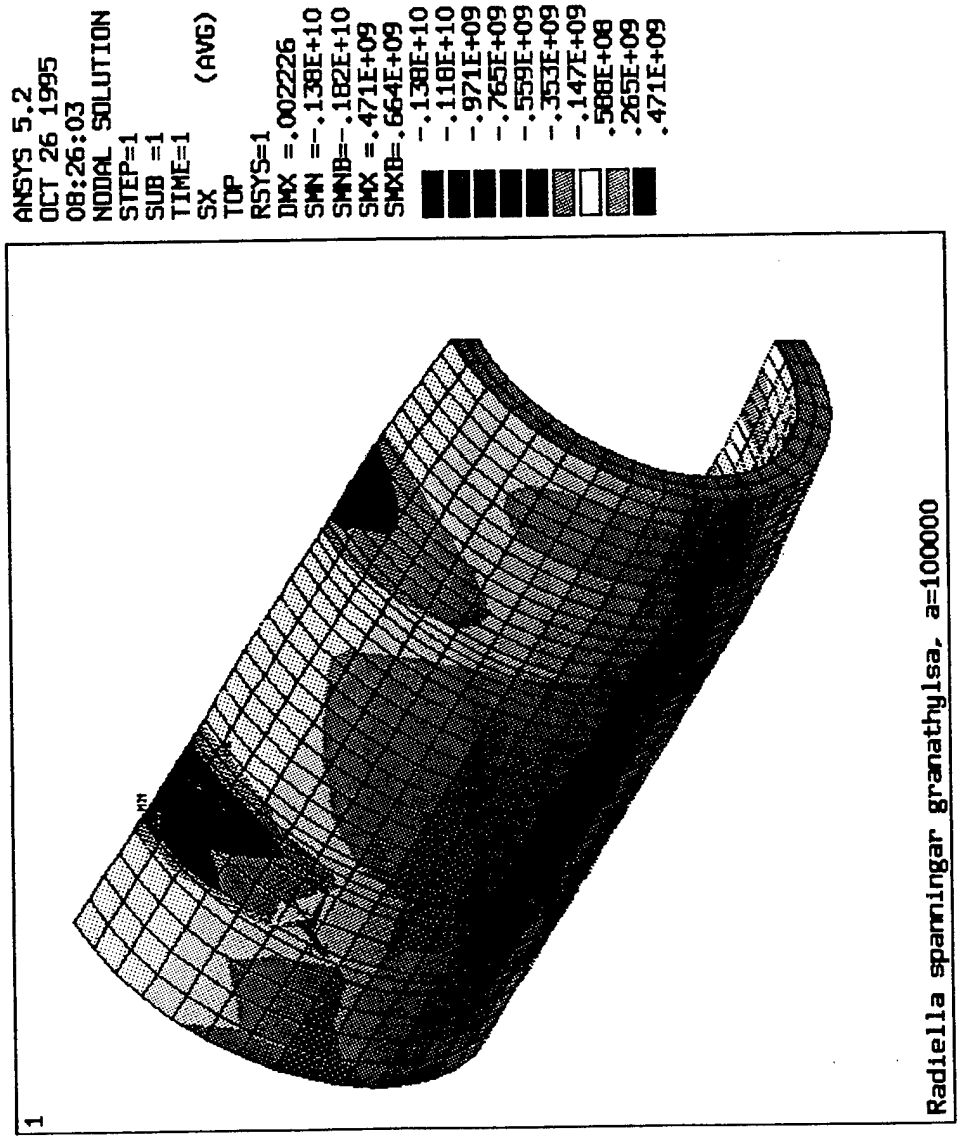

Fig 8. Stress plot, shell.

COMPOSED CASES FOR THE SIMULATION

To reduce the number of cases for simulation earlier experience has been used. The varied parameters are given below:

projectile center of gravity radial offset r_{cg}
" " " " axial offset x_{cg}
" muzzle velocity v_0
inclination of projectile principal axis of inertia
start orientation of the projectile in the barrel (considering center of gravity radial offset)
gap between centering bands and the barrel
bent and drooped barrel

The simulations have been divided into six different cycles. The start orientation of the projectile in the barrel is varied in four angles: 0° , 90° , 180° and 270° . 0° is equivalent to a center of gravity offset upwards, 90° to the right seen from the rear. This gives 24 simulation cases. The projectile center of gravity radial offset is given a constant value in the cycles 1-4. This strategy gives the opportunity to look for other sensitive parameters.
A barrel bent shape and is used in the calculations. The barrel is also deformed by a static droop caused by gravity.

The pressure-time curve is calculated in an internal ballistic computer program. In the simulations the projectile velocity at muzzle passage, v_0, amounts to 959 m/s. The barrel is modelled elastic and is divided into 25 beam elements and the projectile is modelled rigid with elastic centering bands. The barrel is fitted into an experiment cradle with a heavy breech ring.

RESULTS OF LAUNCH DYNAMIC CALCULATIONS IN DADS

One of the most interesting results from the investigation is of course the motion of the projectile. Another is the contact forces between the shell and barrel which can cause wear of the barrel.

The angular velocities at the muzzle passage are presented in the diagram below (see fig 9). The mean pitch and yaw velocities are 1.8 and 3.5 rad/s respectively. Furthermore forces and angles vs time are presented in fig 10, 11 and 12.

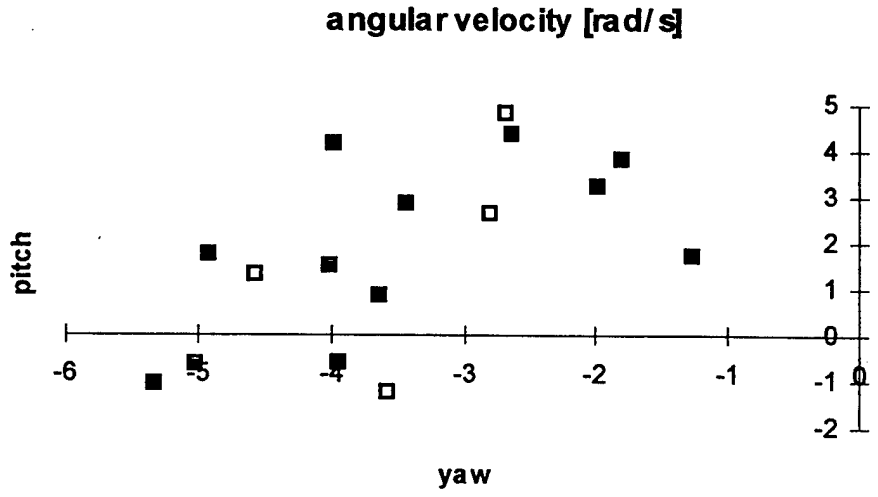

Fig 9. Projectile angular velocity at the muzzle passage.

orientation in the barrel [deg]	pitch angle [mrad]	yaw angle [mrad]	pitch velocity [rad/s]	yaw velocity [rad/s]	rear force centering band [N]	front force centering band [N]
0	2,4	-1,02	-2,64	4,36	77100	38800
90	-1,03	-0,65	-4,02	1,5	59000	69000
180	-2,55	-3,92	-5,02	-0,63	58800	52400
270	1,85	-4,02	-3,99	4,16	47800	49500
Mean	0,167	-2,40	-3,91	2,34	60600	52400
Std dev	2,35	1,81	0,976	2,37	12100	12500
0	1,78	-0,7	0,85	2,24	158900	50200
90	-2,01	-0,87	-1,68	0,33	106700	81200
180	-1,67	-3,88	-2,06	0,83	54900	85500
270	1,66	-3,45	-0,27	2,92	162400	57000
Mean	-0,06	-2,22	-0,79	1,58	120700	68400
Std dev	2,06	1,67	1,33	1,20	50700	17400

Fig 10. Example of results from a parameter variation.

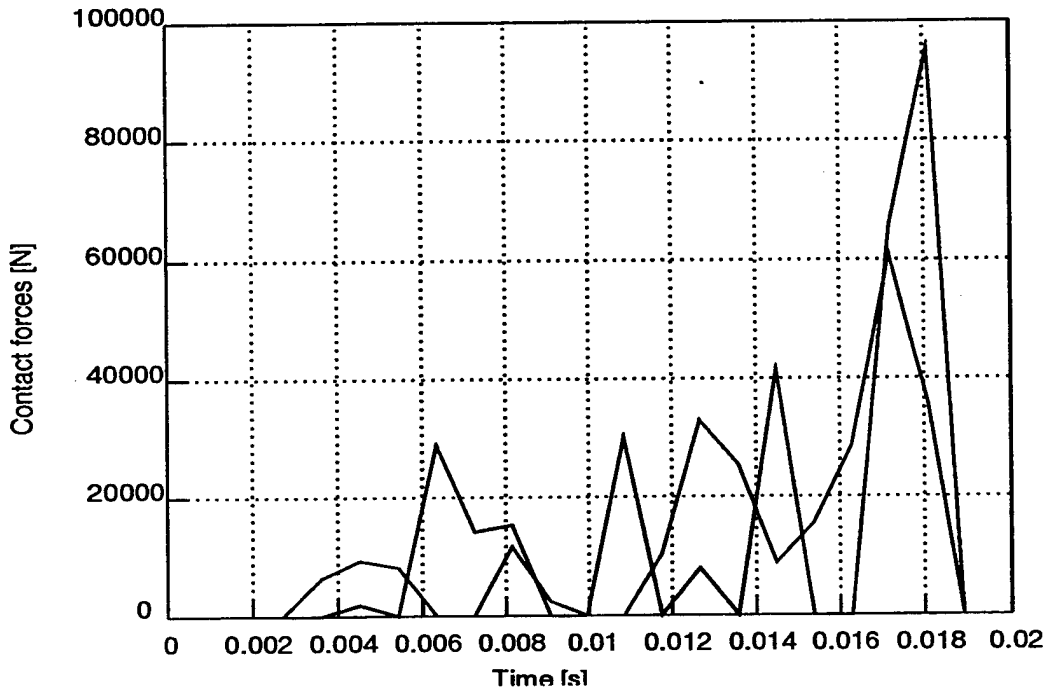

Fig 11. Example of rear (blue) and front (red) centering band forces in the barrel phase.

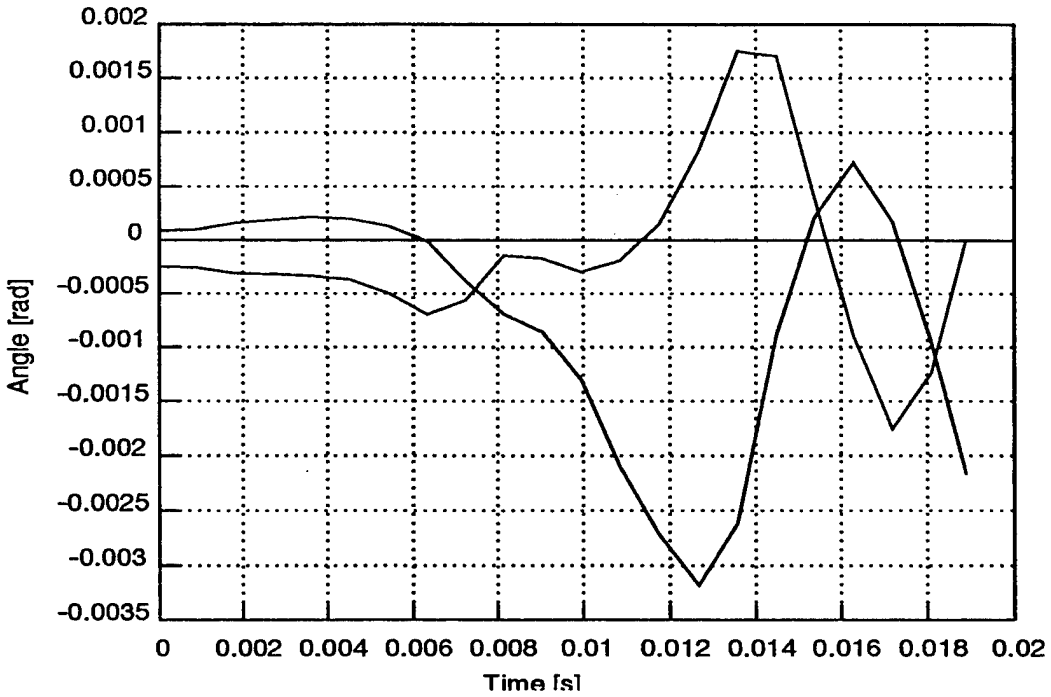

Fig 12. Example of pitch (red) and yaw (green) angles in the barrel phase.

TRAJECTORY CALCULATIONS IN ARTGEN

Since the measurements of the firings are concentrated to projectile attitude at some distance from the muzzle the results from the calculations must be extrapolated to that point. This is done in the external ballistics computer program ARTGEN (developed by BOFORS AB). Trajectory calculations have been made in six degrees of freedom with aerodynamic data valid for HEER (BB). The calculations are based on the Swedish defence standard atmospheric conditions. The projectile angles at the muzzle passage are neglible compared to the angles of attack calculated as a result of the angular velocity. For this reason the angle of attack is calculated for different angular velocities at the muzzle passage. The angles of attack measured at firing tests corresponds quite well to the angular velocities calculated in the DADS model.

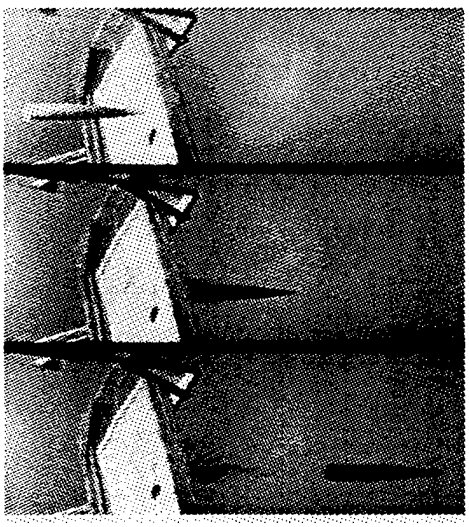

Fig 13. Photo of the projectile attitude in the proximity of muzzle exit.

CONCLUSIONS

Earlier firings in a L/52 barrel that was extended from a L/39 barrel revealed severe wear and inclined projectile attitudes. The barrel consisted of two parts that were joined together. The small radius of bending locally at the joint between the barrel parts was critical in this respect. Firing in a one piece barrel L/52 has shown quite small problems even at muzzle velocities of 1000 m/s for the projectile used in this study.

Some prime actions in order to decrease the angle of attack and the angular velocity vector are:

Most important

- Minimize the displacement of the center of gravity in the radial direction of the projectile
- The barrel should be straight especially close to the muzzle

Important

- Projectile axial center of gravity is placed between the rear and the front centering bands
- Gap between centering bands and the barrel is decreased
- Muzzle velocity is decreased
- Inclination of principal axis of inertia is decreased

Some prime actions in order to decrease the maximum contact forces are:

Most important

- The barrel should be straight especially close to the muzzle

Important

- The gap between the centering bands and the barrel is decreased

For development of the next generation of artillery it is very important to set tolerances for barrels and projectiles due to launch dynamics.

REFERENCES

[1] Larsson C, Studie av utskjutningsstörningar i L/52 kaliber 155 mm (Investigation of launching disturbances in L/52 calibre 155 mm), Technical report document No 2744705 edition No 1, Bofors Weapon Systems AB, Karlskoga, Sweden, 1995.

[2] DADS Reference Manual Revision 8.5, CADSI Inc., Coralville, U.S.A., 1997.

[3] Basic Analysis Procedures Guide Release 5.4, ANSYS Inc., Canonsburg, U.S.A., 1997.

[4] SIMBAD Version 23, Danby Engineering Ltd., North Yorkshire, UK, 1997.

[5] MATRIX$_X$-System Build User's Guide, Integrated Systems Inc., Santa Clara, U.S.A., 1996.

CHARACTERIZATION OF THE DYNAMIC STRAIN EXCITATION FORCE IN GUN TUBES

DAVID F. FINLAYSON
U. S. Army ARDEC
Close Combat Armaments Center
Benet Laboratories
Watervliet, NY 12189-4050

ABSTRACT

The motivation for undertaking this study was to discover the mechanism and nature of the excitation force that results from the movement of the propellant pressure step that follows a projectile in a gun tube. This is accomplished by starting with the concept of multiple periodically space pressure steps (square wave) and proceeding to the limiting case of a single pressure step and thereby introducing the Fourier integral and transform. Using the Fourier transform to analyze the moving pressure step leads to a ring load with specified amplitude and phase spectrums over the entire frequency range. The concept is further demonstrated by using Fourier transformation to sum the response of a simply derived (and simple) shell model of a gun tube to single wave number (frequency) inputs to obtain the response of the tube to a moving pressure step.

INTRODUCTION

The first observations made in gun tubes of what has come to be known as dynamic strain, are recounted in previous papers [1, 2]. What appear to be the earliest investigations of the phenomenon [3, 5], however, took place well before the first observations of it gun tubes; presumably, either in response to observations of the effect in cylindrical shells other than gun tubes, or as natural extensions of the problems of moving loads on beams on elastic foundations. Indeed, the first study done of the response of a cylindrical shell to a moving load was that for a moving ring load [6] which is altogether mathematically analogous to a moving concentrated load on a beam on an elastic foundation [7-9] – just as the problem of a moving uniformly distributed load on a beam on an elastic foundation [10] is mathematically analogous to that of a moving pressure step in a simple shell.

As it turns out to be, practical interest in beam response to moving loads considerably predated that in shells – the first published analysis of the response of a beam on an elastic foundation to a moving load having appeared more than seventy years ago [11]. In consideration of the similarity between beam and shell analysis, it will be shown in the final section how the equation of motion of a simple shell can be easily derived from that for a beam on an elastic foundation.

In all that has gone before, however, no apparent attempt has been made to explain how it is that an expanding pressure step, as exists behind a projectile in the bore of a gun, can be the cause of a localized transient radial displacement of the tube wall that can be several times that caused by a static application of the same pressure. Clearly we have a problem in forced vibration, with the moving pressure step front acting somehow as an excitation force. Discovering the mechanism and nature of this excitation force – that is, expressing it as a forcing function – was the main motivation for undertaking this study. As we shall see in the final section, the method of obtaining the forcing function leads to a powerful method of analysis for the general dynamic strain problem.

REPRESENTING THE EXPANDING PRESSURE STEP

Knowing that the origin of the dynamic strain is the expanding pressure step behind the projectile we may want to examine it in detail with respect to it being the excitation force in a forced vibration problem. That is, we would like to be able to know its harmonic content with the intent of specifying it as the forcing function in a vibration analysis. To accomplish this let us start with something that is familiar by considering the rectangular wave depicted in Figure 1. This would be a good model of the pressure step within a gun tube but for it being periodic. Or to look at it another way, if the period of the wave were infinite it would make an excellent model of a pressure step within a gun tube. In what immediately follows the form of the function is not important, but the periodicity is a problem to be dealt with. Afterward we shall return to the step function.

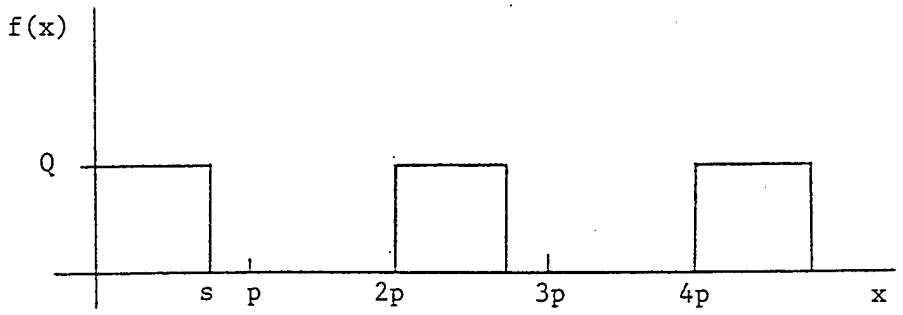

Figure 1. Periodically spaced pressure steps.

Evaluation of periodic functions by the use of Fourier series is a familiar process whereby a function of x with period $2p$ can be represented as

$$f(x) = \frac{1}{2}a_0 + a_1 \cos\frac{n\pi x}{p} + \cdots + a_n \cos\frac{n\pi x}{p} + \cdots + b_1 \sin\frac{n\pi x}{p} + \cdots + b_n \sin\frac{n\pi x}{p} + \cdots \tag{1}$$

$$\text{with } a_n = \frac{1}{p}\int_d^{d+2p} f(x)\cos\frac{n\pi x}{p}\,dx, \tag{2a}$$

$$\text{and } b_n = \frac{1}{p}\int_d^{d+2p} f(x)\sin\frac{n\pi x}{p}\,dx. \tag{2b}$$

Let us make the following substitutions derived from Euler's formula:

$$\cos\frac{n\pi x}{p} = \frac{e^{ni\pi x/p} + e^{-ni\pi x/p}}{2}, \text{ and } \quad \sin\frac{n\pi x}{p} = \frac{e^{ni\pi x/p} - e^{-ni\pi x/p}}{2}. \tag{3a,b}$$

Defining $c_0 = \frac{a_0}{2}$, $c_n = \frac{a_n - ib_n}{2}$, $c_{-n} = \frac{a_n + ib_n}{2}$; (4a-c)

and rearranging terms gives the alternative form

$$f(x) = \cdots + c_{-n} e^{-ni\pi x/p} + \cdots + c_{-1} e^{-i\pi x/p} + c_0 + c_1 e^{i\pi x/p} + \cdots + c_n e^{ni\pi x/p} + \cdots \quad (5)$$

or simply $f(x) = \sum_{n=-\infty}^{n=\infty} c_n e^{ni\pi x/p}$. (6)

Substitution of (3a) and (3b) into (2a) and (2b), and combining terms gives, as well,

$$c_n = \frac{1}{2p} \int_d^{d+2p} f(x) e^{-n\pi x/p} dx . \quad (7)$$

Combining (6) and (7) and substituting $\frac{1}{2\pi}\frac{\pi}{p}$ for $\frac{1}{2p}$ and $-p$ for d gives then

$$f(x) = \sum_{n=-\infty}^{n=\infty} \left[\frac{1}{2\pi} \int_{-p}^{p} f(x) e^{-n\pi x/p} dx \right] e^{ni\pi x/p} \frac{\pi}{p} . \quad (8)$$

The wave number (spatial frequency) for the general term is given by $\kappa_n = \frac{n\pi}{p}$ where successive values of κ_n differ by the amount

$$\Delta\kappa = \frac{(n+1)\pi}{p} - \frac{n\pi}{p} = \frac{\pi}{p}, \quad (9)$$

and since $n\Delta\kappa = \kappa_n$, then

$$f(x) = \sum_{n=-\infty}^{n=\infty} \frac{1}{2\pi} \left[e^{i\kappa_n x} \int_{-p}^{p} f(x) e^{-i\kappa_n x} dx \right] \Delta\kappa . \quad (10)$$

Now let p, the half period, be increased without limit. From (9) it can be seen that $\Delta\kappa$ approaches the infinitesimal. Furthermore, κ_n then approaches the continuous and the summation over n can be replaced by an integral. This suggests that the non-periodic limit of $f(x)$ is given by

$$f(x) = \frac{1}{2\pi} \int_{-\infty}^{\infty} e^{i\kappa x} \int_{-\infty}^{\infty} f(x) e^{-i\kappa x} dx \, d\kappa . \quad (11)$$

Equation (11) is known as the Fourier integral.

Although the above derivation is not considered rigorous*, the result is never-the-less a valid representation of the non-periodic function $f(x)$ - giving its value where it is continuous and the average of its right and left-hand limits at points where it is discontinuous provided that in every finite interval $f(x)$ satisfies the Dirichlet conditions and the integral $\int_{-\infty}^{\infty} |f(x)|\, dx$ exists.

*Proofs of the Fourier integral theorem are quite involved and depend on proving some foundational theorems. The reader is referred to the texts listed in the bibliography for complete proofs.

FROM THE FOURIER INTEGRAL TO THE SPECTRUM OF A FUNCTION

In this section we will take apart the Fourier integral and examine its component's properties. We start by observing that by writing

$$F(\kappa) = \int_{-\infty}^{\infty} f(x) e^{-i\kappa x} dx \tag{12a}$$

we can also write

$$f(x) = \frac{1}{2\pi} \int_{-\infty}^{\infty} F(\kappa) e^{i\kappa x} d\kappa. \tag{12b}$$

Since either one of the above expressions can be obtained from the other by integral transformation, they make up a transform pair. Specifically, they constitute the general form of the Fourier transform pair where $F(\kappa)$ is called the Fourier transform and thus $f(x)$ the inverse Fourier transform. This relationship is expressed compactly in operator notation by

$$F(\kappa) = \Im\left[f(x)\right] \quad \text{and} \quad f(x) = \Im^{-1}\left[F(\kappa)\right]. \tag{13a,b}$$

The Fourier transform is ubiquitous; its forms and areas of application go far beyond what is required of it here. It (and its inverse) will, however, find two applications here. In the following section the Fourier transform will be shown to have a utility comparable to that of the Laplace transform in that just as the Laplace transform can be used to convert an ordinary differential equation into an algebraic equation, the Fourier transform can be used to convert a partial differential equation into an ordinary differential equation.

Of more immediate interest is the use of the Fourier transform by itself to yield insight into the nature of a physical process or phenomenon. Specifically, by obtaining the Fourier transform of a function (whether it be analytic or a collection of data points) one obtains the spectrum/distribution of the constituent wave numbers/frequencies that when given weight according to the spectrum and added together are equivalent to the function. (The addition must be vectorial since there is a variation in phase as well as amplitude with wave number/frequency: both the amplitude spectrum and the phase spectrum are required to give a complete description of the function

By following the derivation of the Fourier integral as given above one can see how the coefficient formula for the Fourier series evolved into the Fourier transform which therefore serves as a weighting function (or spectrum) when the wave number/frequency distribution is continuous. When we obtain the Fourier transform of a real function we form a complex-valued function, say

$$F(\kappa) = u(\kappa) + iv(\kappa), \tag{14}$$

which is sometimes called a phasor (obviously a combination of the words phase and vector) because it can be written as

$$F(\kappa) = a(\kappa)\left[\cos\phi(\kappa) + i\sin\phi(\kappa)\right] = a(\kappa)e^{i\phi(\kappa)} \tag{15}$$

$$\text{where } a(\kappa) = \left| F(\kappa) \right| = \left[u^2(\kappa) + v^2(\kappa)\right]^{\frac{1}{2}}, \tag{16}$$

$$\text{and } \phi(\kappa) = \arg\left[F(\kappa)\right] = \tan^{-1}\left[\frac{v(\kappa)}{u(\kappa)}\right]^{\frac{1}{2}} \tag{17}$$

are the amplitude and phase angle spectrums, respectively.

THE LOAD SPECTRUM OF THE MOVING PRESSURE STEP

We are now in a position to decompose the moving pressure step that is representative of the propellant gas pressure in a gun into its spectrum. Figure 2 depicts a step with magnitude Q and velocity v which is expressed mathematically as

$$P(x,t) = Q\left[1 - \mathrm{H}(x - vt)\right]. \tag{18}$$

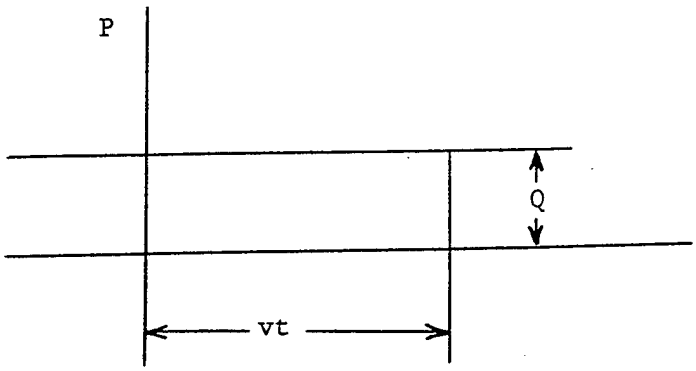

Figure 2. The expanding pressure step.

In this expression H represents the Heaviside unit step function which is defined as equal to zero for negative values of its argument, equal to one half for its argument equal to zero, and equal to one for positive values of its argument.

Alternatively, we can express the moving step as

$$P(x,t) = \frac{Q}{2}\left[1 - \mathrm{sgn}(x - vt)\right] \tag{19}$$

where the function sgn (signum) is defined as equal to -1 for negative values of the argument, zero for 0 argument, and 1 for positive values of the argument.

Expressing the moving pressure step in the second way above allows the Fourier transform of the function to be found by methods that will not be shown here. (Obtaining the Fourier transform by straightforward integration of

$$\Im[P(x,t)] = Q\left[\pi\delta(\kappa) - \frac{1}{i\kappa}e^{-i\kappa vt}\right]$$
$$= Q\left[\pi\delta(\kappa) + \frac{1}{\kappa}(\sin\kappa vt + i\cos\kappa vt)\right] \quad (20)$$

where $\delta(\kappa)$ is the Dirac delta function which is defined as equal to 1 when its argument is zero and equal to zero for all other argument values. Applying equations (16) and (17) gives

$$a(\kappa) = \frac{Q}{\kappa}, \text{ and} \quad (21)$$

$$\phi(\kappa) = \tan^{-1}(\text{ctn}\,\kappa vt). \quad (22)$$

There are some observations to make about equations (21) and (22). First, since from the viewpoint of an observer moving with the pressure step $\kappa s = \omega t$, for the special case of constant velocity where $s = vt$ we have

$$a(\kappa) = \frac{Qv}{\omega} = \frac{Qv}{2\pi f}. \quad (23)$$

This shows the spectrum amplitude to be directly proportional to the pressure, as would be expected; and also the velocity, which while not necessarily is to be expected, is consistent with the requirement that there be no excitation when the velocity is zero. And second, the dimensions of (21) and (23) are seen to be force divided by length which is indicative of a line load; the line in this case being the circle which is the intersection of the circular cylindrical tube bore and the plane of the pressure step .

Thus, the character of the dynamic strain excitation force in gun tubes has been revealed. It is a ring load which is harmonic in nature, comprising the full frequency spectrum with amplitude in inverse proportion to frequency and having phase a function of frequency (wave number) as well.

APPLICATION TO ANALYSIS

Since it is usually a fairly straightforward matter to obtain the dynamic response of a structure to a harmonic input of a single frequency or wave number, having a description of a more complicated input in the form of a spectrum suggests a way to analyze the response of a structure to just such an input. This would be accomplished by operating on the modeling differential equation by Fourier transformation to obtain a frequency or wave number response function with frequency or wave number as a parameter. Then, by applying the inverse Fourier transform to the function, the sum of the responses to the whole spectrum of frequencies or wave numbers is obtained as the response of the structure. A demonstration of this concept follows. But first is needed a differential equation modeling axisymmetric motion of a gun tube.

The simplest equation of motion that can be derived that is applicable is that of a thin circular cylindrical shell, which may be derived using only the results of elementary strength of materials theory. Starting with the differential equation for an element of a beam subjected to a distributed load,

$$EI\frac{d^4w}{dx^4} = F(x), \quad (24)$$

consider the beam to be supported by an elastic foundation according to the Winkler hypothesis so tthat

$$EI\frac{d^4w}{dx^4} + k'w = F(x). \tag{25}$$

This is the equation of a beam on an elastic foundation where k', which is referred to as the foundation modulus, is the constant of proportionality between the deflection of the beam at a point and the foundation resistance.

Since the beam is presumed to be vibrating, the effect of the acceleration of the beam element must be accounted for; which can be done by writing

$$EI\frac{\partial^4w}{\partial x^4} + m\frac{\partial^2w}{\partial t^2} + k'w = F(x,t) \tag{26}$$

where m is the lengthwise mass density of the beam. Note that, with the addition of time as a variable, the equation of motion becomes a partial differential equation.

If the beam has a rectangular cross-section of height h and width b, substitution for the cross-sectional moment of inertia and dividing through by b gives

$$\frac{Eh^3}{12}\frac{\partial^4w}{\partial x^4} + \rho h\frac{\partial^2w}{\partial t^2} + k\,w = P(x,t) \tag{27}$$

where $k = \frac{k'}{b}$ and the change of variable on the right hand side is to indicate the equation now has dimensions of pressure.

When the beam is very wide it becomes a one-dimensional plate of thickness h which, because of the lateral confinement of the material, no longer has a condition of plane stress which is accounted for by application of the equations of linear elasticity to give

$$D\frac{\partial^4w}{\partial x^4} + \rho h\frac{\partial^2w}{\partial t^2} + k\,w = P(x,t)$$
$$\text{where } D = \frac{Eh^3}{12(1-\nu^2)}. \tag{28}$$

Next, imagine a circular cylindrical shell to be formed from a plate rolled into a cylinder and its opposite edges joined. By this arrangement the plate creates its own foundation, the modulus of which is defined by $k = \frac{p}{w}$ where p is the interior pressure. Combining the formula for circumferential stress in a thin cirular cylindrical shell of radius R, $s = \frac{Rp}{h}$, the formula for uniaxial stress, $s = E\varepsilon$, and the formula for circumferential strain in a cylinder, $\varepsilon = \frac{w}{R}$, into $k = \frac{p}{w}$ gives $k = \frac{Eh}{R^2}$.

In the resulting equation of motion,

$$D\frac{\partial^4 w}{\partial x^4}+\rho h\frac{\partial^2 w}{\partial t^2}+\frac{Eh}{R^2}w=P(x,t), \tag{29}$$

w represents displacement of the middle surface of the shell in the radial direction (positive outward) and $P(x,t)$ is the forcing function, which for the purpose of this analysis will be represented by equation 19.

The strategy for solution of equation 29 first involves taking the Fourier transform of both sides of the equation. This has already been done for the right hand side of the equation, and is given as equation 20. On the left hand side of the equation, however, the transform is to be found more conventionally by multiplying each term by $e^{-i\kappa x}$ and integrating from x=-∞ to x=∞. Applying the derivative theorem for the Fourier transform to the spatial derivative term and using a special case of Leibnitz's rule for differentiation under the integral for the time derivative term results in the ordinary differential equation

$$\frac{d^2}{dt^2}F(\kappa,t)+\frac{D}{\rho h}\left[\kappa^4+\frac{Eh}{DR^2}\right]F(\kappa,t)=\frac{Q}{\rho h}\left[\pi\delta(\kappa)-\frac{1}{i\kappa}e^{-i\kappa vt}\right]$$
$$\text{where } F(\kappa,t)=\Im[w(x,t)]=\int_{-\infty}^{\infty}w(x,t)e^{-i\kappa x}\,dx. \tag{30}$$

The complete solution to equation 30 consists of the sum of a particular solution to the non-homogeneous equation and a complementary function obtained from the homogeneous equation that is equation 30 but with zero on the right hand side. Contained in the complementary function are two arbitrary constants of integration that are to be evaluated according to the initial conditions of the problem. For a real gun at time equal to zero the initial displacement and velocity of the wall are zero, as is the applied pressure throughout the tube. The complementary function, which represents the contribution to the tube wall displacement due to the initial conditions is thus zero, leaving only the particular solution to be found. The particular solution, which represents the steady state displacement of the tube wall, is easily found to be

$$F(\kappa,t)=\frac{Q}{D}\left[\frac{\pi\delta(\kappa)}{\kappa^4+\frac{Eh}{DR^2}}+\frac{ie^{-i\kappa vt}}{\kappa\left(\kappa^4-\frac{\rho h}{D}v^2\kappa^2+\frac{Eh}{DR^2}\right)}\right]. \tag{31}$$

Application of the inverse Fourier transform,

$$w=\frac{1}{2\pi}\int_{-\infty}^{\infty}F(\kappa,t)e^{i\kappa x}d\kappa, \tag{32}$$

and substitution of the new variables defined by

$$\kappa_c^2 = \sqrt{\frac{Eh}{DR^2}}, \quad v_c^2 = \frac{2D}{\rho h}\sqrt{\frac{Eh}{DR^2}}, \text{and} \quad \xi = x - vt \tag{33}$$

give the radial displacement of the tube wall

$$w = \frac{QR^2}{2Eh} + i\frac{Q}{2\pi D}\int_{-\infty}^{\infty} \frac{e^{i\xi\kappa}}{\kappa\left(\kappa^4 - 2\kappa_c^2\frac{v^2}{v_c^2}\kappa^2 + \kappa_c^4\right)}d\kappa. \tag{34}$$

Evaluation of the integral in equation 34 is more easily accomplished by starting with its partial fraction expansion which gives

$$\frac{Q}{2\pi D}\int_{-\infty}^{\infty} \frac{e^{i\xi\kappa}}{\kappa\left(\kappa^4 - 2\kappa_c^2\frac{v^2}{v_c^2}\kappa^2 + \kappa_c^4\right)}d\kappa = \tag{35}$$

$$\frac{QR^2}{2\pi Eh}\left[\int_{-\infty}^{\infty}\frac{e^{i\xi\kappa}}{\kappa}d\kappa + 2\kappa_c^2\frac{v^2}{v_c^2}\int_{-\infty}^{\infty}\frac{\kappa e^{i\xi\kappa}}{\kappa^4 - 2\kappa_c^2\frac{v^2}{v_c^2}\kappa^2 + \kappa_c^4}d\kappa - \int_{-\infty}^{\infty}\frac{\kappa^3 e^{i\xi\kappa}}{\kappa^4 - 2\kappa_c^2\frac{v^2}{v_c^2}\kappa^2 + \kappa_c^4}d\kappa\right].$$

Assuming initially that $\xi > 0$, Euler's relation gives

$$\int_{-\infty}^{\infty}\frac{e^{i\xi\kappa}}{\kappa}d\kappa = \int_{-\infty}^{\infty}\frac{\cos\xi\kappa}{\kappa}d\kappa + i\int_{-\infty}^{\infty}\frac{\sin\xi\kappa}{\kappa}d\kappa. \tag{36}$$

Since the first integral on the right hand side above is zero (odd integral) and the second integral is known (from tables) to be equal to π, we have

$$\int_{-\infty}^{\infty}\frac{e^{i\xi\kappa}}{\kappa}d\kappa = \pi i. \tag{37}$$

Provided that $v < v_c$, the remaining two integrals on the right hand side of equation 35 have no real zeros in their denominators. Therefore, simple poles exist in the upper half of the complex plane at

$$z = \left[\pm \left(1 + \frac{v^2}{v_c^2} \right)^{\frac{1}{2}} + i \left(1 - \frac{v^2}{v_c^2} \right)^{\frac{1}{2}} \right] \frac{\kappa_c}{\sqrt{2}}. \tag{38}$$

Evaluation of the integrals is accomplished by application of the residue theorem,

$$\int_c f(z)\,dz = 2\pi \sum_{j=1, z=a_j}^{m} \text{Res}\, f(z). \tag{39}$$

to the contour integration shown in figure 3.

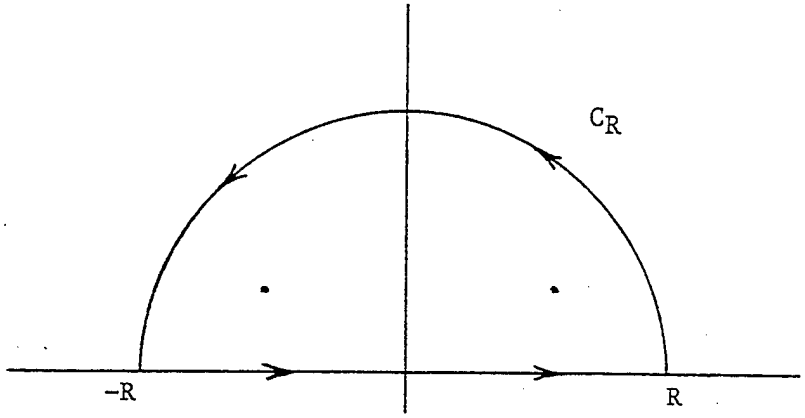

Figure 3. Contour integration for $v < v_c$.

After some considerable work the following expression for the ratio of displacement of the tube wall to that of the tube an infinite distance behind the pressure step is obtained as

$$\frac{w}{\frac{QR^2}{Eh}} = \frac{1}{2} \exp\left[-\left(1 - \frac{v^2}{v_c^2} \right)^{\frac{1}{2}} \frac{\kappa_c}{\sqrt{2}} \xi \right] \left\{ \cos\left[\left(1 + \frac{v^2}{v_c^2} \right)^{\frac{1}{2}} \frac{\kappa_c}{\sqrt{2}} \xi \right] - \frac{\frac{v^2}{v_c^2}}{\left(1 - \frac{v^4}{v_c^4} \right)} \sin\left[\left(1 + \frac{v^2}{v_c^2} \right)^{\frac{1}{2}} \frac{\kappa_c}{\sqrt{2}} \xi \right] \right\}. \quad \xi > 0,\ v < v_c \tag{40}$$

When $v > v_c$ the integrals have real zeros in their denominators. Therefore simple poles exist on the real axis at

$$z = \pm\, a_1 = \pm \left[\left(\frac{v^2}{v_c^2} + 1 \right)^{\frac{1}{2}} - \left(\frac{v^2}{v_c^2} - 1 \right)^{\frac{1}{2}} \right] \frac{\kappa_c}{\sqrt{2}}, \text{ and} \tag{41a}$$

$$z = \pm\, a_2 = \pm \left[\left(\frac{v^2}{v_c^2} + 1 \right)^{\frac{1}{2}} + \left(\frac{v^2}{v_c^2} - 1 \right)^{\frac{1}{2}} \right] \frac{\kappa_c}{\sqrt{2}}. \tag{41b}$$

In this case the integrals are evaluated by applying

$$\int_c f(z)dz = \pi[\mathrm{Res}(-a_2) + \mathrm{Res}(-a_1) + \mathrm{Res}(a_1) + \mathrm{Res}(a_2)] \tag{42}$$

to the contour integration shown in figure 4.

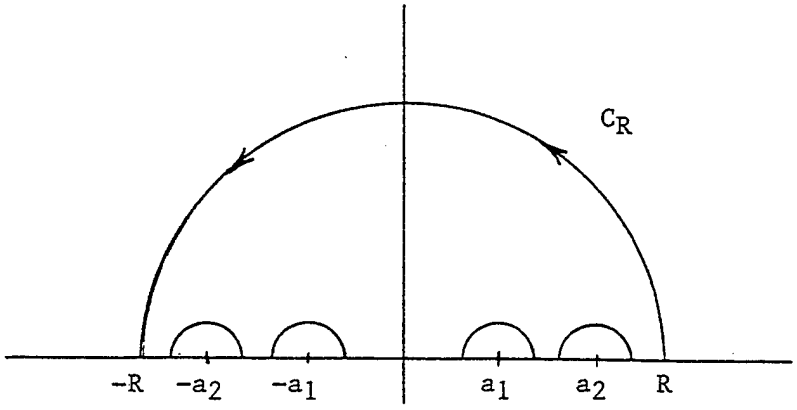

Figure 4. Contour integration for $v > v_c$.

After a similar amount of work the following expression for the ratio of displacement of the tube wall to that of the tube an infinite distance behind the pressure step is obtained as

$$\frac{w}{\frac{QR^2}{Eh}} = \frac{1}{2}\left\{\cos\left[\left(\frac{v^2}{v_c^2}+1\right)^{\frac{1}{2}}\frac{\kappa_c}{\sqrt{2}}\xi\right]\cos\left[\left(\frac{v^2}{v_c^2}-1\right)^{\frac{1}{2}}\frac{\kappa_c}{\sqrt{2}}\xi\right]+\right.$$

$$\left.\frac{\frac{v^2}{v_c^2}}{\left(\frac{v^4}{v_c^4}-1\right)^{\frac{1}{2}}}\sin\left[\left(\frac{v^2}{v_c^2}+1\right)^{\frac{1}{2}}\frac{\kappa_c}{\sqrt{2}}\xi\right]\sin\left[\left(\frac{v^2}{v_c^2}-1\right)^{\frac{1}{2}}\frac{\kappa_c}{\sqrt{2}}\xi\right]\right\}.\quad \xi>0,\ v>v_c \tag{43}$$

Equations 40 and 43 express the response of the gun tube forward of the pressure step. But the real region of interest is behind the pressure step where the largest displacements occur. Assume then that $\xi<0$ so that $(-\xi)>0$ and note that

$$\cos(-\xi)\kappa=\cos\xi\kappa,\ \text{and}\ \sin(-\xi)\kappa=-\sin\xi\kappa. \tag{44a,b}$$

Substitution of $(-\xi)$ for ξ in equations 40 and 43 then gives for the displacement ratios behind the pressure step

$$\frac{w}{\frac{QR^2}{Eh}} = 1-\frac{1}{2}\exp\left[\left(1-\frac{v^2}{v_c^2}\right)^{\frac{1}{2}}\frac{\kappa_c}{\sqrt{2}}\xi\right]\left\{\cos\left[\left(1+\frac{v^2}{v_c^2}\right)^{\frac{1}{2}}\frac{\kappa_c}{\sqrt{2}}\xi\right]+\right.$$

$$\left.\frac{\frac{v^2}{v_c^2}}{\left(1-\frac{v^4}{v_c^4}\right)^{\frac{1}{2}}}\sin\left[\left(1+\frac{v^2}{v_c^2}\right)^{\frac{1}{2}}\frac{\kappa_c}{\sqrt{2}}\xi\right]\right\}.\quad \xi<0,\ v<v_c \tag{45}$$

and

$$\frac{w}{\frac{QR^2}{Eh}} = \frac{1}{2}\left\{\cos\left[\left(\frac{v^2}{v_c^2}+1\right)^{\frac{1}{2}}\frac{\kappa_c}{\sqrt{2}}\xi\right]\cos\left[\left(\frac{v^2}{v_c^2}-1\right)^{\frac{1}{2}}\frac{\kappa_c}{\sqrt{2}}\xi\right]+\right. \tag{43}$$

$$\left.\frac{\frac{v^2}{v_c^2}}{\left(\frac{v^4}{v_c^4}-1\right)^{\frac{1}{2}}}\sin\left[\left(\frac{v^2}{v_c^2}+1\right)^{\frac{1}{2}}\frac{\kappa_c}{\sqrt{2}}\xi\right]\sin\left[\left(\frac{v^2}{v_c^2}-1\right)^{\frac{1}{2}}\frac{\kappa_c}{\sqrt{2}}\xi\right]\right\}.\quad \xi>0,\ v>v_c$$

Equations 40 and 43 express the response of the gun tube forward of the pressure step. But the real region of interest is behind the pressure step where the largest displacements occur. Assume then that $\xi < 0$ so that $(-\xi) > 0$ and note that

$$\cos(-\xi)\kappa = \cos\xi\kappa, \text{ and } \sin(-\xi)\kappa = -\sin\xi\kappa\,. \tag{44a,b}$$

Substitution of $(-\xi)$ for ξ in equations 40 and 43 then gives for the displacement ratios behind the pressure step

$$\frac{w}{\frac{QR^2}{Eh}} = 1-\frac{1}{2}\exp\left[\left(1-\frac{v^2}{v_c^2}\right)^{\frac{1}{2}}\frac{\kappa_c}{\sqrt{2}}\xi\right]\left\{\cos\left[\left(1+\frac{v^2}{v_c^2}\right)^{\frac{1}{2}}\frac{\kappa_c}{\sqrt{2}}\xi\right]+\right.$$

$$\left.\frac{\frac{v^2}{v_c^2}}{\left(1-\frac{v^4}{v_c^4}\right)^{\frac{1}{2}}}\sin\left[\left(1+\frac{v^2}{v_c^2}\right)^{\frac{1}{2}}\frac{\kappa_c}{\sqrt{2}}\xi\right]\right\}.\quad \xi<0,\ v<v_c \tag{45}$$

and

$$\frac{w}{\frac{QR^2}{Eh}} = 1 - \frac{1}{2}\cos\left[\left(\frac{v^2}{v_c^2}+1\right)^{\frac{1}{2}}\frac{\kappa_c}{\sqrt{2}}\xi\right]\left\{\cos\left[\left(\frac{v^2}{v_c^2}-1\right)^{\frac{1}{2}}\frac{\kappa_c}{\sqrt{2}}\xi\right]+\right. \tag{46}$$

$$\left.\frac{\frac{v^2}{v_c^2}}{\left(\frac{v^4}{v_c^4}-1\right)^{\frac{1}{2}}}\sin\left[\left(\frac{v^2}{v_c^2}+1\right)^{\frac{1}{2}}\frac{\kappa_c}{\sqrt{2}}\xi\right]\sin\left[\left(\frac{v^2}{v_c^2}-1\right)^{\frac{1}{2}}\frac{\kappa_c}{\sqrt{2}}\xi\right]\right\}.\ \xi<0,\ v>v_C$$

The steady state solution to equation 29 with $P(x,t)$ as given by equation 19 is now seen to consist of standing waves in the moving coordinate system that represent the sums and differences of the spectrum of waves propagating away from the pressure step. Since these waves (which can also be thought of as interference patterns) are stationary with respect to the moving coordinate system, they move in the gun tube with the pressure step.

CONCLUSION

In this final section some observations will be made regarding the foregoing results and a suggestion for further work put forward as well.

The goal of discovering and characterizing the source of the dynamic strain was met, and then exceeded by obtaining a solution to a simple differential equation describing the response of a tube by means of a mathematical method (Fourier transformation) that is analogical to the physical process involved. As it happens, this solution method has advantages beyond the ability to demonstrate the physical process.

One of these advantages is its ability to find solutions without the specification of boundary conditions. What makes that important here is the fact that more traditional methods of solution require the specification of more boundary conditions than are available – in particular for the case where v is greater than v_c – thus precluding the obtainment of a complete solution.

But perhaps the most important advantage this solution method has to offer is its ability to accommodate mathematical models consisting of coupled partial differential equations. This is made possible by the conversion of the partial differential equations by Fourier transformation. With but the one additional step of solving for the Fourier transform(s) of the variable(s) of interest from a set of ordinary differential equations, the solution would proceed as above. As to the motivation for undertaking a more elaborate analysis, one only has to make some observations regarding the above analysis.

Probably the first and most important observation to be made is that as v approaches v_c in equations 40, 43, 45 and 46 the resulting displacement ratios approach infinity. This would seem to indicate the existence of a critical velocity at $v = v_c$. However, although there is plenty of evidence demonstrating that at velocities near v_c tube wall displacements may be several times that caused by an equivalent static pressure, there is not to this writer's knowledge any confirmation of displacements so large as to approach infinity – either by physical test, finite element simulation or any other means.

Furthermore, equations 43 and 46 predict that the response of the tube will be undiminished at infinitely large distances from the moving step in pressure when v is greater than v_c, which is contrary to reality. (This finite

response at infinite distance is the root of the problem in using conventional methods to solve the case where v is greater than v_c).

The origin of these discrepancies can only lie with equation 26 itself – or, more to the point, the simplifying assumptions that are built into the equation. What these are can easily be seen by reference to the equations of a "Timoshenko beam" on an elastic foundation

$$EI\frac{\partial^2\psi}{\partial x^2}+\gamma AG(\frac{\partial w}{\partial x}-\psi)-\rho I\frac{\partial^2\psi}{\partial t^2}=0\text{, and} \tag{47a}$$

$$\rho A\frac{\partial^2 w}{\partial t^2}-\gamma AG(\frac{\partial^2 w}{\partial x^2}-\frac{\partial\psi}{\partial x})+k'w=F(x,t) \tag{47b}$$

where γ is the shear deformation coefficient and ψ is the angle of rotation of an initially vertical cross-section of the beam. By simply assuming the contribution of the rotational acceleration term to be negligible and also that cross-section rotation is due entirely to bending produces equation 26 from equations 47a and 47b.

By eliminating the effects of rotational inertia and shear deformation, however, we are in the very least introducing error into the analysis. This is because, as shown earlier, the excitation of the tube consists of large amounts of high frequency/short wavelength input which, to be accounted for completely and correctly, requires the solution of the equations for a "Timoshenko shell". Such equations, as given in [12] for example, would present no particular difficulty for the method of solution presented here.

BIBLIOGRAPHY

Books which contain proofs of the Fourier integral theorem:

1. Tolstov, Georgi P., *Fourier Series*, Dover Publications, New York, 1976.
2. Broman, Arne, *Introduction to Partial Differential Equations*; Dover Publications, New York, 1989.
3. Brown, James Ward and Ruel V. Chruchill, *Fourier Series and Boundary Value Problems*, 5th edition, McGraw-Hill, New York, 1993.

Books on the theory of Fourier transforms:

1. Cartwright, Mark, *Fourier Methods for Mathematicians, Scientists and Engineers*, Ellis Horwood, New York, 1990.
2. Gaskill, Jack D., *Linear Systems, Fourier Transforms, and Optics*, John Wiley and Sons, New York, 1978.
3. Bracewell, Ronald N., *The Fourier Transform and Its Applications*, 2nd edition, McGraw-Hill, New York, 1986.

REFERENCES

1. Simkins, T.E., "*Resonance of Flexural Waves in Gun Tubes," in: Proceedings of the Fifth U.S. Army Symposium on Gun Dynamics*, ARCCB-SP-87023, Benet Laboratories, Watervliet, NY, 23-25 September 1987, pp. 65-78.

2. Hasenbein, R.G., A. Gabriele, D. Finlayson, B. Artus, G. Cunningham, and R. Gast, "Dynamic Strain Waves - A Development Perspective," in *Proceedings of the Sixth U.S. Army Symposium on Gun Dynamics*, ARCCB-SP-90015, Benet Laboratories, Watervliet, NY, 15-17 may 1990, Vol. II, pp. 286-297.

3. Reismann, H., "Response of a Prestressed Cylindrical Shell to Moving Pressure Load, Developments in Mechanics," *Solid Mechanics – Proceedings of the Eighth Midwestern Mechanics Conference,* Pergamon Press, Part II, Vol. 2, 1965, pp. 349-363.

4. Tang, S.-C., "Dynamic Response of a Tube Under Moving Pressure, "*Journal of the Engineering Mechanics Division, Proceedings of the ASCE*, Vol. 91, No. EM5, October 1965, pp. 97-122.

5. Schiffner, K., and C.R. Steele, "Cylindrical Shell with an Axisymmetric Moving Load, "*AIAA Journal,* Vol. 9, No. 1, January 1971, pp. 37-47.

6. Jones, P., and P.G. Bhuta, "Response of Cylindrical Shells to Moving Loads," *Journal of Applied Mechanics*, Vol. 31, No. 1, Trans. ASME, Vol. 86, Series E, March 1964, pp. 105-111.

7. Kenney, J. T., "Steady-State Vibrations of Beams on Elastic Foundations for Moving Load," *Journal of Applied Mechanics*, Vole 21, No. 4, Trans. ASME, Vol. 76, December 1954, pp. 359-364.

8. Crandall, S.H., "The Timoshenko Beam on an Elastic Foundation," *Proceedings of the Third Midwestern Conference on Solid Mechanics*, Ann Arbor, MI, 1952, pp. 146-159.

9. Achenback, J.D. and C.T. Sun, "Moving Load on a Flexibly Supported Timoshenko Beam," *International Journal of Solids and Structures*, Vol. 1, 1965, pp. 353-370.

10. Steele, C.R., "The Timoshenko Beam With a Moving Load," *Journal of Applied Mechanics*, Vol. 35, No. 3, Trans. ASME, Vol. 90, September 1968, pp. 481-488.

11. Timoshenko, S., "Method of Analysis of Statical and Dynamical Stresses in Rail," *Proceedings of the Second International Congress of Applied Mechanics*, Zurich, 1927, pp. 1-12.

12. Naghdi, P.M., and R.M. Cooper, "Propagation of Elastic Waves in Cylindrical Shells, Including the Effects of Transverse Shear and Rotatory Inertia," *Journal of the Acoustical Society of America*, Vol. 28, No. 1, January 1956.

Dynamic Analysis of a 155 mm Cannon Breech

G. Peter O'Hara
Elmhurst Research
165 Jordan Rd.
Troy NY 12181

Abstract

This report describes a finite element analysis of the breech closure for the 155 mm Cannon M199, which is normally mounted on the Towed Howitzer M198. In this configuration it has has an excellent record for reliability in the field and is easy to service. However when the breech is used in an ammunition test environment, some maintenance problems exist. The analysis is for a 9 body problem with 13 contact surfaces and was solved for both static and dynamic load cases. The two dynamic loads were of similar shape with different loading times. The 9 bodies in the model include, a facility mount, four major structural components, the obturator seal and 3 minor components. The results show that the major components are normally subjected to quasi-static loading but under fast 'pressure spike' loadings, the dynamic effect can be important. This is particularly true for the contact between minor components which can show extreme behavior with the fast loading rates.

Introduction

The 155 mm Towed Howitzer M198 has been in service since with the U.S. Armed Services since 1978 and has proven to be a reliable weapon with few problems in service. This system uses the 155 mm Cannon M199 which was designed at the Benét Laboratories, with an Eastman style interrupted screw block breech, and a Debange obturator seal. Interrupted screw threads used for the breech block to breech ring connection are also used for the breech ring to barrel connection and in the breech ring to recoil mount joint. A similar interrupted lug joint is used to assemble the firing mechanism housing to the obturator spindle, as a means of allowing easy assembly in the field. While the normal maintenance record of gun is excellent, there have been some problems with the breech when it is used on ballistic guns for ammunition testing. In this environment the breech is subjected to prototype propellant systems and other conditions which may produce 'ragged' pressure time histories. These histories are characterized by large pressure spikes which apparently do not affect the primary structure but do produce failure in the small components such as the firing mechanism housing. The case in point was the lugs on the obturator spindle which retain the housing on the spindle. These lugs were noted to produce bearing failures which made the components difficult to dissemble. This analysis was intended to explore this effect and demonstrate the value of the analysis of a full cannon breech.

This report will describe the static and dynamic finite element analysis of the breech closure of the M199 cannon. The work compares three different time frames:

a static case and dynamic cases using a normal pressure time curve and a very fast pressure spike. The analysis is done at a medium level of detail with the components described by 8 node axisymmetric elements and the various contact surfaces modeled using an appropriate interface formulation. The three major threaded connections are modeled with the individual threads smeared to an equivalent orthotropic continuum and contact modeled using the appropriate kinematics conditions. Other contact surfaces are modeled using either a small sliding or large sliding formulation. All of the necessary analysis tools were available in the ABAQUS Standard finite element code (1,2).

Description of Component Models

The initial objective of this study was to produce individual models of all necessary structural component of the cannon breech and link them to produce the overall system model. This was done with 8 node axisymmetric elements (CAX8) which is a reasonable assumption for these components. The breech ring and block both have non symmetric features but they can be ignored in favor of the more general solution goals. The block carrier is a totally non symmetric structure but this has been ignored because it does not play a structural role during firing. The firing mechanism is another non-symmetric structure, but this level of detail is not appropriate to this analysis. However, it was necessary to include the mass of the firing mechanism in the model of the firing housing.

A cross section drawing of the breech is shown in Figure 1 with the major components labeled and a brief description given below. The diagonal lines show the kinematic direction of the thread bearing surfaces.

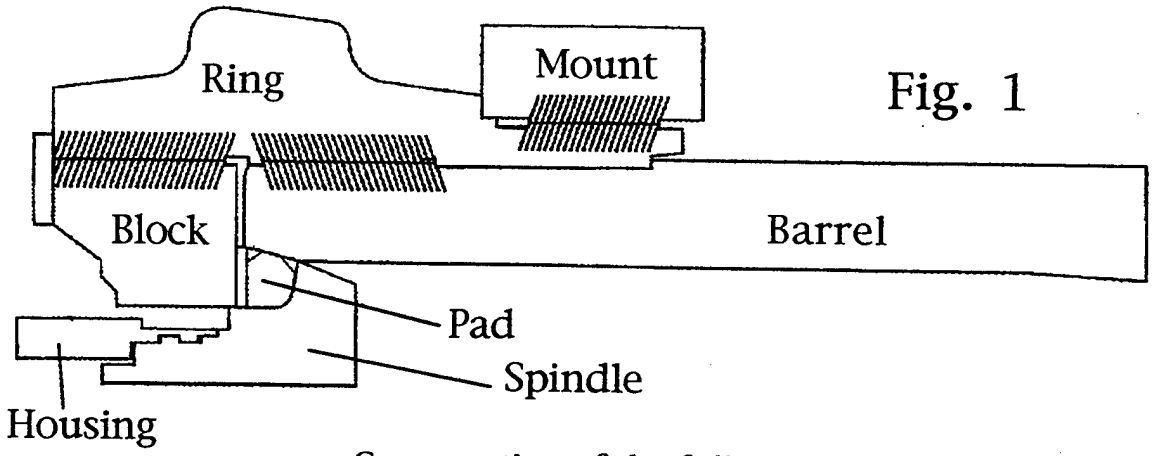

Fig. 1

Cross section of the full system model

1) Barrel Assembly: This model includes about 0.6 meter of the breech end of the barrel including the obturator pad seat, tube to ring threads and two pilot surfaces. A small portion at the forward end uses an increased mass to replace the unmodeled portion of the barrel assemble. To further enhance the model the nodes at the muzzle end are constrained to a constant axial displacement.

2) Breech ring: This model is an axisymmetric approximation of the breech ring with tube to ring threads, block to ring threads, mount to ring threads, the two pilot surfaces for the tube and a pilot surface for the mount. The outer surface contour is a rather unusual shape which resulted from a complicated development history and a need for a specific breech weight.

3) Breech Block: This is a full model of the block including the block to ring threads on the outer diameter and the block-to-disk contact surface on the muzzle face.

4) Obturator Spindle: This is a model of the spindle including the housing to spindle contact surfaces, the spindle to pad contact surface and the pad to disk contact. The small extension at the breech end retains the primer and is normally not on the centerline of the gun but has been moved in this model. The material stiffness for the lugs is reduced to model the fact that they are interrupted in the actual components.

5) Obturator pad and rings: The pad and rings are included as one body because sliding contact between them can be ignored. The fact that the pad is an elastomers and the rings are steel is modeled. Also since the rings are split rings the steel is given a very low hoop stiffness.

6) Disc: This is a simple washer located between the obturator pad and the breech block. It has a small sliding surface on each axial face.

7) Mount: The mount is modeled as a short cylinder with the ring-to-mount threads on the inside along with a mount-to-ring pilot surface. The outer volume uses the increased mass property to replace the mass of a facility mount.

8) Cam Plate: This is a non-structural plate which is bolted to the breech face of the block and is included because of it's inertial load on the block. The bolts are modeled using three simple springs which are preloaded by using a small interference of the contact surface with the block.

9) Housing: The housing model includes the mass of the firing mechanism, a contact surface at the muzzle end with the obturator spindle and the housing-to-spindle lug connection.

The dimensions for these component were taken directly from the Benét Laboratories drawings for the individual component and use the nominal dimensions for all of the gaps between contact surfaces.

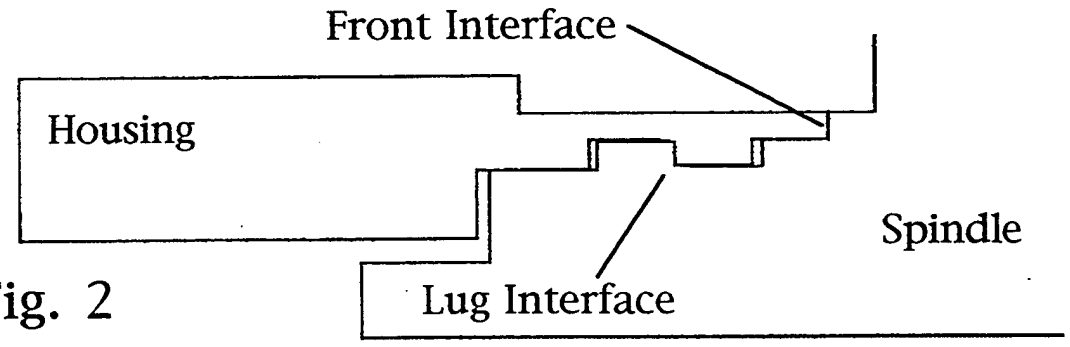

Fig. 2

Detail of the Housing to spindle connection

Figure 2 is a detail of the housing and spindle showing how the housing is retained between the spindle body at the front (muzzle end) and a set of interrupted lugs at the breech end. With this system the assembly method is to insert the spindle into the housing, until it bottoms on the front interface and then a simple 1/4 turn locks in both the spindle and housing (using a spring pin). This requires a small gap or play between the two interfaces to allow easy assembly, which is a minimum of

0.000254 meter (0.010 inch) on the drawings. This fact will play a role in the conclusions of the analysis.

Contact Surfaces

There are three types of interfaces in the overall model, small sliding contact, large sliding contact and the complex thread interaction model. The small sliding surface formulation in ABAQUS (INTER3A) is used for the 3 pilot surfaces which close a radial gap and the five contacts surfaces which act in the axial direction and are all initially closed. The Slide Line (ISL22A) formulation for large sliding contact was used for obturator pad/spindle interaction and the obturator pad/barrel interaction. The pad is an elastomer which is subjected to very high loads and deformations. These deformations allow the pad/rings to have substantial motions relative to the barrel, breech block and spindle.

The three threaded connections are modeled using a combination of material replacement for threads and a set of oriented one-dimensional gap elements to provide the proper kinematics of the thread contact surfaces. This method has been used for several years (3) and was originally suggested by Bretel (4). The first step is to calculate an equivalent orthotropic material with the same global stiffness as the full height of the threads. This material will occupy the space between the thread root and the pitch cylinder on each side of the connection. A detailed analysis of a single thread tooth was used to establish these properties using methods similar to work done in studies of thread performance (5,6,7). The individual threads are then smeared into two rows of elements, with one row attached to each of the adjoining components. These rows meet at the pitch cylinder of the threads in a set of independent node pairs. The pairs are linked with 1-dimensional gap elements (GAPUNI), in a coordinate system which enables sliding parallel to the thread contact surface direction. The two connected points are at the same point in space and the direction vector for gap is defined normal to the thread contact surface. These two techniques model the stiffness and kinematics of the thread contact without resorting to defining individual thread teeth.

Loading

The primary loads are the pressure load in the chamber of the gun and the inertial loads from recoil. The pressure load covers the muzzle surface of the spindle, the bore surface (forward of the obturator pad) and the ID of the flame hole in the spindle. The pressure load is also reflected in a small concentrated load on the housing to simulate the axial load of the primer on the firing mechanism. The inertial loads are applied as a constant body force in the static solution and by using the free recoil condition for the dynamic solutions.

The three loads used reflect the behavior of M203 charge in an M199 Cannon. The basic pressure-time in Figure 3 data was obtained from a XNOVAKTC (8,9,10) Interior Ballistic solution for this charge and was entered into ABAQUS as a table of 148 X-Y pairs. In this IB solution the projectile motion starts at 0.0048 seconds with the peak pressure of 310 mPa. is at 0.0099 seconds. Shot exit is at 0.020 seconds and the data table is cut off at 0.025 seconds. The peak pressure was used for the static solution along with a body force calculated from simple rigid body mechanics. The full pressure-time curve was used for the first dynamic solution to model the normal behavior of the breech. For the pressure spike case the time of the M203 charge was simply divided by 10 to produce a spike of the same pressure an shape but with a duration of 0.0025 seconds.

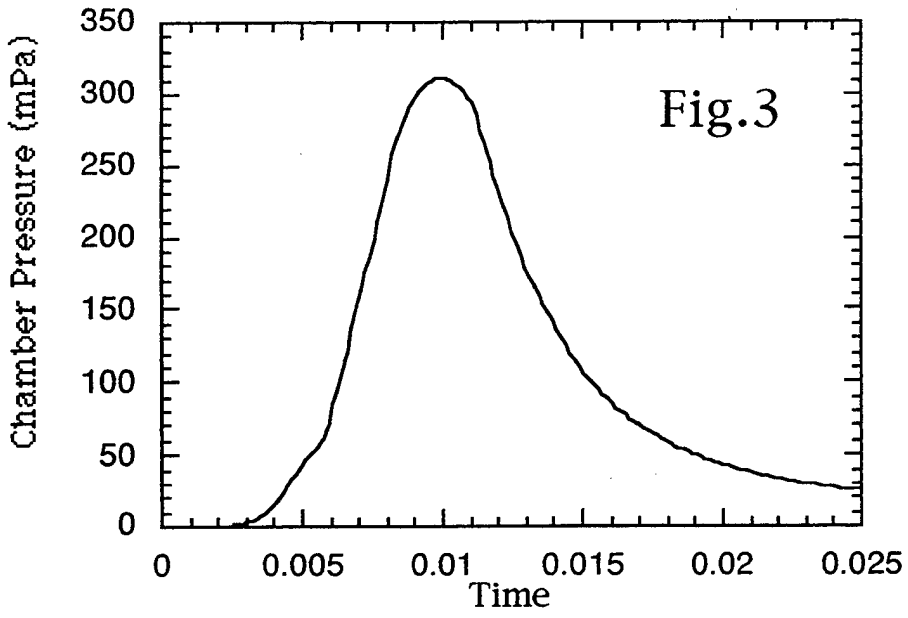

Results

The overall system model was debugged as a static problem and a test of the various contact surfaces. As always, in this sort of problem, most of the modifications made were in favor of a more realistic model, which generally makes the solution faster and more reliable. A case in point was that the disk was originally included as an extension on the block model, however this would not converge or would converge to an incorrect deformed shape. The disc is a bearing which operates to release the shear deformation between the block and the pad. Without fully modeling this function the 'hourglass' mode of the elements became a dominate behavior and produced a incorrect deformed shape. Inclusion of the disk as a separate component, with two contact surfaces, solved this problem.

The stress contour plot in Figure 4 is typical of the general Mises stresses at the maximum pressure. Note the high stresses near the bore of the chamber, in the breech block and in the pad fillet of the spindle. Also note that there are no contours in the obturator pad which is in a state of hydro static compression. There is also a stress concentration in the ring at the thread relief for the block end threads. This rather mild stress concentration links with the stress concentration of the threads to produce the actual fatigue failure point in the ring.

After the static model was completed the dynamic solutions proceeded easily and the major problem became selecting and displaying the important results. An early decision was the selection of 4 points to use for stress comparisons of the various solutions. These points were all at high stress points of the major components. The first was at the bore of the barrel (3111-1), then one in the thread relief of the ring (6152-1), another in the block near the central hole (1166-7) and the last the pad fillet of the spindle (8201-1). Mises equivalent stresses for these four points and the three loading conditions are shown in Table I. Note that there is no difference

between the static solution and the standard M203 charge solution. The Pressure spike solution produces modest stresses increases of as little as 1 % for the bore of the tube to a high of 48 % for the spindle. All of these were recorded at the time of maximum pressure in the chamber.

Fig. 4

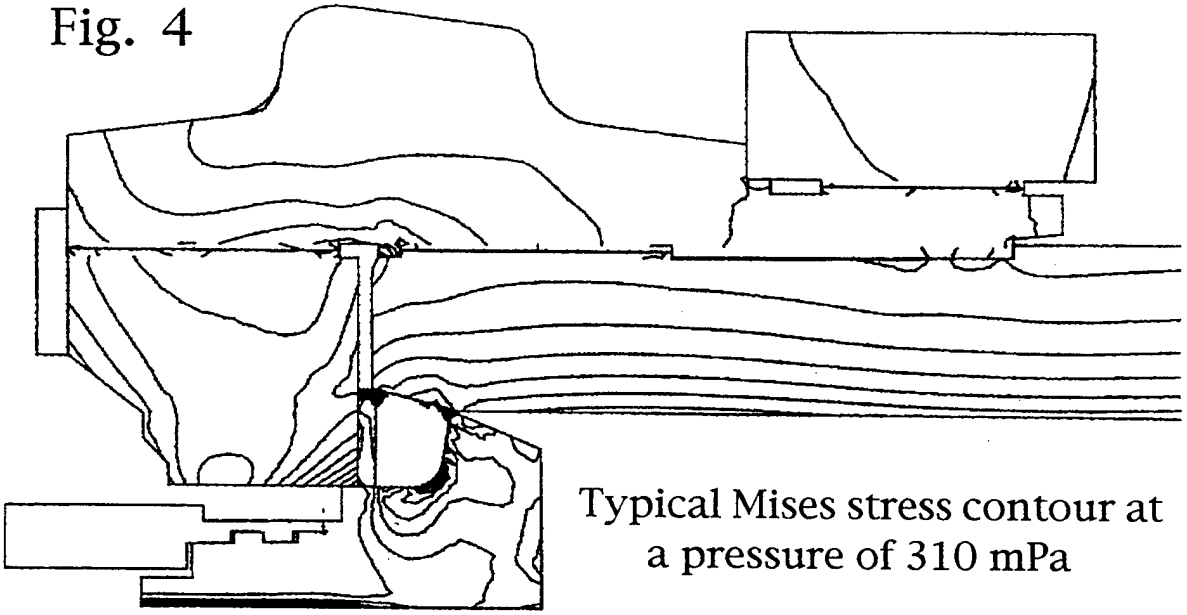

Typical Mises stress contour at a pressure of 310 mPa

Table I

Mises Stress Comparison for three loading rates and four major components with stress in mPa.

Component	Static	M203 Charge	Pressure Spike
Tube			
3111-1	807.8	808.0	817.0
Ring			
6152-1	384.8	381.0	530.6
Block			
1166-7	999.8	993.6	1301.4
Spindle			
8208-1	883.2	878.0	1319.2

The spindle movement is a critical part of the operation of the obturator pad seal in this style of cannon. This is a Bridgeman unsupported area seal and uses the spindle to increase the pressure on the pad and force it against the pad seat of the barrel. The elastomer pad is compressed by the full axial pressure load on the spindle and is restrained on the pad seat and breech block . This seat is tapered so that as the pad moves rearward it must expand to meet the new diameter of the tube. At the same

time the tube is expanding from the pressure load of the pad and the block is deflecting backward from the axial load in it. All of these combine to produce the spindle movement of 2.2 mm relative to either the block or the tube. This movement opens a large space between the spindle and the tube, which would allow the elastomer pad to extrude out if the split rings were not in place. The front split ring prevents this extrusion along with its mating split ring in the smaller space between the tube and the disc.

The first dynamic solution used the pressure-time data for the M203 charge and some of the basic structural information reported in Table I. This was a free recoil case which yielded a rigid body displacement of 0.0075 meter at the time of peak pressure and 0.088 meter at shot exit. The corresponding recoil velocities were 3.98 and 9.92 meter/second. These numbers tended to reinforce the quality of the solution. However a major goal was to study the contact conditions on the lugs and the front contact surfaces of the housing. This was done by plotting the contact stress against time, as shown in figure 5. This plot shows a rather complex behavior which is influenced by local natural frequencies. The general stress level is low with a maximum of about 55 mPa on the lugs. The front contact surfaces is only activated twice between .004 and .007 seconds. Certainly one would not predict any sort of failure from this response.

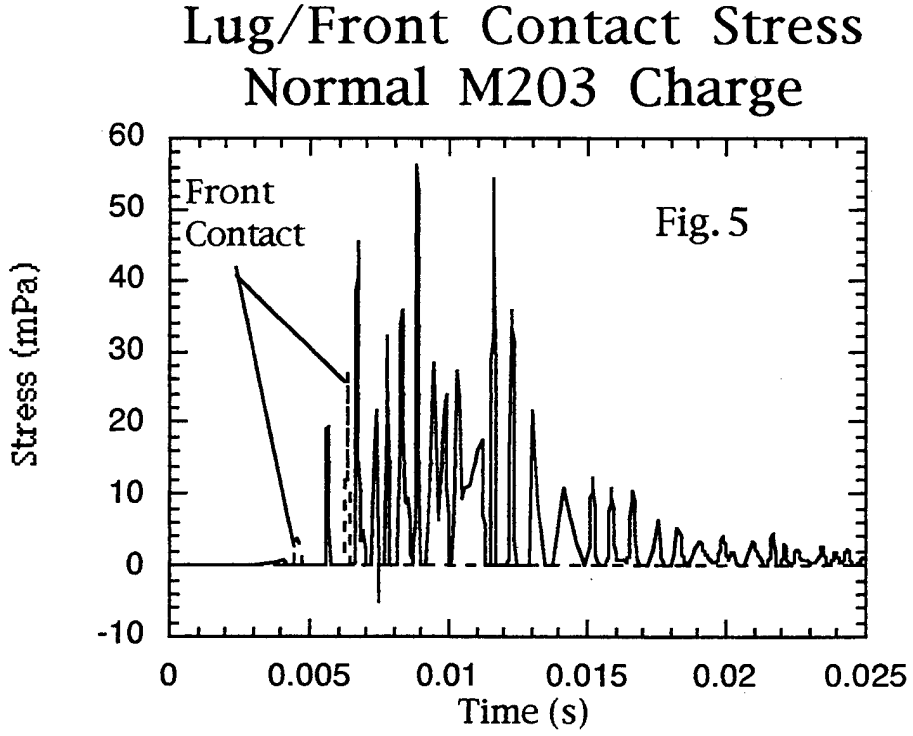

The last solution, for the pressure spike, was generally similar to the other two cases with some increase in general stresses as noted in Table I . This small increase is not the case for the lug contact stress in the spindle and housing. Here a plot of contact stresses vs. time for the lugs and the front contact surface reveal a very different picture of the stress levels and a clear behavior is demonstrated. The maximum contact stress on the lugs has become 1125 mPa and the front contact surface is very active. At this high loading rate the housing bounces across the gap

impacting heavily on both surfaces. The maximum stress has increased by a factor of 20 and the contact stress is approaching the yield strength of the steel. Clearly one could predict a possible failure for this case.

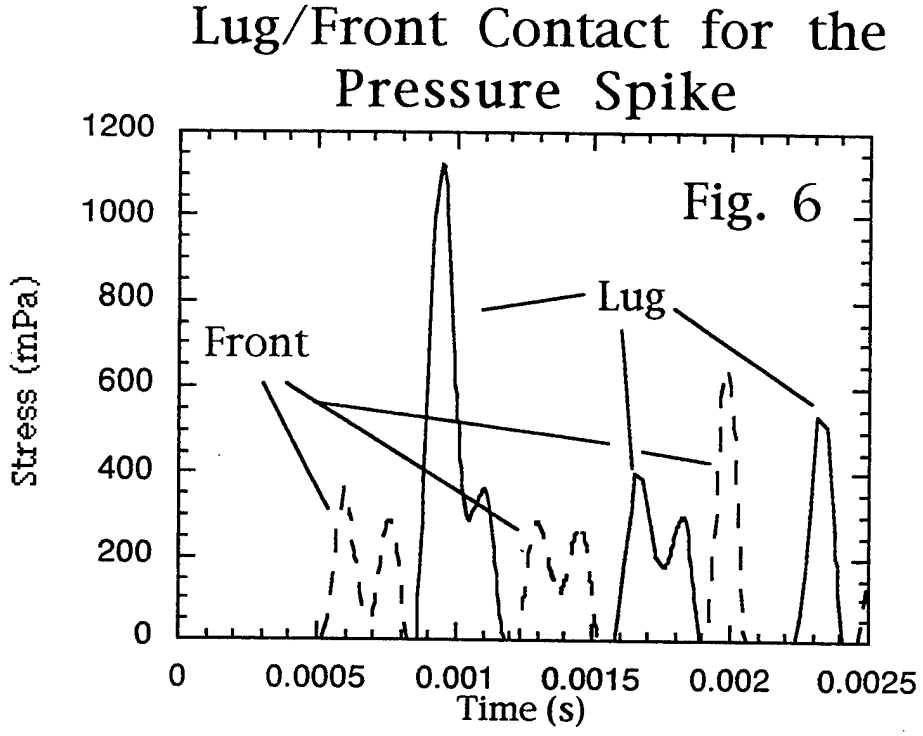

Discussion

The three solutions in this report are for quite different time frames and show different data when viewed from different perspective. When the data is viewed from a general structural viewpoint some important effects can be demonstrated. An example of this is that static analysis may be a valid assumption for the design of large cannon components, if the analysis is for a normal well behaved charge. If the propellant does not burn smoothly and pressure spikes are generated some components may be subject to increased stress conditions. This is the case for the spindle fillet which shows a 48% gain in Mises stress. However when we look in detail at the spindle/housing interactions a rather different picture emerges. In the static case there is nothing of any interest the primer load pushes the housing against the spindle lug at an average of 11.4 mPa and nothing more. However when the normal pressure time curve is introduced a much more complex behavior is introduced and the contact load varies rapidly, at low stresses. Then at very high rate loads, another behavior is demonstrated in which the the housing bounces rapidly between the front contact surface and the lug surface resulting in high contact surfaces and possible failure of the lugs.

It is not enough to solve large complex finite element models of complicated structures and casually view the results. These models create enormous volumes of information which must be critically evaluated to find the pertinent information. In this case the initial request was look at for an explanation for the bearing failure of the spindle lugs which prompted the investigation of the lug contact stresses. The

information on variation of general stresses with loading rate is one of the many other areas that may be investigated along with the primary analysis goal. Another point is the necessity of doing more than one analysis. The interesting part of this study is the comparison of three different loading rates and not the results of any single computer run. It should be pointed out that the results shown in this paper are for three runs using the same structural model, the same computer code (ABAQUS) and the same solution tolerance for the dynamic load cases. While the work may continue to make the solutions more efficient, this report provides a consistent set which can be used for comparisons.

Conclusion

This work tends to validate the very old idea that structural analysis of cannon breeches can be done by quasi-static methods. The burning of propellants is not an explosion, but a deflagration which should result in a rather smooth and (relatively) slow pressure time curve. However this is only true for the major structural components and a well behaved propellant charge. When high level pressure spikes are involved the stress picture changes and the changes can be rather dramatic.

Acknowledgement

The author wishes to acknowledge the support of Mr. Richard Hasenbein and Mr. Stephen VanDyke-Restifo of Benét Laboratories for support in this work. The author also wishes to thank Mr. George Pflegl for his advice and council.

Reference List

1) ABAQUS Theory Manual Version 5.7, Hibbitt, Karlsson & Sorenses, Inc., 1080 Main St., Pawtucket RI, 1997

2) ABAQUS Users Manual Version 5.7, Hibbitt, Karlsson & Sorenses, Inc., 1080 Main St., Pawtucket RI, 1997

3) O'Hara,G.P., "Analysis of a Large High Pressure Vessel Closure", ASME Pressure Vessels & Piping Conference, Orlando FL, PVP Vol. July 1988
Also
US Army Armament Research Development and Engineering Center (ARDEC), Technical Report, ARCCB-TR-89003, January 1989

4) Bretl, J.l., "Finite Element Analysis for General Solids and Threaded Connections", University of Wisconsin-Madison, Ph.D. Thesis Applied Mechanics, 1978

5) O'Hara, G.P., "Stress Concentrations in Screw Threads", Eighth NASTRAN Users' Colloquium, Goddard Space Flight Center, NASA Conference Publication 2131, pp 65-77, October 1979
Also
US Army Armament Research Development and Engineering Center (ARDEC), Technical Report, (with appendix) ARLCB-TR-80010, April 1980

6) O'Hara, G.P. and "Elastic-Plastic Comparison of Three Thread Forms", Proceedings of the Eighth U.S. Army Symposium on Gun Dynamics, Newport RI, pp 18-1-18-10, May 1996

7) O'Hara, G.P. and "Elastic Comparison of Four Thread Forms", ASME Pressure Vessels & Piping Conference, Orlando FL, PVP Vol. 344, July 1997

8) Gough, P.S., "The NOVA Code: A users Manual", Indian Head Naval Ordnance Station, Contractor Report, IHCR- 80-8, 1980

9) Gough, P.S., "The XNOVA: A Users Manual", Indian Head Naval Ordnance Station, Contractor Report, N00174-86-M-4336, PGA 88-2, December 19878

10) Gough, P.S., "The XNOVAKTC Code", U.S. Army Ballistic Research Laboratory, Final Report, Contract DAAK11-85-D-00002, Task II, PGA-TR-86-1, March 1986

A METHOD OF ESTIMATING BLAST ENVELOPE DURATION

Robert Dillon
Rose-Hulman Institute of Technology
Terre Haute, IN 47803

The blast signature of large caliber cannons was studied in order to capture the random jet noise which can strongly affect the acceptability of the blast overpressure. The jet noise theories of Lighthill and Nagamatsu were used to provide an estimate of the pressure fluctuations produced by the supersonic turbulent free jet of the muzzle as the cannon emptied. The free jet produced pressure fluctuations were superposed on the pressure waveform predicted by the method of Fansler et.el. This composite pressure signal was compared was compared to the free field blast signal for a 155mm cannon. The method described here predicted the blast envelope duration with good agreement with the experimental data available

INTRODUCTION

There is a need to accurately predict the blast envelope pressure duration of large caliber cannons in order to incorporate the blast overpressure limits imposed by MILSTD 1474D early in the design process. Failure to do so may result in weapons systems being rejected by the acquisition process late in the design process at large expense in both cost and failure to field a needed system.

When a cannon is fired, the high pressure propellant gases still have an large amount of available energy at the muzzle. At the muzzle, these propellant gases have completed their task, that is, they have accelerated the projectile from zero velocity to the muzzle velocity. These propellant gases, having completed their major task and yet still possessing a great deal of available energy can still be put to work in attenuating the recoil impulse felt by the carriage during the firing of the weapon. The use of recoil mounts serves to lessen the peak force encountered during firing but the overall recoil impulse remains unchanged. Only by fitting a muzzle brake to a closed-breech weapon can we reduce the recoil impulse felt by the carriage. To be able to fully understand the functioning of a muzzle brake and the possible detrimental effect it may have on the crew, the blast field created by the cannon must be described.

The muzzle blast field created by the release of the high pressure propellant gases is complex, and time dependent. This muzzle blast field is characterized by a highly underexpanded supersonic exhaust plume, which terminates at a strong shock, an expanding front of exhaust gases (the contact surface), and an expanding, nearly spherical outer shock (the blast wave), figure 1. This process is generated twice for every round fired. The first or precursor develops as the air ahead of the projectile is forced out of the gun. The second, the propellant gas jet, develops as the projectile leaves the muzzle and uncorks the cannon. The muzzle pressure level of the precursor is typically an order of magnitude lower than that of the propellant gases. As a consequence, the precursor shock is rapidly engulfed by the propellant blast. The

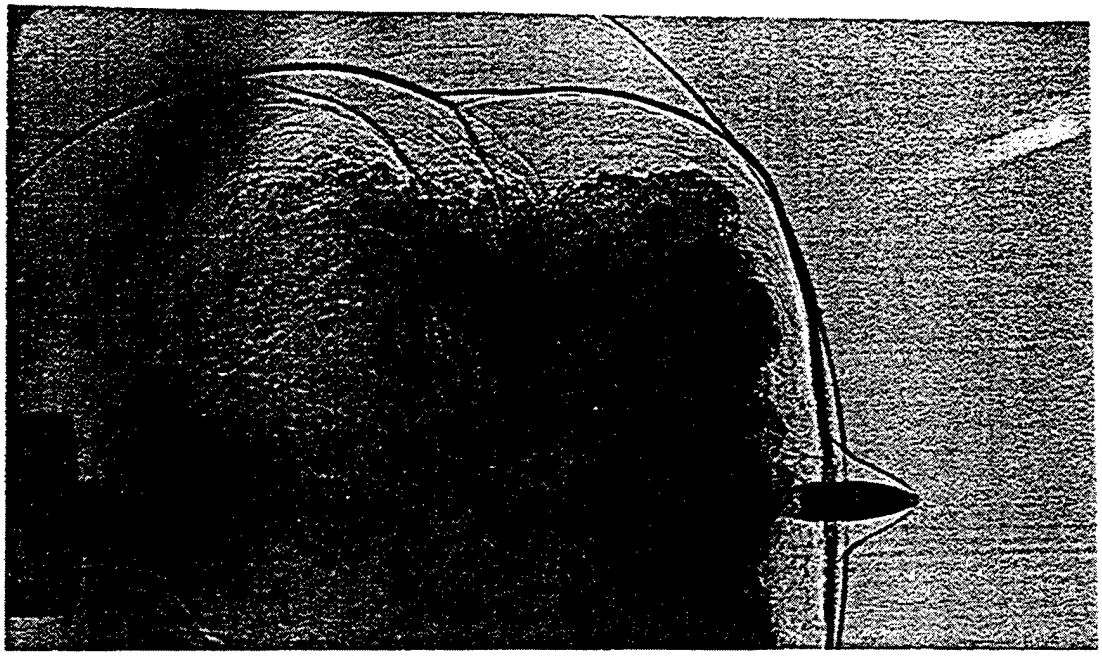

Figure 1. Muzzle blast flow field

propellant gas plume growth is influenced by the precursor flow, the projectile, and the ambient conditions. The resulting waveform is complex and contains superposed waves from reflections as well as a great deal of noise from the turbulence of the jet of propellant gases issuing from the muzzle. A representative free field blast pressure history is shown in figure 2. Notice the main blast wave and the high noise level followed by the second blast wave arrival, due to the ground reflection.

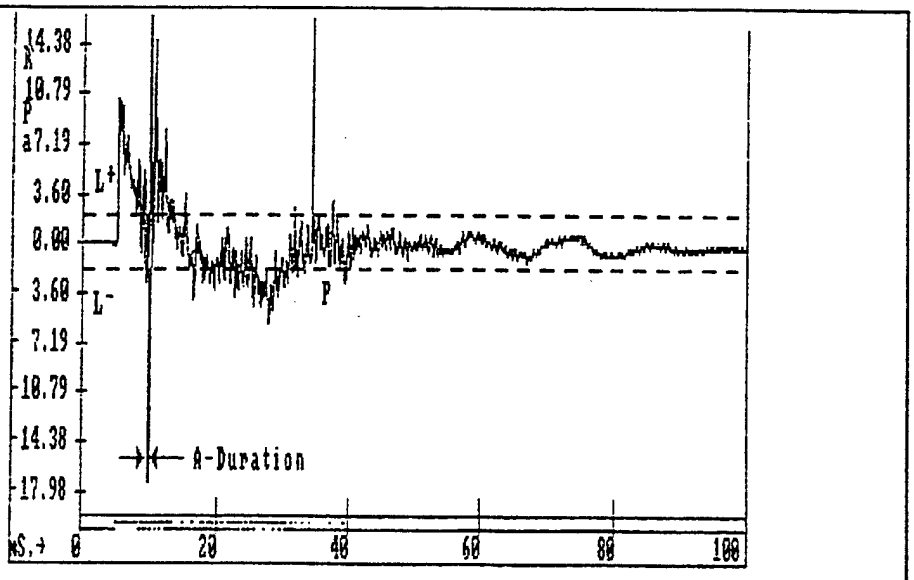

Figure 2. Blast overpressure signal.

The noise limits for Army material producing impulse noise is set forth in MILSTD-1474D. In order for any cannon to meet the noise limits imposed by the MILSTD the blast pressure level must not exceed the permissible envelope pressure duration or B-level duration. This envelope pressure is a function of the peak pressure level (PPL) and is taken as plus or minus 20 dB of the PPL recorded at that station. In order for a person to be allowed to be exposed to a source of impulse noise, the PPL and B-duration must fall below the line seen in figure 3.

BACKGROUND

The blast pressure wave can be numerically modeled in the near field and has been done extremely well in the past. The most promising results are from Carofano [1] who used Harten's Total Variation Diminishing (TVD) scheme to capture the fine details of the muzzle flowfields. It is computationally expensive, however, to carry Carofano's efforts to the crew positions due to the large storage requirements and the consequently fast processor speed required for the accuracy demands in predicting the envelope pressure duration.

Another approach used to predict the peak pressure levels for various cannons has been to develop scaling laws from experimental data into predictive empirical equations. Previous investigators [1-10] have done excellent work in developing extremely useful relation relations for predicting the time of arrival, peak overpressure level, positive phase duration and negative pressure duration of the blast signature of large and small caliber weapons. Unfortunately, these efforts did not attempt to capture the blast pressure envelope duration.

At this point, there appear to be three possible approaches to determine the envelope duration: numerical via CFD, analytical via jet noise theory, and scaling via experimental data. The first effort used her will be to attempt to use steady-state supersonic jet noise theory to predict the jet noise from the muzzle of the cannon and add this noise to the well established impulse pressure waveform. As additional experimental data become available they will be used to empirically correct the initial pressure signal predicted by the jet noise theory.

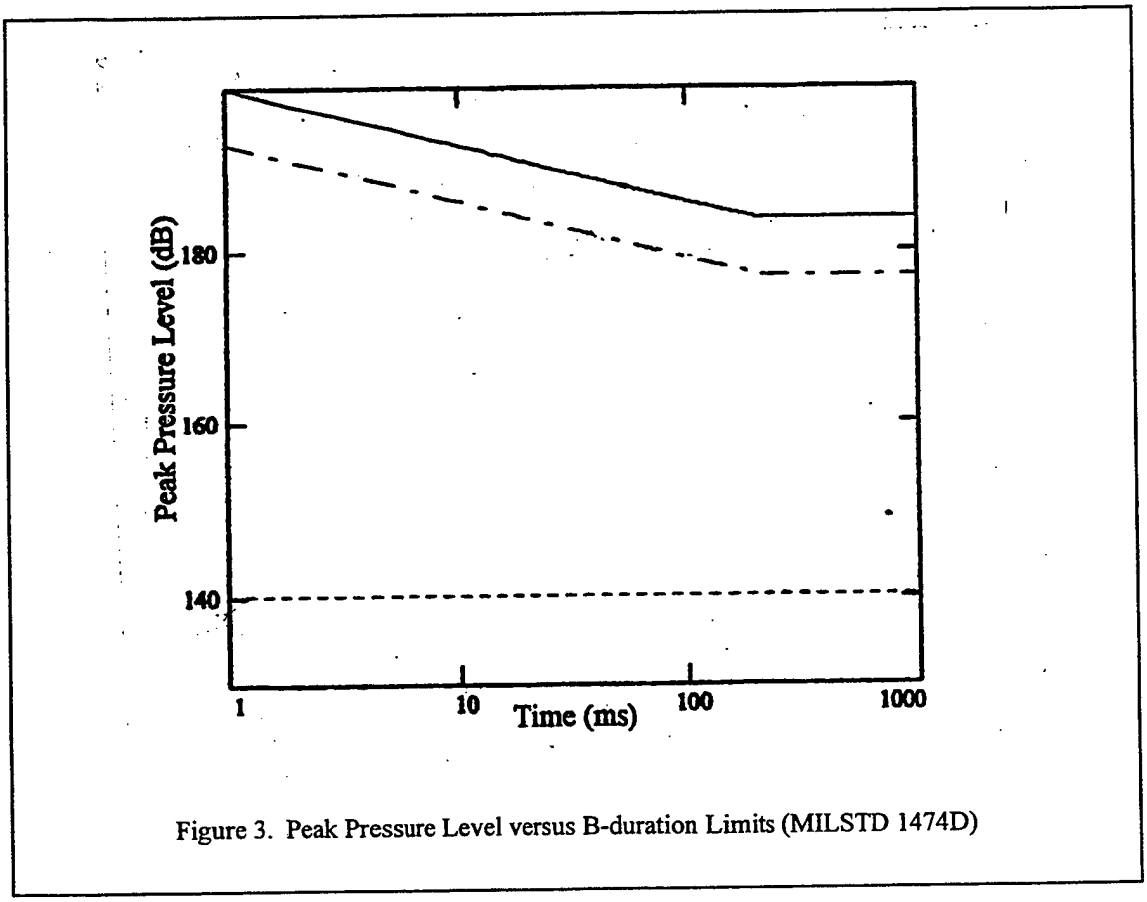

Figure 3. Peak Pressure Level versus B-duration Limits (MILSTD 1474D)

JET NOISE THEORIES

The first step in predicting the envelope pressure duration is to examine the quasi-steady state noise Lighthill [41] developed an expression for the steady state noise from supersonic jets. This expression gives the square of the overpressure fluctuations due to the interaction of the high velocity jet and the quiescent ambient air.

$$(p-p_0)^2 = \rho_0 a_0^5 \{\frac{V_e \omega^4 \overline{T}^2}{\rho_0 a_0} \frac{1}{4\pi r^2} \{(1-M_e \cos\theta)^2 + (\frac{\omega l}{a_0})^2\}^{\frac{-5}{2}}\}$$

where

a_0 is the ambient acoustic velocity
l is the length scale of a single eddy
M_e is the Mach number of the jet (jet velocity/ambient acoustic velocity)
p_0 is the ambient pressure
r is the distance from the jet noise source to the point of interest
T^2 is a typical mean square value of the quadrupole strength T_{ij}
$T_{ij} = \rho v_i v_j + p_{ij} - a_0^2 \rho \delta_{ij}$
V_e is the turbulent eddy volume
ρ_0 is the ambient density
θ is the angular measure from the axis of the jet to the point of interest
ω is the frequency of turbulent fluctuation

This expression when applied to the supersonic jets of the muzzle exhaust plume yields a value for the magnitude of the pressure fluctuations. The main difficulty in applying Lighhill's noise theory is to estimate the values of the jet characteristics such as l, T_{ij}, V_e, and ω

Another useful expression which may be used here is the one developed at NASA Lewis [41] which yields the acoustic power radiated by jets up to speeds of 600 m/s. Although the speeds are lower than those encountered in high velocity cannons the expression may still be useful and is given as

$$P = \rho_0 U^8 A / a_0^5$$

where

A is the nozzle (muzzle) area

Nagamatsu et al [37] used a similar expression and obtained empirical corrections for supersonic jets from converging nozzles. The total acoustic power output of a supersonic jet can be estimated by

$$P = \frac{10^{-4}}{9.6} \dot{m} \frac{\rho}{\rho_0} \left(\frac{a}{a_0}\right)^5 \left(a^2 M_j^2\right)\left(5M_j^2 + 0.8\right)\left(\frac{M_j^{-\alpha} + M_j^{-\beta}}{2} + \frac{M_j^{-\beta}}{5}\right)$$

where

$\alpha = 6.2$
$\beta = 2.4$

Now that the total acoustic power from the decaying muzzle jet can be estimated it can be added to the scaled blast pressure signal predicted by Fansler. To do this it must be brought back to the pressure level. The following expression from [44] is used to calculate first the sound power level and then the sound pressure level once the sound power level is known.

$$L_W = 10\log_{10}\frac{P}{P_{ref}}$$

where $P_{ref} = 10^{-2}$ Watts

$$L_p = L_w - 20\log_{10} r - 8dB$$

where r is in meters

Now the pressure can be calculated and added to the predicted impulse waveform.

$$p = p_{ref}10^{\frac{L_p}{20}}$$

where $p_{ref} = 20\ (10^{-6})$ Pa

Now that we have methods of estimating the jet noise form the muzzle exhaust plume we can apply them to the impulse noise signal calculated from the methods put forth by earlier investigators. Comparisons to the experimental data using the jet noise theories resulted in the pressure envelope duration being much shorter than that seen experimentally. It is theorized the quasi-steady turbulent noise produced by the muzzle jet is of less importance in predicting the envelope duration than the pressure fluctuations caused by the blast wave reflection off solid objects in the pressure field. In order to gain an estimate of the magnitude of the pressure fluctuations the experimental data were thoroughly reviewed. The method of dimensional analysis was used to determine what, if any, the relevant scaling parameters were in this approach. The jet noise theories could be adjusted by the use of empirical corrections obtained by scaling.

Scaling

Scaling has been used very successfully in the past and is being used here. A brief history of relevant efforts in maturing the scaling approach to the blast problem is presented now.

Pater [13] developed some very useful scaling relations for the prediction of recoil reduction and peak pressure level for baffled muzzle brakes. Fansler and Schmidt [25, 29] developed very good methods to model the blast of cannons and documented their efforts to develop useful scaling laws from several sources of experimental data over many calibers [22-33]. From their results the peak pressure level, the time of arrival, positive phase duration, and time until return to zero pressure level are all modeled. A detailed description of their method used in scaling is presented in reference 25. Figure 4 shows the resulting pressure signal predicted by this method. As stated earlier this pressure signal alone cannot be used to estimate the number of exposures a crewman could endure safely. There exists a need to capture the noise seen in the pressure traces to provide an estimation of the B-duration. For this present effort the scaling method is modified to include the prediction of the B-duration. This will allow the MILSTD to be employed to estimate the exposure levels permissible with candidate muzzle brake designs.

In order to scale the B-level duration an extensive analysis was done on all the free field blast pressure histories. The frequencies and amplitudes as well as the decay characteristics of the embedded noise was estimated and correlated as a function of radial position and distance from the muzzle. Since all pressure traces were obtained with the same interior ballistic solution, no scaling of those effects were conducted. Once an estimate of the intensity and decay characteristics of this embedded jet noise was made, the method of Nagamatsu, et. al. [36-39] was used to generate this noise for the scaled predictions. For this interior ballistic solution the Reynolds number based on bore diameter at the muzzle varies from a

high of about 980 million at shot ejection to a low of about 8 million when the muzzle jet has decayed to subsonic velocities. Nagamatsu [36] modified the theory of Lighthill [40, 41] to model the steady state jet noise from subsonic and supersonic underexpanded jets. For this case we use his method for supersonic jets. The characteristic length for the turbulent eddies is taken as the bore diameter (in the absence of any data otherwise) and the pressure fluctuations given by Nagamatsu's method yield the steady state noise level and decay patterns used to model the random noise seen in the actual blast signals.

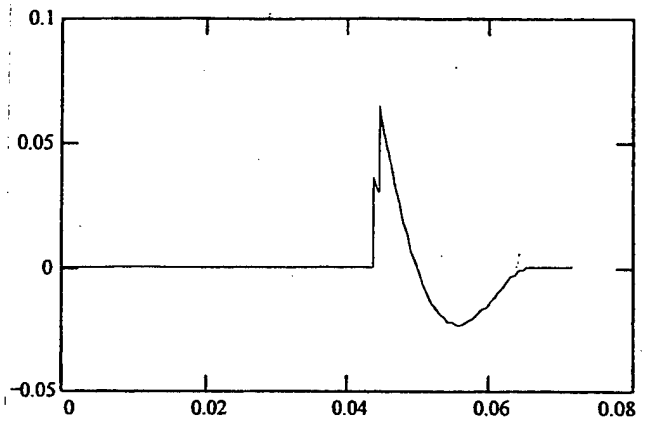

Figure 4. Blast pressure signal predicted by Schmidt

This noise was generated and added to the "clean" pressure wave from Fansler and Schmidt's scaled predictions and a representative trace can be seen in figure 5. The existing signals from the full-scale firing tests were then compared to these artificially generated noise signals to determine where any unacceptable deviations occurred. Available free field blast data were correlated and used to provide empirical corrections to the noise predictions obtained by Nagamatsu's method.

This artificially generated jet noise now allows the calculation of the B duration and then the number of exposures at each level of hearing protection may be predicted using the method of MILSTD-1474(D). An actual trace for this position is shown in figure 6.

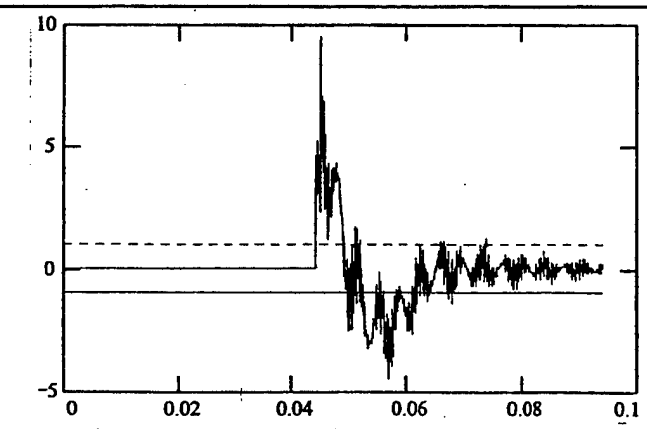

Figure 5. Scaled blast signal with jet noise added.

Now that the blast signature can be duplicated, various muzzle brake designs can be tested with this method to determine if there is the possibility of a blast overpressure problem. This will be extremely useful both is saving time and the expense of full scale tests.

RESULTS

The method developed was compared to the blast signature of a developmental 155 mm cannon equipped with an integral perforated muzzle brake. The cannon was fired horizontally with maximum zone. Two free field stations recorded the blast signal. The stations were located on a ray 135 ° measured from the axis of fire and at distances of 7.75 and 15.5 meters from the muzzle.

Figure 6 shows a comparison of the actual pressure signal with the estimated pressure signal for the 7.75 meter location. The actual pressure signal is the top trace. The estimated trace qualitatively agrees well with the actual signal and this method appears promising for estimating the envelope duration.

The comparison for the 15.5 meter location is given in figure 7. Again the actual signal is the tope trace while the lower trace is the estimation. Again the qualitative agreement is good and the traces seem to agree well. The peak pressure level and the envelope duration are computed and compared in Table 1.

Table 1 Comparison of Predicted and Measured Blast

155mm XM297 Cannon, Zone 6, $\beta = 0.7$, $\theta = 135^{\circ}$ Level Cannon						
		PPL(dB)			B-duration(ms)	
r(m)	Measured	Predicted	Error	Measured	Predicted	Error
7.75	179.9	176.6	-2%	31	32	3%
15.5	181.6	173.5	-4%	60	42	-30%

CONCLUSIONS

The method developed here was able to predict the pressure envelope duration with good results. For the first time a mathematical tool exists which can give an estimate of the blast overpressure acceptability of a cannon while in the initial design stage. The model developed here shows great promise and can easily be improved as more firing data become available. The scarcity of accurate measurements of the B-duration limits the accuracy of the method at this time.

The areas where the model must be improved are in accounting for the dynamic interactions between the expanding blast waves and the nearby obstacles. The model only accounts for the jet noise of the cannon exhaust plume. The Mach disk is a source of very large pressure fluctuations and must be modeled as well.

Overall however the method worked very well and is capable of providing the designers and managers an initial estimate of the total blast signature of a cannon while it is still on the drawing board.

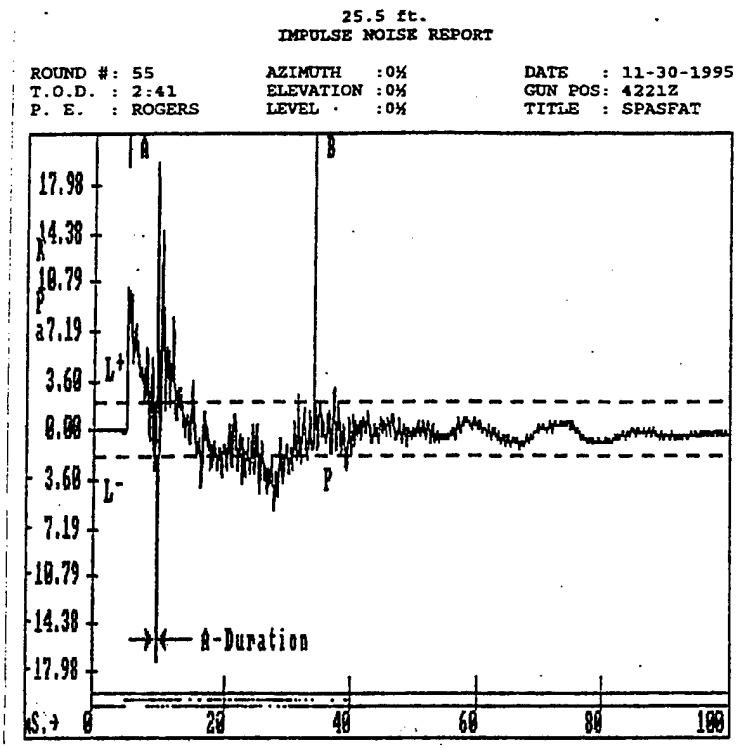

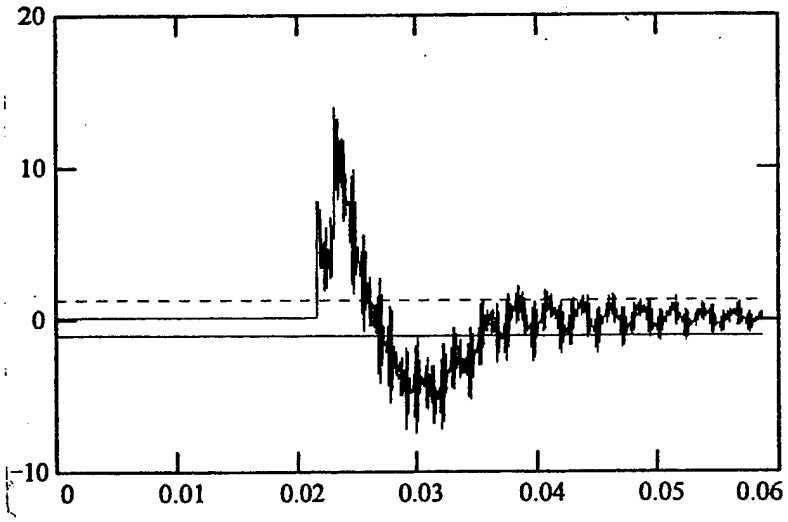

Figure 6. Blast Signatures from the 7.75m Free Field Station. Top - Actual, Bottom - Calculated

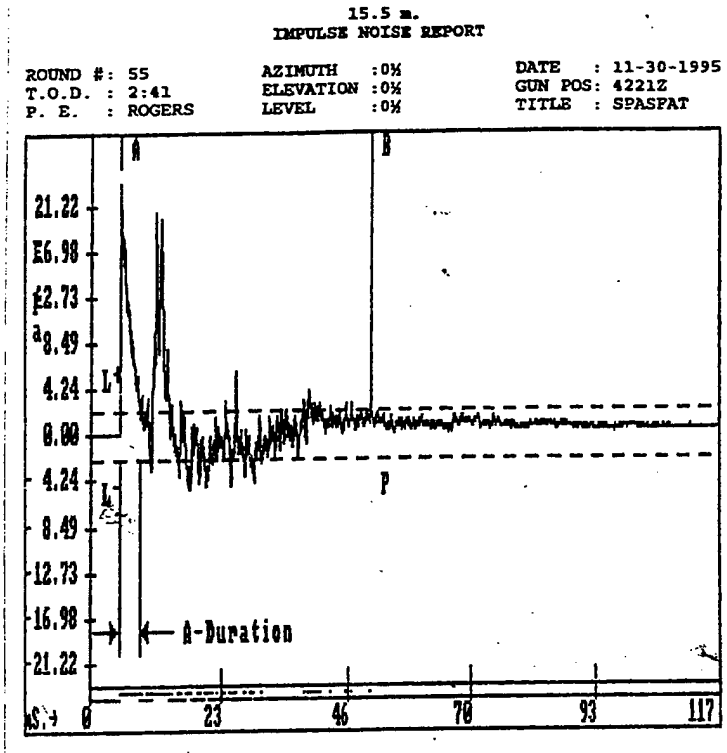

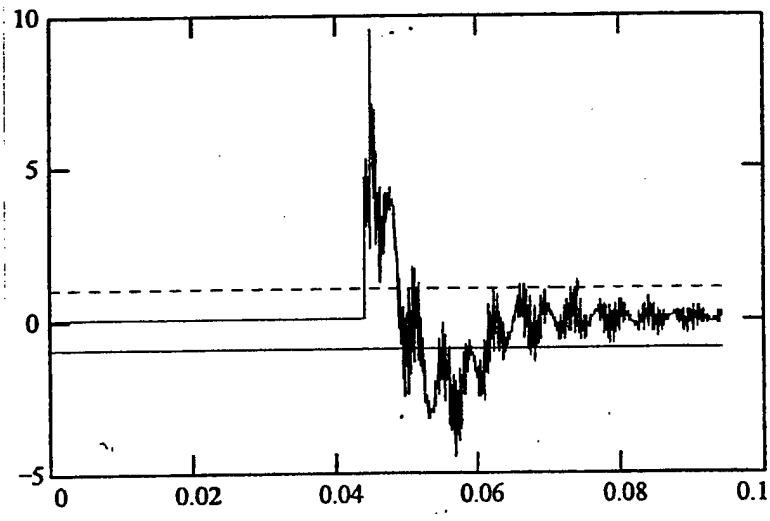

Figure 7. Blast Signatures from the 15.5m Free Field Station. Top - Actual, Bottom - Calculated

REFERENCES

1. Carofano, G.C., "The Blast Field Produced by a Cannon Having a Perforated Muzzle Brake," Technical Report ARLCB-TR-88043, Benet Laboratories, Watervliet, NY, December, 1988.

2. Dillon, R.E., "A Parametric Study of Perforated Muzzle Brakes," Technical Report ARLCB-TR-84015, Benet Weapons Laboratory, Watervliet, NY, May, 1984.

3. Dillon, R.E., "Wall Thickness and Vent Area Effects on Perforated Muzzle Brake Performance," Technical Report ARLCB-TR-84020, Benet Weapons Laboratory, Watervliet, NY, May, 1984.

4. Dillon, R.E. and Nagamatsu, H.T., "An Experimental Study of Perforated Muzzle Brakes," Technical Report ARLCB-TR-84004, Benet Weapons Laboratory, Watervliet, NY, February, 1984.

5. Dillon, R.E. and Nagamatsu, H. T., "A Method of Analyzing Perforated Muzzle Brake Performance," Technical Report ARLCB-TR-84002, Benet Weapons Laboratory, Watervliet, NY, February, 1984.

6. Dillon, R.E. and Nagamatsu, H.T., "An Experimental Study of Perforated Muzzle Brakes," AIAA Paper 84-1642 Presented at the AIAA 17th Fluid Dynamics, Plasma Dynamics, and Lasers Conference, Snowmass, CO, June 25-27, 1984.

7. Carofano, G.C., "The Gasdynamics of Perforated Muzzle Brakes," Technical Report ARCCB-TR-8806, Benet Laboratories, Watervliet, NY, February, 1988.

8. Carofano, G.C., "Blast Computation Using Harten's Total Variation Diminishing Scheme," Technical Report ARLCB-TR-84029, Benet Weapons Laboratory, Watervliet, NY, October, 1984.

9. Carofano, G.C., "Blast Field Contouring Using Upstream Venting," Technical Report ARCCB-TR-93009, Benet Laboratories, Watervliet, NY, march, 1993.

10. Carofano, G.C., "A Comparison of Experimental and Numerical Blast Data for Perforated Muzzle Brakes," Technical Report ARCCB-TR-90034, Benet Laboratories, Watervliet, NY, December, 1990.

11. Carofano, G.C., "Perforated Muzzle Brake Efficiency Measurements Using a 20-mm Cannon," Technical Report ARCCB-TR-93010, Benet Laboratories, Watervliet, NY, March, 1993.

12. Plostins, P. and Clay, W.H., "Performance of Lightweight 105-mm Cannon Designs [U]," Technical Report BRL-TR-2749, Ballistic Research Laboratory, Aberdeen MD, July, 1986.

13. Savick, D.S. and Baur, E.H., "Test Performance Characteristics for a 120-mm Perforated Muzzle Brake [U]," Memorandum Report BRL-MR-3816, Ballistic Research Laboratory, Aberdeen, MD, May, 1990.

14. Pater, L.L., "Scaling of Muzzle Brake Performance and Blast Fields," Technical Report NWL TR-3049, Naval Surface Weapons Center, Dahlgren, VA, October, 1976.

15. Pater, L.L., "Muzzle Brake Parameter Study," Technical Report NSWC/DL TR-3531, Naval Surface Weapons Center, Dahlgren, VA, October, 1976.

16. Moore, G.R., "Finite Difference Calculations of the Free-Field Gun Blast About the Muzzle of a 5"/54 Naval Gun, Technical Report TR-2794, Naval Weapons Laboratory, Dahlgren, VA, September, 1972.

17. Moore, G.R., "Calculation of 5"/54 Muzzle Blast Using a Multi-Material Hydrodynamic Code [U]," Technical Report TR-3008, Naval Weapons Laboratory, Dahlgren, VA, February, 1974.

18. Walther, M.F., "Gun Blast from Naval Guns," Technical Report TR-2733, Naval Weapons Laboratory, Dahlgren, VA, August, 1972.

19. Soo Hoo, G. and Yagla, G.G., "Use of a Conical Muzzle Device to Control Gun Blast," Technical Report NWL TR-2793, Naval Weapons Laboratory, Dahlgren, VA, August, 1972.

20. Pater, L.L., "Gun Blast Far Field Over Pressure Contours," Technical Report TR-79-442, Naval Surface Weapons Center, Dahlgren, VA, March, 1981.

21. Pater, L.L and Shea, J.W., "Use of Foam to Reduce Gun Blast Noise Levels," Technical Report TR-81-94, Naval Surface Weapons Center, Dahlgren, VA, March, 1981.

22. Schmidt, E.M., Gion, E.J. and Fansler, K.S., "A Parametric Study of the Muzzle Blast from a 20mm Cannon," Technical Report ARBRL-TR-02355, Ballistic research Laboratory, Aberdeen, MD, August, 1981.

23. Gordnier, R.E., "Effect of Gun Tube Evacuation on Free Field Blast Pressures and Comparison with Proposed Models," Memorandum Report ARBRL-MR-03160, Ballistic Research Laboratory, Aberdeen, MD, March, 1982.

24. Schmidt, E.M. and Thompson, W.G., "The Effect of Muzzle Device Configuration on the Blast Overpressure Levels on the AH-1S TOW Sight Unit," Memorandum Report ARBRL-MR-03266, Ballistic Research Laboratory, Aberdeen, MD, May, 1983.

25. Fansler, K.S. and Schmidt, E.M., "The Prediction of Gun Muzzle Blast Properties Using Scaling," Technical Report ARBRL-TR-02504, Ballistic Research Laboratory, Aberdeen, MD, July, 1983.

26. Schmidt, E.M., "Muzzle Blast Pressure Loadings upon Aircraft Surfaces," Memorandum Report ARBRL-MR-03336, Ballistic Research Laboratory, Aberdeen MD, February, 1984.

27. Schmidt, E.M., Baur, E.H. and Thompson, W.G., "Comparison of the Performance of Candidate Muzzle Devices for 30mm Cannon," Memorandum Report BRL-MR-03337, Ballistic Research Laboratory, Aberdeen, MD, February, 1984.

28. Baur, E.H. and Schmidt, E.M., "Design Optimization Techniques for Muzzle Brakes," Interim Memorandum Report BRL-IMR-841, Ballistic Research Laboratory, Aberdeen, MD, March 1985.

29. Heaps, C.W., Fansler, K.S., and Schmidt, E.M., "Computer Implementation of a Muzzle Blast Prediction Technique," Memorandum Report BRL-MR-3443, Ballistic Research Laboratory, Aberdeen, MD, May, 1985.

30. Kietzman, J., Fansler, K.S., and Thompson, W.G., "Muzzle Blast from 105mm M735 Round," Memorandum Report BRL-MR-3957, Ballistic Research Laboratory, Aberdeen MD, January, 1992.

31. Fansler, K.S., et. al., "A Parametric Investigation of Muzzle Blast," Technical Report ARL-TR-227, Army Research Laboratory, Aberdeen, MD, September, 1993.

32. Fansler, K.S., "Prediction Model for Blast from Recoilless Guns," Technical Report ARL-TR-235, Army Research Laboratory, Aberdeen, MD, June, 1995.

33. Fansler, K.S., "Prediction Model for Blast from Recoilless Gun Blast in Enclosures," Memorandum Report ARL-MR-303, Army Research laboratory, Aberdeen, MD, April, 1996.

34. Skews, B.W., "The Shape of a Diffracting Shock Wave," Journal of Fluid Mechanics, Vol. 29, Part 2, 297-304, 1967.

35. Skews, B.W., "The Perturbed Region Behind a Diffracting Shock Wave," Journal of Fluid Mechanics, Vol. 29, Part 4, 705-719, 1967.

36. Nagamatsu, H.T., Sheer, Jr., R.E. and Bigelow, E.C., "Mean and Fluctuating Velocity Contours and Acoustic Characteristics of Subsonic and Supersonic Jets," Report No. 70-C-391, General Electric Corporate Research and Development Center, Schenectady, NY, October, 1970.

37. Nagamatsu, H.T., Sheer, Jr., R.E. and Bigelow, E.C., "Subsonic and Supersonic Jet Flow and Acoustic Characteristics and Supersonic Suppressors," Report No. 72-CRD-264, General Electric Corporate Research and Development Center, Schenectady, NY, September, 1972.

38. Nagamatsu, H.T., Sheer, Jr., R.E. and Gill, M.S., "Flow and Acoustic Characteristics of 191 Tubes and 191 Shrouds Supersonic Jet Noise Suppressor," Report No. 70-C-354, General Electric Corporate Research and Development Center, Schenectady, NY, October, 1970.

39. Nagamatsu, H.T. and Sheer, Jr., R.E., "Flow, Thrust, and Acoustic Characteristics of 50 Tubes with 50 Shrouds Supersonic Jet Noise Suppressor," Report No. 71-C-258, General Electric Corporate Research and Development Center, Schenectady, NY, September, 1971.

40. Lighthill, M.J., "On Sound Generated Aerodynamically," Proceedings of the Royal Society of Aeronautics, Vol. 211, 564-587, 1952.

41. Lighthill, M.J., "Jet Noise," AIAA Journal, Vol. 1, No. 7, 1507-1517, 1963.

42. VanDyke, M., An Album of Fluid Motion, The Parabolic Press, Stanford, CA, 1982.

43. MILSTD -1474D, "Noise Limits for Army Materiel"

Dispersion Analysis of the XM881APFSDS Projectile

Thomas F. Erline
Weapons and Materials Research Directorate
U.S. Army Research Laboratory
Aberdeen Proving Ground, MD 21005-5066

Alan F. Hathaway
Arrow Tech Associates
1233 Shelburne Road
Suite D8, Pierson House
South Burlington, VT 05403

This study compares the results of a dispersion test with mathematical modeling. A 10-round group of modified 25-mm XM881 Armor Piercing Fin Stabilized Discarding Sabot projectiles was fired from the M242 chain gun into a designated target. The mathematical modeling results come from BALANS, a product of Arrow Tech Associates. BALANS is a finite-element lumped parameter code that has the capability to model a flexible projectile being fired from a flexible gun. It also has the unique feature of an automated statistical evaluation of dispersion. This study represents an effort to establish a combined experiment and simulation approach to reduce system error.

INTRODUCTION

The US Army has a need to improve its understanding of the effectiveness of medium-caliber cannon systems. One of the methods for advancement toward this understanding is to perform experimental aerodynamic jump tests and mathematical modeling simulating the jump tests. One fielded system of major interest is the 25-mm M242 Autocannon, which is found on the Bradley Fighting Vehicle. This gun system was selected for study by the U.S. and German Defense Exchange Agreement Number 1132. This system is ideal for setup in a small-caliber range, like the Aerodynamics Range Facility at the US Army Research Laboratory at Aberdeen Proving Ground.

The current service round, used with the 25-mm M242 Autocannon, is the M919 Armor Piercing Fin Stabilized Discarding Sabot (APFSDS) projectile used for armor penetration. This round has a depleted uranium penetrator that would contaminate the experimental facility. Therefore the XM881, which has tungsten penetrator and was a precursor of the M919, presents itself as a suitable substitute. The XM881 has a flight vehicle that is geometrically similar to the M919 including matching threads for fitting the sabot, however, the discarding sabot of the XM881 was totally different from the M919. To better emulate the M919, it was decided to replace XM881 sabots with the sabots used on the M919.

The dynamic state of a projectile at shot exit is determined in part by the in-bore launch disturbances experienced by the projectile as it traverses the length of the barrel. A contributing factor is the initial misalignment of the projectile's principle axis and center-of-gravity (CG) offset with respect to the bore centerline. As the projectile is driven axially down bore by the propellant gas pressure, it is also forced to travel a lateral path that is determined by static and dynamic curvatures. Tube droop in the vertical plane is a gravity-induced static curve, and the bore straightness profile is a static curve due to the manufacturing processes' inability to produce a perfectly straight bore. The firing of the gun produces an array of complex interdependent events. Axial travel of the projectile and propellant gas pressure will impart forces on the gun for recoil and slight bending in the barrel. The projectile reacts in flexure to the massive barrel and the barrel responds to the projectile loads. The dynamic lateral path then becomes a boundary condition of projectile balloting.

The balloting analysis program, BALANS, from Arrow Tech Associates, Inc., was chosen for this study because of its multifunctional abilities. It has the capability to perform a single shot deterministic case in either two or three dimensions and target impact dispersion analysis using a stochastic approach.

Under this mission for investigating the experimental performance of the XM881, it is believed that good agreement between the experimental results and modeling results with the BALANS program will allow modeling to point to areas that need improvement. This is especially true in the area of gun tube straightness and projectile-gun tube interactions. In this study, for example, both experiment and modeling show the in-bore balloting reactions to be a significant contribution to dispersion.

EXPERIMENTAL APPROACH

Overview of the Experiment

The M242 chain gun was setup at the Aerodynamics Range of the ARL, APG. A schematic of the test setup is shown in Figure 1. Two eddy probe stations that measure lateral displacements were positioned about the muzzle brake of the gun to capture the muzzle motion. A pressure probe trigger was located just outside the muzzle to start the experimental equipment. A sabot catcher plate positioned several meters from the muzzle. Six orthogonal x-ray stations were positioned within two meters of the muzzle to capture velocity, yaw, and yaw rates. There were 25 orthogonal shadowgraph stations to measure the flight vehicle motion (see Figure 2). At 100 meters from the muzzle, a target setup recorded shot fall. The muzzle displacements, pointing angles, transverse velocity and angular velocity were determined using data reduction analysis techniques found in reference [1].

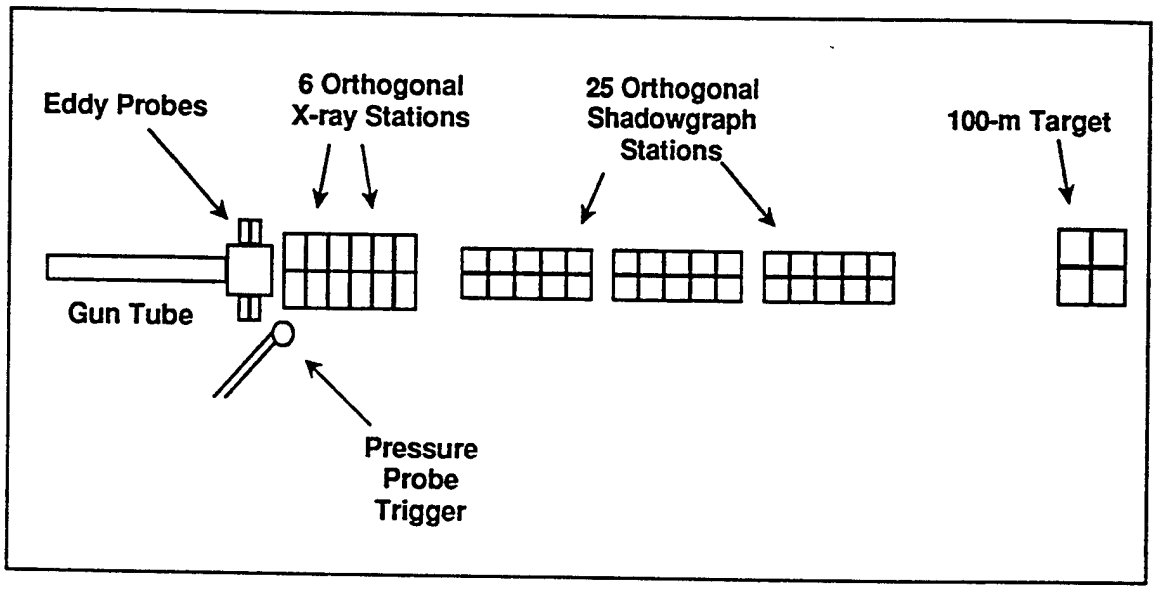

Figure 1. Jump Test Instrumentation.

Description of the XM881

The XM881 is a 25-mm APFSDS experimental round that has gone through a number of design iterations. The XM881 specimens available did not match the particular version of the penetrator drawings found. Therefore, detailed measurements were performed. The total length of the flight vehicle is 153.0 mm with the penetrator length of 82. 8 mm and threaded length of 29.4 mm starting at 64.4 mm from the base of the flight vehicle. Refer to Figure 2 showing a print of a shadowgraph of the flight vehicle from the test. The original sabots were removed from the flight vehicle and replaced with those found on the M919.

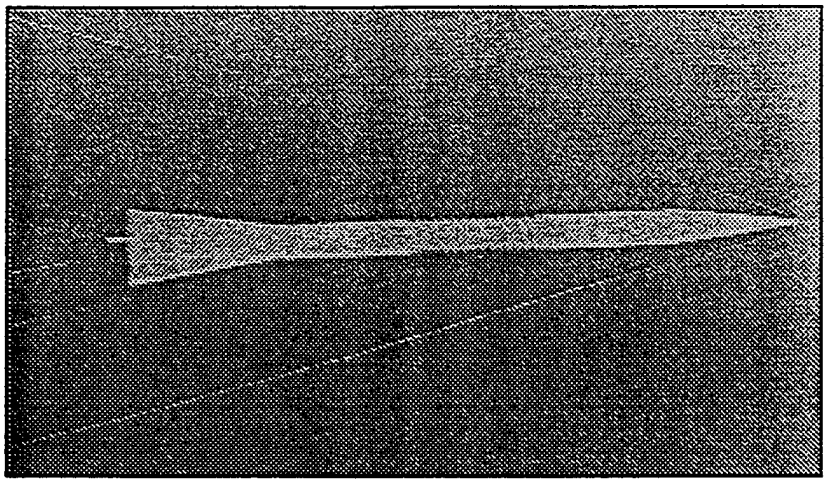

Figure 2. XM881 Flight Vehicle at Mach 4.0

Bore Straightness

The M242 chain gun was setup with barrel serial number (SN) 273 that was measured for centerline straightness, and bore gauging for service condition. The vertical (without gravity droop) and horizontal centerline referencing the rear face of the tube (RFT) of SN273 is shown in Figure 3. The manufacturing irregularities noted in the centerline are typical with positive up and to the gunner's right.

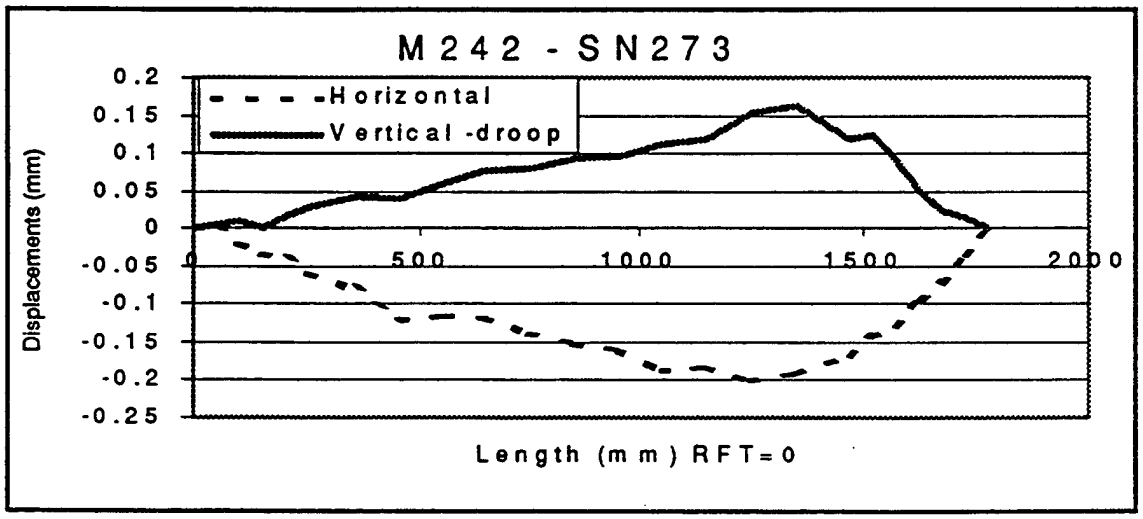

Figure 3. M242 Barrel Serial Number 273 for the 25-mm Chain Gun.

Experimental Results

The experimental results are utilized in jump and dispersion models that are defined in reference [2]. The means of major angular components of jump and dispersion are displayed in Figure 4 in milliradians. The muzzle pointing angle component is noted as "PA". The muzzle of the gun has transverse velocity noted as "CV" which imposes on the projectile at shot exit. The angular deviation of the projectile center of gravity relative to a coordinate system attached to the muzzle at shot exit is known as projectile "CG" jump. The "CG" jump is caused by in-bore balloting, muzzle blast, projectile mechanical disengagement and sabot discard. The component noted as "AJ" is aerodynamic jump which is the mean angular deviation of the projectile swerve trajectory. There was no measurable evidence of disturbance from sabot discard on the projectile "CG" jump. The sabot discard was completed within 0.15 meters from muzzle, which is too close to the muzzle to capture in the x-ray stations. In Figure 4 positive is up and to the right.

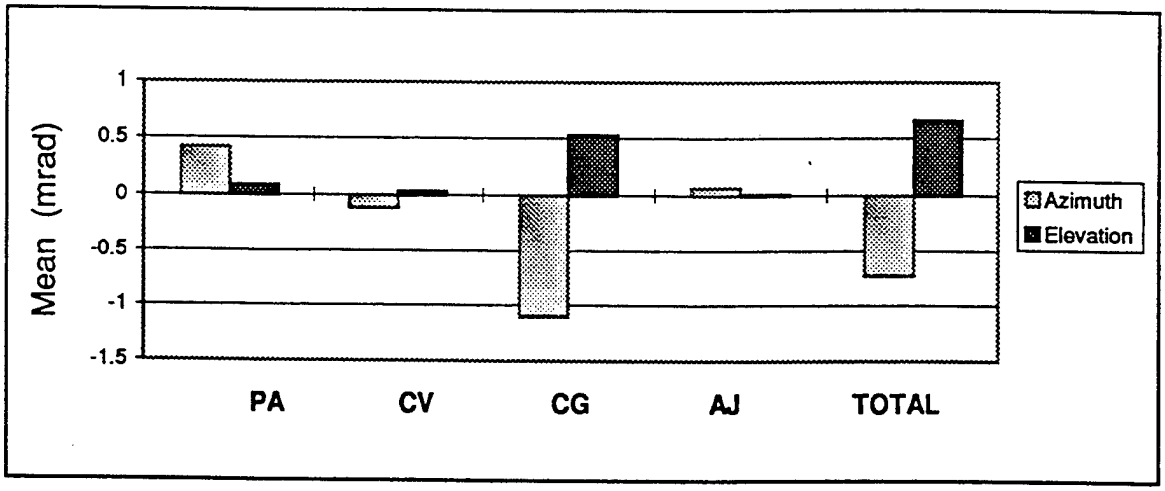

Figure 4. The 25-mm XM881 Means of Jump Components.

The standard deviations of the components of jump are displayed in Figure 5. The dispersion model may be simple if the total dispersion is the result of the sum of the independent individual jumps. The square of the standard deviations of the individual jump components will sum to the square of the impact dispersion. This empirical model appears to be best suited for this type of experiment.

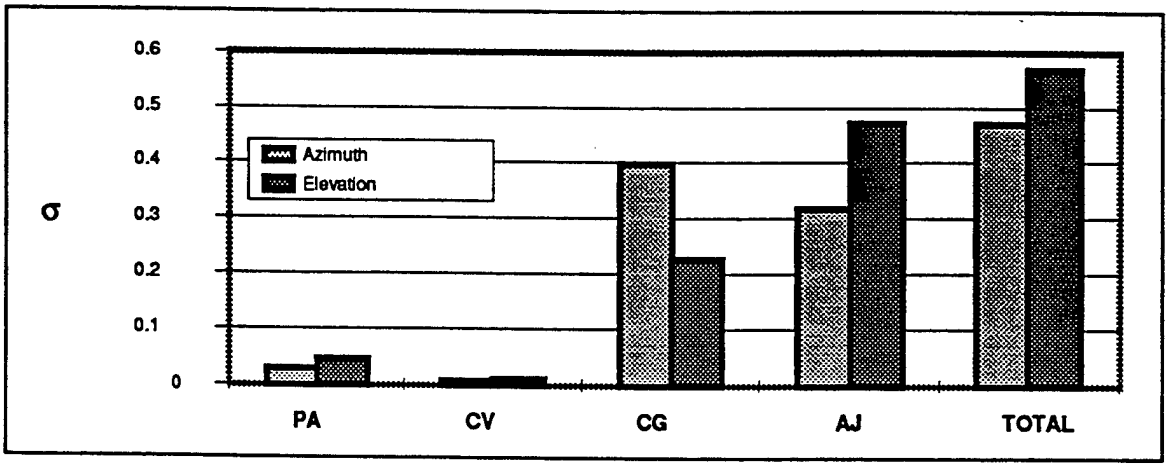

Figure 5. The 25-mm XM881 Dispersion of Jump Components.

ANALYTICAL APPROACH

Overview of BALANS

BALANS [3] simulates the dynamic response and interaction of a flexible projectile and a flexible gun tube during in-bore travel. It also includes the effects of a curved bore profile. The simulation utilizes individual models of the projectile and gun tube, in a time step iterative solution. Pertinent motion and load data are periodically saved during the analysis to produce selective summary graphical displays. BALANS takes advantage of the interior ballistics simulation and CG offset calculations of PRODAS [4] and an automatic lumped parameter modeling capability to assist in building a BALANS model.

The analytical procedure utilized in BALANS presupposes that the projectile is initially misaligned within the gun tube due to manufacturing tolerances. During firing, this misalignment produces secondary forces causing transverse displacement and yawing motion of the projectile as it travels from breech to muzzle. The resulting yaw angle, angular rate, and transverse velocity at muzzle exit are then analyzed for their effect on dispersion. It should be noted that BALANS calculates the projectile state (yaw, yaw rate, transverse velocity) at muzzle exit while the experimental setup determines the state of the tube and bore at the projectile exit.

Figure 6 contains a flow diagram of this stochastic method for predicting dispersion. Whether trying to predict dispersion on a new design or solve a dispersion related problem on a current design, the approach is very similar. It begins with gathering basic technical information such as manufacturing dimensional data, assembly drawings and/or specifications, analytical results from other analyses or test such as a finite element analysis or experimental results of the sabot front borerider. This information is critical to building the accurate analytical model of the projectile to be used during all analyses within this approach. From this information, a tolerance study can also be performed for input into the in-bore balloting analysis.

The second piece of information required is production history information such as Statistical Process Control (SPC) information. Even if working with a new projectile design for which there is no production history, it is valuable to obtain this information for a similar design or a projectile with similar characteristics.

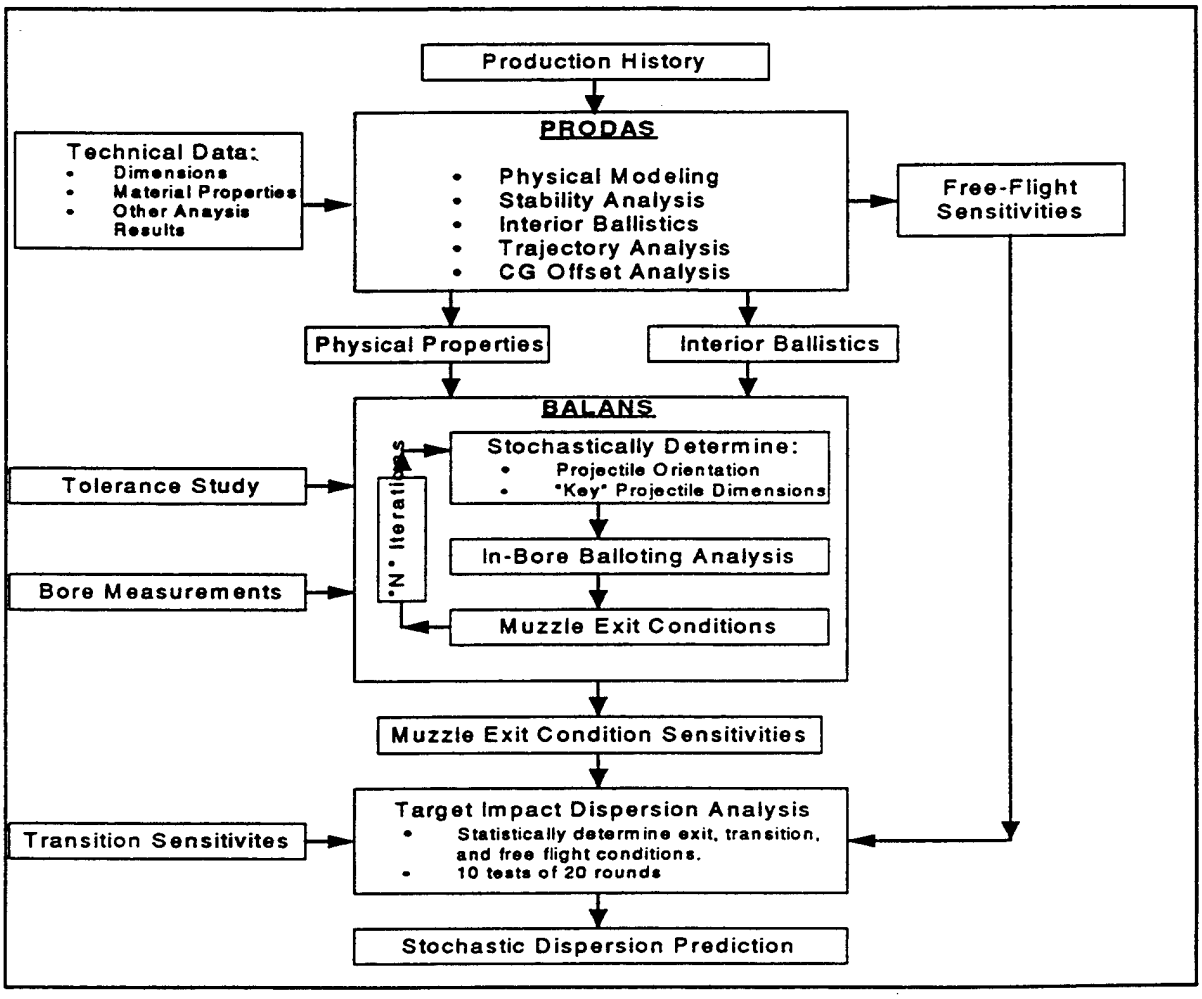

Figure 6. Analytical Approach to Predicting Dispersion.

Since some of the inputs to this approach are statistical in nature, the historical data provides a foundation from which to derive the statistical information.

The last type of information required is test and/or measurement that is important to predicting dispersion but is not derived from analysis. This includes bore centerline measurements, boresight errors inherent within a test fixture or boresight tool, known sabot discard issues from tests of similar sabots, etc.

As can be seen in Figure 6, the drawings, production history, and results from previous analyses are used for physical modeling of the projectile which in turn is the basis for several analyses to be described in the following sections. Each of the analyses results in dispersion component sensitivities that are then used in predicting dispersion.

BALANS Model of the XM881

The basic inputs for the in-bore balloting analysis are a lumped parameter model of the projectile that properly characterizes its mass properties and flexibility, a forcing function, and several distances and runouts that are used to orient the projectile within the gun tube. The lumped parameter model is generated automatically from the PRODAS geometric model.

Figure 7 is an example of the XM881 as a lumped parameter model automatically generated from PRODAS. As shown, the upper half of the model is the actual projectile as generated from PRODAS. The lower half attempts to mirror the upper half by reflecting the lumped parameter node/element model.

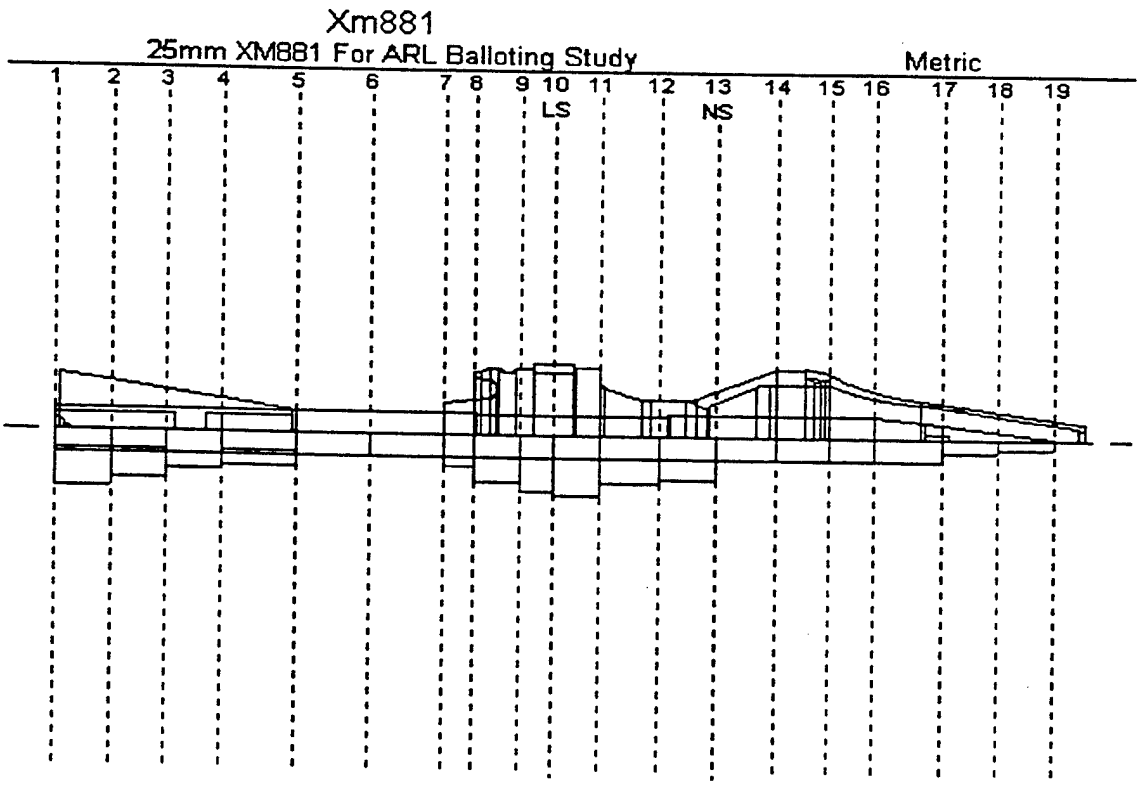

Figure 7. Graphical Representation of the XM881 Lumped Parameter Model.

The forcing function required for the balloting analysis is provided directly from the PRODAS interior ballistics analysis module. PRODAS uses the Baer-Frankl methodology to simulate combustion of propellant grains and calculate the time-dependent parameters of base pressure (that is applied to the projectile aft of the obturator during the balloting analysis), spin velocity and acceleration (that is used to calculate centrifugal forces during in-bore travel), and axial acceleration (that is used to calculate axial forces during in-bore travel). Transverse forces are calculated from the induced balloting motion.

In addition to the lumped parameter model, the dispersion analysis requires manufacturing dimensional and tolerance information and transition and free-flight sensitivity information. The manufacturing information consists of several critical dimensions and tolerances necessary for in-bore balloting. These define the locations of the projectile / gun tube interfaces and some of the critical projectile dimensions which effect dispersion. The statistical in-bore balloting analysis uses these dimensions and their tolerances to randomly orient the projectile in the gun tube. Several hundred in-bore balloting analyses are generally required to obtain statistically valid muzzle exit yaw, yaw rate, and transverse velocity predictions [5].

The transition and free-flight sensitivity information is used to determine those components of dispersion after the projectile has left the gun tube. Transition sensitivities are separated into sabot discard and boresight sensitivities. Errors induced by sabot discard may have significant variation from one projectile configuration to another. They have both a physical component which can occur due to asymmetric loads applied to the core during discard and an aerodynamic interference component. Sabot discard is the least well understood of the major contributors to dispersion and therefore is generally determined from test, observation, and/or experience. Boresight errors are the error associated with pointing the gun at the target. Boresight errors vary between calibers, gun crews, and instrumentation.

The free-flight dispersion component sensitivities include muzzle velocity, aerodynamic jump, aerodynamic trim angle, cross winds, and aerodynamic/mass asymmetries. All of these parameters are determined via trajectory analysis within PRODAS as follows:

- The muzzle velocity sensitivity factor is the drop variation due to muzzle velocity variation and can be calculated by comparing the drop of trajectory simulations made by perturbating muzzle velocities.
- The aerodynamic jump sensitivity relates dispersion to the muzzle exit yaw rate of the projectile. This factor is dependent upon the physical and aerodynamic characteristics of the projectile as well as the projectile spin and velocity.
- The cross wind sensitivity of the projectile is determined by trajectory simulations of the projectile flight to the range of interest both with and without a nominal crosswind applied.
- The aerodynamic trim angle of a projectile configuration (due to manufacturing tolerances) may be calculated from PRODAS predictions of the body alone and fin alone center of pressure and normal force coefficients, and from the expected one sigma value of the angular misalignments of the nose and tail sections.
- The aerodynamic/mass asymmetries factor is determined by simulating trajectories with a trim angle assumed to be oriented at orthogonal and diametrically opposed orientations.

Deterministic Analysis

Once the lumped parameter model of the projectile and gun system is finished, one needs to run test cases. Start with the most basic analysis before proceeding to more complex simulations. First, run the simplest case, for example, a 2-dimensional single shot simulation using a straight centerline including gravity droop. When the results appear reasonable then move on to a simulation that includes the measured centerline from SN273. Now, one simple way of obtaining insight from the modeling results is to compare the results from the straight centerline to the measured centerline SN273. In Figure 8a is seen the projectile lateral forces from interacting with a smooth straight centerline. Though the loads are low, it is immediately apparent that balloting causes high frequency disturbance. Next, in Figure 8b are seen the projectile lateral forces from interacting with a centerline that includes manufacturing irregularities. The loads are only slightly higher except for some higher forces noted near shot exit delivered to the rear contact of the projectile.

The deterministic analysis provides a detailed analysis at each node in the lumped parameter model in terms of bending moments, shear forces, nodal displacements, and projectile shape at each time step as well as exit conditions. It is equivalent to performing a *single shot* experiment to investigate issues other than dispersion. Since the analysis presupposes an initial projectile orientation in the gun tube which is difficult to determine

experimentally, the deterministic analysis has limited usefulness when trying to evaluate overall projectile performance parameters such as dispersion.

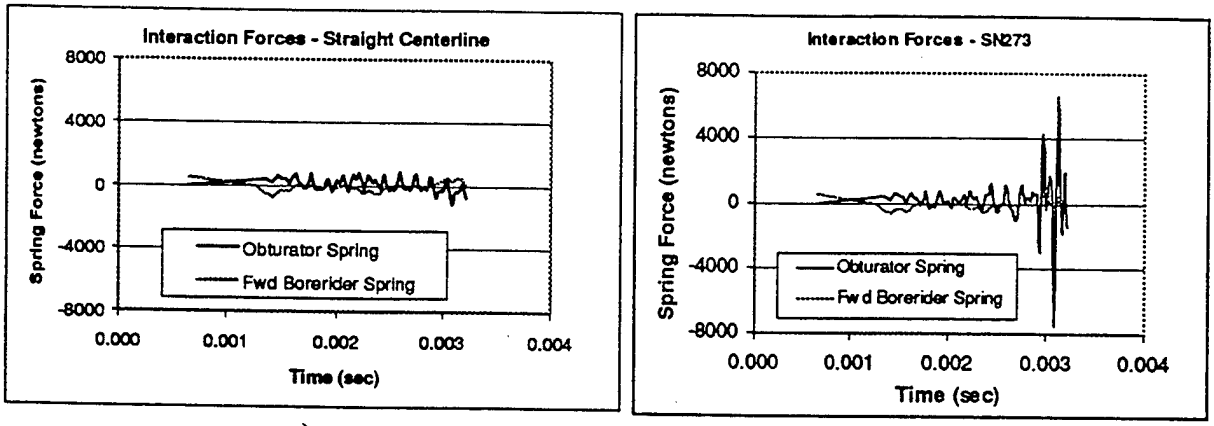

a) b)

Figure 8a & 8b: Interaction Forces

Stochastic Analysis

Since production history information such as SPC information does not exist for the XM881 specimens in our inventory, the parameters required for input had to come from either measurements or estimate based on M919 data. For the sensitivity values found in Table 2. the muzzle velocity data comes from the experiment. Aerodynamic jump, yaw factor and spin rate come from the PRODAS segment. Bore sight, sabot discard, and miscellaneous error numbers are engineering best guess values based on experience with similar projectiles. For simplicity, values that were assumed to be zero, such as wind factors, aerodynamic and mass asymmetries, and others are not shown in the table.

Tables 1 and 2 contain sensitivity data and manufacturing information required for the simulation. Generally, this data is obtained from previous simulations, testing, drawings, and/or SPC data collected by the manufacturer. For this simulation, the source of the data was either through measurements (meas.) or from engineering estimates (est.) which are based on previous experience in simulating and testing of similar rounds.

Table 1. XM881 Sensitivity Data

Characteristic	Value	Data Source
Aerodynamic Jump Factor(dimensionless)	0.030	est.
Muzzle Velocity Standard Deviation(m/s)	8.419	est.
Muzzle Velocity Factor(dimensionless)	0.005	est.
Boresight Error(dimensionless)	0.050	est.
Sabot Discard Error(dimensionless)	0.050	est.
Miscellaneous Errors(dimensionless)	0.100	est.
Muzzle Velocity (m/s)	1398.4	meas.
Initial Yaw Factor (mils)	0.010	est.
Muzzle Spin Rate (rads/s)	2900.0	est.

Table 2. Manufacturing Tolerance Information

Characteristic	Value (mm)	Data Source
Distance to Obturator	63.0941	meas.
Distance to Forward Spring	101.143	meas.
Distance to Bore Rider	110.236	meas.
Bore Diameter	25.100	meas.
Forward Bourrelet Mean Diameter	24.970	est.
Forward Bourrelet Standard Deviation	0.015	est.
Forward Bourrelet Runout (Mean to Penetrator)	0.025	est.
Forward Bourrelet Runout Standard Deviation	0.010	est.
Rear Bourrelet Runout (Mean to Penetrator)	0.025	est.
Rear Bourrelet Runout Standard Deviation	0.010	est.
Sabot Inside Diameter at Fwd Bourrelet	8.273	meas.
Sabot Inside Diameter at Fwd Bourrelet Std Dev	0.000	est.
Core Outside Diameter at Fwd Bourrelet	8.273	meas.
Core Outside Diameter at Fwd Bourrelet Std Dev	0.000	est.

The BALANS dispersion results presented here in Table 3 are the result of 10 different simulations of 10 rounds each stochastically determining projectile orientations and other key dimensions as described earlier to develop the muzzle exit conditions of yaw, yaw rate and center of gravity velocities. To perform the target impact dispersion analysis, the muzzle exit sensitivities are combined with the transition sensitivities and free-flight sensitivities. Table 4 shows the components of dispersion for one of the simulations.

Table 3. Simulated TID Results of 10 Simulations of 10 Round Tests

Simulation No.	Horizontal (mrads)	Vertical (mrads)
1	0.320	0.418
2	0.384	0.469
3	0.377	0.463
4	0.350	0.441
5	0.402	0.484
6	0.321	0.419
7	0.460	0.533
8	0.292	0.397
9	0.381	0.467
10	0.408	0.489
Average	**0.369**	**0.458**
Std. Dev.	**0.050**	**0.040**

Table 4. Components of Dispersion (from Simulation #3)

Dispersion Component	Horizontal (mrads)	Vertical (mrads)
Yaw Rate	0.304	0.304
Muzzle Velocity	0.000	0.269
Windage	0.000	0.000
Boresight	0.050	0.050
Sabot Discard	0.050	0.050
Aero/Mass Asymmetries	0.000	0.000
Yaw Angle	0.001	0.001
Transverse Velocity	0.058	0.058
Muzzle Spin	0.204	0.204
In-Bore Total (Yaw Rate + Yaw Angle + Transverse Velocity + Muzzle Spin) =0.371		

COMPARISON BETWEEN EXPERIMENTAL AND ANALYTICAL RESULTS

This project is still a work in progress. The Aerodynamics Branch of ARL and Arrow Tech Associates are continuing the dialog necessary to resolve all the parameters definitions, and understand all the translations that maybe required to make BALANS output results correlate to the similar quantities that are used in the experimental arena. At the present time, the two parties believe the bottom line quantities of horizontal and vertical standard deviations (sigma's) for total dispersion can be compared directly (see table 5.)

Table 5. Total Dispersion Comparison

Test	Sigma-Horizontal (mrads)	Sigma-Vertical (mrads)
Experiment (10 rounds)	0.470	0.570
Simulation (10 simulations each with 10 rounds)		
- Minimum	0.292	0.397
- Maximum	0.460	0.533
- Mean (of 10 simulations)	0.369	0.458
- Standard Deviation (of 10 simulations)	0.050	0.040

From a strict comparison point of view, the differences between the experimental values and the mean of the simulation values appears to be quite large. However, the difference between the minimum and maximum values of the ten simulations is also significant. This implies that there is some variability in a ten round sample size. Another source for the differences is in the number of simulation parameters that had to be estimated

SUMMARY AND CONCLUSIONS

The full scope of correlating the experimental work with the modeling efforts is incomplete at this time. However, despite the lack of closure on this project, this work has brought the following insights:

- Use of this combined experimental and analytical approach can lead to more effective test plans by providing engineers with the relative magnitude of dispersion improvement to be expected by changes in a configuration.
- The experimental approach complements the analytical approach by providing accurate aerodynamic coefficients, a necessary ingredient to determining the free-flight sensitivities for the analytical approach.
- The BALANS analytical approach is useful in the investigation of piece part dimensional tolerances and their effect on dispersion.
- Since dispersion is a combination of random independent and interdependent events, statistics becomes an important issue. The most important issue is whether one can experimentally predict an overall projectile performance parameter such as dispersion from a ten round group.
- When combining the experimental approach with mathematical simulation approach, the modeler should be involved in the experimental methodologies to allow for more understanding of detailed comparisons.

REFERENCES

1. B. T. Haug and J. A. Bornstein, "Gun Dynamics Measurements for Tank Gun Systems," Proceedings of the Fifth U. S. Army Symposium on Gun Dynamics, T. E. Simpkins and C. G. Homan eds., U. S. Army ARDEC, BENET Laboratories, Watervliet, NY 12189, 1987.
2. P. Plostins, I. Celmins, J. Bornstein and J. E. Diebler(Battelle Pacific), "The Effects of Sabot Front Borerider Stiffness on the Launch Dynamics of Fin-Stabilized Kinetic Energy Ammunition," BRL-TR-3047, Oct., 1989.
3. "BALANS Version 2. Users/Technical Manual", Arrow Tech Associates, South Burlington, Vt, August 1998.
4. "PRODAS Version 3.9 Users/Technical Manual", Arrow Tech Associates, South Burlington, Vt, January 1998.
5. A. F. Hathaway and J.R. Burnett Jr. "Stochastic Approach to Predicting Dispersion", in: Proceedings, 49th Aeroballistic Range Association Meeting, The Hague, Netherlands, and October 1998.

ACKNOWLEDGEMENTS

Mr. T. Marrs of Aberdeen Test Center performed centerline measurements. From the ARL, Mr. B. Hudler performed projectile measurements, Mr. B. Patton performed testing with Mr. D. McClelland of Defense Services, Inc. Mr. B. Guidos performed the jump analysis, and provided the authors with constructive guidance. Mr. K. Severkson, Dr. P. Plostins, and Mr. R. Whyte of Arrow Tech contributed to the yaw analysis.

Spatial Multi-body Simulation Validation Techniques and Their Application to a Heavy Truck – Towed Gun Combination

David D. Gunter and Michael D. Letherwood
U.S. Army Tank-automotive and Armaments Command, RD&E Center
MS#157, AMSTA-TR-VP, Bldg. 215
Warren, MI 48397-5000

This paper describes an effort by the US Army Tank-automotive and Armaments Command, Research, Development & Engineering Center (TACOM-TARDEC) to validate a dynamic model of an M923 5-ton cargo truck towing an M198 medium 155mm Howitzer. It also describes the use of the model to investigate the dynamic performance of the vehicle combination, conducting a full matrix of "virtual" field tests to evaluate its stability and handling during braking. Also described is an analysis intended to determine the influences that the 7257+ kilogram (kg) howitzer has on the stability of the truck during braking maneuvers when the truck is operating in an unloaded condition.

INTRODUCTION

The purpose of this effort was to collect field data to support the development and validation of high resolution, spatial, computer-based M923 truck/M198 howitzer analytical model (Figure 1) and accurately predict system performance for the follow-on braking performance analysis and investigation. Simulation and test results are compared and contrasted with field-test vehicle (Figure 2) data to identify model and design deficiencies.

Once the models are known to accurately replicate representative samples of measured system performance, they can be confidently extrapolated to predict quantitative (or at least qualitative) effects of design excursions. The objective of this report is to compare data from a set of instrumented field tests to a series of analytical simulation results to determine how well the data sets correlate so that it can be used to answer field-related questions. This branch has a working, validated model of the M923 truck which is described in (Letherwood 1996) and, hence, this analysis will address the validation and use of a recently developed M198 howitzer model being towed by a M923 truck. This report documents the effort to validate the model by direct comparison of model simulation results to field-test results, and to conduct a follow-on braking and stability analysis.

METHODOLOGY

Many studies have been conducted on the analysis of dynamic performance of the Army's fleet of combat and

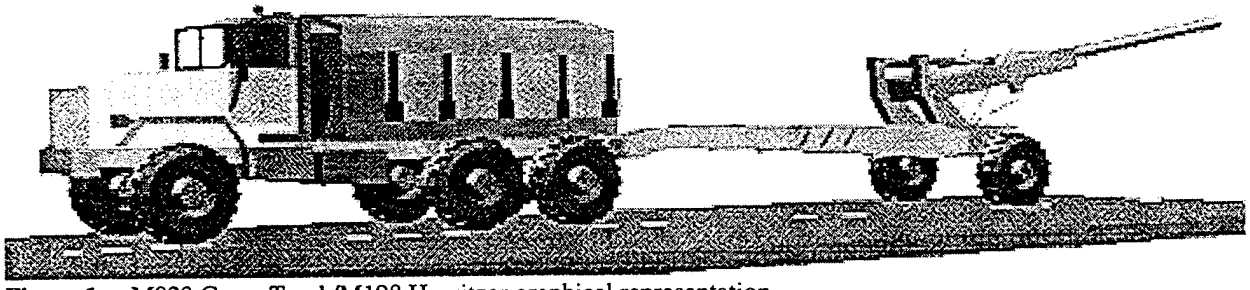

Figure 1 M923 Cargo Truck/M198 Howitzer graphical representation.

tactical equipment using linearized models, but these models generally fall short in determining the upper bounds of safe and acceptable usage. This is primarily because large subsystem displacements often involve many nonlinearities which, if incorrectly modeled, could lead to erroneous predictions and conclusions. Thus it is vital to accurately characterize and model critical components and to validate predictions against controlled and instrumented field and laboratory tests. Subsystem characterization and model validation through carefully controlled and instrumented laboratory and field tests are the most valuable tools available

The Dynamic Analysis and Design System, or DADS methodology (CADSI 1977) was used to assemble the analytical models, run the simulations and analyze and display the simulation results. The DADS computer program is a highly detailed general purpose modeling and simulation method for determining the spatial, transient-dynamic response of controlled, articulated multibody mechanical systems to excitation by irregular external and internal effects. The DADS program consists of three main parts, a preprocessor, main processor and post processor. The preprocessor allows much of a system's parametric and topological properties to be defined in an interactive environment without having to be concerned with the supporting equations. The main processor also has a number of user interface subroutines which allow more detail to be added to the model then possible with the primitive building blocks. This feature makes the representation of highly nonlinear vehicle system properties possible and yields much more representative models. The main processor also automatically integrates the resulting equations of motion for a specified period of time and outputs the states at regular time intervals. The post processor allows these states to be plotted and, when supplied with geometrical outline descriptions of the bodies comprising the system, can generate animations of the results. A description of the DADS M923 truck/M198 Howitzer model is beyond the scope of this paper.

FIELD-VALIDATION TESTS AND RESULTS

During preliminary dynamic stability studies, a number of field tests on the M198 howitzer combination were conducted and used to develop and validate high resolution models. In order to obtain carefully controlled and representative off-road transient response data for model validation, the most effective and least expensive field test procedures for system characterization and model validation involve the incorporation of short duration, transient inputs into the system with carefully controlled initial conditions, and direct comparison of the dynamic response characteristics with identical simulations. In the field, the M923 truck speed and pitman arm steering angles were recorded. The trajectory of the M923 truck pintle was recorded by using a pressurized water/paint bottle methodology that laid down a trace on a carefully constructed grid from which longitudinal and lateral position points could be measured. This methodology worked well at slow speeds and calm wind conditions but tended to degrade quickly as speeds increased above 40 kilometers per hour (KPH). Relative chassis/suspension and axle displacements were measured using string potentiometers and displacement transducers. Triaxial rate gyros were used to measure roll, pitch and yaw rates. Accelerometers were placed on the axles to determine precisely when critical events such as bottoming out, wheel lift-off and contact with ground or obstacles occurred. The field tests were intended primarily to study the howitzer dynamic responses, and consequently, to verify the model. A SOMAT series 2000 Field Computer System set at a sample rate of 500 Hz was used to record the data. A Rochester Instrument Systems (RIS) SUPERCAL II was used to calibrate the SOMAT Field Computer System channels. The calibration of the SUPERCAL II is traceable to the National Bureau of Science and Technology standards.

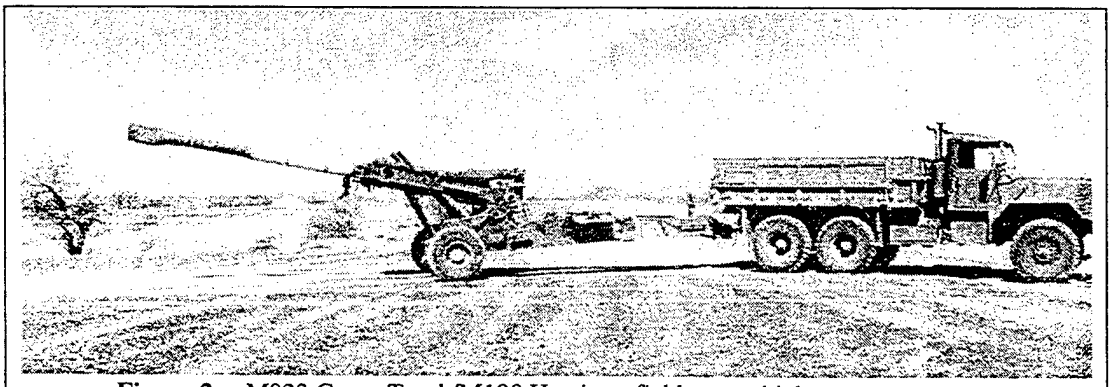

Figure 2 M923 Cargo Truck/M198 Howitzer field-test vehicles.

	SPEED (Kilometers per Hour)											
	4	8	12	16	20	24	28	40	48	56	65	72
COURSE												
Slalom				X		X	X	X	X	X	X	
15 cm Bump		X		X		X	X	X				
30 cm Bump		X	X	X	X							
45 cm Bump	X	X										
15 cm Hole				X		X	X					
23 cm Hole	X	X		X								
30 cm Hole	X	X	X									

Table 1 Field/Simulation Validation Tests.

Analytical And Field Test Data Comparisons

The analytical models were simulated through the exact same tests and conditions as the field test vehicles (Heydinger 1991). The first set of simulations consisted of driving the left side of the truck/howitzer combination over a number of specially designed positive and negative ramps to study dynamic roll stability. The vehicle speed, ramp slopes and heights/depths were varied to emulate the field tests exactly. The systems were also simulated at various speeds through a slalom course measuring 3.35 meter by 83 meter. The models were carefully instrumented to replicate the physical instruments used at the test site and the instruments were placed at the same locations as recorded by test personnel. Comparisons with the simulations were made on 27 field tests as outlined in Table 1.

The discrete event tests such as those described above drive the subsystems into highly nonlinear regions of operation. Short duration, discrete event tests allow the initial conditions to be carefully controlled. They avoid excessive phase and amplitude differences between measured and simulated results which could completely mask correlation studies in highly nonlinear systems (Weir 1991). Direct visual comparisons are made between superimposed plots of measured and simulated states. Examination of the overlay plots shows that in most cases the response curves were replicated in a consistent manner with the field test measurements as illustrated in plots 1 through 12 in each of the sections below. Model validation and refinement is a critical part of system simulation. By simulating actual field tests, it is possible to determine, with good confidence, which parameters should be adjusted and where the model needs to be improved.

An error analysis was performed on the simulation data set against the field data. This analysis consisted of shifting the simulation data in time in order to maximize the correlation between the two signals. This shifting was necessary due to transient differences between the test driver's control actions and the speed and steering control algorithms implemented in the model. Once these transients are corrected for, the difference between the two signals are computed for each data point. Each of these differences is divided by the peak maximum and peak minimum for the field data, and then multiplied by 100 to produce a percentage of error for each data point. The absolute value of these errors are summed up and divided by the number of the data points in the signal, to give us indicator of the absolute value of the percent error for the signal of interest (|%E|avg). Similarly, the standard deviation was computed for all of these errors to determine %Esd. The results of each of these error analyses are provided below in tables 2, 3 and 4.

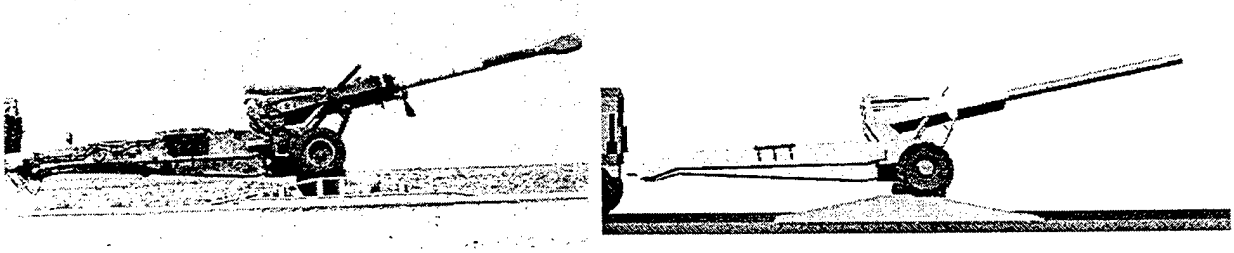

Figure 3 M198 Howitzer on 45 cm Bump @ 16 KPH.

Positive Bump Course Comparisons and Correlation

Comparisons were made between the DADS simulation data and the field test data for vehicle speeds varying from 1.6 (idle) to 40 KPH and bump heights of 15, 30 and 45 centimeters (cm). Figure 3 shows examples of the truck traversing the 45 cm bump at 16 KPH during the field and simulation-based validation tests. The M198 howitzer traversed the 15 cm ramps up to 48 KPH at which time the tests were stopped. The howitzer experienced some roll instabilities and de-stabilized considerably as the speeds approached 48 KPH. The system traversed the 30 and 45

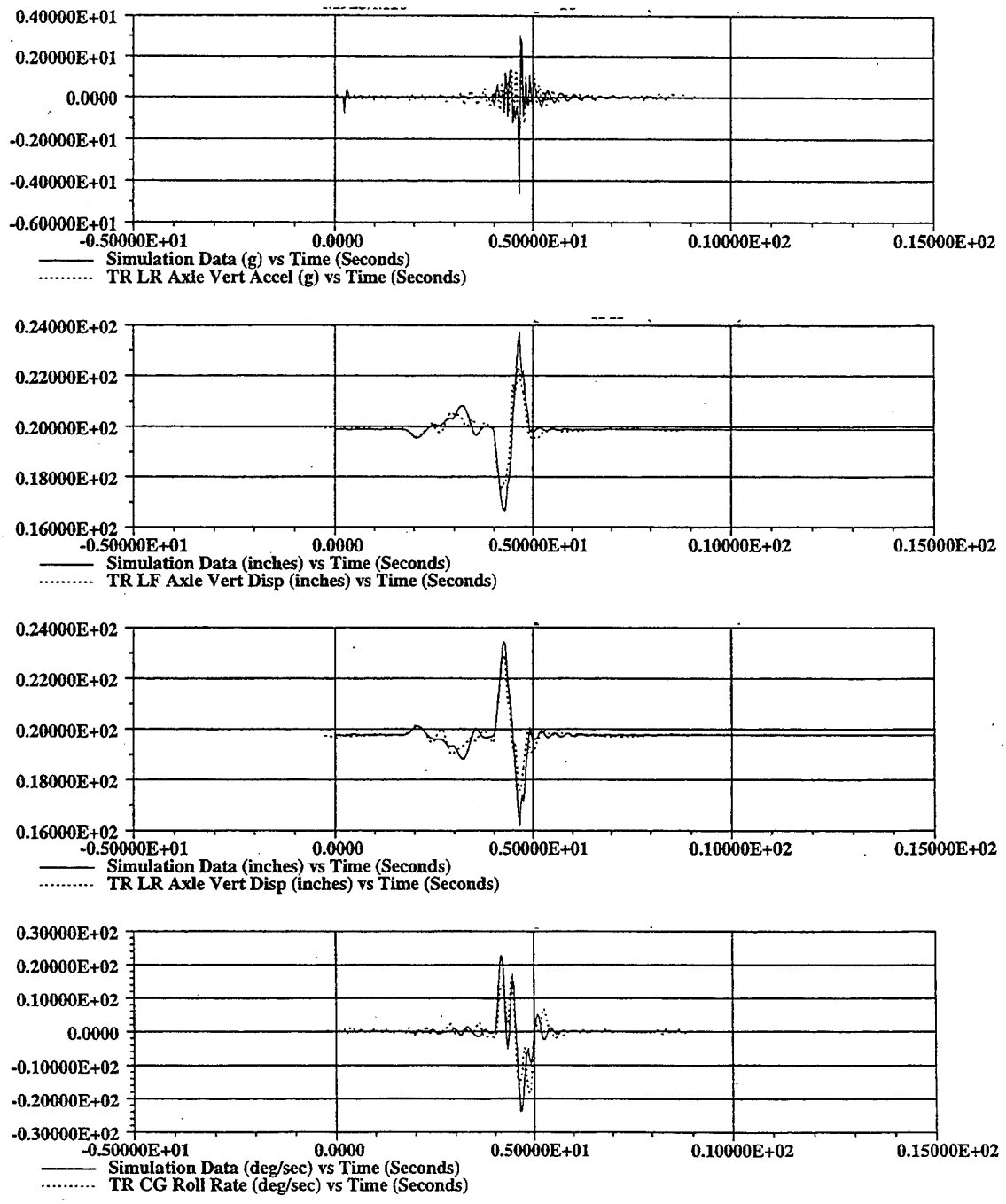

PLOTS 1 through 4 Trailer (Howitzer) Field-test vs Simulation Test Results. 15 cm bump.

CH#	CHANNEL NAME	|%E|avg	%Esd
1	Howitzer left axle vertical accel.	7.0	12.3
2	Howitzer right axle vertical accel.	7.3	12.6
3	Howitzer chassis X acceleration	6.6	10.8
4	Howitzer chassis Y acceleration	8.8	13.6
5	Howitzer chassis Z acceleration	8.2	13.5
6	Truck chassis pitch rate	10.0	15.0
7	Truck chassis roll rate	7.2	12.6
8	Truck chassis yaw rate	9.5	15.4
9	Howitzer chassis pitch rate	10.7	16.5
10	Howitzer chassis roll rate	8.0	14.1
11	Howitzer chassis yaw rate	8.5	13.7

|%E|avg = average absolute value of percent error
%Esdv = standard deviation of percent error
%E=100*(field data-simulation data)/(field data maximum-field data minimum)

Table 2 Average Values For All Bump Simulations.

cm ramps at speeds up to 20 and 8 KPH, respectively. Higher speeds were not attempted during tests due to interference problems between the howitzer and the obstacles. No noticeable truck instabilities were observed due to he relatively low vehicle speeds. The intent of these tests was not to identify vehicle rollover thresholds, but to provide adequate inputs in the system for model validation efforts. Individual overlay plots of various state variables were generated and matched well. The results are all tabulated and summarized in Table 2.
The results of the correlation studies show that the average standard deviation of percent error (%Esd) per channel is about 5.2 percent on all channel comparisons across all bumps. The maximum absolute value percent error (|%E|) for each channel ranges from 1.2 to 16.4 percent. Plots 1 through 4 show the magnitudes and signal shapes of four data channels of field versus simulation test results during a 15 cm bump run.

Pothole Course Comparisons and Correlation

Comparisons were made between the DADS simulation data and the field test data for vehicle speeds varying from 1.6 (idle) to 32 KPH and pothole depths of 38, 58 and 76 cm. Figure 4 shows examples of the howitzer traversing the 30 cm pothole at 8 KPH, during the field and simulation-based validation tests.

The M198 howitzer traversed the 15, 23, and 30 cm holes at speeds up to 32, 16, and 12 KPH, respectively, at which time the tests were stopped due to vehicle interference or perceived instabilities. The howitzer experienced some roll instabilities at the slower speeds and stabilized considerably as speeds increased. As the speeds increased, the left

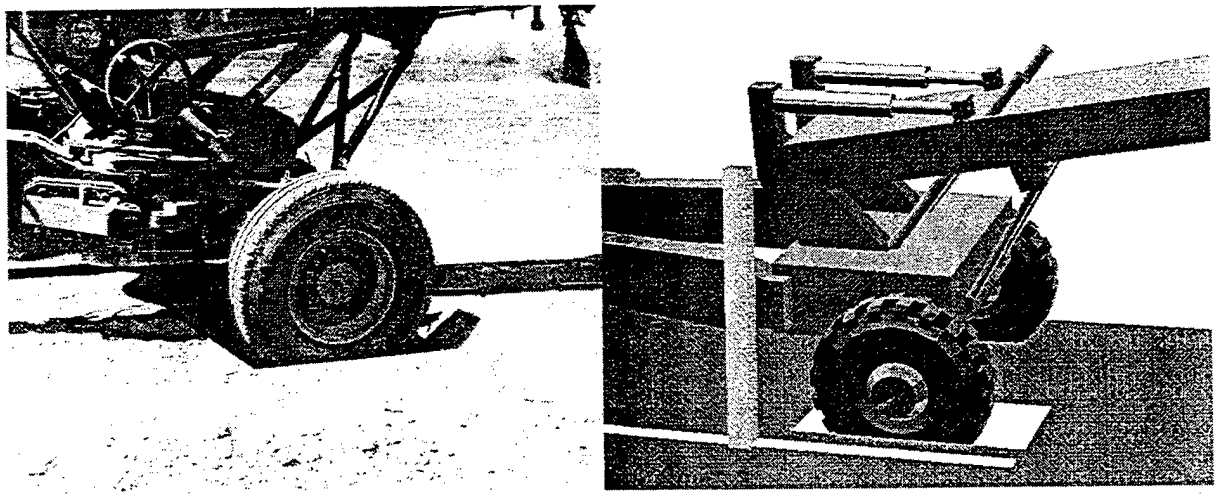

Figure 4 M198 Howitzer on 30 cm Pothole @ 8 KPH via field-tests and simulation.

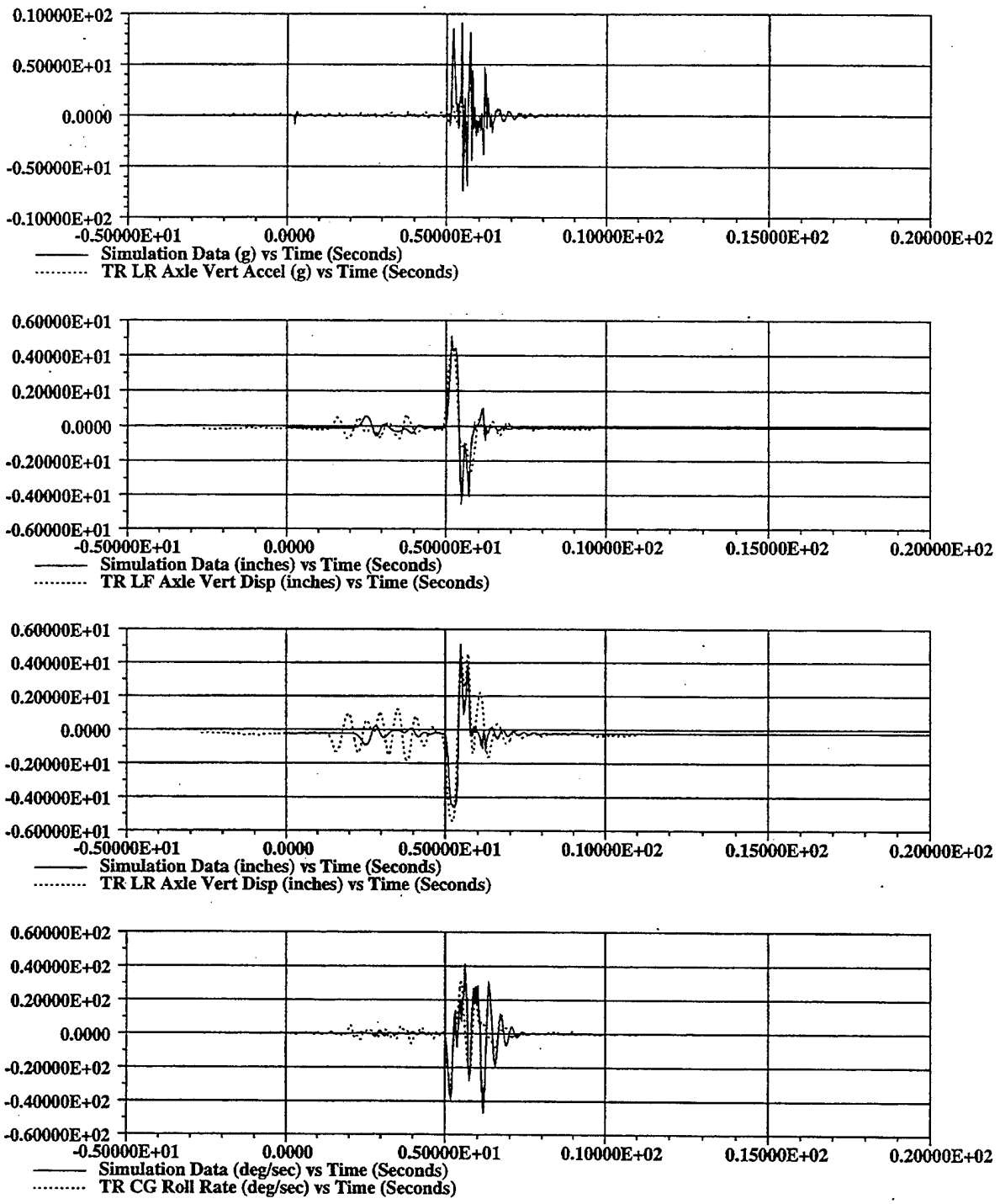

PLOTS 5 through 8 Trailer (Howitzer) Field-test vs Simulation Test Results. 30 cm Pothole.

tires were increasingly unable to drop to the bottom of the hole, and consequently, hit the opposite side of the hole very hard. This could result in vehicle damage. Higher speeds were not attempted due to interference problems between the howitzer and the hole or because some stability and handling instabilities occurred. Individual overlay plots of various state variables were generated and matched well. The results are all tabulated and summarized in Table 3.

CH#	CHANNEL NAME	|%E|avg	%Esd
1	Howitzer left axle vertical accel.	4.1	8.3
2	Howitzer right axle vertical accel.	4.5	9.0
3	Howitzer chassis X acceleration	3.9	8.4
4	Howitzer chassis Y acceleration	6.4	11.3
5	Howitzer chassis Z acceleration	5.7	10.2
6	Truck chassis pitch rate	8.1	13.9
7	Truck chassis roll rate	5.1	10.0
8	Truck chassis yaw rate	7.3	12.3
9	Howitzer chassis pitch rate	7.9	14.2
10	Howitzer chassis roll rate	4.2	9.5
11	Howitzer chassis yaw rate	4.1	8.5

|%E|avg = average absolute value of percent error
%Esdv = standard deviation of percent error
%E=100*(field data-simulation data)/(field data maximum-field data minimum)

Table 3 Average Values For All Pothole Simulations.

The results of the correlation studies show that the average standard deviation of percent error (%Esd) per channel is about 5.6 percent on all channel comparisons across all potholes. The maximum absolute value percent error (|%E|) for each channel ranges from 1.1 to 15.5 percent. Plots 5 through 8 show the magnitudes and signal shapes of four data channels of field versus simulation test results during a 30 cm pothole run.

Slalom Course Comparisons and Correlation

Comparisons were made between the DADS simulation results and the field test data for vehicle speeds varying from 16 to 65 KPH. Figure 5 shows examples of the M198 howitzer traversing the 3.35 meter by 83 meter slalom course at 48 KPH, exactly as the tests were conducted during the field and simulation-based validation tests.

The howitzer had little difficulty traversing the course up to 48 KPH. From 56 KPH and higher, there was some excessive sliding as the combination maneuvered from one lane to another. Individual overlay plots of various state variables were generated and matched very nicely. The results are all tabulated and summarized in Table 4. The results of the correlation studies show that the average standard deviation of percent error (%Esd) per channel is about 13.7 percent on all channel comparisons across all slalom maneuvers. The maximum absolute value percent error (|%E|) for each channel ranges from 1.6 to 24.3 percent. The errors on these comparisons tend to run somewhat higher than the bumps and pothole correlations. This is attributable to the errors introduced into the simulations by the simplified steering and tire models which come into play in much greater way in the slalom courses. Simplified, yet representative tire models included in DADS, requiring measured tire properties are used to account for interaction between tire and terrain. A normalized longitudinal slip curve, represented, is used to compute the longitudinal tractive force in terms of vertical tire force and longitudinal slip. A vertical force versus deflection curve is used to compute the vertical force between the tire and terrain as a function of vertical tire deflection. This

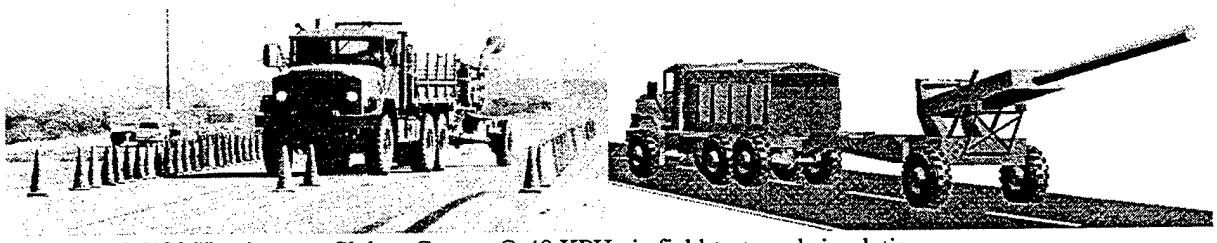

Figure 5 M198 Howitzer on Slalom Course @ 48 KPH via field-tests and simulation.

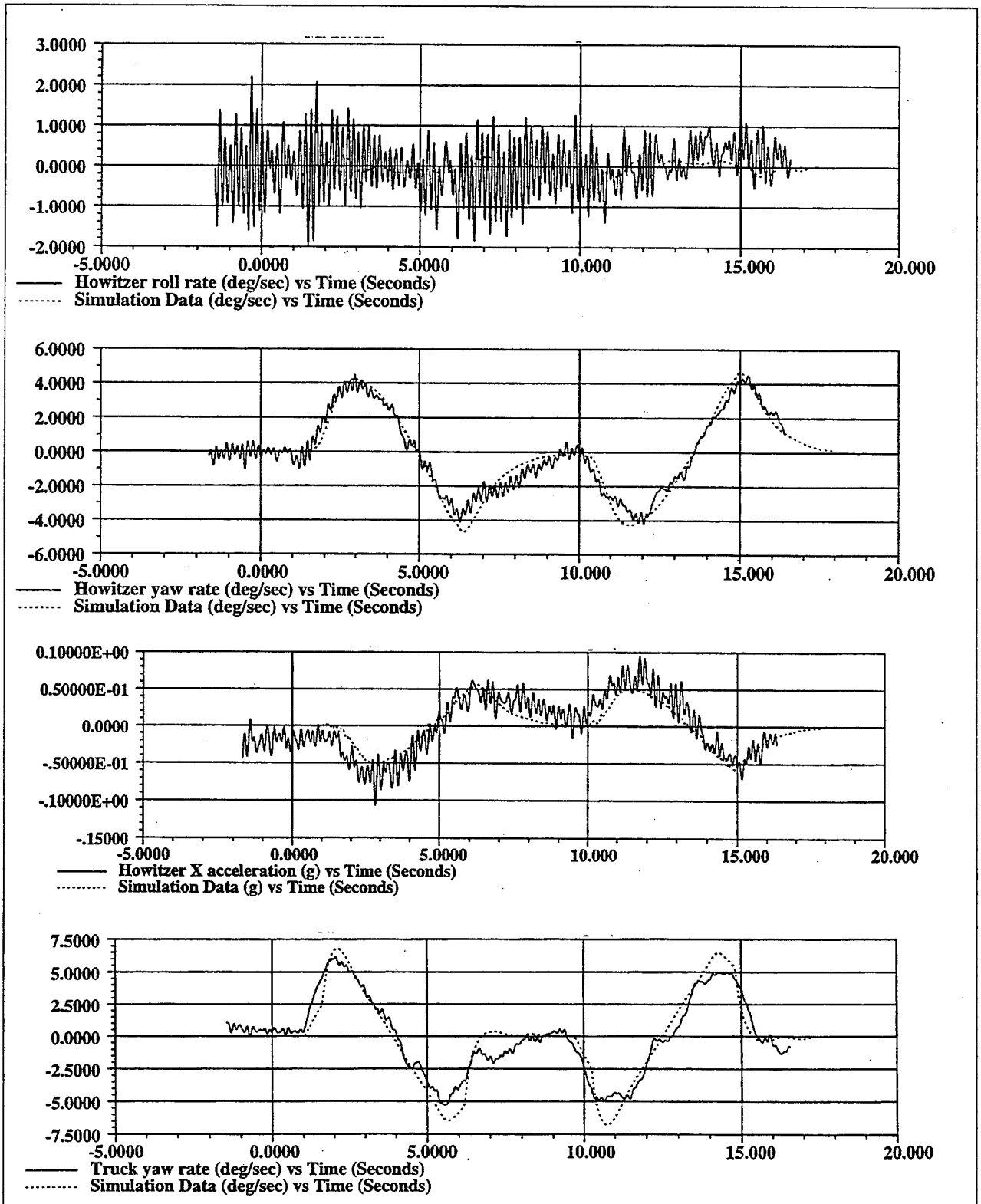

PLOTS 9 through 12 Trailer (Howitzer) Field-test vs Simulation Results. 16 KPH Slalom.

curve has been modified from the data provided to approximate the effect of tire stiffening due to encountering the rim at large deflections. Additional data causing the curve to increase non linearly to emulate hardening effects due to bottoming out on the rims was also added. Also the output force is zero for all negative displacements. The

CH#	CHANNEL NAME	|%E|avg	%Esd
1	Howitzer left axle vertical accel.	13.3	16.9
2	Howitzer right axle vertical accel.	13.9	17.6
3	Howitzer chassis X acceleration	7.9	10.2
4	Howitzer chassis Y acceleration	12.9	17.3
5	Howitzer chassis Z acceleration	14.9	19.1
6	Truck chassis pitch rate	11.3	15.8
7	Truck chassis roll rate	13.5	18.1
8	Truck chassis yaw rate	9.0	11.5
9	Howitzer chassis pitch rate	11.2	15.9
10	Howitzer chassis roll rate	17.0	21.7
11	Howitzer chassis yaw rate	7.7	10.0

|%E|avg = average absolute value of percent error
%Esdv = standard deviation of percent error
%E=100*(field data-simulation data)/(field data maximum-field data minimum)

Table 4 Average Values For All Slalom Simulations.

vertical stiffness rate corresponds to a cross country tire inflation of a pre-determined rate. The tire model also computes the relative slip velocity between the bottom of the tire and ground. This slip velocity is used to compute a fore-aft slip between zero and 100 percent which is inserted into the longitudinal friction curve. The coefficient of friction from this curve is then multiplied by the normal force to obtain the longitudinal frictional force. This force always acts on the tire in the opposite direction of the relative slip. A lateral slip angle in radians is also computed from the two components of forward and lateral slip velocity and inserted into the curve. To find lateral tire forces for vertical force, the curves are interpolated with vertical tire force and slip angle values to obtain lateral force magnitudes and directions. These forces are applied to the wheel bodies to support the vehicle and control it.The model is steered by a simplified second order controller model which minimizes the angle between its centerline and the tangent to a specified trajectory, and which minimizes the lateral displacement of a vehicle midpoint relative to the trajectory. Steering commands on the truck is supplied by driving the pitman arm. This insures that all wheel steering angles are accurately maintained for any pitman arm angle and that roll steer effects are also included. The second order algorithm provides position and velocity feedback for a more stable control. The error signal is converted to a torque which is divided between left and right front kingpins and applied to the torsional spring on the pitman arm which transfer these torques to the respective wheel hubs. The gain in this controller model was made inversely proportional to vehicle speed to reduce steering sensitivity at higher speeds for better steering stability. Plots 9 through 12 show the magnitudes and signal shapes of four data channels of field versus simulation test results during a 16 KPH slalom run. The underlying high frequency signal in these plots are due to the tri-axial accelerometer and rate gyro mounting bracket flexure. In order to mount these instruments near the center of gravity of the Howitzer, a steel bracket was fabricated onto which the instrumentation was mounted. Unfortunately, we see the natural frequency of that bracket in the field data signals, but if one neglects the high frequency noise on these data signals, we show adequate aggreement with the field data.

Validation Summary

An extensive analysis was performed on all tests and, in most cases, the magnitude and shape of the vehicle dynamic responses were very similar to field test responses. The results of the field tests show that the analytical simulation M923 truck/M198 howitzer model is capable of predicting system response and stability under normal operating conditions which do not demand highly accurate steering and powertrain inputs. The final complete averages indicate that the model results produce an average of about 8% error per channel of data with an average standard deviation of approximately 11% per channel. Displacements and rates correlate extremely well over the wide range of tests conducted while accelerations do not correlate as well. The largest errors were present in much of the acceleration data due to road noise and structural ringing. There are many ways to interpret these numbers and it is very undesirable to put a single number on such a large array of comparisons between simulations and tests, especially when there is so much room for potential errors. Better correlations could have been achieved if only the displacements had been compared, instead of lumping comparisons between all of the signals together. Unless obvious errors were found, all field test data collected were considered correct and were used as a baseline for comparison with the simulation data. Lastly, recording of the exact locations of the instruments (in 3 dimensions)

	SPEED (Kilometers per Hour)				
COURSE	4	8	12	16	20
90° J-Turn Dry-Braking w/ no load	X	X	X	X	X
90° J-Turn Dry-Braking w/ 2267 kg	X	X	X	X	X
90° J-Turn Dry-Braking w/ 4535 kg	X	X	X	X	X
90° J-Turn Dry-Braking w/ 6803 kg	X	X	X	X	X
90° J-Turn Dry-Braking w/ 9071 kg	X	X	X	X	X
90° J-Turn Wet-Braking w/ no load	X	X	X	X	X
90° J-Turn Wet-Braking w/ 2267 kg	X	X	X	X	X
90° J-Turn Wet-Braking w/ 4535 kg	X	X	X	X	X
90° J-Turn Wet-Braking w/ 6803 kg	X	X	X	X	X
90° J-Turn Wet-Braking w/ 9071 kg	X	X	X	X	X

Table 5 90° J-Turn Braking Simulation Tests.

may have been in error. Exact dimensions are crucial in the simulations. The analytical representation of instruments must be in the exact locations as the field instruments so their output quantities can be compared on a one-to-one basis. A secondary objective was to more closely approximate the field test results by performing a number of parameter and design sensitivity studies using parameter estimation techniques. To accomplish this we iteratively modify suspension springing and damping rates to more accurately reflect response measured in the field. After an extensive set of parameter and design studies, it was determined that better correlations between the simulation results and the field tests results could not be achieved partly because of errors introduced into the model results by the use of simplified tire, powertrain, and steering models.

BRAKE EVALUATION

Experience with the M923 truck tells us that the braking performance of the truck is very good as far as stopping distance is concerned. The impetus behind this study was to evaluate the braking stability of the vehicle combination during panic braking applications. 90° J-turn braking and straight braking course simulations were used to evaluate the on-road braking performance of the M923 truck/M198 howitzer combination. Data was collected on twenty-six 90° j-turn braking and straight braking courses in wet and dry conditions and at varying speeds to provide limited field validation data to evaluate TACOM-TARDEC's braking subsystem models. However, information was also used from the slalom, bump, and pothole course simulations, where applicable, if discrepancies in performance were found due to operational or configuration changes. Comparisons were made between the simulations and field tests, matching the amplitude and width of the pulses well on most channels across the maneuvers.

90° J-Turn Braking Course Analysis

Comparisons were made between the DADS simulation data and field-test data for vehicle speeds varying from 4 to

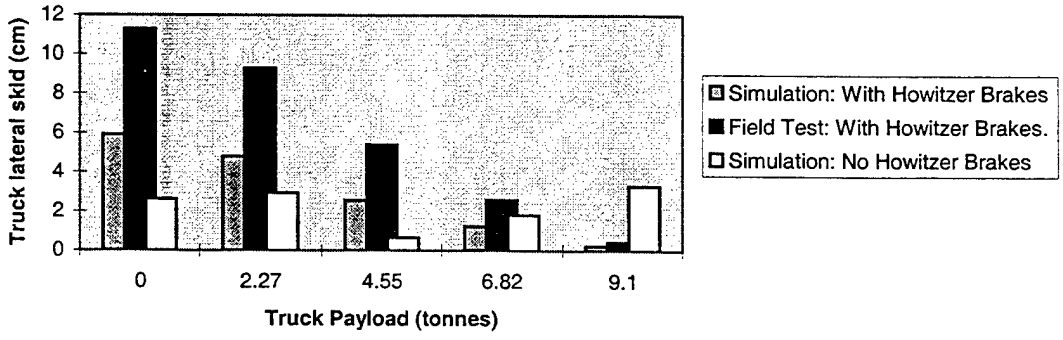

Table 6 90° J-Turn Braking Simulation Test Results (Dry).

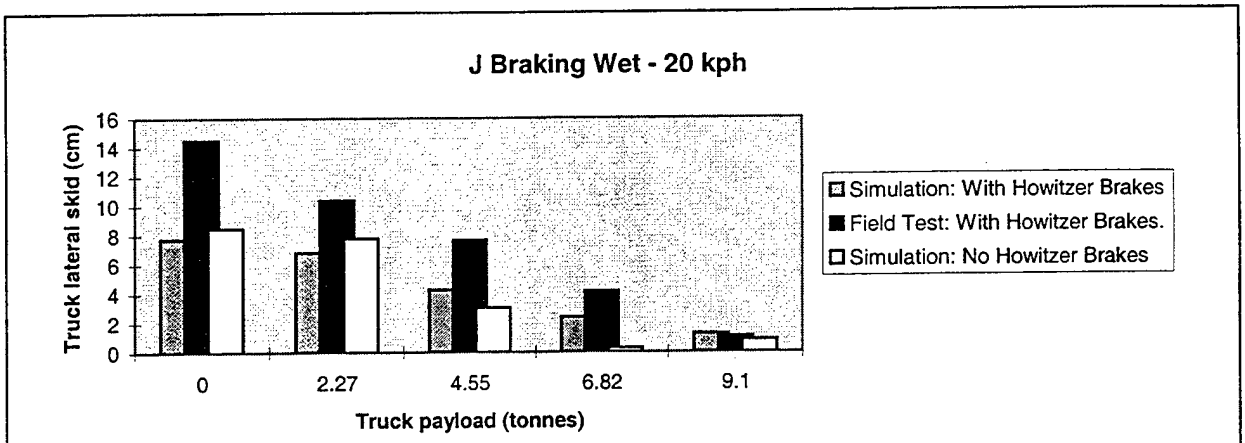

Table 7 90° J-Turn Braking Simulation Test Results (Wet).

20 KPH, in wet and dry conditions, with and without howitzer brakes, and at vehicle measured application times. Figure 6 shows an example of the howitzer combination traversing a specially designed course on the virtual testing environment.

The j-turn braking simulations were conducted at 5 different truck payload weights, at 5 different speeds, and in wet and dry conditions with the payloads centered over the truck's rear tandem axle as depicted in Table 5. This test matrix was conducted without howitzer brakes and then with howitzer brakes using vehicle measured brake application times. The results of the simulations are shown in Tables 6 and 7. The results in Tables 6 and 7 indicate that adding a payload to the M923 truck (w/ 14.0 x R20 tires) shows a marginal improvement on the stability and handling of the M923 truck / M198 howitzer combination during the 90° J-turn braking maneuver. As speeds and payloads are incrementally increased from 4 to 20 KPH and 0 to 9071 kg, respectively, improvement is seen in vehicle slew/lateral displacement. In general, the trends in the simulation data follow along the same trends that were seen in the limited field data that was collected. Those being that lateral displacement of the overall vehicle and axles increases with speed and load, especially on axle #3, and brake stopping times are marginally affected by the above mentioned operational factors, including wet and dry conditions.

Straight Braking Course Analysis

Comparisons were made between the DADS simulation data and field test data for vehicle speeds varying from 8 to 65 KPH, in wet and dry conditions, with and without howitzer brakes, and at vehicle measured brake application times. Figure 7 shows an example of the howitzer combination traversing a specially designed course on the virtual proving ground.

SPEED (Kilometers per Hour)								
COURSE	**8**	**16**	**24**	**32**	**40**	**48**	**56**	**64**
Straight Dry-Braking w/ no load	X	X	X	X	X	X	X	X
Straight Dry-Braking w/ 2267 kg	X	X	X	X	X	X	X	X
Straight Dry-Braking w/ 4535 kg	X	X	X	X	X	X	X	X
Straight Dry-Braking w/ 6803 kg	X	X	X	X	X	X	X	X
Straight Dry-Braking w/ 9071 kg	X	X	X	X	X	X	X	X
Straight Wet-Braking w/ no load	X	X	X	X	X	X	X	X
Straight Wet-Braking w/2267 kg	X	X	X	X	X	X	X	X
Straight Wet-Braking w/4535 kg	X	X	X	X	X	X	X	X
Straight Wet-Braking w/6803 kg	X	X	X	X	X	X	X	X
Straight Wet-Braking w/9071 kg	X	X	X	X	X	X	X	X

Table 8 Straight Braking Simulation Tests.

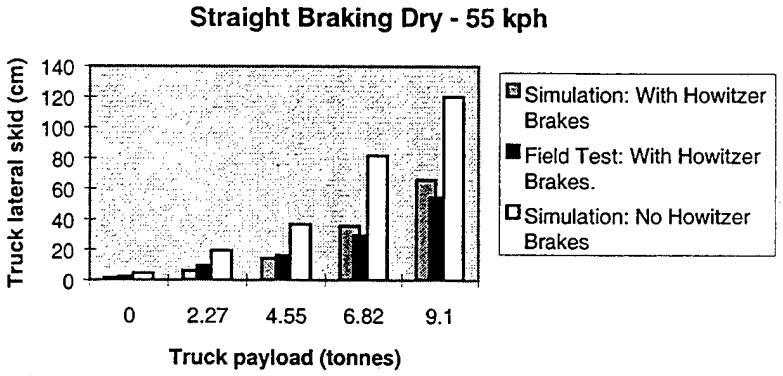

Table 9 Straight Braking Simulation Test Results (Dry).

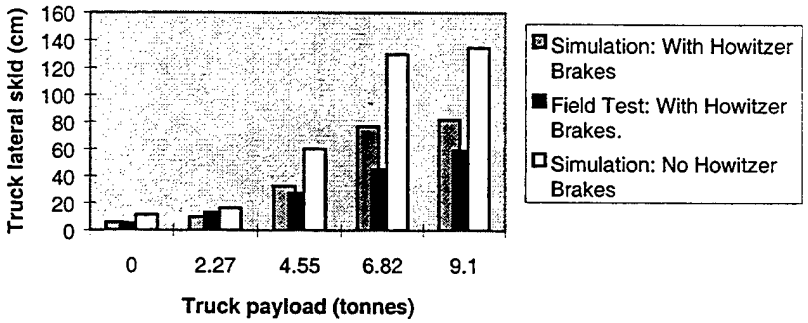

Table 10 Straight Braking Simulation Test Results (Wet).

The straight braking simulations were conducted at 5 different truck payload weights, at 8 different speeds, and in wet and dry conditions with the payloads centered over the truck's rear tandem axle as depicted in Table 8. This test matrix was conducted without howitzer brakes and then with howitzer brakes using vehicle measured brake application times. The results of the simulations are summarized in Tables 9 and 10. The results in Tables 9 and 10 indicate, once again, that adding a payload to the M923 truck (w/ 14.0 x R20 tires) has little or no effect on the stability and handling of the M923 truck / M198 howitzer combination during the straight braking maneuver. As speeds and payloads are incrementally increased from 8 to 65 KPH and 0 to 9071 kg, respectively, no improvement is seen in vehicle slew/lateral displacement during panic braking lock-up conditions. In general, the trends in the simulation data follow along the same trends that were seen in the limited field data that was collected. Those being, as speeds and loads are increased, vehicle slew, lateral displacement of the overall vehicle and axles increases, and brake stopping times are unaffected by the above mentioned operational factors, including wet and dry conditions. No significant increases in braking stability were realized during straight braking maneuvers due to loads in the truck during panic braking lock-up conditions.

BRAKE ANALYSIS CONCLUSIONS

Because the mass of the M198 Howitzer is so large, it is not unreasonable to think that towing the Howitzer could have a destabilizing affect on the M923 truck when the brakes are applied or when performing aggressive maneuvers requiring harsh steering inputs. In addition to the size of the Howitzer, the fact that the Howitzer has no suspension and is at the limit of the truck's towed load allowance also adds to the potentially destabilizing effects it could have on the combination if operated improperly. Lugged off-road tires designed for military vehicle use have reduced lateral and longitudinal slip force characteristics than tires designed for highway use. Additionally, an empty vehicle requires much less brake pressure to lock the wheels when braking. The fact that the M923 truck, when towing the

howitzer, is operating in an empty condition makes it more likely that the rear tires will lock up during "panic" brake applications. Once wheel lock-up occurs, the tire lateral force generated by the ground/tire interaction is greatly reduced. Reduced lateral force makes the likelihood of skidding into adjacent lanes of traffic more likely.

It was thought that adding a payload to the back of the M923 truck would serve to reduce the incidence of wheel lock-up, acting to stabilize the combination during braking. The payload would act to increase the tire to ground normal force, thereby increasing the friction force available to brake the vehicle and prevent excursion out of lane. The field test results and simulations (tables 6 and 7) indicate that the increase in system weight provides only marginal improvement to lateral braking stability. The braking gains made by payloading the truck must be weighed with the penalty that comes with the increased payload acting to raise the system center of gravity. Raising the system center of gravity results in reduced roll stability which will force a reduction in the safe-use speeds allowed for the vehicle combination.

Due to its size, weight, and the wide range of possible payloads that the M923 truck carries, the braking performance of this combination varies substantially in its daily operation. A wide range of loading conditions can present a challenge to brake system designers. These conditions are worsened considerably whenever wheel lockup occurs. If the front wheels lockup, steering control is lost, and the combination will continue straight ahead or plow out of a turn. If the M923 truck rear axles lock during braking, the combination may fold under the influence of the howitzer pushing on the pintle, resulting in jackknife. Locking the howitzer's wheels may cause the Howitzer to swing out of lane. None of these phenomena are desirable for safe operation.

SUMMARY

In this paper we were able to describe a modeling and validation effort undertaken by engineers at the US Army Tank-automotive and Armament Command's Research Development and Engineering Center. We were able to show good dynamic response agreement for the truck/howitzer combination executing lane change maneuvers, bump maneuvers and pothole maneuvers. We used these models to evaluate the vehicle combination's braking performance and achieved good agreement on the trends but not so good agreement as far as the actual stopping times and distances. This is disappointing but not unexpected due to the complex nature of the tire to ground interface, which is even more complex when braking, as well as the difficulty in obtaining accurate brake system data. The tire ground interface questions are the subject of several research projects around the world. And when the tire problems are solved, everyone's attention will be turned to solving the braking questions. These models represent a first step in a long process which will be undertaken to develop good, accurate tire/ground interface and braking models that can be used to evaluate braking and handling performance of vehicle systems.

However, these models are relevant for the questions that we are trying to answer. Namely, vehicle dynamic response during braking. Whether or not the stopping distances are correct does not preclude us from applying these models to evaluate performance gains or losses due to payloading changes, braking efficiency changes, or even to evaluate anti-lock braking, traction control and yaw instability control schemes. These models allow us to identify trends that system modifications have on the system, and from these trends we can provide configuration control guidelines to the managers and users of the systems.

6 References

CADSI (Computer Aided Design Software, Inc.) (1977), Dynamic Analysis and Design Systems, PO Box 203, Oakdale, Iowa 52319.

Heydinger, G.J., Garrott, W.R., Chrstos, J.P., and Guenther, D.A., (1991) 'A Methodology for Validating Vehicle Dynamics Simulations', SAE Preprint 900128.

Letherwood, M.D. and Gunter, D.D. (1996) 'Field-Validation of a Spatial, High-Resolution, Computer-Based, M923 Truck Analytical Model' US Army Tank-automotive and Armaments Command, Research, Development & Engineering Center (TACOM-TARDEC) Report#13692.

Weir, D.H., Shortwell , C.P., and Johnson , W.A., (1967) 'Dynamics of the Automobile Related to the Driver Control', SAE Preprint 680194.

A Coolant Loop Model for Crusader Armament Thermal Predictions

Michael Kneer
United Defense L.P.
4800 E. River Rd.
Minneapolis, MN, 55421

A thermal model was developed to predict the transfer of thermal energy from the Crusader gun tube and recoil modules to a cooling system comprising forced convection liquid-to-air heat exchangers. This armament thermal simulation incorporates modular computational programs to model the armament thermal system. The armament thermal model was successfully calibrated using test data, and the model demonstrated the essential physics to predict thermal performance for other firing conditions and designs. The objective Crusader system is predicted to meet the rate of fire requirement of 10 rounds per minute for 3 minutes followed by 3 rounds per minute for up to 60 rounds at the maximum charge zone six and ambient temperature limit 52°C.

ARMAMENT DESCRIPTION

Crusader's firing rate require liquid cooling of the main armament. Both the gun tube and recoil modules absorb large thermal loads induced by the firing event. The gun tube cooling system is sized for the firing scenario (rate, duration, and charge zone) and the maximum temperature allowable for safe operation.

The Thermal Dissipation Subsystem (TDS), a component of the Crusader turret, transfers heat generated by the gun tube and recoil modules to the ambient environment. Separate cooling circuits and heat exchangers are required for the gun tube and recoil modules for improved heat transfer and due to the different coolant temperatures. Ambient air is blown through each heat exchanger by a high capacity fan. The rearmost one-third portion of the XM297 gun tube has longitudinal coolant channels located mid-wall. The forward section of the tube uses a cooling jacket to route coolant along the exterior surface. The XM200 gun mount has external cooling sleeves around the outside of each of two recoil modules.

THERMAL MODEL DESCRIPTION

Figure 1 is a schematic of the cooling system modeled. The armament thermal model assumes: the heat exchanger fouling and air flow blockage degrade efficiency to 85%, the heat exchanger capacity factor is constant, and the ambient cooling air is held at a constant temperature.
The armament cooling simulation models the dissipation of thermal energy during cannon firings (gun tube, recoil module) to ambient (exhaust air) in the Crusader turret. The model implements several computation routines to simulate this thermal system.

Gun tube cooling is modeled using one-dimensional, radial, conduction segments. Segments are used for the midwall portion of the gun tube and the rest of the tube is modeled as a solid tube with coolant flowing along the outside through the formed annulus.

Recoil cylinder cooling is modeled using annular fluid segments for the centrally located rod and outer sleeve. The recoil cylinder cooling model uses a one-dimensional transient conduction solver. Due to its high viscosity and large Prandtl number, the recoil heat transfer mode is conduction limited.

The heat rejection rate of the heat exchangers are determined by their capacity factors, and the temperature difference between the coolant and the ambient air. The coolant contained in the expansion tanks is also modeled. The thermal mass of the system comprises the coolant, plumbing, and heat exchanger.

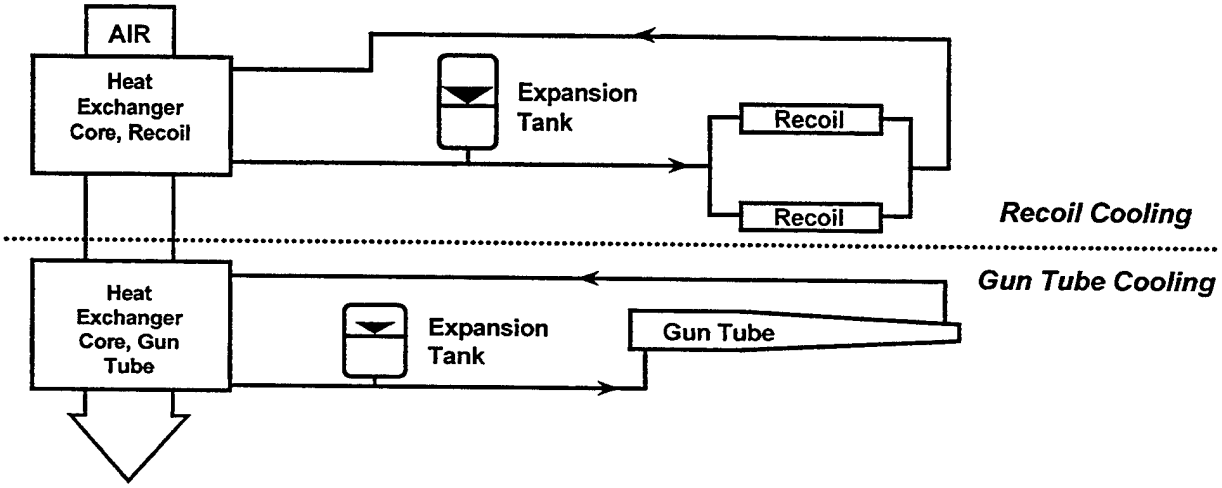

Figure 1. Schematic for Armament Thermal Model

The armament thermal model is implemented in two software codes: one each for the gun tube and recoil cooling circuits. The cooling air connects the gun tube and the recoil codes. The outlet air temperature from the recoil model is input to the gun tube model.

THERMAL MODEL CALIBRATION

A series of cannon firings, on a Thermal Hardstand (THS), generated data to calibrate the model. The THS test fired 15 rounds at a rate of 8 rounds per minute. Data from one of the 15 round firings are presented below for model calibration, with discussions for the gun tube and recoil fluid thermal model calibration.

Gun Tube Bore Temperatures

Figure 2 compares predicted and measured gun tube bore temperatures. The firing phase of the cycle compares very well. The large "sawtooth" pattern is typical of surface temperatures during short high heat flux pulses.

However, there is a slight deviation during the cooldown phase of the cycle. Initially, the model predicts higher temperatures than measured for approximately 100 seconds, but after that it predicts lower values than those measured. The average difference between the plots is acceptable and only 8.3° (4.7%)[1].

[1] Model accuracy is calculated as $\left|\frac{T_{predicted} - T_{meas}}{\Delta T_{max}}\right| \times 100\%$

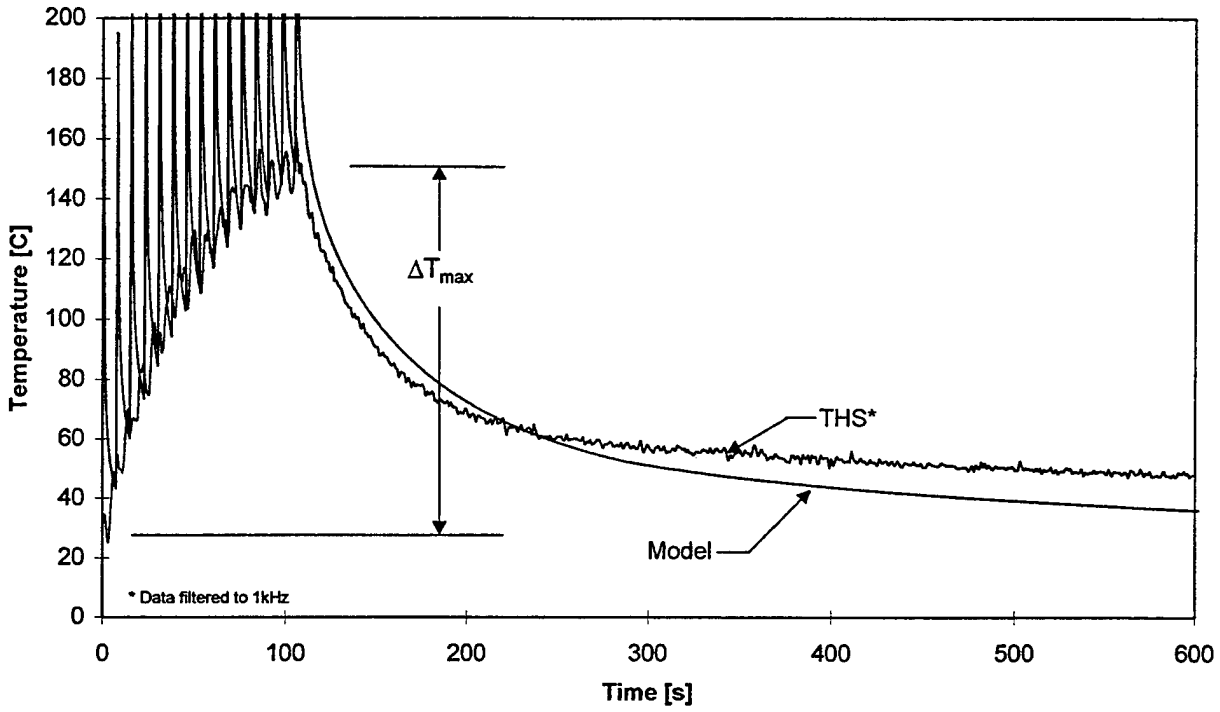

Figure 2. Predicted vs. measured gun tube bore temperatures 2 mm below the surface.

Recoil Fluid Temperatures

Figure 3 compares predicted vs. measured recoil fluid temperatures during the firing phase of the cycle. Again, there is a good correlation between the model and the test data. The average temperature difference between the model and the test data is acceptable and only 5.7°C (8.6%).

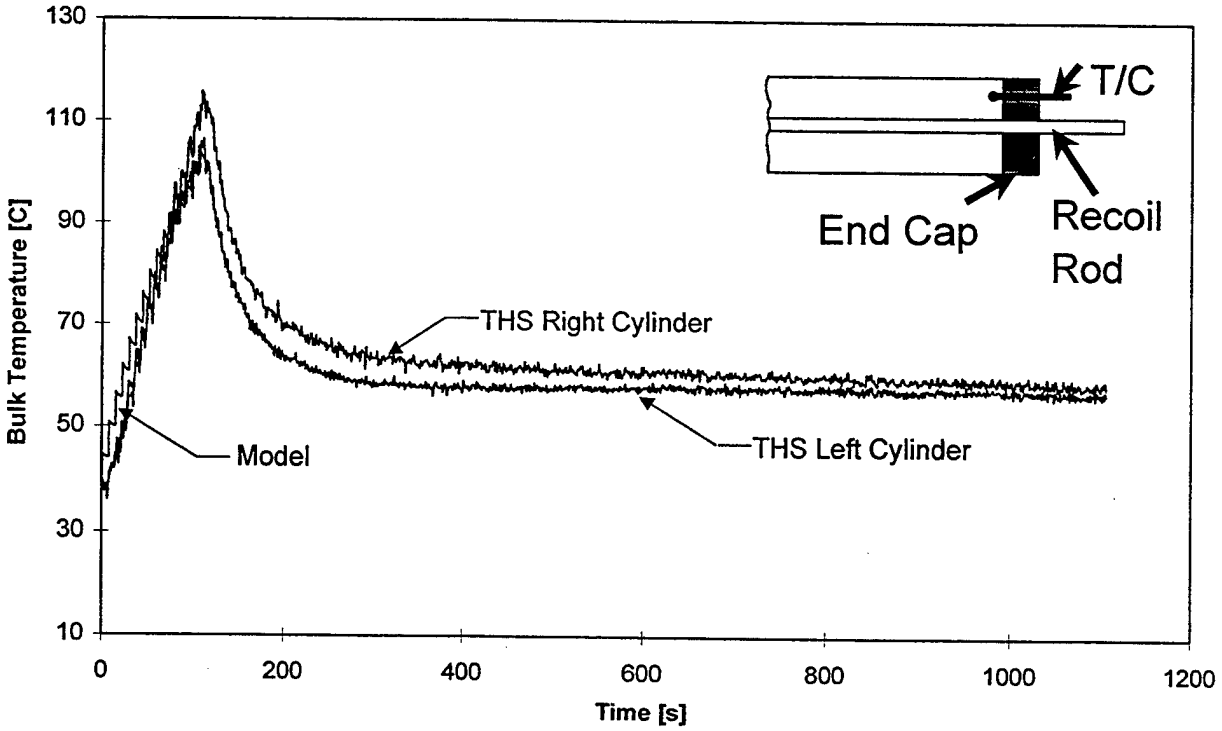

Figure 3. Predicted vs. measured recoil fluid temperature

The model predicts the bulk (or average) temperature of the recoil fluid. However, due to the poor penetration of the thermocouple used to measure and record fluid temperature, the test data likely do not indicate true recoil fluid temperature. As shown in figure 3, thermocouple is mounted in the endcap of each cylinder, protruding only about 6mm past the wall into the fluid. Due to heat conduction effects near the endcap, this penetration is likely inadequate to accurately measure fluid temperature during cool down. During the firing phase of the cycle, the rapid mixing of fluid in the recoil cylinder certainly improves heat transfer to the thermocouple and the measurement is affected less by endcap conduction. Hence, the model cooldown results for the cooldown phase of the cycle are not presented in Figure 3.

Recoil Cylinder Inlet and Outlet Coolant Temperatures

Figure 4 compares model predictions and test data for the record cylinder inlet and outlet coolant temperatures. The data and model match well, and the average difference over the entire firing/cooldown cycle for the inlet and outlet temperature is 2.3°C and 0.8°C (9.7% and 3.5%), respectively.

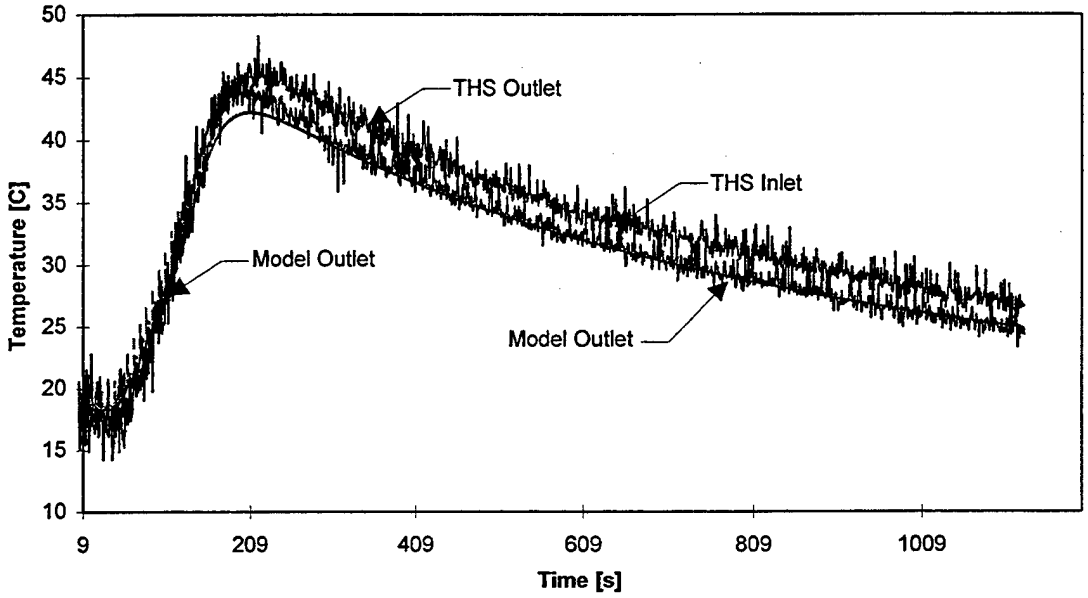

Figure 4. Predicted vs. measured record cylinder inlet and outlet coolant temperatures

Radiator Coolant Inlet and Outlet Coolant Temperatures

Figure 5 compares predicted vs. measured coolant temperatures into and out of the radiator. Unlike the Crusader armament TDS, the THS used a single radiator for cooling both the recoil cylinder and gun tube. Measured data for the inlet temperature are unreliable and are not shown.

There is a good correlation between the model and the test data, i.e., average difference is only 2.0°C, 8.3%.

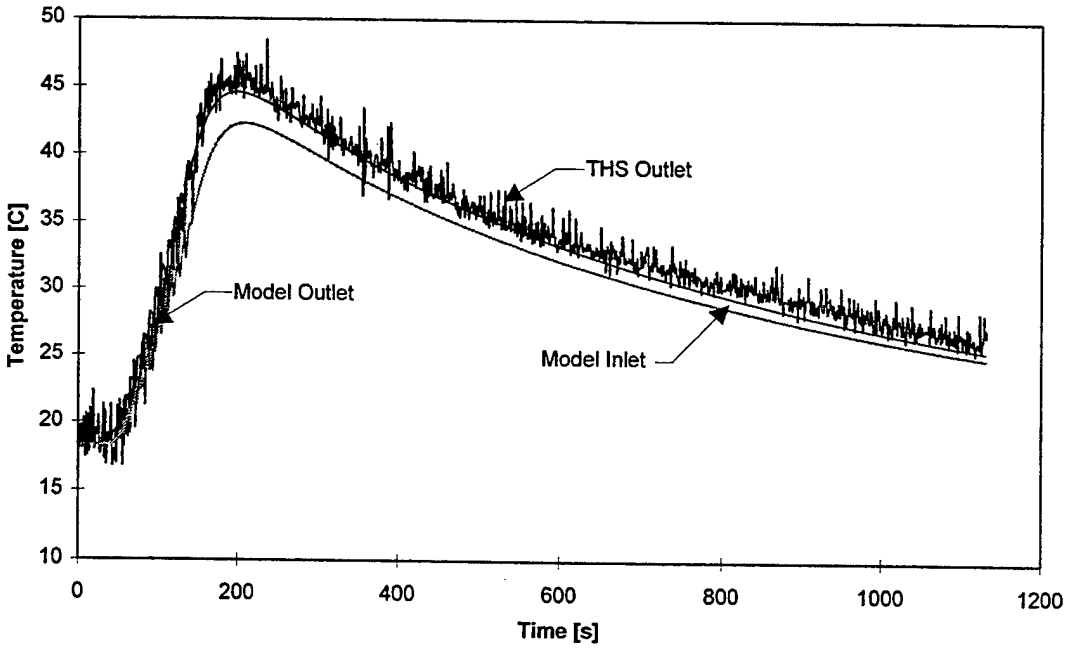

Figure 5. Predicted vs. Measured Radiator Inlet and OutletCoolant Temperatures

Model Prediction for Crusader Armament

The thermal model is applied to the following firing scenario:

1) Fire 30 rounds at 10 rounds per minute
2) Fire 30 rounds at 3 rounds per minute (or until propellant or projectiles are expended)
3) Allow system to cool for 12 minutes

All rounds are fired at the maximum charge (zone 6). The howitzer vehicle is not expected to fire all 60 projectiles at the zone 6 because the propellant magazines hold 72% of the effective maximum charge. As a result, only 43 zone 6 rounds can be fired before the vehicle empties the propellant magazine. There will still be some unfired projectiles in these cases (i.e. all propellant will be used up after firing 43 zone 6 rounds).

The maximum ambient temperature of 49°C is assumed for this analysis. The combination of firing scenario, charge, and ambient temperatures is considered to be a worst case scenario that would occur infrequently with the fielded system.

Figure 6 shows the prediction for the gun tube temperatures using the calibrated model. The maximum acceptable gun tube temperature is based on the cook-off limit of the propellant. Cook-off occurs when propellant is in a hot environment which causes it to spontaneously combust. The chamber temperature is normalized in Figure 6 to the analysis cook-off limit[2].

[2] The normalized temperatures in Figures 6 and 7 are calculated by: $T_{norm} = \frac{T - T_0}{T_{limit} - T_0}$

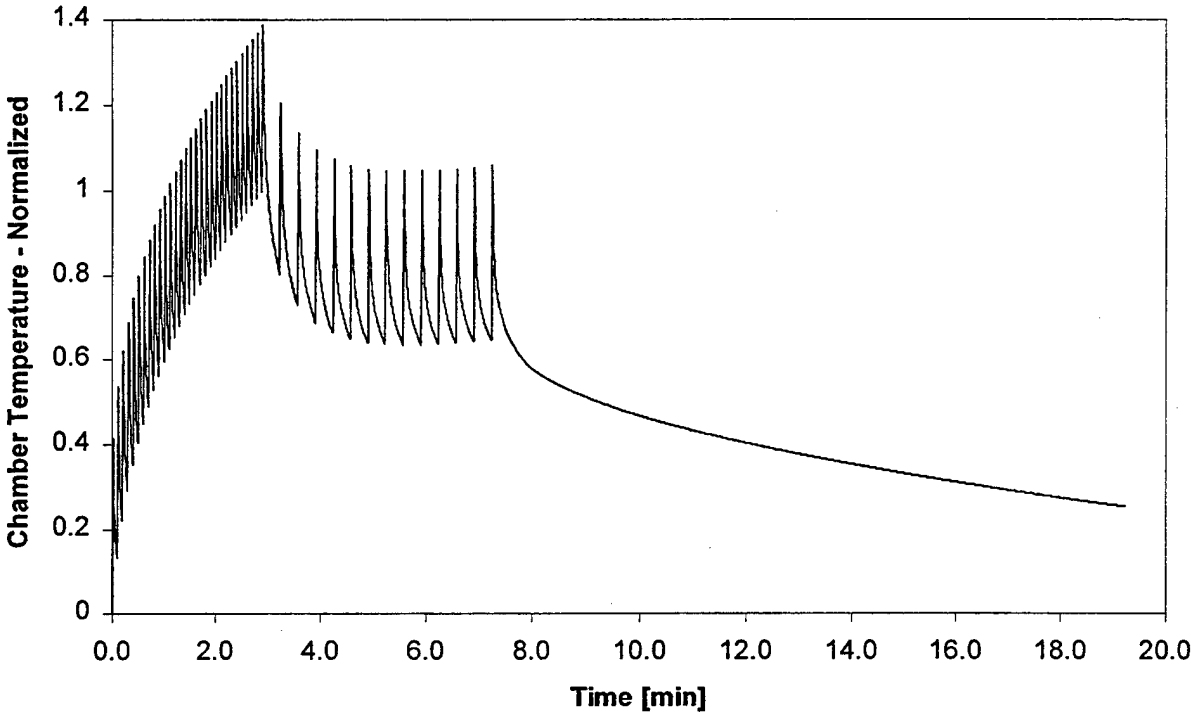

Figure 6. Normalized Gun Tube Bore Temperature (Origin of Rifling)

During a firing, the bore surface temperature increases significantly for a short time. After the propellant is done burning, the heat close to the surface conducts into the tube and the surface temperature drops quickly. The gun tube temperature is compared to the temperature limit only during that critical portion of the scenario where propellant is present in the gun tube. Since propellant is loaded just before ignition, only the last 1.2 seconds of each cycle are required to remain below the temperature limit.

Using the calibrated thermal model, the predicted recoil fluid temperature profile is shown in Figure 7, for the same firing scenario (see footnote on page 6).

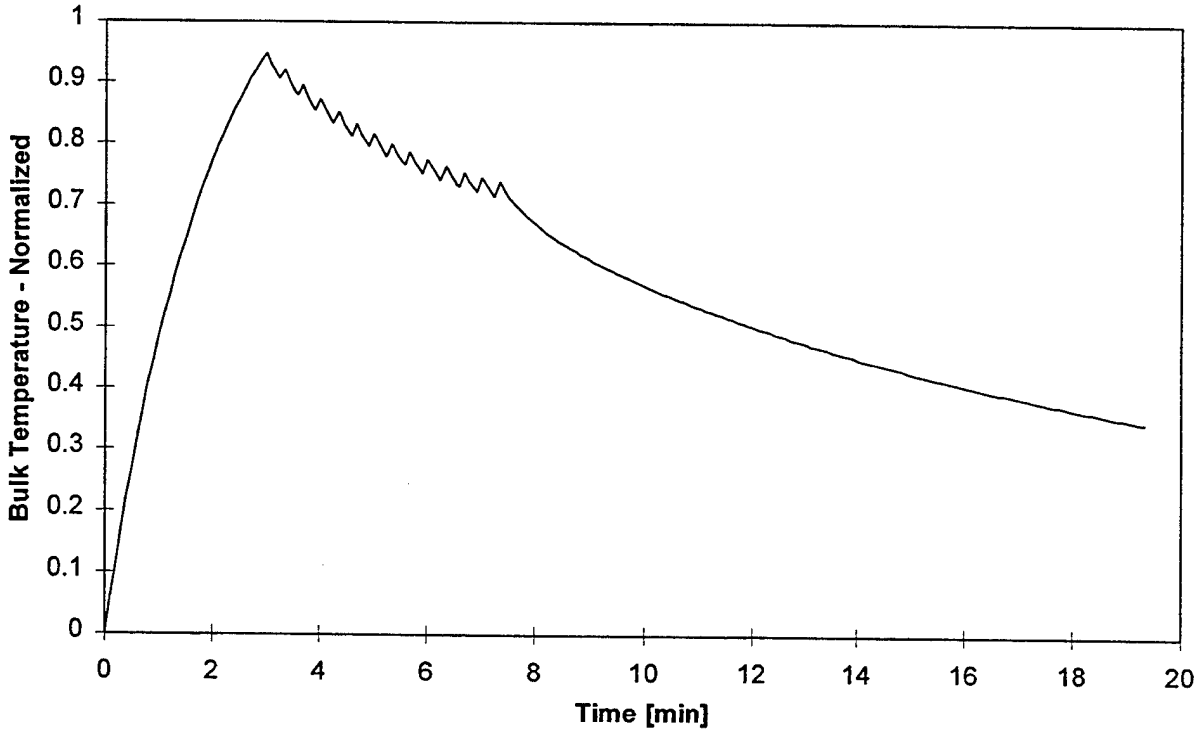

Figure 7. Normalized Recoil Fluid Bulk Temperature

The analysis indicates a peak recoil fluid temperature which is 95% of the fluid allowable for this worst case scenario. Therefore, the peak temperature is acceptable for the recoil fluid. If necessary, some temperature excursions above the operating limit may be acceptable for limited time periods without adversely affecting the recoil fluid. Additional investigations would be required to determine what short term temperature limits the fluid is capable of withstanding.

CONCLUDING REMARKS

The calibrated armament cooling system model shows good correlation between predictions and available measured data. The model has supported the cooling system size decision rationale to meet ROF requirement of 10 rounds per minute for 3 minutes followed by 3 rounds per minute for the remaining rounds at top zone and high ambient temperature.

Successful calibration of the model allows for a better understanding of the thermal performance of the TDS, Gun Tube and Recoil Modules. Confidence in the results has precluded extensive and costly design iterations and additional confirmation tests.

THERMAL RESPONSE OF SAPPHIRE TO PROPELLANT COMBUSTION

Mark Bundy
US Army Research Laboratory
AMSRL-WM-BC
Aberdeen Proving Ground, MD 21005-5066

Laser ignition is a relatively new approach to initiating the combustion of gun propellant. In this application, the laser pulse is transmitted into the combustion chamber through a window, typically made of sapphire, located in the breech face. In order to evaluate the long-term effects of propellant combustion on the laser window itself, it is important to know the window temperature during firing. This paper presents temperature data on a sapphire sample located in the region of the laser window in a laser-ignited 155-mm M199 cannon, firing various charge configurations. It was found, for example, that the sapphire surface temperature peaked at 1,200-1,400° C during the combustion event. It was also found that the surface of the sapphire sample sustained physical damage (cleaving, pitting, and plugging) with each shot fired.

BACKGROUND

Conventional large-caliber guns ignite the main charge in one of two ways. Direct-fire weapons, such as tank guns, typically use a bayonet-type igniter, which consists of a long, perforated metal tube that extends down the central core of the propellant bed. When the electrical firing signal passes through a resistive heating element in the primer head of the igniter tube, it kindles the juxtaposed igniter charge. Jets of hot gas spew from the igniter openings, thereby setting off the main propellant charge. After firing, the stub base, with its long protruding igniter tube, is discarded.

The second type of conventional ignition train, typically used with indirect-fire weapons, such as artillery, is one that utilizes a small breech-end powder charge (base ignition pad) in place of a metal igniter tube. In this system, the firing signal (pin) activates a small primer charge (cartridge) that is externally loaded into the breech block after it is closed. Hot gases, ejected by the primer, impinge on and thereby set off the base ignition pad. Flame-spreading from the base pad throughout the combustion chamber ignites the main charge. There are several concerns associated with this type of ignition system (Barrows et al. [1]), such as, for a less than full charge configuration the free chamber volume will allow the base pad to move beyond the activation range of the primer jet. Furthermore, the design of future autoloaders is complicated by the requisite loading of a primer cartridge before each firing.

As described, conventional ignition methods rely on a series of convective heat transfer events (ignition train) to set off the main charge. On the other hand, the ultimate goal of laser ignition technology is to use radiation heat transfer to "light" the main charge directly. If laser ignition is successful, it could simplify the combustion process by eliminating some of the mechanical prerequisites and residual ignition hardware that accompanies conventional methods.

In laser-based ignition, radiation is transmitted from an outside laser source into the combustion chamber by means of a fiber-optic cable connected to a "laser window" located in the spindle face of the breech block, e.g., Fig. 1.

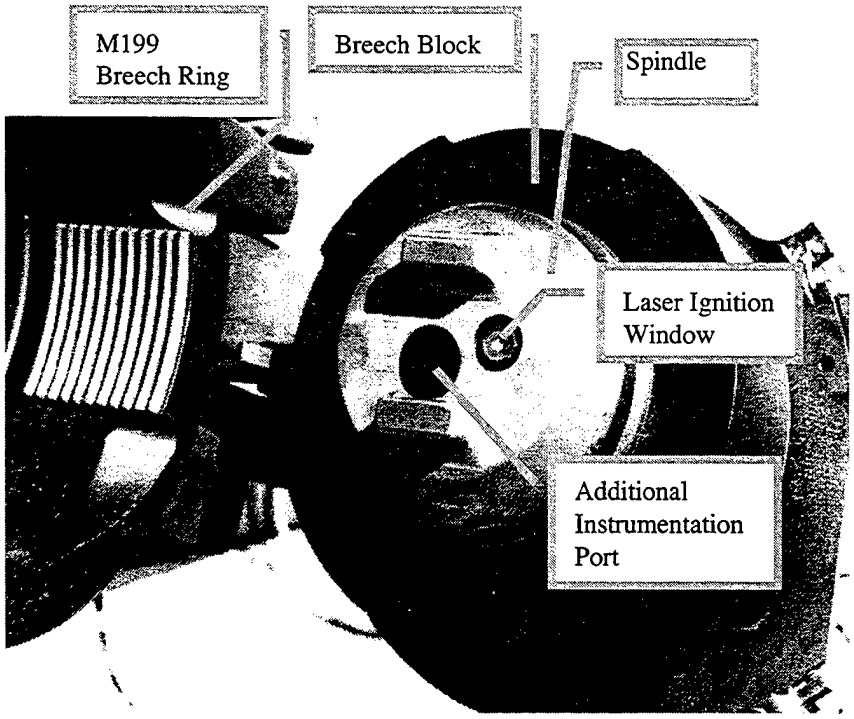

Fig. 1. View of the M199 Breech Ring, Breech Block, Spindle, and Experimental Laser Ignition Window.

The laser window must, obviously, be transparent to laser radiation, but it must also be capable of withstanding the high pressures and temperatures generated by the main charge combustion. The material of choice for this application is sapphire (Al_2O_3). Sapphire has a melting point of 2,040° C, and is reputed to be chemically stable at high temperatures (Schmid, Khattak, and Felt [2]). It is also high strength: at room temperature it has a tensile strength along the optical axis of ~425 MPa, with a compressive strength of ~1,950 MPa (Harris and Schmid [3]). However, at elevated temperature, its compressive strength may dramatically decrease, incurring a 97–98% loss (to ~50MPa) above 600° C (Harris and Schmid [3]).

Kerwein [4] noted both cracking and, what appears to be, changes in the surface chemistry on a previously fired laser window. Such findings bring into question whether or not the sapphire surface can reach temperatures high enough to allow mechanical and chemical degradation to take place during the combustion event. Hence, the following experiment was designed to address this question.

EXPERIMENT

Purpose

The test objective was to provide inaugural measurements of the surface temperature on a sapphire sample located where the laser window would be in a 155-mm M199 cannon (e.g., Fig. 1) firing various charge configurations.

Instrumentation

A current laser window design is shown in Fig. 2. It consists of a sapphire crystal, 14 mm in diameter, contained within a 25-mm hexagonal (socket) head. When threaded into the spindle, the sapphire surface of the window is flush with the combustion chamber.

Alongside the laser window in Fig. 2 is a K-type thermocouple (TC) probe that was used to replicate the window shape and means of attachment to the spindle. A second TC probe type (thin film on sapphire), along with the K-type, is shown threaded in place on the spindle face of an M199 breech block in Fig. 3 (both TC probe types were custom made for this test by Medtherm Corp., Huntsville, AL).

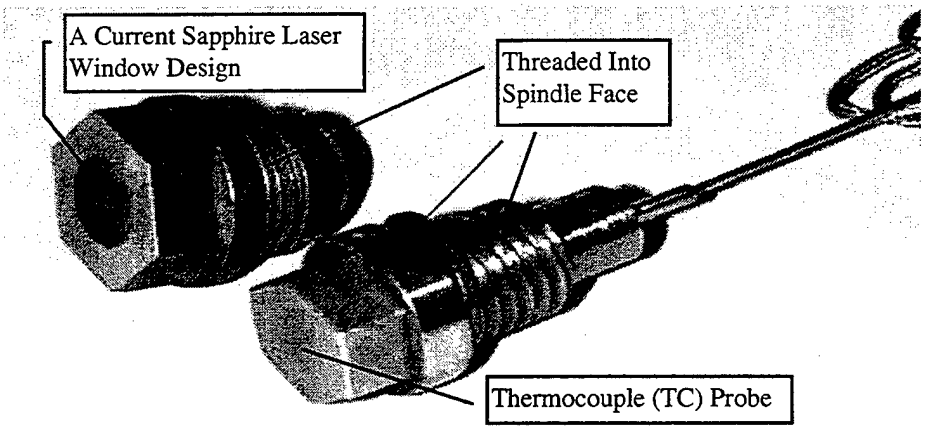

Fig. 2 A Conventional Laser Window and One (of Two) TC Probes Used to Measure Temperature.

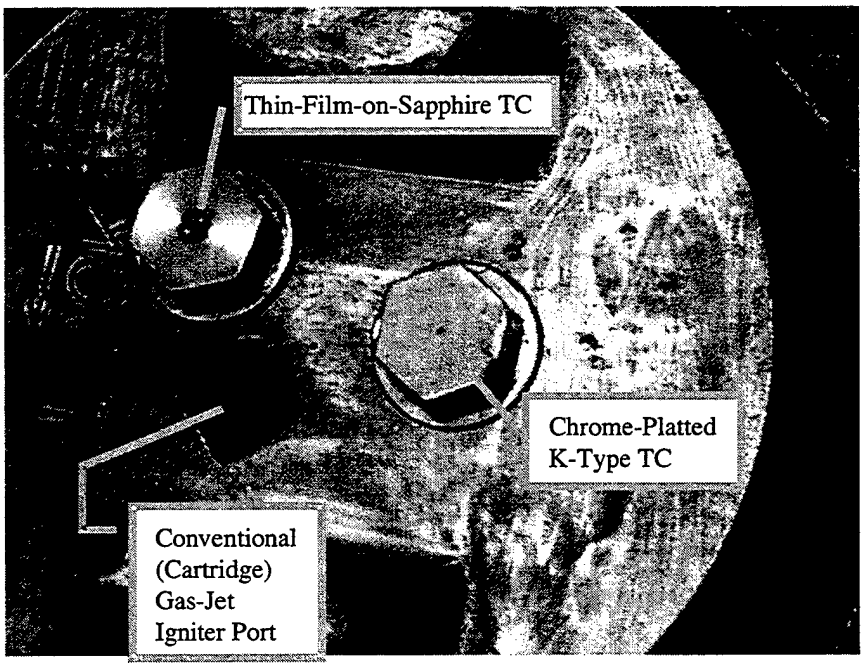

Fig. 3. Location of Thermocouples in M199 Spindle Face.

The K-type TC is composed of a central wire of alumel that is separated from an outer coaxial wire of chromel by a thin insulating layer of ceramic. The thermocouple junction was formed by vapor depositing a thin film (1–2 μm) of chromium (Cr) over the sensing end of the coaxial wires, Fig. 4. The thin-film nature of the TC junction gives this type of thermocouple an extremely fast response time, reputed to be on the order of microseconds (Medtherm [5]). Bear in mind, the measured surface temperature is actually that of the probe material itself, which, for the most part, consists of the central alumel wire and surrounding chromel tube. For comparison, the thermal properties (conductivity and diffusivity) of these materials are close to that of the stainless steel housing.

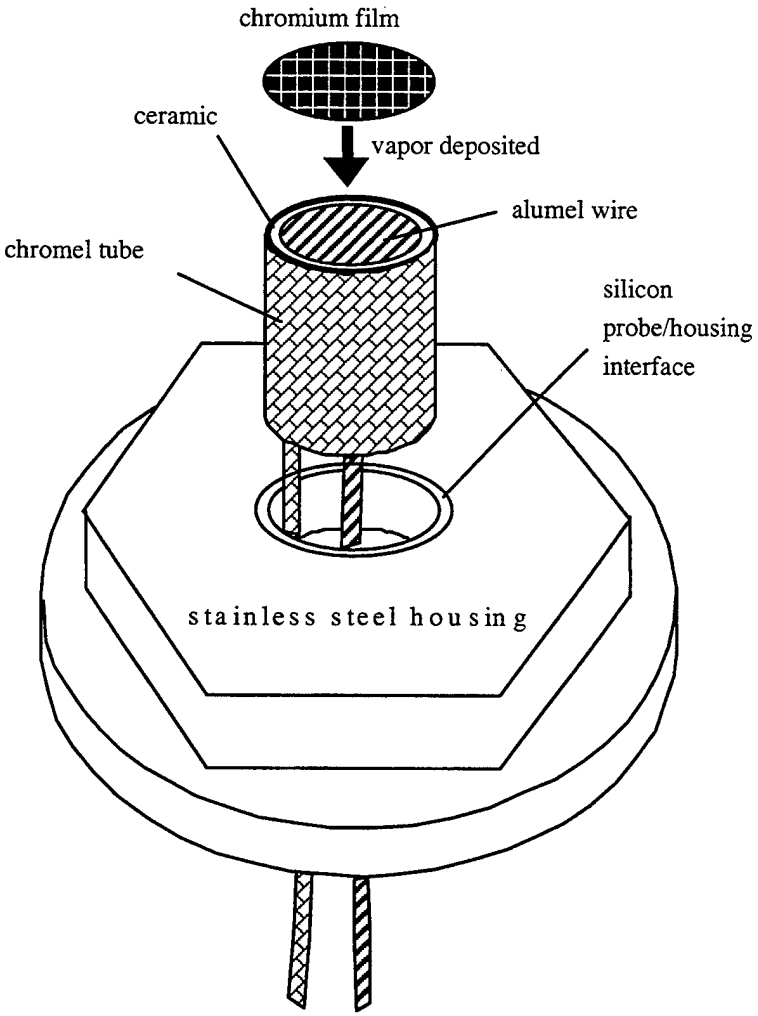

Fig. 4. K-Type TC Probe Construction.

The sapphire TC was made from a thin film (0.5–1.0 μm) of rhodium (Rh) and platinum (Pt) vapor deposited on a sapphire crystal, 4 mm in diameter. The thermocouple junction was formed in a central region of thin-film overlap, as shown in Fig. 5. Wires of platinum and rhodium transmitted the temperature-dependent voltage from the bimetallic junction to a signal-processing data recorder. Typical of thin-film TCs, the response time is on the order of microseconds. This sapphire TC provided identical laser window material for duplicating the heat conduction and diffusion effects. Thus, the temperature measurements from this probe should give an accurate assessment of the laser window surface temperature in the gun chamber environment.

A broader perspective of the test setup is shown in Fig. 6, where the spindle, breech block, and breech ring are included in the view. The thermocouple lead wires extended through and out the back of the spindle, connecting to a data recorder located inside the firing bunker.

In addition to the TCs, two copper crusher gauges (M11 type) were used to measure the peak internal combustion pressure in the chamber region for each round fired. Also, the muzzle velocity of each round was recorded with a Weibel (Model 680) Doppler radar system. These two sources of information (chamber pressure and muzzle velocity) provided an independent check that the firing was "typical" for a given propellant charge configuration.

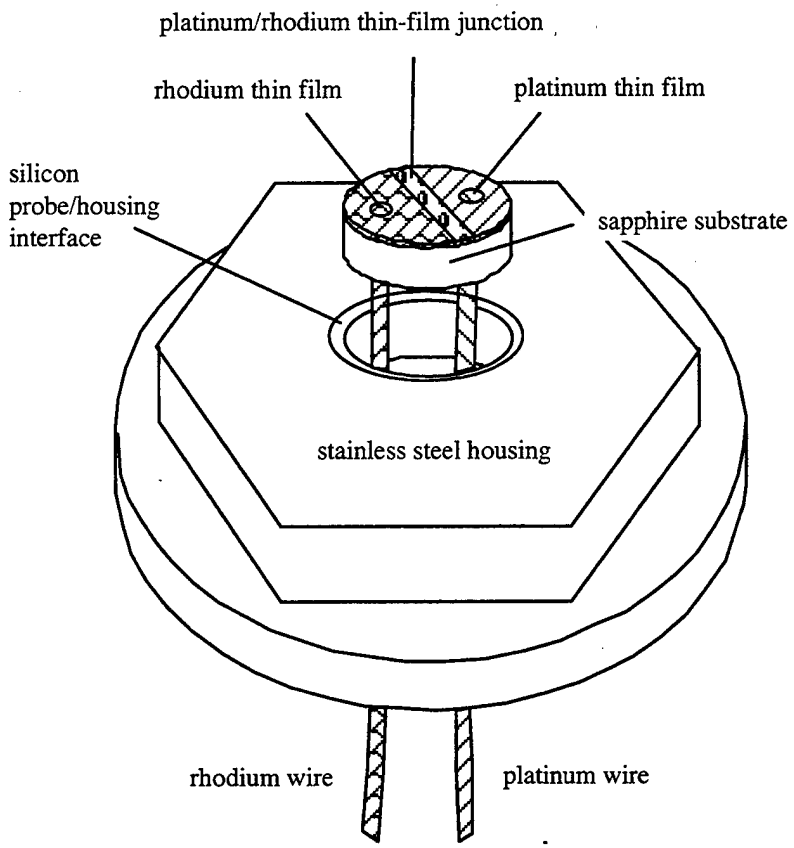

Fig. 5. Thin-Film-on-Sapphire Probe Construction.

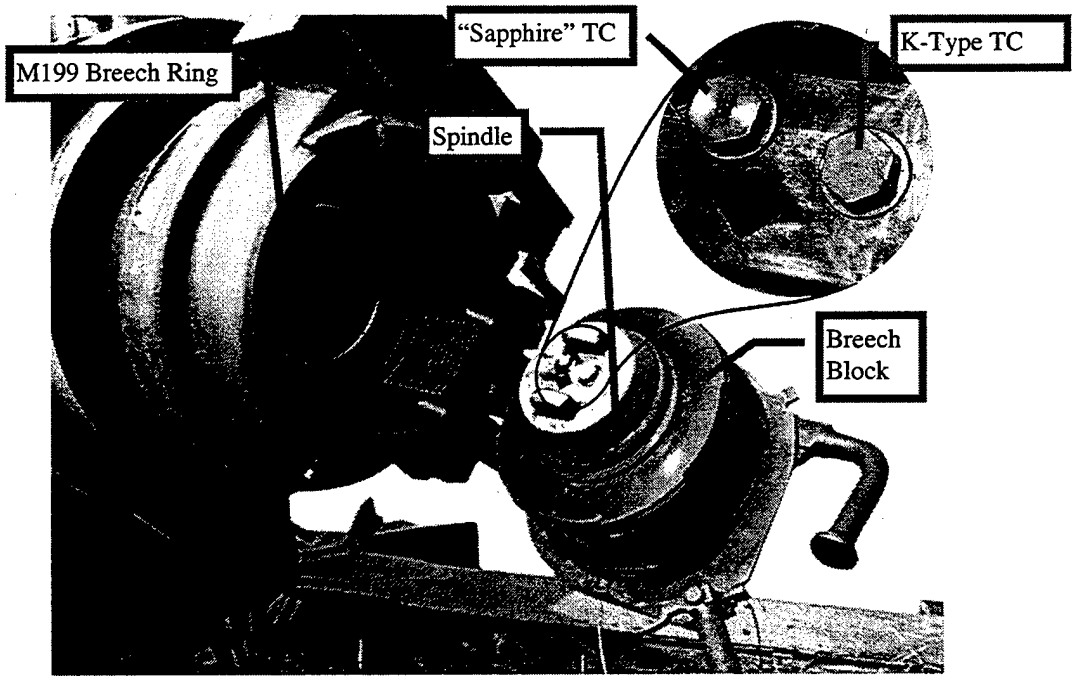

Fig. 6. Open-Breech View of TC Probe Locations.

Test Matrix

Temperature data were obtained from a ten-round firing program, as described in Table 1. In total, there were five different propellant charge configurations (groups); two rounds of each type were fired. The five groups spanned a range of propellant combustion conditions from low to high charge. The first group, M3A1 zone 5, is made up of five (unequal) increments (zones 1–5) of bagged M1 granular propellant (flame temperature = 2,176° C), totaling 5.5 lb (24.5 N). The second group, M4A2 zone 5, consists of three of a possible five bags (zones 3–7) of M1 granular propellant, totaling 7.1 lb (31.4 N). The third group, M4A2 zone 7, uses all five bags of M1 propellant, totaling 13.3 lb (59.1 N). The fourth group, M119A2 zone 7, is a single bag of M6 granular propellant (flame temperature = 2,298° C), weighing 20.7 lb (92.1 N). The fifth group, M203A1 zone 8, was a single bag of M31A1E1 stick propellant (flame temperature = 2,301° C) weighting 26.3 lb (117.0 N). The M101 projectile (weighting 96 lb [427 N]) was used for all firings. The M101 is the (obsolete) predecessor of the M107 projectile, having the same weight, the only difference being in the width of the rotating band.

Table 1. Firing Test Sequence

Round Number (Group Number)	Propellant Charge Designation (weight, N)
1 (1)	M3A1 zone 5 (24.5)
2 (2)	M4A2 zone 5 (31.4)
3 (3)	M4A2 zone 7 (59.1)
4 (4)	M119A2 zone 7 (92.1)
5 (5)	M203A1 zone 8 (117.0)
6 (5)	M203A1 zone 8 (117.0)
7 (4)	M119A2 zone 7 (92.1)
8 (3)	M4A2 zone 7 (59.1)
9 (2)	M4A2 zone 5 (31.4)
10 (1)	M3A1 zone 5 (24.5)

RESULTS

Chamber Pressure and Muzzle Velocity

The average pressure and muzzle velocity results are tabulated in Table 2. As is typical for this gun system, the peak chamber pressure (averaged over both chamber gauges) was repeatable to within <10% for rounds in the same group. It is also typical for the muzzle velocities to repeat within ~1%, as they did. An instrumentation failure prevented a muzzle velocity measurement for round seven. In general, the chamber pressure and muzzle velocity went up with increasing propellant charge weight (Table 1) in going from group one to group five. The one exception to this correlation was group two, which had a lower chamber pressure than group one, even though it had more propellant and a higher muzzle velocity than group one. The explanation lies in the fact that the propellant grain geometry was slightly different for the M1 propellant in group two than group one, giving it a different burn-rate history.

Breech-Face Temperatures

In general, rounds were fired every 30 min. Probe temperatures were monitored for several seconds prior to and after firing each round. During the combustion event, temperature data were recorded at a 10-kHz rate. Figure 7 shows a plot of the breech-face surface temperature recorded on the K-type gauge for the first round in the first group. It is speculated that the initial (small) spike, ΔT ~35° C, is coincident with the primer initiation of the base pad. The peak temperature rise (above ambient) from combustion of the main charge, Δt_{max}, is ~720° C, occurring ~70 ms after the primer impulse. A large part of the temperature rise occurred in a short time span, e.g., the temperature rose 235° C in 1 ms, as shown in Fig. 8. It can also be seen from the expanded view of Fig. 8 that the temperature remained within 5% of its peak value (715–755° C) for a period of 4 ms. It decayed to 50% of Δt_{max} in 22–23 ms.

Table 2. Maximum Chamber Pressure and Muzzle Velocity Results

Round Number (Group Number)	Charge Designation	Chamber Pressure (MPA)	Muzzle Velocity (m/s)
1 (1)	M3A1 zone 5	112	369
2 (2)	M4A2 zone 5	78	396
3 (3)	M4A2 zone 7	195	569
4 (4)	M119A2 zone 7	223	696
5 (5)	M203A1 zone 8	351	848
6 (5)	M203A1 zone 8	350	846
7 (4)	M119A2 zone 7	223	no data
8 (3)	M4A2 zone 7	181	570
9 (2)	M4A2 zone 5	79	402
10 (1)	M3A1 zone 5	105	371

Figure 9a displays the temperature time profiles of the first three rounds, as recorded sequentially on the same K-type TC. The relative time scale was adjusted so that the igniter pulse from all three plots is, more or less, coincident. For the second round Δt_{max} is 750° C, while, for the third round it is 870° C. For round four, Fig. 9b, Δt_{max} is 830° C, and for round five, Δt_{max} is 770° C.

Recall that for each firing there are two TC probes (Fig. 6). One probe is a K-type (Fig. 4), and the other is a thin-film-on-sapphire type (Fig. 5). As noted in the Background section, it has been reported that the compressive strength of sapphire along the optical axis drops to ~50 MPa at temperatures above 600° C. Table 2 shows that, in all cases, the peak chamber pressure was $\geq$75 MPa, and Fig. 9 shows that in all cases the peak surface temperature exceeded 600° C. Based on the thermal conductivities and diffusivities of sapphire, compared to alumel, the core material of the K-type probe (Fig. 4), the surface temperature of the sapphire probe should be even higher than the K-type probe. If the optical axis of the sapphire TC was, by chance, closely aligned with its axis of symmetry, then the combination of high pressure and temperature would indicate that the sapphire TC might fail mechanically in this environment. In fact, this may have been the case, since only two of the four sapphire probes procured for this test survived one round (but not the second); the other two probes malfunctioned on their initial firing. Comparatively, the K-type TCs worked well; one K-type gauge operated for nine consecutive rounds.

For the first five rounds, the only round where a sapphire gauge functioned properly was for round three, Fig. 10 (the K-type TC temperature is also shown for comparison). As anticipated, the peak sapphire temperature (1,235° C) was higher (320° C) than the K-type probe. Although the absolute temperature values may have been different, both gauges registered the initial temperature spike, and the peak temperature, at virtually the same time.

After the third sapphire probe failed, with the firing of only the fourth (of ten) round(s), a K-type TC was threaded into the sapphire port. Thus, for round five, both temperature sensing probes were of the K-type. Figure 11 shows the temperature recorded on the breech face by the side-by-side K-type TCs. It can be seen that the primer pulse and the peak temperatures are very nearly aligned in time, and, that the peak temperatures differ by only ~55° C. This 7% difference between adjacent probes of the same type gives some indication that the 30% difference between the K-type and sapphire TCs in round three (Fig. 10) was due primarily to the difference in their thermal properties.

The K-type TC that was used in the sapphire TC port for round five failed on round six. In its place, the last sapphire probe was installed. Fortunately, this probe functioned properly for round seven (though it failed on round eight). Its peak surface temperature was measured to be 1,405° C, compared with a reading of 1,020° C from its adjacent K-type probe, Table 3. The same K-type probe that recorded round one, recorded all rounds up through nine, but failed on round ten. Table 3 gives a probe-temperature summary for all ten rounds.

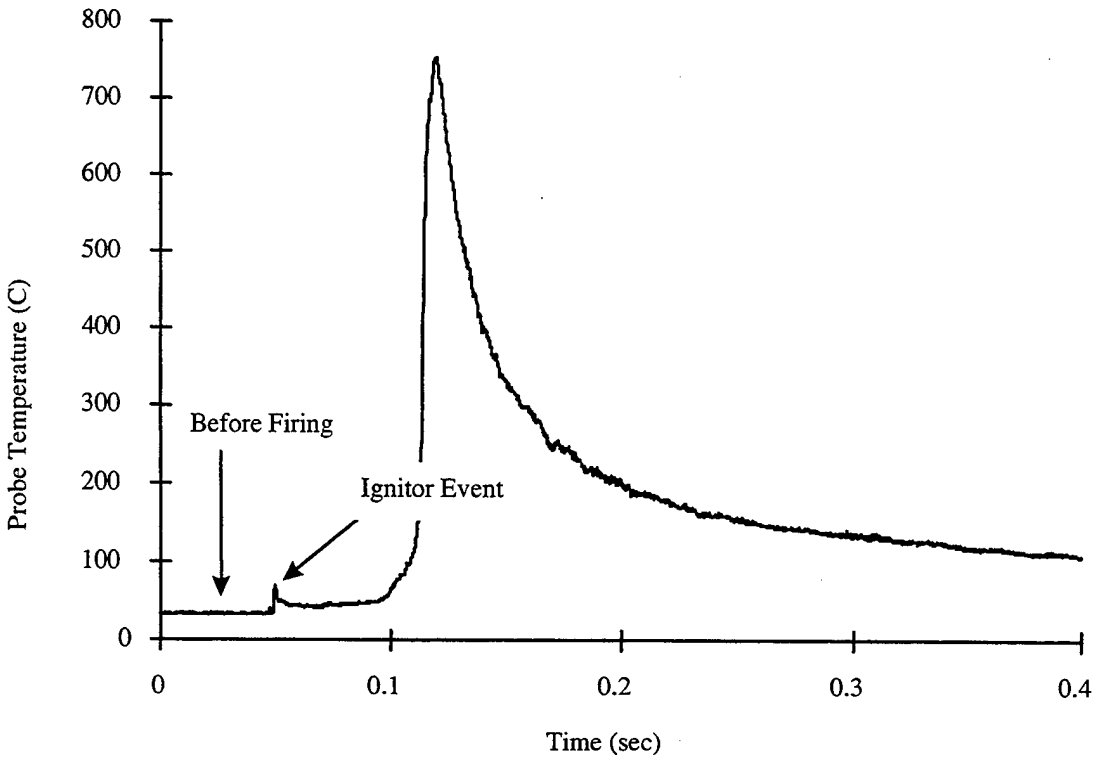

Fig. 7. Breech-Face Surface Temperature (K-Type TC) from Firing an M3A1 (Zone 5) Charge.

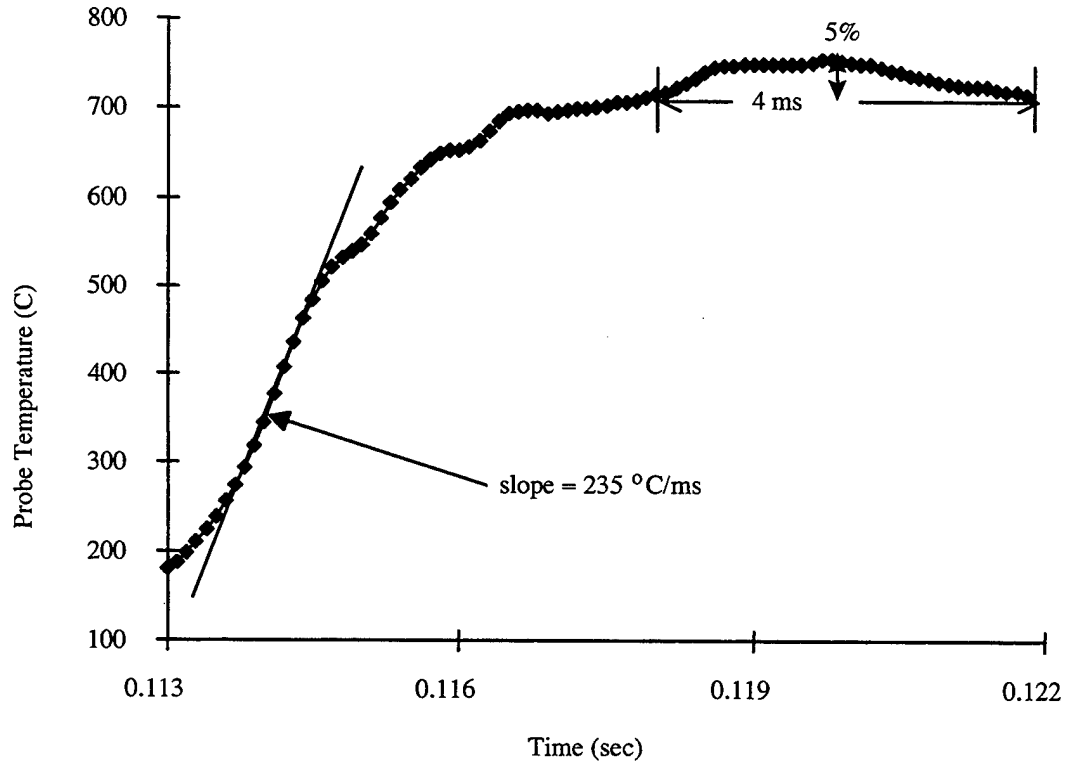

Fig. 8. Region of Maximum Temperature Rise, and Peak Temperature, From Fig. 7.

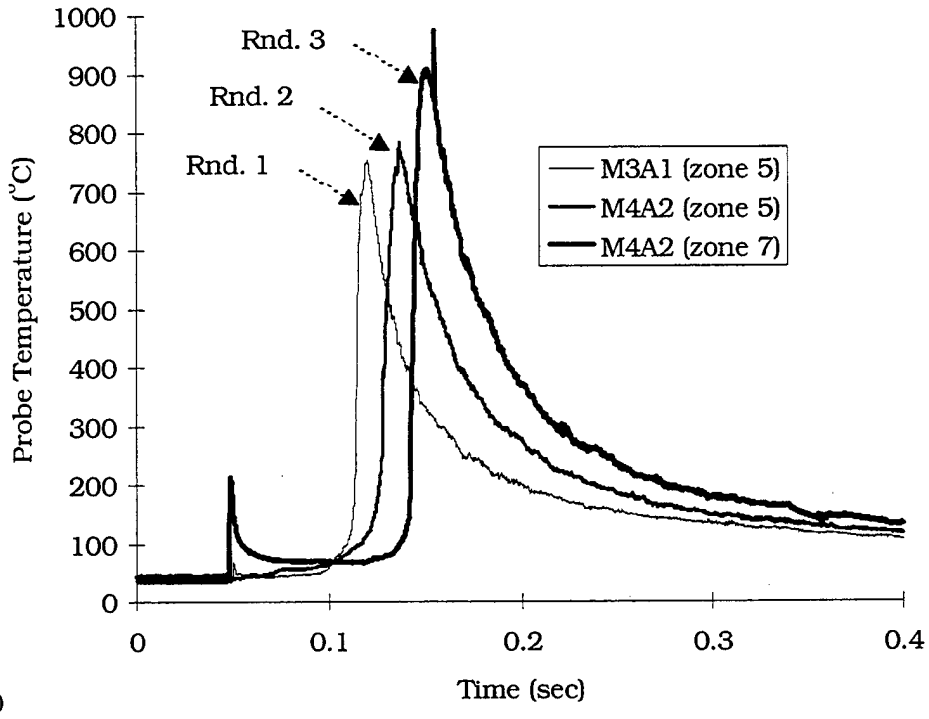

a)

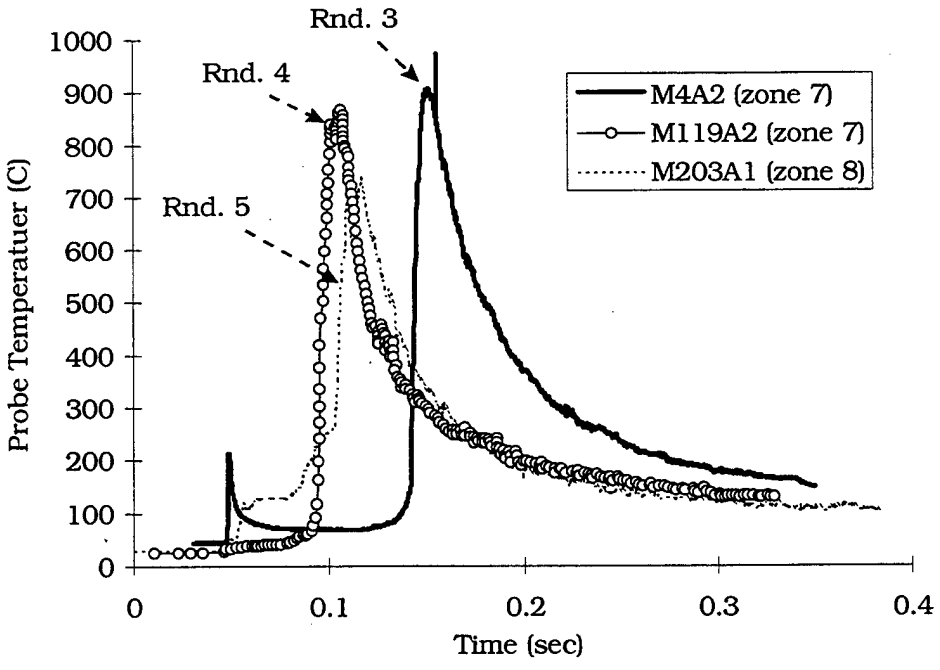

b)

Fig. 9. Breech-Face Surface Temperature (K-Type Probe) for a) Rnds. 1–3, b) Rnds. 4–5.

As alluded to earlier, it is apparent from the scatter in peak temperatures of Table 3, that round-to-round variation is relatively large. For instance, a 55° C probe-to-probe difference was noted in round five, whereas, a 310° C round-to-round difference (measured with the same probe) was noted between rounds two and nine (i.e., between the first and second firing of the M4A2 zone 5 charge). On average, there was about a 185° C temperature difference between the first and second firing of the same charge. Therefore, at the risk of generalizing from such a small sample size, the round-to-round temperature difference might be as much as three times larger than the probe-to-probe temperature variation.

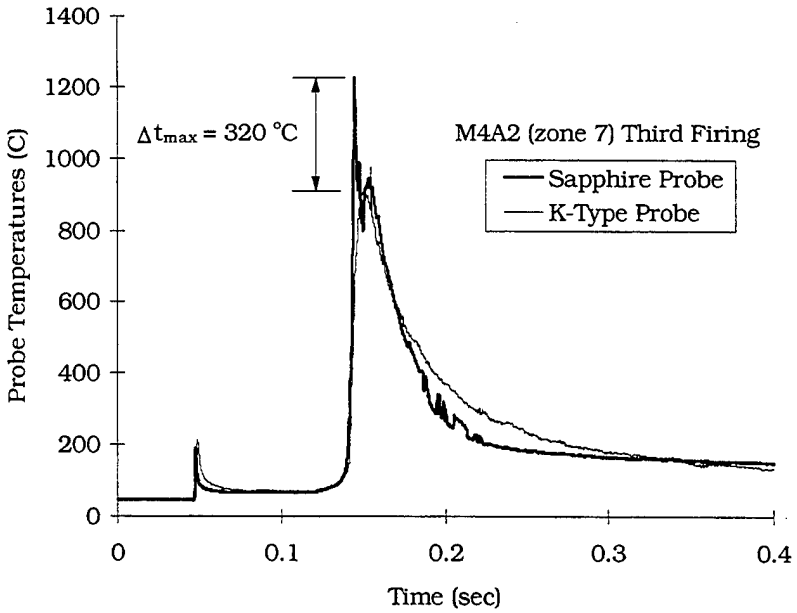

Fig. 10. Breech-Face Surface Temperatures of Both Probes for Round Three.

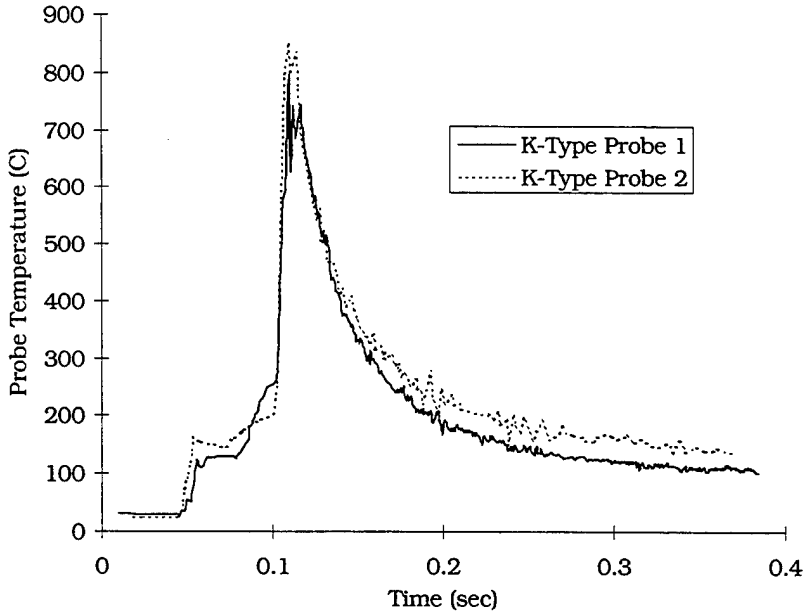

Fig. 11. Breech-Face Surface Temperature at Two Adjacent K-Type Probes, for Round Five.

Sapphire (Probe) Surface Damage

Having implied that the cause of failure in the sapphire TCs was mechanical damage to the crystal from the combination of high temperature and pressure, evidence for this claim is now shown. Figure 12 is a scanning electron micrograph (SEM), magnified 20×, of the surface of one of the sapphire TC probes (profiled in Fig. 5), as it looked before firing. Although the rhodium and platinum thin-film coatings are not distinguishable in this image, the rhodium and platinum wires running through the sapphire crystal are perceptible.

Figure 13 is an SEM (27×) of a sapphire probe after one firing. Clearly, there is physical damage. For instance, the semicircular cleavage line near the outer edge of the probe face is evidence of crystal fracture. Figure 14

provides a close-up SEM view (85×) of the fracture site. Also shown in the field of view of Fig. 13, but more clearly in Fig. 14, is a small crater-like pit, or surface depression in the crystal, roughly 100 μm in diameter.

In addition to fracture and pitting, there are hole-like regions on the crystal surface of Fig. 13, magnified in Fig. 15, where it appears that a "plug," or "core" of crystal material is missing. These plugs/cores are 20–100 μm in diameter (depth unknown).

Table 3. Peak Temperatures

Round Number (Charge Designation)	K-Type TC (°C)	Sapphire TC (°C)
1 (M3A1 zone 5)	755	TC failure
2 (M4A2 zone 5)	785	TC failure
3 (M4A2 zone 7)	915	1235
4 (M119A2 zone 7)	855	TC failure
5 (M203A1 zone 8)	795	850 (K-type TC)
6 (M203A1 zone 8)	955	TC failure
7 (M119A2 zone 7)	1,020	1,405
8 (M4A2 zone 7)	1,030	TC failure
9 (M4A2 zone 5)	1,095	TC failure
10 (M3A1 zone 5)	TC failure	TC failure

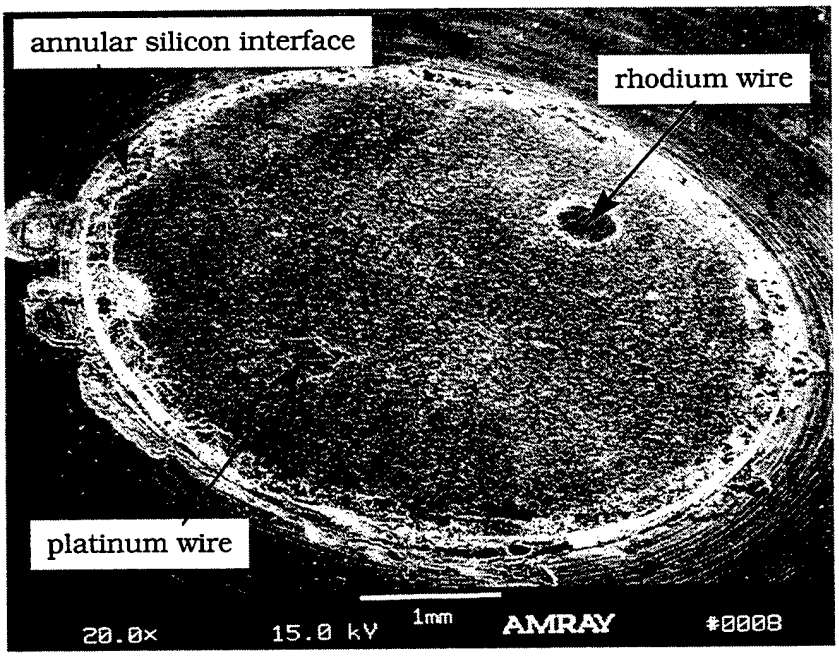

Fig. 12. SEM of Sapphire Probe Surface Before Firing.

It is conceivable that pits and plugs could both be caused by the same phenomenon. Reasoning, after peak pressure, the compressed crystal will "spring" back to its original shape. However, bonding in the crystal is weakened by high temperature (Harris and Schmid [3] not only showed that the compressive strength, but also the tensile strength of sapphire decreased along the optical axis with increased temperature). Conceivably, the inertia of the returning surface may exceed the restraining capacity of the bonds in some regions. If so, these regions could break away from the surface, leaving voids that appear as pits and holes. Although speculation on the mechanism of

mechanical damage is engaging, it is beyond the scope of this investigation. However, surface chemistry is within this study's scope, as taken up next.

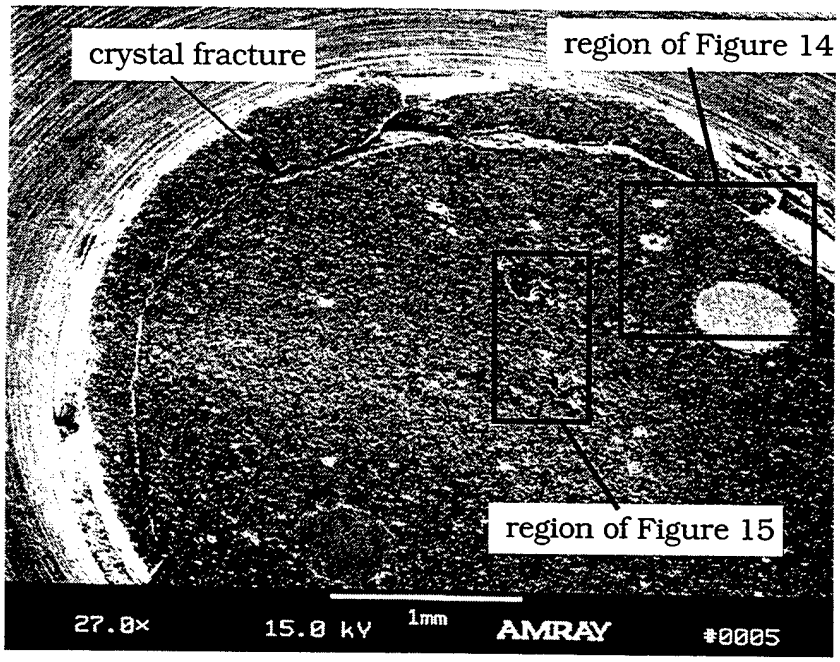

Fig. 13. SEM of Sapphire Probe Surface After Firing One Round.

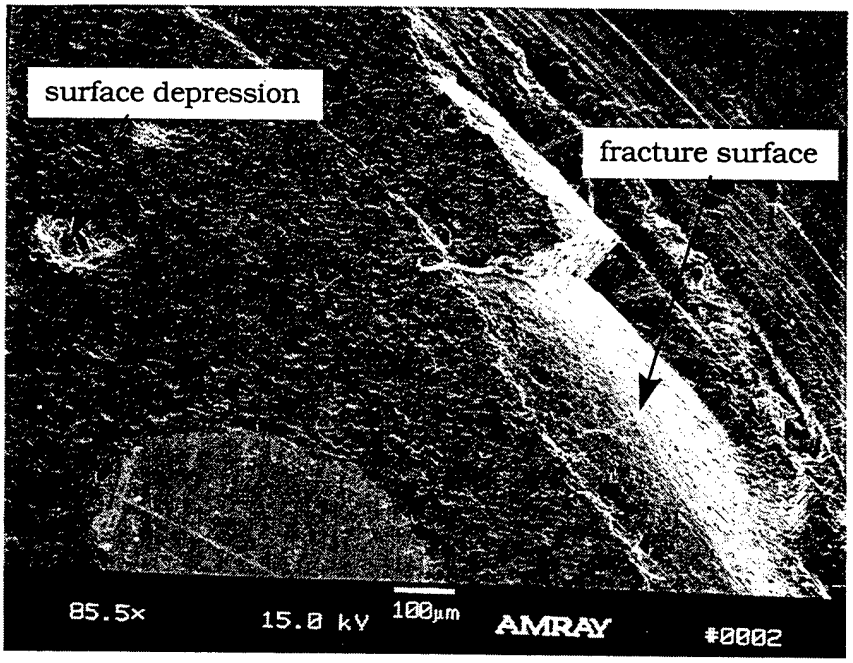

Fig. 14 Close-Up SEM of Crystal Fracture, and Crater-like Surface Depression (Magnified From Fig. 13).

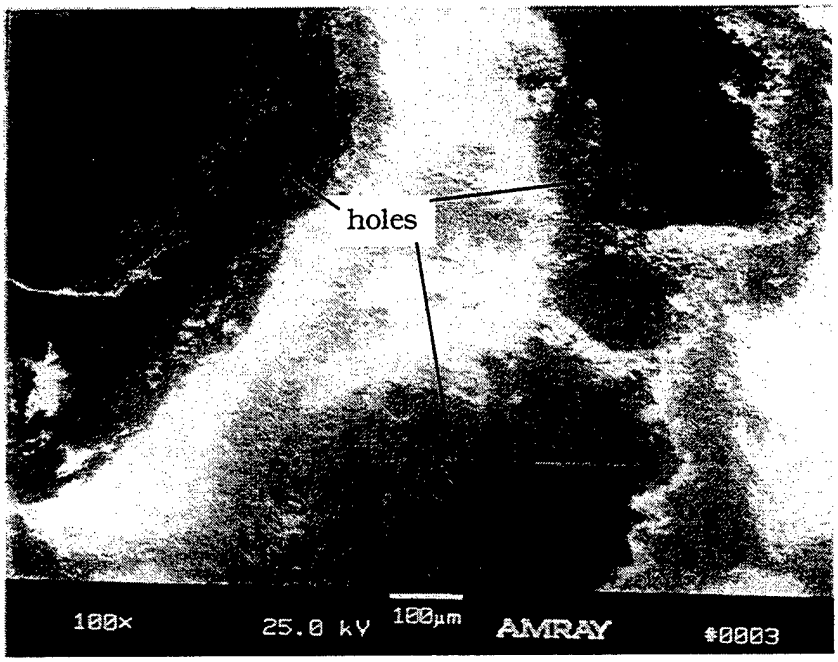

Fig. 15. Close-Up SEM of Holes in the Post-Fired Sapphire Surface (Magnified From Fig. 13).

Elemental Analysis of Sapphire Surface

Using an energy dispersive x-ray (EDX) technique, elements (above magnesium, [Mg]) were identified on the surface of the sapphire probe. Before firing, the surface constituents were found to be: aluminum (Al), rhodium (Rh), and platinum (Pt), with trace amounts of sulfur (S), phosphorus (P), silicon (Si), chromium (Cr), and iron (Fe). As expected, the primary element in each half, Fig. 16, was either Rh or Pt, with the secondary element being the substrate material—Al. It is not known why there were trace elements of S, P, Si, Cr, and Fe found on the surface.

After firing, the percentage of surface area that was primarily Rh or Pt decreased dramatically, as shown in Fig. 17. Out of five areas sampled sequentially across the Pt-side of the probe, two were found to be primarily Al, rather than Pt. Apparently, a significant fraction of the thin-film coatings of Pt and Rh was removed by the combustion event. A trace amount of potassium (K) was also found on the post-fired surface, this is not unusual, since K (as well as S) is an element of the propellant.

Lastly, in the area of the holes in Fig. 15, the primary element was Al, secondary elements were Si, S, K, and P, with traces of Cr and Fe, Fig. 18. Noteworthy, Pt is absent, even as a trace element, in these hole regions.

SUMMARY AND COMMENTARY

Sapphire is the window material of choice for laser pulse transmission (through the breech and into the chamber) in laser-ignited guns. However, very little is known about the thermal response of sapphire in this environment. This report expounds on first-of-a-kind measurements where sapphire was the substrate of a thin-film TC mounted in the same location as a laser window in a 155-mm (M199) cannon. Various charge configurations were fired and the surface temperature measured. The results indicate that a sapphire laser window will incur a peak temperature exceeding 1,000° C in this environment, regardless of charge configuration. (In the two cases where the sapphire probe did not fail, the surface temperature peaked at 1,235° C, for an M4A2 zone 7 charge, and 1,405° C for an M119A2 zone 7 charge.)

Physically, the cylindrically shaped sapphire probe sustained significant damage with each round fired. Semicircular cleaving of the 4-mm-diameter crystal was observed. In addition, there was evidence of surface pitting and plugging, with these features as large as 100 µm in diameter. Although it is not known where the optical axis of the sapphire probe was, in relation to the compression axis, the observed damage would be consistent with a near alignment between the two. Since, in that case, the reported reduction in tensile strength at elevated temperature,

coupled with decompression (after the peak chamber pressure is reached) could be the cause of both pitting and plugging on the surface. (Bear in mind, in discussing the possible thermomechanical effects here, it has been tacitly assumed that the peak pressure and temperature occur, more or less, simultaneous. However, in a more detailed failure analysis, it would be important to know the temporal relationship [phase] between pressure and temperature.)

As a commentary, in spite of the rather significant damage incurred by these sapphire samples—after just one firing—sapphire windows have, in general, proven themselves fairly resilient to multiple firings. The explanation for this discrepancy may lie in the details of crystal fabrication for laser windows (vs. thermocouples) and/or in the method of mounting sapphire into a laser window fixture.

Finally, it should be cautioned that the findings of this study, for laser windows in artillery guns, should not be assumed to hold for laser windows in tank gun applications. In artillery, the propellant flame temperature and peak pressure are around 2,300° C and 350 MPa, respectively; whereas, in a tank gun, these values approach 3,200° C and 500 MPa, respectively. This 40% increase in temperature and pressure will, undoubtedly, have a significant effect in the areas reported on here.

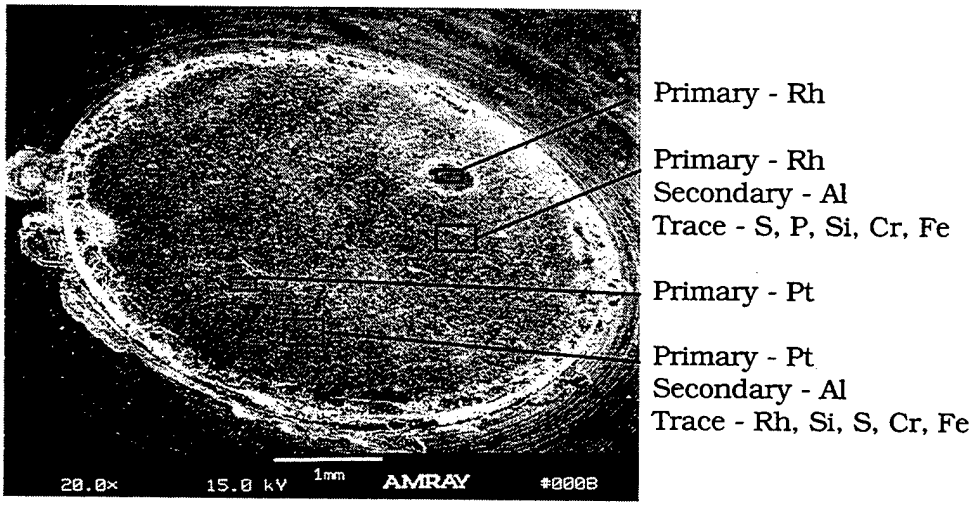

Fig. 16. Elemental (EDX) Analysis of Sapphire Probe Before Firing.

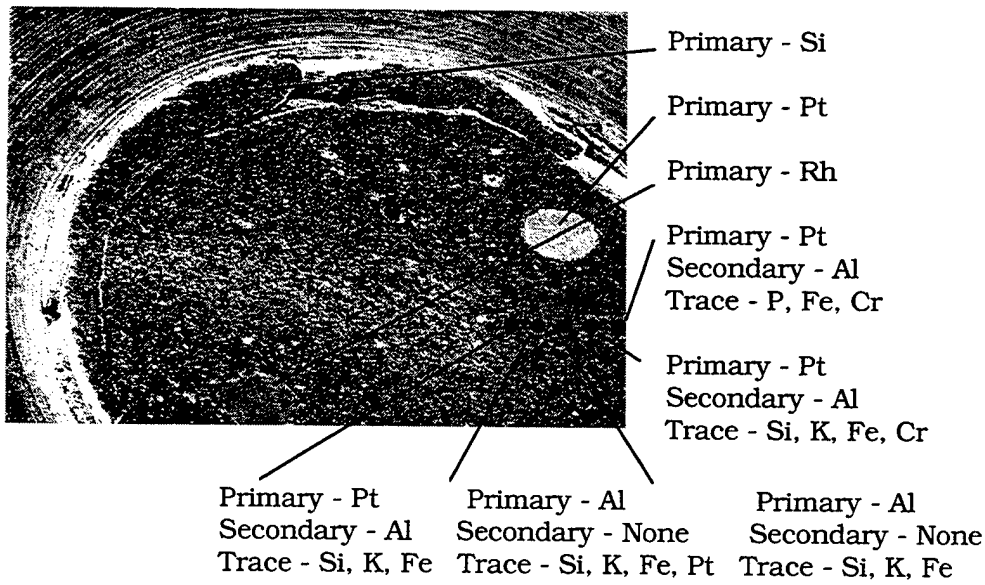

Fig. 17. Elemental (EDX) Analysis of Sapphire Probe After Firing.

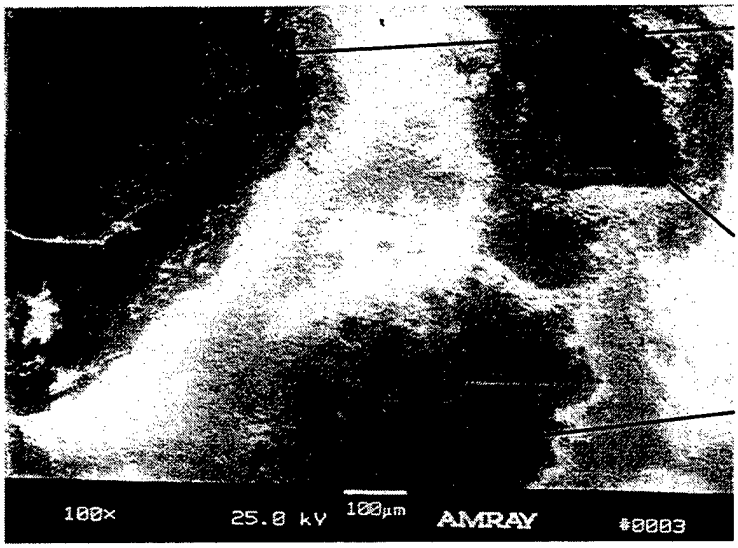

Primary - Al
Secondary - Si, S, K, P
Trace - Cr, Fe

Primary - Al
Secondary - Si, S, P
Trace - Cr, Fe

Primary - Al
Secondary - P, S, K
Trace - Cr, Fe

Fig. 18. Elemental (EDX) Analysis of Plug Areas on Sapphire Surface.

REFERENCES

1. Barrows, A. W., B. E. Forch, R. A. Beyer, A. Cohen, and J. E. Newberry, February 1993, "Laser Ignition in Guns, Howitzers and Tanks: The LIGHT Program," ARL-TR-62, U.S. Army Research Laboratory, Aberdeen Proving Ground, MD.

2. Schmid, F., C. P. Khattak, and D. M. Felt, "Producing Large Sapphire for Optical Applications," *American Ceramic Society Bulletin*, February 1994, Vol. 73, No. 2, Salem, MA.

3. Harris, D. C., and F. Schmid, "Mechanical Strength of Sapphire at Elevated Temperature," *Proceedings of the 6th DOD Electromagnetic Windows Symposium*, Huntsville, AL, October 1995.

4. Kerwien, S. C., December 1996, "Materials Analysis and Characterization of a Laser Ignition System Window," (Internal report) U.S. Army Armament Development and Engineering Center, Picatinny Arsenal, NJ.

5. Medtherm Corporation, "Measure Surface Temperature With a Response Time as Little as 1 Microsecond," *Bulletin 500*, November 1994, Huntsville, AL.

INVESTIGATING WORST-CASE HEAT TRANSFER CONDITIONS IN THE STORAGE OF UNSTABLE SOLID ROCKET FUEL

Mark Bundy
US Army Research Laboratory
AMSRL-WM-BC
Aberdeen Proving Ground, MD 21005-5066

Given time, it's possible for the chemical payload of an M55 (nerve-agent carrying) rocket to leak into its solid propellant fuel compartment. If this happens, the exothermic agent-propellant reaction can raise the reactant temperatures. It is conceivable that the rise in temperature might trigger ignition (i.e., autoignition), unless the heat loss to the surrounding environment is sufficient to limit the temperature increase. An experiment was done, and is reported on here, to determine the convection coefficients governing heat loss in the M60 rocket (the inert surrogate of the M55) in various long-term storage scenarios. This information is made available to assist in subsequent modeling of the autoignition problem. Also furnished, based on the results, is a hierarchy of best- to worst-case rocket storage conditions for mitigating this problem.

INTRODUCTION

Rockets bearing nerve-agent payloads have been banned as weapons-of-war by international treaty. However, a large number of such pre-treaty weapons are still stockpiled, awaiting demilitarization. The M55 rocket is one such example; it is designed to deliver either the chemical nerve agent GB or VX to the target. It is configured with the payload compartmentalized ahead of, and separate from its M28 double-base rocket propellant. M28 consists of nitrocellulose and nitroglycerin, which degrade slowly under normal storage conditions. Although the degradation process is exothermic, it occurs slowly under ordinary conditions and is not considered a safety hazard. However, laboratory experiments indicate that if the propellant is exposed to the chemical agent carried in the payload section, it greatly accelerates the degradation process, increasing the heat generation rate. Thus, in the unlikely event that a stored M55 rocket was leaking agent into the propellant compartment, there is concern that the heat generation may be sufficient to autoignite the contaminated propellant.

To date, experimental measurements have been obtained on the caloric heat output from the agent-propellant reaction of a single propellant sample. The potential for propellant autoignition will be evaluated by extrapolating the heat release from the single sample to a full propellant grain. However, knowledge of the heat generation rate, alone, is not enough to determine under what conditions, if any, a leaking rocket will autoignite. A suitable heat transfer model must also have a value for the rate at which heat is lost (primarily through conduction and convection) to the surroundings. Textbook values for heat transfer coefficients are only applicable to simple configurations, unlike the relatively complex case of a rocket stowed singly, or in some combination with other rockets. The only way to obtain reliable heat transfer coefficients under these circumstances is to conduct experimental heat transfer measurements under similar conditions.

Therefore, an experimental test was designed, and is reported on here, to acquire temperature measurements on an M60 rocket, Fig. 1, the inert surrogate of the M55, with a simulated agent-propellant (heat-generating)

reaction, under various conditions. An estimate of the nominal heat transfer coefficient was obtained from this test; however, evaluating the potential for propellant autoignition was beyond the scope of this investigation. It was possible, however, to assess which storage conditions, of the forty-two tested, provided the best, and worst, cooling environment for an unstable rocket.

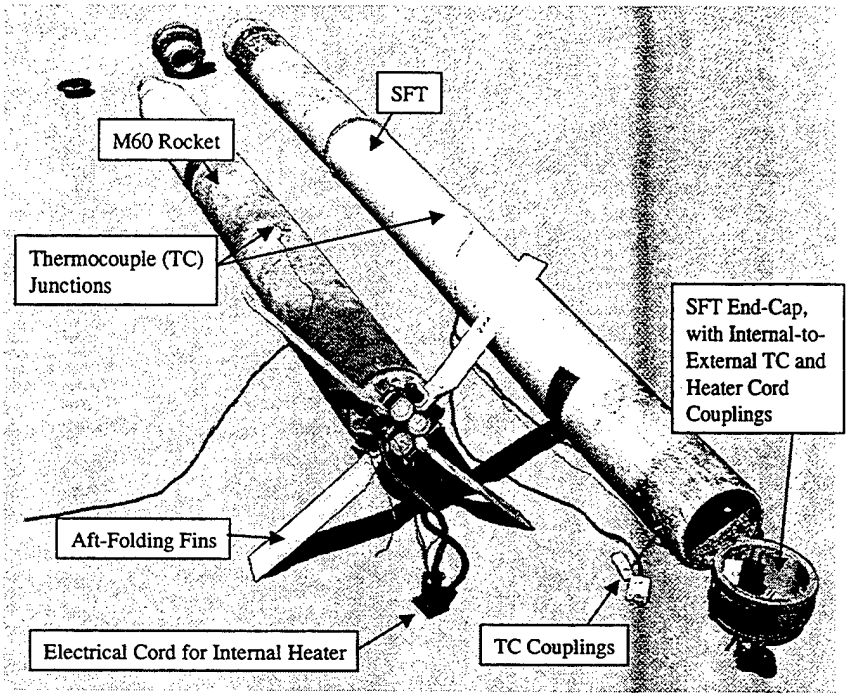

Fig. 1. An M60 Rocket, the Inert Surrogate of the M55 (Chemical Payload) Rocket, Alongside Its Shipping and Firing Tube (SFT).

EXPERIMENT

Objective

Design and conduct an experiment to investigate heat transfer in an M60 rocket under various storage conditions simulating the (abnormal) exothermic chemical decomposition of the M55's solid rocket fuel.

Methodology

The M55 rockets are normally stored (fins folded) inside shipping and firing tubes (SFTs), Fig. 1. In the case of a leaking rocket or other abnormal condition the rocket and its surrounding SFT, are (over)packed, Fig. 2, inside either 1) an end-sealed/flanged PIG-type container; 2) a mid-sealed/flanged "PIG-type" container; or 3) a single round container (SRC).

Roughly 400,000 M55s are stored in magazines at five sites around the country. Rocket-filled SFTs are palletized in a 3-high by 5-across configuration. Palletization of SFT-filled SRCs also occurs in the 3-high by 5-across arrangement. Palletization of fully-loaded PIG-type containers usually occurs in a 3-high by 4-across configuration. Depending upon quantities and available space, pallet stacking may occur up to 5 high for SFTs, 6 high for SRCs, and 4 high for PIGs. It was not possible to duplicate all aspects (conditions and environments) in which an unstable M55 rocket could be found, however, a total of forty-two cases were investigated.

The inert M60 uses a mass-equivalent steel sleeve in place of the M55's solid rocket fuel; the sleeve was removed for this test. A custom-made (Thermal Devices, Mt. Airy, MD) heater was produced to fit within the (sleeveless) solid fuel rocket compartment. As shown in Fig. 3, the heater consisted of a ¾-in. (19-mm) diameter by 24-in. (610-mm) length stock heating element held within a frame-like structure used to center the element in the

rocket fuel cavity. The heater frame was also designed to allow a filler, in particular, granular magnesium oxide (MgO), to be "poured" around it, thus filling the void between the heating element and the rocket chamber walls. Connecting the internal heater to a variable power supply allowed this modified M60 to serve as a surrogate for the M55 in various stages of rocket-fuel decomposition (internal heat generation).

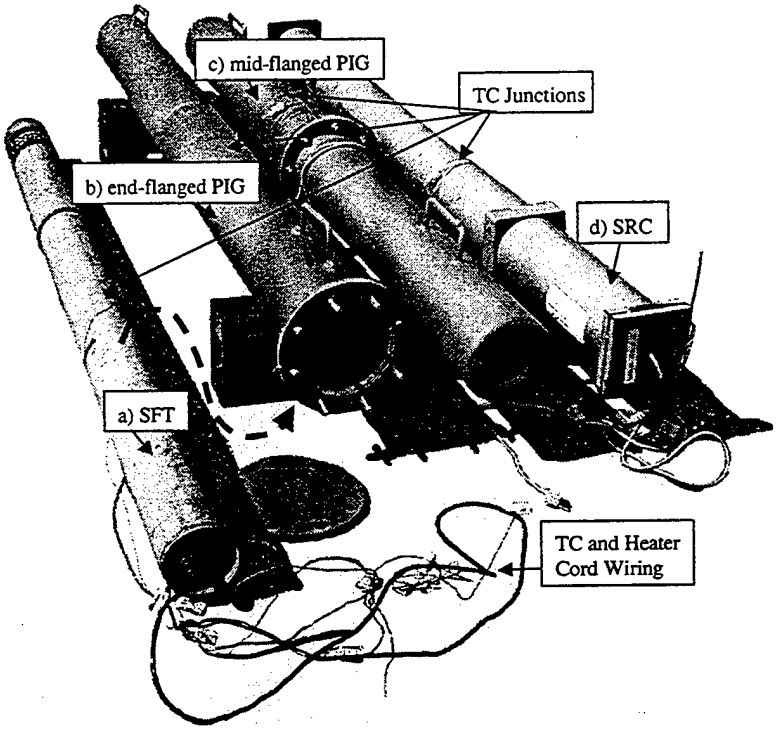

Fig. 2. Four Different Packing Containers for the M55 Rocket, a) an SFT, b) an end-flanged PIG, c) a mid-flanged PIG, and d) an SRC.

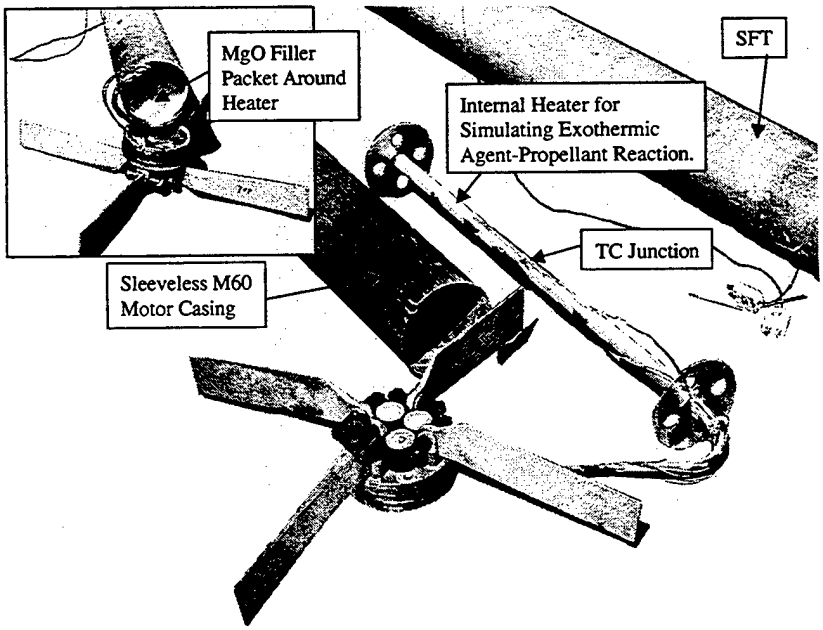

Fig. 3. Heating Element Designed to Fit Within the M60's Empty Fuel Cavity, Surrounded by MgO Filler.

Thermocouples (TCs) were used to measure the temperature of the heating element, the M60 rocket body, the SFT body, and any additional external containment structures, henceforth called overpacks, such as an SRC or PIG (Fig. 2). All TCs were located along the intersection line between the vertical plane and the plane through the central cross section of the heating element. The TCs were numbered as diagramed in Fig. 4. There are two TCs on each structure, one on top and one on the bottom. These duel measurements not only provided redundancy from two circumferentially separated measurements on the cylindrically symmetric bodies, but they also provided an opportunity to observe the vertically-stratified effects of gravity on heat conduction and convection in and around the structures. TCs 1 and 2 were located on the heater itself, TCs 3 and 4 were on the outside wall of the rocket motor/propellant case. TCs 4 and 5 were on the outside surface of the SFT, while TCs 7 and 8 were placed on the outside surface of the overpacks. TCs 9 and 10 were suspended in the air, roughly 10–50 mm away from TCs 7 and 8, depending on the stacking structure (~10 mm for SRCs, ~20 mm for SFTs, and ~50 mm for PIGs). However, if the rockets were not overpacked, TCs 7 and 8 served the role of TCs 9 and 10 (i.e., they were air-suspended around TCs 5 and 6, respectively). In general, it was not physically possible (within reason) to locate TCs on the inside surface of the cylindrical bodies (e.g., rocket, SFT, or overpack), nor was it necessary, since such temperatures would be nearly identical to their outer-surface counterparts on the relatively thin-walled structures. (Furthermore, inner diameter temperatures can be calculated from outer diameter temperatures based on the laws of heat conduction.) Nevertheless, there was one case where the assumption that the two temperatures will be nearly identical can be easily verified, that being the case with the mid-flanged PIG containment tube. There, TCs 7 and 8 were located on the inner surface (just inside the flange), while TCs 9 and 10 were adhered to the opposite, outer surface (as will be shown, these TCs always registered the same values, at least, within the TC error limits). In this special case, TCs 11 and 12 were suspended in air outside TCs 9 and 10, respectively.

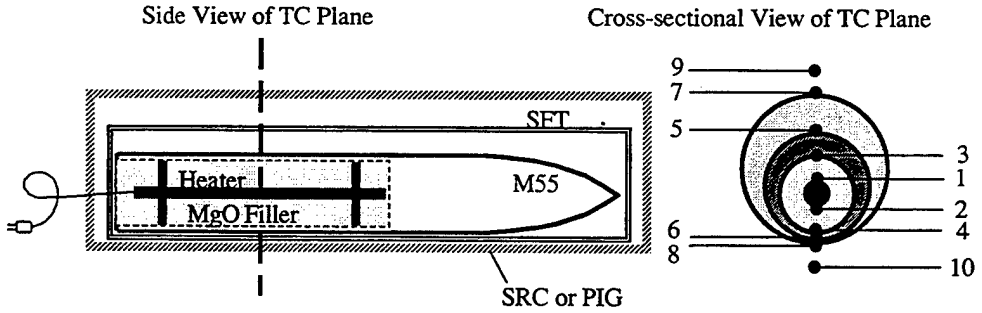

Fig. 4. Schematic of TC Locations and Gauge Numbering Scheme Around the Internal Rocket Heater.

Test Plan

The M55 rockets are normally stored in an igloo-type magazine large enough to contain several thousand rockets. However, it was not possible in this test to simulate such large-scale storage conditions. Rather than the typical 12-ft (3.7-m) high by 81-ft (24.7-m) long by 26-ft (7.9-m) wide earth-covered igloo, a 7-ft (2.1-m) high by 14-ft (4.3-m) long and 10-ft (3.0-m) wide partially earth-covered bunker was used for this test (Fig. 5a). Instead of thousands of M55-filled SFTs and/or SRCs/PIGs, only 30 M60-filled SFTs (two pallets worth), two unfilled SRCs, and two unfilled PIGs (one end-flanged and one mid-flanged) were available for simulation testing. The stacking configuration of these items in this test facility is shown in the schematic of Fig. 5b. Four of the 30 filled SFTs were removed from one of the pallets and placed inside the two SRCs and two PIGs. Their place in the SFT pallet was then filled by 4 empty SFT-like shells. Likewise, to create somewhat of a pallet-like environment for the SFT-filled SRCs and PIGs, 5 empty overpack-like shells were stacked around the filled overpacks, as indicated in Fig. 5b.

Studies done on a propellant sample (Christman [1]) indicated that, at the high end, there may be as much as 1200 μW/g of heat generated by the contaminated rocket fuel. For 19.3 lbs. (8755 g) of propellant this would equate to ~10.5 W of internal heating in the fuel chamber.

To cover the low and high end of the possible heating spectrum, there was a total of twelve heating scenarios, six at a moderate bunker temperature (~20 °C), and the same six at a high bunker temperature (~40 °C). Three of the six at each bunker temperature were for internal heater settings on rockets A–F of 4 W, 8 W and 12 W, the remaining three were for the same wattages, with the exception that the heater in rocket B was not be turned on, Table 1. Since the location of rocket B is relatively far away from all other rockets, except A, this last heating scenario only had an affect on the temperature measurements of rockets A and B. (It was felt that having a scenario where two unstable rockets are in close proximity [A and B] was as important as the case where a single unstable rocket [A alone] is located at an interior pallet location, or the case where a single unstable rocket [C alone] is located on the periphery of the pallet).

a)

b)

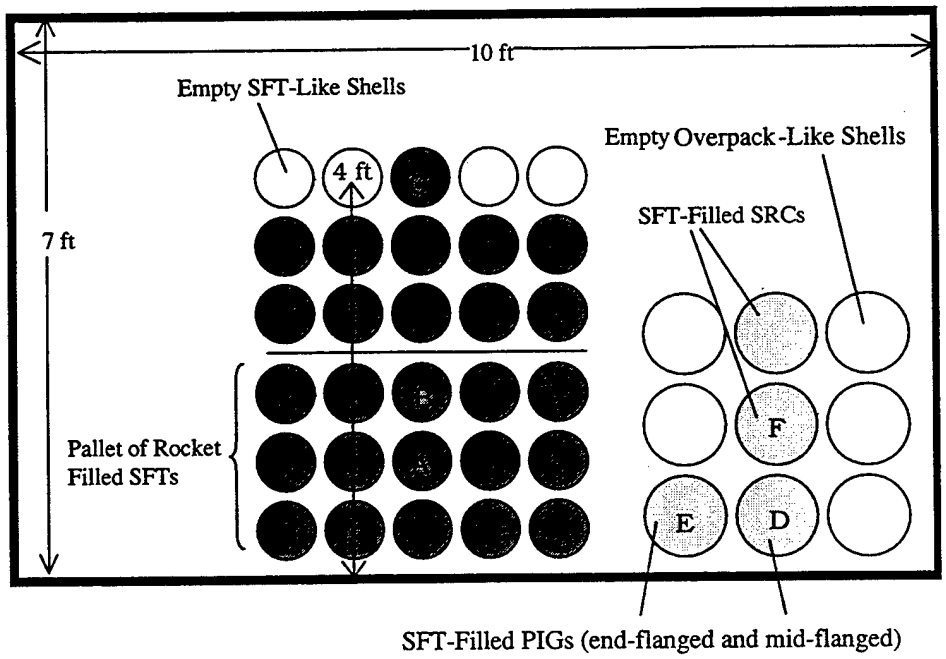

Fig. 5. Bunker Test Environment, a) Outside View, b) Inside Cross-Sectional Dimensions and Rocket Stacking Configuration.

Table 1. Test Matrix

Rockets	Wattage Controller Settings for Internal Rocket Heaters (W)											
	Moderate Temperature Bunker (~20° C)						High Temperature Bunker (~40° C)					
	Case 1	Case 2	Case 3	Case 4	Case 5	Case 6	Case 7	Case 8	Case 9	Case 10	Case 11	Case 12
A	4	4	8	8	12	12	4	4	8	8	12	12
B	4	0	8	0	12	0	4	0	8	0	12	0
C	4	4	8	8	12	12	4	4	8	8	12	12
D	4	4	8	8	12	12	4	4	8	8	12	12
E	4	4	8	8	12	12	4	4	8	8	12	12
F	4	4	8	8	12	12	4	4	8	8	12	12

MEASUREMENTS

Gauge Calibration

Given any two commercial-grade TCs (such as the 30-gauge K-type TC from Omega Engineering, Inc., used in this experiment) it is unlikely that they will register identical temperatures for the same object. Slight differences in material composition and physical makeup of the TC wires and their junctions will create slightly different EMFs at the same temperature. For example, the TCs used in this test are guaranteed by the manufacturer to have an accuracy of ±2.2 °C (the American National Standards Institute, ANSI, standard for K-type TCs). If greater accuracy is sought, then each TC must be individually calibrated. A calibration procedure was instituted, Bundy [2], to insure that all TC readings were as accurate as practically possible (~ ±0.1 °C).

Temperature

Figure 6 displays a representative set of temperature data, taken from rockets A–C in a bunker that was heated to simulate storage conditions in a warm climate (ref. the test matrix of Table 1). The conditions monitored during this time interval include the turning down of the internal rocket heaters from 8 W to 4 W in rockets A and C, and the complete turning off of the internal heater in rocket B (i.e., from 8 W to 0 W). It can be seen that, in all cases, the effect of the heater change no longer influences the temperature measurement 12 (or more) hrs after the change. As anticipated, the gauge temperature in rocket C is higher than its counterpart in rocket A, since C is located higher in the vertically-stratified bunker temperature gradient. Also, note that both A and C are greater than the (floor-to-ceiling) average bunker air temperature, as expected, since they are internally heated. Furthermore, the equilibrium temperature of rocket B is lower than both the ceiling temperature and that of its 4-W heated counterparts in rockets A and C, but it is higher than the floor temperature.

The listed gauge temperatures in subsequent tabulations are actually the average for that gauge over a period of roughly 10 min (~100 TC samplings). The 10-min period is arbitrary, with the caveat that it must be at least 12 hrs after any change in the internal heating conditions (e.g., changing the internal rocket heater outputs from 0 W to 4 W). Additionally, there should not be any unusual changes in the gauge readings over this 10-min period

(resulting from, for example, a temporary power outage, or the opening of the bunker door for routine system inspection, etc.).

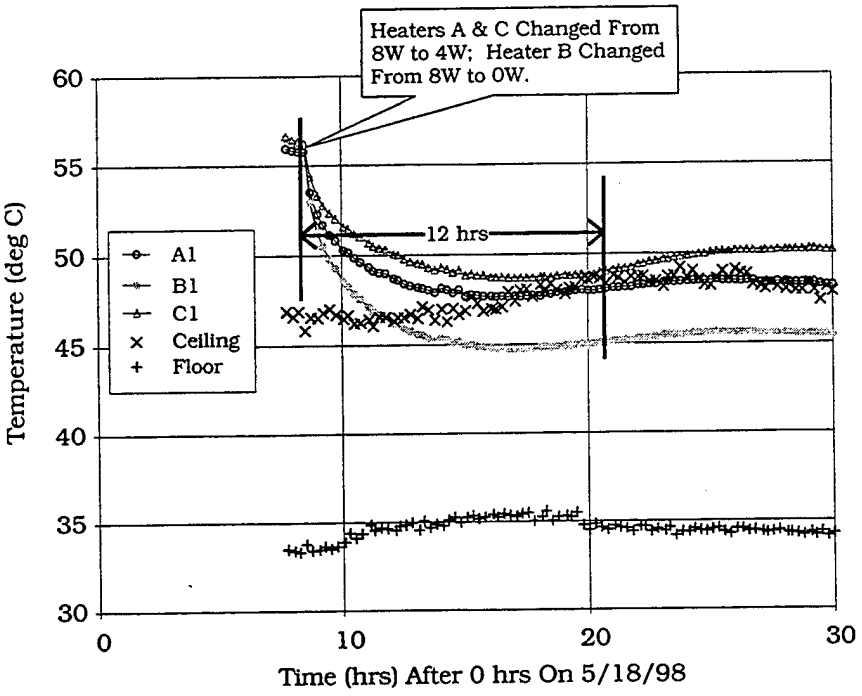

Fig. 6. Illustration of Equilibration Time for Internal Heater Changes.

<u>Internal Heating at Moderate Storage Temperatures:</u> The results in this section pertain to TC temperatures measured when the internal rocket heaters are set to output 4 W, 8 W, and 12 W (±0.5 W). Recall, Fig. 6 showed a glimpse of the 4-W heating results for gauges A1 and C1 in a relatively high overall bunker temperature environment, ~40 °C. This phase of the experiment deals with internal heating results in a moderate temperature bunker, ~20 °C (note, the total heat generated by all the internal rocket heaters [e.g., 6×12 W = 72 W] is not sufficient to noticeably raise the bunker temperature).

Figure 7 illustrates the temperature changes in and around the heating element (gauges B1 and B2), the rocket walls (gauges B3 and B4), the SFT (containment tube) (gauges B5 and B6), as well as the SFT-surrounding air temperature (gauges B7 and B8), after switching from 0 W to 4 W in a moderate temperature bunker environment.

From Fig. 7, any 10-min period after ~22 hrs on 5/4/98 is acceptable for characterizing the effects of 4-W heating. This being the case, the time interval from 24.0 hrs to 24.17 hrs was sampled, with the temperature averages for each of the 56 gauges tabulated in Table 2.

There are two sets of data in Table 2 for the ceiling and floor TCs as well as the TCs surrounding rocket A. The second (parenthetical) data set represents 10-min temperature averages for the case where rocket A has 4-W internal heating but rocket B (which is directly above rocket A, see Fig. 5) has no internal heating (ref. Table 1). Although there was also data available for this case from rockets C–F, there is no reason to believe, nor did it appear to be the case, that it would be changed by the heating conditions of rocket B, which is relatively far away.

Similarly, Tables 3 and 4 give 10-min temperature averages when the internal heaters set at 8 W and 12 W, respectively.

It can be seen that the unevenness in rocket B's wall temperature is caused by an external heating/cooling asymmetry. That is, note in Tables 2–4 for rocket B that the bottom-vs.-top air-temperature difference (gauge 8-7) is more extreme than the bottom-vs.-top SFT-wall temperature difference (gauge 6-5), which in turn, is more extreme than the bottom-vs.-top rocket-wall temperature difference (gauge 4-3). Thus, this greater bottom-vs.-top temperature difference is seen to "work" its way inward in rocket B. The ultimate cause of this temperature difference is obviously rocket A, which lies below rocket B (Fig. 5) and therefore heats it from below. (Note, even though it could be said that rocket D heats rocket F from below, the more massive, thermally conducting overpack tends to both shield and even out the effects of external heating asymmetries.

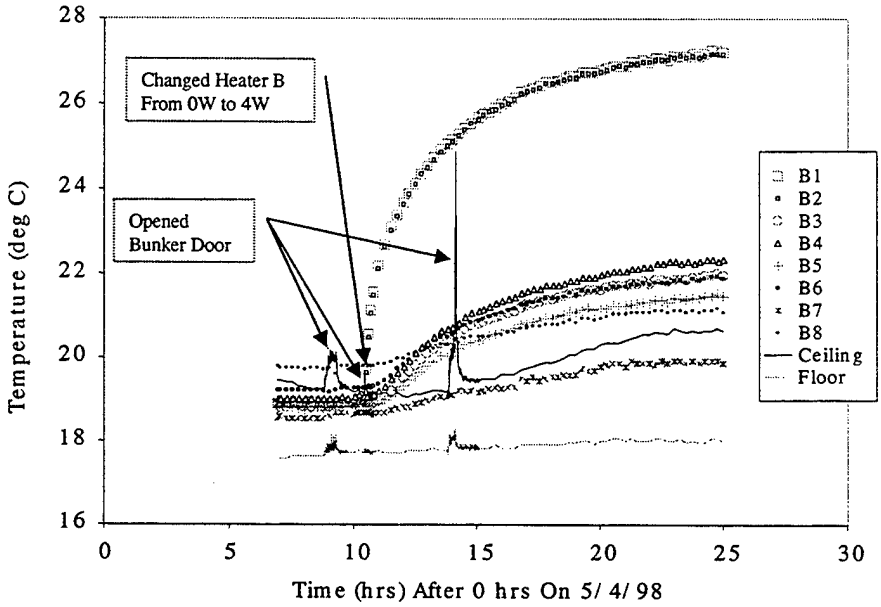

Fig. 7. Effects of 4-W Internal Heating on the TC Gauges Surrounding Rocket B.

Table 2. Temperatures for 4-W Internal Heating in a Moderate Temperature Storage Environment

Gauge No.	Floor TC	Ceiling TC	10-min Average Gauge Temperatures (°C) by Rocket Location (Fig. 5)					
			A	B	C	D	E	F
1			26.8 (26.2)	27.2	26.8	25.6	25.6	26.9
2			26.8 (26.2)	27.1	26.8	25.6	25.7	26.9
3			21.7 (21.1)	21.9	22.1	21.4	21.4	21.8
4			21.8 (21.1)	22.2	22.1	21.3	21.3	21.8
5			21.6 (20.6)	21.4	21.6	20.8	20.7	21.4
6			21.1 (20.6)	21.9	21.7	20.8	20.6	21.3
7			21.0 (19.7)	19.9	20.9	19.0	19.4	20.2
8			19.7 (19.0)	21.1	20.5	18.8	19.3	20.2
9						19.0	19.4	19.7
10						18.9	18.4	19.3
11						19.1		
12						18.3		
NA	18.0 (17.6)	20.6 (19.4)						

Table 3. Temperatures for 8-W Internal Heating in a Moderate Temperature Storage Environment

Gauge No.	Floor TC	Ceiling TC	10-min Average Gauge Temperatures (°C) by Rocket Location (Fig. 5)					
			A	B	C	D	E	F
1			33.7 (32.7)	34.0	33.6	33.4	33.1	34.4
2			33.6 (32.6)	33.9	33.6	33.5	33.4	34.4
3			23.9 (22.9)	24.0	24.1	24.4	24.3	24.6
4			24.0 (22.8)	24.5	24.2	24.1	24.1	24.6
5			23.5 (21.8)	22.9	23.1	23.1	23.0	23.4
6			22.8 (21.9)	23.8	23.5	23.1	22.8	23.4
7			22.4 (20.2)	20.2	21.6	19.1	20.0	21.5
8			19.8 (18.8)	22.5	20.7	19.0	19.9	21.4
9						19.1	19.4	21.1
10						19.0	18.2	19.7
11						19.5		
12						18.0		
NA	17.4 (16.9)	20.2 (18.4)						

Table 4. Temperatures for 12-W Internal Heating in a Moderate Temperature Storage Environment

Gauge No.	Floor TC	Ceiling TC	10-min Average Gauge Temperatures (°C) by Rocket Location (Fig. 5)					
			A	B	C	D	E	F
1			39.2 (39.3)	39.8	38.3	39.8	38.8	40.5
2			39.2 (39.3)	39.6	38.4	40.0	39.2	40.4
3			25.0 (25.0)	25.0	24.6	26.5	26.2	26.2
4			25.2 (25.0)	25.9	24.7	25.9	25.8	26.3
5			24.0 (23.2)	23.3	23.0	24.5	24.3	24.2
6			23.5 (23.5)	24.6	23.6	24.6	24.1	24.3
7			22.7 (21.0)	19.0	20.7	18.4	20.0	21.8
8			18.5 (18.4)	22.8	19.4	18.7	19.8	21.7
9						18.6	19.2	20.9
10						18.6	17.8	19.3
11						19.1		
12						17.1		
NA	16.6 (16.8)	19.0 (17.9)						

Internal Heating at High Storage Temperatures: The results in this section parallel those of the last section, however, in these experiments the bunker is heated by electrical wall heaters, raising the background temperature ~20 °C above that of the previous test conditions and thus simulating a high storage temperature environment. The room heaters were located so that there was no direct flow of hot air onto the test items. Thermostats on the heaters kept the bunker temperature environment fairly stable. Figure 6 gives an indication of temperature in the supplementally heated bunker. It can be seen that the floor and ceiling temperatures not only have a wider spread in values than their unheated bunker counterparts (e.g., Fig. 7), but the apparent noise in the temperature traces seems to be greater as well. This "noise" factor is witness to the fact the room heaters actually came on and off (roughly every 5–10 min), which gives rise to a small perturbation on the floor and ceiling temperature profiles. Tables 5–7 for the high temperature storage environment are analogous to Tables 2–4 for the moderate temperature environment. (Note, there was an unexpected power outage during the heater-A-on, heater-B-off phase of the 8-W, high storage temperature test, this was not realized until after testing was completed. Therefore, there are no [parenthetically offset] data points for this category in Table 6.)

Table 5. Temperatures at 4-W Internal Heating in a High Temperature Storage Environment

Gauge No.	Floor TC	Ceiling TC	Average Gauge Temperatures (°C) by Rocket Location (Fig. 5)					
			A	B	C	D	E	F
1			49.5 (48.4)	51.5	51.1	44.0	44.3	48.1
2			49.3 (48.2)	51.4	51.2	43.9	44.3	48.1
3			45.6 (44.6)	48.3	47.6	40.7	40.9	44.4
4			46.1 (45.1)	48.1	48.1	40.5	40.8	44.2
5			46.2 (45.1)	48.1	46.5	40.4	40.3	44.0
6			44.7 (43.7)	47.6	48.6	40.1	40.1	44.0
7			45.4 (44.4)	47.9	45.9	39.5	40.2	43.4
8			43.3 (42.6)	45.5	48.0	38.5	38.7	43.0
9						39.5	41.4	42.9
10						38.5	35.8	42.4
11						42.0		
12						35.8		
NA	35.3 (34.5)	49.6 (48.8)						

Table 6. Temperatures at 8-W Internal Heating in a High Temperature Storage Environment

Gauge No.	Floor TC	Ceiling TC	Average Gauge Temperatures (°C) by Rocket Location (Fig. 5)					
			A	B	C	D	E	F
1			55.1	55.8	55.6	49.7	49.3	53.1
2			55.0	55.8	55.6	49.6	49.3	53.1
3			45.8	47.8	47.3	41.5	41.3	44.6
4			46.3	47.9	47.8	41.1	41.2	44.5
5			45.6	46.9	45.5	40.4	40.2	43.5
6			44.3	46.9	47.4	40.1	39.8	43.6
7			43.8	45.4	43.9	37.4	38.5	41.9
8			41.1	43.9	46.4	36.5	37.1	41.5
9						37.4	39.5	41.5
10						36.5	33.5	40.4
11						40.0		
12						33.5		
NA	32.7	46.6						

Table 7. Temperatures at 12-W Internal Heating in a High Temperature Storage Environment

Gauge No.	Floor TC	Ceiling TC	Average Gauge Temperatures (°C) by Rocket Location (Fig. 5)					
			A	B	C	D	E	F
1			59.9 (62.1)	61.7	58.4	55.1	55.2	58.7
2			59.7 (61.8)	61.5	60.4	55.3	55.4	58.7
3			47.7 (50.0)	49.9	49.1	44.5	44.6	47.1
4			48.3 (50.4)	50.1	49.8	44.0	44.3	47.1
5			47.3 (49.1)	48.6	47.0	43.0	43.1	45.7
6			46.1 (48.1)	48.8	49.1	42.7	42.7	45.7
7			44.9 (46.5)	46.2	45.2	38.8	40.1	43.2
8			42.0 (44.4)	45.0	47.4	38.2	39.1	43.0
9						38.8	40.7	43.0
10						38.1	35.5	41.2
11						40.8		
12						35.4		
NA	34.7 (36.4)	47.5 (49.9)						

It is noteworthy, and without an obvious explanation, that the temperatures in rocket C during all three internal heater settings, Tables 5–7, are hotter on the bottom than on the top. Although this was also found to be the situation for rocket B in the moderate temperature storage environment (Tables 2–4), it was expected there, since rocket B was heated from below by rocket A. However, in all other cases, the temperatures outside the rocket were higher on top than the bottom, consistent with the effects of gravity (i.e., "hot air rises"). Perhaps it is the case that the room heaters, used to elevate the bunker temperature, were positioned to create a room recirculation current that resulted in a temperature inversion across rocket C. Some corroboration for this conjecture is found in the fact that with the room heaters left on, but all internal heaters turned off, there was the expected top-hotter-than-bottom temperature pattern across all rockets in the bunker except rocket C, where the temperature inversion persisted.

HEAT TRANSFER

Conduction

The heat, Q, transferred from the heating element (outer radius r_{heater}) to the rocket wall (inner radius $r_{rocket\ wall}$) will be governed by the law of heat conduction. In cylindrical coordinates this is given by (e.g., Holman [3])

$$Q = \frac{2\,\pi\,k_{MgO}\,L\,(T_{heater} - T_{rocket\ wall})}{\ln(r_{rocket\ wall} / r_{heater})}\ , \tag{1}$$

where k_{MgO} is the thermal conductivity of the MgO filler between the heating element and the rocket wall, L is some effective length (≥ heating element length), T_{heater} is the temperature of the heating element, and $T_{rocket\ wall}$ is the temperature of the rocket wall.

The value for k_{MgO} in the loose-fill condition of this experiment is somewhat speculative, since textbook listings give k_{MgO} for MgO in the solid (crystal) form, and the value used for k_{MgO} by manufactures of heating elements is for MgO in the highly compacted, high-temperature state. In the later case (Acres [4]),

$$k_{MgO}^{packed} = 1.9\ W/m\cdot{}^{\circ}C\ . \tag{2}$$

A simple analysis was used by Bundy [2] to arrive at a loose-fill value of

$$k_{MgO} = 0.32\ W/m\cdot{}^{\circ}C\ , \tag{3}$$

which is far less than k_{MgO}^{packed}, Eq. 2, but is a reasonable extrapolation to high porosity granular MgO from (the only available) low-porosity data (Acres [4]). Coincidentally, the thermal conductivity of solid rocket fuel is 0.27 W/m·°C, which is virtually identical with Eq. 3.

If Eq. 1 is evaluated using Eq. 3, along with values of

$$\begin{aligned} r_{heater} &= 0.375\ in.\ (0.0095\ m)\ , \\ r_{rocket\ wall} &= 2.125\ in.\ (0.054\ m)\ , \\ L &= 30\ in.\ (0.762\ m)\ , \end{aligned} \tag{4}$$

then the following values (Table 8) are obtained for Q for the various heating scenarios of Tables 2–7, with T_{heater} given by the average of TC gauges 1 and 2, and $T_{rocket\ wall}$ equated to the average of gauges 3 and 4. Note, although the length of the heater is 24 in., L is taken to be 30 in. (for use in Eq. 1), since that is roughly the length of the heated, MgO-filled rocket-fuel cavity.

Table 8. Computed Power Output for Each Heater in the 4-W, 8-W, and 12-W Heating Experiments

Wattage (W) Settings (±0.5 W) on A–F Heater Controls		Heater Wattage (W) Computed from Eq. 1					
		A	B	C	D	E	F
Moderate Temperature Bunker	4	4.5 (4.5)	4.5	4.1	3.8	3.8	4.5
	8	8.6 (8.7)	8.6	8.3	8.1	8.0	8.7
	12	12.5 (12.6)	12.4	12.1	12.1	11.5	12.5
High Temperature Bunker	4	3.1 (3.0)	2.9	2.9	3.0	3.0	3.4
	8	7.9 (NA)	7.0	7.1	7.4	7.1	7.6
	12	10.4 (10.4)	10.2	8.8	9.7	9.6	10.2

It can be seen from Table 8 that in the moderate temperature bunker (~20 °C), the computed heater wattage is, for the most part, within the ±0.5 W error window of the heater control setting. However, in the high temperature bunker (~40 °C), the computed heater output is consistently lower than the heater control settings, usually by more than –0.5 W. It is speculated that the decrease in thermal conductivity of the MgO filler used inside the heater element, itself, with an increase in bunker temperature, causes a temperature increase in the heater filament, which subsequently changes its resistance and current levels, and ultimately reduces the wattage output of the heater.

Although the assumptions that produced values for k_{MgO} and L, for use in the computation of Q, are sensible, they are not rigorously defendable. Nevertheless, they give reasonable predictions for Q, when compared against the wattage settings on the control unit. Moreover, any inaccuracies in k_{MgO} and L will enter into all computations for Q, unlike the ±0.5 W controller setting error, which can vary from one heater output to the next. Therefore, the values for Q given in Table 8 are henceforth assumed to be heater outputs for all subsequent computations. To facilitate their description, Q will be given a subscript that designates the rocket location (A–F) and a superscript that denotes the wattage controller setting (4, 8, or 12) as well as the bunker temperature (high or mod). For example, $Q_C^{8,high}$ equates to 7.1 W in Table 8.

Having reached the outer rocket surface via conduction through the (steel) wall, it is assumed that the heat will bridge the small rocket-to-SFT air gap, ~0.025 in. (~0.6 mm), by conduction as well (i.e., convection is assumed to be minimal across such a small air gap), viz.,

$$Q\Big|_i^{j,k} = \frac{2\pi k_{air} L (T_{rocket\ wall} - T_{SFT})}{\ln(r_{SFT} / r_{rocket\ wall})}\Bigg|_i^{j,k} , \tag{5}$$

where T_{SFT} would be the average of TC gauges 5 and 6, and k_{air} is assumed to be

$$k_{air} = 0.026\ W/m\cdot{}^{o}C . \tag{6}$$

For example, using Eq. 6 for k_{air}, and Eq. 4 for L, with

$$r_{SFT} = 2.25\ in.\ (0.057\ m) \quad , \quad and \quad r_{rocket\ wall} = 2.225\ in.\ (0.0565\ m) \quad , \tag{7}$$

Equation 5 yields for Q across the gap in the case of i = A, j = 4, and k = mod, $Q\Big|_A^{4,mod} = 4.46$ W, which rounds to the same value predicted in Table 8 for this case. (Note, $r_{rocket\ wall}$ is smaller in Eq. 4 than in Eq. 7 because in the former case it referred to the inside radius of the rocket wall and in the later case it refers to the outside radius.) Having shown how the temperature data can be used to compute the conduction heat transfer to the outside SFT wall, the next section discusses how heat is transferred from the SFT to the surroundings, via heat convection.

Convection (Coefficients)

In view of the underlying subject matter, viz., the potential for a "runaway" reaction in decomposing solid rocket fuel, it is not only the heat generated by such a chemical reaction, but the temperature of the reacting fuel, which governs the rate at which the reaction will progress. The temperature of the fuel is analogous to the temperature of the MgO filler, taken to be the average of T_{heater} and $T_{rocket\ wall}$ ($\equiv T_{filler}$). An effective convection coefficient for the transfer of heat Q from the filler to the surrounding ambient temperature air can be defined as:

$$h_{effective} \equiv \frac{Q}{A_{effective}\,(T_{filler} - T_{ambient})} \quad . \tag{8}$$

Replacing $A_{effective}$ in Eq. 8 by $2\pi r_{rocket\ wall}L$, were $r_{rocket\ wall}$ is given by Eq. 7, and L is given by Eq. 4, yields Table 9 for $h_{effective}$.

Table 9. Average Effective Convection Coefficients (Over the Top and Bottom Surface)

Wattage (W) Settings (±0.5 W) on A–F Heater Controls		$h_{effective}\|_i^{j,k}$ (W/ m^2·°C) from Eq. 8					
		A	B	C	D	E	F
Moderate Temperature Bunker	4	4.2 (3.8)	4.1	4.1	2.9	3.1	3.4
	8	4.1 (3.9)	4.1	4.0	3.0	3.0	3.5
	12	4.1 (3.7)	3.9	3.9	3.0	3.0	3.5
High Temperature Bunker	4	3.5 (3.6)	3.4	4.2	3.3	2.8	3.5
	8	3.6 (NA)	3.6	4.1	3.1	3.0	3.6
	12	3.7 (3.6)	3.7	4.0	3.1	3.0	3.5
Column Average		3.8 (3.7)	3.8	4.0	3.1	3.0	3.5

There are several observations that can be made from Table 9, for instance,

- Comparing moderate- vs. high-temperature results, $h_{effective}$ does not show any immutable (over all columns) storage temperature dependence.
- Furthermore, comparing 4 W vs. 8 W vs. 12 W at either storage temperature, $h_{effective}$ does not show any noticeable heat input dependence.
- On average, the worst-case configurations for storing an unstable rocket, lowest average $h_{effective}$, is when it is stored in an overpacked SFT, viz., rockets D–F, with the PIG-type overpacks, D and E, providing the least rocket cooling.
- Conversely, the best-case configurations for storing an unstable rocket, highest $h_{effective}$, is when it is stored in an unpacked SFT, rockets A–C, with the most effective location being the one that is most exposed, viz., on the periphery of the pallet (rocket C, Fig. 5).
- The closeness of the $h_{effective}$-values for the case where nearest neighbor rockets A and B are both heated, vs. the case where just rocket A is heated (the parenthetical values under column A in Table 9), implies that cooling conditions are not strongly influenced by the stability, or instability, of adjacent rockets in the stack.

SUMMARY

The analysis of the previous section establishes a hierarchy of cooling conditions for an unstable (agent-contaminated, heat-generating) M55 rocket contained within its shipping and firing tube (SFT). Reiterating,

- More cooling will occur if the SFT, surrounding an unstable rocket, is left unpacked (i.e., not overpacked).
- If left unpacked, the highest cooling rate will occur if the SFT is on the periphery of the palletized stack. Presumably, a single, unpacked and isolated SFT (e.g., by itself on the floor) will yield even higher cooling rates than tested here.
- The cooling rates for unpacked SFTs (and presumably overpacked, as well) are not strongly influenced by instabilities (heat generation) in neighboring SFTs.
- If an unstable SFT must be overpacked, it will cool the most in an SRC, as opposed to a PIG-type overpack.

Heat convection coefficients were not strongly influenced by either the heat input or the room temperature of the storage bunker.

Although the results obtained in this test would make it possible to quantify the fuel temperature in an unstable rocket, given the internal heat generation rate and storage room temperature, it must be assumed that the heat generation rate from an exothermic reaction will, itself, depend on the fuel temperature. Hence, it is not possible to predict from these test results, alone, whether contaminated propellant will reach its autoignition temperature. However, these results, in particular, the convection coefficients, will make it possible to properly evaluate a more comprehensive (temperature-dependant and chemistry-based) solution to the potential M55 autoignition problem.

REFERENCES

1. Christman, D., April 1998, Private communication on the testing of GB contaminated M28 propellant, SAIC Inc., Edgewood, MD.

2. Bundy, M., 1998, "Investigating Worst-Case Heat Transfer Conditions in the Storage of Unstable Solid Rocket Fuel," to be published, U.S. Army Research Laboratory, Aberdeen Proving Ground, MD.

3. Holman, J.P., 1981, *Heat Transfer*, Fifth Edition, McGraw-Hill, New York.

4. Acres, J., July 1998, Private communications on the thermal and material properties of granular MgO, Muscle Shoals Minerals, Inc., Cherokee, AL.

CANNON -PROJECTILE GAS DYNAMICS

C. A. Andrade
Benét Laboratories, ARDEC

This work describes development of Computational Fluid Dynamics (CFD) applied to cannon-projectile flows; herein to leakage flow that can occur in a Zone six firing of an M549A1 with imperfect obturation. The steady, axisymmetric flow was determined by use of the NPARC flow solver, given inflow boundary values at points on the ballistics path. Pressure distributions on the projectile are obtained assuming a smooth cannon surface and a cannon-projectile wear gap of 0.02-inch. The obturator protrudes 70% into the gap. Integration of the axial pressure distribution over the projected lateral surface of the projectile gives an estimated side force of about 500 tons on the projectile as it enters the integral-perforated-brake section of the tube. In a yawed attitude, such forces would effect inertial instabilities on the projectile; which may contribute to balloting or hydroplaning, hence, mechanical wear of the tube. The same numerical solution computes local heat transfer rates on the obturator and rotating band surfaces. Results are presented at two points on the ballistics trajectory, 2.212 and 5.256 meters from the rifle origin. The cannon wall heat transfer rates at the two leakage flow locations are estimated to be 105 and 132 Btu/ft^2/sec, respectively.

INTRODUCTION.

The most striking evidence for cannon blow-by flow can be inferred by shadowgraphs of rifle muzzle flow fields [1]: A series of shadowgraphs of the M16 muzzle blast field show that bore residue particles accelerate across the blast wave [2] which, in turn, has accelerated ahead of the exiting 7.62 mm projectile in the muzzle flow field. Fig 1 shows the residue particles, which were expelled either by leakage flow over the boattail - during exit dynamics - or, became entrained by the in-tube leakage past the projectile. It has not been determined which scenario prevails; but, after many firings, it is likely that both processes occur: in-tube and exit flow expansions of the propellant gases entrain particles of unburned propellant, graphitic carbon and water vapor smoke and; extrapolating to the case of artillery, particles of eroded materials from the obturator, rotating band and gun steel. Evidence for the 155 mm cannon muzzle-end wear problem was given by Hasenbein [3] who presented measurements indicating disproportionate increases in cannon diameter, toward the muzzle-end of the barrel, that correlate with increasing number of rounds fired. These data constitute the basis for a first hypothesis: that balloting, a mechanical instability of the projectile as it approaches the muzzle, is the cause of muzzle-end wear. Examining the same data at the breech-end indicates that the wear slope is significantly less there, than at the muzzle-end, for the number of rounds fired; thereby, supporting a second hypotheses: that turbulent boundary layer flow in the projectile's wake is the predominant flow mechanism initiating heat transfer to the barrel and high temperature gas-surface reactions, which cause erosion at the origin of rifling (O.R.) and downbore. The latter has been the basis for several recent modeling efforts designed to predict gun tube wear and erosion [4, 5, 6, 7].

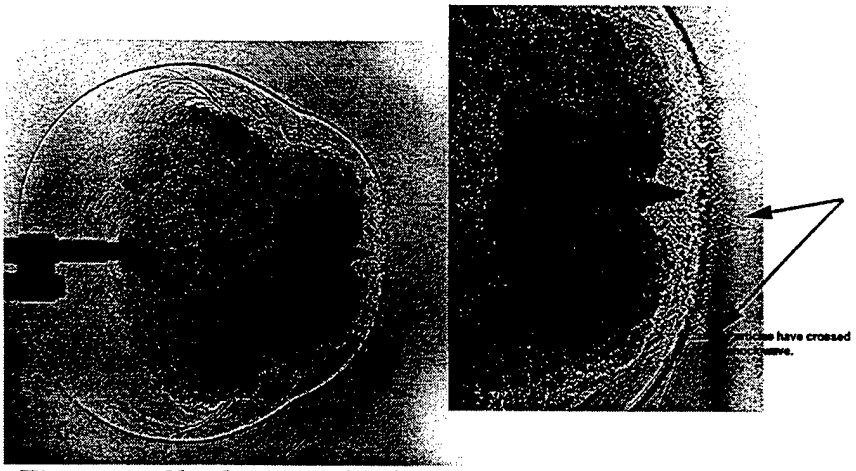

Figure 1. Shadowgraph of M16 Muzzle Blast Flow. In-Bore Particles Cross Blast Wave. (Courtesy of Dr. E.M. Schmidt.)

Blow-by flow, or leakage past the projectile, has been investigated by Hasenbein [8], Ahmad [9], Buckingham [10], and Lawton [7, 11]. While most of these authors dealt with inferences from field observation, evidence of gas wash on projectile fragments and barrel section metallurgical examination have led to the construction of mathematical models, and their laboratory validations, given restricted blow-by flow systems [10, 11] aimed at understanding and reduction of tube erosion. For example, Buckingham has studied particle-gas flow to examine the use of cannon wear reduction additives, while Lawton has adapted an interior ballistics code to correlate the observed gas leakage temperature rise on 30 and 40 mm guns. Projectile body engraving may be evidence of the imbalance of forces due to blow-by, indicating that sufficiently high temperatures occur, either by friction or blow-by gas or both, as to leave large deposits of the band material on one side of the body. Thus, it is thought that blow-by gas dynamics may contribute to projectile instabilities, which can cause balloting, body engraving, and mechanical wear at the muzzle-end of the barrel.

The present work is thus motivated by a desire to better understand the mechanical problem. Moreover, Lawton's [11] measurements of the in-bore temperature, pressure and heat transfer on the barrel walls of 30 mm Rarden and 40 mm Bofors guns indicate that at least half of the heat transfer to the barrel near the O.R. is due to blow-by gas leakage, Fig 2. These data also show large transient temperature fluctuations, near the origin of rifling, that exceed the melting point of gun steel – albeit, samples that produced these results were 10 % of the total population fired. Thus, a second motivation for the present work is to obtain an assessment of the local surface heat transfer rates during blow-by flow through a narrow gap. This is considered preliminary toward the calculation of the blow-by heat pulse during the ballistic cycle. Also, the computation of local surface heat transfer rates, temperature and pressure distributions about the projectile can be useful in the design of obturators and rotating bands.

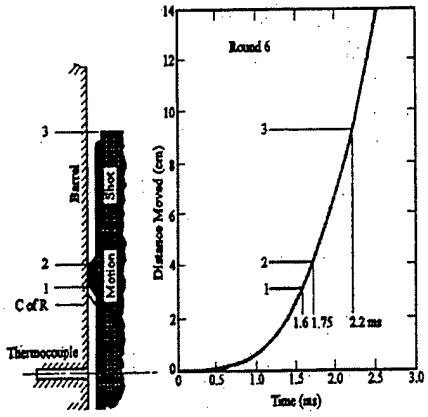

Fig 2a. Shot Travel for 40 mm Bofors Gun, Computed from the Pressure-Time Data.

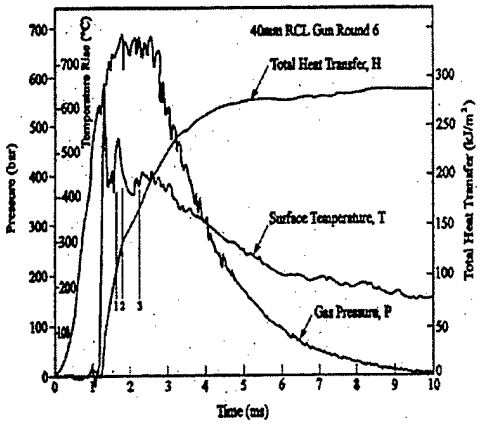

Fig 2b. Wall Temperature, Heat Transfer & Pressure vs Time. (Due to Prof. Bryan Lawton

PROBLEM DESCRIPTION

Underlying effects of blow-by flow on the cannon wear and erosion can be studied, as with other modeling solutions, by examining the fundamental gas dynamic equations. For a viscous, compressible, and reacting propellant gas, the Navier-Stokes equations and constitutive laws provide the basis for solution. To ease the computational burden, and because the heat transfer gradients, $-\nabla\bullet(k\nabla T)$, are critical at the wall, subsets of these equations have traditionally been used to model only the viscous boundary layer at the barrel wall. These models [4, 6] are evolving. At first, these account for equilibrium reacting gases in the turbulent wake of the projectile, presently including finite rate chemistry, and eventually (when present work warrants) incorporating blow-by in a composite interior ballistics code. Contrasting the wake boundary layer approach, the present work seeks to understand the baseline core flow, which can be validated by controlled laboratory measurements, and which can serve to guide experiments both in the laboratory and in the field, thus aiming to reduce the cost of field experimentation. The present solution set is thus the full set of flow equations for the perfect gas to be used as control medium. These are the well-known conservation laws for mass, momentum and energy [12], respectively,

$$\rho_{,t} + (\rho u_i)_{,i} = 0 \tag{1}$$

$$\rho(u_{j,t} + u_i u_{j,i}) - \sigma_{ij,i} = 0 \tag{2}$$

$$\rho(e_{,t} + u_i e_{,i}) - \sigma_{ij} u_{j,i} + Q_{i,i} = 0, \tag{3}$$

where the comma notation denotes partial differentiation with respect to time and with respect to spatial derivatives of the density, ρ, velocity components, u_i, deviatoric-pressure tensor, σ_{ij}, specific internal energy, e, and components of the heat flux vector, Q_i. (i = 1, 2, and

3 for three-dimensional flow.) In the NPARC [13] code formulation, the equations were recast according to the Reynolds averaging procedure. The averaged variables then define the solution in terms of the state vector, $\mathbf{q} = \mathbf{q}(\rho, m_i, E)^T$, consisting of up to five components when the flow is three dimensional. In the present, axisymmetric study, the solution four-state vector obtains two momenta, $m_i = \rho u_i$ (i = 1,2). The total energy density obtained is given by

$$E = p/(\gamma - 1) + m_i m_i/2\rho \tag{4}$$

for the perfect gas, $\gamma = 1.25$, considered.

We provide results of numerical solutions to the conservation equations of gas dynamics applied to the problem of blow-by flow. The asymptotic steady-state solution obtains viscous and pressure stresses on the projectile. This allows calculation of drag and side forces that can destabilize the projectile. The temperature field and local transient heat transfer rates on the tube and projectile surfaces are obtained as by-products of that solution. We use the NPARC code, Version 2.2, which simulates perfect gas flows by solving the Navier-Stokes equations. The code was tailored for the blow-by problem and is implemented on the SGI Power Challenge and Origin 2000 computers at the Benét Laboratories, USARDEC. The code also operates on the IBM SP2 at the Rensselaer Polytechnic Institute, where it was used in the initial stages of this Computational Fluid Dynamics project [14]. The present CFD assumes a hot propellant gas, defined by the specific heat ratio, $\gamma = 1.25$, for the burned solid propellant in the gun chamber. That value was assumed constant, but may be varied as a function of the bore average gas temperature, T, and projectile base pressure, P_b, assumed as equilibrium values. The inflow boundary conditions were taken at travel points 2.212 and 5.256 m on the ballistic base pressure curve obtained from the IBHVG2, interior ballistics code [15], Fig 3. Outflow conditions were calculated to account for the precursor shock wave.

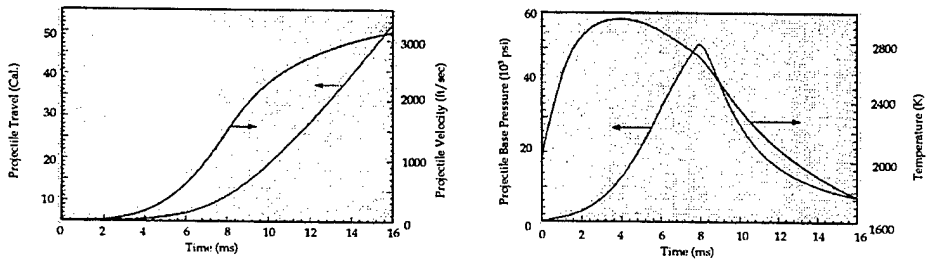

Figure 3. Simulation of Inflow Boundary Conditions for M549A1/XM230/Zone 6, using the IBHVG Code

National Project for Applications-oriented Research in CFD (NPARC). The NPARC flow solver, Versions 2.2 - 3.1, were developed by the NPARC Alliance, a joint NASA and U.S. Air Force (Arnold Engineering Development Center) effort to produce a flow simulation code for problems in internal propulsion gas dynamics [13, 16]:

The time-dependent, compressible, Navier-Stokes flow equations were formulated in the divergence form which include the perfect gas equation. The numerical code was built upon the Beam-Warming algorithm [17] which uses a Taylor series linearization of the governing equations and an approximate factorization to decouple the spatial directions. The code is a finite-volume scheme, second-order accurate in space and first-order in time. Second and fourth order artificial viscosity terms are employed to reduce dispersive oscillations that can appear downstream of shock waves and contact surfaces. We calculate the Reynolds number to be about 10^6 with respect to gap height, choked flow conditions, and Sutherland's law of viscosity for the propellant gas, given the initial viscosity computed with NASA's thermochemical code [18] at the interior ballistics gas state (P_b, T). Although both the laminar and several turbulent flow options are given in NPARC, we selected the laminar flow option. To decide which of these models validates the requisite certification for real-gas blow-by code, we have proposed [19] conducting pressure and thin film heat transfer measurements on a shock tunnel model of the projectile-cannon annular flow region. Thus, we apply the time-dependent NPARC solver to compute the asymptotic steady-state simulation of flow in the narrow gap between a traveling 155 mm projectile and smooth cannon bore, adjusting the flow solution to account for the relative velocity between cannon and projectile. It is important to select a set of assumptions that facilitate extension of these investigations from the present compressible, laminar, perfect gas flow to the real multi-component gas that can ablate the surface material, causing barrel erosion.

GRID/DOMAIN

The annular computational domain is described on Figure 4. Following NPARC procedure, the grid was constructed by using quadrilateral elements with their nodes regularly connected in a curvilinear coordinate system - within the solid border shown on the figure.

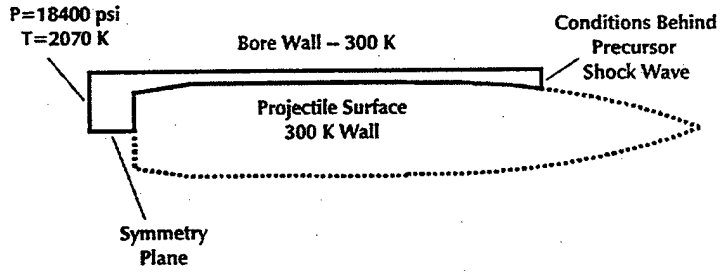

Figure 4. Boundary Conditions on Computational Domain at 2.212 m from O.R.

The blow-by simulations for projectile without obturator and band employed 110,843 nodes. That number increased to 129,492 nodes for the obturated projectile in order to maintain

accuracy in the high gradient region and to extend the domain from 1.7 to 6.7-inches upstream of the projectile base.

BOUNDARY CONDITIONS

Six boundary conditions were imposed on the flow boundaries. Common to both cases, i.e., projectile with and without obturator and band, are the symmetry axis, inflow and outflow free surfaces, with input values from Fig 3 and the shock precursor, respectively. No-slip, isothermal, boundary surfaces for viscous flow were applied at the cannon wall, the projectile base and body, with adjustments to accommodate the obturator and band geometry. Fig 4 shows the no-obturator case. The assumed blow-by gap of 0.02-inches (0.508-mm) is consistent with measured data for several 155-mm tubes [3, 19]. That gap is narrowed at the obturator to 0.006-inches (0.1524-mm).

PROCEDURE

Four flow problems were run, with and without obturator and band, for two points on the ballistic curve. After selection of the initial boundary conditions, and construction of code input in the form of a restart file, each solution was executed for several thousand time steps. Initially large maximum time step sizes and artificial viscosity were used to allow the incremental limit on flow values to limit the time step size. This procedure allowed the solution to develop from the initial restart through several restarts to a form that resembles the final steady-state result. Visualization of these results were obtained with the NASA postprocessor, FAST [20]; but convergence is usually assured by running subsequent restarts with decreasing time step size limits to values small enough that the maximum percentage change in pressure or density is less than the maximum allowed value (about 10%) and that the total residual is decreasing. However, solution convergence was interrupted by large increases in the total residual when the relative velocity between projectile and tube wall was introduced, thus requiring several tens of thousands of time steps for as much as 30 restarts before the acceptable (steady-state) convergence criteria were achieved.

POSTPROCESS

To postprocess and visualize results in a current restart file, the required grid and solution output files are suitably formatted for FAST (Flow Analysis Software Toolkit) by executing the restart operation file given in the NPARC source directory.

RESULTS

Figure 5 is a composite of numerical simulation results visualized by FAST for the blow-by flow field at the 5.256-m ballistics travel point of Fig 3. The total gap height for the annular flow region between cannon and projectile is 0.020-inches (0.5080-mm). The obturator protrudes 70% into that gap. The color bars indicate the range of values obtained by the solver, normalized to the reference values. The maximum pressure in the field is the solid color aft of the projectile, representing boundary condition, P_b = 10,250 psi, in a reservoir that extends 6.7-inches aft of the projectile base. The other flow quantities pictured show compressibility effects at the base. Flow expansion over the ogive cools the gas rapidly to the isothermal value, T = 300 K, on the surface; but at the image resolution of Fig 5, the solution gas state (p, ρ, T) appears indistinguishable from that which was imparted by the precursor shock wave. Magnifications of the axial velocity confirmed the boundary no-slip condition for viscous flow. Nearly equal magnifications of the pressure field, Fig 6, show a shock expansion on the corner of the obturator (Fig 6a) with pressure exceeding the reservoir value on the cannon wall.

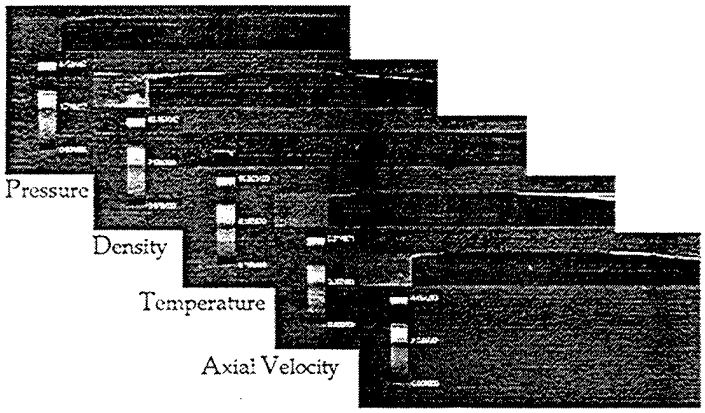

Figure 5. Composite Blow-By Flow Field, M549A1 Projectile at 5.256 m from the O.R.; 0.02 inch (0.508 mm) gap height.

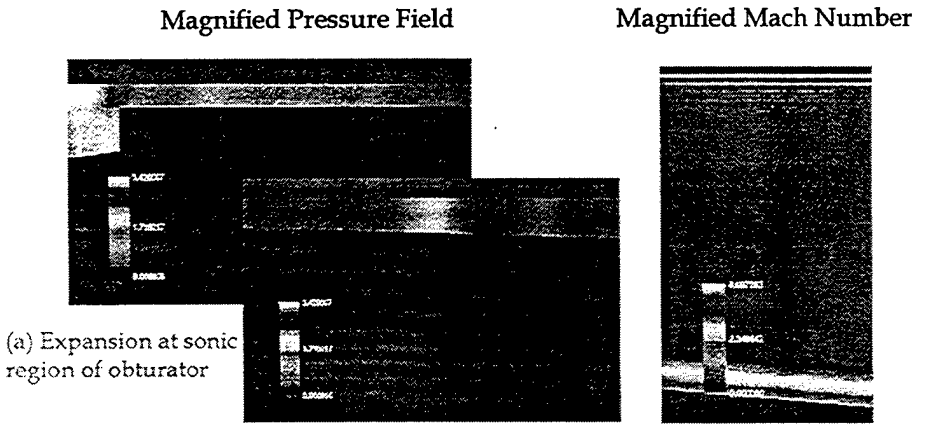

Figure 6. Magnified Pressure and Mach Number Fields Indicating Shock Structures Over Projectile at 5.256 m

Downstream there are subsequent expansion and compression waves, first over the obturator, then further downstream over the rotating band, Fig 6b. The Mach number color bar on Fig 6c indicates that maximum flow velocities over the ogive are nearly five times the sound speed at maximum expansion. Such speeds are expected because propellant gases *subsequently* exit the muzzle much faster than the projectile, expanding about the boattail as in the case of the M16 muzzle flow field, Fig 1 and Ref 1.

CONCLUSIONS

Figure 7 presents pressure distributions on the projectile, for the case of no-obturator or band, at ballistic travel points: (a) 2.212 m, and (b) 5.256 m. Approximate integration of the distribution (b) over the projected lateral surface of the projectile gives an estimated side force of 500 tons through the projectile center of pressure as it enters the brake section of the tube. In a yawed attitude, such forces become unbalanced and effect inertial instabilities on the projectile which contribute to balloting and mechanical wear of the tube.

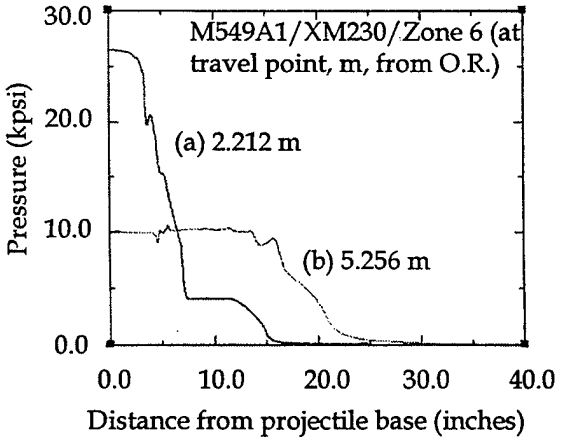

Figure 7. Pressure Distribution on the Projectile; no obturator nor band; (a) Proj at 2.212 m, (b) at 5.256 m

For a projectile with obturator and band, Figure 8 gives the local heat transfer flux to the barrel wall, relative to the wall heat flux in the boundary layer 6.7-inches upstream of the projectile base. This ratio peaked at 2040 for the projectile at 2.212 m from the O.R. and dropped more than an order of magnitude for the projectile at 5.256 m from the O.R. Although the larger peak might seem to be more accurate because convergence was carried out to 30 restarts, the low peak solution was converged with the 18th restart file. Given these results, the explanation is that the temperature gradient is dropping off faster than total enthalpy does as the projectile approaches the muzzle. An illustration of solution convergence in terms of the heat transfer output, Fig 9, shows how the heat transfer evolves from initial restart through final restart for a projectile, without the obturator and rotating band, at the first travel point. (The x-axis coordinate is normalized by the gap height, HO = 0.020 inches.)

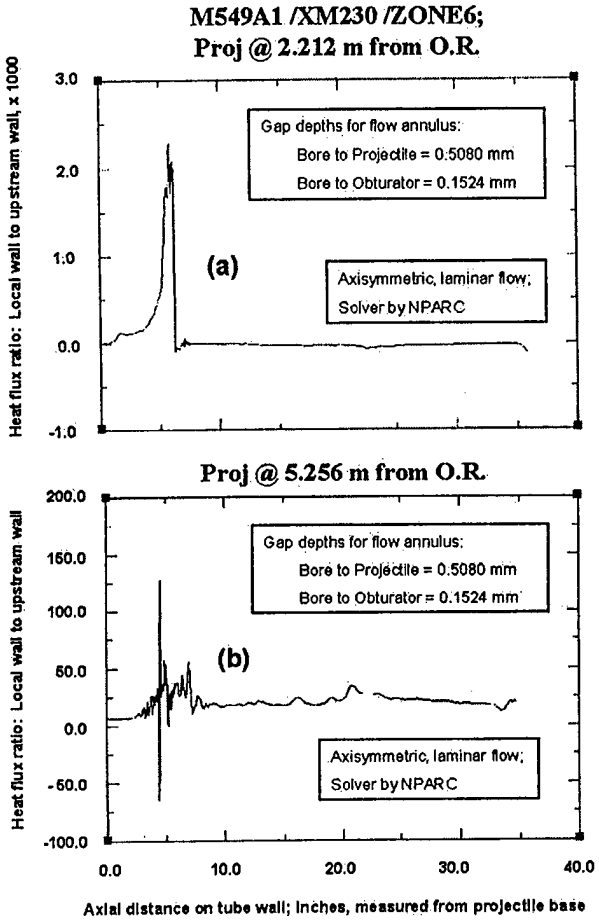

Figure 8 - Heat Transfer Stanton Number Ratio: Bore Wall to Projectile Wake Boundary Layer (a) Proj at 2.212 m, (b) at 5.256 m.

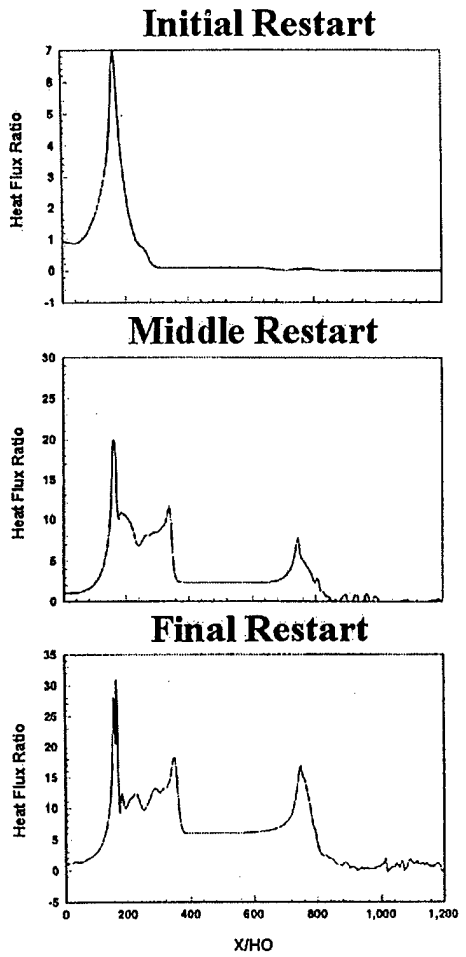

Figure 9 - Illustration of Convergence on Heat Transfer Calculation. Projectile at 2.212 m from O.R.

Another illustration is important: Results are presented at two points on the ballistics trajectory, 2.212 and 5.256 meters from the rifle origin. Local heat transfer to the barrel wall is obtained for projectiles with and without obturator and band. At the 2.212 meter location, the latter (Fig 9) yielded maximum local heat transfer rates on the barrel surface that exceed 30 times the heat transfer computed 1.7-inches upstream of the projectile's base, i.e., in the projectile's wake boundary layer. With the obturator and band, and at the same travel point (Fig 8a), the heat transfer ratio peaked at 2040, normalized to the wake heat transfer computed at 6.7-inches upstream of the projectile's base. Other than the expectation of much higher temperature gradients, obtained with the much smaller gap for the obturator and band, the normalizing factor was obtained further upstream of the base where the wake has thinned out and the heat transfer is less. Hence these two results cannot be used for comparison.

Nominal heat transfer results from these computations, not included in an interim report [21], were calculated for the two points on the ballistics trajectory, as follows: The tube wall Stanton Number ratios, $C_h = T_{,y}(HO)/P_rR_e(T_w - T_{Ref})$, averaged over the length of the projectile, are 10 and 15 respectively, for the travel points 2.212 and 5.256 meters. These ratios represent the tube wall heat flux rate in the blow-by gap, compared to that aft of the projectile where film coefficients are determined by ballistics. Given these coefficients [22], we then determine the total conductive heat input to the cannon at the two travel points to be 10.5 and 8.8 Btu/ft^2-sec. Thus, the product of the blow-by Stanton Number ratios with the total cannon heat inputs gives 105 and 132 Btu/ft^2-sec on the tube wall in the blow-by gap.

In addition to computation of the Navier-Stokes blow-by flow solution, the overall scope of this work included computation of pressure forces and heat transfer rates on the cannon wall and projectile surfaces. Heat transfer on the projectile and its components is available from the saved data. The perfect-gas solutions reported here represent 850 CPU-hours. This work is considered baseline to the methodology that requires laboratory measurements to determine the degree of turbulence that can modify and validate predictive models of the blow-by flow. It is basis for future three-dimensional, time-dependent, models for prediction of wear and erosion of barrel surfaces effected by a balloting projectile in a multi-component gas flow that reacts with the substrate. Notwithstanding, the principal value of the present perfect gas solution to the Reynolds Averaged Navier-Stokes equations is that it provides start-up files for the more accurate model (WIND) recently installed at Benét. WIND, the upgrade to NPARC, includes developer model templates that allow construction of source files for computation of finite rate chemical reactions in the gas phase.

RECOMMENDATIONS

The effect of blow-by flow heat transfer on tube erosion is a factor that is not well understood. Extension of the present work can provide a basis for further understanding the combined effects of abrasive and chemical erosion.

The extension of this work for time-dependency, for 3-D, and including finite rate chemistry, is estimated at 4500 CPU-hours (one Origin 2000 processor) and is best performed at High Performance Computing facilities to take full advantage of the speed-up offered by parallelization techniques. New versions of NPARC, will treat reacting gas flows. Chemical reactions require a set of diffusion equations, for the production and annihilation of each species considered, in addition to equations (1) - (3) listed above. The NPARC Alliance has developed a new solver code from the full set of equations for finite-rate chemically reacting flows, called WIND. Benét recommends its eventual use for subsequent blow-by flow CFD, or for an erosion model CFD validation task in which Picatinny's Vented Combustor would provide the experimental platform.

ACKNOWLEDGEMENTS

The author hereby expresses his gratitude to members of the Tube Wear Working Group at the Benet Laboratories, particularly Drs. Ron Gast, John Santini; Messrs. Tony Gabrielle, Rick Hasenbein, Russ Fiscella (Director, Benét Laboratories); Mr. Kok Chung, Picatinny Arsenal, and Emeritus Research Prof. Henry T. Nagamatsu, Rensselaer Polytechnic Institute, for giving their support and critique. Special thanks is given to Ms. Barbara Cunningham, Benét Laboratories, and to Dr. Donald G. Messitt, Rensselaer Polytechnic Institute, who assisted with their considerable computational skills.

REFERENCES

1. Schmidt, E.M., and Shear, D.D., "Optical Measurements of Muzzle Blast," J. AIAA, v.13 (8) p. 1086-1091, August, 1975.

2. Schmidt. E.M., Figure 1 is from a set contributed by Ed Schmidt (BRL, 1984).

3. Hasenbein, R.G., "BACK TO THE FUTURE: A Twenty Year Perspective on Artillery Wear & Erosion," Proc. of the Sagamore Workshop on Gun Barrel Wear & Erosion, Sponsored by the U.S Army Research Laboratory, July 1996; see also "155MM XM198 Howitzer Muzzle Wear," Report WVT-TR-75024, Benét Laboratories, Watervliet Arsenal, NY, 1975.

4. Sopok, S., Pflegl, G., O'Hara, P., Dunn, S. and Coats, D., "Thermochemical Erosion Modeling of Original M242/M919 Gun System," Benét Laboratories Report ARCCB-TR-97005 (ADA323941), Watervliet Arsenal, NY, 1997.

5. Seiler, F., Zimmermann, K., Raupp, J., and Zettler, G., "Bore Erosion and Heat Transfer Measurements in 20 and 60-mm-Caliber Compared With Predictions of Model Calculations," ARCCB-SP-96032, Proc. Of the 8th U.S. Army Symposium on Gun Dynamics, Newport, RI, 14-16 May 1996.

6. Conroy, P.J., Weinacht, P., & Nusca, M.J.,"ARL Tube Erosion Code (ATEC)," Proc. of the 32nd JANNAF Combustion Subcommittee Meeting, Huntsville, June 1995; see also "Surface Chemistry Effects on High Performance Tank Ammunition," loc. Cit., ARCCB-SP-96032 (Ed. Pflegl, G., Benet Laboratories, Watervliet NY) 14-16 May 1996.

7. Lawton, B., "Heat Transfer and Erosion in Gun Barrels," Royal Military College of Science, Cranfield U., U.K., June 1994.

8. Hasenbein, R.G., "Analysis of Wear Data for the 155MM XM198," Benét Laboratories Report WVT-TR-75023, Watervliet NY, May 1975.

9. Ahmad, I., "The Problem of Gun Barrel Erosion: An Overview," in Gun Propulsion Technology, Ed. Ludwig Stiefel, Vol. 109, American Association of Aeronautics and Astronautics Series, 1984.

10. Buckingham, A.C. "Modeling Additive and Hostile Particulate Influences in Gun Combustion Turbulent Erosion," Lawrence Livermore Laboratory Report UCRL-82756, 27 September 1979.

11. Lawton, B. and M.P.B. Laird, "Influence of Gas Leakage on Heat Transfer and Wear in Gun Barrels," Royal Military College of Science, U.K., Proc. 16th International Ballistics Symposium and Exhibition, S.F., CA, 23-27 Sept 1996.

12. Thompson, P.A., "Compressible-Fluid Dynamics," McGraw-Hill, 1972.

13. Sirbaugh, J.R., Cooper, G.K., Smith, C.F., Jones, R.R., Towne, C.E., & Power, G.D., "A User's Guide to NPARC, Versions 2 and 3," Arnold Engineering Development Center, Internet home page at < http://info.arnold.af.mil/nparc/index.html >, November., 1994.

14. Messitt, D.G., Nagamatsu, H.T. and Myrabo, L.N., "Numerical Simulation of High Pressure, High Temperature Flow Through Bore Evacuator Seals and Blowby Past Projectiles," Dept. of Mechanical, Aeronautical Engineering and Mechanics, Rensselaer Polytechnic Institute, Final Report for Army Contract DAAA22-96-M-0570, December 1996.

15. Anderson, R.D. and Fickie, K.D., "IBHVG2-A User's Guide," Army Research Laboratory Report ARBRL-TR-2829, Aberdeen Proving Ground MD, 1987.

16. Messitt, D.G., "Computational and Experimental Investigation of 2- and 3-D Scramjet Inlets and Flow Over a Sharp Flat Plate at Mach Numbers From 10 to 25 in a Hypersonic Shock Tunnel," Rensselaer Polytechnic Institute , Ph.D. Thesis, December 1998.

17. Beam, R.M., and Warming, R.F., "An Implicit Finite-Difference Algorithm for Hyperbolic Systems in Conservation-Law Form," Journal of Computational Physics, Vol. 22, No. 1, p. 87-110, September 1976.

18. Gordon, S., & McBride, B.J., "Computer Program for Calculation of Complex Chemical Equilibrium Compositions and Applications," I. Analysis, NASA Reference Publication 1311, October 1994.

19. Andrade, C.A., Nagamatsu, H.T., Messitt, D.G., and Myrabo, L.N., "Shock Tube Investigation of Bore Surface Heating and Related Erosion Chemistry in the Blow-by Region," loc. Cit., Proc. of the Sagamore Workshop on Gun Barrel Wear & Erosion, July 29-31, 1996.

20. Walatka, P.P., Clucas, J., McCabe, R.K., Plessel, T., and Potter, R., "FAST User's Guide," NASA Ames Research Center, October, 1993.

21. Andrade, C.A., Cunningham, B., Nagamatsu, H.T., and Messitt, D.G., "The Cannon-Projectile Blow-By Flow Field," Benét Laboratories Technical Report ARCCB-TR-98017, Watervliet NY, 12189-4050, September 1998.

22. Witherell, M., Benét Laboratories, Personal Communication.

Electrothermal-Chemial (ETC) Gun Propulsion Advantages and Technical Status

William Oberle, Gary Katulka, and Gloria Wren
US Army Research Laboratory, Weapons and Materials Research Directorate
Aberdeen Proving Ground, MD 21005-5066

Bradley Goodell, and Jahn Dyvik
United Defense, L.P., ASD, 4800 East River Road, Minneapolis, MN 55421-1498 (USA)

The objective of this paper is to review the status of utilizing electrothermal-chemical (ETC) armament systems on U. S. Army weapon platforms. Toward this end, systems issues associated with the weaponization and integration of electrothermal-chemical (ETC) based guns into weapon platforms will be discussed. Next, recent ETC test data applicable to future Army direct (tank) and indirect fire (artillery) weapon systems will be presented. Finally, discussions concerning the potential application of ETC technology in the medium caliber arena will be provided.

INTRODUCTION

At the present time, electrothermal-chemical (ETC) gun technology attempts to utilize electrical energy in the form of a plasma to augment and control the release of chemical energy stored in propellants in order to achieve significant performance enhancements using existing conventional guns. The propellants being used are existing solids, developmental solids, and experimental hybrid solid/liquid slurries. The performance enhancing benefits provided by an ETC gun system are: improved accuracy/hit probability with precise ignition timing; maximum performance at all temperature conditions with temperature compensation; increased lethality and range with higher muzzle velocities; soft launch of g-sensitive munitions; and hypervelocity potential.

A schematic of a generic ETC gun is shown in Fig 1. The three major subsystems are (1) the pulse power system, consisting of energy storage devices such as batteries or flywheels; power condition devices such as converters, alternator rectifiers, or pulsed alternators; and power compression devices such as capacitive based pulse forming networks (PFN), or pulsed alternators; (2) the ammunition which includes the launch package, propellant and the plasma generator (located either in the cartridge case or the breech); and (3) the cannon, inclusive of gun barrel, breech, and power connection.

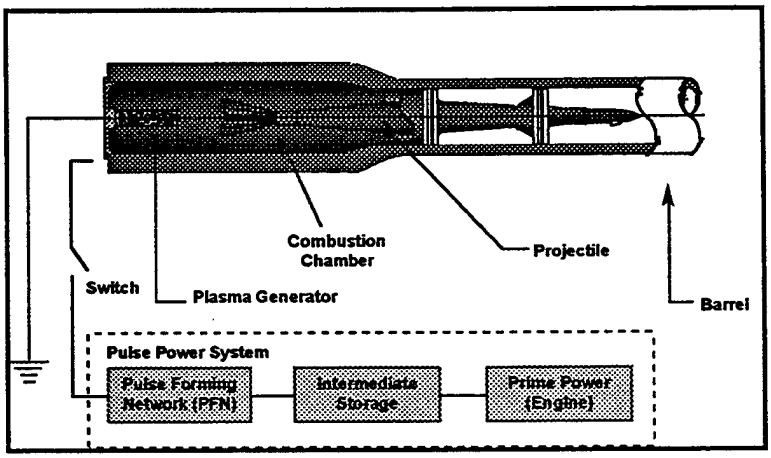

Figure 1. Schematic ETC Gun.

Although many specific ETC configurations have been proposed, generally the ETC interior ballistic (IB) process is initiated by a high electrical current discharge from the PFN into the plasma generator which causes vaporization and subsequent ionization of fuse material associated with the plasma generator. As the high electrical current continues to be discharged from the PFN, the plasma generator converts the electrical energy to thermal energy with both radiative and convective components. In theory, controlling the electrical energy discharge, and subsequent conversion to thermal energy, results in the tailoring of the IB pressure profile to achieve enhanced gun performance.

The objective of this paper is to review the status of utilizing electrothermal-chemical (ETC) armament systems on U. S. Army weapon platforms. First, systems issues associated with the weaponization and integration of electrothermal-chemical (ETC) based guns into weapon platforms will be discussed. Next, recent ETC test data applicable to future Army direct (tank) and indirect fire (artillery) weapon systems will be presented. Finally, the paper concludes with a discussion concerning the potential application of ETC technology in the medium caliber arena.

SYSTEMS ISSUES

The development of ETC technology and pulse power began before the fall of the Iron Curtain and the demise of what was then known as the Soviet Union. When that development began, ETC was looked upon primarily as a means of getting more performance out of large caliber cannon systems that were physically approaching the limits of what could be put inside a tank and still be protected. In more recent years, the Army and others have been conducting experiments and war gaming exercises, like Force XXI and Army After Next (AAN) to determine what capabilities will be needed on the 21st Century battlefield. The results emerging from these war games and experiments have lead to the postulation of vehicle concepts that are significantly smaller and lighter than their predecessors. Of concern, to those who have to develop the technologies and systems to implement these changes, is that many of these vehicles are also postulated to be more lethal, more mobile and more survivable than their predecessors. While down sizing alone will be challenging enough, the implementation of greater capabilities will make it even more so.

To put this challenge in perspective, consider the current main battle tank. The M1 Abrams weighs approximately 70 tons, achieves 48 km/hr cross-country speed and is equipped with a 120 mm cannon and 40 rounds of ammunition. Initial war-gaming efforts postulated that the next new tank-like vehicle would have to weigh on the order of 40 tons, travel at speeds in excess of 96 km/hr as well as preserve significant other combat capabilities including a more lethal cannon and at least as much ammunition. Still more recently, additional results emerging from studies such as AAN postulate combat vehicles that are even lighter weighing in at 15-20 tons.

Without knowing what the specific functionality or mission equipment is, or what capabilities it might possess, the magnitude of the down sizing trend and the potential implications can be illustrated, see Fig 2. Mission equipment is defined as the main armament (or equivalent), survivability, C4I and other mission unique equipment that is required to perform the combat mission of the vehicle. It can be thought of as that combination of equipment that makes one vehicle a tank, another a scout vehicle and another a howitzer. Mission equipment also includes any plus-ups in the basic crew, prime power, mobility platform structure etc. that is required to accommodate the unique performance requirements of the mission equipment. The technology assumed for the suspension, and vehicle structure are in general the current state-of-the-art technologies for tracked vehicles. For the power train, the Blue Ribbon Committee [1] sizing estimates for an advanced diesel technology were used. The data shown in this figure are still preliminary, but are sufficiently accurate to show the scale of the problem.

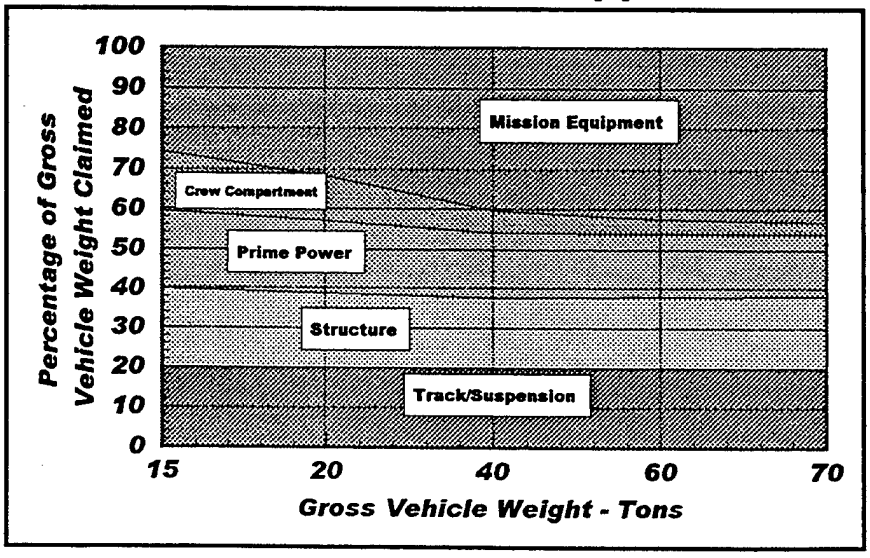

Figure 2. Percentage Weight Fractions For All Sub-systems.

As can be seen from Fig 2, the track/suspension, the hull structure and prime power scale almost directly with GVW, though the latter two, hull structure and prime power become a slightly larger percentage with lower weights. Because the crew and the number of crew does not change, the weight and volume remain constant and become an ever larger percentage of the whole. The net result is that the residual weight remaining for mission equipment is a significantly lower percentage as a fraction of the total vehicle. A similar effect would be observed for volume as well. The questions for ETC technology is whether the reduced weights and volumes are compatible with the requirements of the ETC weapons system (gun, mount, recoil, pulsed power systems, etc.) needed to meet the desired enhanced lethality.

ETC Integration Considerations

Integration and weaponization of ETC and pulse power systems into combat vehicle systems is well within the state-of-the-art of the technologies currently being developed and those that are expected to be developed in the near future. However, the integration of ETC is not just simply a matter of fitting the "biggest" gun and pulse power system into the available space and weight allowances. Successful integration of ETC will involve the consideration of many issues, some seemingly unrelated but nevertheless real, and require that many difficult choices be made in the course of successfully developing a balanced system design. The successful system will have a "balance" of capabilities that matches it's lethality with it's mobility, survivability, etc.

In general, the issues and concerns that need to be considered fall into three principal areas. While, closely related, it is useful to think about and consider each area separately in order to avoid misunderstandings, unrealistic expectations and to fully exploit the maximum potential offered by this, or any other technology for that matter. The three areas to consider are: (1) Matching expectations to evolving combat vehicle trends, (2) Sizing the weapon and pulse power systems for a balanced system design and (3) Weaponizing ETC & pulse power technology

Matching Expectations: In the first area, the issue of matching expectations to evolving vehicle trends can be captured in the idea of "right sizing" or the matching of the weapon and pulse power systems to be commensurate with the overall capacity and capabilities of the vehicle on which it is integrated. Driven by economic and strategic deployability needs, the trend is toward significantly smaller combat vehicles. The concern is whether the expectations for the performance of the technologies that are to be integrated are being adjusted accordingly. What levels are ETC and other advanced technologies expected to support? What performance levels can they support? It would be unrealistic to expect that the launch energies would be the same as what it might have been installed on today's 70 ton legacy vehicles. There is a reason why 16 inch guns are not installed on destroyers and it holds true on ground combat vehicles. To illustrate consider Fig 3, where the allowable minimum vehicle weight as a function of cannon bore and muzzle brake efficiency is plotted. [2]

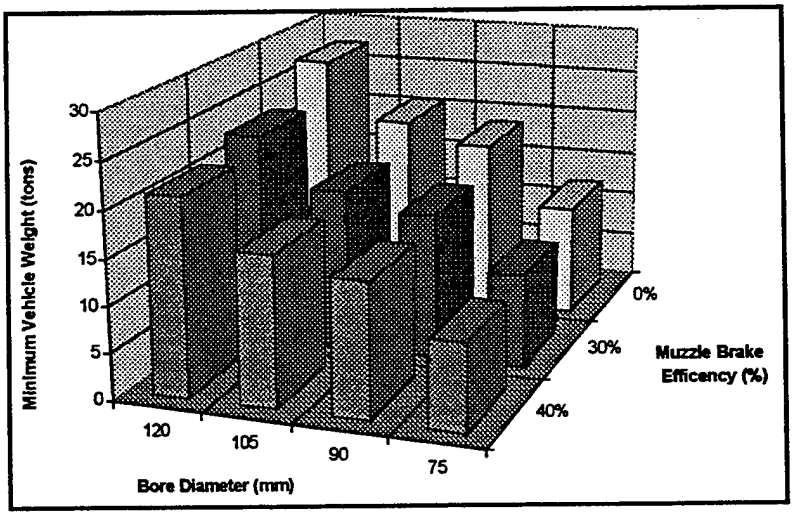

Figure 3. Minimum Allowable Vehicle Weight.

Sizing the Weapon: The second set of issues is associated with the sizing of the weapon and pulse power systems. They are also closely related and inseparable from the "right-sizing" concerns, but these revolve around

the balancing and trade off of performance related capabilities both within the armament system and within the overall vehicle system. It is not enough to be in the right ball park, the weapons system must also be a part of the system in which it is integrated. In these tradeoffs, the warfighting benefits provided by the weapons systems is balanced with those provided by survivability, mobility and other system capabilities. The exploitation of synergism between the various sub-systems in the tradeoffs will be critical. For ETC and its pulse power system, one such synergistic technology is Hybrid Electric Drive and the development of an all electric vehicle architecture. Such an architecture is being developed under the Defense Advanced Research Projects Agency (DARPA) Combat Hybrid Power Systems (CHPS) program. This architecture is shown in block diagram form in Fig 4.

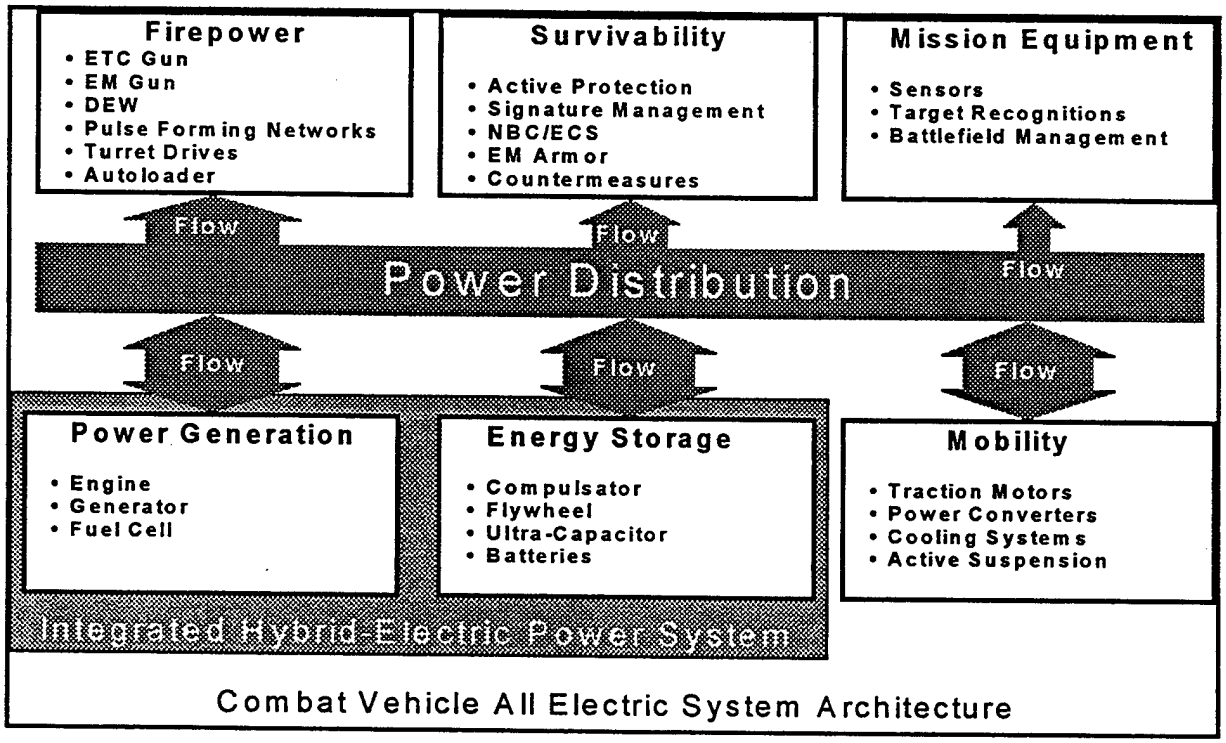

Figure 4. Combat Vehicle All Electric System Architecture

Weaponization of ETC: The third area of consideration is the weaponization of ETC and pulse power technology. Even assuming that the ETC and pulse power weapons system has been diligently "right sized" and balanced for the objective capabilities that are targeted, weaponization is not yet done. ETC and pulse power will still have to be useable and operable by normal, everyday soldiers under the pace and tempo of future battlefield conditions. For ETC and pulse power, the principal weaponization issues revolve around the following areas: (1) Ruggedization and Other Weaponization Issues, (2) Operator and Maintainer Safety, (3) Managing Failure Modes and Graceful Degradation, and (4) Accomplishing Battle Damage & Repair. While these issues are not trivial, they are not insoluble if dealt with early in the development and weaponization effort and from a system perspective. ETC is amenable to providing satisfactory weaponization solutions that should be as good or better than those employed for conventional armament technology. Similarly the energy and power levels used in the pulse power system have a long history of safe and reliable operation in commercial power and industrial applications. That experience needs to be translated into the combat vehicle environment so that the soldier usability, safety, maintainability are as good as they need to be to meet the needs of the future battlefield.

DIRECT FIRE APPLICATIONS

Under the EEF Follow-on Program, funded by the U.S. Army Research Laboratory, a series of 120-mm test firings have recently been conducted in order to demonstrate particular advantages of ETC propulsion concepts.

Dual Ignition

The 120mm ETC gun fixture used in these firings is a smooth bore M256 cannon with an overall projectile travel length of 4.75 meters (39 calibers). Fig 5 shows the gun, mount, and breech assembly. Two separate breech blocks were used to support both conventional and ETC firings modes (Fig 6). The conventional tests were fired with the standard breech block. The ETC tests were fired with a modified breech block, Fig 6 on the right, that allowed a coaxial power connection to transfer power through the block to the plasma injector. It has been demonstrated, however, that both ETC and conventional firings can be conducted using only the modified breech block. The conventional firings require a small ignition pulse to initiate the conventional primer. This can be accomplished with the PFN trigger generator and the ETC power connection with no impact on the conventional performance.

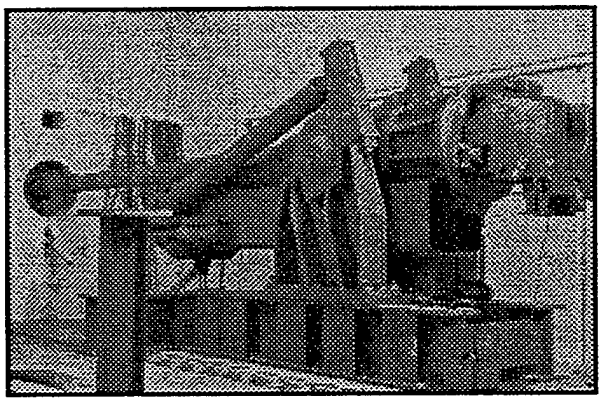

Figure 5. EEF Follow-on 120mm Gun Fixture.

Precision Ignition

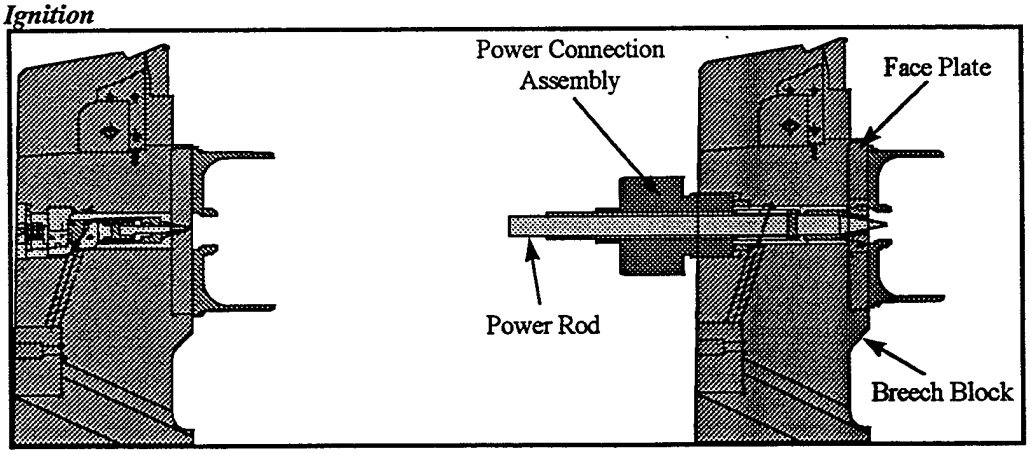

Figure 6. EEF Modified Breech Block, Conventional (Left), ETC (Right).

The main objective of the precision ignition gun study was to demonstrate that variations in conventional large-caliber gun ignition delays can be minimized using the ETC ignition design. As reported at the 16th International Ballistics Symposium and Exhibition [3], it has been demonstrated that large-caliber (120-mm) ETC tank gun firings produced significantly (factor of 25-75) reduced propellant ignition time variability in comparison to conventionally ignited rounds. Simulations indicate that this improvement in ignition time variability could provide a greater than 10% increase in accuracy.

Temperature Compensation

The purpose of the temperature compensation effort was to demonstrate that the ETC ignition process can compensate for the varying velocity of 120-mm tank rounds at different temperatures. The intent was to show that by adjusting the profile of the electrical energy deposition, both spatially and temporally, the combustion process can be controlled in such a way as to produce hot round performance over a wide range of preconditioned round temperatures. Typically, a conventionally ignited round will perform differently at varying temperatures. Cold rounds tend to produce lower peak pressures and lower velocities while hot rounds usually give higher pressures

and velocities. The ability to boost performance of colder rounds to match that of a hot round means that mission effectiveness can be maintained at its highest level at all temperatures. Operating at the hot round performance level for any given temperature means that most current firing scenarios could be improved by increasing lethality and range. The temperature compensation test program was divided into two phases using the two different 120mm rounds, DM13 and M829A2.

Phase 1: First, a series of tests was conducted using the German DM13 (7 perf JA2) 120-mm round. Conventional tests used the standard configuration with the M125 primer. The ETC tests used a modified DM13 round that replaced the M125 primer with a piccolo style plasma igniter. Fig 7 shows the conventional performance levels along with the levels of performance achievable with ETC ignition. An electrical power pulse (pulse A), delivering 580 kJ, brought an ambient round up to the hot round level of performance. Cold rounds required a nominal electrical energy transfer of 650 kJ to achieve hot round performance. Note that for this particular configuration, similar pulses produced greater enhancement in the colder rounds as shown by the shots using pulse A and pulse B (Fig 7). Pulse A gave a 53 m/s increase in a cold round and only a 14 m/s increase in the ambient round. Pulse B produced a 14 m/s increase in the ambient round and a 6 m/s increase in the hot round. Finally, temperature compensation in the DM13 is reproducible as demonstrated by a ten shot repeatability series at 0 C with a muzzle velocity standard deviation of 0.49% of the mean. In addition, this approach to temperature compensation proved to "fail-safe" in that using the 650 kJ pulse with a round conditioned to 52 C (hot) did not result in an over pressurization of the gun.

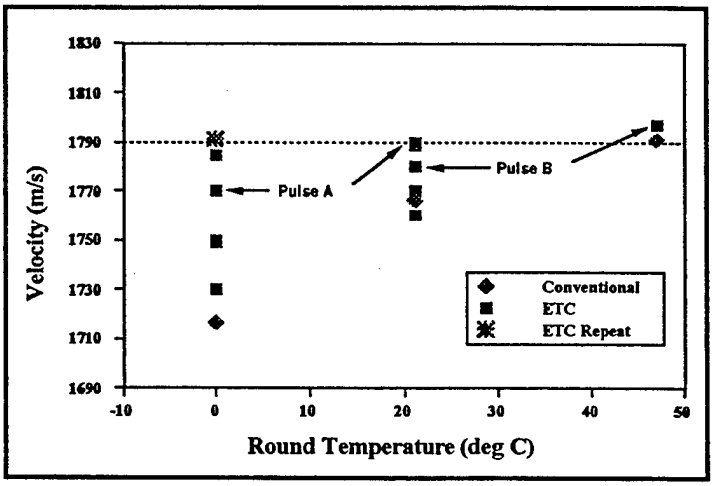

Figure 7. DM13 Temperature Compensation Results.

Phase 2: The second temperature compensation test sequence was conducted using the M829A2 slug round with similar results to Phase 1. Approximately 500 kJ of electrical energy was required to bring conditioned cold rounds to hot performance.

INDIRECT FIRE APPLICATIONS

ETC technology can offer several potential performance enhancements for indirect fire applications. These improvements are in the areas of precision ignition and shorter ignition time delays, low-zone performance enhancement through minimized residue and sticker, center-core simultaneous ignition at all zones, better overlaps among various zones (improved MRSI), and increased range at all zones in combination with advanced high energy propellants.

Precise Ignition

ETC offers the same advantage in the indirect fire as demonstrated in the direct fire application by providing precise time of ignition in all the firings, and reducing the time delay to ignition. Unlike other ignition mechanisms that take in the order of 40-50 ms from the time of fire to the start of the pressurization in the chamber, it has been demonstrated that ETC would reduce that time to 2-10 ms depending on the amount of electrical energy input to the ignitor. It also ignites the charge at exactly the same time from shot to shot as opposed to conventional ignitors with varying time delays. This precise ignition would support consistent shot start condition and minimizes variation in muzzle velocity, resulting in improved accuracy.

Low-Zones Enhancement

The common problems of residue and projectile "stickers" at low zones in the artillery systems can be improved using ETC technology. These problems are generally associated with using large-web grains in gun chambers with a large fraction of ullage. The energy and properties associated with the plasma and the effects it has on the propellant burning rate needs to be investigated further and used properly to help minimize the residues from unburned propellant and combustible case, and improve the acceleration profile along the travel at these low zones.

Center-Core Ignition

The plasmas generated from ETC ignitors have been shown to have velocities between 1500-2000 m/s in air. This high penetration velocity combined with the low-density high-temperature species content of the plasma offers an effective means of providing true center-core simultaneous ignition of the modular charges. This arrangement offers several advantages to the existing system. It eliminates the requirement of having the ignition train within the center core of the modules. These cores typically contain black powder. It also allows the cases to extend radially in size since there would be no need for leaving ullage space around the modules for flame spread, and that results in higher loading volume for propellant and therefore improved performance.

Improved MRSI

The ability of increasing the chamber pressure in the gun for a given propellant mass by dissipating electrical energy would result in improving the muzzle velocity at various zones. This effect can be used to improve the velocity overlap among different zones, and help enhancing the multiple rounds simultaneous impact (MRSI) mission. The level of electrical energy varies at various zones; expected to be higher at low zones with larger amount of ullage than at high zones. If the plasma affects the burning rate of the solid propellant, improvement in MRSI mission could be achieved with lower electrical energy as opposed to the case when electrical energy would be used as pure thermal energy to increase the gun pressure and muzzle velocity. Fig 8 shows results of calculations illustrating the projected improvement in MRSI using ETC (MACS plus Modular Disks) versus today's technology (MACs Only).

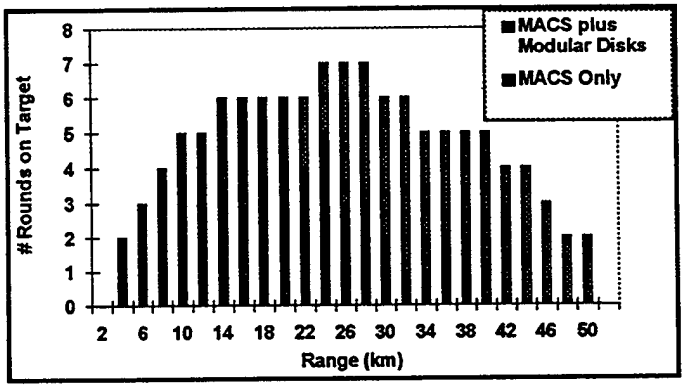

Figure 8. MRSI Mission And Range Potential.

Increased Range and Soft Launch

With the advancements in the composite propellant technology such as Thermoplastic Elastomer (TPE) propellants and geometries that support high loading densities with high level of progressivity, it is possible to achieve greater performance and range for artillery at the current gun operating pressures (35% increase demonstrated) or achieve current performance at reduced pressures to minimize g-loading on the projectile, i.e. soft launch (35% decrease in g-loading demonstrated). These high loading density propellants need to be ignited in an effective manner to ensure uniform and simultaneous ignition of the entire propellant bed. ETC ignition has been demonstrated to be a precise and efficient means of igniting such configurations.

MEDIUM CALIBER APPLICATIONS

As discussed in the previous sections, significant recent advances in ETC technology development have been made in the large caliber guns. Although 30mm testing is routine for propellant screening and development, little work has been conducted recently with testing of tactical medium caliber weapon systems. Several years ago,

researchers at United Defense conducted a limited series of ETC tests with 30mm gau-8 cartridge cases and experimental launch packages provided by Kaman Sciences. Although the tests were successful and demonstrated the potential of ETC technology as applied to the medium caliber arena, work was stopped. This decision was largely driven by the desire of the U.S. Army to focus on large caliber.

Recent studies indicate that the benefits of ETC: improved accuracy/hit probability with precise ignition timing; maximum performance at all conditions with temperature compensation; increased lethality and range with higher muzzle velocities; soft launch of g-sensitive munitions; and hyper velocity potential are all translatable to medium caliber. As discussed in previous sections, many of these benefits have already been successfully demonstrated in large caliber.

The questions that impact medium caliber ETC are largely driven by systems issues. Yes, the technology is scaleable, but what are the system benefits, given the unique nature of medium caliber weapon systems. (Their main focus is not to launch sabot rounds, or to launch heavy projectiles tens of kilometers.) United Defense and the U.S. Army have begun a cooperative investigation to answer the following questions:

- To what extent can the lethality (both penetration and behind armor effects) of a conventional round be matched or overmatched with a smaller caliber ETC round?
- To what extent will precision ignition enhance system accuracy to increase probability of hit, or to extend battlespace beyond that of conventional weapons?
- Will the enhanced accuracy provided by ETC reduce the necessary rate of fire typical of medium caliber cannons?
- What new target sets could an ETC medium caliber weapon service that a conventional system can not?
- Given a reduced number of rounds required per kill, what is the vehicle weight and volume impact of fewer required stowed rounds?
- What is the performance enhancement offered to bursting munitions provided by precise ignition timing?
- What is the lethality enhancement offered by temperature compensation?
- What are the war-fighting gains (depending on measures of effectiveness) that can be estimated in war gaming exercises?

Integration of pulse power systems into vehicle power trains poses several systems issues, but are not considered significant. As future vehicle concepts develop, the synergy provided by an all-electric vehicle will simplify integration of pulse power systems. Recent estimates by researchers at the U. S. Army Research Laboratory indicate that the size of pulse power and the required prime power are well within current vehicle envelopes.

SUMMARY

This paper has summarized efforts in ETC gun propulsion related to U. S. Army applications. Although formidable challenges remain in meeting future Army weapon platform goals in terms of weapon lethality and downsizing, the authors, as indicated by the discussions and results presented in this paper, believe that ETC technology can play an important role toward realizing these goals.

REFERENCES

1. Blue Ribbon Committee Report - *Research Needed For More Compact Intermittent Combustion Propulsion Systems For Army Combat Vehicles.* Interim Report TFLRF No. 296, by Blue Ribbon Committee, (BRC), prepared for U.S. Army Tank-automotive and Armaments Command (TACOM), U.S. Army Tank-Automotive Research, Development and Engineering Center (TARDEC), Warren, Michigan 48397-5000, Contract No. DAAK70-92-C-0059, November 1995.

2. *Technology of Tanks", Volume I,* Richard M. Ogorkiewicz, Jane's Information Group Limited, Sentinel House, 163 Brighton Road, Coulsdon, Surrey CR5 2NX, United Kingdom. ISBN 0-7106-0595-1.

3. W. F. Oberle and B. Goodell, *The Role of Electrothermal-Chemical (ETC) Gun Propulsion In Enhancing Direct Fire Gun Lethality*, Proceeding of 16th International Ballistics Symposium and Exhibition, San Francisco, CA, September 1996.

Recoil Characteristics of Electromagnetic Cannon

Edward M. Schmidt
Army Research Laboratory
Aberdeen Proving Ground, MD 21005-5066

Abstract - The recoil from an electromagnetic (EM) railgun is discussed and compared with that from conventional, propellant gas driven cannon. It is shown that, under similar launch conditions, the recoil of the EM gun is less than that of the powder gun; however, use of a muzzle brake on a powder gun can alter this relative behavior.

INTRODUCTION

Electromagnetic launchers have experienced renewed interest over the past ten to fifteen years. They have the potential to deliver both hypervelocity and hyperenergy launch while eliminating the potential hazards associated with gun propellants and reducing the size of the cartridge. The two main classes of electromagnetic launcher are the coil gun and the railgun. Within the latter, there are many configurations of rails such as simple, augmented, transaugmented, contra-augmented, etc. For the present paper, only simple railguns are considered, Fig. 1. These have two conducting rails separated by adjacent insulators that run the complete length of the launcher. The projectile is accelerated by the Lorentz Force developed from the interaction of the magnetic field (generated by current flowing up one rail and down the other) with the current passing through the armature. The Lorentz Force is expressed as $\mathbf{F_L} = q\,\mathbf{v}\times\mathbf{B}$. In the railgun, the magnitude of this force is $F_L = L'I^2/2$, where L' is the inductance gradient of the rails (typical values are 0.35 - 0.55 μH/m) and I is the current in amperes. The current is provided by a suitable pulsed power system. This could be a capacitor bank, battery-inductor array, or a rotating machine such as an homopolar generator or compulsator. Typically, L' is a constant and I varies with time depending upon the characteristics of the pulsed power system in use. Since there is current flowing in the rails which are immersed in the magnetic field of their partner, a rail repulsion force is developed which must be resisted by the structure of the launcher.

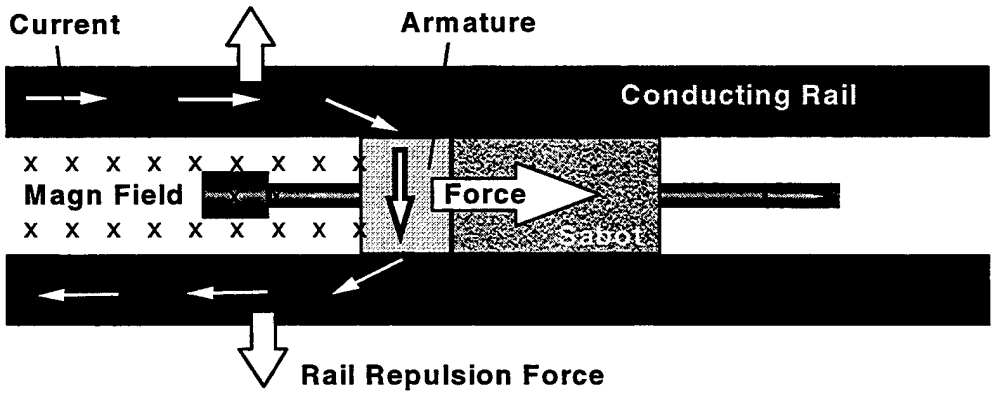

Figure 1. EM Railgun Schematic

RECOIL

With a powder gun, the accelerative force is provided by the high pressure gases generated from the propellant combustion process. Clearly, the recoil force is transmitted at the breech of a powder gun by the pressure exerted by the propellant gases. The time integral of this force is the recoil impulse and for a powder gun is equal to the momentum imparted to both the projectile and the propellant gases as they exit the muzzle.

In the case of EM, there is neither a breech nor propellant gas. As such the recoil impulse is simply equal to the momentum imparted to the projectile at shot exit, $I_t = m_p V_o$, but where is the recoil force applied? The fact that EM guns must recoil is obvious from first principles and has been measured by mounting an EM gun in a ballistic pendulum[1]. Witalis[2] postulates that the recoil force is transferred in part at the rails themselves. Marshall and Wood[3] counter that the relativistic effects Witalis claims for rail recoil are simply to small to account for the actual recoil levels. They place the recoil forces at the buswork and power supply. Clearly, the buswork connecting the power circuit to the gun experiences substantial loads as is evidenced by the frequent failure of these components in test. It would be of interest to conduct a careful experiment to define the location of the recoil force. It will be assumed in this paper that the position taken by Marshall and Wood is correct.

To make a comparison with the powder guns, their recoil impulse is estimated as the sum of the projectile momentum and powder gas momentum efflux at the weapon muzzle[4] :

$$I_t = m_p V_o + m_c (RT_o)^{1/2} (2/(\gamma+1))^{3/2} (1+(\gamma+1)m_c/(12\gamma m_p)) \quad (1)$$

$$RT_o = RT_{ad} - 0.26(1/6 + 4m_p/7m_c)V_o^2 \quad (2)$$

where m_p, m_c are the projectile and charge masses; V_o is the projectile muzzle velocity; R, γ are the gas constant and ratio of specific heat; and T_{ad}, T_o adiabatic flame temperature and average gas temperatures at shot exit. As a simple means to develop the trend in the impulse with velocity, a fit[5] to the correlation presented in Fig. 2 is used.

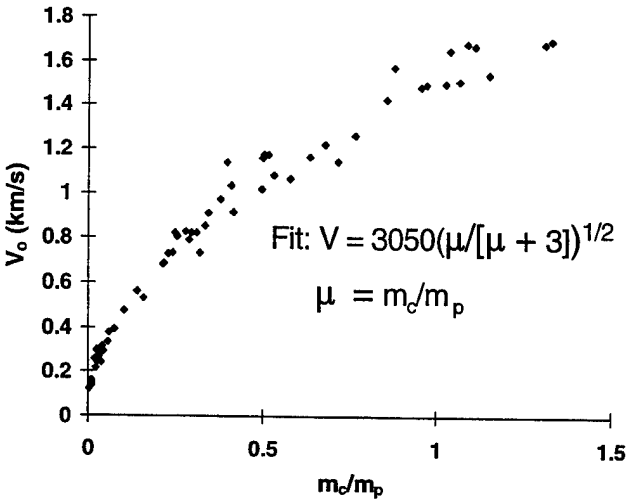

Figure 2. Velocity vs Charge to Mass Ratio for a Wide Range of Powder Guns

Using the fit above, Eq (1) and (2) are rearranged to

$$I_t/m_p = 3050\,(\mu/[\mu+3])^{1/2} + \mu(RT_o)^{1/2}\,(2/(\gamma+1))^{3/2}(1+(\gamma+1)\mu/(12\gamma) \quad (3)$$

$$RT_o = RT_{ad} - 2.4\text{x}10^6\,(1/6 + 4/7\mu)(\mu/[\mu+3]) \quad (4)$$

For a sample calculation, a 20mm cannon using WC870 propellant is assumed. For this case, γ=1.25, R=365.5 m^2/s^2K, and T_{ad}=2577 K. The variation in the impulse ratio for a powder gun is computed and compared to that for an EM gun, $I_t/m_p = V_o$, in Fig. 3. This ratio is effectively the impulse imparted for firing a constant launch mass. It can be seen that the recoil impulse of the powder and EM are quite similar at low velocities; however, beyond 1800 m/s the recoil impulse ratio for the powder gun begins to increase dramatically as the propelling charge mass grows.

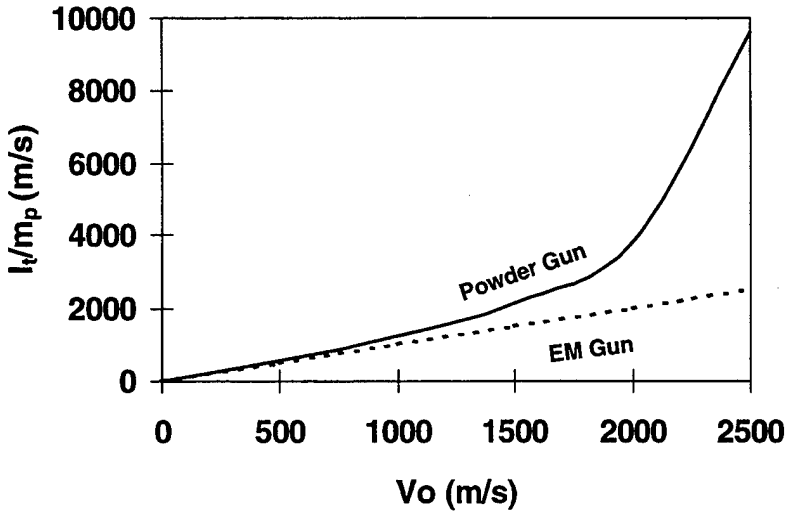

Figure 3. Impulse Ratio vs Velocity

Often, comparisons are made by assuming that the gun muzzle energy is constant across the range of launch velocities, Fig. 4. The EM gun behavior simply reflects the fact that the recoil momentum varies as the energy divided by the velocity. For the powder gun, the recoil impulse is similar to that of the EM gun until 1800 m/s where it begins to climb. However, for the constant energy case, the increase is less dramatic due to the decreasing launch and propellant masses as velocity increases. For powder guns, there is the potential to decrease the recoil impulse through the use of a muzzle brake.

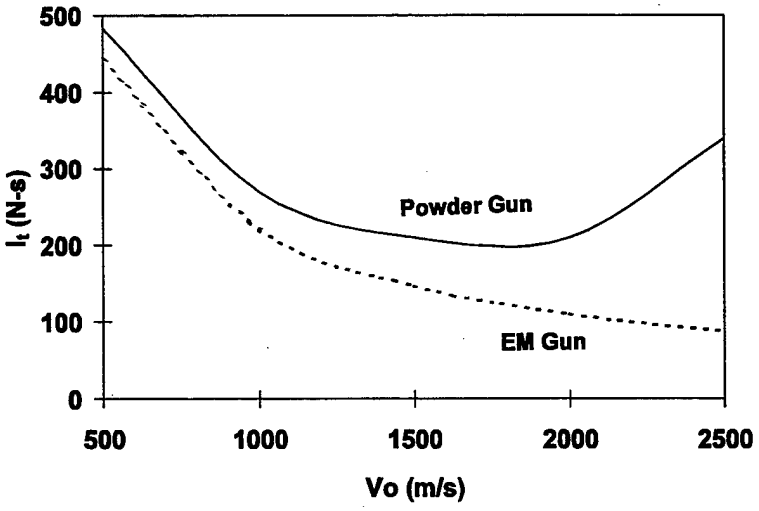

Figure 4. Constant Energy Case

MUZZLE BRAKES

Muzzle brakes deflect the exhausting propellant gases laterally thereby recovering axial momentum. The M109 brake, Fig. 5, is a high efficiency device employed on a 155mm self-propelled howitzer. Baur and Schmidt[6] measured the recoil attenuation of 20mm scale models of M109 and M198 brakes, Fig. 6. The brake momentum efficiency factor is defined as

$$\beta = (I_{wo} - I_w)/(I_{wo} - m_p V_o) \qquad (5)$$

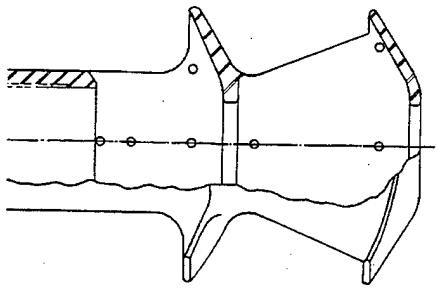

Muzzle Brake

The numerator is simply the difference in total recoil impulse with and without the brake in place and the denominator is the total momentum available in the propellant gases. This ratio can exceed 100% since the gases may be both turned rearward and further expanded. The behavior of β in Fig. 6 reflects this. For the 20 mm cannon as the launch velocity increases, the muzzle pressure also increases. The dimensions of the propellant gas exhaust plume also grow with muzzle pressure. The M198 brake is only 1.6 calibers in radius and is swept away from the muzzle; thus, its outer edge allows gases to escape as the plume grows. However, the M109 brake has a radius of 2.0 calibers and is swept toward the muzzle. Figure 5. M109

This baffle captures more of the plume as pressure increases and the brake efficiency grows. Eventually, the supersonic core of the plume should fully envelop both brake surfaces and variation with velocity (pressure) should level out. These data may be used to estimate the impulse imparted to the cannon as velocity increases.

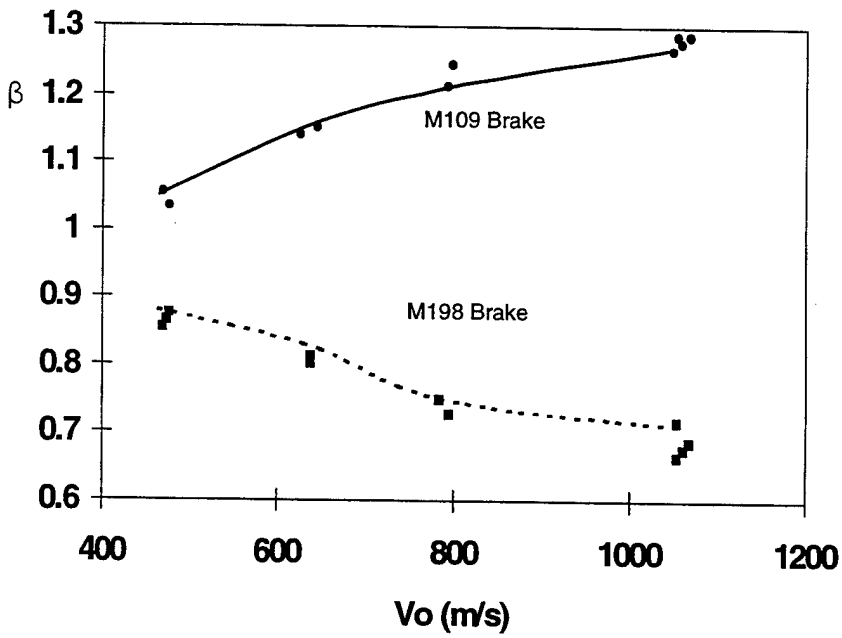

Figure 6. Muzzle Brake Efficiencies

By courageously fitting the M109 data in Fig. 6 and extrapolating to velocities up to 2500 m/s, the impulse of a powder gun with a high efficiency brake may be compared to the impulse of an EM gun over a similar range, Fig. 7. Since the efficiency of the M109 brake is greater than one, the total impulse imparted to the powder gun with the brake installed is lower than the impulse imparted to the EM gun, i.e., the momentum imparted to the projectile. There are drawbacks to employing a muzzle brake. The M109 brake is quite massive and affects the gun dynamics and the design of the elevating and trasversing mechanisms. Also, the employment of a muzzle brake greatly increases the muzzle blast overpressure behind the weapon. This may not be a problem with a vehicle having a closed hatch, but infantry moving with an armored fighting vehicle could be injured.

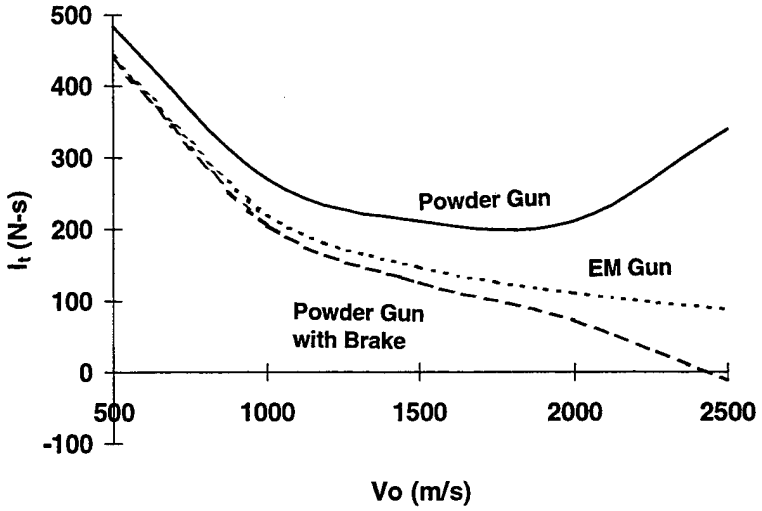

Figure 7. Constant Muzzle Energy Case with Muzzle Brake

CONCLUSIONS

The recoil characteristics of an electromagnetic railgun are considered and compared with those of a powder gun. The EM gun is shown to have less recoil impulse imparted to it than does the powder gun, particularly at high velocities. However, the installation of a muzzle brake can alter this comparison to the point where the recoil imparted to a powder gun equipped with a high efficiency brake is lower than that of an EM gun.

REFERENCES

1. Zielinski, A., private communication (1998) of results presented at the 11th EM Launcher Association Meeting, Sep 93.

2. Witalis, E., "Origin, Location, Magnitude, and Consequences of Recoil in Plasma Armature Railgun," *IEEE Proc. A*, Vol 142, No 3, 1995.

3. Marshall, R. And Woods, L., private communication (1996) of draft paper responding to Witalis.

4. Lang, C., "Muzzle Devices," AMCP 706-251, AMC, Alexandria, VA, May 68.

5. Schmidt, E. "A Ballistic Evaluation of Electromagnetic Launch and Flight," *Proceedings of 17th Int'l Symposium on Ballistics*, NDIA, Arlington, VA, May 98.

6. Baur, E. And Schmidt, E., "Relationship between Efficiency and Blast from Gas Dynamic Recoil Brakes," AIAA Paper 85-1718, Jul 85.

Fin Stabilised Munitions: A Review Of Current UK Concept Studies

Mr S Smith (1)
Mr R Meddes (2)
Dr A Groves (3)

1. Technology Leader, Indirect Fire Ammunition, Weapons Systems Sector, DERA, UK
2. Senior Research Scientist - Composite Fabrication, Structural Materials Centre, DERA, UK
3. Technology Chief - Composite Structures, Structural Materials Centre, DERA, UK

INTRODUCTION

The aim of the Concept Shell programme, previously known as Payload Augmented Munition (PAM), is to explore the potential of new technologies for enhancing the performance of indirect fire munitions in terms of accuracy, range and lethality. The munition is fin rather than spin stabilised so that length and payload are not constrained by gyroscopic stability considerations.

The programme is intended to address the performance of fin stabilised munitions, to examine the means by which range extension techniques such as a rocket motor, base bleed and/or gliding might be employed combined with developments in Global Positioning System (GPS) course correction techniques, small rugged inertial autopilot/guidance control systems and seekers/sensors to provide improved accuracy at the target.

Other objectives include the assessment and test of high specific strength composite materials in fin stabilised carrier shell concepts. Materials such as carbon fibre reinforced plastics (CFRP) or glass reinforced plastic (GRP) have been proposed. The improved mass efficiency of composites offers the potential for greater payloads to be delivered to the target area. Alternative warhead natures (as a carrier shell PAM is intended to be versatile), and in particular those lethal mechanisms (e.g. tandem shaped charge, high capacity blast) for which PAM is particularly suited because of its size, configuration and modus operandi, are being studied. Issues of stealth and resistance to countermeasures (e.g. GPS jamming) are being addressed.

Related issues include the effects of improvements to bomblet sub-munitions and dispersal techniques. Dispersion is being examined using a test rig to simulate deployment of bomblets by various methods.

The potential of adopting a modular approach is of particular interest for operational and logistics reasons. Different components could be linked together quickly and easily depending on the target type and particular operational requirement - e.g. nose guidance assembly, payload body assembly, rocket motor/base bleed integrated fin unit assembly, etc. Modularity

provides robustness to developments in both munition and target technology. Projectile length becomes a secondary issue if multiple part assemblies can be simply joined together in the depot or at the gun by the implementation of a non-complex, reliable joint mechanism requiring the minimum of tooling and mechanical expertise.

A number of firing trials have been conducted, with the successful launch of projectiles at gun design pressures and representative muzzle velocities. Ranges to date have been short to enable the shells to be recovered and examined to aid decisions on the direction of future research. A range of photographic techniques have been used to record the condition of shell during flight and these have yielded valuable trials information. A summary of the initial concepts is given in the next chapter.

INITIAL CONCEPTS

Figure shows a typical arrangement for a fin stabilised canard controlled carrier shell concept.

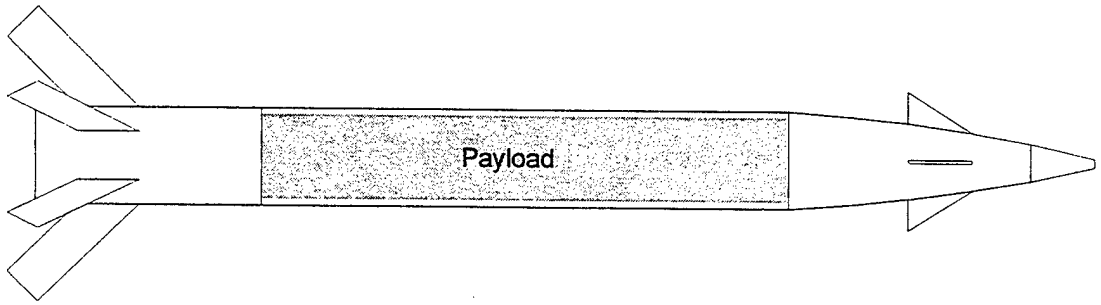

Figure 1: Fin stabilised carrier shell concept

Materials Selection

Shell Body

In order to reduce the parasitic weight of the projectile, it was recognised that high specific strength and stiffness (strength and stiffness to weight ratios) materials would be required. Currently the materials with the highest specific properties at acceptable cost and risk are advanced fibre-reinforced composites, consisting of low density continuous fibres encapsulated in a polymer matrix. The fibres offer strength and stiffness, while the polymer matrix provides load sharing/transfer across adjacent fibres. A summary of composite material options (fibres and matrix) for artillery applications is given in chapter 3 of the complementary symposium paper [1]. In this paper the material properties and costs are given and compared with high performance lightweight metallic alloys.

From [1] it is clear that a thermoset matrix carbon fibre composite holds the greatest potential for case weight reduction, with specific compressive properties at least twice those of the aerospace light alloys considered. It should be clearly noted that the properties shown are for a conservative ± 45° lay-up. For the shell case, where the most severe loading is essentially unidirectional, i.e. in the axial direction, a different lay-up could be chosen with materials properties approximately 60-70% greater than those presented, yielding specific properties

some three times those of the metallic options. It is interesting to note that material cost is bounded by the magnesium and titanium alloys, both of which are extensively used for defence applications.

The manufacturing route chosen for the first generation composite body was that of filament winding [2]. This process involves the placement of fibres on to a rotating mandrel of the required shape. A schematic of the filament winding process is shown in Figure 2.

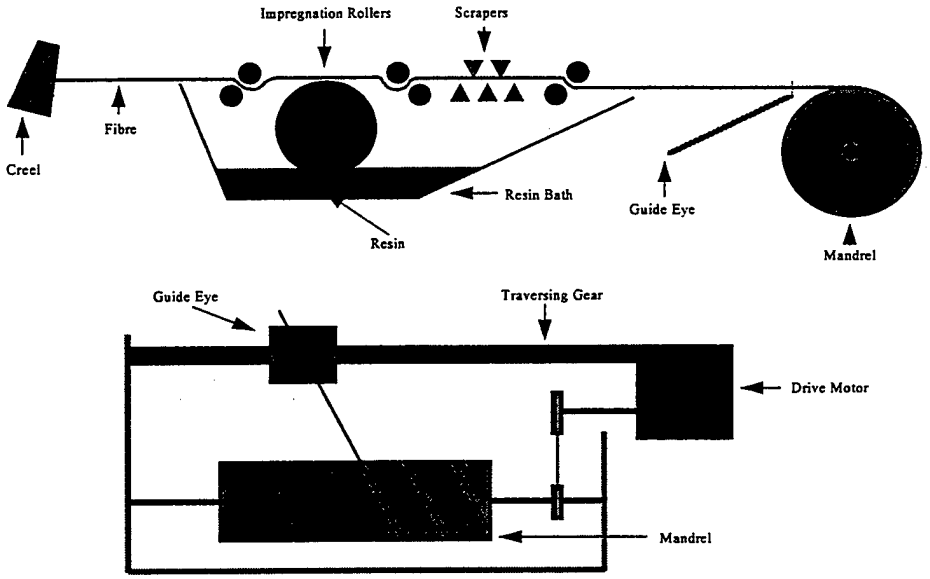

Figure 2: Schematic of the filament winding process

Fibre orientation is achieved through computer control of the mandrel rotation speed, carriage and cross feed movement, plus winding eye rotation. The fibre is impregnated with a polymer matrix in the resin bath shown. By adjusting the winding speed and fibre tension, composites of a very high quality can be produced with minimal porosity and fibre volume fractions of the order of 60%. A photograph of a carrier shell case being filament wound is shown in Figure 3.

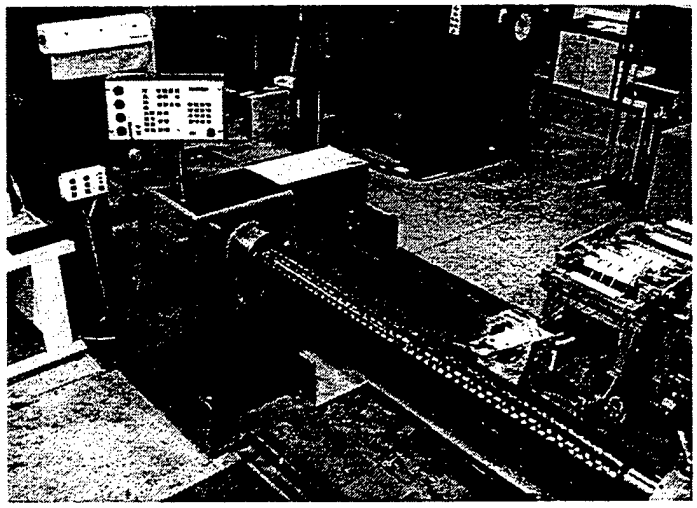

Figure 3: Carbon fibre carrier shell case during winding at DERA

The polymer matrix is cured in accordance with the manufacturers specifications.

Lower cost alternatives to filament winding are currently being considered and involve options such as pultrusions and pull-winding [2]. However, this work remains at an exploratory stage.

Fin unit and fins

In order to minimise technical risk and programme costs, 7075 aluminium alloy aged to its maximum strength (T6) condition was employed for the fin unit. This aluminium alloy is well known to the projectile community, is readily available and easily machined to achieve some of the more intricate features required for the fin unit and inserted sub-components, e.g. the fin opening dampers.

For the fin blades, two materials have been trialed, 7075-T6 aluminium alloy and a carbon fibre composite. The aim of the latter was to reduce weight, although clearly cost was considerably greater.

The composite fins for the demonstrator trials were manufactured by a standard hot press approach, in which epoxy pre-impregnated carbon fibre fabrics were laid up to the required form and thickness and then cured under pressure and heat in a hot press. The fins were then final machined from the resulting flat panel.

While this can yield composites of good quality, it can be an expensive fabrication route since it is both labour intensive and requires machining to produce the final product. Alternative manufacturing approaches are being considered within DERA including the RTM process briefly described in [1] and [2]. Here the hand lay-up element is automated and virtually all machining eliminated. A pre-form (of unimpregnated fibres) can be manufactured by one of three possible methods:

- automatic stacking system;
- 3-D jacquard weaving;
- tailoring of fabrics (semi-automated).

The pre-form is inserted into a tool steel die and then infused with resin under pressure. The resulting component is manufactured to near as net shape as possible, although some removal of flash and skimming of the profile remains inevitable.

An RTM moulded fin produced in support of the UK Concept Shell programme is shown in Figure 4 and a photograph of the projectile in flight in Figure 5. In this photograph, the composite case and fins are clearly visible.

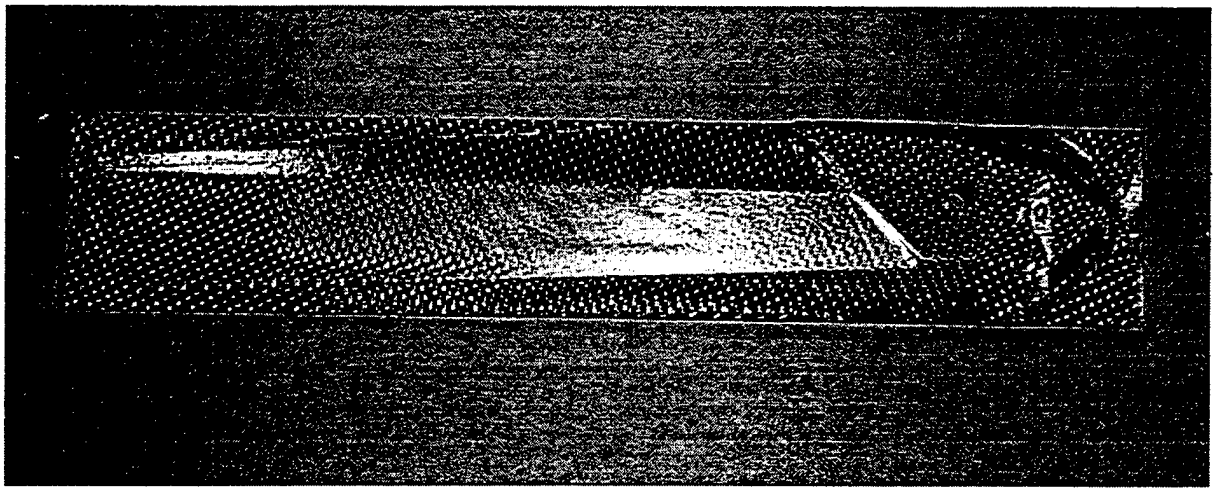

Figure 4: RTM Carbon fibre composite fins

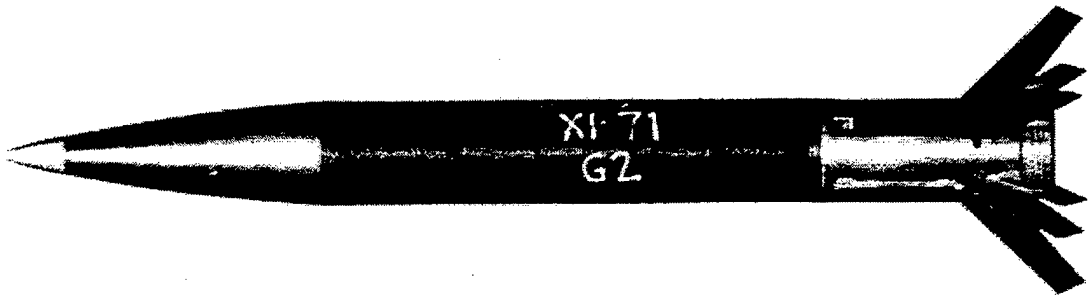

Figure 5: UK Concept shell with CFRP case and fins, 50 m from the muzzle

In view of the success of the trials to date, which have clearly demonstrated the concept of the shell, work is now ongoing to develop the shell into a highly versatile delivery system for use by the British Army.

FUTURE CONCEPTS

In view of successful trials, future work is now moving towards a numbers of issues which will enhance the performance of the current demonstrator munitions. These involve:

- Firing at greater range to gather ballistic data;
- Adopting a more wide spread use of advanced composite materials;
- Use of navigational guidance systems;
- Use of canards for flight control;
- Modularity of design for operational flexibility and improved potential for mid-life improvements.

EXTENDED RANGE

Projectile based range extension methods considered for an extended range projectile were:

- low drag design;
- base drag reduction using base bleed;
- sub-calibre projectiles;
- rocket assistance;
- ramjet assistance;
- glide trajectories.

Low drag design

A projectile decelerates during flight due to its aerodynamic drag which, for long ranges, must be minimised. The main components of drag are:

- **Profile drag:** Profile drag is associated with the aerodynamic shape of the projectile and tends to be very low at low Mach numbers (< 0.5) but becomes the major source of zero incidence drag at higher Mach numbers (e.g. M > 3).
- **Base drag:** Base drag provides the greatest source of drag and is caused by the sub-atmospheric pressure which develops in the wake of a projectile due to flow separation.
- **Skin friction drag:** Skin friction is typically the major source of drag at low Mach numbers (M < 0.5). It depends on the Reynolds number, surface finish and wetted area. A novel technique for reducing skin friction drag involves the use of riblets parallel to the flow to modify the boundary layer. This technique has applications for racing yachts, but the depth of riblets has been found to be too small to be practical for a projectile due to the high Reynolds numbers which occur in high speed flight.

Drag reduction:

- **Nose:** for low profile drag at supersonic speeds, a slender nose is desirable. A secant ogive about three calibres (cal) long is recommended.
- **Boattail:** tapering the aftbody reduces the base drag, but incurs some profile drag. A tapered aftbody (boattail) reduces the lift of a projectile and tends to be de-stabilising; so that fin stabilised projectiles require larger fins when a boattail is used offsetting any advantage obtained.
- **Base bleed:** the use of a base bleed unit to reduce base drag can typically extend the range of a projectile by around 20%. A propellant burnt at a low pressure is used to produce gases which are injected into the region of sub-atmospheric pressure which develops behind the projectile. It is most effective when base drag is high, i.e. during the initial phase of flight when the projectile is flying at supersonic speeds and low altitudes.

- **Lifting surfaces:** The drag of aerodynamic lifting surfaces can be significant and a fin stabilised projectile can lose about 20% range (in ballistic flight) due solely to the presence of the fins. The drag of lifting surfaces is mainly due to skin friction and to profile drag and therefore, they should be designed to have as small a thickness:chord ratio as possible.

Rocket assisted projectile

Rocket motor case design: The design of a rocket motor case for a gun launched projectile is complicated by the fact that at very high accelerations it is necessary to assume that the "solid" propellant behaves as a liquid due to its low shear strength (i.e. the propellant ceases to be self-supporting).

Conventionally, the rocket motor would be sealed from the gun chamber with a nozzle plug. The walls of the motor case carry the setback loads of the forebody, bulkhead and payload, during launch. At the base of the motor case, the walls must carry the additional loads due to the setback of the rocket motor and the propellant. As the propellant behaves as liquid under very high accelerations, the setback of the propellant generates a significant internal pressure, and hence radial and hoop stresses in the motor. Since the wall stresses increase significantly towards the base of the case, the walls need to be tapered in order to minimise their mass.

Breech pressurised rocket motors: Unconventional designs of rocket motor are under consideration with the aim of minimising the casing mass and maximising the propellant mass. The preferred option is considered to be an end burning grain in a 'breech pressurised' case. In this scheme, the rocket motor case is open to the gun chamber (breech) pressure, through the nozzle, so that the gun pressure is applied directly to the rocket motor propellant and thence to the bulkhead which carries the payload and forebody setback loads. This arrangement can significantly reduce the longitudinal setback loads acting on the rocket motor case.

A 'breech pressurised' rocket motor for use in a smoothbore barrel could probably be designed such that the rocket motor case carries the longitudinal setback loads and radial pressure loads, with the gun barrel carrying the circumferential hoop loads. A low friction plastic sleeve (placed around the rocket motor) is likely to be required. Suitable materials and manufacturing processes are currently under investigation.

In a breech pressure equalised design, the pressure gradient is matched along the outside of the rocket motor case and hence there would be no hoop stresses in the motor case wall. The main stress would be a longitudinal tensile stress, due to the fin unit and base of the rocket motor being pulled rather than pushed. The difficulty in this design is in matching the internal and external pressure gradients during transient conditions (especially those at muzzle exit).

For a rifled barrel, pressure matching is probably best obtained by having a small clearance between the rocket motor case and the bore. The grooves in a rifled barrel will assist pressurisation, so that the clearance between the bore and the rocket motor casing could probably be quite small. This type of design is used in the US Navy Extended Range Guided Munition (ERGM) with a 'breech pressure equalised' rocket motor. The main difficulty in this

scheme is that with a small nozzle, the internal pressurisation of the rocket motor case may lag behind the external pressurisation, possibly resulting in the case walls collapsing inwards.

The response of the rocket motor propellant to the high chamber pressure also needs careful study since:

- it will tend to contract axially when the pressure is applied, giving rise to shear stresses at the case walls;
- there will be dynamic 'ringing' effects;
- the propellant will 'bounce back' when the pressure is removed, generating undesirable tensile stresses; it will then be required to perform as a normal rocket propellant a few seconds later.

Both types of 'breech pressurised' rocket motor must be designed to survive the loads at muzzle exit. Here, the setback loads would be relatively small but, as the motor emerges from the barrel, external pressurisation or barrel support would be lost. The magnitude of the pressure at muzzle exit and the resulting stress levels in the motor case need to be evaluated.

Other rocket motor options include the use of an annular, radial burning charge instead of an end burning charge. The disadvantage is that the volumetric filling efficiency is generally less than 80%, due to the size of the central hole that is necessary to avoid erosive burning. Generally, with a conventional rocket motor, the central hole must be filled with an inert fluid of similar density to that of the propellant so as to prevent the charge from collapsing at the base. If the case is pressurised by the gun chamber gases during launch, a central support may not be required, but the pressure rise time will be affected by the relatively large free volume within the case, possibly making pressure equalisation difficult to achieve.

Rocket motor operating conditions: For a high specific impulse, the chamber pressure should be as high as possible and the nozzle expansion ratio (exit/throat area ratio) should be optimised for the chamber/ambient pressure ratio. (The optimum expansion ratio is the ratio which produces an exit pressure equal to the ambient pressure at the nozzle exit plane.)

Ambient pressure: It is generally accepted that the range of a rocket assisted projectile is maximised when the rocket motor operates at a high altitude because of the low drag associated with low atmospheric pressures. In the parametric studies, the mean altitude for optimum rocket motor operation was found to be around 15 km. At this altitude, the atmospheric pressure is only 12 kPa; this is nearly a tenth of the sea-level pressure and permits the use of a nozzle with a greater expansion ratio than could be used at low altitudes.

Sub-calibre projectiles

One method for reducing drag is to reduce the projectile's cross-sectional area. If the projectile is merely scaled down, the mass reduction is greater, but the drag reduction and the in-flight deceleration are increased, thus reducing the range for a given muzzle velocity. However, if the mass can be maintained, or only slightly reduced, then longer ranges can be obtained. Maintaining the mass of a sub-calibre HE shell or bomblet carrier requires either the substitution of a high density material, such as steel, for some of the relatively low density

payload, or an increase in length. The latter is only likely to be possible with fin stabilisation. However, increased length means that some of the drag reduction is lost due to increased skin friction.

The disadvantages of sub-calibre projectiles include:

- the maximum allowable payload diameter is reduced;
- an increased payload length is necessary to maintain payload volume and could result in structural problems (e.g. the self-supporting height of a bomblet stack is limited by setback loads on the bottom row);
- the mass of the sabot, which must be used to carry the sub-calibre projectile in the gun barrel, results in a proportion of the available kinetic energy being imparted to the sabot rather than to the projectile; in some systems, the sabot may be as heavy as the projectile and half of the gun's energy is wasted.

Sub-calibre projectiles are particularly suited to direct fire applications such as kinetic energy penetrators. These require low in-flight deceleration for a high impact velocity, rather than for a long range. The only known example of an indirect fire sub-calibre projectile used in service is the German second world war Peenemunde Arrow Shell. This sub-calibre fin stabilised projectile holds the record for the longest range achieved in service by a gun launched projectile. The 136 kg, 120 mm calibre projectile had a range of 151 km when fired from a 31 cm smoothbore gun with a muzzle velocity of 1525 m/s. (The gun was a 28 cm K5(E) rifled gun with a bored-out barrel.) It should be noted that the projectile's long range was obtained with a kinetic energy at muzzle exit of about eight times the energy that the 155 mm ERO can provide.

Rocket assistance and base bleed

It has generally been found that the most effective use of propellant is obtained when base bleed is used for the first 10 to 20 seconds of flight and is immediately followed by rocket assistance for around 10 seconds. Fitting a conventional base bleed unit around a rocket motor nozzle is relatively straightforward, provided that the nozzle is not too large.

The combination of base bleed and rocket assistance had been under consideration for the US 155 mm XM982 carrier projectile. However, glide has been adopted as the range extension technique for the projectile currently being produced by Raytheon-Texas Instruments Systems (RTIS).

Glide

Range can be extended by gliding from the apogee of a ballistic trajectory using aerodynamic lift to reduce the effect of gravity. Lift can be generated by forcing the projectile to fly at incidence. The glideslope angle, which must be shallow for long range, depends on the lift to drag ratio of the projectile. Body lift alone can be used for gliding, but the lift to drag ratio can be enhanced using aerodynamic lifting surfaces. Hence, on this basis, fin stabilised projectiles are more suitable than spin stabilised projectiles for gliding to extreme ranges.

Gliding is only possible if the projectile can be flown under control to maintain the appropriate attitude. This implies the use of a control system, however, since an extreme range projectile would require some means for minimising its dispersion in both range and line, the use of a control system is inevitable in any practical design.

COMPOSITE MATERIALS

To date, composite materials have been used only for the case, ogive (in early versions) and fins. This selection was based on identifying those areas where the most benefits could be achieved by adopting lightweight materials at low technical risk and within the funding limits available. The use of composites can, in future, be extended to the fin unit.

Fin Unit

As discussed, all fin unit designs to date have used high strength aerospace aluminium alloys. However, it is recognised that with a proof strength of some 400-500 MPa , the material is being pushed to its structural limit when used in conjunction with a base mounted obturator and that any scope for further weight reduction will necessitate a move to lower density materials of similar if not greater strength. While CFRP is likely to be the prime candidate due to its high strength and low density, it is clear from the data given in chapter three of the symposium paper [1] that glass (either solid or hollow fibres) could be considered as an alternative, particularly if cost is of a greater priority than overall weight saving. An intermediate option is the use of hybrids e.g. carbon and glass fibres, to obtain a trade-off between cost and weight savings. This is currently being assessed as part of the DERA research programme. In order to minimise the fin unit production costs, two fabrication routes are being explored.

Pultrusion

The first option considers the use of pultrusions, in which tows of fibres are pulled through a shaped die. The resin is infused into the fibres and cured within the die itself. The resins are generally polyesters, but epoxies can be used. An illustration of a pultrusion machine is shown in Figure 6.

The pultrusion process is recognised as being able to produce composite components at very competitive costs if a high degree of fibre unidirectionality is acceptable for the product and the cross section remains the same along its length. The fin unit broadly fits into this category, although some post machining will be required to achieve some of the more intricate features required.

Manufacture could be accomplished by using a single pultruded component, or by assembling a series of segments by bonding and/or mechanical fixtures (pins/bolts). The latter method is attractive in that it permits smaller dies to be used and thus reduces cost for die manufacture. However, additional costs are incurred by the need to carry out assembly of the resulting segments. The use of smaller dies also permits greater control over component quality.

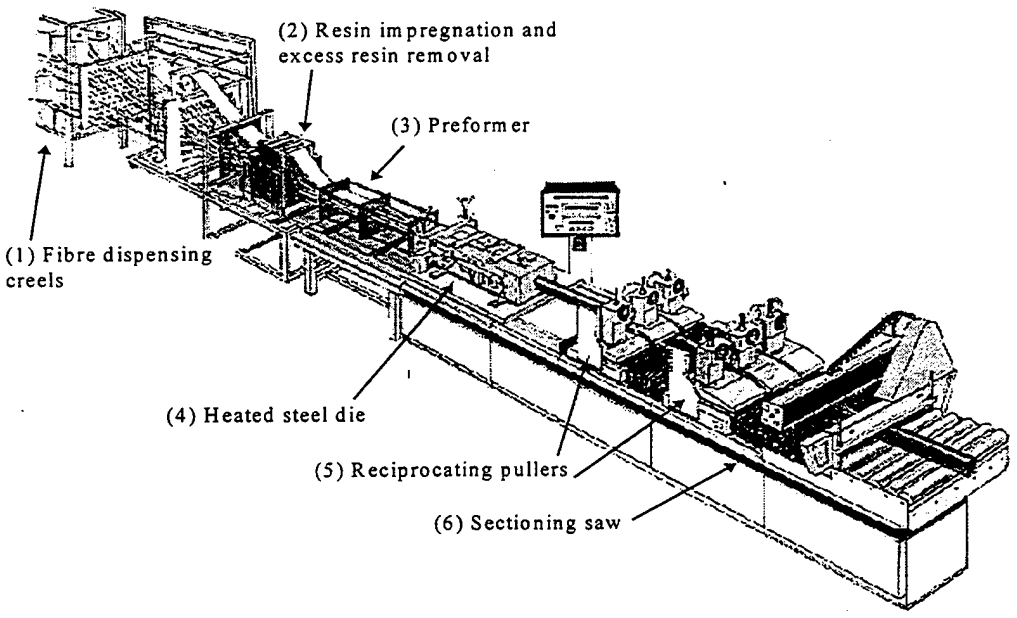

Figure 6: Pultrusion machine - Courtesy of Fibre-Force Ltd.

Large sections of composite are particularly susceptible to fibre waviness, voids and variable fibre volume fraction. Moreover, heat transfer through the component during resin cure becomes problematic, due to the thermal insulating properties of the composite materials. Exothermic reactions (causing over-heating) can also become a serious problem leading to internal defects. Thus, curing of thick sections needs considerable attention to detail and the pultrusion feed rates can become considerably slower than would be otherwise desired. However, it is clear that by using a single die, assembly costs will be eliminated. Which of these ultimately yields the lowest cost product at acceptable quality remains to be resolved and is part of DERA's ongoing projectile materials work programme.

Resin Transfer Moulding (RTM)

An alternative technique is the resin infusion process as summarised in [1] and [2]. For the fin unit, it is likely that unimpregnated fibres (pre-form) will be placed into a high quality tool steel closed die into which the polymer matrix is pumped under high pressure. This produces composites of high quality, deemed essential for the fin unit given the loads imparted on the projectile during launch. While the cost of the die can be expensive, the cost of the die is quickly recuperated on large production runs. Furthermore, the die can be designed to produce a net shape product, a major attraction of the RTM process to reduce composite manufacturing costs. The only major drawback is the manufacture of the fibre perform. This can be both complex and costly; furthermore, the perform must be very carefully located into the die. However, this is recognised as a generic problem area to RTM for complex components and is being actively researched world-wide.

Inertial navigation systems

A typical inertial navigation system (INS) consists of an inertial measurement unit (IMU) with an associated navigation processing unit. The IMU contains sensors which provide the basic angular rate and acceleration information input to the navigation system as well as providing data on the weapon position to the control system or autopilot. An INS is based upon the principle of 'dead-reckoning' navigation whereby, given an initial position, speed and altitude, the inertial sensors measure the change in position and attitude with time and thus establish the current position based upon these measurements. The accuracy, or drift, of the instruments with time is thus of paramount importance.

The sensors are required to withstand setback loads resulting from high launch accelerations of gun fired munitions. This eliminates many of the conventional mechanical gyroscopes and accelerometers based upon spinning wheels and pendulous mass technology respectively. These instruments generally have bearing support systems for the moving parts which are not sufficiently robust to withstand forces generated by accelerations likely to be in excess of 16000 g at launch.

Some mechanical instruments have been specially gun hardened - the two axis gimballed spinning wheel gyroscope used in the US Copperhead projectile being a notable example, but a sensor based on solid state technology is likely to be inherently better at surviving gun launch. Such instruments include optical gyroscopes; ring laser gyroscopes (RLG) and fibre optic gyroscopes (FOG), and micro-machined devices such as rate sensors, accelerometers, magnetometers etc.

Micro-machined devices which exploit the deposition, lithography and etching technologies from the silicon micro-electronics industry offer significant benefits in terms of size, cost, mass, and launch shock survivability. They could be manufactured as part of the same process which produces the INS electronic control circuit on a single integrated chip. The technology is at this stage somewhat immature. Only accelerometers have been manufactured in any quantity and devices capable of achieving the estimated error budget requirements are currently available on the commercial market. Complementary devices for measuring angular rate are under development and their future commercial availability is assured. It is confidently predicted that by the year 2005 micro-machined rate sensors with necessary performance levels (approaching 1 deg/hr) should be available.

The US Navy ERGM programme is known to favour the use of FOGs in its pre-production versions, but development of micro-mechanical rate sensors is parallel funded with a view to replacing the FOG based system with a potentially smaller, lighter and cheaper micro-machined based sensor package once that is available and achieving adequate performance levels.

It is unlikely that micro-mechanical devices would provide the necessary accuracy for a stand-alone INS, since they would result in excessive dispersion. However, if external navigation

aids are available to supplement the INS, it may be possible to use a lower quality (and hence less costly) IMU to achieve similar performance.

GPS

The Global Positioning System (GPS) is considered most likely to provide the means of updating the INS. The system is globally available and GPS receivers are currently undergoing gun hardening development. Total reliance upon GPS for navigation would permit the use of relatively low quality inertial instruments which would satisfy only the lesser autopilot requirements. However, the vulnerability of GPS to local area jamming is well known and total reliance upon GPS would compromise operational effectiveness since position data would be lost during crucial phases of flight. Effectively GPS would be used as the prime position finder. Its data would be used to periodically update and reset the sensors in the INS so that they would have an accurate starting point should GPS fail due to countermeasures.

Clearly there is a compromise where intermediate quality and less costly inertial instruments could be used in combination with GPS to provide both control and navigation requirements at an acceptable accuracy and cost.

Canard control

Canards are considered to provide the most suitable form of control, positioned as far aft on the nose (ogive) section as practicable for maximum efficiency. They can be stowed in the ogive until the end of the ballistic phase of flight so as to minimise drag and then deployed at the commencement of a range extending controlled glide phase at or near apogee.

Two canard configuration options are considered to be feasible. These are:

- four canards, with opposite canards coupled together and actuated with sufficient dynamic performance to be able to control a slowly rolling airframe in pitch and yaw;
- a roll controlled nose section carrying two canards coupled together.

Canards tend to be destabilising and are likely to be ineffective for roll control of the whole projectile due to their small span. Downwash from the canards onto the tail fins may also produce a counter-torque. For these reasons, consideration should be given to de-coupling the roll between the tail section and the nose by an intermediate bearing.

Thrust control

Lateral thrusters could be used and, as for aerodynamic control with canards, an ogive mounted system is likely to be the most effective. Options include intermittent 'on-off' control of stored pressurised gas, continuous control of gas generated by a solid propellant, or the use of an array of single-shot squibs. The latter is, mechanically, the simplest control

system, but the control authority is limited. Such a system is most suited to a low accuracy guidance system, in which only a few trajectory corrections are made.

Base fin control

Tail control is preferred for controlling the projectile in roll, but has a number of disadvantages in comparison with canard control for course adjustment. These include:

- tail forces oppose the body lift forces so that the net lift is lower than with canards;
- fins need to be considerably larger than canards, and the actuation power requirements are greater;
- there is limited space for the actuation system at the tail due to the structural requirements of a high 'g' launch;
- the internal volume of the ogive can be used to contain both the control and guidance systems without significantly affecting payload volume.

Preferred configuration

The most suitable configuration for bomblet and other sub-munition/warhead delivery is considered to be a canard controlled rocket assisted projectile with base bleed. A range of 150 km (meeting NFS aspirations) would be a realistic goal in the first instance with the possibility of extension to over 200 km. The goal of 150 km is estimated to require a total launch propellant mass of about 7.5 kg (0.7 kg base bleed and 6.8 kg rocket motor). The exact mass of propellant required would depend on the final aerodynamic design (e.g. canard size, fin size, nose profile, body length etc.) and on the rocket motor design (propellant, pressure, nozzle dimensions etc.)

It is estimated that a range of 150 km could be achieved with a conventionally designed rocket motor, but for ranges of over 150 km, it is likely that a lightweight rocket motor would need to be developed. The design and development of such motors is probably more straightforward for smoothbore applications than for rifled barrel applications.

The number of canards (either two or four) has little effect on range. There is a marginal increase in range when only two canards are used, and the control system using two linked canards and a roll controlled nose section may be simpler. If the GPS aerials are mounted on the roll controlled nose section they could be pointed away from the ground, to avoid low level jammers, without the need to aerodynamically roll control the projectile. The latter requires the rotating fin unit to be de-coupled.

The design of a lightweight CFRP forebody and ogive is thought to be relatively straightforward compared with the design of a lightweight rocket motor. However, aerodynamic heating will need to be considered, especially when a large rocket motor is used, because of the long period of flight spent at high Mach numbers. The resin used to bond the carbon fibres is unlikely to be able to withstand surface temperatures above about 300°C for any length of time and, although overall strength may not be seriously impaired, the surface finish may deteriorate, leading to increased drag.

With the high overall lift to drag ratios that can be obtained with aerodynamic lifting surfaces (such as fins, canards and wings), a gliding fin stabilised projectile offers the possibility of greatly increased ranges. Such projectiles require some form of guidance and control in order to reduce their dispersion at the target to acceptable levels. The installation of a control system makes gliding a practical proposition.

Wings are attractive for long gliding ranges, but the stowage space within the projectile is a major drawback, especially if a large payload and rocket motor are to be incorporated.

The distance that a projectile can glide depends on its speed and altitude at the start of the glide. It would be advantageous to consider both rocket assistance and base bleed as means for maximising these parameters, and hence the range.

MODULARITY

As discussed, the carrier shell concept lends itself to a modular concept. This would permit flexibility hitherto unavailable to the British Army in terms of logistics and fire power. Modularity also greatly assists in mid-life improvements in that particular shell elements can be upgraded, without withdrawal from service of the whole round. In essence the 'shell' becomes a series of simply 'clipped' together components comprising :

- Nose assembly
  - ◊ dumb
  - ◊ GPS guided using canards.
- Munitions case into which the munitions are loaded via a simple cartridge
- Fin unit
- Range assist
  - ◊ Rocket motor
  - ◊ Base bleed

These options are illustrated in Figure 7.

Work on joint options is currently underway and the principal design features sought are summarised below:

- Ease of assembly.
- Dimensional accuracy and stiffness to prevent flexural vibrations in the shell during launch and flight.

For composite materials this offers a number of challenges, particularly when low cost is an important driver. However, two routes are being considered. One consists of a conventional metallic end-ring joint, with titanium alloy being considered as a suitable material. Titanium to composite attachment will require care, but DERA possesses considerable expertise in the design of bonded and pinned joints from a range of military and civil projects. Alternatively, if weight, is to be minimised a composite variant could be considered, but it is unlikely that

this would be as durable as a metallic solution if repeated assembly/disassembly is sought. Several manufacturing routes have been identified ranging from filament winding/machined through to RTM moulded connectors.

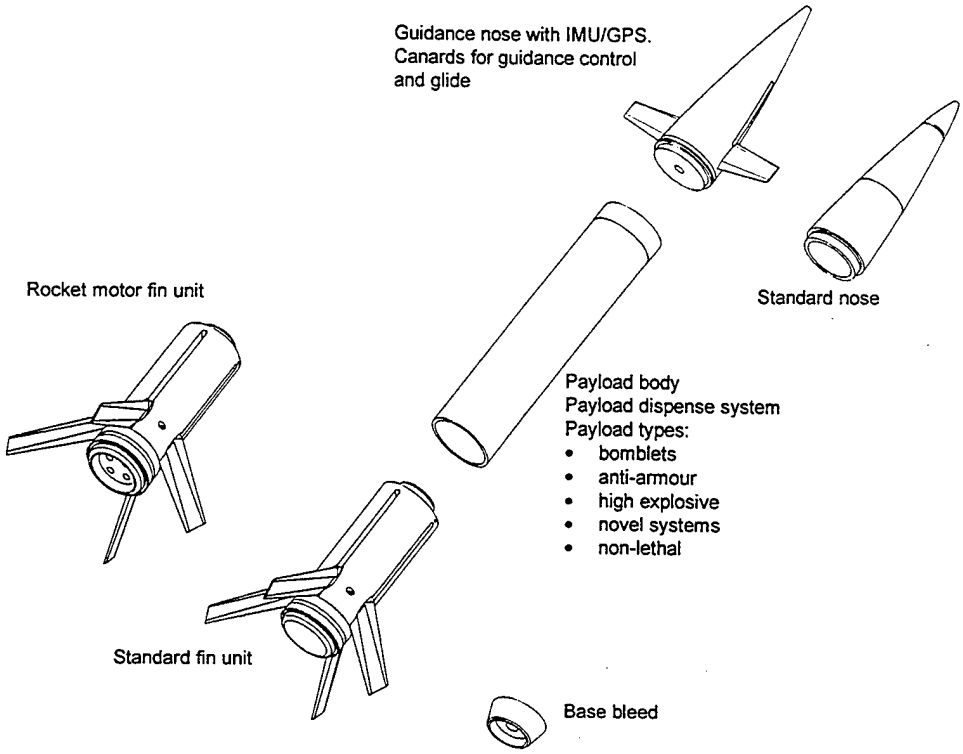

Figure 7: Modularity concepts for the UK Carrier shell

SUMMARY

In essence the carrier shell represents a generic family of munitions rather than a single shell so that military solutions can be made available in a number of configurations. The modularity concept provides logistics flexibility as well as facilitating in-service improvements and updates resulting from technological advances.

The programme will maintain the expertise possessed by DERA for research into indirect fire support (IFS) munitions and thus will enable the UK to make an effective contribution to any international discussions on, or analysis of, future munition concepts.

References

1 A. Groves, J. Woolard. "Sub-9000 lb. Mobile Lightweight Artillery: Systems and Materials Requirements". *9th US Army Gun Dynamics Symposium*, November 1998. McLean Va.

2 Payload Augmented Munition: a multi-role concept shell for future artillery; DERA report DERA/WSS/WX6/CR980586/1.0, August 1998.

AERODYNAMIC JUMP: A SHORT RANGE VIEW FOR LONG ROD PROJECTILES

Mark Bundy
US Army Research Laboratory
AMSRL-WM-BC
Aberdeen Proving Ground, MD 21005-5066

It is shown that aerodynamic jump for a nonspinning kinetic energy penetrator is not—as conventional definitions may infer—a discontinuous change in the direction of motion at the origin of free flight, nor is it the converse, a cumulative redirection over a domain of infinite extent. Rather, with the aid of an alternative kinematical definition, it is shown that aerodynamic jump for such a projectile is a localized redirection of the center-of-gravity motion, caused by the force of lift due to yaw over the relatively short region from entry into free flight until the yaw reaches its first maximum. A rigorous proof of this statement is provided, but the primary objective of this paper is to provide answers to the questions: what is aerodynamic jump, what does it mean, and what aspects of the flight trajectory does it refer to, or account for.

INTRODUCTION

The motion of a projectile can be separated into two general regions: the free-flight, FF, region and the launch-disturbance, LD, region (prior to FF). For instance, if the projectile is a saboted long rod (or, kinetic energy, KE) penetrator, then the LD region begins in-bore and extends downrange to the point where shock waves from the discarding sabot petals no longer interact with the rod. The end of the LD region marks the beginning of the FF region, where the phenomenon known as aerodynamic jump (AJ) occurs. The KE penetrator is chosen to facilitate the ensuing discussion and illustrations on the subject of AJ.

Although AJ occurs in the FF region, its magnitude is influenced by events that take place in the LD region. Hence, a brief discussion of LD effects is in order. A KE projectile consists of a long rod with an aerodynamically shaped nose and stabilizing tail fins. The high mass-density, sub-caliber rod is held centered in the gun bore by a low mass-density, full-caliber sabot. The rod can undergo small, lateral, center-of-gravity (cg) displacements and rotations while being propelled longitudinally down the bore. Such in-bore motion permits the projectile cg to exit the barrel with a velocity vector oriented at an angle $\angle CG$ with respect to the instantaneous bore axis. In addition to the rod moving relative to the bore axis, the barrel itself can be moving. Thus, the rod can be launched with the instantaneous pointing angle of the bore axis, $\angle PA$, different from the original muzzle sight line. Furthermore, the instantaneous bore axis can have a lateral (crossing) velocity that is transferred to the projectile cg motion. The angular change in the projectile cg velocity due to this barrel crossing motion is denoted by $\angle CV$. Outside the gun, it is possible for asymmetric sabot discard to create uneven mechanical and aerodynamic forces on the rod that add yet another transverse cg velocity component, and redirection angle, $\angle SD$. The net effect of these four pre-free-flight LDs can give the projectile cg a cumulative transverse deflection angle, $\angle LD = \angle CG + \angle PA + \angle CV + \angle SD$, at the point where it enters FF, Fig. 1. (Bornstein et al. [1] discuss techniques to measure these LD components.)

After traveling through the LD region, the KE rod enters FF. The motion of the projectile in FF is influenced by time-dependent side forces that cause the projectile cg to oscillate (swerve) about a mean FF path (swerve axis) as it travels to the target, Fig. 2. For a typical KE rod (which is statically stable, near-symmetric, and virtually nonrolling), the swerve curve can be approximated by a damped sine wave in both the vertical and horizontal directions.

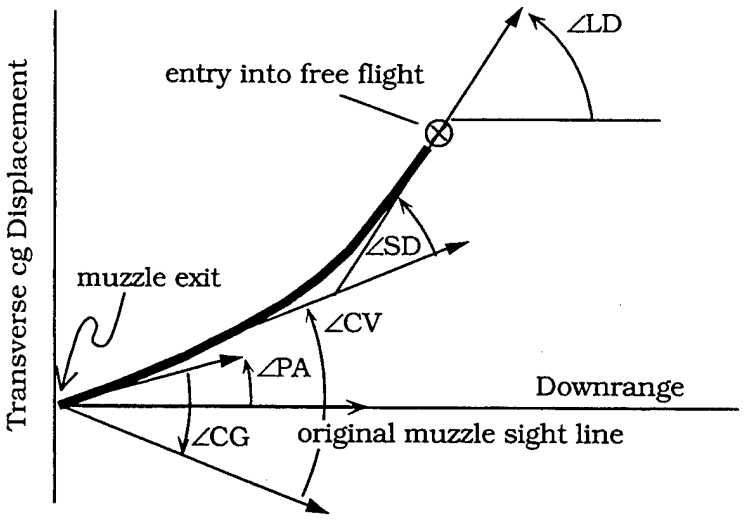

Fig. 1 Hypothetical Planar CG Motion of a KE Rod Caused by Launch Disturbances.

As the trajectory of Fig. 2 is extended to a distant target, the swerve amplitude decays to near zero and the point of impact lies close to the axis of swerve symmetry, Fig. 3. (Note, the effects of gravity and the Coriolis force on the trajectory are not included in this discussion because they are not aerodynamic in nature; if warranted, their influence can simply be superimposed on the swerve motion.)

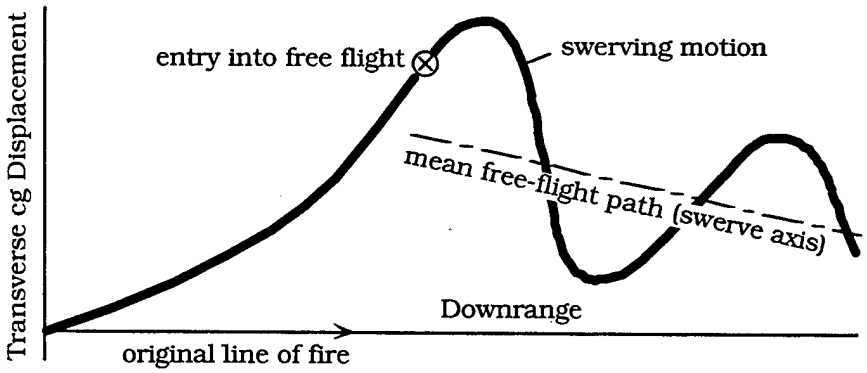

Fig. 2. Transition of CG Trajectory Into Free Flight.

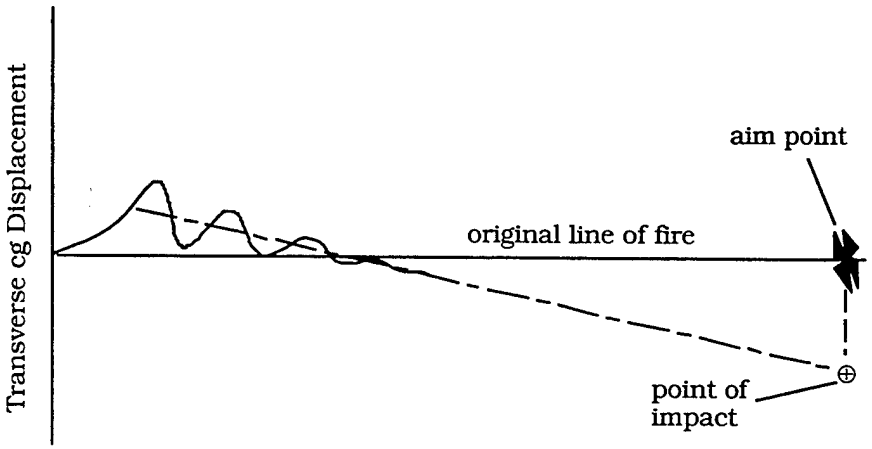

Fig. 3. Hypothetical CG Trajectory Extended to the Target.

Thus, the axis of swerve symmetry has special significance because it is closely aligned with the point of impact on a distant target. As indicated by Figs. 2 and 3, the swerve axis can be, and most often is, different from the direction given to the projectile cg as it leaves the LD region. This change in direction is caused by FF aerodynamic side forces. The term "aerodynamic jump," AJ, is used to quantify this change in direction.

One of the earliest descriptions of AJ was given by Murphy [2], stating that AJ is "the angle between the bore sightline and the 'average' trajectory when other contributors to jump are neglected." Although this definition describes AJ as an angle, it is actually the tangent of the described angle. However, for small angles (typical for AJ), the angle and its tangent are nearly one and the same. Neglecting other contributors to jump, as per Murphy [2], would mean setting, or assuming, $\angle LD = 0$ in the previous discussion. In this case, Fig. 3 would transform into Fig. 4.

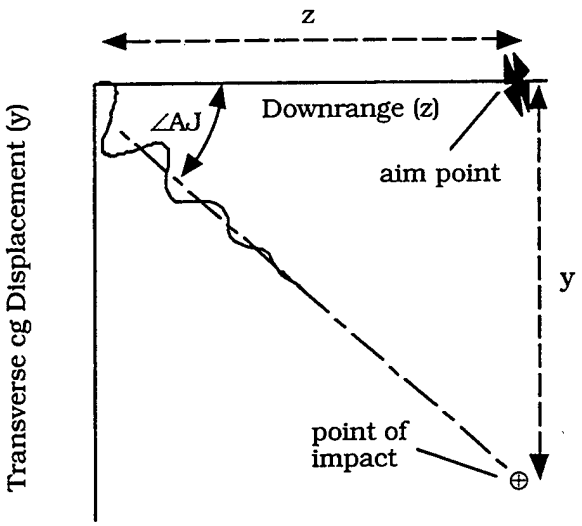

Fig. 4. Geometrical View of $\angle$AJ, Neglecting $\angle$LD.

From Fig. 4, when the FF trajectory approaches infinity, AJ and $\angle$AJ can be defined by

$$AJ = \lim_{z\to\infty}\left[\frac{y}{z}\right] \quad ; \quad \angle AJ = \tan^{-1}\{AJ\} \underset{AJ,\ \angle AJ << 1}{\approx} AJ \ , \tag{1}$$

where y represents the transverse cg displacement and z represents the longitudinal, or downrange, displacement. (Note, for later reference, the sign convention for the direction of positive y in Eq. 1 will determine the sign convention for positive AJ.) Both Murphy [2] and Murphy and Bradley [3] begin their discussions of AJ based on Eq. 1. A more inclusive expression for AJ, one that does not neglect "other contributors to jump," is put forth later by Murphy [4]. This more general definition states:

$$AJ = \lim_{z\to\infty}\left[\frac{y - y_o}{z - z_o}\right] - \left.\frac{dy}{dz}\right|_{z_o} \quad ;$$

$$\angle AJ \underset{\lim_{z\to\infty}\left[\frac{y-y_o}{z-z_o}\right],\ \left.\frac{dy}{dz}\right|_{z_o} << 1}{\approx} \lim_{z\to\infty}\left[\frac{y - y_o}{z - z_o}\right] - \left.\frac{dy}{dz}\right|_{z_o} \ , \tag{2}$$

where y_o is the transverse cg displacement and $dy/dz|_{z_o}$ is the tangent to the cg displacement, both at the origin of FF. Figure 5 (an annotated version of Fig. 3) gives the geometrical interpretation of Eq. 2.

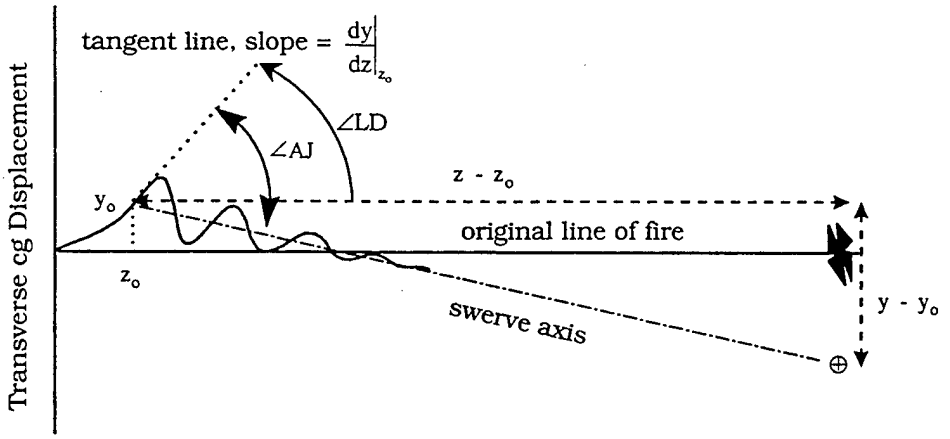

Fig. 5. Geometrical Interpretation of Eq. 2.

Equations 1 and 2 are kinematical definitions for AJ. Their more familiar dynamical counterparts are derived from them by solving, then substituting for y and z based on the equations of motion (as done later in this paper). Although the dynamical expressions for AJ may be more useful in practical applications, the simple geometry-based definitions of Eqs. 1 and 2 are the most helpful for those seeking to visualize the effect of AJ on the cg trajectory. However, because the definitions in Eqs. 1 and 2 call upon the limit as the trajectory approaches infinity, some may erroneously infer from this that AJ is an effect that "accumulates" with downrange distance. In other words, they may wrongly assume from these infinity-based definitions that it takes a near-infinite amount of space to establish the AJ. The purpose of this paper is to dispel any such notions by showing that the bending of the "average" trajectory, referred to as AJ, is due to aerodynamic forces acting over a relatively short segment of the FF trajectory. This will be done, in triplicate, by first giving an alternative geometry-based, or kinematical definition for AJ (one that does not invoke a limiting case). Then, a physically sound explanation, supporting this definition, is given. And finally, the theoretical consequences promulgated from the alternative kinematic definition are shown to produce the same dynamical expression for AJ as that derived from Eqs. 1 and 2.

AN ALTERNATIVE KINEMATICAL DEFINITION FOR AJ

From Eq. 2 and Fig. 5, $\angle AJ$ is the angular change between the tangent to the cg trajectory at the transition point between the LD and FF regions (oriented at $\angle LD$ with respect to the original line of fire) and the axis of swerve symmetry. As shown in Fig. 6, and proven in Bundy [5], the axis of swerve symmetry runs parallel to the tangent to the swerve curve at any and all of the local swerve maxima (positive or negative maxima with respect to the swerve axis). Hence, $\angle AJ$ can also be defined as the angular difference between the tangent to the cg trajectory at the origin of FF and the tangent to the swerve curve at the first (or second, or third, etc.) local maximum in the swerving motion. In equation form, this alternative definition is stated as:

$$\angle AJ = \tan^{-1}\left\{\left.\frac{dy}{dz}\right|_{z_{\text{swerve maxima}}}\right\} - \tan^{-1}\left\{\left.\frac{dy}{dz}\right|_{z_{\text{origin of free flight}}}\right\} \approx \left.\frac{dy}{dz}\right|_{z_{\text{swerve maxima}}} - \left.\frac{dy}{dz}\right|_{z_{\text{origin of free flight}}} \quad (3)$$

where the subscripts identify the locations at which the derivatives are to be evaluated. Note, unlike Eqs. 1 and 2, the definition for $\angle AJ$ given in Eq. 3 does not call upon the limit as the trajectory approaches infinity.

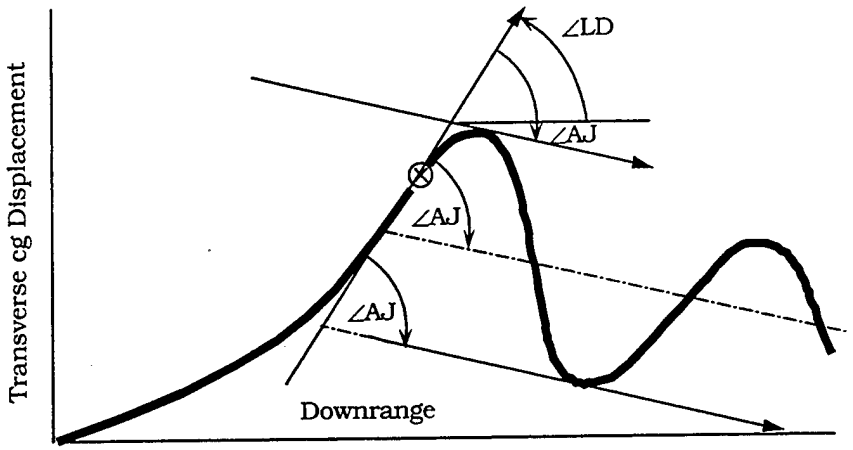

Fig. 6. Alternative Geometrical Definitions for ∠AJ .

Even though ∠AJ can be defined using the tangent line at any of the local maxima, as depicted in Fig. 6, it is clear that the minimum distance needed to establish the orientation of the swerve axis is the distance to the first swerve maxima, z_1. Thereafter, the cg motion simply oscillates back and forth about this axis, albeit with damped amplitude.

The "limitless" definition of Eq. 3 facilitates additional insights into the kinematic relationship between ∠AJ and the initial conditions at the origin of FF. Take the special cases illustrated in Figs. 7a and 7b, unlike Fig. 6, the swerve axes in these two cases are nearly parallel with the LD direction, hence, ∠AJ is nearly zero. From Fig. 7a, for instance, the distance between the origin of free fight, z_o, and the first swerve maximum, z_1, is relatively small, at least in comparison with the wavelength of the swerve curve, λ. On the other hand, in Fig. 7b, $z_1 - z_o$ is relatively large. Contrasting the larger ∠AJ of Fig. 6 with that of Figs. 7a and 7b, it can be inferred that the largest ∠AJ will occur when $z_1 - z_o = \lambda/4$. In fact, if the swerve curve is approximated by a sine wave of the form $y = A\sin(2\pi[z-z_o]/\lambda)$, at least for the first cycle, then, from Eq. 3, the maximum ∠AJ would be given by

$$\left|\angle AJ_{max}\right| = \left| \left.\frac{d\left\{y=A\sin\left(\frac{2\pi[z-z_o]}{\lambda}\right)\right\}}{dz}\right|_{z_1=z_o+\lambda/4} - \left.\frac{d\left\{y=A\sin\left(\frac{2\pi[z-z_o]}{\lambda}\right)\right\}}{dz}\right|_{z_o} \right| \qquad (4)$$

$$= \frac{A\,2\pi}{\lambda}$$

To appreciate the significance of Eq. 4, Fig. 8 illustrates how $\angle AJ_{max}$ varies with A and λ, for two cases where y conforms to $A\sin(2\pi[z-z_o]/\lambda)$. From the depiction, a larger A and smaller λ produce a larger $\angle AJ_{max}$. For large-caliber guns, A may be on the order of several millimeters, whereas λ is on the order of tens of meters; hence, $\angle AJ_{max}$, from Eq. 4, will be small—on the order of milliradians.

In summary, Figs. 6–8, and the discussions thereabout, illustrate that the axis of swerve symmetry is fixed in space by the time the rod reaches its first swerve maximum, as implied by Eq. 3. They also provide visible examples that support the contention that it is not necessary to take the swerving motion to infinity, as called for in Eqs. 1 and 2, in order to establish the swerve axis. However, geometry alone does not provide physical insight into how the cg path can turn away from the LD direction after the rod enters FF. Next, a physical model is constructed that identifies the aerodynamic force that causes such a change in direction to occur.

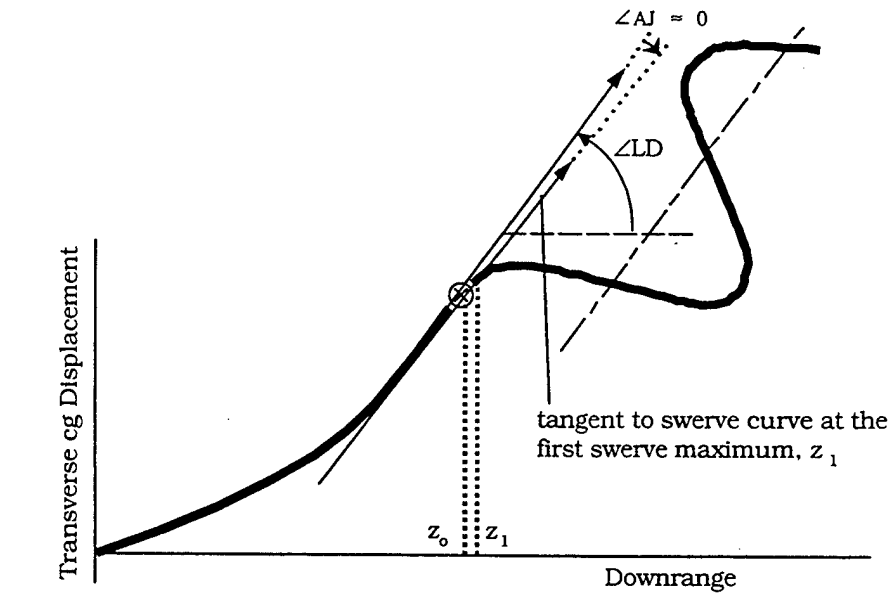

a)

b)

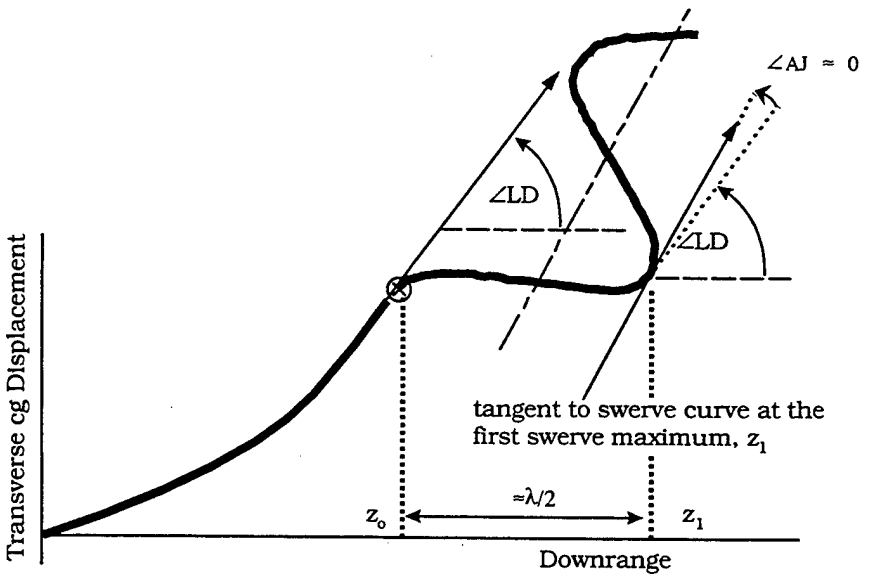

Fig. 7. The Influence of Initial (Swerve) Conditions on AJ, a) Entry Into FF at $z_o \approx z_1$, and b) Entry Into FF at $z_o \approx z_1 - \lambda/2$.

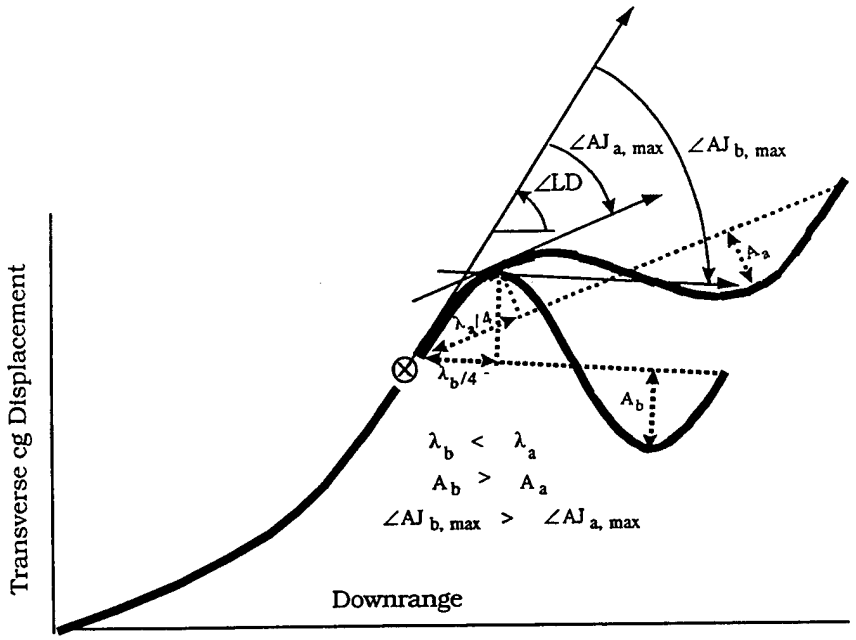

Fig. 8. Depiction of Variation in $\angle AJ_{max}$ With Amplitude and Wavelength of the Swerve Curve

A PHYSICAL EXPLANATION FOR AJ

A KE penetrator is also called a long-rod penetrator, conveying the fact that its fundamental shape is a high length-to-diameter ratio cylinder. It is fin stabilized, with only a small roll rate (assumed here to be zero). There are two fundamental aerodynamic forces on such a rod, one is drag, $\vec{D}$, and the other is lift, $\vec{L}$. The combination of drag and lift produces a resultant force, $\vec{R}$ $(=\vec{L}+\vec{D})$, acting at the center of pressure, cp, as shown in Fig. 9. The drag force is opposite in direction to $\vec{u}$, while the lift force is perpendicular $\vec{u}$. However, lift is only nonzero if the angle of yaw (α) between the symmetric rod axis and $\vec{u}$ is nonzero. Since the Magnus force is absent for a nonrolling projectile, lift is the only aerodynamic force that is capable of producing the type of lateral cg motion needed to explain AJ.

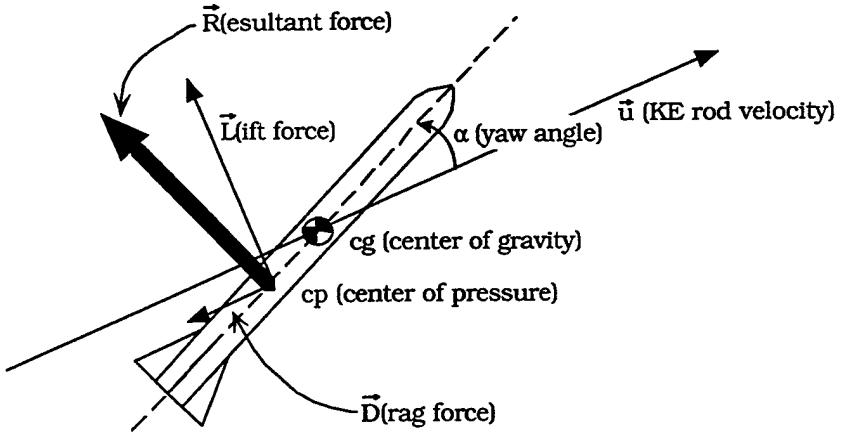

Fig. 9. Illustrating the Lift and Drag Force Directions, as Well as the CG and CP Locations.

In order to understand how the lift force can, in fact, account for AJ, it is necessary to discuss the factors that control α (thereby controlling lift). By Newton's second law for angular motion, yaw will be controlled by the aerodynamic moment, $\vec{M}$, that acts about the projectile cg. For a properly designed nonspinning KE rod, $\vec{M}$ will tend to decrease α, aligning the rod axis with $\vec{u}$. Consider then, what happens when such a KE penetrator enters FF.

Suppose, as shown in Fig. 10 (which displays the same cg motion as Figs. 2, 3, 5, 6), the transverse component of the cg velocity is positive at the point where the rod enters FF, i.e., $\dot{y}_o > 0$ at y_o, z_o (attributed to a particular combination of LD effects, e.g., Fig. 1). Furthermore, assume that at entry into FF, the KE rod has a negative initial yaw, $\alpha_o < 0$ (represented, as a clockwise rotation of the rod axis below the impinging airstream in Fig. 10) and a negative initial yawing rate, $\dot{\alpha}_o < 0$ (given a clockwise arrow). Under these conditions, the flow of air will create an initial lift force with a negative-y component (reducing $\dot{y}$), and a negative-x directed moment $\vec{M}$, which (in lieu of being out of the page in Fig. 10) is depicted as a counterclockwise arrow. Eventually, the negative lift force will turn the cg motion around, so that $\dot{y} < 0$. Likewise, the counterclockwise $\vec{M}$ will eventually turn the angular motion around, changing the yaw rate from its initial negative value (clockwise) to a positive one (counterclockwise), $\dot{\alpha} > 0$. These changes in direction occur around the first local maximum in the swerve curve. In fact, it can be shown (Bundy [5]) that the yaw angle will be at its maximum at the local swerve maximum.

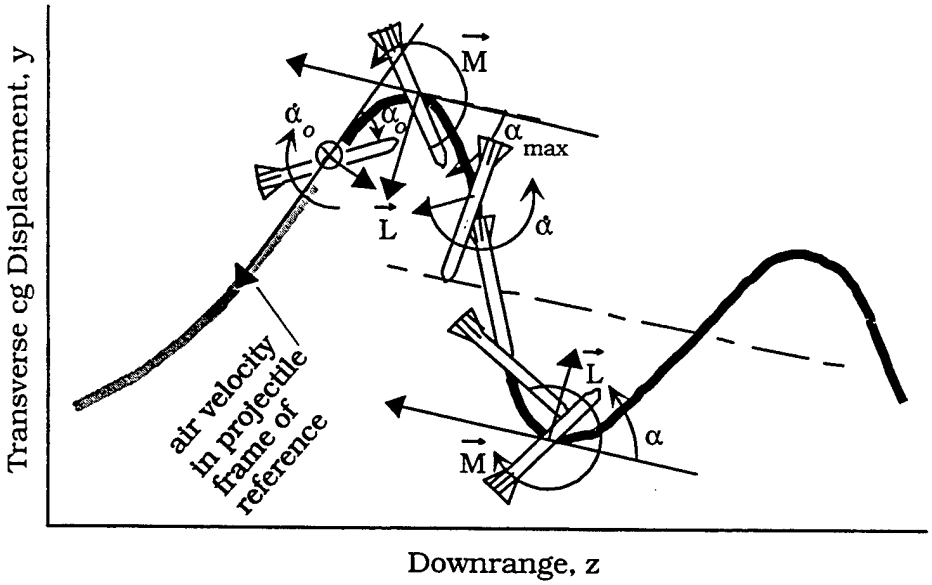

Fig. 10. Angular Orientations of a KE Rod Consistent With the CG Trajectory of Figs. 2, 3, 5, and 6.

After bringing the clockwise rotation to a halt at its maximum (negative) yaw angle, α_{max}, the counterclockwise moment in the first half cycle reverses the yaw rotation and eventually brings α to zero. This occurs when the y component of the rod's cg crosses the swerve axis, as pictured. Throughout this period of time, the lift force remains negative; thus, the rod cg will enter the second half cycle of the swerve motion with negative-y momentum. Similarly, the counterclockwise angular momentum rotates α past zero at the swerve axis, giving the rod a positive yaw in the second half cycle. However, when α becomes positive, it generates a positive lift force and a positive-x directed (into the page) clockwise moment $\vec{M}$ that opposes further increases in α, as depicted in Fig. 10. Such projectiles are said to be statically stable, which simply means that if the projectile is held statically at some nonzero yaw angle, and then released (as might be the case in a wind tunnel experiment), the yaw will decrease.

Hence, the conditions present in the first half cycle of FF are exactly reversed in the second half of the swerve cycle. Therefore, with the exception of a reversal in directions, the explanation for events in the second half cycle will be identical to that which accounted for the first half cycle motion. In a like manner, each cycle in the swerving motion of the KE rod cg can be understood as resulting from the oscillation in lift created by a periodic motion in yaw.

Although the previous arguments infer that the change in cg direction between the point of entry into FF and the first maximum yaw ($\equiv \angle AJ$) is attributable to the force of lift due to yaw over this region, the dependence of $\angle AJ$ on initial conditions cannot be fully appreciated until Fig. 7 is compared with Fig. 6 in the following manner.

Figure 11, displays a set of initial and subsequent FF conditions that are consistent with the cg motion of Fig. 7. Specifically, as illustrated, the initial yaw angle of the rod as it enters FF is near its maximum (albeit negative) value, $\alpha_o \approx \alpha_{max}$, therefore, the initial yaw rate is near zero, $\dot{\alpha}_o \approx 0$. Furthermore, since the initial

yaw is negative, $\bar{L}$ is initially directed toward the swerve axis and $\bar{M}$ is initially in the negative-x direction (out of the page). These are exactly the same conditions that were present at the first local maximum in the swerving motion of Fig. 10. Therefore, from the point of first maximum yaw onward, the lift force affecting the cg motion of Fig. 11 is exactly the same as that governing the cg motion of Fig. 10. Yet, the direction of the swerve axis is seen to be noticeably different, in particular, the $\angle AJ$ is noticeably different. The significance of this observation is the sum and substance of this paper. That is, since the aerodynamic force on the KE rod is essentially the same from the first maximum onward in both Figs. 10 and 11, yet $\angle AJ$ is significantly different in the two figures, it must be the case that $\angle AJ$ is due to differences in the lift force prior to the first maximum yaw. Once again, implicating that AJ is a regional effect, occurring from the point of entry into FF up to the point of first maximum yaw.

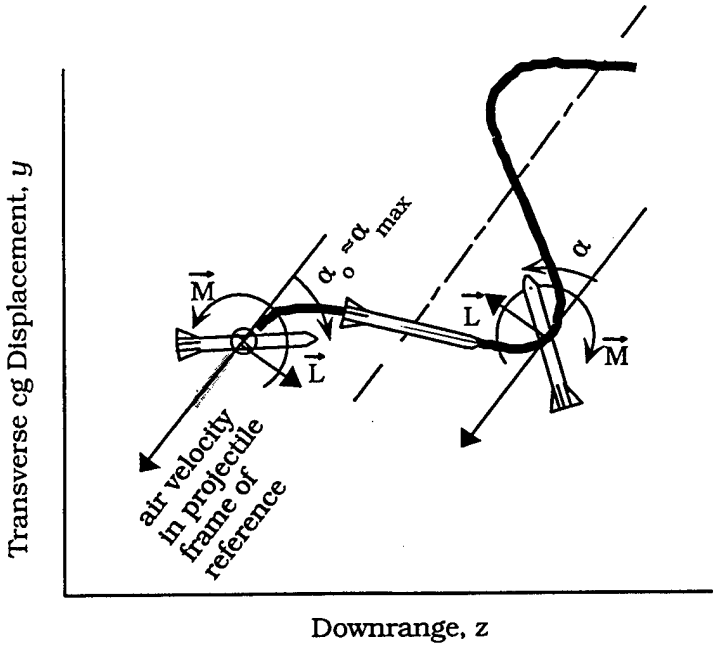

Fig. 11. Angular Orientations of a KE Rod Consistent With the CG Trajectory of Fig. 7.

Ultimately, differences in the lift force, more correctly, differences in the integrated lift force, up to the point of first maximum yaw are governed by differences in the initial conditions. That is, in both Figs. 10 and 11 the rod enters FF with an appreciable initial yaw angle, but only in the case of Fig. 10 was the initial yaw rate, $\dot{\alpha}_o$, notably different than zero. Comparing this with the observation that $\angle AJ$ was only substantial for the initial conditions of Fig. 10, it can be deduced that $\angle AJ$ is not dependent upon the initial yaw angle, but rather, it is dependent on the initial yaw rate. It is shown later that, indeed, the mathematical expression for $\angle AJ$ of a nonspinning KE rod depends on the initial yaw rate, not yaw. (Bear in mind, for the more general case of a spinning projectile, $\angle AJ$ depends on both yaw and yaw rate.)

In summary, based on the physical and kinematical developments of this and the previous section, respectively, it is now a simple matter to derive a dynamical expression for AJ. However, before such an expression can be formulated, it is necessary to review the basic aerodynamic forces and moments.

BASIC AERODYNAMIC FORCES AND MOMENTS ACTING ON A NONSPINNING KE PENETRATOR

The force of friction, drag, on the projectile is commonly expressed as

$$\bar{D} = -\frac{1}{2} C_D \rho A |\bar{u}| \bar{u} , \tag{5}$$

where C_D is called the drag coefficient, ρ is the air density, A is the cross-sectional area of the projectile, and, by virtue of the minus sign, drag is in the direction opposite $\vec{u}$, the cg velocity vector (Fig. 9). For small yaw (e.g., $\alpha < 5°$), typical of KE rods, C_D can be considered a constant.

The expression for lift is conventionally written as

$$\vec{L} = \frac{1}{2} C_L \rho A |\vec{u}|^2 \hat{L} , \tag{6}$$

where C_L is referred to as the lift coefficient. The unit-vector direction of the lift force, $\hat{L}$, is perpendicular to the drag force and is in the yaw plane.

Here, yaw is the vertical(z–y)-plane angle, α, between the projectile's tail-to-nose axis and the tangent to its trajectory (or, equally suitable, $\vec{u}$). As is typical, it is assumed here that a positive α means the nose of projectile is above $\vec{u}$. A projectile flying at zero yaw has no lift, whereas one having a positive α generates a positive lift (the case depicted in Fig. 9) and one having a negative α creates a negative lift (the initial conditions depicted in Figs. 10 and 11). A yaw dependence of this type is characteristic of an odd-power series in α. For small yaw, the expansion can be truncated after the first power in α:

$$C_L = C_{l_\alpha} \alpha , \tag{7}$$

where C_{l_α} is the derivative of the lift coefficient with respect to α.

Suppose the original line of fire is defined to be the z axis, and that gravity and the Coriolis force are ignored. Furthermore, assume the cg motion is 2-D planar, in particular, assume the motion is confined to the vertical plane, then $\vec{u} = \dot{z}\hat{z} + \dot{y}\hat{y}$ (where a dot indicates time differentiation), as shown in Fig. 12.

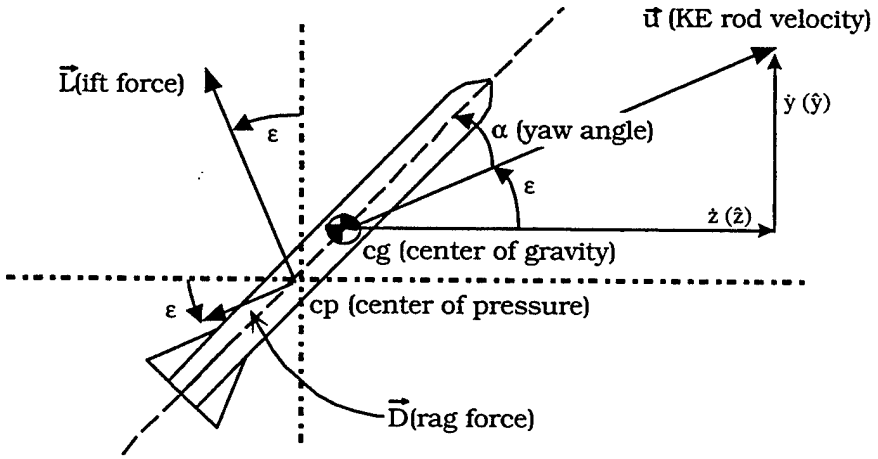

Fig. 12. Illustration of 2-D Planar Force and Velocity Components.

From Newton's second law for linear motion in the $\hat{y}$ direction,

$$m \frac{d\dot{y}}{dt} = \vec{L}\cdot\hat{y} + \vec{D}\cdot\hat{y} = \frac{\alpha}{|\alpha|}\left\{ |\vec{L}| \cos\varepsilon \right\} - |\vec{D}| \sin\varepsilon , \tag{8}$$

where m is the mass of the projectile, and the ratio $\alpha/|\alpha|$ accounts for the positive or negative influence of yaw on lift. The counterclockwise (positive) angular deviation, ε, of $\vec{u}$ from the original line of fire is assumed small;

nevertheless, it is not necessary to neglect ε entirely in order to simplify Eq. 8. If the coordinate axes $\hat{z}$ and $\hat{y}$ are simply rotated by the angle ε (i.e., the $\tan^{-1}$ of the cg trajectory) at z_1 and y_1, and thereafter denoted $\hat{s}$ and $\hat{Y}$, respectively, as shown in Fig. 13, then the equation of motion in the $\hat{Y}$ direction becomes

$$m \frac{d\dot{Y}(s)}{dt} = \bar{L} \cdot \hat{Y} + \bar{D} \cdot \hat{Y} \approx \frac{\alpha}{|\alpha|} |\bar{L}| \quad , \tag{9}$$

where lift is nearly parallel with, and drag nearly perpendicular to, the Y axis (even though it may not appear this way in the not-to-scale illustration of Fig. 13.). In this coordinate system, the locus of points Y(s) defines the swerve curve, which oscillates about the swerve axis, $\hat{s}$. Note, $\bar{u}$ will actually oscillate about some average vector; however, the magnitude of this oscillation is small, so that, $\bar{u} (= \dot{z}\hat{z} + \dot{y}\hat{y}) \approx \dot{s}\hat{s}$.

(Note also, for future reference, if the direction of positive $\hat{y}$ and positive $\hat{Y}$ had been defined as opposite of that assigned here [viz., if $\hat{y}$ and $\hat{Y}$ were defined as positive downward], yet α was still considered positive when the nose of the KE rod is above its cg velocity vector, then the right-hand side of Eqs. 8 and 9 would change signs. This minus sign would carry through in subsequent equations; ultimately, it would change the sign of the final expression for AJ. In other words, as stated in the kinematical discussion of AJ, the sign convention for positive transverse displacement will affect the sign convention for AJ.)

Simply stated, Eq. 9 establishes that lift is the primary cause of swerve, and, from Eqs. 6 and 7, lift is proportional to yaw; hence

$$m \frac{d\dot{Y}(s)}{dt} = \frac{\alpha}{|\alpha|} \left| \frac{1}{2} \rho A |\bar{u}|^2 C_{l_\alpha} \alpha \right| = \frac{1}{2} \rho A |\bar{u}|^2 C_{l_\alpha} \alpha \quad . \tag{10}$$

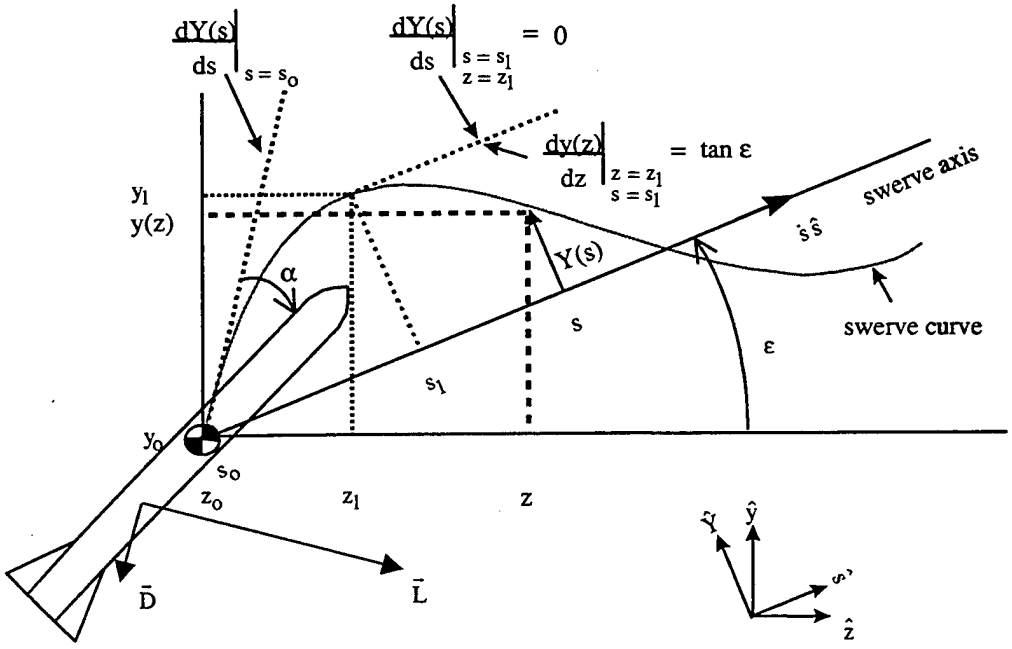

Fig. 13. Swerve-Fixed $(\hat{s}, \hat{Y})$ and Earth-Fixed $(\hat{z}, \hat{y})$ Coordinate System (Illustrated Dimensions are Not to Scale).

The expression for α must satisfy the torque equation, viz.,

$$m k^2 \frac{d\dot{\alpha}}{dt} (-\hat{x}) = \bar{M} \quad , \tag{11}$$

where k^2 is the radius of gyration of the KE rod about its transverse (x) axis. Furthermore, in accordance with the right-hand rule, a counterclockwise angular acceleration of the rod (relative to the positive-s(werve) axis) must be represented by a negative-x directed vector (which points out of the page), hence, the negative unit vector, $\bar{u}$, appears in Eq. 11.

In FF, the axis of the projectile will oscillate about its cg trajectory (i.e., the z, y or s, Y curve, depending on the coordinate system chosen). Just as air opposes the forward motion of the projectile, it will also oppose this oscillating motion. Hence, there will be a resisting torque, known as the damping moment, that varies with the yaw rate. As the name implies, the damping moment causes the yaw magnitude to diminish with time of flight. However, since it has been argued in the previous illustrations (e.g., Figs. 6–8) that $\angle$AJ is established within a relatively short segment of the trajectory, the effect of damping on AJ can be ignored. In this case, the moment $\bar{M}$ about the cg will only be due to the resultant force, $\bar{R} = \bar{L} + \bar{D}$, located at the center of pressure, cp (Fig. 12). Thus,

$$\bar{M} = |cg - cp| \left(|\bar{D}| \sin\alpha + \frac{\alpha}{|\alpha|} |\bar{L}| \cos\alpha \right) \hat{x} \approx |cg - cp| \left(|\bar{D}| \alpha + \frac{\alpha}{|\alpha|} |\bar{L}| \right) \hat{x} \quad , \tag{12}$$

for small α (e.g., < 5°). Note, a positive α will generate a positive-x directed $\bar{M}$.

Using Eqs. 5–7 in Eq. 12, yields

$$\bar{M} = \frac{1}{2} \rho A |\bar{u}|^2 |cg - cp| \alpha \left(C_D + C_{l_\alpha} \right) \hat{x} = - \frac{1}{2} C_{m_\alpha} \rho A |\bar{u}|^2 d\alpha \, \hat{x} \quad , \tag{13}$$

where C_{m_α} ($\equiv - [C_D + C_{l_\alpha}] |cg - cp| / d$) is called the derivative of the restoring (overturning, or pitching) moment coefficient with respect to α, and d is the rod diameter. By definition, C_{m_α} is negative for a statically stable projectile. The coefficients C_D, C_{l_α}, and C_{m_α} can all be determined from wind-tunnel measurements, or, they can be numerically predicted using computational fluid dynamics (CFD).

Substituting Eq. 13 into Eq. 11 produces

$$m k^2 \frac{d\dot{\alpha}}{dt} = \frac{1}{2} C_{m_\alpha} \rho A |\bar{u}|^2 d\alpha \quad . \tag{14}$$

Since C_{m_α} is negative for the KE projectile, this differential equation for α is of the form $\ddot{\alpha} \propto -\alpha$. Such an equation has a sinusoidal solution; thus, from Eq. 10, Y(s) will have a sinusoidal solution (however, α and Y will be 180° out of phase). It is now proven that this oscillatory motion, coupled with the lift force, can account for AJ.

A MATHEMATICAL FORMULATION FOR AJ

It was stated in the kinematical discussion surrounding Eq. 3, that an alternative definition for $\angle AJ$ is:

$$\angle AJ = \tan^{-1}\left\{ \left.\frac{dy}{dz}\right|_{z_1} \right\} - \tan^{-1}\left\{ \left.\frac{dy}{dz}\right|_{z_o} \right\} \approx \left.\frac{dy}{dz}\right|_{z_1} - \left.\frac{dy}{dz}\right|_{z_o} \quad , \tag{15}$$

$$\left(= \left.\frac{\dot{y}}{\dot{z}}\right|_{z_1} - \left.\frac{\dot{y}}{\dot{z}}\right|_{z_o} \approx \frac{\dot{y}(z_1) - \dot{y}(z_o)}{\dot{z}} \right)$$

where, it will be recalled, z_1 is taken to be the downrange coordinate of the first local swerve maxima (relative to the swerve axis), while z_o is the designation for the downrange coordinate at the origin of FF (cf., Figs. 7 and 13). Hence, from Eq. 15, $\angle AJ$ can be viewed as a change in slope of the cg trajectory from z_o to z_1 (or, it can be viewed as a change in transverse velocity from z_o to z_1, nondimensionalized by the longitudinal velocity [assumed to be constant from z_o to z_1]).

Equations 3 and 15 define $\angle AJ$ in terms of dy/dz, to find its equivalent expression in terms of dY/ds, it is necessary to find the transformation algorithm between y and Y, and z and s. To that end (with the aid of Fig. 13), it can be shown that

$$\begin{aligned} y(z) &= Y(s)\cos\varepsilon + (s - s_o)\sin\varepsilon \\ z &= (s - s_o)\cos\varepsilon - Y(s)\sin\varepsilon \end{aligned} \tag{16}$$

From Eq. 16,

$$\frac{dy(z)}{dz} = \frac{\frac{dy(z)}{ds}}{\frac{dz}{ds}} = \frac{\frac{dY(s)}{ds}\cos\varepsilon + \sin\varepsilon}{\cos\varepsilon - \frac{dY(s)}{ds}\sin\varepsilon}$$

$$\approx \frac{dY(s)}{ds} + \tan\varepsilon \quad , \quad \text{for} \quad \frac{dY(s)}{ds},\ \varepsilon << 1 \tag{17}$$

Hence, from Eqs. 15 and 17,

$$\angle AJ = \left.\frac{dy}{dz}\right|_{z_1, s_1} - \left.\frac{dy}{dz}\right|_{z_o, s_o} = \left.\frac{dY}{ds}\right|_{s_1, z_1} - \left.\frac{dY}{ds}\right|_{s_o, z_o}$$

$$\left(= \left.\frac{\dot{Y}}{\dot{s}}\right|_{s_1} - \left.\frac{\dot{Y}}{\dot{s}}\right|_{s_o} \approx \frac{\dot{Y}(s_1) - \dot{Y}(s_o)}{|\vec{u}|} \right) \quad , \tag{18}$$

where the subscript notation z_1, s_1 (for example) refers to the point on the swerve curve with coordinate z_1 along the z axis and s_1 along the s axis (cf. Fig. 13), and time and space derivatives are related by

$$\dot{Y} \equiv \frac{dY}{dt} = \frac{dY}{ds}\frac{ds}{dt} \approx |\vec{u}|\frac{dY}{ds} \quad . \tag{19}$$

In effect, Eq. 18 states the obvious—the difference in slopes between two points on the swerve curve does not change if the coordinate system, used to describe the curve, is rotated through an angle ε.

Combining Eqs. 9, 10 and 14, it can be shown that

$$d\dot{Y} = \frac{\left(\vec{L}\cdot\hat{Y}\right)dt}{m} = \frac{C_{l_\alpha}\,k^2}{d\,C_{m_\alpha}}\,d\dot{\alpha} \quad . \tag{20}$$

Denoting $\dot{\alpha}_o$ and s_o as the initial conditions at entry into FF and $\dot{\alpha}_1$ and s_1 as the conditions at the first local maximum in the swerve curve, then integration of Eq. 20 yields

$$\dot{Y}(s_1) - \dot{Y}(s_o) = \int_{\dot{Y}(s_o)}^{\dot{Y}(s_1)} d\dot{Y} = \frac{1}{m}\int_{t(s_o)}^{t(s_1)}\left(\vec{L}\cdot\hat{Y}\right)dt = \int_{\dot{\alpha}_o}^{\dot{\alpha}_1}\frac{C_{l_\alpha}\,k^2}{d\,C_{m_\alpha}}\,d\dot{\alpha} = \frac{C_{l_\alpha}\,k^2}{d\,C_{m_\alpha}}\left(\dot{\alpha}_1 - \dot{\alpha}_o\right) \quad . \tag{21}$$

Combining Eqs. 18 and 21, yields

$$\angle AJ = \left.\frac{dY}{ds}\right|_{s_1,\,z_1} - \left.\frac{dY}{ds}\right|_{s_o,\,z_o} \approx \frac{1}{m\,|\bar{u}|}\int_{t(s_o)}^{t(s_1)}\left(\vec{L}\cdot\hat{Y}\right)dt = \frac{C_{l_\alpha}\,k^2}{d\,C_{m_\alpha}\,|\bar{u}|}\left(\dot{\alpha}_1 - \dot{\alpha}_o\right) \quad . \tag{22}$$

Equation 22 shows that $\angle AJ$ can be viewed as a change in the slope of the cg trajectory from z_o to z_1, or, it can be related to a change in angular rates from z_o to z_1 (s_o to s_1). Furthermore, the insertion of the lift correlation in Equation 20 and its retention in Equations 21 and 22 serves to underscore the physical explanation given earlier, viz., that $\angle AJ$ is due to the (integrated) effect of lift, caused by yaw, from z_o (s_o) to z_1 (s_1).

Note, Eqs. 18, 21, and 22 could have been simplified by setting $dY/ds\big|_{s_1,\,z_1} = 0$ and $\dot{Y}(s_1) = 0$, since, by definition, Y(s) is at a local maxima at s_1, z_1. (This would also mean [from Eq. 17] that $dy/dz\big|_{z_1,\,s_1} = \tan\varepsilon$, as marked in Fig. 13.) Moreover, since α and Y are 180° out of phase, when $\dot{Y}(s_1) = 0$, $\dot{\alpha}_1 = 0$; hence, Eq. 22 can be simplified to:

$$\angle AJ = -\left.\frac{dY}{ds}\right|_{s_o,\,z_o} = -\frac{C_{l_\alpha}\,k^2}{d\,C_{m_\alpha}\,|\bar{u}|}\,\dot{\alpha}_o \quad . \tag{23}$$

From Equation 22, it can be seen that $\angle AJ$ will increase if either the integrand (viz., the lift force) or the domain of integration (viz. the lift force action time) increases. In more fundamental terms (noting that C_{m_α} will always be negative for a KE rod, and C_{l_α}, k, *d*, and $|\bar{u}|$ are all positive), $\angle AJ$ will increase if either 1) C_{l_α} increases (so that the lifting force per degree yaw increases), 2) k increases (in which case, the rod would rotate slower, and hence the lifting force would act longer), 3) $\dot{\alpha}_o$ increases (so that, once again, it would take more time to bring the rod to rest), or 4) C_{m_α} decreases (so that the overturning moment per degree yaw decreases, again lengthening the action time for the lifting force).

Other, equivalent expressions for AJ that can be found in the literature include:

$$\angle AJ = -(+)\frac{C_{l_\alpha}\,k^2}{d\,C_{m_\alpha}\,|\bar{u}|}\,\dot{\alpha}_o \equiv -(+)\frac{C_{l_\alpha}\,I_t}{m\,|\bar{u}|\,d\,C_{m_\alpha}}\,\dot{\alpha}_o \equiv -(+)\frac{C_{l_\alpha}\,I_t}{m\,d^2\,C_{m_\alpha}}\,\alpha'_o \quad , \tag{24}$$

where I_t ($= mk^2$) is the moment of inertia of the (symmetric) projectile about its transverse axis, and α'_o is the initial FF yaw rate with respect to the trajectory arc length, measured in rod diameters (i.e., $\alpha'_o \equiv d\alpha / d[s/d]\,|_{s_o,z_o}$).

Depending on the coordinate system used, there may or may not be a negative sign on the right-hand side in the equalities/identities of Eq. 24. The convention chosen here is to define both the positive vertical axis (y) and positive yaw (α) as up (up for α means its nose is above the cg velocity vector). However, it is more common in the field ballistics to define the positive vertical axis as down, and positive yaw as up; in this case, the negative sign convention is absent in Eq. 24 (thereby explaining the plus signs in parentheses). The plus-sign form of the expression for $\angle AJ$ is, by far, the most common construction (e.g., Murphy and Bradley [3], Murphy [4], Fansler and Schmidt [6], Schmidt [7]). There is one other sign variation that may appear in the literature; if both the positive vertical axis and positive yaw are defined as down, then the sign remains negative in Equation 24 (e.g., Murphy [2], Lijewski [8]). Regardless of the sign convention for the coordinate system used, it is always the case, as Murphy and Bradley [3] state, that "jump due to α_o' is in the direction of α_o'."

CONCLUSIONS AND COMMENTARY

Equation 3 (or 15) provides a "limitless" kinematical definition for $\angle AJ$, which, reassuringly, leads to the traditional dynamical expression for $\angle AJ$, viz. Eq. 24. The origins of possible variations in the sign convention of Eq. 24 were explored, but the paper's primary objective was to answer the questions: what is AJ, what does it mean, and what aspect of the flight trajectory does it refer to, or account for.

For instance, one misconception about AJ can arise from the fact that Eq. 24 only shows a dependence on the initial yaw rate at the origin of FF (concealing the fact that it is actually a difference in rates, Eq. 22, that happens to equal the initial rate, Eq. 23). Therefore, some may conclude from this (apparent) point dependence that AJ is a "point-based" phenomenon, i.e., that it results from (aero)dynamical effects that occur at the origin of FF. Others, seeking a geometrical explanation for AJ, may forgo the dynamical definition of Eq. 24 and return to its origin in the kinematical definition adopted, for example, by Murphy [2] or [4]. However, those geometry-based definition for AJ (viz., Eq. 1 or 2) call for the cg coordinates to be evaluated in the limit of an infinite trajectory. Thus, there is some risk that those drawing upon this definition to explain AJ will erroneously assume that it is a transformation that accumulates with downrange distance (not realizing that the swerve axis is actually a constant, established long before the trajectory reaches infinity).

The central theme of this paper is to show that AJ is neither a change in direction that takes place at a point, nor is it a curving change that takes place over a domain of infinite extent, but rather, it is a regional transformation. In particular, using an alternative kinematic definition, it was illustrated geometrically (in terms of the cg trajectory), argued physically (in terms of yaw and lift), and proven mathematically (based on Newton's equations of motion), that $\angle AJ$ for a (nonspinning) KE penetrator can be accounted for by the change in transverse cg velocity—due to lift—acting for the short period of time and space from entry of the projectile into FF until it reaches its first local maxima in yaw (or swerve).

REFERENCES

1. Bornstein, J., I. Celmins, P. Plostins, and E. M. Schmidt, December 1988, "Techniques for the Measurement of Tank Cannon Jump," BRL-MR-3715, U.S. Army Ballistic Research Laboratory, Aberdeen Proving Ground, MD.

2. Murphy, C. H., April 1957, "Comments on Projectile Jump," BRL-MR-1071, U.S. Army Ballistic Research Laboratories, Aberdeen Proving Ground, MD, AD 132323.

3. Murphy, C. H., and J. W. Bradley, May 1959, "Jump Due to Aerodynamic Asymmetry of a Missile With Varying Roll Rate," BRL-R-1077, U.S. Army Ballistic Research Laboratories, Aberdeen Proving Ground, MD, AD 219312.

4. Murphy, C. H., July 1963, "Free Flight Motion of Symmetric Missiles," BRL-R-1216, U.S. Army Ballistic Research Laboratories, Aberdeen Proving Ground, MD.

5. Bundy, M. L., December 1998, "The Regional Nature of Aerodynamic Jump," to be published, U.S. Army Research Laboratory, Aberdeen Proving Ground, MD.

6. Fansler, K. S., and E. M. Schmidt, June 1975, "The Influence of Muzzle Gasdynamics Upon the Trajectory of Fin-Stabilized Projectiles," BRL-R-1793, U.S. Army Ballistic Research Laboratory, Aberdeen Proving Ground, MD.

7. Schmidt, E. M., "A Technique for Reduction of Launch-Induced Perturbations," *Proceedings of the Eighth U.S. Army Symposium on Gun Dynamics*, G.A. Pflegl, Ed., Benet Special Publication ARCCB-SP-96032, Newport, RI, 14-16 May, 1996, pp. 12-1–12-7.

8. Lijewski, L. E. "Aerodynamic Jump Prediction for Supersonic, High Fineness Ratio, Cruciform Finned Bodies," *Journal of Guidance, American Institute of Aeronautics and Astronautics*, September–October 1982, Vol. 5, No. 5, pp. 521–528.

Sabot Front Borerider Stiffness vs. Dispersion: *Finding the Knee in the Curve*

Alan F. Hathaway and John R. Burnett, Jr.

Arrow Tech Associates
1233 Shelburne Road
Suite D8, Pierson House
South Burlington, Vermont 05403
E-mail: arrowtech@prodas.com
http://www.prodas.com

It is a well-known fact that in the design of fin-stabilized projectiles, the radial stiffness of the sabot front borerider has a significant impact on the projectile's dispersion characteristics and is therefore, an important design consideration. Whether designing a new projectile or trying to improve on an existing design, projectile designers can achieve front borerider stiffness without understanding its affect on dispersion characteristics. There is a ***knee*** in the stiffness vs. dispersion curve at which a change in the sabot front borerider stiffness will have a significant impact on dispersion or no impact at all depending on whether the stiffness is increased or decreased. The subject of this paper is an analytical approach to quantitatively determining the *knee in the curve*. Results from using this approach on the M865 APFSDS projectile are also presented.

INTRODUCTION

The ability to predict the dispersion of a projectile is a challenging task due to the fact that dispersion is a combination of independent and interdependent random launch "events" occurring throughout the complete projectile environment from propellant ignition to target impact. There are many parameters that influence each of these "events". One of the more important parameters affecting these "events" is the stiffness of the sabot front borerider.

If the stiffness is insufficient, testing during projectile development might reveal that the dispersion is outside the design specifications; this leads to design changes and additional testing. However, since dispersion is a combination of "events", insufficient stiffness could be masked by other "events" during this phase of testing. It is also unlikely that sufficient testing is performed during development to provide assurance that, across the total range of manufacturing tolerances for every part/assembly, all combinations of these "events" have been tested. During production, insufficient stiffness could mean failing a Target Impact Dispersion (TID) Lot Acceptance Test (LAT) requirement; this type of failure can be very costly.

The in-bore balloting components of dispersion which are directly affected by sabot bore rider stiffness can be analytically determined using a worst case scenario in terms of muzzle exit conditions. However, it is often very time consuming and requires many trials to find the specific initial conditions that produce the worst muzzle exit conditions.

This paper summarizes an analytical method that combines in-bore balloting analyses, dispersion sensitivity determination, and manufacturing tolerance information into a stochastic approach for predicting dispersion with varying sabot front borerider stiffness.

OVERVIEW OF STOCHASTIC APPROACH TO PREDICTING DISPERSION

Why Stochastic Approach

One of the primary contributors to the in-bore balloting component of dispersion is the accumulation of tolerances in the manufactured projectile parts and assembly of those parts into a projectile whose CG does not lie on the geometric center of the projectile. With high velocity, conventional guns, very small CG offsets can produce catastrophic results. While a user may want to know what the worst possible launch scenario may be, he/she may also be interested in the likelihood of a failure occurring. Use of a stochastic approach enables the analyst to determine the probability of failure (either structural or launch induced dispersion). It also gives the user the range and mean of expected behavior.

Due to the fact that the relationship between maximum balloting loads and the initial orientation of projectile CG offset and principal axis tilt is not intuitive, selection of a "worst case" analysis condition could require several trial and error analysis replications. An analytical procedure that is set up to only run one set of conditions at a time is of limited value and can prove to be very time consuming. It has been Arrow Tech's experience that an approach that randomly selects initial conditions and continues with a sound analytical solution can prove very useful in determining the probability of occurrence of the outcome.

The question is sometimes asked: "Why do I need a stochastic approach when I only launch one or, at most, a handful of projectiles at a time?"

The answer to this question is, at the same time, both simple and complex. Projectiles launched from high performance gun systems are sensitive to small imperfections. While it is true that high performance projectiles are fabricated with significant precision, the center of mass is not perfectly aligned with the geometric center of the projectile. Assembly of the piece parts and/or manufacture of any projectile is also imperfect (dimensional and runout tolerances). These small differences of the mass axis from perfection can have an orientation with the geometric axis that is not predictable.

Another random source of error is the placement of the projectile within the bore. The projectile (even if perfectly manufactured) will never be positioned exactly the same way within the bore. The small differences in this, and the projectile mass axis offsets, when combined with the bumps in the gun tube (due to lack of straightness) can produce different maximum stress conditions within each projectile firing.

Approach Considers the Complete Projectile Environment

This approach considers the complete projectile environment from propellant ignition to target impact as shown in Figure 1. The environment includes the following three major phases:

1. Propellant ignition to muzzle exit
2. Muzzle exit until sabot discard
3. Sabot discard through target impact

Each of these distinct phases involves parameters that have an impact on dispersion and requires a specific type of analysis to determine the components of dispersion.

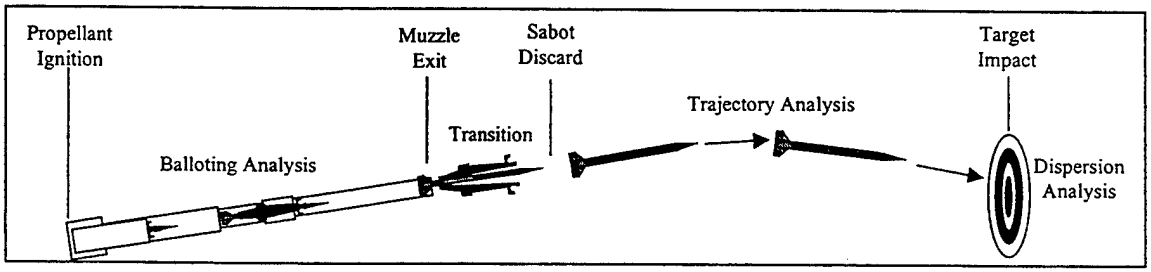

Figure 1: The Complete Projectile Environment

Propellant ignition to muzzle exit implies an in-bore balloting analysis is performed to determine the muzzle exit condition components of dispersion. Arrow Tech's BALANS analysis software is used for the balloting analysis. The basic inputs for the in-bore balloting analysis are a lumped parameter model of the projectile that properly characterizes its mass properties and flexibility including the sabot front borerider stiffness, a forcing function, and several diameters and runouts that are used to orient the projectile within the gun tube.

Muzzle exit to sabot discard dispersion components consist of a bore site component and a sabot discard component. These transition parameters are very difficult to determine analytically. For this reason, the bore site component is usually determined via test set-up measurements and the sabot discard component is determined from experience with testing of similar projectiles.

Sabot discard through target impact is the free-flight trajectory of the projectile. The dispersion components are muzzle velocity variation, wind sensitivity, aerodynamics jump and trim angle, and aerodynamic mass asymmetries. Arrow Tech's Projectile Design and Analysis system, PRODAS, is used for determining the sensitivities to these dispersion components.

The dispersion components from the complete projectile environment are then combined in a statistical Target Impact Dispersion (TID) analysis to determine the overall dispersion both horizontally and vertically.

ANALYSIS SYSTEM FOR DETERMINING DISPERSION vs. STIFFNESS

Input Data Requirements

The process begins with gathering basic technical information such as manufacturing, assembly drawings and/or specifications, analytical results from other analyses such as a finite element analysis of the sabot front borerider. This information is critical to building the accurate analytical model of the projectile to be used during all analyses within this approach. From this information, a tolerance study can also be performed for input into the in-bore balloting analysis.

The second piece of information required is production history information such as Statistical Process Control (SPC) information. Even if working with a new projectile design for which there is no production history, it is valuable to obtain this information for a similar design or a projectile with similar characteristics. Since some of the inputs to this approach are statistical in nature, the historical data provides a foundation from which to derive the statistical information.

The last type of information required is test and/or measurement that is important to predicting dispersion but is not derived from analysis. This includes bore centerline measurements, bore site errors inherent within a test fixture or bore site tool, known sabot discard issues from tests of similar sabots, etc.

System Is Based On PRODAS and BALANS

PRODAS is a projectile design and analysis system with several analysis modules and is used to determine free-flight characteristics. The analysis modules that are key to this approach for predicting dispersion are the following:

- *Model / Edit Module* - The physical description of the projectile using PRODAS is used throughout the modeling effort. The lumped parameter model for in-bore balloting is automatically built from the geometric model created in this module.
- *Physical Properties Module* - This module uses the element / component definition from the Modeling Module to determine element, component and assembly physical properties that are used, not only in subsequent PRODAS analyses, but also in the in-bore balloting analysis.
- *Stability Module* - This module predicts the aerodynamic and stability coefficients for a given projectile configuration. Output from this module includes the Aerodynamic Jump Factor and the Aerodynamic Trim Coefficients.

- *Interior Ballistics Module* - This module's output is a tabulation of time, base pressure, chamber pressure, travel, spin rate, spin acceleration, axial acceleration, and axial velocity. These parameters form the forcing function for the in-bore balloting dynamic analysis.
- *Trajectory Module* - Both 4 DOF and 6 DOF trajectory options are used to assess the free-flight dispersion sensitivities.
- *CG Offset Module* – This module provides the ability to estimate the mean and standard deviation of projectile center of gravity radial offset and tilt of the principal axis from projectile drawings.

BALANS simulates the dynamic response and interaction of a flexible projectile and a flexible gun tube during in-bore travel. It also includes the effects of a curved bore profile. The simulation utilizes individual models of the projectile and gun tube, in a time step iterative solution. Pertinent motion and load data are periodically saved during the analysis to produce selective summary graphical displays. BALANS takes advantage of the Interior Ballistics simulation and CG Offset calculations of PRODAS and an automatic lumped parameter modeling capability to assist in building a BALANS model.

The analytical procedure utilized in BALANS presupposes that the projectile is initially misaligned within the gun tube due to manufacturing tolerances. During firing, this misalignment produces secondary forces causing transverse displacement and yawing motion of the projectile as it travels from breech to muzzle. The resulting yaw angle, angular rate, and transverse velocity at muzzle exit are then analyzed for their effect on dispersion.

Propellant Ignition to Muzzle Exit: In-Bore Dispersion Components

Balloting, within the context of this paper, refers to any transverse motion of a projectile in the gun tube. Some of the causes of balloting are discussed below.

- Projectile center of gravity (CG) and principal axis may be offset from the bore centerline. Even with a perfectly concentric projectile, it is possible to insert a projectile into a gun tube with less than perfect alignment with the bore centerline. Even if perfect insertion were achievable, projectile wear during travel may not be uniform, thereby producing CG or principal axis misalignment with the bore centerline.
- Projectiles, as manufactured, are not perfectly concentric. This lack of concentricity produces a transverse separation between the projectile geometric centerline (referenced from the bourrelet diameter) and the projectile CG.
- Projectile/gun tube (and wear induced) clearances may exist at projectile surfaces. These clearances enable the projectile to assume a skewed and/or non-symmetric position (CG shifted off-axis) within the gun bore.
- Insufficient stiffness of the projectile / gun tube interface will exacerbate conditions caused by minimal balloting. When a projectile is subjected to lateral loads, the radial stiffness of the projectile at the bourrelet, limits the radial deflection of the CG and potential tilt of the principal axis. Excessive deflection produces CG offsets that contribute to further deflection and balloting.
- Projectile wear produces or widens gaps (clearances) between the projectile bourrelet surfaces and the gun bore. Wear, therefore, enables the projectile to tilt its principal axis and/or translate the CG off the bore centerline.
- Gun tube curvature (including bore irregularities) exists in all gun tubes. While gun tube profiles are monitored during manufacture, some local tube curvature exists. Any tube curvature will induce balloting.
- Gas dynamics produce irregular pressures at the projectile base. These pressure spikes tend to exacerbate any existing projectile misalignment with the gun tube.

The basic inputs for the in-bore balloting analysis are a lumped parameter model of the projectile that properly characterizes its mass properties and flexibility, a forcing function, and several diameters and runouts that are used to orient the projectile within the gun tube. The lumped parameter model is generated automatically from the PRODAS geometric model.

Figure 2 is the lumped parameter model of the 120mm M865 APFSDS projectile that was automatically generated from the PRODAS geometric model; also shown is a lumped parameter model of a 120mm gun tube. As shown, the upper half of the model is the actual projectile as generated from PRODAS. The lower half attempts to mirror the upper half by reflecting the lumped parameter node/element model.

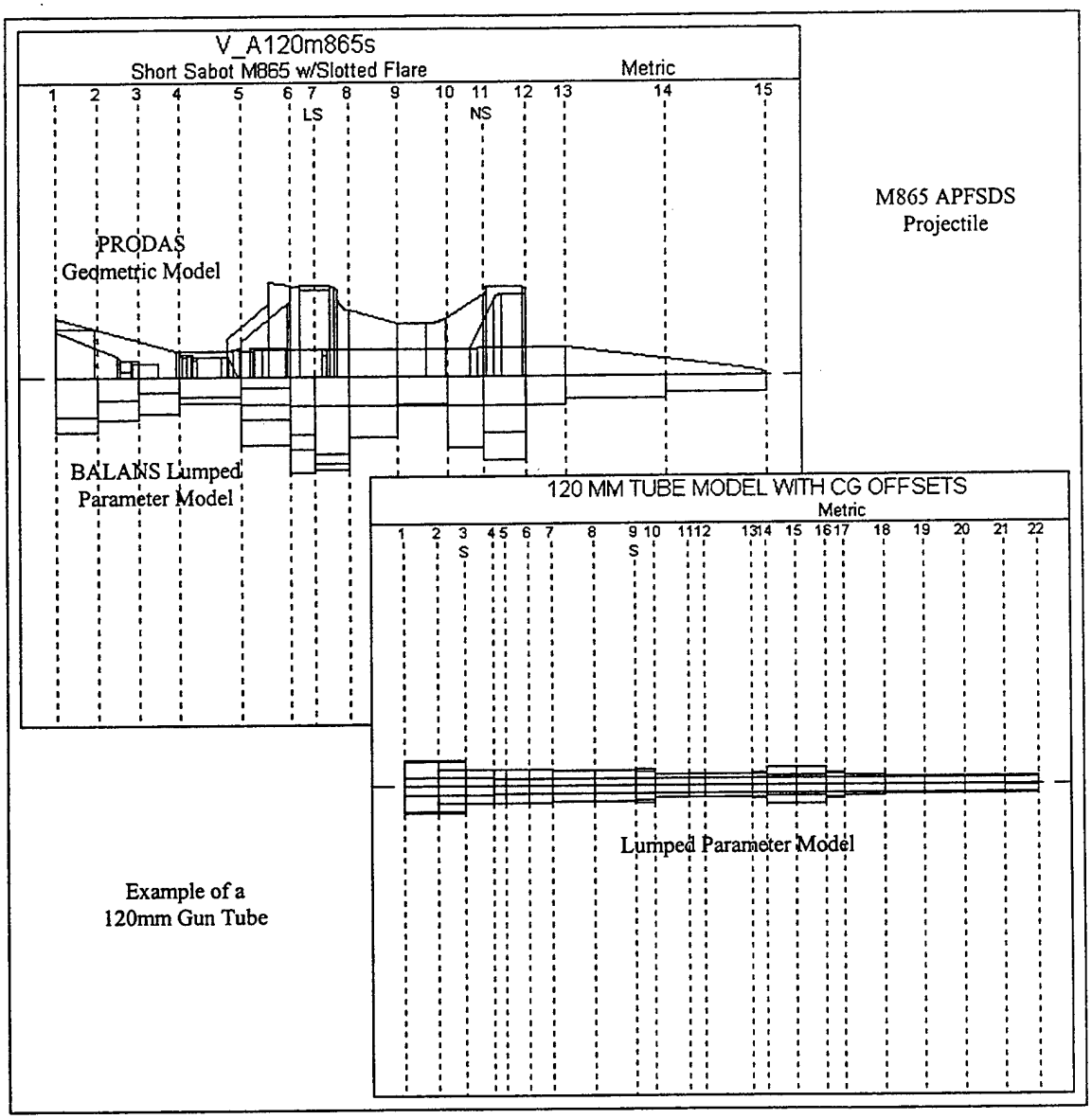

Figure 2: Lumped Parameter Models of the Projectile and the Gun Tube

The forcing function required for the balloting analysis is provided directly from the PRODAS interior ballistics analysis module. PRODAS uses the lumped parameter Baer-Frankl methodology to simulate combustion of propellant grains and calculate the time-dependent parameters of base pressure to be applied to the projectile aft of the obturator during the balloting analysis. Spin velocity and acceleration are computed and used to calculate centrifugal forces during in-bore travel; axial velocity and acceleration are computed and used to calculate axial forces during in-bore travel. Transverse forces are calculated from the induced balloting motion.

The diameters and runouts that are used to orient the projectile within the gun tube are shown in Figure 3 . These define the locations of the projectile / gun tube interfaces and some of the critical projectile dimensions which effect dispersion. The runouts and tolerances for these dimensions are also required.

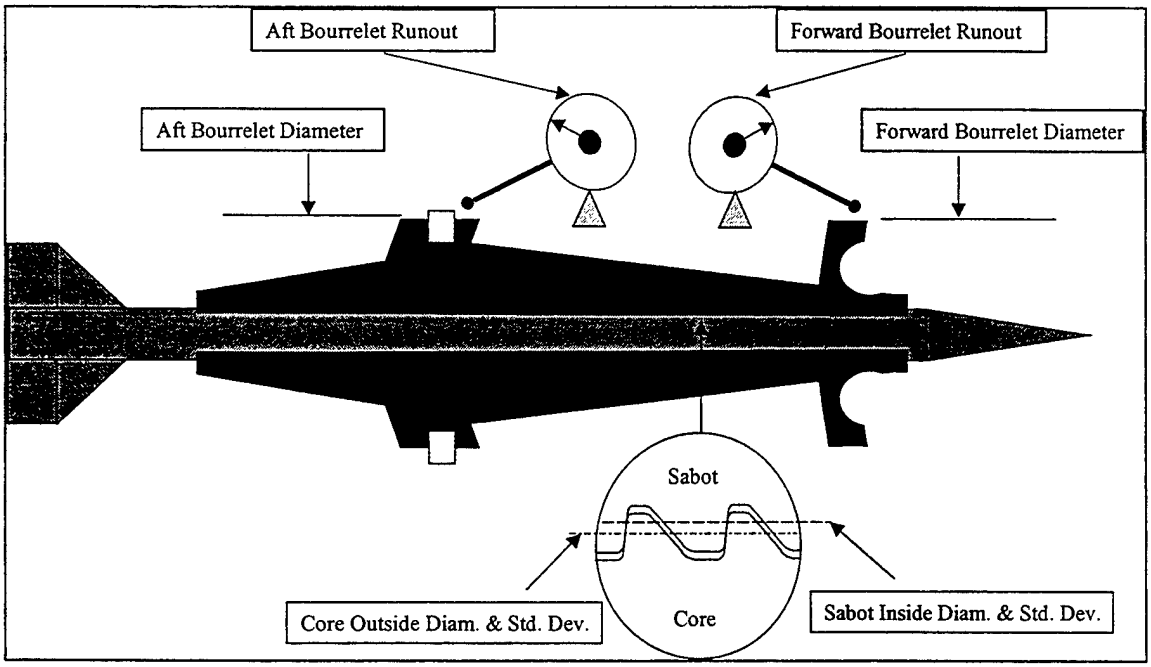

Figure 3: Balloting Analysis Variables

The statistical in-bore balloting analysis uses these dimensions described above and their tolerances to randomly orient the projectile in the gun tube. Several hundred in-bore balloting analyses are generally required to obtain statistically valid muzzle exit yaw, yaw rate, and transverse velocity predictions. To further illustrate this, the in-bore balloting analysis sequence number versus the cumulative average standard deviation of yaw rate is plotted in Figure 4. Each sequence number represents a different in-bore balloting analysis with different projectile dimensions.

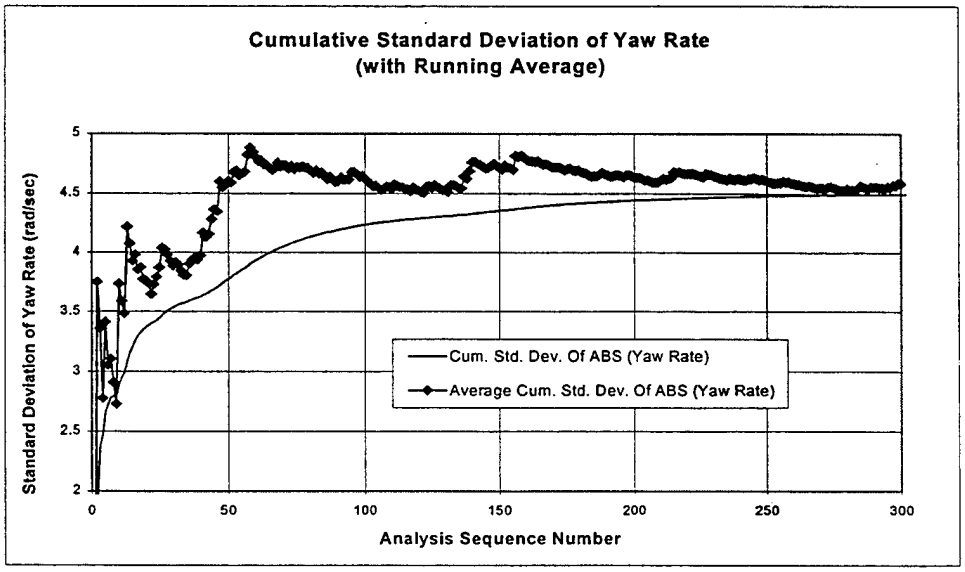

Figure 4: Analysis Sequence No. vs. Cumulative Standard Deviation of Yaw Rate

Muzzle Exit to Sabot Discard: Transition Dispersion Components

Transition sensitivities are separated into sabot discard and bore site sensitivities. Errors induced by sabot discard may have significant variation from one projectile configuration to another. There is both a physical component which can occur due to asymmetric loads applied to the core during discard and an aerodynamic interference component as shown in Figure 5.

Sabot discard is the least well understood of the major contributors to dispersion and therefore is generally determined from test, observation, and/or experience.

Bore site errors are the error in pointing the gun at the target. Bore site errors vary between calibers, gun crews, and instrumentation.

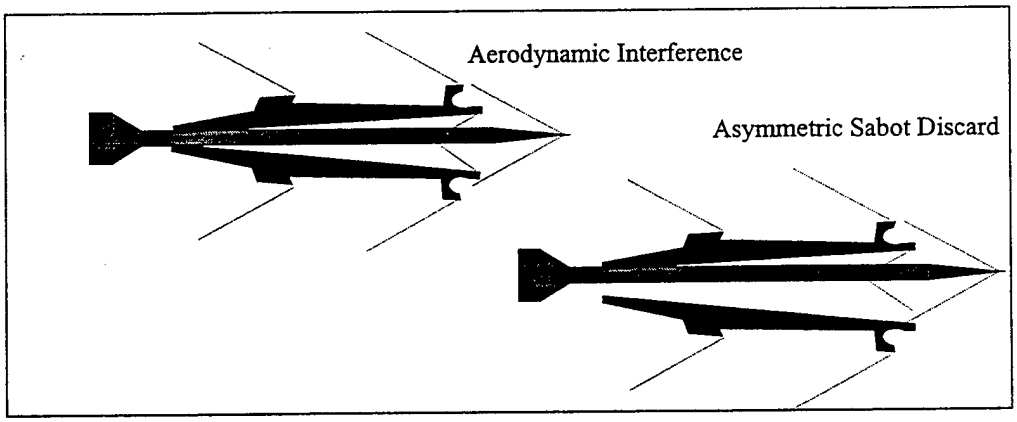

Figure 5: Sabot Discard Components of Dispersion

Sabot Discard to Target Impact: Free-Flight Dispersion Components

The free-flight dispersion component sensitivities include muzzle velocity, aerodynamic jump, cross winds, aerodynamic trim angle, and aerodynamic/mass asymmetries. All of these parameters are determined via trajectory analysis within PRODAS as follows:

- The muzzle velocity sensitivity factor is the drop variation due to muzzle velocity variation and can be calculated by comparing the drop of trajectory simulations made by perturbating muzzle velocities (typically 10 M/S). The resulting "delta drop" at the range of interest is then divided by the muzzle velocity difference to obtain the factor. Variations in muzzle velocity add primarily to the vertical projectile dispersion. Muzzle velocity standard deviation, which is also required, is generally available for ammunition lots.
- The aerodynamic jump sensitivity relates dispersion to the muzzle exit yaw rate of the projectile. It may be calculated using PRODAS. This factor is dependent upon the physical and aerodynamic characteristics of the projectile as well as the projectile spin and velocity.
- Typically, the cross wind sensitivity of the projectile is determined by trajectory simulations of the projectile flight to the range of interest both with and without a nominal crosswind applied (5 m/s). The "delta drift" in mils is then divided by the applied wind velocity to derive the factor. Cross wind standard deviation of the variation of the true wind velocity from the measured value (from range MET data).
- The aerodynamic trim angle of a projectile configuration (due to manufacturing tolerances) may be calculated from PRODAS predictions of the body alone and fin alone center of pressure and normal force coefficients, and from the expected one sigma value of the angular misalignments of the nose and tail sections. The calculated angle of the projectile geometric principal axis with the air stream flow assuming no spin. (This is analogous to the angle a projectile would take if suspended in a wind tunnel by its center of gravity.)

- The aerodynamic/mass asymmetry factor is determined by simulating trajectories with a trim angle assumed to be oriented at orthogonal and diametrically opposed orientations. This will produce an impact pattern at a specified range that can be fitted with a circle whose radius (in mils) can then be divided by the assumed trim angle to calculate the factor.

Sabot Front Borerider Stiffness vs. Dispersion

Total dispersion is computed by performing a root-mean-square combination of the following dispersion components:

- Propellant Ignition to Muzzle Exit (from In-Bore Balloting)
  - Yaw
  - Yaw Rate
  - Transverse Velocity
  - Muzzle Spin (combination of yaw, aerodynamic jump, spin rate)
- Muzzle Exit to Sabot Discard (from Experience/Experimental Results)
  - Sabot Discard
  - Bore Site
- Sabot Discard to Target Impact (from Free-Flight Trajectory Analysis)
  - Muzzle Velocity
  - Wind Component
  - Aerodynamic and Mass Asymmetries

The in-bore balloting analysis is automatically performed for a range of stiffness values to arrive at a curve of stiffness vs. dispersion as shown in Figure 6. Dispersion components from muzzle exit to sabot discard and sabot discard to target impact are held constant for this analysis since they are not a function of the sabot front borerider stiffness.

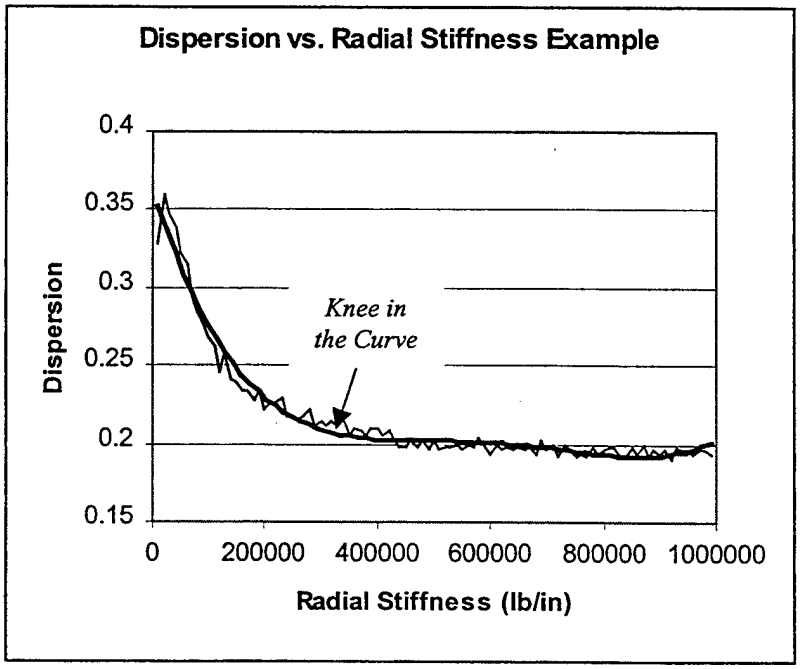

Figure 6: Example of Sabot Front Borerider Stiffness vs. Total Dispersion

SAMPLE RESULTS: DISPERSION VS. STIFFNESS IN THE 120MM M865

The 120mm M865 APFSDS production round was selected to illustrate this analysis process. In addition to the technical data package, statistical process control (SPC) data was collected to develop the necessary manufacturing tolerances of the diameters and runouts required by this analysis system.

Figure 7 is a plot of the sabot front borerider stiffness vs. dispersion (dispersion values have been normalized) for the M865 projectile. From testing, the normalized dispersion value for the M865 is approximately 0.085. It is obvious that a radial stiffness above 800000 lb./in provides little or no improvement in dispersion. This point will vary depending on the projectile/sabot configuration.

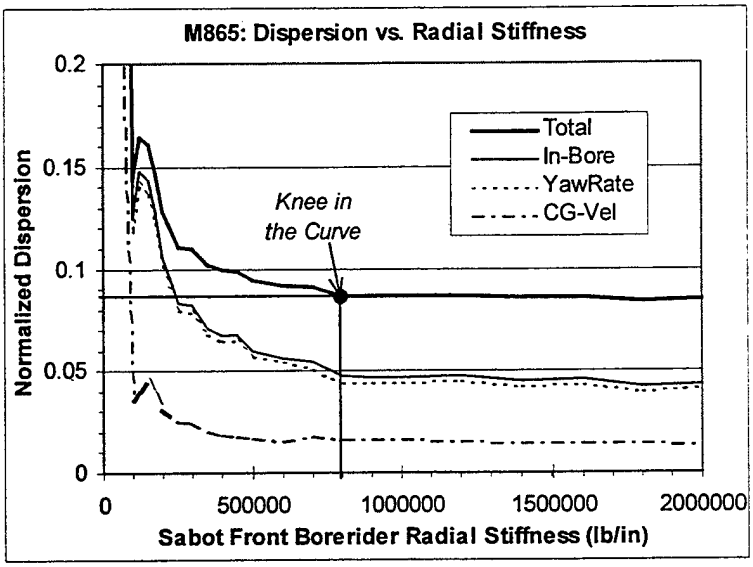

Figure 7: M865 Test Case, Radial Stiffness vs. Normalized Dispersion

SUMMARY AND CONCLUSIONS

The analysis process described in this paper can not only determine the effect of a change in front borerider stiffness but it can also identify the components of dispersion and their relative contribution as shown in Figure 8. This can greatly assist the projectile designer in choosing a dispersion source to *attack* in trying to improve dispersion.

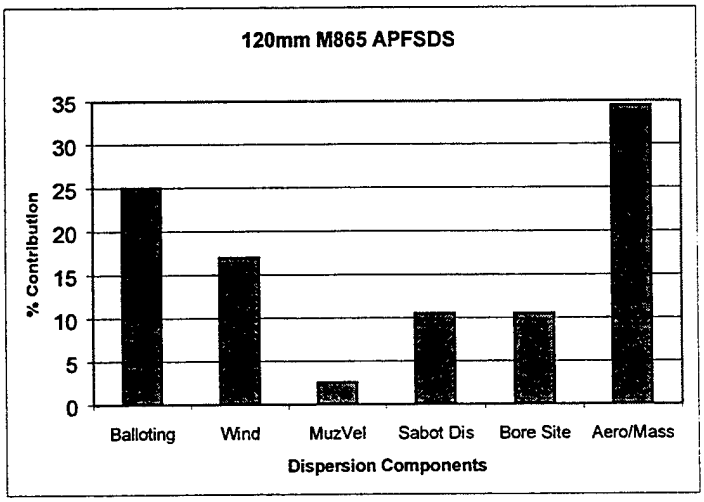

Figure 8: M865 Dispersion Components

Following are some conclusions based on the use of this system for predicting dispersion and solving dispersion-related problems on several projectiles:

- This approach enables isolation of the primary cause of dispersion.
- Use of this system can lead to cost effective test plans by giving the engineer the relative magnitude of dispersion improvement to be expected by changes in configuration.
- This approach provides realistic expectations for a projectile design's dispersion capability.
- Use of this system has proven to be very useful when coupled with data from spark range testing that can provide accurate aerodynamic coefficients and average trim estimates.
- The system is useful in the investigation of piece part dimensional tolerances and their effect on dispersion.
- The system provides insight into which parameters need to be modified to enhance projectile dispersion and/or minimize external effects (i.e., wind) while testing for dispersion.

REFERENCES

1. Hathaway, A.F. and Burnett, J.R., *Stochastic Approach to Predicting Dispersion*, Proceedings, 49th Aeroballistic Range Association Meeting, The Hague, Netherlands, October, 1998

2. Stearns, B.K. and Burnett, J.R., *Simulation of Projectile Balloting in Hypervelocity Launchers,* Proceedings, 45th Aeroballistic Range Association Meeting, Huntsville, Alabama, October, 1994.

3. Whyte, R.H., Stearns, B.K., Burnett, J.R., and Siewert, J.A. *M865 Short Sabot and M831 Dispersion Sensitivity Analysis*, Internal Report, Arrow Tech Associates, South Burlington, Vermont, September 1990

4. Siewert, J.A., Stearns, B.K. and Burnett, J.R., *Aluminum and Plastic M865 Variants, Aeroballistic Analysis, Dispersion Prediction, and Balloting Response Analysis*, Internal Report, Arrow Tech Associates, South Burlington, Vermont, April 1994.

5. Lyons, D.H., *Radial Stiffness Measurements of 120MM Projectiles*, Aberdeen Proving Ground, Proceedings of the Seventh U.S. Army Symposium on Gun Dynamics, ARCCB-SP-93034 Newport, R.I., Sponsored by: Benet Laboratories, Watervliet, N.Y. 11-13 May, 1993, pp. 167-186.

6. Simkins, T.E., *Transverse Response of Gun Tubes to Curvature-Induced Load Functions*, Proceedings of the Second U.S. Army Symposium on Gun Dynamics, ARLCB-SP-78013, Renselaerville, N.Y., Sponsored by: Benet Laboratories, Watervliet, N.Y., September 1982, pp. I-67 - 77.

7. Arrow Tech Associates, *PRODAS Version 3.9 Users and Technical Manual*, Arrow Tech Associates, South Burlington, Vermont, January 1998.

8. Arrow Tech Associates, *BALANS Version 2.00 Users and Technical Manual*, Arrow Tech Associates, South Burlington, Vermont, August 1998.

IMPACT DISPERSION OF A SMART EXTENDED RANGE PROJECTILE FROM MUZZLE DISTURBANCES*

by:

Mark F. Costello†
Department of Mechanical Engineering
Oregon State University
Corvallis, Oregon 97331

Abstract

This effort investigates the extent to which moveable canards can extend the range of indirect fire munitions using both projectile body and canard lift. The implications on terminal velocity, time of flight, and impact dispersion using this mechanism to extend range are also documented for various canard configurations. The study is carried out using a six degree of freedom simulation model which has previously been validated against range data. The projectile dynamic equations are formed in the body frame and aerodynamic loads from the body and canards are Mach number and angle of attack dependent. The projectile body aerodynamic moments include unsteady aerodynamic damping. The focus of the study is directed toward low cost competent munitions that extend range and as such a simple flight control system is considered which utilizes only timer, roll rate, and roll attitude inputs.

Symbols

x, y, z : Position vector components of the center of mass expressed in the inertial reference frame.

ϕ, θ, ψ : Euler roll, pitch, and yaw angles.

u, v, w : Translation velocity components of the center of mass resolved in the body reference frame.

p, q, r : Components of the angular velocity vector of both the forward and aft bodies expressed in the body reference frame.

X, Y, Z : Total external force components on the projectile expressed in the body reference frame.

L, M, N : Total external moments components on the projectile expressed in the body reference frame.

m : projectile mass.

$[I]$: Mass moment of inertia matrix.

$[T]$: Transformation from the projectile body frame to the inertial frame.

$[S]$: Skew symmetric cross product operator on the projectile body angular velocity components.

D : Projectile characteristic length.

C_i : Projectile aerodynamic coefficients.

q_a : Dynamic pressure at the projectile mass center.

α : Longitudinal aerodynamic angle of attack.

β : Lateral aerodynamic angle of attack.

V : Magnitude of mass center velocity.

ϕ_{C_i} : ith canard azimuthal angle.

γ_{C_i} : ith canard sweep angle.

δ_{C_i} : ith canard pitch angle.

Introduction

Traditionally, field artillery target effects are produced by firing a sufficient number of rounds with known accuracy at a given target so that, statistically, the target is neutralized. The goal of improving field artillery systems boils down to increasing achievable range and improving terminal accuracy of the projectile.

It is obvious that a round with extended range enjoys the flexibility of being able to engage a greater number of targets over a larger land area. A less

* Proceedings of the 9th Annual US Army Gun Dynamics Symposium, November 17-19, McLean, Virginia.
† Assistant Professor.

obvious, yet equally important advantage of extended range is that the system with greater range requires fewer repositionings on the battlefield and can provide fire support for a higher percentage of time. This becomes particularly important in today's highly mobile battle environment, where a significant portion of time is spent moving into position. Since a long-range projectile can cover a large area of land, rounds can be fired at many different targets on the battlefield in a short period of time. Thus, a long range projectile adds increased flexibility to the field artillery commander, allowing him to influence a much greater portion of the battlefield, for longer periods of time.

The intensity of Army operations dictates that the field artillery optimize target effects with every round fired. One method of improving target effects is to increase the terminal accuracy of each round.[1,2] Current field artillery doctrine requires large numbers of rounds to be fired in order to neutralize a particular target. Statistically, only a small percentage of these rounds actually produce effects on the target. Increased accuracy provides that the 'extra' rounds, those not having effects on target, are never fired. If more rounds than necessary are fired, the firing unit accepts an unnecessary risk of being acquired by enemy target acquisition assets and subsequently engaged with counter fire. When the firing unit comes under steady counter fire, the unit will reposition and be rendered unavailable for other missions while in transit. Also, firing more than the minimum number of rounds needed to eliminate a target wastes expensive munitions and burdens the resupply system. Every extra round expended on a particular target represents an opportunity cost that could have been directed at another objective on the battlefield. More importantly, target effects decrease exponentially as a function of the number of projectiles fired at a particular target due to the lack of surprise. The first volley fired is by far the most important volley to achieve maximum target effectiveness. Furthermore, if rounds are inaccurate, targets will reappear on the battlefield. Potentially, this will require additional artillery engagements and negatively affect the outcome of the overall battle plan. Thus, increased terminal accuracy increases target effects by landing more first hits, reduces vulnerability by firing less shots, and uses less material, which reduces the burden on the supply system - all contributing to a more effective and lethal field artillery unit.

The notion of utilizing canards as an aerodynamic control mechanism is by no means new and has been successfully applied to aircraft and missiles for some time. A significant aerodynamic data base has amassed on aerodynamic modeling of missile configurations with canards.[3] However, few studies have specifically addressed the use of canards to extend the range of a ballistic projectile. Smith, Smith, and Topliffe[4] studied the use of canards on a spin stabilized projectile with the intended use of accuracy improvement. The canards, which were relatively small, were controlled by a seeker. To reduce the required control moments and actuator bandwidth, the canards were mounted on a bearing spinning at a different rate than the main body.

The work reported here evaluates the potential of extending the range of a field artillery projectile using moveable canards. It begins with a description of the simulation model used to predict projectile motion. This is followed with the definition of a representative extended range projectile configuration. With this model data, a parametric study is conducted which includes different canard geometry and deflection profiles.

Projectile Dynamic Model

The mathematical model describing projectile motion admits 6 rigid body degrees of freedom comprised of three body inertial position coordinates as well as three Euler angle body attitudes. The equations presented below use the ground surface as an inertial reference frame. The body frame is defined in the conventional manner[5] and the dynamic equations are written with respect to this coordinate system. The projectile translation and rotation kinematic and dynamic equations are given by Equations (1) through (7).[5,6]

$$\begin{Bmatrix} \dot{x} \\ \dot{y} \\ \dot{z} \end{Bmatrix} = [T] \begin{Bmatrix} u \\ v \\ w \end{Bmatrix} \tag{1}$$

$$\begin{Bmatrix} \dot{\phi} \\ \dot{\theta} \\ \dot{\psi} \end{Bmatrix} = \begin{bmatrix} 1 & s_\phi t_\theta & c_\phi t_\theta \\ 0 & c_\phi & -s_\phi \\ 0 & s_\phi / c_\theta & c_\phi / c_\theta \end{bmatrix} \begin{Bmatrix} p \\ q \\ r \end{Bmatrix} \tag{2}$$

$$\begin{Bmatrix} \dot{u} \\ \dot{v} \\ \dot{w} \end{Bmatrix} = \begin{Bmatrix} X/m \\ Y/m \\ Z/m \end{Bmatrix} - [S] \begin{Bmatrix} u \\ v \\ w \end{Bmatrix} \tag{3}$$

$$\begin{Bmatrix} \dot{p} \\ \dot{q} \\ \dot{r} \end{Bmatrix} = [I]^{-1} \left[\begin{Bmatrix} L \\ M \\ N \end{Bmatrix} - [S][I] \begin{Bmatrix} p \\ q \\ r \end{Bmatrix} \right] \tag{4}$$

$$[T]=\begin{bmatrix} c_\theta c_\psi & s_\phi s_\theta c_\psi - c_\phi s_\psi & c_\phi s_\theta c_\psi + s_\phi s_\psi \\ c_\theta s_\psi & s_\phi s_\theta s_\psi + c_\phi c_\psi & c_\phi s_\theta s_\psi - s_\phi c_\psi \\ -s_\theta & s_\phi c_\theta & c_\phi c_\theta \end{bmatrix} \quad (5)$$

$$[S]=\begin{bmatrix} 0 & -r & q \\ r & 0 & -p \\ -q & p & 0 \end{bmatrix} \quad (6)$$

$$[I]=\begin{bmatrix} I_R & 0 & 0 \\ 0 & I_P & 0 \\ 0 & 0 & I_P \end{bmatrix} \quad (7)$$

As shown in Equations 8, the total applied force is composed of weight (W), body aerodynamic force (A), and canard aerodynamic force (C).

$$\begin{Bmatrix} X \\ Y \\ Z \end{Bmatrix}=\begin{Bmatrix} X_W \\ Y_W \\ Z_W \end{Bmatrix}+\begin{Bmatrix} X_A \\ Y_A \\ Z_A \end{Bmatrix}+\begin{Bmatrix} X_C \\ Y_C \\ Z_C \end{Bmatrix} \quad (8)$$

The weight portion of the external loads is given by Equations 9,

$$\begin{Bmatrix} X_W \\ Y_W \\ Z_W \end{Bmatrix}=mg\begin{Bmatrix} -s_\theta \\ s_\phi c_\theta \\ c_\phi c_\theta \end{Bmatrix} \quad (9)$$

while the aerodynamic force contribution is given by Equations 10.

$$\begin{Bmatrix} X_A \\ Y_A \\ Z_A \end{Bmatrix}=q_a D\begin{Bmatrix} C_{X0}+C_{XA2}\alpha^2+C_{XB2}\beta^2 \\ C_{YB1}\beta+C_{YB3}\beta^3+C_{YB5}\beta^5 \\ C_{ZA1}\alpha+C_{ZA3}\alpha^3+C_{ZA5}\alpha^5 \end{Bmatrix} \quad (10)$$

The longitudinal and lateral aerodynamic angles of attack are computed using Equations 11.

$$\alpha=\tan^{-1}\left(\frac{w}{u}\right) \qquad \beta=\tan^{-1}\left(\frac{v}{u}\right) \quad (11)$$

The aerodynamic coefficients in Equations 10 are functions of the local Mach number at the projectile mass center. They are computed using linear interpolation from a table of data.

The aerodynamic force due to a single canard is modeled as a point force acting at the lifting surface aerodynamic center. Canard orientation is defined by azimuthal angle (ϕ_{C_i}), sweep angle (γ_{C_i}), and pitch angle (δ_{C_i}). In this study, canard pitch angle is controlled during flight. The ith canard force is given by Equation 12,

$$\begin{Bmatrix} X_{C_i} \\ Y_{C_i} \\ Z_{C_i} \end{Bmatrix}=q_{C_i}S_i[T_{C_i}]\begin{Bmatrix} C_L s_{\alpha_i-\delta_i}-C_D c_{\alpha_i-\delta_i} \\ 0 \\ -C_L c_{\alpha_i-\delta_i}-C_D s_{\alpha_i-\delta_i} \end{Bmatrix} \quad (12)$$

where q_{C_i} is the dynamic pressure at the canard computation point, S_i is the canard reference area, and T_{C_i} is the transformation from the local canard reference frame to the projectile body frame. In Equation 12, the canard lift and drag coefficients are expanded in terms of canard angle of attack and Mach number.

$$C_L=C_{L1}\alpha_i+C_{L3}\alpha_i^3+C_{L5}\alpha_i^5 \quad (13)$$

$$C_D=C_{D0}+C_{D2}\alpha_i^2+C_I C_L^2 \quad (14)$$

The coefficients in Equations 13 and 14 are Mach number dependent. Canard angle of attack is computed in the same manner as the body angle of attack except the local relative velocity at the canard computation point is used.

The right hand side of the rotation kinetic equations contains the externally applied moments. The external moment components are given by Equations 15 and contain contributions from steady body (SA), unsteady body (UA), and canard (C) aerodynamics.

$$\begin{Bmatrix} L_A \\ M_A \\ N_A \end{Bmatrix}=\begin{Bmatrix} L_{SA} \\ M_{SA} \\ N_{SA} \end{Bmatrix}+\begin{Bmatrix} L_{UA} \\ M_{UA} \\ N_{UA} \end{Bmatrix}+\begin{Bmatrix} L_C \\ M_C \\ N_C \end{Bmatrix} \quad (15)$$

The steady body aerodynamic moment is computed by a cross product between the distance vector from the center of gravity to the center of pressure and the steady body aerodynamic force vector above. Like the aerodynamic coefficients, the center of pressure

location is dependent on local Mach and is computed by linear interpolation. The unsteady body aerodynamic moment provides a damping source for projectile angular motion and is given by Equations 16.

$$\begin{Bmatrix} L_{UA} \\ M_{UA} \\ N_{UA} \end{Bmatrix} = q_a D^2 \begin{Bmatrix} C_{DD} + \dfrac{pDC_{LP}}{2V} \\ \dfrac{qDC_{MQ}}{2V} \\ \dfrac{rDC_{NR}}{2V} \end{Bmatrix} \qquad (16)$$

The canard moment is computed through a cross product operation similar to the steady body aerodynamic moment.

Air density is computed using the center of gravity position of the projectile in concert with the standard atmosphere.[7]

The mathematical model described in this section has been validated against spark range data for a generic 25mm fin stabilized sabot launched projectile.[8] Agreement between the model and range data is excellent.

Configuration Data

Consider a representative extended range field artillery projectile that is fired from a 155mm cannon. The projectile is 6 ft. long and weighs 120 lb. The projectile is equipped with pop-out rear fins and forward canards. The mass center is located 2.75 ft. from the base.

The body aerodynamic coefficients are shown in Figures 1 through 3 while the canard aerodynamic data is shown in Figures 4 and 5. Various size canards are considered in the following, however, all canard configurations share the same aerodynamic properties shown in Figures 4 and 5.

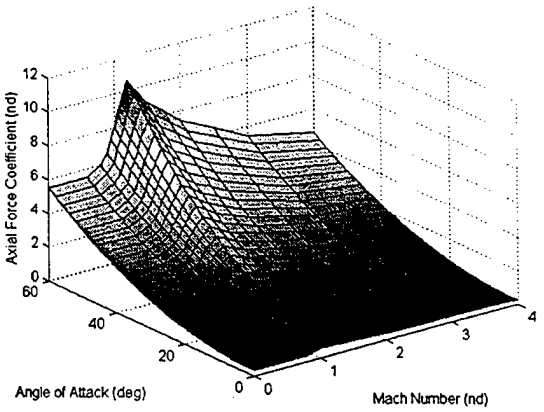

Figure 1 – Body Axial Force Coefficient (nd)

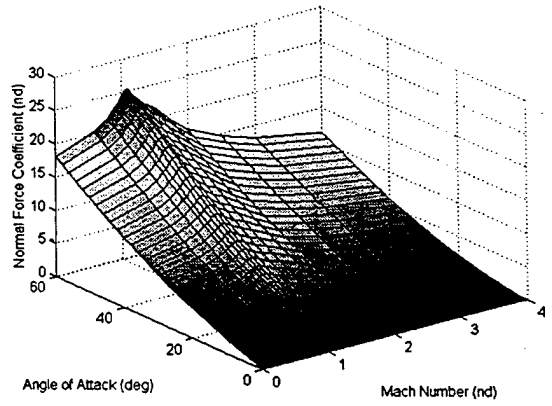

Figure 2 – Body Normal Force Coefficient (nd)

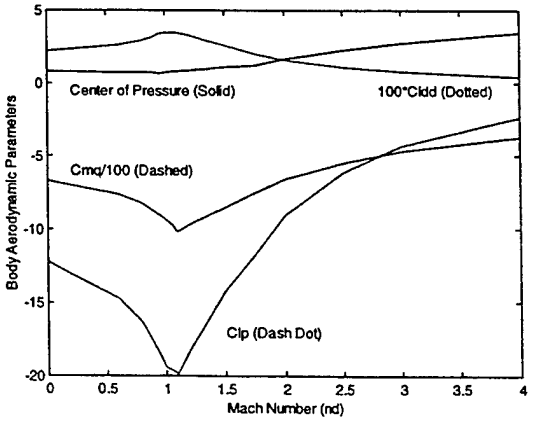

Figure 3 – Body Aerodynamic Parameters

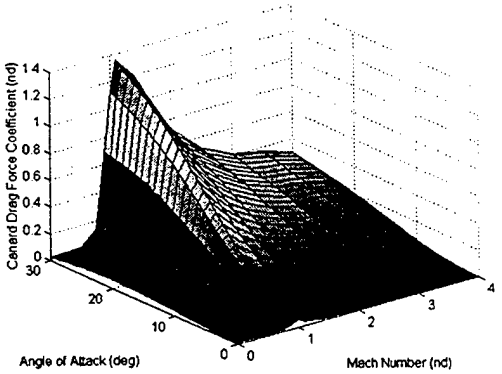

Figure 4 – Canard Drag Force Coefficient (nd)

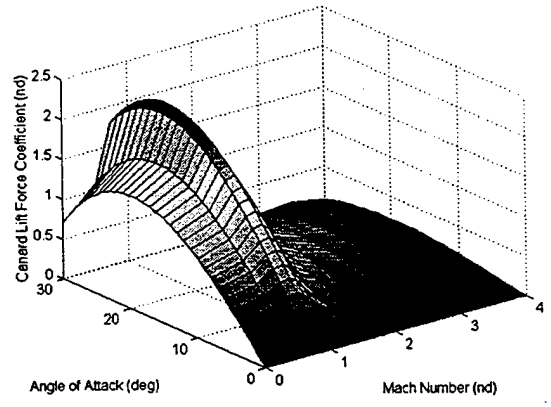

Figure 5 – Canard Lift Force Coefficient (nd)

Simulation Results

Figures 6 through 13 compare the nominal trajectory and the extended range trajectory for the projectile described above. Range extension is accomplished with 4 equally spaced canards, each with a reference area of 0.07 ft^2 or a reference area ratio of 0.35. A reference area ratio of 0.7 represents a practical upper limit on what could be installed in a production round. The initial forward body velocity is 750 m/s, the initial roll rate is 31 rad/s, and the gun elevation is 45 degrees. The fins are slightly canted to provide a slowly rolling projectile in steady state. For the range extension trajectory, a proportional plus integral (PI) roll control system is used prior to canard activation. The 2 canards in the body pitch plane are activated at the apex of the trajectory to an angle of 6 deg. Figure 6 compares range with and without movable canards installed. Under the conditions mentioned above, range is more than doubled from 17.5 km to 39.9 km. The small discrepancy between the nominal and canard configuration trajectories before the onset of the canard activation is due to the drag of the canards, which are not present on the nominal projectile. From the altitude versus time, it can be seen that the time of flight of the canard controlled projectile dramatically increases from 71 to 195 sec. Subsequent to canard pitch activation, a slight steady state yaw rate develops that alters the azimuth of the projectile hence creating a difference in the cross range between the two trajectories. Figure 8 shows pitch attitude. At launch, both trajectories have a 45 deg. pitch attitude; however, the baseline trajectory pitch attitude monotonically decreases with time, whereas the controlled trajectory experiences some transient oscillations immediately after the pitch command is executed. After transient oscillations settle, pitch attitude of the controlled trajectory approaches a value of –10 deg. The forward velocity trace, given in Figure 9, shows the nominal trajectory arrives at the terminal point with a velocity of 300 m/sec. compared to the controlled trajectory at a velocity of 166 m/sec. Furthermore, the decreased velocity is present throughout a large portion of the flight. The roll rate time history, given in Figure 10, shows the PI roll control eliminates roll rate from 31 rad/sec to 0 within 5 sec. whereas the nominal trajectory has a steady state roll rate due to rear fin cant. This is absolutely necessary for this range extension strategy, since the pitch attitude commands assume the projectile will maintain near zero roll rate and angle from the start of pitch commands to the terminal point. Figure 11 shows the total aerodynamic angle of attack of the projectile for both the nominal and controlled case. The nominal angle of attack is small, less than half a deg., and does not show up on the chart. However, the canards induce maximum angle of attack oscillations slightly over 7 deg. and a steady state glide angle of attack of 4.1 deg. As canard angle of attack will basically mimic body angle of attack, the canards can stall during the transient part of the response. For this reason, the higher order expansion of canard lift and drag coefficient is important to model. Figure 12 plots the body and canard aerodynamic forces in the axial direction. Body drag dominates the axial force with the canards contributing more near launch. However, Figure 13 plots the magnitude of the normal force from the body and canards where the body and canards contribution to the normal force is the same order of magnitude. Figures 6 through 13 show that range of a projectile can be significantly increased by using body and canard lift achieved by pitching the projectile upward using the movable canard lifting surfaces. While a dramatic increase in range is achievable, an equally dramatic increase in the time of flight and decrease in the impact point velocity is realized. Thus, the action of the moveable canards is to facilitate a transfer of kinetic

energy to potential energy, allowing the projectile to stay aloft longer.

Figures 14 through 18 show range, flight time, terminal velocity, terminal pitch angle, and glide angle of attack for various canard areas and various canard command angles. The canard command was executed at the apex of flight in all cases. The general trends from these figures is that increasing canard area or canard command angle increases range, flight time, steady state angle of attack, and terminal pitch attitude while decreasing terminal velocity.

Figure 19 shows range versus time of canard activation. For the case shown, the apex of flight was reached 31.5 seconds into flight. Figure 19 shows that for maximum range, the canard command should be executed at the apex of flight. Also, the curve is relatively symmetric about the maximum range point.

Figures 20 and 21 plot range dispersion versus initial pitch and yaw rate disturbances caused by muzzle rotational motion. The magnitude of the initial angular disturbance is 0.1, 0.5, and 1.0 rad/s and the phase angle of the disturbance is random. Figure (20) shows dispersion for the nominal projectile and it is seen that increasing the initial angular disturbance decreases total range and increases the cross range dispersion. Figure (21) shows dispersion for the canard controlled case and trends similar to the nominal case are noticed, however, amplified. The exception is that the down range dispersion increases due to the long glide phase of flight.

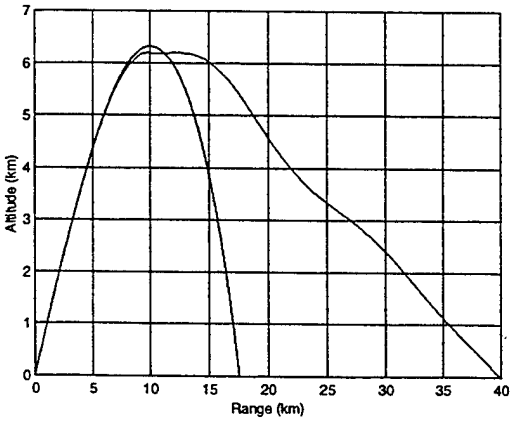

Figure 6 – Altitude vs. Range
(Solid=Nominal, Dotted=Extended)

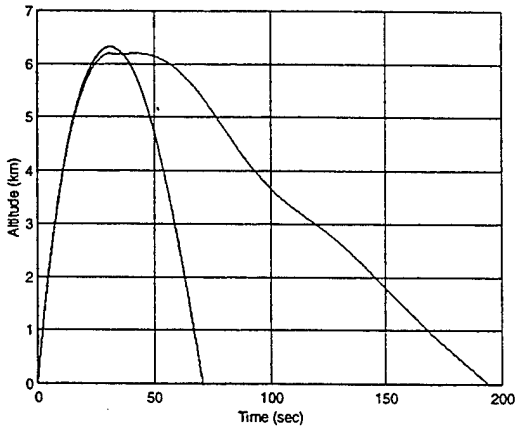

Figure 7 – Altitude vs. Time
(Solid=Nominal, Dotted=Extended)

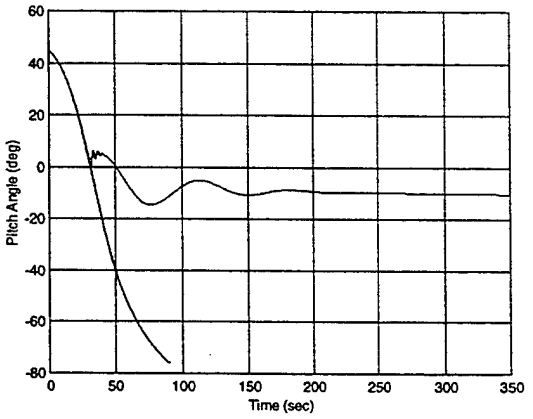

Figure 8 – Pitch Attitude vs. Time
(Solid=Nominal, Dotted=Extended)

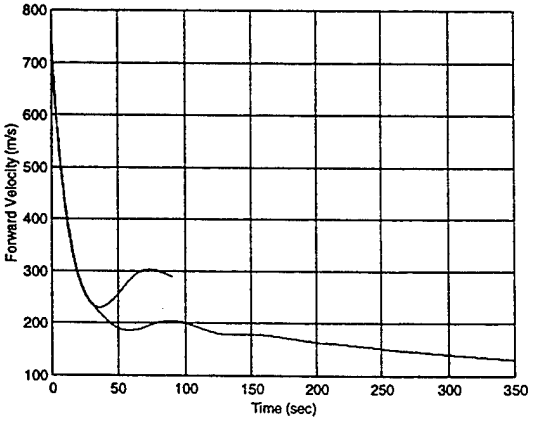

Figure 9 – Forward Body Velocity vs. Time
(Solid=Nominal, Dotted=Extended)

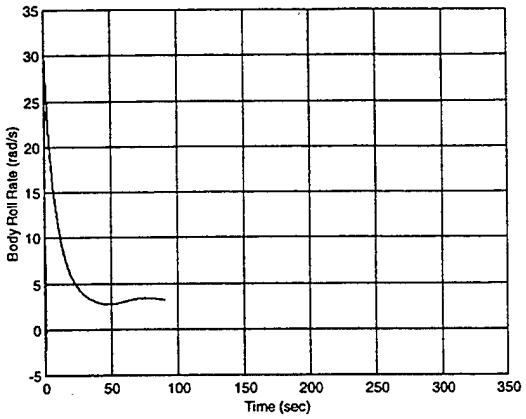

Figure 10 – Roll Rate vs. Time
(Solid=Nominal, Dotted=Extended)

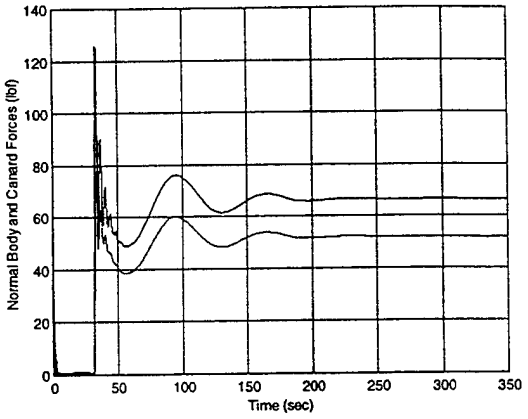

Figure 13 – Normal Body Force vs. Time
(Solid=Nominal, Dotted=Extended)

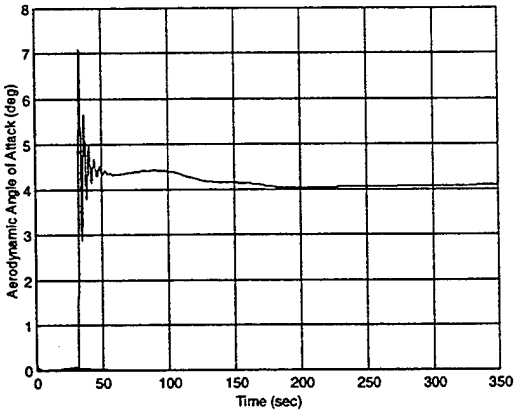

Figure 11 – Total Angle of Attack vs. Time
(Solid=Nominal, Dotted=Extended)

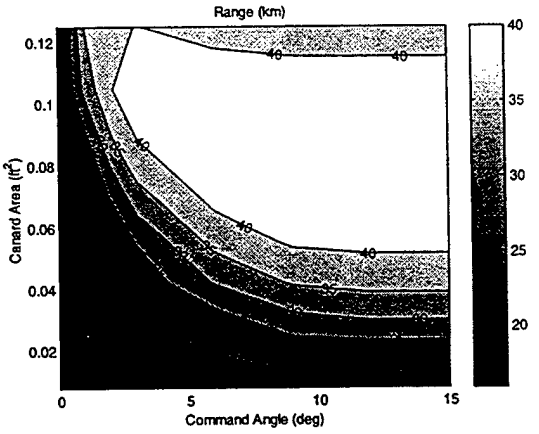

Figure 14 – Range vs. Canard Area and Angle

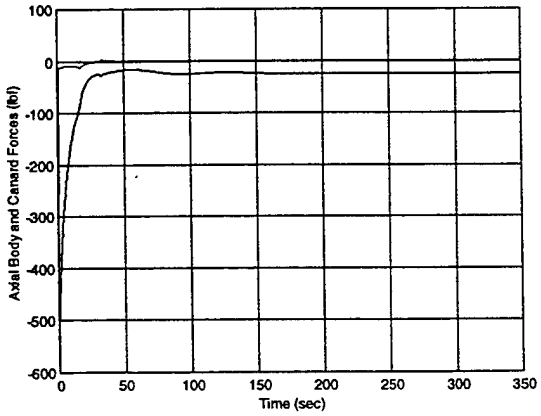

Figure 12 – Axial Body Force vs. Time
(Solid=Nominal, Dotted=Extended)

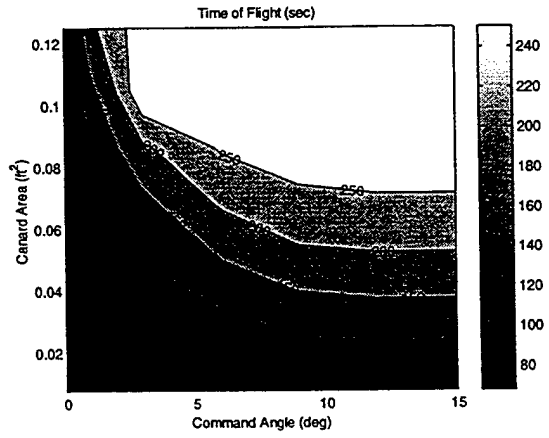

Figure 15 – Flight Time vs. Canard Area and Angle

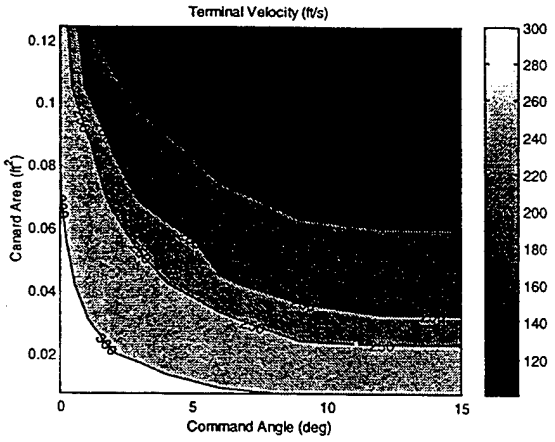

Figure 16 – Terminal Vel. vs. Canard Area and Angle

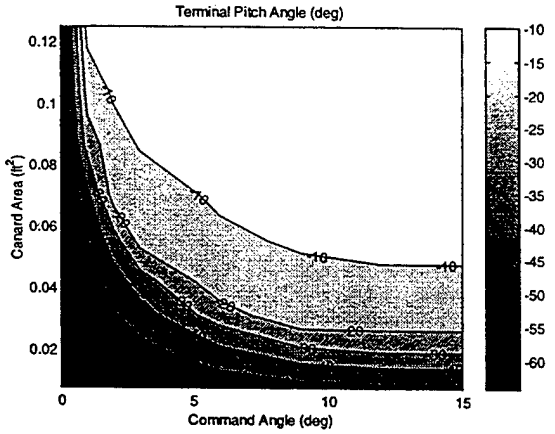

Figure 17 – Terminal Pitch Angle vs. Canard Area and Angle

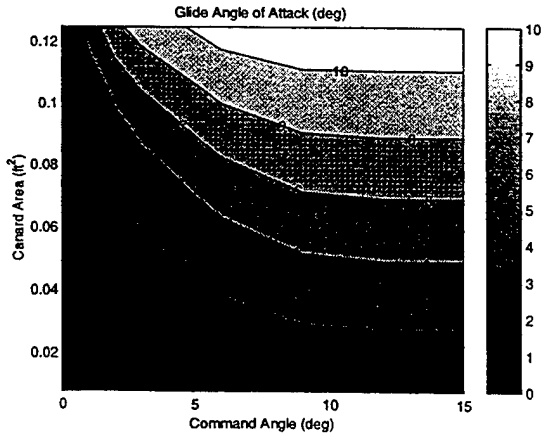

Figure 18 – Glide Angle of Attack vs. Canard Area and Angle

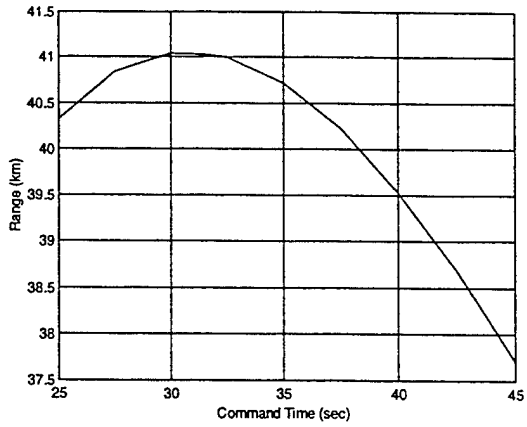

Figure 19 – Range vs. Command Time

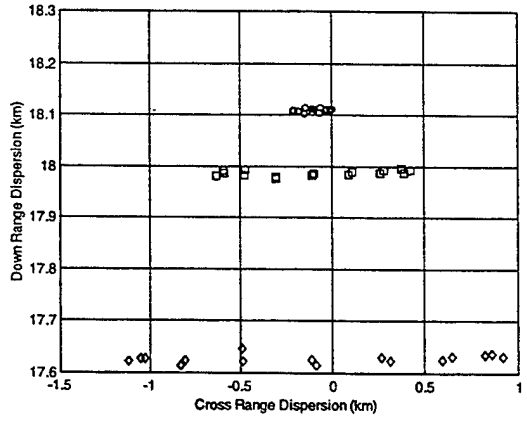

Figure 20 – Impact Dispersion (Nominal, Circle = 0.1rad/s, Square=0.5 rad/s, Diamond=1 rad/s)

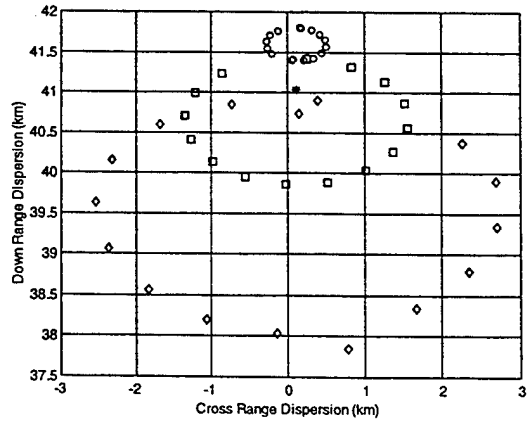

Figure 21 – Impact Dispersion (Range Extension, Circle = 0.1rad/s, Square=0.5 rad/s, Diamond=1 rad/s)

Conclusions

Using a modified 6 degree of freedom trajectory simulation driven by projectile data representative of an indirect fire field artillery round, it is found that using a relatively small set of four canards, projectile range can be dramatically increased. The side effects of increased range using this mechanism are:

1) Decreased terminal velocity.
2) Increased flight time.
3) Increased nose-up terminal attitude.
4) Increased aerodynamic angle of attack.
5) Increased range dispersion.

Generally, maximum range is attained when the canards are activated at the apex of the trajectory

References

1. R.W. Pointer, C.E. Dean, "Cannon Artillery May One Day Soon Provide Crisis Logistics To Ground Forces," *National DEFENSE*, Vol. LXXX, Num. 518, May 1996.

2. C.E. Dean, W.P. Wiesman, "Combat Resupply by Artillery," *Army RD\&A*, Vol. PB70-96-1, January 1996.

3. USAF Stability and Control DATCOM, AFFDL Wright Patterson AFB, Ohio, November 1965.

4. J.A. Smith, K.A. Smith, R. Topliffe, Feasibility Study for Application of Modular Guidance and Control Units to Existing ICM Projectiles, U.S. Army Armament Research and Development Command, Contractor Report ARLCD-CR-79001, November 1978.

5. B. Etkin, Dynamics of Atmospheric Flight, John Wiley and Sons, New York, 1972.

6. C. Murphy, Free Flight of Symmetric Missiles, Ballistics Research Laboratory Report BRL-1216, Aberdeen Proving Ground, Maryland, 1963.

7. R. Von Mises, Theory of Flight, Dover Publications Inc., New York, 1959.

8. M.F. Costello, D.A. Anderson, "Effect of Internal Mass Unbalance on the Stability and Terminal Accuracy of a Field Artillery Projectile," Proceedings of the 1996 AIAA Atmospheric Flight Mechanics Conference, San Diego, CA, 1996.

Dynamic Response and Fracture of Composite Gun Tubes

Jerome T. Tzeng
US Army Research Laboratory
Weapons and Materials Research Directorate
Attn: AMSRL-WM-MB
Aberdeen Proving Ground, MD 21005-5066

ABSTRACT

The fracture behavior due to dynamic response in a composite gun tube subjected to a moving pressure has been investigated. The resonance of stress waves result in very high amplitude and frequency strains in the tube at the instant and location of pressure front passage as the velocity of the projectile approaches a critical value. The cyclic stresses can accelerate crack propagation in the gun tube with an existing imperfection and significantly shorten the fatigue life of gun tubes. The fracture mechanism induced by dynamic amplification effects is particularly critical for composite overwrap barrels because of a multi-material construction, anisotropic material properties, and the potential of thermal degradation.

INTRODUCTION

When a stress wave of sufficiently large amplitude travels through a solid, it might produce fracture or accelerate the rate of propagation of an existing crack. The fracture mechanism under a transient loading condition is different from that produced by relatively static loading. This is because the velocity of the stress wave is in general much higher than the velocity of the crack propagation. Cracks might not grow in time as the stress waves pass through them. In addition, the structural deformation is non-uniform and time dependent under transient loading conditions. From a material point of view, both fracture toughness and strength can change due to various loading rates. A ductile material, such as reinforced polymer composite, might behave more brittle. The fracture toughness and strength measured in static loading conditions might not be suitable for a transient case. In this paper, stress waves due to a dynamic response in a composite wrap steel liner are modeled to study fracture behaviors of composite gun tubes. A strain energy integration approach [1] is proposed to evaluate crack propagation at the interface of the composite and steel liner. A discussion on the energy integration for prediction of the crack propagation is also included from an implementation point of view.

A very high amplitude and frequency strain, commonly referred to as dynamic strain amplification, develops in a gun tube at the passage of projectile. The phenomenon is caused by the resonance of flexural waves when the moving pressure approaches the velocity of wave propagation in the gun tube. The resonance response of a isotropic cylinder subjected to moving pressure loads has been investigated by Taylor [2], Jones and Bhuta [3], Tang [4], and Reismann [5]. More recently, Simkins [6] and Hopkins [7] investigated the dynamic response of flexural waves in steel gun tubes. Recently, Tzeng [8] extended the research on the dynamic strain effect in cylinders made of fiber-reinforced composite materials overwrap with a metal liner. The results

are very applicable to lightweight composite cylinders used for gun tubes and high pressure piping systems.

ANALYSIS

In this section, the dynamic response and fracture of a composite overwrap cylinder subjected to a moving pressure is investigated based on closed-form analytic as well as finite element methods. As a first approximation though, Love's thin shell theory can be used to derive a closed-form expression for the critical velocity. The critical velocity at which resonance occurs is greatly influenced by tube geometry and material properties. The finite element solution is obtained using a version of Dyna2d [9], which has been modified to allow accurate modeling of the moving pressure front. This approach allows modeling both the moving pressure front and the composite cylinder geometry with initial cracks in sufficient detail to simulate the actual loading conditions. Finally, an integration of strain energy density along a specific path within a cylinder is computed as an indication to determine crack propagation.

Integration of Energy Density

Consider a crack at the interface of the composite overwrap and steel liner as shown in Figure 1. The strain fields near the crack tip are difficult to determine, especially in a bi-material system with anisotropy of composite laminates. Let's assume that the crack at the interface is axisymmetric and sufficiently large. Accordingly, the analysis can utilize a two-dimensional model for the far-field and crack analyses. Rice [1] proposed an approximate method known as J-integral, which bypasses the complexity of solving a boundary value problem at the crack tip. Integration along the crack tip with a path Γ can be defined as

$$J = \int_{\Gamma} \left(\omega \, dy - T \cdot \frac{\partial u}{\partial x} \, ds \right) + \int_{V} \left(\rho \ddot{u} \frac{\partial u}{\partial x} \right) dV \quad , \tag{1}$$

where "ω" is strain energy density and can be defined as

$$\omega = \omega(\varepsilon) = \int_{0}^{\varepsilon} \sigma_{ij} \, d\varepsilon_{ij} \quad , \tag{2}$$

'T' is the traction vector along the path, 'u' represents the displacement vectors, 'ds' is an element of arc length along 'Γ', and 'V' is a volume integration.

Atluri [10] and Doyle [11] investigated the contribution of acceleration from the internal movement of the material for a beam structure. Based on linear fracture mechanics, the J-integral is equivalent to strain energy release rate at the crack and the following expression is obtained:

$$J = -\frac{\partial V}{\partial a} = G = G_I + G_{II} + G_{II} \quad , \tag{3}$$

V is potential energy of elastic body, and 'a' is a crack length in the body. 'G' is the total strain energy release rate resulting from three fracture modes. Accordingly, the strain energy release rate is related to stress intensity as follows:

$$G = \frac{1-\nu^2}{E}\left(K_I^2 + K_{II}^2 + \frac{K_{III}^2}{1-\nu}\right) \quad , \qquad (4)$$

where K_I, K_{II}, and K_{III}, are stress intensity factors associated to different modes.

The integration of strain energy can be carried out with an implementation of finite element technique. An overwrapped composite cylinder with an initial crack at the interface of the composite/liner is modeled in detail. Stress and strain fields at the surrounding region can be obtained through a transient analysis. Strain energy density and its integration are then calculated element by element through a specific path. The results will then be ready for comparison with empirical data and serve as a useful design and fabrication parameter.

Dynamic Response of Cylinders

The critical velocity of a flexural wave in a cylindrical tube can be obtained from Love's thin shell theory. The closed form solution is valuable in illustrating and understanding the important parameters that determine the dynamic response of the cylinder. The results can also be compared with the critical velocity values obtained using finite element techniques. The finite element values will approach the exact solution as the mesh discretization increases. Consider a thin orthotropic cylinder of radius R subjected to a transient pressure load (e.g., a moving internal pressure, P). Figure 2 shows the geometry, coordinate system, and pressure loading condition being considered. The governing equation for this model with a moving internal pressure front, expressed as Heaviside step function, can be shown to be given by

$$m\frac{\partial^2 W}{\partial t^2} + D_x\frac{\partial^4 W}{\partial x^4} + \frac{12(1-\nu_{\theta x}\nu_{x\theta})}{h^2R^2}D_\theta W = P\,(1-H(x-Vt)) \quad , \qquad (5)$$

in which W is the radial displacement, dependent upon time, t, and axial position coordinate, x, m is the mass, which is equal to ρh, ρ is the density of shell material, h is the thickness of the shell, P is the internal pressure, and V is the pressure front velocity, which is assumed constant. The shell bending stiffness in the axial and circumferential directions is given by the expressions in Eq. (6) and Eq. (7), respectively.

$$D_x = \frac{E_x h^3}{12(1-\nu_{\theta x}\nu_{x\theta})} \quad \text{and} \quad D_\theta = \frac{E_\theta h^3}{12(1-\nu_{\theta x}\nu_{x\theta})} \quad , \qquad (6)$$

in which Ex and E_θ are the effective (smeared) elastic moduli, and $\upsilon_{x\theta}$ and $\upsilon_{\theta x}$ are the effective Poisson's ratios of the composite material in the axial and circumferential directions, respectively. For a composite tube with cross-ply laminate construction, the shell bending stiffness is different in the axial and circumferential directions and is determined by the axial-to-hoop layer ratio. The loading function, P(1 - H(x-Vt)) in Eq. (5), represents the internal pressure front traveling in the axial direction with constant velocity V. H(x-Vt) is the Heaviside step function. Accordingly,

$$P(1-H(x-Vt)) = 0 \quad \text{when} \quad x > V$$
$$= P \quad \text{when} \quad x \le Vt \quad . \qquad (7)$$

The critical velocity for an orthotropic cylindrical shell can be derived from the characteristic function obtained from Eq. (1) by author [8] as

$$V^2_{cr,comp} = \sqrt{\frac{1}{3(1-\nu_{\theta x}\nu_{x\theta})}} \left(\frac{h}{R}\right) \left(\frac{\sqrt{E_\theta E_x}}{\rho}\right) \tag{8}$$

Eq. (8) shows that the critical velocity of an orthotropic cylinder subjected to a moving pressure front is a function of the tube geometry, density, Poisson's ratios, and elastic moduli. The critical velocity increases when either of the elastic moduli increase as well as when the shell thickness to radius ratio increases. From a design point of view, a tube constructed with high stiffness and lightweight materials is preferred for dynamic loading conditions. However, Eq. (8) indicates that a larger wall thickness is required in general for the tube geometry when a high-velocity pressure front is present. It also shows that both axial and hoop moduli (e.g., E_θ and E_X) have influence on the critical velocity. Accordingly, the optimal design can be achieved by varying the laminate architecture of composite cylinders. The derived equation can also be applied to isotropic case such as steel liner, which has equal modulus and Poisson's ratio in all directions.

RESULTS

The described closed-form solution can be applied accurately to a cylindrical shell under the assumption of infinite length. For a finite length cylinder with varying cross-sectional area along its length and multimaterial construction, the finite element method allows a more expedient and straightforward procedure for determining the critical velocity. Since the composite tube is a laminated construction, ideally a ply-by-ply model will yield the best result and accuracy. However, this would dictate the use of many thousands of elements in the finite element model. The level of detail, coupled with the very short time step interval required for a dynamic analysis, would lead to an unreasonably long computational time. Accordingly, a smeared properties for the composite laminate is used. These properties, which are representative of the unique layup construction of the tube, were calculated using a model developed by Alexander and Tzeng [12]. The smeared property approach allows a single finite element to contain several layers and reduces the size of the finite element model.

The cylinder used in this analysis is 100 in long with a constant wall thickness. The steel liner and composite overwrap are 0.075 in and 0.125 in thick, respectively. The effective properties for a composite tube composed of 25% axial (x-direction) and 75% hoop (q-direction) plies are listed in Table 1. The properties are calculated based on the use of an IM7 graphite / 8551-7 epoxy composite. The cylinder is equally divided into 400 elements along the axial direction and 10 elements through the wall thickness. There are 4 elements representing the steel liner and 6 elements representing the composite overwrap. In all, the model contains 4,000 elements. The cylinder is subjected to a moving internal pressure of 6,000 psi.

Effects of Projectile Velocity

Two pressure front velocities, a sub-critical velocity of 2,500 ft/s (Case 1) and a supercritical velocity of 3,500 ft/s (Case 2), are performed to demonstrate the dynamic effects.

The total time for the pressure front to traverse down the tube was about 3.33 and 2.43 ms for Cases 1 and 2, respectively. The time increment used in the analysis was on the order of 10^{-6} sec; therefore, approximately 3,500 - 4,000 time steps were used per analysis. The finite element models including the composite cylinder and the dummy material block are shown in Figure 3 at a time instant when the block is about 20 inch from the initial position. The block is then given an initial velocity, which is held constant throughout the analysis. Finally, because an axisymmetric model was employed, only one-half of the cylinder is shown. A fringe plot of the radial displacement in the neighborhood of the projectile with velocity of 3500 ft/s at this specific instant is shown in Figure 4. The fringe pattern clearly shows the stress oscillation due to induced bending boundary layer stresses in the wall of the cylinder as it is subjected to a moving pressure front. There are no strain and stress waves occurring at a low velocity. The maximum displacement is located very close to the pressure front where pressure discontinuity is located. The displacement then decreases with increasing axial distance from the location of the pressure front discontinuity. The deformation is transient and cyclic with time and position.

Deformations and stresses can also be presented at a particular axial location as a time history. Figure 5 illustrates the radial deformation at the inner radius of composite as the projectile runs through the tube. A dramatic difference is obtained in the magnitude of peak displacement as well as in temporal behavior of the oscillations as the projectile velocity changes, Case 1 versus Case 2. Before the arrival of the pressure front, the cylinder at these observed locations is basically undeformed. The small oscillations that occur just before projectile arrival are real and represent stress oscillations due the moving pressure front. Similar behavior is predicted by thin wall shell theory. It is seen that at the instant the pressure front passes, the radial displacement undergoes a rapid increase. However, for sufficiently low velocities, similar to Case 1, the displacements and stresses are still close to what would be predicted based upon a static internal pressure loading. In Case 2, a very large radial displacement occurs for this case where the pressure front velocity is 3,500 ft/s. In fact, this velocity exceeds the critical velocity of the overwrapped composite cylinder. The peak magnitude of the radial displacement is seen to be about 1.5 times the peak magnitude of the radial displacement of Case 1 where the velocity is only 2,500 ft/s. As the projectile moves farther away from this axial location, the radial displacement approaches the same magnitude ($\sim 7.5 \times 10^{-3}$ in) as would be predicted by a static analysis. This is shown to be true for both Case 1 and Case 2. Since the velocity of Case 2 is above the critical velocity, the peak radial displacement is much greater than the average value with oscillation. If the projectile is accelerated from 2,500 ft/s to 3,500 ft/s gradually, the highest amplitude would happen when the critical velocity is reached. This would have resulted in a resonant condition as described previously. A similar characteristic was also found in other stress and strain components such as hoop, axial, and shear (not illustrated).

Cylinders with an Initial Crack

A composite overwrap tube with delamination (crack) at the interface was modeled by adding a slideline into the finite element model developed previously. It is also assumed that there is no friction at the sliding interface. Due to singularity, the stress and strain fields are not accurate in the very near region of the crack tip. Nonetheless, the far-field stress and strain are reasonably accurate and can be used to calculate strain energy density surrounding the crack. Accordingly, a

superfine finite element mesh is not necessary if the dynamic response can be fully modeled. This approach can significantly reduce computation time.

Figure 6 illustrates the finite element model near the crack tip and the path of integration. Figure 7 shows the hoop strain in steel element 484 which is near the embed crack. The magnitude of strain is much larger (about double) comparing to the one calculated from the model without crack. The integration path is chosen to be along to the coordinate axes to reduce computational efforts. It is also traction free along the path, which furthermore reduces the complexity of the calculation. The integration can be performed element by element along the path. The strain energy density is calculated at the center of each element and assumed to be uniform in each element. As the density of finite element model increases, the integration will approach to an exact solution.

The integration of strain energy density is conservative or path independent. If there is no crack existing, the integration along any closed loop will be equal to zero theoretically. This can be verified numerically by integrating strain energy density along a closed loop using the results from the previous finite element analysis. For a case with cracks, the stress and strain fields surrounding the crack are no longer the same as those calculated from a model without cracks. Accordingly, the integration of strain energy density along the path yields to the energy release rate at this specific crack. Furthermore, the integrated energy release rate is determined by the size of crack if the velocity and magnitude of pressure are constant.

Analysis was performed for a model with a crack size of 0.75 inch along the interface of composite and liner, which is large enough to cause failure of the cylinder by a rapid crack propagation. The internal pressure is about 6000 psi and the velocity of pressure front is 3500 ft/sec. Figure 8 shows the hoop stress in the steel liner near the crack. It is significantly larger than in a tube without crack. The strain energy density can be calculated from the calculation for specific instant along the selected path. The energy release rate is calculated to be 10 psi-in or 0.01 ksi-in from radial, axial, and through thickness shear components. The elastic modulus of the epoxy interface is about 500 ksi; accordingly, we can get the combined toughness as follows

$$K = \sqrt{K_I^2 + K_{II}^2} \approx 5.0\ ksi - in^{1/2}$$

The mode III toughness is not included since there is no contribution of in-plane shear components. It is noted that the computed combined stress intensity (K) is much larger than the fracture toughness measured under a static condition. The K_{1c} is about 1.2 ksi-in$^{1/2}$ and K_{2c} is about 1.5 ksi-in$^{1/2}$ for toughened epoxy. The dynamic fracture toughness is not available for the rate of interests generally. It is expected that the fracture toughness will be lower as loading rate increases. Currently, experiments are conducted to measure dynamic toughness for selected materials.

CONCLUSIONS

The dynamic analysis of a composite overwrap tube indicates high magnitude strains and stresses occurring in the cylinder at the pressure front that traverses along the length of the

cylinder. The amplification is caused by the resonance of stress wave attributed to the movement of loading. This dynamic strain effect will potentially cause crack growth and leads to a short life cycle of gun tubes. The propagation of fracture due to the stress waves is particularly critical for the lightweight composite cylinders. This is attributed to the low shear and tensile strength at the interface of different materials, thermal degradation, and potential loading rate dependence in polymer composite materials. The proposed analysis provides a straightforward method to evaluate the dynamic response and fracture mechanism in a composite gun barrel, which also exposes the shortcomings of static analysis used in traditional gun tube design.

REFERENCE

1. Rice, J. R., "A Path Independent Integral and the Approximate Analysis of Strain Concentration by Notches and Cracks," Journal of Applied Mechanics, June 1968, pp. 379-386.
2. Taylor, G. I., "Strains in a Gun Barrel Near the Driving Barrel of a Moving Projectile," A.C. 1851/Gn. 104, U.K. Ministry of Supply, London, England, March 1942.
3. Jones, J. P. and Bhuta, P. G., "Response of Cylindrical Shell to Moving Loads," Journal of Applied Mechanics, Vol. 31, Trans, ASME, Vol. 86, Series E, March 1964, pp. 105 - 111.
4. Tang, S., "Dynamic Response of a Tube Under Moving Pressure," Journal of the Engineering Mechanics Division Proceedings of the ASCE, October 1965, pp. 97-122.
5. Reismann, H., "Response of a Prestressed Cylindrical Shell to Moving Pressure Load, Development in Mechanics," Solid Mechanics - Proceedings of the Eighth Midwestern Mechanics Conference, Pergamon Press, Part II, Vol. 2, 1965, pp. 349-363.
6. Simkins, T. E., "Response of Flexural Waves in Gun Tubes," Tech. Report ARCCB-TR-87008, US Army ARDEC, Benet Weapons Laboratory, Watervliet, NY, July 1987.
7. Hopkins, D. A., "Predicting Dynamic Strain Amplification by Coupling a Finite Element Structural Analysis Code with a Gun Interior Ballistic Code," BRL-TR-3269, US Army Ballistic Research Laboratory, APG, MD, September, 1991.
8. Tzeng, J. T., and Hopkins, D. A., "Dynamic Response of Composite Cylinders Subjected to a Moving Internal Pressure," Journal of Reinforced Plastics and Composites, Vol. 15, No. 11, November 1996, pp 1088-1105.
9. Hallquist, J. O., "User Manual for DYNA2D - An Explicit Two-Dimensional Hydrodynamic Finite Element Code With Interactive Rezoning and Graphical Display," Lawrence Livermore National Laboratory, 1987.
10. Atluri, S. N. Computational Methods in Mechanics of Fracture, Springer-Verlag, NY, 1985, Chapter 5.
11. Doyle, J. F. and Farris T. N., "Interaction of Longitudinal Waves With a Lengthwise Crack in a Beam," ESM Proceedings, Portland, June 1988. 1253-1260.
12. Alexander, A. and Tzeng J. T., "Three Dimensional Effective Properties of Composite Materials for Finite Element Applications," Journal of Composite Materials, Vol. 31, No. 5, 1997, pp. 466-485.

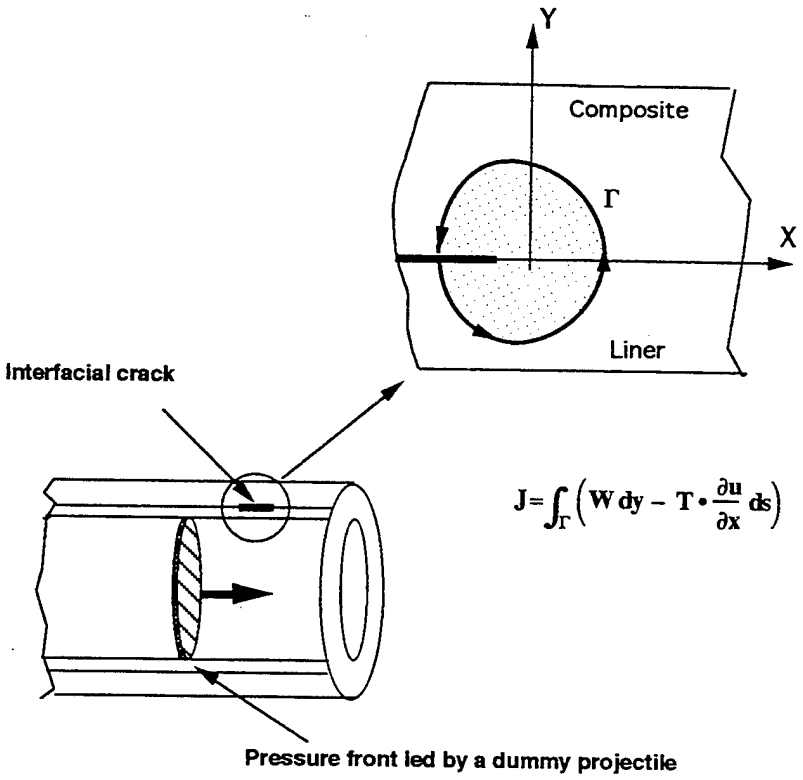

Figure 1: Energy integration defined along an interface crack.

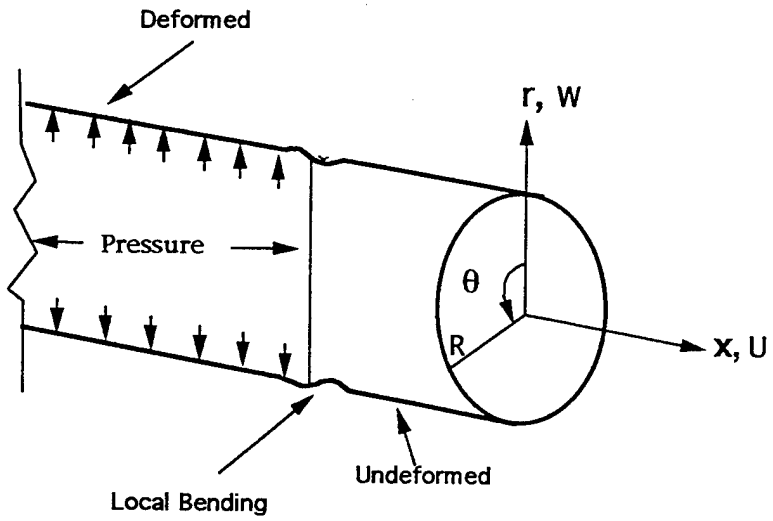

R : Radius of cylindrical shell
W: Radial displacement
U : Axial displacement
r, θ, x : Cylindrical coordinates

Figure 2: Deformation of cylinder subjected to a moving pressure front.

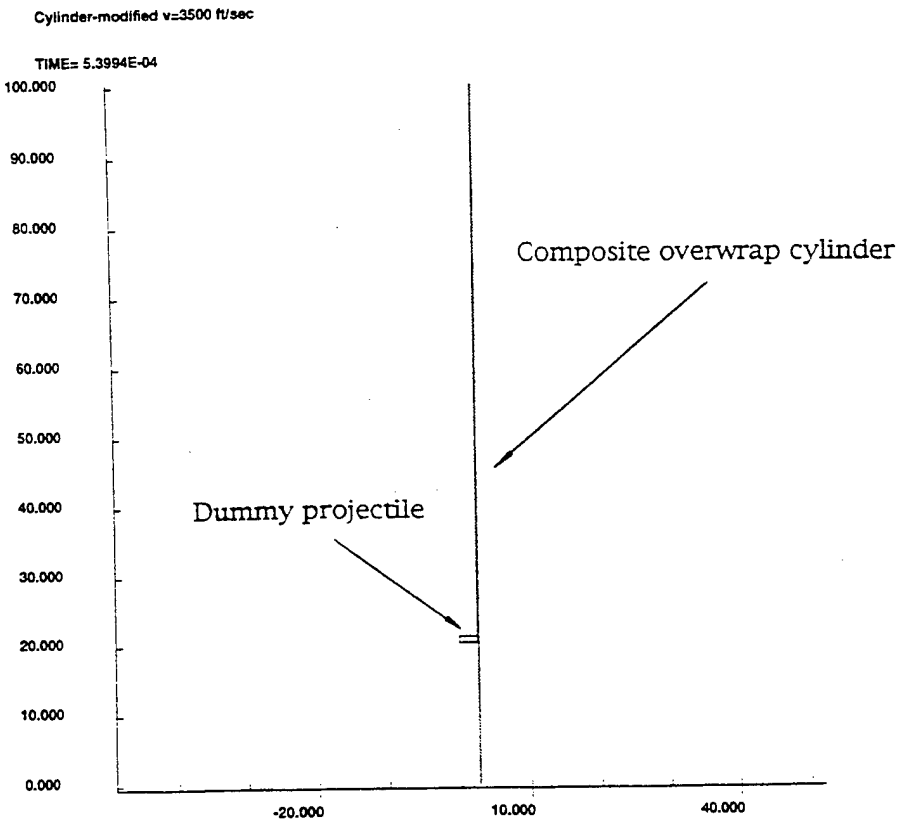

Figure 3: FEM model of a projectile moving along a gun tube

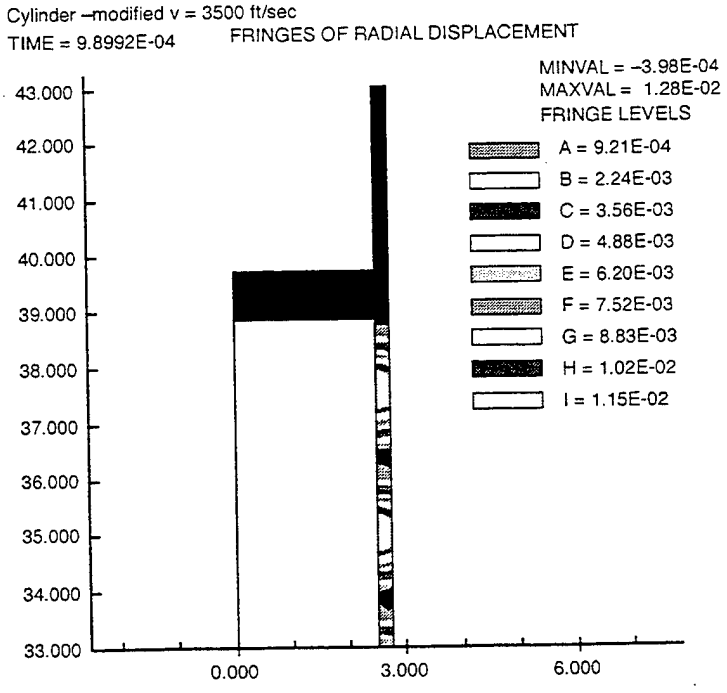

Figure 4: Radial displacement in the vicinity of projectile passage.

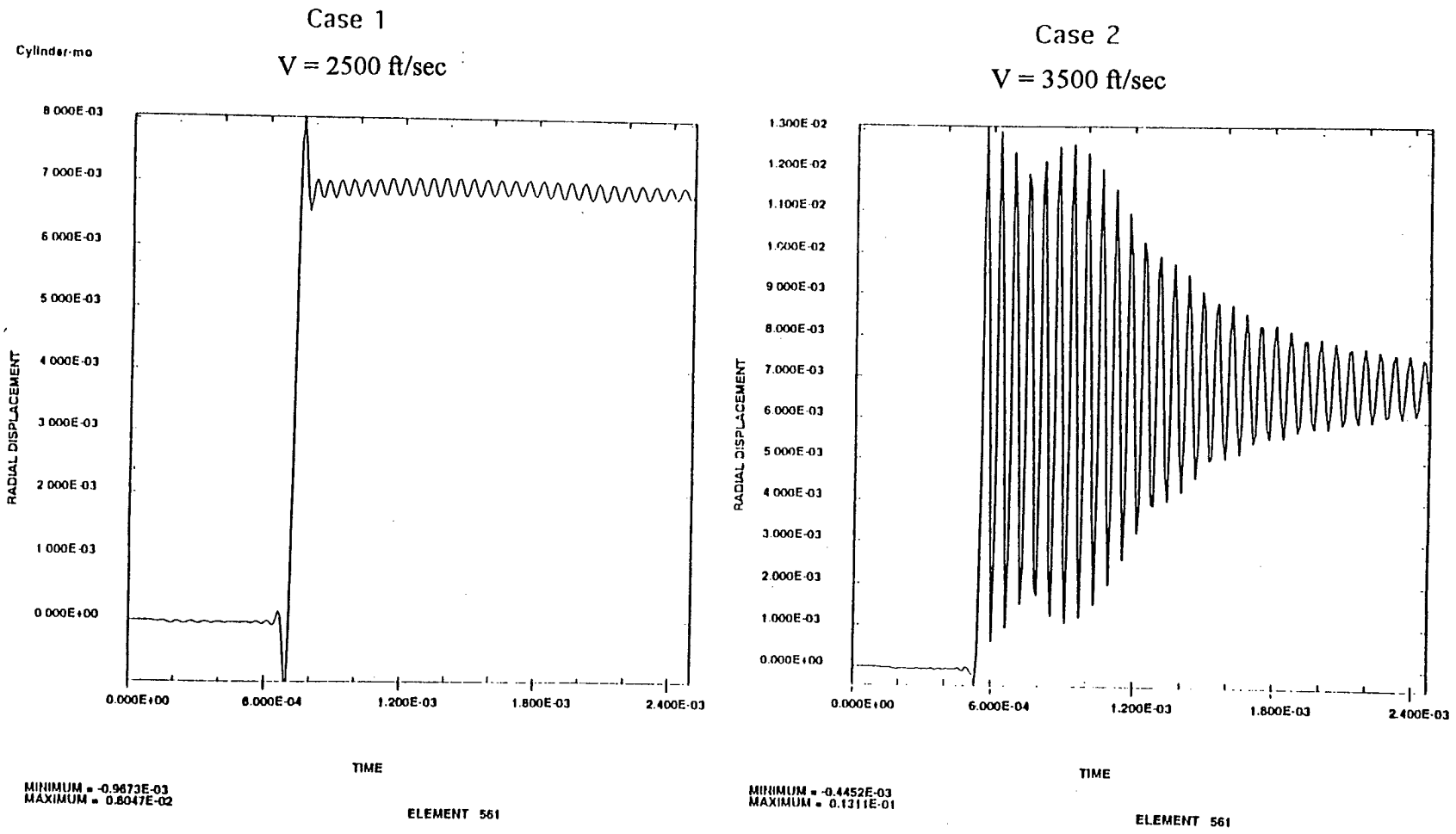

Figure 5: Radial displacement at the inner radius of composite wrap.

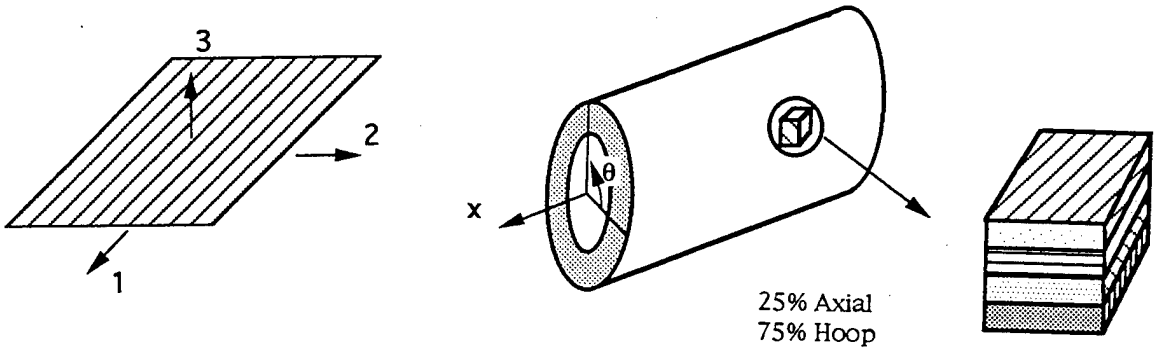

E_{11} = 25.0E+06	G_{12} = 7.0E+05	E_r = 1.298E+06	G_{rx} = 4.095E+05
E_{22} = 1.2 E+06	G_{13} = 7.0E+05	E_x = 7.214E+06	$G_{\theta r}$ = 4.610E+05
E_{33} = 1.2 E+06	G_{23} = 5.3E+05	E_θ = 19.10E+06	$G_{\theta x}$ = 7.000E+05
ν_{12} = 0.33	ν_{23} = 0.31	$\nu_{\theta r}$ = 0.3825	ν_{xr} = 0.338
ν_{13} = 0.33		$\nu_{\theta x}$ = 0.0556	(unit in psi)

Table 1: Effective properties of the composite wrap.

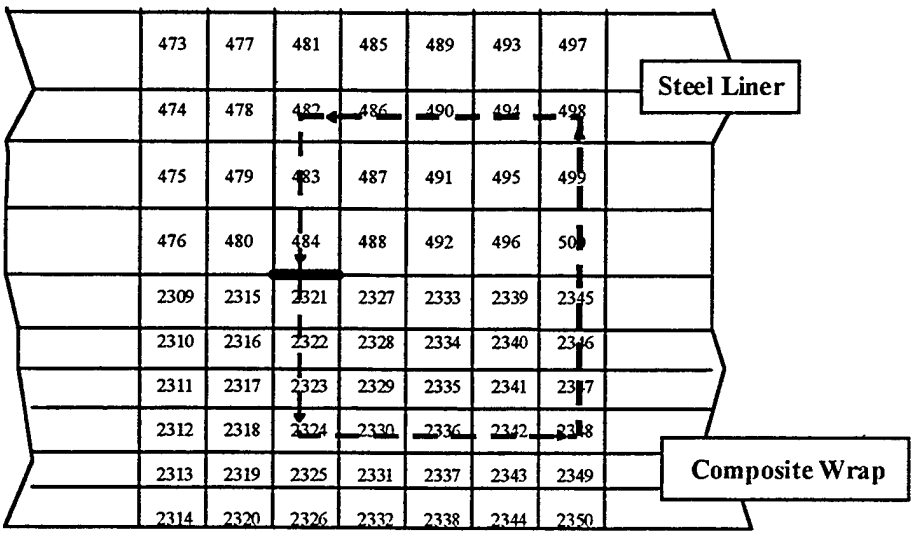

Figure 6: FEM model and integration path near the crack.

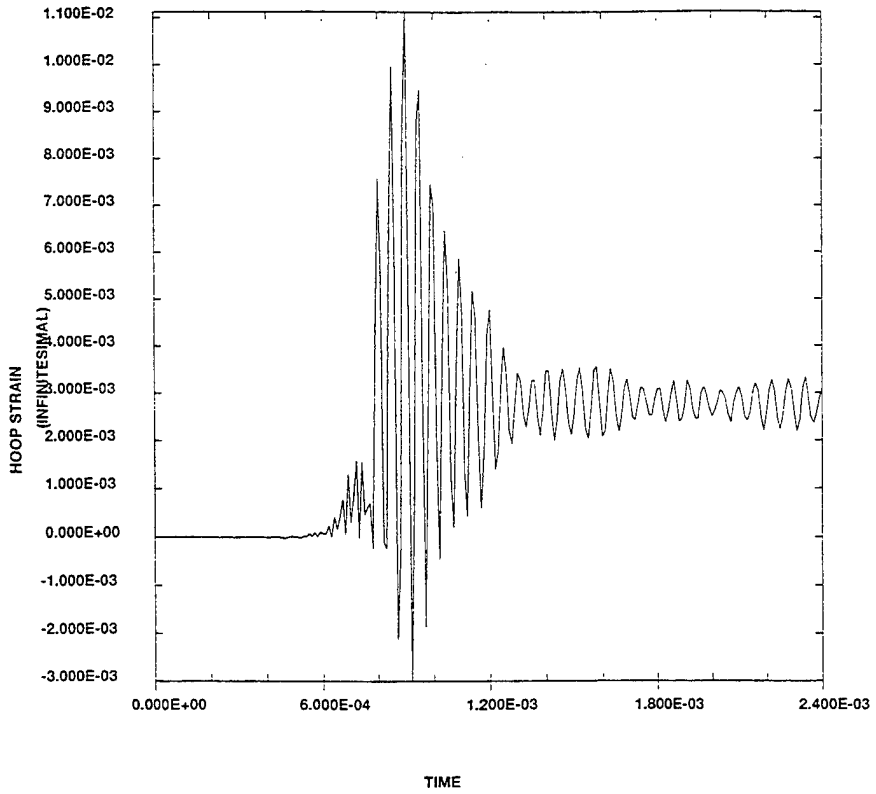

Figure 7: Hope strain in an element near the crack.

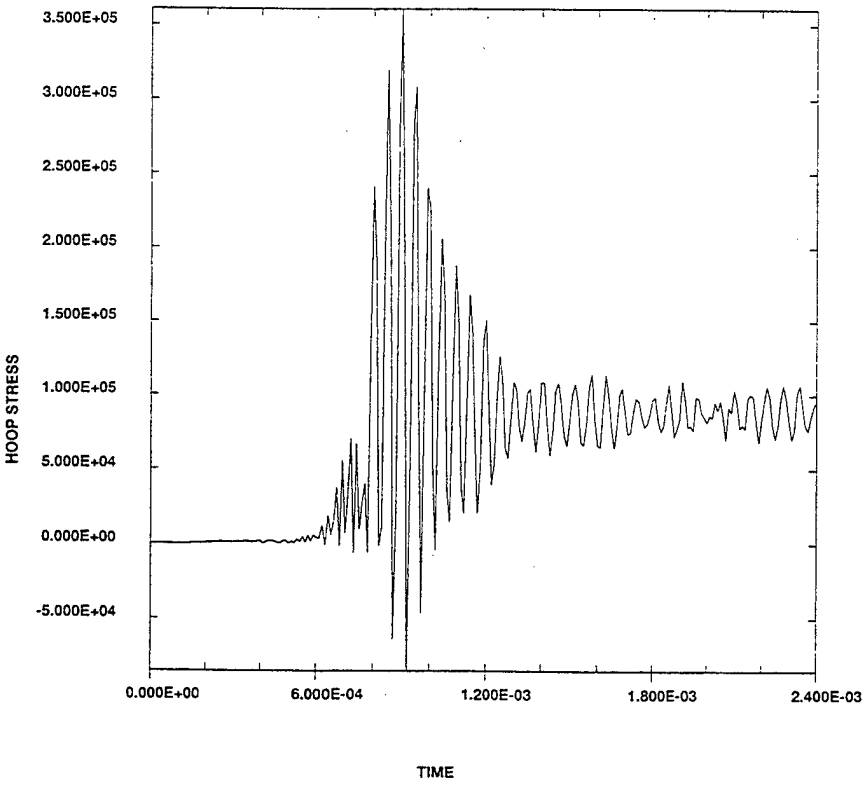

Figure 8: Hope stress in an element near the crack

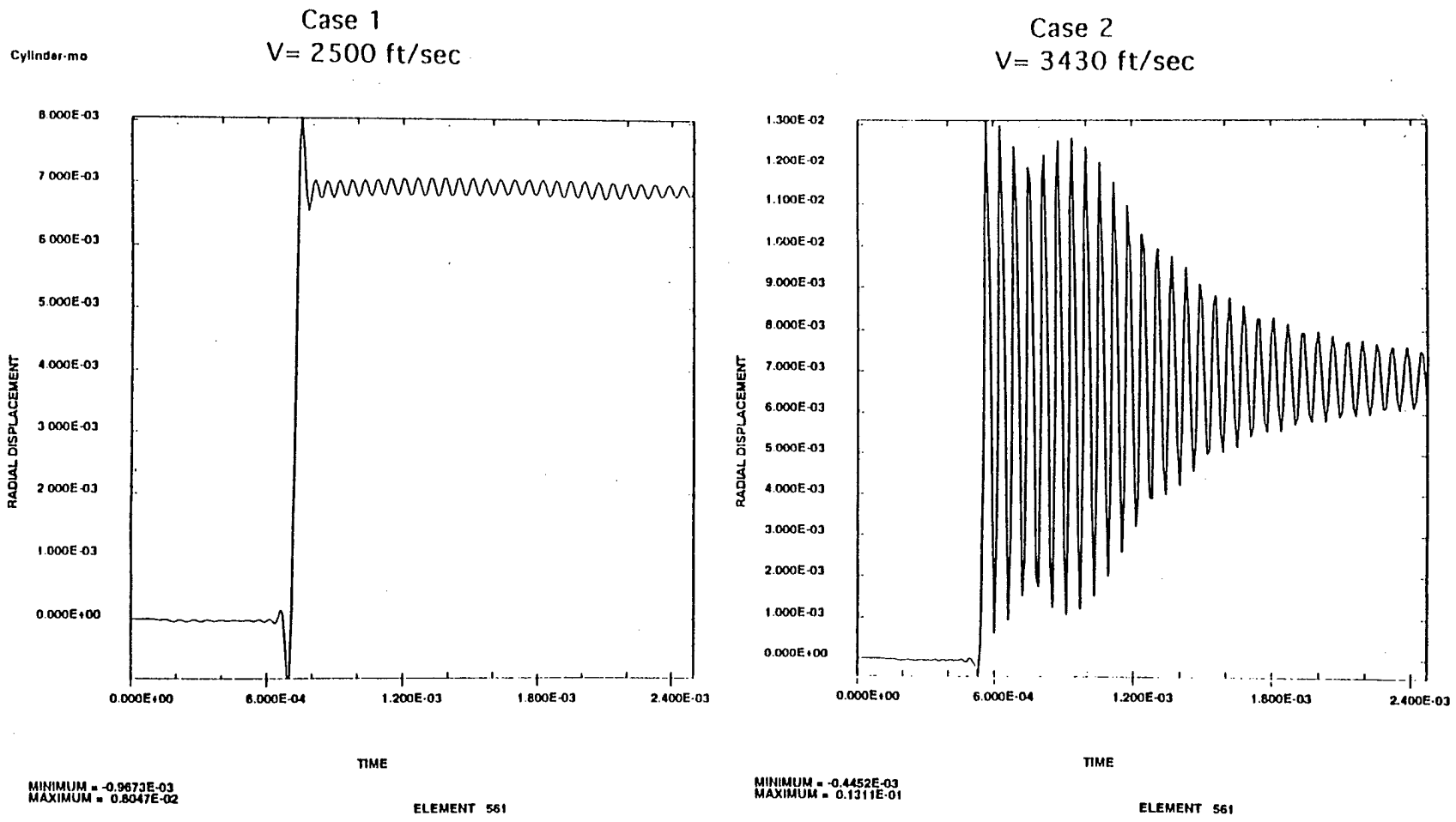

Figure 5: Radial displacement at the inner radius of composite wrap.

Sub-9000lb. Super Lightweight Towed Artillery: Materials and Systems Requirements

Dr A Groves (1)
Mr J A Woolard (2)

1. Technology Chief - Composite Structures, Structural Materials Centre, DERA, UK
2. Technical Manager - Indirect Fire Support: Recoil, Weapons Systems Sector, DERA, UK

INTRODUCTION

For towed artillery, platform weight is of great operational importance. Unless the platform, together with crew and adequate ammunition stock, can be readily deployed via a maximum of two medium lift helicopters the viability of the system in support of rapid mobile forces becomes increasingly an area of major concern.

UK industry is at the forefront in developing lightweight, 39 calibre 155mm towed howitzers; two systems having been successfully demonstrated recently, see Figure 1.

Royal Ordnance Plc; LTH
Picture courtesy Royal Ordnance Plc

VSEL: UFH
Picture courtesy VSEL

Figure 1, UK 9000 lbs artillery demonstrator platforms

However, given the current and projected helicopter lifting capacity available to the British armed forces, there is an imperative to seek even further weight reduction, particularly when considering the introduction of add on features like: autoloaders, pointing aids and electronic power packs. While the platforms can be split, in practice this is an unattractive option, since this greatly reduces logistical efficiency. Moreover, it doubles the risk of gun inoperability through helicopter failure or loss.

To mitigate this problem, weight reductions can be achieved via a move to shorter (29 calibre) barrels. However, for the British Army this is not considered a satisfactory option due to

option due to resulting range limitations. An alternative route, albeit at present with a higher level of risk, is to consider using a lightweight composite 39 calibre gun barrel in conjunction with soft recoil. Further weight savings can be achieved via the application of composites for other parts of the gun system: e.g. trails, baseplate, carriage, etc. A weight objective of some 7000-7500 lb is considered an interim goal with an ultimate target weight of 5000 lb. This will not only provide scope for air lift by all but the smallest of helicopters, but moreover enables the gun to be towed by a very small vehicle and to be relatively 'man handleable' for rapid movement on the battlefield.

In this paper a summary of current DERA research and development activities related to lightweight towed artillery is presented. Particular emphasis is given to novel recoil management systems, which is believed to hold the key to the long term ambition of a 5000 lb weight target for a 39 calibre gun with a composite barrel; otherwise a serious reduction in gun stability may occur. Emphasis is then placed on alternative materials/designs for the current titanium alloys adopted. The associated manufacturing routes are discussed. Potential weight savings and technical risks are reviewed.

SOFT RECOIL

As discussed in the introduction, if a superlightweight field gun is to be achieved with stabilty commensurate with existing towed artillery, soft recoil may hold the key to success. While advanced lightweight, high strength/stiffness materials can assist in the weight reduction exercise, unless gun stability can be managed to ensure round to round consistency, no military gain will be achieved. Indeed in an inferior delivery system may result. Of course this is irrespective of the material selected, be it metallic. e.g. aluminium or titanium, or fibre reinforced composites.

Recoil is the natural reaction to the firing sequence of a conventional gun system. The function of the recoil systems function is to absorb the energy of the recoiling parts over a convenient distance, and return the gun into a position for further firing. It is the absorption and the controlled dissipation of this energy that reflects the working efficiency and ultimate accuracy of the weapon system.

Therefore, recoil management needs to be concerned with a number of issues which influence the operational characteristics of the weapon system. These can be defined as follows:

- The smooth absorption of recoil energy in a pre-defined stroke.
- The control of the momentum recoiling parts in run-out.
- The retention of the recoiling parts at the battery position irrespective of elevation.
- The controlled dissipation of energy to ensure the stability of the weapon system at all times.

Recoil systems design considerations

The recoiling mass consists of the barrel, muzzle brake, breech and breech ring and a proportion of the recoil mechanism. The percentage of the recoil mechanism which is part of the recoiling mass is dependant upon a number of factors which influence the overall design of the gun. In attempting to maximise the recoiling mass to reduce recoil length, the designer may wish the recoil cylinders (usually the heavier) to be included, with the buffer and recuperator rods being fixed to the cradle. Conversely the cylinders may be fixed to the cradle with the rods free to move; this allows for a reduction in the trunnion pull, but extends the recoil stroke. Given the desire to move to very lightweight composite overwrapped barrels, the latter option is very much likely to be the preferred route for a an ultra-lightweight gun system.

A significant factor in the performance of any weapon system during firing and run-out is stability. None more so than with towed systems. Stability can be controlled by careful management of the recoil event, with movement of the gun kept within acceptable limits. However, this problem becomes more acute the lighter the system.

Stability is more prevalent at lower angles of elevation where the line of action of recoil tends to the horizontal. The problem can be exacerbated when the gun is traversed from the centre of arc. Firing from this position creates an imbalance in the forces reacted by the structure.

In previous towed gun designs, the ratio of the recoiling mass to overall mass is approximately 1:4 to 1:5. The design of guns proposed during the recent American LW155 competition have ratios of 1:2.23 to 1:2.25. All of these guns are 39 calibre and fire similar ammunition; they therefore produce the same reaction with respect to recoil force. It follows that the smaller the ratio, stability becomes more important in the design of lightweight systems. The problems facing the designer with regard to the stability of lightweight systems is illustrated in Figure 2; World Artillery Developments.

This figure shows energy (joules) per unit of mass (kg) of the system against range (metres). The points on the graph represent a variety of towed gun systems since the 1930's; the more familiar systems are shown in the darker points. The trend is clearly mass increase with energy and range. The two extreme data points, (8 and 9) illustrate the significant departure of the 9000 lb lightweight (e.g. LTH and UFH) guns (point 8) and a superlightweight 5000 lb 39 calibre (point 9) from this trend.

Factors which affect the stability of a gun when firing can be defined as follows:

- **Trunnion height:** The height of the trunnion is significant as it reflects the magnitude of the overturning moment produced from gun recoil. The lower the trunnion height, the lower the moment and the more stable the gun.

- **Trunnion pull:** The force reacted by the trunnions during recoil in the direction of the recoil path. This is the force element of the overturning moment. The lower the trunnion pull, the more stable the gun.

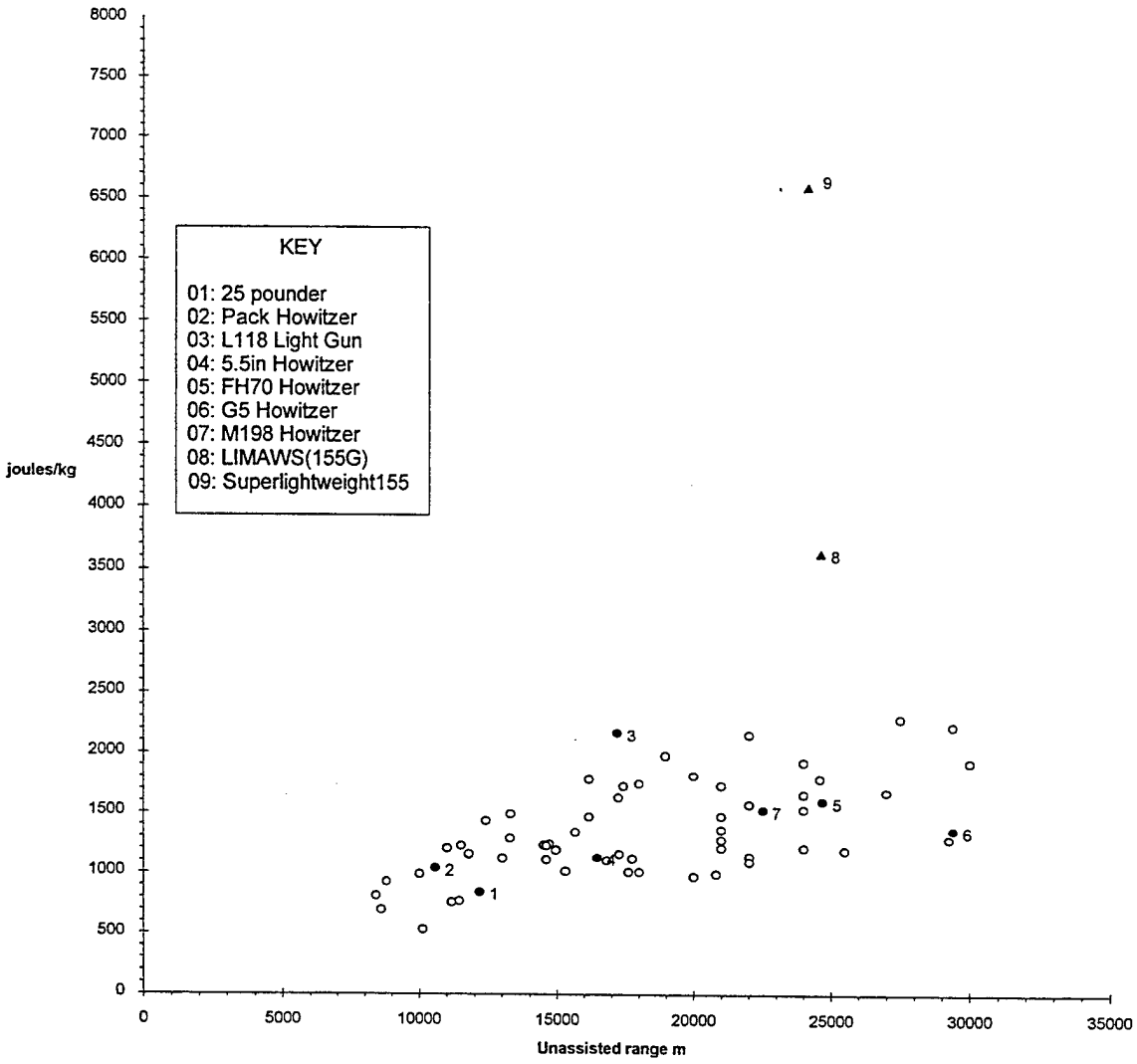

Figure 2 World Artillery Development

- **Gun elevation:** As gun elevation is increased the horizontal component of the recoil force decreases. This reduces the overturning moment by allowing a greater proportion of the reaction to be absorbed vertically downwards into the gun carriage/platform. The higher the elevation, the more stable the gun.

- **Mass of the recoiling parts:** The lighter the recoiling parts, the greater the Kinetic Energy (KE) imparted and the more work needed to bring them to rest. The heavier recoiling parts, the less work needed and the more stable the gun.

- **Length of trail legs-mass of carriage:** To counter the overturning moment from the gun, a restoring moment must be in place; a significant element of this moment is the length and position of the trail leg/carriage. The longer the trail leg and the heavier the carriage, the more stable the gun.

An illustration of the forces acting on the weapon and structure when firing is shown in Figure 3.

However, what is evident is that future lightweight towed howitzer(s) recoil needs will not just rely on one technology, and that the recoil system will form only one part of the recoil management solution.

The demands towards even lighter weight systems while maintaining or increasing range will undoubtedly grow. In trying to meet these aims, it will be important to realise that no single approach will offer a solution. Excessive movement of the gun carriage will adversely effect weapon efficiency, consistency, and increase crew fatigue. Equipment stress levels and fatigue limits will also suffer. The demands in absorbing higher impulses from the gun and the need to keep the weapon platform stable suggest that the problem can only be resolved by adopting a total system approach.

In this respect a total system approach would need to encompass those parts of the superstructure which could be used to dissipate and transfer energy uncontrolled by the recoil system. Current gun carriage designs have to be flexible to absorb the high forces that are imparted through the structure, but they are absorbed in an uncontrolled way, with no inherent damping capability. This can often lead to early fatigue of structural components which is countered by sections having to increase in size resulting in a corresponding weight penalty. The use of composites at critical sections may permit the absorption of energy and its regulated release in slow time, allowing greater control of the recoil event and thereby enhanced stability.

Muzzle brakes (MB) must be considered as part of the total system approach when considering the management of recoil. Nearly all artillery systems employ the use of a muzzle brake to absorb some of the energy from the escaping propellant gases and thus reduce the recoil forces acting on the gun. The design and characteristics of the brake is important as this will reflect the proportion of energy absorbed. It will also dictate the overpressure effects on the gun crew and their resulting safe exposure limit.

The design parameters for the more common type of muzzle brakes used to-day were established over 50 years ago. These parameters/rules define the method by which the efficiency of the brake could be determined. However, no account of the effects of muzzle blast over pressure or how it could be reduced was taken in to account in the formulation of these rules.

Since WW2 MB types such as Multi-baffle and Pepper-pot have been investigated but without significant progress in the efficiency versus overpressure issue. Therefore, the need is to identify the muzzle brake configuration which offers the best compromise between blast over pressure and efficiency. Currently research in this area is on-going; early indications are that results are dependant upon gun configuration, but improvements to efficiency are expected.

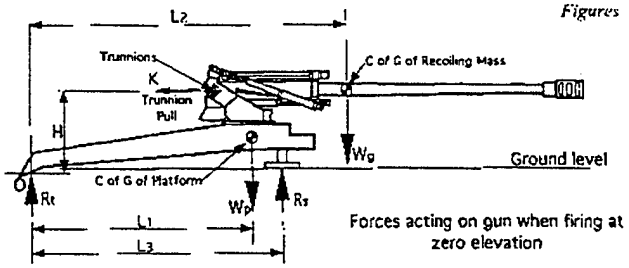

For equilibrium to take place, moments about O. Wp x L1 + Wg x L2 = K x H + Rs x L3
For the gun to remain stable throughout recoil. Wp x L1 + Wg x L2 - K x H = Rs x L3

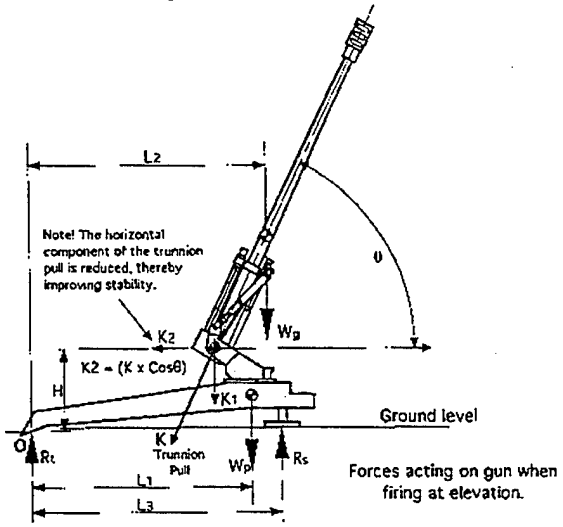

For equilibrium to take place, moments about O. Wp x L1 + Wg x L2 = K2 x H + Rs x L3
For the gun to remain stable throughout recoil. Wp x L1 + Wg x L2 - K2 x H = Rs x L3

Figure 2 Forces acting on weapon when firing

Figure 3. Forces acting on platform when firing

Operational efficiency of the weapon system will continue to be dictated by its stability. Therefore, it is important to recognise how this can successfully be controlled and how it should be applied to lightweight structures.

One concept of recoil management that would significantly enhance the stability of lightweight systems would be the use of soft-recoil. Soft-recoil is a system that uses the momentum of the counter-recoiling mass to reduce[1] the trunnion pull and thereby improve stability of the gun.

The concept of soft-recoil has been around for some considerable time and was put to use by the French in their "Cannon de 65 (montagne) modèle 1906", which was extensively used in the first World War.

The only serious development of soft-recoil for artillery systems has been undertaken in the US, during the 1970s, by Rock Island Arsenal who were responsible for the XM204. This was a 105 mm field gun of which eight prototypes were manufactured and successfully demonstrated. Since that time, a 39 calibre 155 mm gun has been developed by Rock Island known as the 'VIPER'. This incorporates a system of recoil referred to as 'hybrid' soft-recoil (HSR).

1 theoretical figures of greater than 50% reduction for a 'pure' soft-recoil cycle are claimed.

The hybrid soft-recoil differs from the XM204 design in that charge initiation is distance-dependent and not velocity-dependent. Thus VIPER can accommodate the misfire and cook-off scenarios, which have often been cited as disadvantages of soft-recoil systems, and can fire current charge systems without the usual dependence on precisely-timed ignition events.

The US are investigating the reduction of launcher mass towards their goal of 5000lb. This is being conducted as a technology demonstration programme by ARDEC and its specification has been outlined in a recent white paper entitled 'Advanced Technology Light Artillery Systems'.

The future may hold many advances for lightweight systems. The concept of ultra-lightweight guns with composite over-wound barrels and composite or lightweight alloy platforms, may make stability an even greater issue. Soft-recoil for 155 mm systems is by no means proven but it does offer the potential to improve the stability of future systems like for LIMAWS, and will certainly allow it to be a major contender for any future growth requirements such as 52 calibre towed gun.

LIGHTWEIGHT MATERIALS

Although soft-recoil may hold the key to the development of a superlightweight 39 calibre 155mm field gun, it is clear that if significant weight savings are to be realised, a move to materials with greater specific strengths and stiffness (i.e. strength and stiffness to weight ratios) will be required from those currently used. Since both aluminium and titanium alloys are extensively used for field gun platforms, it is clear that the most realistic options currently available for significant weight gains is via continuous fibre-reinforced composite materials.

Description of continuous fibre-reinforced composite materials

Continuous fibre-reinforced composites are a family of materials which combine one or more materials to provide a 'composite' with properties (e.g. strength, stiffness, etc.) well in excess of those obtainable from its constituent parts. The most commonly known composites are those using a polymeric matrix with either glass, carbon or Kevlar continuous fibres as the reinforcing medium. In principle, other matrix/fibre options are availabl; examples include aluminium or titanium matrices for metal matrix composites (MMCs), and alumina, silicon carbide and boron fibres for the reinforcement. However, relative to the more commonly used composites, these are extremely expensive, some commercially very immature and others are only likely to find a relatively small niche market, certainly in the near term. It is for this reason, therefore, that this paper will concern itself only with the widely used composites, thereby endeavouring to minimise technical risk for a next generation superlightweight field gun.

Strength and stiffness are dependant of fibre orientation which can be tailored to satisfy the applied loads. For example, stiffness and strength of an I-beam can be maximised by producing flanges from a unidirectional fire composite. For the shear web, where maximum shear strength is required, a $\pm 45^{\circ}$ lay-up can be employed. This, in essence, is the great attraction of composites, in that they can be tailored for

the application and all material redundancy removed.

Polymer Matrices

Two generic types of polymeric systems are available to the gun designer: thermosets and thermoplastics. Thermosets are the most widely adopted and embrace the cross-linked polymers such as polyesters, vinyl-esters, epoxies and polyimides. In these materials, the polymer chains are effectively 'locked' together via a complex chemical cross linking process so that on application of heat they do not soften, but will degrade and eventually char. By contrast, thermoplastics have no cross-linking and soften on heating and can be remoulded to shape. This lack of cross-linking makes them particularly tough, which can yield benefits in terms of the damage tolerance of the resulting composite - a notable deficiency of thermoset composites. Notable thermoplastic matrices include the commonly used industrial thermoplastics, e.g. polypropylene, through to the high-performance polymers like polyetheretherketone (PEEK) and polyphenylene sulfide (PPS).

While thermoplastic matrices continue to receive much attention, there has been much interest in automobile manufacturing because of the short processing times, their complex processing routes, often involving high temperature and pressure, has resulted, to date, in them being less attractive than their thermosetting counterparts, which are by far the most widely used.

In terms of the thermosets, while polyesters and vinyl-esters are widely used in the marine environment due primarily to their low cost, epoxies almost reign supreme where extreme high performance is required. This is combined with hot/wet performance and good compressive properties. This is further aided by their processing adaptability, being used in virtually all of the principal composite manufacturing routes available. Their only major drawback, as far as ordnance is concerned, is their relatively low maximum operating temperature, circa 180°C, which is inadequate for barrel applications. For this reason the polyimides are preferred, namely the Bismaleimide resins which are the most easy to process of the polyimide family. However, it must be recognised that all polyimides are difficult to process when compared to epoxy resin systems, requiring complex processing parameters if high quality components are to be produced.

Fibre selection

Fibre selection is limited for artillery platforms to the well known fibres: glass, Kevlar and carbon fibre.

Glass fibres are widely available and very cheap, circa £2/kg for E-glass, have excellent strength but are not particularly stiff. A hollow version of the fibre is available, although not widely. It's reduced density and large second moment of area infer improved specific properties over conventional glass fibres.

Kevlar fibre, which is very tough (widely used for ballistic armour for example) has very poor compressive properties. Furthermore, while strength is good, stiffness is not significantly higher than glass; the fibres are also expensive. It is for these reasons that

Kevlar is unlikely to have a significant structural role in a gun platform, although its toughness could be harnessed to improve damage tolerance and wear resistance in specific locations.

By contrast to glass and Kevlar fibres, carbon fibres are very stiff and have excellent strength and good compression properties. Cost, however, can be high, although it is unlikely that anything other than the lower cost high strength/standard modulus carbon fibre would be considered for a next generation superlightweight field gun.

Typical material properties

Examples of the in-plane specific properties of composite materials, based on a typical 60% fibre volume fraction ± 45° lay-up, are given in Table 1. Compressive properties are presented since these are inferior to the tensile properties.

It is unlikely that such a simple lay-up will be used for all gun components; a much more orthotropic lay-up will be selected due to the asymmetry of the component loading. Nevertheless, these figures do provide a 'conservative' estimate of the properties available for the gun platform, against which comparisons can be made with the light alloys data presented. For completeness, the cost of the raw materials per kg is given. While composites are more expensive than aluminium and magnesium, the cost is very competitive to titanium alloys. However, final cost is a function of the manufacturing route chosen for a particularly component, details of which are now discussed in the next chapter.

60% V_f Composite ± 45° lay-up properties	Density kg/m^3	Modulus GPa	Specific Comp. Modulus GPa/sg	Comp. Strength MPa	Specific Comp. Strength GPa/sg	Material Cost £/kg
E-glass/epoxy	2000	23	11.5	500	0.25	2-3
Hollow S2 glass/epoxy	1560	19	12.2	550	0.35	~12
Kevlar 49/epoxy	1360	33	24.3	120	0.09	20
Standard Modulus carbon fibre/epoxy	1540	65	42.2	700	0.45	18
Light Alloys						
Magnesium	1740	45	26	350	0.2	14
Titanium	4500	100	22	1000	0.22	25
Aluminium 7075-T6	2700	72	26	540	0.2	7

Comp. = Compressive sg = Specific gravity V_f = Fibre volume fraction

Table 1, Typical material properties for candidate artillery composite materials

COMPONENT SELECTION

In this section of the paper, the key components of a typical 'lightweight' field gun are considered from which potential weight savings can be identified via a materials substitution approach. In addition, material selection, potential design solutions and manufacturing routes are briefly described for each component considered. For the purposes of weight saving, titanium is taken as the reference material, given its accepted use as a field gun material.

From the consideration of the principal components of a 'typical field gun' (see Figure 4) and the associated illustrative weight breakdown details (Table 2), it is clear that,

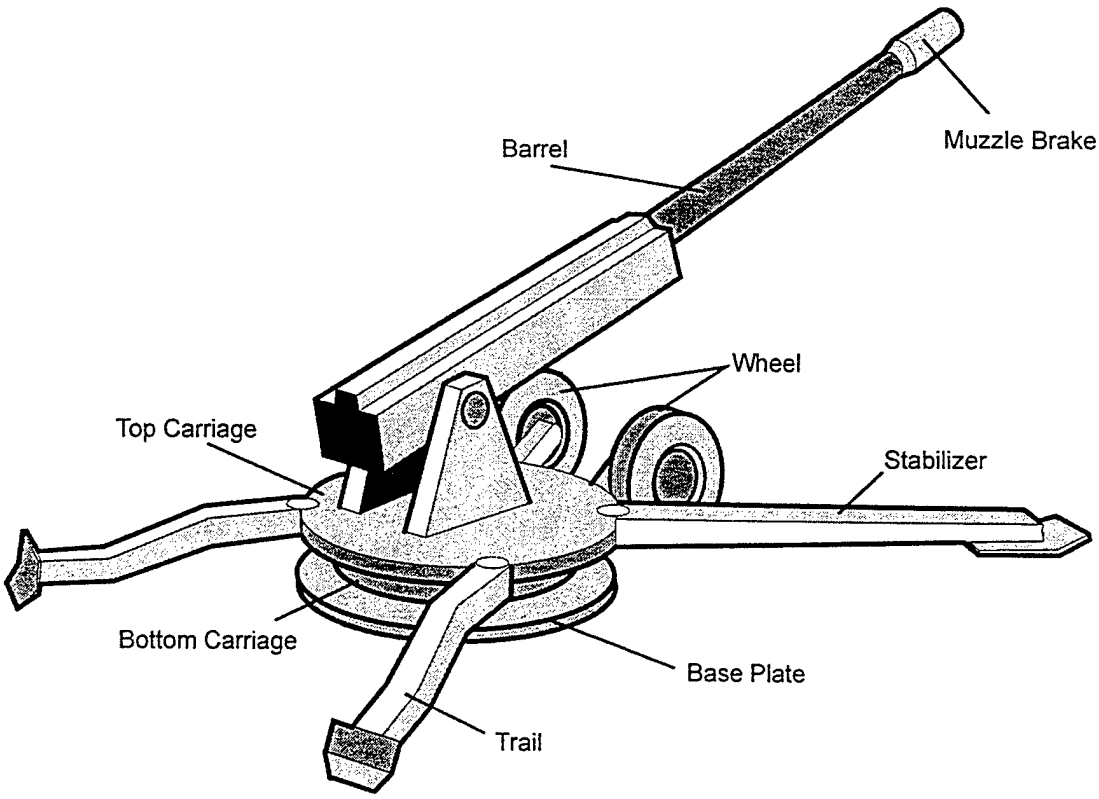

Figure 4 Typical field gun principal components

if significant weight savings are to be realised for a field gun, then efforts must be focused on the gun barrel, the stabilisers, base plate, upper/lower carriage and wheels. In principle, other components could be considered for material substitution, but for the most part they are either very complex to design from composites (e.g. the cradle) or alternatively the weight/cost trade-off reaches a point of diminishing returns.

Component	% of total system weight	Cumulative weight %
Trails / Stabiliser	20	20
Gun Barrel, excluding breech	35	55
Base plate	7	62
Upper & lower carriage	12	74
Wheels/Tyres	8	82
Remainder, e.g. cradle, breech, etc.	18	100

Table 2 Typical component weight breakdown for a field gun

Gun barrel

DERA has been undertaking active research into the exploitation of composite overwraps to reduce the weight of conventional launch gun barrels. A typical composite barrel would consist of a thin steel liner, to provide a wear resistant/gas tight seal to the projectile, overwrapped with a standard modulus carbon fibre composite to provide circumferential strength. Axial stiffening, if required, would be provided by an axially aligned intermediate modulus carbon fibre composite sleeve. A schematic diagram of a typical barrel is shown in Figure 5.

Because of the high temperature requirements sought from an artillery gun barrel, a high temperature polyimide resin is adopted as opposed to a standard epoxy. The overwrap is applied in the form of a prepreg tow, manufactured by a route developed within DERA. The overwrapping process is very similar to filament winding, with the steel liner forming the rotating mandrel. Furthermore, the overwrap is applied under substantial tension levels to pre-stress the liner. This is undertaken for several reasons: maintaining/increasing barrel fatigue life; thermal expansion mis-match (avoid gap formation between the steel and overwrap at temperature extremes); matching of the strain limits of the two materials (steel 0.5%ε; composite overwrap 2%ε). The overwrap is then cured using standard DERA developed procedures.

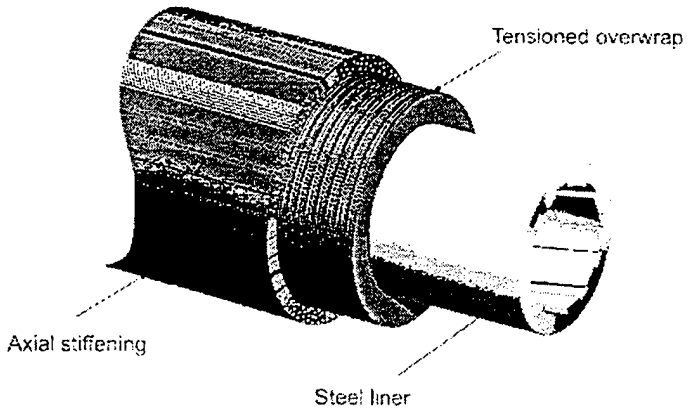

Figure 5 Schematic of a fibre composite overwrapped barrel

A number of barrels have been produced to demonstrate the technology, both at cannon calibre and 120mm calibre; examples are shown in Figure 6. Lifing issues of the overwrap are being researched, while axial stiffening is currently being addressed. While the latter is not straightforward, potential solutions have been identified and are currently being assessed.

Weight saving assessments, based on a 60% steel barrel wall reduction configuration, suggest that the weight of a 39 calibre barrel could be reduced by some 35%. Mounting of the barrel into the cradle will require careful consideration, but a rail/cruciform approach is considered to be a viable approach.

30mm Overwrapped Barrel

120mm Overwrapped Barrel

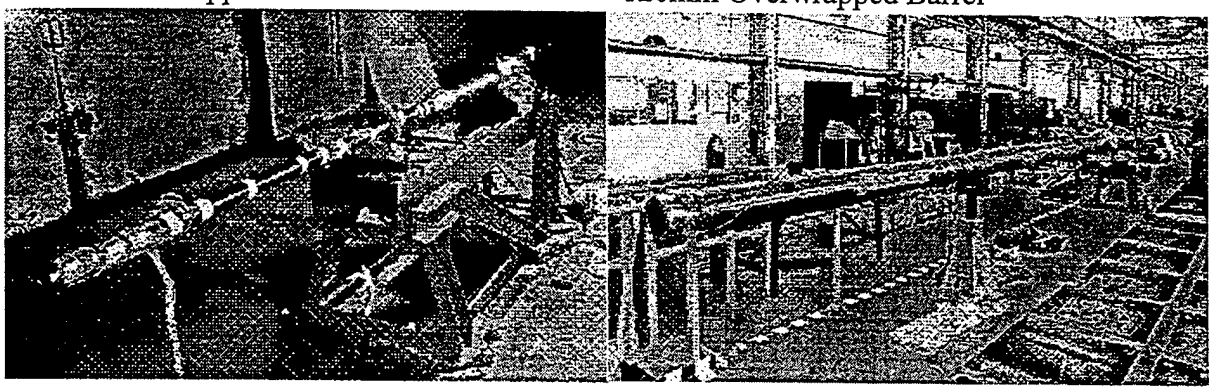

Figure 6 Overwrapped Demonstrator Barrels

Baseplate

Since the weight of the base plate represents some 7% of the total system weight, it seems logical to consider a composite replacement, even though the component is subjected to a harsh environment, both in terms of applied loads and abrasion.

As the baseplate needs to withstand very high loading, from consideration of Table 2,

(which holds given that a $\pm 45^{\circ}$ lay-up would be considered for this component) it is clear that both hollow S2-glass or standard modulus carbon fibre/epoxy composites (CFRP) are viable options. In terms of cost, S2-glass offers the greatest benefit. Moreover, the lower stiffness of this composite material could be seen as beneficial, offering baseplate flexibility to conform to the underlying terrain. However, if costs are not the only driving factor, then carbon fibre will yield the greatest weight saving, whilst retaining a similar stiffness to a titanium component.

In practice, a hybrid structure could be considered, possibly consisting of a carbon fibre/epoxy composite core with protective skins consisting of a Kevlar fabric. For composite bridging, Kevlar has shown excellent durability to extensive military vehicle wear and abrasion trials. A glass/carbon fibre hybrid core could also be considered as a mechanism to reduce cost, although weight savings would be compromised. Thus a detailed cost/weight trade-off analysis would need to be conducted. A cross section of a possible composite baseplate in shown in Figure 7. Adhesively bonded rubber pads are shown to protect the base of the component. Such pads are well known for tracked military vehicles to reduce road damage from the steel links. In addition, a titanium boss is retained to aid connection to the lower carriage.

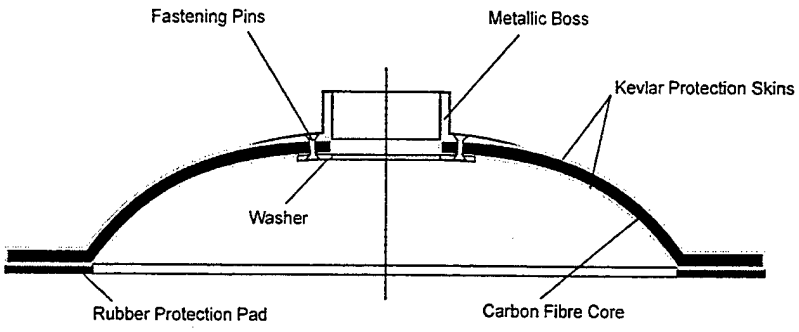

Figure 7 Schematic of a composite baseplate

Manufacture of a composite baseplate can be achieved via one of two routes. The first would embrace the use of pre-preg composite materials carefully laid-up into the required format. A mixture of pre-preg materials would be required to achieve the core configuration and Kevlar skins. Curing and consolidation of the resulting product is then achieved by the application of heat and pressure. Given that this is a fairly complex structure, with built in corrugations for stiffness, this is likely to be a achieved via the aid of an autoclave. Here the component is placed within a rubber bag in a large pressure chamber to apply pressure whilst simultaneously heating the component. The mould, to which the pre-preg is applied to achieve shape, can be either metallic or composite in nature. A schematic of the autoclave process is shown in Figure 8. Resin volatiles are removed during cure by the application of a vacuum..

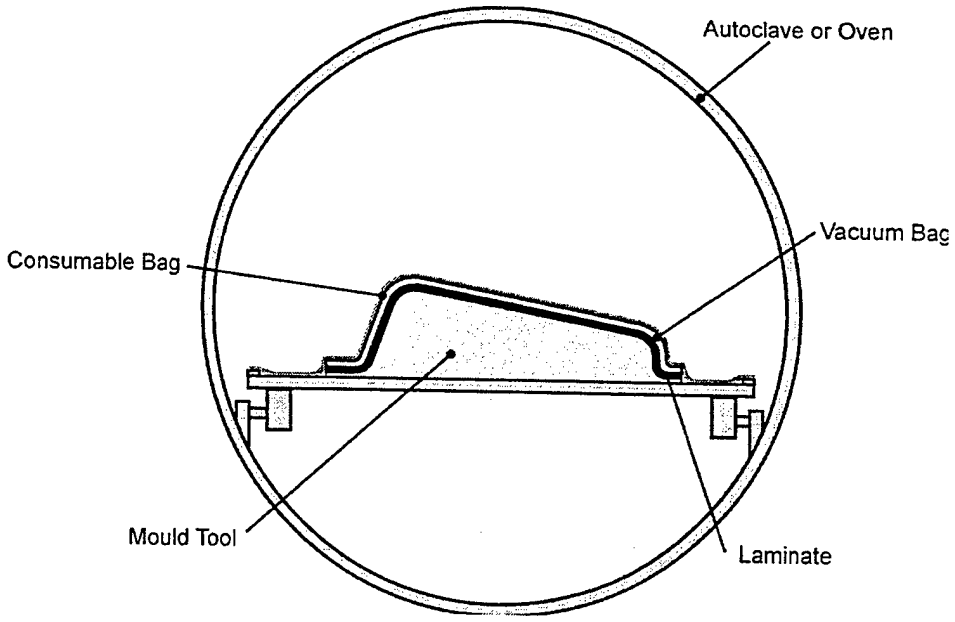

Figure 8 Autoclave manufacturing

An alternative, and potentially cheaper route, is via the resin infusion process. For a baseplate, it is likely that a resin infusion process could be considered, whereby the fibre pre-form (the dry fibre reinforcement) is placed over a mould and covered with a porous release film. This in turn is covered by a resin distribution media and finally vacuum sealed to the mould. A vacuum is then applied and the resin drawn in through the fibres to produce a composite of high quality, with fibre volume fractions of the order of 50-55%. This compares favourably with volume fractions of 60% achieved by the autoclave process, although voidage content can be worse. The resin infusion process is receiving world wide attention as a viable low cost composite manufacturing route in various disguises; the Seimans Composite Resin Infusion Manufacturing Process (SCRIMP); Resin Infusion Flexible Tooling (RIFT); Resin Injection Moulding (RIM), etc. The Resin Transfer Moulding (RTM) process is similar, but in this case the resin is pumped under pressure into a complex closed die to produce composites of a higher quality, i.e. approaching the pre-preg autoclave route. However, due to the high pressures entailed, the tooling is costly. Thus RTM is essentially only suited to large volume production. A schematic of the vacuum resin infusion process in given in figure 9.

Weight savings for a composite baseplate are shown in Table 2. For a carbon fibre composite configuration it is not unreasonable to assume that a 35% weight saving should be possible, even greater if the loading endured by the component is significantly reduced with the use of soft recoil.

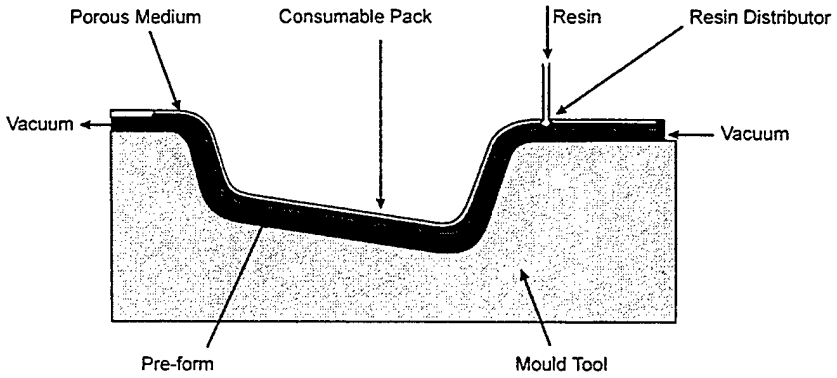

Figure 9 Resin infusion manufacturing process

Stabilisers/Trails

Composite stabilisers/trails for artillery have been addressed by a number of organisations in the past, but with little success. This is mentioned not to suggest that a composite option is not feasible, but to illustrate the complexity of the problem and that considerable attention to detail must be given if a successful design is to be achieved. History has shown that problems usually occur at joints or metallic/composite interfaces. This is a common problem to all composite structures, particularly where attachment to dissimilar materials is involved. Adhesive bonding, frequently aided by rivet / bolt fasteners to minimise peel loads and aid load transfer across the two sub-components, is the common and preferred jointing route for composite materials.

Given that these components see very substantial loads, it is unlikely that any other material other than carbon fibre will yield a satisfactory design solution.

Since stabiliser/trails are essentially beams in nature and high direct compressive loads occur as the gun is forced rewards at low elevation firings, several design solutions and thus fabrication routes can be identified. However, the simple I-beam approach can be quickly eliminated due to the need to avoid torsional instability and collapse.

The first approach is that of a comparatively simple box beam, with bulk heads/rib-stiffeners located at strategic point along the section to avoid buckling. This builds very much on aircraft technology and work currently being undertaken in the UK in support of low cost manufacture of aircraft primary parts. This work is not only addressing the design of the wings and fuselage sections, but also the associated manufacturing routes to reduce overall cost. Work on metallic bushes also forms an extensive element of this aircraft programme, which will have direct relevance to the hinged connections required for connection to the lower carriage and spades. The carbon fibre composite materials selected for aircraft primary parts can also be readily 'read across' to the trails/stabilisers. A composite stabiliser/trail leg schematic consisting of an outer skin with integral bulkheads and stiffeners is shown in Figure 10.

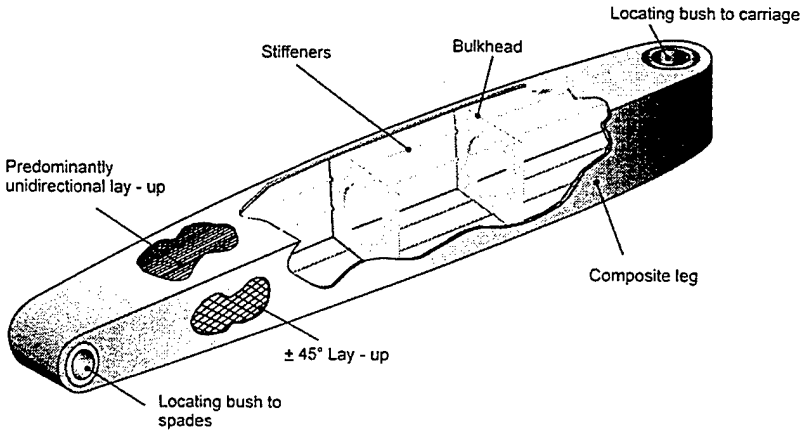

Figure 10 Composite trail/stabiliser schematic

Manufacture can be achieved via the autoclave process, with the individual components being manufactured as separate sub-components and then bonded together to produce the final component. While in principle this produces excellent structures, concerns over joint strengths will prevail. Furthermore, this approach represents a very costly manufacturing route.

Alternatively, it may be preferable to manufacture the box beam in two parts. These would be a U-shaped channel, into which the stiffeners and bulkheads are applied afterwards, followed by the application of the final face, if required.

Another approach is the manufacture of the beam skin as a single component. This can be achieved via several routes such as filament winding and resin infusion. However, the basic concept remains common to both. For this route either a rib-stiffened structure is adopted, in which case the pre-manufactured stiffeners and bulkheads will need to be held in place on a lightweight mandrel. This mandrel can be manufactured from a range of simple low cost materials, e.g. a simple thermoplastic bottle which remains in situ, through to soluble mandrels which are removed after manufacture. The mandrel also prevents sag of the composite fabric skin prior to cure.

A third approach is the use of a sandwich structure, in which a considerably thicker skin is used with a lightweight core of, for example, a lightweight polyurethane foam. Such techniques are again widely adopted in the aircraft industry. However, at this stage this option is more speculative than that of a more conventional stiffened structure and will require considerably more attention to assess its overall viability.

Given that this structure may contain a number of metallic parts, particularly for carriage/spade interfaces, weight savings could be of the order of some 30%. Further weight savings could be achieved via shorter length stabilisers due to a more favourable CofG position offered by composite overwrapped barrels. Moreover, a move to a tripod platform could also offer further weight reductions, but issues such as gun stability will need to be carefully addressed.

Carriage

Compared with the baseplate and trails/stabiliser, these are more complex in shape and design and thus represent an even greater challenge to the design engineer. Nevertheless, if a platform with a weight in the 5000-6000lb regime is to be developed the adoption of a high-specific strength carriage must be considered.

The upper and lower carriages provide the function of transmitting the recoil loads from the recoiling mass down in the trail legs and baseplate. The lower carriage may be expected to come into contact with the ground and possibly act as a baseplate, rather than have two separate components. In this respect the component requires similar properties to the baseplate described above. However, it is unlikely that any composite other than CFRP will be adequate to withstand the severe loading conditions experienced and satisfy the stiffness requirements to maintain good platform stability. However, Kevlar/epoxy composite skins could be employed to enhance overall ruggedness. The use of a thin rubber ground/carriage interface pad could again be considered to aid ruggedness.

For the upper carriage, similar structural requirements exist to the lower carriage, but with the added role of interfacing with the cradle and elevating gear. Ruggedness requirements are somewhat less than that of the lower carriage, in that ground contact will not be required.

Since the carriage will interface with the trail/stabilisers, carriage traversing gear and elevating gear, it can be assumed metallic inserts and complex joint arrangements will be required. These are likely to be high risk areas and there are few areas of work involving the application of such high dynamic loadings to composite structures that useful read across can be obtained. Furthermore, the inclusion of metallic inserts is likely to limit the overall weight reduction to approximately 20%.

Given the substantial loadings seen in the carriage, it can be assumed that in the absence of a detailed design study, a composite of extremely high quality will be required. While the resin infusion process can achieve good quality composite parts, the use of autoclaved composites may be more desirable. Metallic inserts, be they for the trail/stabiliser interface, the traversing gear or the cradle, can be built into the structure during manufacture, although very careful consideration of thermal expansion mismatch during curing/cooling will need to be addressed. This may also lead to component distortion, which again will require considerable thought.

Alternatively, the more conventional approach would be adopted whereby individual components are pre-fabricated and then connected using the techniques previously discussed.

Wheels

Composite wheels are not new, indeed several studies have concentrated on their use for weight reduction. For example the Motor Wheel Corporation designed,

manufactured and tested a composite wheel around 1982; these were manufactured from Sheet Moulding Compounds (SMCs), fitted to a road car and road tested for several million km on all terrain's including Alaska. Prototype wheels for tanks were also made in mid 1980's by ACG using pre-preg materials.

Where weight saving is of major importance, carbon fibres are used, but where the application is cost sensitive, glass fibres are used.

Most structural resin systems, e.g. epoxy, vinyl-esters, etc., are suitable for wheels operating in ambient conditions. Resin selection depends on the manufacturing process, which in turn depends on production volumes. The resin infusion process can also be considered as a viable route.

The potential weight savings depend on the application, but savings of 10 to 15% can easily be achieved, inclusive of the tyre.

Most composite wheel applications have been difficult to establish because they are a direct replacement for steel where the tooling for manufacture has already been paid for. Tooling for composite wheels is therefore considered to be an extra cost and the tooling cost for existing steel product is neglected. Composites will only be used in either new applications or where there is an imperative which is more important than the tooling cost, viz. a viz. the lightweight artillery platform.

Discussion

In this paper a review has been presented of the possible systems and advanced lightweight composite materials options which could be employed to significantly reduce the weight of towed 9000lb field guns. The principal gun components have been identified, from which potential weight savings can be considered. The results to this study are summarised in Table 3.

From this study it is clear that by using essentially conventional gun configuration concepts and available advanced composites combined with soft recoil and state-of-the-art manufacturing routes, a lightweight gun can in principle be manufactured at similar cost to an existing titanium design, but at a weight of circa 6750lb While this does not meet the long term 5000lb objective, it nevertheless yields a gun which is significantly more mobile than the current 9000lb systems. However, if a further 1750lb weight saving is to be achieved, three possible options can be identified:

- ◊ Platform configuration; to date this has assumed a 4 legged cruciform, but a move to a three legged tripod layout could be considered to reduce weight by some 300 - 400lb

- ◊ To consider the manufacture of the cradle, elevating gear and pressure bottles from composites or other composite/metallic hybrids; this would yield a further 250lb weight saving

- ◊ Shorter composite overwrapped barrel; this follows the thinking in the US of using a shorter barrel to reduce weight and may yield about a 300-400lb

weight saving.

◊ Reducing material volumes such that the materials operate at higher stress levels; the weight saving here is difficult to estimate but 400-500lb should not be seen as an unrealistic objective.

Component	% weight of gun (A)	Principle Material(s) (B)	% weight saving (C)	% weight saving of gun (A) * (C)
Trails/stabiliser	20	CFRP	30	6
Gun barrel, excl breech	35	CFRP/Steel	35	12.25
Baseplate	7	GFRP	25	1.75
Upper/lower carriage	12	CFRP	25	3
Wheels, including tyres	8	GFRP	12	1
Other	18	Mixture	15	2.7
TOTAL	**100**	-	-	**26.7**

Table 3 Summary of weight savings

These weight savings collectively approach a total system weight of approximately 5250 lbs. However, in so doing the technical risks are increased in terms of component development, particularly for the cradle. Increased concern over gun stability is also an issue. The shortened barrel will reduce range, unless more innovative shells are developed, e.g., carrier shells. UK work in this area is reported separately.

Acknowledgements

The authors acknowledge the support given by:

Mr R Selleck, Mr R Clay and Mr D Wallington of the Weapons Systems Sector, DERA Fort Halstead and Professor M Hinton, Dr D Bray and Mr C Wheatley of the Structural Materials Centre, DERA Farnborough for their valued contributions to this report.

Thermal Analysis of Lightweight Mortar Tubes
9th U.S. Army Symposium on Gun Dynamics

Larry Burton and Paul Conroy
U.S. Army Research Laboratory
Weapons and Materials Directorate
Aberdeen Proving Ground, MD 21005-5066

There is an interest in applying lightweight materials to the design of mortar barrels to facilitate the man-portability of the weapon. For this reason, aluminum and titanium alloys, and graphite-epoxy composites were considered candidates for barrel materials. A principal design consideration for a mortar tube is the thermal response to both rapid and sustained rates of fire.

The M252 81-mm mortar system was chosen as the baseline for comparison to examine the feasibility of using lightweight materials to sheath a steel liner in order reduce barrel weight while maintaining the rate-of-fire requirements. This necessitated an investigation of each lightweight material's thermal response under repetitive fire.

Modeling of lightweight mortar barrels in the 81-mm caliber was done with the interior ballistic code XKTC and the U.S. Army Research Laboratory's (ARL) XBR-2D barrel heating code. The XKTC interior ballistic code simulated the firing of the M821A1 projectile. The results from this interior ballistic model were used as input conditions for the barrel heating calculations. The barrel heating code required modifications to account for the convective heating losses due to the radiating cooling fins on the M252 design. This modified version of the code was then used to calculate barrel heating under maximum firing rates until an equilibrium temperature was attained.

INTRODUCTION

The use of lightweight materials in gun barrels has been primarily restricted to systems that function at very low operating temperatures. This implies that lightweight materials only have application on systems that do not have high, sustained rate-of-fire requirements. The principal reason for this is that materials typically undergo a reduction in their load-carrying capacity with increased temperature. This loss of strength with increasing temperature can transform a viable design under ambient conditions to one destined to fail at elevated temperatures. As far back as 40 years ago, titanium was considered for mortar applications [1]. More recently, titanium alloys have been used to lighten extended length tank cannons [2]. Graphite-reinforced epoxies (GREP) have been used to provide a 90% weight reduction in a Navy 5-inch gun as part of a demonstration of the FIREBOX concept, which used multiple lightweight barrels to maintain rate of fire but reduced the sustained rate requirement for a single barrel [3].

However, the Army has increased its emphasis on reducing the weight of weapon systems to facilitate its desire for increased mobility. In order to achieve significant weight reductions, it is necessary to introduce lightweight metal alloys and composite materials and analyze the specific application to make the most appropriate material selection.

An investigation was undertaken in an attempt to reduce the weight of the U.S. Army's 81-mm mortar system, the M252. The barrel for this system, the M253, experiences maximum operating temperatures of 550° C (1,022° F) [4].

Under such an extreme operating environment, it was necessary to do a thermal evaluation of the material candidates prior to any structural analysis of a possible design. This paper provides the results from of a thermal analysis of the 81-mm mortar system and was used as the basis for material selection for a lightweight mortar tube that exhibited a 30% weight reduction over the M252 [5].

BARREL HEATING CODE

The ARL XBR-2D heat transfer/conduction code used in this study is an extension of the Veritay XBR-2D heat transfer/conduction code [6] and consists of a 2-D axisymmetric implicit finite-difference heat conduction model. Several inputs are required for the code; the primary ones being a barrel geometry model, an interior ballistic representation that includes the propellant product gas velocity, pressure, and temperature, as well as material properties of the barrel materials to include conductivity and diffusivity. Output from the XKTC interior ballistic code [7] model of the M821A1 81-mm projectile provided the necessary inputs for the barrel heating code.

The inner boundary condition consists of forced convective heat transfer over flat plates as discussed by Conroy [8] and may be written as

$$-k\left(\frac{\partial T}{\partial r}\right)=h\left(T_{gas}-T_{wall}\right), \tag{1}$$

where k is the thermal conductivity, T_{gas} is the combustion product gas temperature, and T_{wall} is the wall temperature. The convection coefficient, h, is provided from a correlation of correlations given as

$$h=0.037\frac{\mu^*}{\chi}Re^{*0.8}\frac{C_f}{C_{fi}}C_p. \tag{2}$$

In equation (2), μ^* is the viscosity computed from a form of Sutherland's law, χ represents the equivalent flat-plate length to the axial position of interest, and C_p is the specific heat of the wall material. The Reynolds number, Re, is defined to equal $\chi\rho u/\mu^*$, where ρ is the density of the gas and u is the axial velocity of the propellant gases. The compressible to incompressible skin friction ratio is given by

$$\frac{C_f}{C_{fi}}=\left[1+(\gamma-1)^2M^2\right]^{-0.6}. \tag{3}$$

The outer boundary condition consists of both convective and radiative heat transfer and is expressed as

$$Q_w=h_{conv}\left(T_{wall}-T_\infty\right)+\sigma\varepsilon\left(T_{wall}^4-T_\infty^4\right). \tag{4}$$

In equation (4), ε is the emissivity of the wall, σ is the Boltzmann constant, and T_∞ is the temperature of the surroundings. The convection coefficient, h_{conv}, is represented by one of two models, depending on the value of the Reynolds number. For buoyant laminar flow, in air, the convection coefficient is expressed as

$$h_{conv}=1.32\left(\frac{T_{wall}-T_\infty}{D}\right)^{0.25}, \tag{5}$$

where D is the outer diameter of the barrel wall. The units are accounted for in the coefficient. For buoyant turbulent cross flow, in air, the convection coefficient is

$$h_{conv}=1.2(T_w-T_\infty)^{1/3}, \tag{6}$$

where, again, the units are accounted for in the coefficient.

Use of equations (1) - (6) allows for the modeling of a gun barrel's heat transfer at both its bore surface and outside wall. This modeling capability has been used previously to model both direct-fire tank cannons and indirect-fire howitzers, and the results matched reasonably well with the experimentally determined values [9-15]. This investigation was the first attempt at applying the code to examine thermal heating in mortar barrels.

The XBR-2D code did not account for the additional heat loss provided by the radiating cooling fins of the M252 81-mm mortar. Accounting for this required the external convection coefficient to be modified to enable incorporation of a fin augmentation factor. This was accomplished by combining the heat-transfer characteristics of an unfinned tube with a correlation for the heat transfer of an externally finned tube. The total external heat transfer may be expressed as

$$q_w = N\eta_f q_{max} + q_o \,, \tag{7}$$

where the q_o term represents the heat loss from the unfinned cylindrical barrel surface area and may be written as

$$q_o = h(T_{barrel} - T_{air})(L - Nt)*2\pi r. \tag{8}$$

The term $(L - Nt)*2\pi r$ is the unfinned surface area with N being the number of fins, L is the total barrel length, t is the fin's thickness at its base, and r is the radius from the bore centerline to the base of the fins.

The first term on the right hand side of equation (7) represents the increase in heat transfer due to the contribution of the fins, where N is the total number of fins, η_f is the fin efficiency coefficient, and q_{max} is the maximum rate that the fin can dissipate heat. The fin efficiency is a measure of the cooling fin's effectiveness in removing heat via convection to the surrounding air and is primarily a function of its surface area, its shape, and the material's thermal conductivity. The mortar fins are annular in shape, and Figure 1 shows a graph of fin efficiency that is reprinted from Incropera and DeWitt [16].

BARREL MATERIAL MODELING

The current M253 barrel is a British design and is made from a British-alloy steel. The required temperature property data for this steel was not available, so the properties from a representative U.S. gun steel, 4340, were used in modeling the all-steel barrel configuration. For the lightweight barrel configurations, it was decided to maintain the steel as the bore surface to minimize problems with propellant-induced erosion and eliminate the need to consider coatings or plating technologies. The steel liner for the lightweight barrels was kept fixed to maximize the achievable weight savings and assumed to be a hollow cylinder having a wall thickness of 0.040 in (0.102 cm). The barrel geometry is modeled by providing a bore size, the liner thickness, and an outside wall diameter. The outside wall diameter was given as the the dimension across the base of the fins. The lightweight materials considered were an aluminum alloy, a titanium alloy, and a GREP.

The GREP was chosen because of the availability of published thermal property data [20]. It is understood that the choice of different fibers, resins, and architecture lay-up could alter the thermal reponse and influence the results. However, a survey of existing composite material databases showed the properties to be representative of other GREPs and were therefore adopted. Note that there is no fin efficiency provided for the GREP design in Table 1. This is because it was felt that fabrication of such radiating cooling fins would be very difficult and, in fact, an existing lightweight design by Lockheed-Martin does not incorporate any cooling fins [21]. Thus, the composite overwrapped barrel was treated as an unfinned cylinder and equation (7) would reduce to $q_w = q_o$.

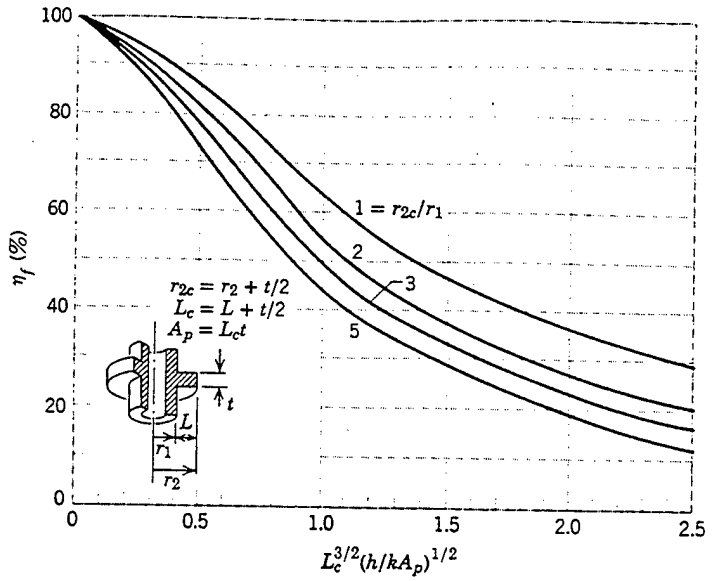

Figure 1. Estimation of Fin Efficiency

Table 1. Material Property Data

Material	Conductivity (W/m/K)	Diffusivity (m^2/s)	Fin Efficiency η_f
Steel, 4340	34.1	5.7×10^{-6}	0.89
Aluminum, 7075T6	120.0	5.2×10^{-5}	0.96
Titanium, TIMET21s	11.8	4.98×10^{-6}	0.80
Graphite-Reinforced Epoxy, Fiberite 976	0.71	5.1×10^{-7}	unfinned

The M252 is required to fire at 30 rounds per minute for the first 2 minutes with a sustained firing rate of 15 rounds per minute [22]. During this analysis, the barrel configurations were subjected to a sustained firing rate of 15 rounds per minute for a period of 11 minutes. The duration of the firing was based on the initial analysis runs that showed the weapon systems reaching an equilibrium temperature condition within that timeframe. The initial high rates of fire were not modeled in this exercise, but the barrel heating code does have the capability of modeling a varying rate of fire which would be necessary if going through a complete design iteration.

RESULTS

The M253 barrel configuration of the M252 mortar system was modeled to simulate the thermal heating that results from the launch of the M821A1 round. Figure 2 shows a plot of the outside wall temperature at five locations along the finned region of the barrel. The point of maximum heat transfer, 13.8 in (35.0 cm) from the base of the chamber, corresponds to the location of maximum barrel temperature. The maximum temperature, as predicted by the code, is 526° C (978° F) and is within 5% of the maximum operating temperature of the M252 weapon. Slight adjustments to the results could have been achieved by tweaking the fin efficiency, but it was felt that the agreement between the simulated results and experimental values [4] was satisfactory.

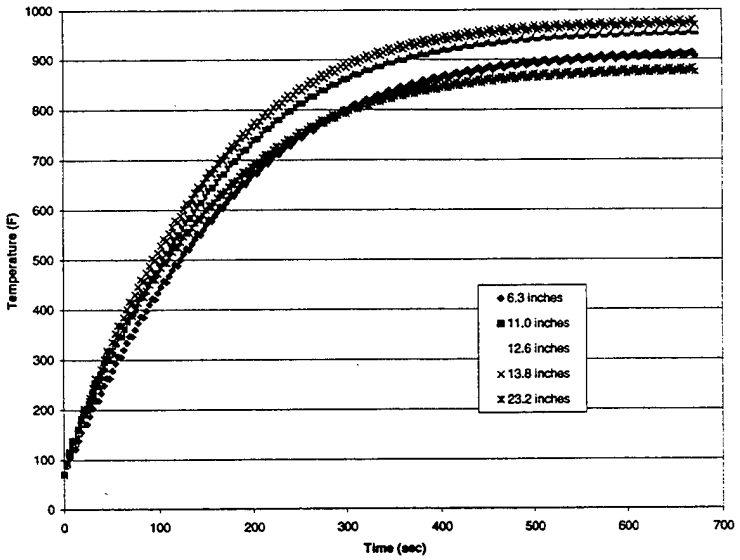

Figure 2. Outside Wall Temperature of the M252 Mortar System Barrel

Subsequent runs were made for steel-lined barrels that were sheathed with titanium- and aluminum-alloy barrels that had cooling fins. Also considered was a steel liner overwrapped with GREP, having no fins. Again, the maximum outside wall temperature occurred at the point of maximum pressure for each barrel configuration. Figure 3 provides a plot of the temperature for each barrel configuration, including the M252 all-steel design, at the same axial location, namely 13.8 in (35.0 cm) from the base of the chamber. The results of the lined barrel analysis runs were quite surprising in that they predicted temperatures well below those of the M252 configuration. The expectation was that, since both the titanium alloy and the GREP have poorer thermal conductivity than steel, they would act as insulators and cause an increase in heat to the sheathing material. Figure 3 shows that this was not the case.

Because of these surprising results, an additional material geometry was analyzed with the barrel heating code. An all-titanium-alloy barrel, having the same thermal properties as those listed in Table 1, was modeled, and the results from this calculation are also included on the plot in Figure 3. Note that the maximum temperature experienced by this design is greater than 500° C (932° F), nearly equivalent to that of the M252 barrel prediction. However, the steel-lined titanium-alloy barrel exhibits temperatures 25% less than the homogeneous titanium-alloy barrel. The through-the-thickness temperatures of the sheathed barrel configurations were examined to see if there was an appreciable increase in heat to the steel liner. While a gradient was present through the thickness, it was not excessive and it did not appear that the sheathed materials were "blocking" the heat transfer across the material interface and subsequently reducing the heat to the outside wall.

In attempting to explain the temperature reductions in the lined barrels, it was noted that the initial temperature gradient of the all-titanium barrel was steeper than any of the other cases (see Figure 3). This gradient can be explained when comparing its reponse to that of the M252 steel design. The calculations were made for the same projectile charge system and the heat flux, q_o, is assumed to be equal for each calculation. Fourier's Law expresses the heat flux as

$$q_o = -k\frac{dT}{dr} \quad . \tag{9}$$

From Table 1, the thermal conductivity, k, of steel is greater than the titanium alloy, so, for a fixed heat flux, the temperature difference, dT/dr, in the titanium must be greater than that of steel. Thus, as seen in Figure 3, the all-titanium-alloy barrel heats up more quickly than the steel design.

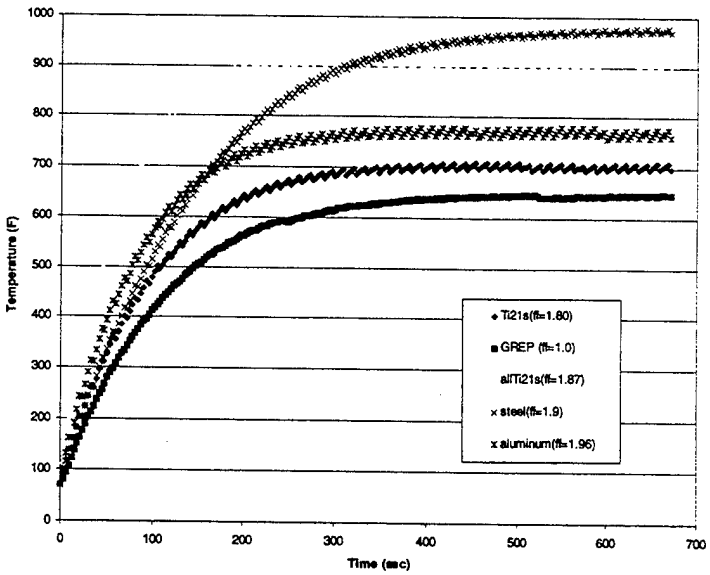

Figure 3. Comparison of Outside Wall Temperature for Different Material Configurations of an 81-mm Mortar Barrel

However, over time, the energy imparted to the bore wall equals the energy dissipated from the outer barrel surface. Again, looking at equation (9), it would be expected that, over time, the temperature gradient through the thickness of the titanium-alloy sheath would be greater than the steel as a result of their difference in thermal conductivity. This effect works to the benefit of the titanium-alloy design in that it reaches an equilibrium state much faster than the steel.

Examining the lined barrel cases, it is seen that each barrel, regardless of sheath material, tends to have an initial temperature gradient that mimics the all-steel configuration. This is not unexpected if one considers the aforementioned explanation for the initial temperature gradients and realizes that all of these designs have a steel liner. However, over time, as energy builds up in the sheathing, the heat transfer begins to reflect the characteristics of the sheathing material. Figure 3 shows that the steel-lined titanium-alloy barrel closely follows the steel barrel's temperature characteristics for 90 s before the gradient alters and begins to respond like the titanium-alloy sheathing.

This effect can best be viewed if one considers an energy balance, where, over a long period of time, the energy emparted to the bore surface will equal the energy dissipated at the outer tube wall. This energy balance may be expressed in terms of the heat flux as

$$k_{inside} \frac{dT_{inside}}{dr} = k_{outside} \frac{dT_{outside}}{dr}. \qquad (10)$$

For a homogenous barrel, the thermal conductivities are the same on each side of equation (10), and thus have equivalent temperature gradients. However, for the lined cases, the k values are not equal, and in the case of the titanium-alloy barrel, since $k_{outside} < k_{inside}$, then $dT_{outside} > dT_{inside}$. Thus, it appears that the lined barrels follow the low initial temperature gradient that corresponds to their steel liner but then adopt the response of their sheathing material that results in an overall lower equilibrium temperature.

CONCLUSIONS

As part of an effort to design a lightweight 81-mm mortar barrel, a thermal analysis of candidate lightweight materials was performed. The study used the ARL XBR-2D barrel heating code to calculate the thermal response of sheathed barrels having a steel liner. The sheating materials considered were an aluminum alloy, a titanium alloy, and a graphite-reinforced epoxy. A model of the all-steel M252 mortar system was also analyzed and served as a baseline comparitor.

The analysis results showed that the maximum operating temperatures were significantly lower that those predicted for the M252 system. This occurs because the lined barrels demonstrate an initial temperature gradient similar to that of steel, their liner material. However, over time, the sheathing material begins to dominate the heat-transfer event so that thermal equilibrium is reached more quickly and at a lower tempertature level.

All calculations for this study were made assuming the 15-rounds-per-minute sustained rate-of-fire that is a requirement of the M252 81-mm mortar. The higher initial firing rate of 30 rounds per minute was not addressed here but will need to be considered because it will likely increase the predicted maximum operating temperatures.

The ramifications of this study's findings, that lined bimaterial mortar barrels have lower maximum operating temperatures than the existing steel configuration, are that a lightweight sheath's material strength will not degrade as severely as originally anticipated because it experiences lower temperatures than expected. For instance, in the case of the Ti21s, its yield strength at 371° C (700° F) is 50% greater than at 550° C (1,022° F). This makes the lightweight candidates more viable as structural design materials for mortar barrel applications.

REFERENCES

1. Poughkeepsie, F. B. "Thermal Studies of 81-mm Titanium Mortar Barrel," DPS-405, Development and Proof Services, Ordnance Corps, Aberdeen Proving Ground, MD, December 1961.

2. Hasenbein, R., E. Hyland, G. Cunningham, April 1989, "Titanium-Jacketed Cannon Tube Program," ARCCB-TR-89009, U. S. Army Armament Research, Development and Engineering Center, Benet Laboratories, Watervliet, NY.

3. Tzeng, J. T. and P. J. Conroy, to be published. "FIREBOX Composite Gun Barrel," Draft Report, U.S. Army Research Laboratory, Aberdeen Proving Ground, MD.

4. Andrews, J., August 1991, "Final Report – Preproduction Qualification Test (PPQT) of M821E1/M889E1 81-mm High Explosive Cartridges," USACSTA-7159, U. S. Army Combat Systems Test Activity, Aberdeen Proving Ground, MD.

5. Burton, L. W., to be published, "Analysis of a Titanium-Sheathed 81-mm Mortar Barrel," Draft Report, U.S. Army Research Laboratory, Aberdeen Proving Ground, MD.

6. Crickenberger, A.B., Talley, R.L., and Tally, J.Q., April 1994, "Modifications to the XBR-2D Heat Conduction Code," ARL-CR-126, U.S. Army Research Laboratory, Aberdeen Proving Ground, MD.

7. Gough, P.S., February 1990, "The XNOVAKTC Code," BRL-CR-627, U.S. Army Research Laboratory, Aberdeen Proving Ground, MD.

8. Conroy, P. J., December 1991, "Gun Tube Heating," BRL-TR-3300, U.S. Army Ballistic Research Laboratory, Aberdeen Proving Ground, MD.

9. Bundy, M. L., P. J. Conroy, and J. L. Kennedy, "Experimental and Simulated Bore Surface Temperatures for 120-mm Ammunition," *Journal of Defense Science,* October,1996.

10. Conroy, P. J., P. Weinacht, and M. J. Nusca, October 1997, "Surface Chemistry Effects on High Performance Tank Ammunition," ARL-TR-1526, U.S. Army Research Laboratory, Aberdeen Proving Ground, MD.

11. Hollis, M. S. L., B. J. Guidos, and P. J. Conroy, August 1997, "Thermal Analysis of a Subminiature Telemetry Sensor Mounted in a Kinetic Energy Projectile Base," ARL-TR-1425, U.S. Army Research Laboratory, Aberdeen Proving Ground, MD.

12. Keller, G. E., P. J. Conroy, T. P. Coffee, and J. Barnes, June 1995, "Liquid Propellant (LP) Cookoff Considerations for the Advanced Field Artillery System (AFAS) Cannon," ARL-MR-799, U.S. Army Research Laboratory, Aberdeen Proving Ground, MD.

13. Conroy, P. J., M. L. Bundy, and J. L. Kennedy, June 1995, "Experimental and Simulated Bore Surface Temperatures for 120-mm Ammunition," ARL-TR-770, U.S. Army Research Laboratory, Aberdeen Proving Ground, MD.

14. Conroy, P. J., T. P. Coffee, and G. E. Keller, September 1994, "RLPG Chamber Heating," ARL-MR-179, U.S. Army Research Laboratory, Aberdeen Proving Ground, MD.

15. Keller, G. E., A. W. Horst, P. J. Conroy, and T. P. Coffee, May 1993, "The Influence of Propulsion Technique and Firing Rate on Thermal Management Problems in Large-Caliber Guns," ARL-TR-130, U.S. Army Research Laboratory, Aberdeen Proving Ground, MD.

16. Incropera, F. P. and D. P. DeWitt, 1981, *Fundamentals of Heat Transfer*, Wiley & Sons, New York.

17. Touloukian, Y. S., R. W. Powell, C. Y. Ho, and P. G. Klemens, 1970, *Thermophysical Properties of Matter – The TPRC Data Series, Volume 1 - Thermal Conductivity – Metallic Elements and Alloys*, Plenum Publishing Corporation, NY, NY.

18. Touloukian, Y. S., R. W. Powell, C. Y. Ho, and M. C. Nicolaou, 1973, *Thermophysical Properties of Matter – The TPRC Data Series, Volume 10 - Thermal Diffusivity – Metallic Elements and Alloys*, Plenum Publishing Corporation, NY, NY.

19. "Data on World Wide Metals and Alloys," *Alloy Digest,* 1993.

20. Tzeng, J. T. and A. C. Loos, "A Cure Analysis for Axisymmetric Composites," *Composites Manufacturing*, 1993, Vol 4, No 3, pp.157-165.

21. Hendricks, W. L., 1994, "Lightweight 120mm Mortar," Infantry Conference, Fort Benning, Ga.

22. Headquarters, Departments of the Army and the Air Force, 1990, "Mortars," FM 23-90/TO 11W2-5-13-21.

The Introduction of Spin to an Existing Flexible Shot Model within a Gun Dynamics Simulation

David N Bulman
DANBY ENGINEERING Ltd.
High Gill House, Low Row, Richmond,
North Yorkshire, DL11 6NE, UK.
Tel: +44 (0) 1748 886345 Fax: +44 (0) 1748 886014

The paper describes the enhancement of an existing gun dynamics simulation package, to introduce spin to the flexible shot model. The original one or two piece flexible shot model was based on finite element beam theory, and therefore spin needed to take into account the moments of inertia at each node. Each node is therefore treated as an independently spinning body, each with its own spinning axes which can be related to the next node so that stiffness forces between them can be calculated. The stiffness coefficients are recalculated as deformation takes place, which is particularly important with long rod penetrators because of the high accelerations involved which induce buckling moments in the rod as it bends. The relationship between the nodes and the stiffness coefficients is maintained by updating the direction cosines for each node, plus a set for the overall beam.

The final model has been validated against known rigid model cases, by increasing stiffness until flexing is reduced. Comparisons have then been made with standard whirling cases.

INTRODUCTION

The modelling of barrel and shot motion during firing is now an accepted part of gun design procedure. Analysis has been carried out on guns with bore sizes ranging from 12.5mm to 155mm, and in some cases it is known that the models have been used on a bore size as small as 6mm [1]. Comprehensive simulations now include flexible and recoiling barrels, effects of bore wear, non-linear supports, flexible cradles, rigid or flexible shots, and the supporting vehicle [1,2,3] . The rigid shot models have usually included spin and the mathematics is well understood. Originally the flexible shot models were specifically designed to analyse the long rod penetrators of 120mm APFSDS rounds. In this case spin is of less importance as in many cases they are fired from smooth bore barrels, or have slipping driving bands which keep spin to a controlled minimum.

The first non-spinning flexible shot models were based on non-spinning flexible beams [4,5]. They have been shown to give very good results with the smooth bore guns for which they were initially designed. However, even with slipping driving bands, the spin induced in a shot can be considerable and the use of non-spinning flexible shot models for these cases is not acceptable. Furthermore, gun dynamics modelling is being used more extensively with smaller calibres which include rifling, and with an increased requirement to model long rod penetrator type shots. The ability to simulate spinning flexible shots is therefore essential in a comprehensive gun dynamics simulation.

This paper describes the enhancement of an existing gun dynamics simulation package, SIMBAD [2], to introduce spin to the flexible shot model. The original one or two piece flexible shot model was based on finite element beam theory [5]. This type of model was used because of its simplicity, and its ability to produce good results with relatively few elements. It keeps simulation times short, and enables parameter studies to be made with ease. More

complex models, using 'brick' elements [6,7], can offer the possibility of providing a deeper understanding of the deformation of the shot, but require a much greater time to develop a specific model, and the run times can be very long which makes their use in parameter studies unlikely.

Most dynamic simulations which use finite element methods assume the inertia forces for a particular freedom at each node to be equal to the acceleration multiplied by the mass. This also applies to nodes with moments of inertia where the inertia torques are assumed to be equal to the angular acceleration multiplied by the moment of inertia. For elements which are only described by point masses at each node (normally brick elements with 3 degrees of freedom at each node) this assumption is valid for any general motion. For elements which are described by point masses plus moments of inertia at each node, this assumption is valid for any general motion provided that the angular velocities are small enough so that 'gyroscopic' effects can be neglected. This applies to beam models which have 6 degrees of freedom at each node relating to the three translations and three rotations.

It is for this reason that the simple dynamic analysis used with beams can not be used for the analysis of spinning flexible shots. Each node needs to be treated as an independently spinning body, each with its own spinning axes. The 'gyroscopic' inertia torques then need to be included in the analysis, and the motion of one node related to the next node so that stiffness forces between them can be calculated. This requires the stiffness coefficients to be known, and these need to be recalculated as deformation takes place. This is particularly important with long rod penetrators because of the high accelerations involved which induce buckling moments in the rod as it bends [5]. (Note: This is important will all types of elements.)

BASIC THEORY

The existing model from which the final model was constructed is based on standard finite element type theory. The shot is divided into a number of beam elements, and a stiffness matrix is produced so that:

$$[F] = [F_s] \tag{1}$$

where $[F_s] = [K][\delta]$ and may be known as the stiffness force vector.

This is the normal equation used in the finite element analysis of structures where the stiffness matrix [K] relates the displacements $[\delta]$ at the nodes to the applied forces [F] at those nodes. The displacements include the longitudinal and transverse displacements, and also the angular displacements about three fixed orthogonal axes, normally known as the global axes, $Ox_gy_gz_g$. It will be seen later that $[F_s]$ requires special treatment when the shot is spinning.

In a dynamic situation [F] is a function of time, and will be composed of externally applied forces plus inertia and damping forces. The equation will then hold true at any instant in time. Hence, let:

$$[F] = [F_t] - [M][\ddot{\delta}] - [C][\dot{\delta}] \tag{2}$$

where
- $[F_t]$ are the applied external forces which may be time dependent,
- $[M]$ are the equivalent masses and inertias of the shot at the nodes, and in this case is a column vector
- $[C]$ are the viscous damping coefficients at the nodes, a column vector
- $[\dot{\delta}]$ are the global velocities,

and
- $[\ddot{\delta}]$ are the global accelerations.

Replacing [F] by $[F_s]$ from equation (1), the 'standard' form of equation (2) can be written:

$$[M][\ddot{\delta}] + [C][\dot{\delta}] + [F_s] = [F_t] \tag{3}$$

Equation (3) represents a set of simultaneous second order differential equations. The formation of the relevant matrixes [M] and [C] is already well documented, and it is now a relatively simple matter to solve the equations for any particular combination of applied forces $[F_t]$. For a conventional gun, the forces consist of the pressure forces (normally on the base), and the reactions between the shot and the bore. For an electromagnetic gun, the pressure forces may be replaced by a distributed force along the shot which accelerates it along the bore. The reactions with the bore can be obtained by assuming a non-linear elastic interface, with or without clearance [1,2,8]. The actual solution is made by rearranging the equations so that

$$[\ddot{\delta}] = [M]^{-1}\,[F_{all}] \tag{4}$$

where $[F_{all}] = [F_t] - [C][\dot{\delta}] - [F_s]$

A modified Runge-Kutta routine is then used to solve equation (4).

These equations are satisfactory for a non-spinning shot, provided that the stiffness coefficients are recalculated during the simulation [5]. When the shot is spinning such that the gyroscopic torques are significant the term $[M][\ddot{\delta}]$ is no longer valid for the rotational degrees of freedom. Also the simple form of the stiffness force vector, $[F_s] = [K][\delta]$, will no longer be valid, and must now take into account the rotation of the shot.

First consider the changes due to the effect of the gyroscopic torques. For a single node, the linear motion in the global directions is valid and can remain, but the 'inertia' torques must be replaced by Euler's Dynamical Equations. In this case

$$Q_x = I_{xx}\,\dot{\omega}_x - (I_{yy}-I_{zz})\,\omega_y\,\omega_z \tag{5a}$$
$$Q_y = I_{yy}\,\dot{\omega}_y - (I_{zz}-I_{xx})\,\omega_x\,\omega_z \tag{5b}$$
$$Q_z = I_{zz}\,\dot{\omega}_z - (I_{xx}-I_{yy})\,\omega_x\,\omega_y \tag{5c}$$

where Q_x, Q_y, Q_z are the torques on each axis (damping, stiffness and applied),
I_{xx}, I_{yy}, I_{zz} are the principal moments of inertia about each axis,
$\dot{\omega}_x, \dot{\omega}_y, \dot{\omega}_z$ are angular accelerations about each axis,
and $\omega_x, \omega_y, \omega_z$ are angular accelerations about each axis.

All the terms in these equations refer to the inertia torques about the principal axes of the nodal mass. These will be referred to as the local axes, $Ox_ly_lz_l$, for the node, which are fixed to the node and move with the node. A transfer matrix, $[T_L]$, containing the direction cosines of the local axes, must therefore be set up to relate the local axes of the node to the global axes. Let

$$[\text{GLOBAL}] = [T_L] * [\text{LOCAL}] \tag{6}$$

Therefore, referring to equations (4) and (5), for the **rotational freedoms** of a **single node** we can write:

$$[\dot{\omega}] = [M_s]^{-1} * [\,[T_L]^{-1}\,[[F_{st}] - [C_s][\dot{\theta}] - [F_{ss}]] + [R]\,] \tag{7}$$

where $[\dot{\omega}]$ contains $\dot{\omega}_x, \dot{\omega}_y, \dot{\omega}_z$,
$[M_s]$ contains I_{xx}, I_{yy} and I_{zz}.
$[F_{st}]$ contains the associated terms from $[F_t]$,
$[C_s]$ contains the associated terms from $[C]$,
$[\dot{\theta}]$ contains the associated terms from $[\dot{\delta}]$,
$[F_{ss}]$ contains the associated terms from $[F_s]$,

and [R] contains terms $(I_{yy}-I_{zz})\,\omega_y\omega_z$, $(I_{zz}-I_{xx})\,\omega_x\omega_z$, $(I_{xx}-I_{yy})\,\omega_x\omega_y$.

Equation (7) can be written as

$$[\dot{\omega}] = [M_s]^{-1} * [F_r] \tag{8}$$

If we take $[F_{all}]$ from equation (4) and replace the components concerned with the rotational freedoms with the terms from $[F_r]$ for each node, we can write for the complete shot:

$$[\ddot{\delta}_{LG}] = [M]^{-1}\,[F_{allLG}] \tag{9}$$

where $[\ddot{\delta}_{LG}]$ contains the Local rotations and Global linear motion,
and $[F_{allLG}]$ contains the Local moments and Global linear forces.

Provided that $[F_s]$ is calculated as shown below, the solution of this can now be made in the same way as equation (4), and will give the global linear velocities and displacements, plus the local angular velocities and displacements. For each step in the solution, the step increments in angular displacements about the local axes can be used to update the transfer matrix $[T_L]$.

It is still necessary to know the global angular velocities and displacements, both to appreciate the motion of the shot, and to calculate some of the terms required in $[F_t]$. For each node, the global angular velocities can be derived directly by using equation (6). It is not possible to use the transfer matrix to convert angular displacements, but for the relatively small angular displacements expected about y_l and z_l we can show that the global angular displacement about x_g is the same as the local angular displacement about x_l. Also for the angular displacement about y_g and z_g we can use the projection of the local x_l axis onto the global x_gz_g and x_gy_g planes respectively. This gives:

angular displacement about global y = $-T_L(3,1)$ (10a)
angular displacement about global z = $T_L(2,1)$ (10b)

Hence we can update $[\delta]$ and $[\dot{\delta}]$, which are then used to obtain the relative displacements and velocities between the shot and the barrel, and hence the contact forces at the shot bands.

We must now consider the recalculation of the stiffness coefficients during the solution [2,5] and the calculation of the stiffness force vector, $[F_s]$, given in equation (1). It may be noted that the term $[K][\delta]$ referred to the global directions, but because the shot is spinning the stiffness terms in [K] refer to the spinning directions, and [K] is not valid to be used with $[\delta]$ which is in global directions.

We therefore introduce another set of axes, $Ox_sy_sz_s$, initially coincident with the global axes, but which have angular motion about the global x_g axis which is equal to the spin angle of the node at the driving band of the shot. These therefore spin with the shot, and the shot then has small displacements relative to these axes. These displacements need to be found so that the new stiffness coefficients and the stiffness forces can be calculated in these directions. We introduce another transfer matrix so that:

$$[\text{SPIN AXES}] = [T_S] * [\text{GLOBAL}] \tag{11}$$

The linear displacements at a node in the spin axes directions x_s, y_s and z_s can be given directly by the above equation. For small angular displacements about local y_l and z_l, we can show that the angular displacement about the spin axis x_s is the same as the local angular displacement about x_l minus the angular displacement of the spin axes. For the angular displacement of a node about spin axes y_s and z_s we can use the projection of the local x_l axis onto the x_sz_s and x_sy_s planes of the spin axes respectively. It can be shown that this is given by:

angular displacement about spin axes y = $-(T_{S(3,2)}.T_{L(2,1)} + T_{S(3,3)}.T_{L(3,1)})$ (12a)

angular displacement about spin axes y = $T_{S(2,2)}.T_{L(2,1)} + T_{S(2,3)}.T_{L(3,1)}$ (12b)

To calculate the new stiffness coefficients during the simulation, the y_s and z_s displacements calculated above are added to the original positions of the nodes at the start of the simulation. The stiffness coefficients are then calculated in the usual way.

The stiffness forces are calculated by taking the new stiffness matrix and multiplying it by the calculated linear and angular displacements in the spinning axes directions. The transfer matrix $[T_S]$ is then used to convert these stiffness forces to the global directions to give the term $[F_s]$ which is required in equations (4) and (7).

In practice, the actual model is specifically designed for use with a one or two piece shot. The two piece shot involves a separate sabot and penetrator, and in this case each part is simulated individually with an interaction between the two parts. This interaction assumes a circular cross-section of the penetrator and sabot at the interface, and is based on the resultant relative displacement between the two parts [8]. This was unchanged between the non-spinning and spinning models.

VALIDATION

It is very difficult to obtain good experimental data to validate the complex model of a spinning flexible shot. The only satisfactory method would be to measure the flexing of the shot as it travelled down the bore. There are great practical difficulties with this, although some work has been done for non-spinning flexible shots [6,7,9] and methods for measuring pitch and yaw for rigid shots have been developed [10,11]. However, at the time of writing no experimental data is known by the author for the complete motion of a spinning flexible shot as it travels down the barrel. A different approach was therefore taken.

The first part of the validation was to remove the pressure and band forces from the shot, and then support the shot at either end in pin-joints. This was done in the program through the 'User Defined Routines' [2]. A small bend was placed in the shot which was then spun at various speeds to encourage a whirling condition. In this case the shot was a simple thin rod, for which the natural whirling frequency could be calculated.

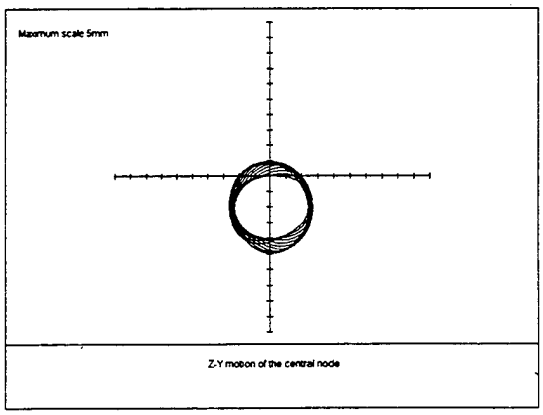

Figure 1. Spin speed 10Hz.

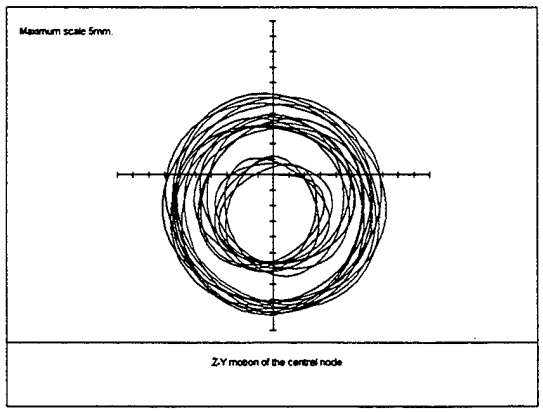

Figure 2. Spin speed 20Hz

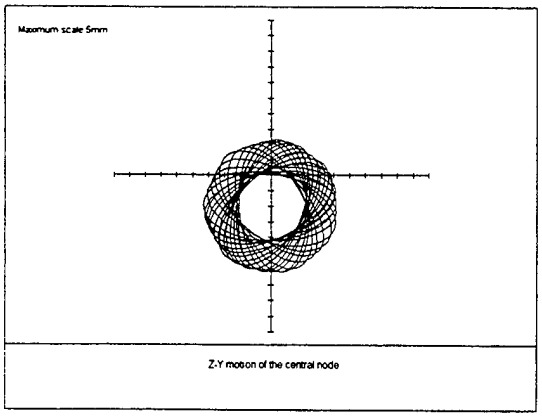

Figure 3. Spin speed 40Hz.

For each speed, the transverse displacement of the centre node was recorded and the simulation continued until steady state conditions were achieved. The amplitude of the displacement was plotted against speed, and the result compared with the theoretical whirling frequency. This was repeated for a two piece shot, in which the composite of the two pieces was equivalent to the single rod, and the interface was made very stiff. In order to keep run times to a minimum, only 10 elements were used for each part, and the thickness and the length of the rod was such as to keep the natural frequency relatively low.

The results showed that the maximum amplitude occurred at the expected natural whirling frequency. Figures 1 to 3 show the motion of the centre node in a plane at right angles to the spin axis from the start of the simulation up to a time of 1 second. It may be noted that the zero point on the plot is the starting point of the node, which was 1mm above the spin axis. It can clearly be seen that at the natural frequency of 20Hz the amplitude was increasing rapidly. The reason why the motion is not symmetrical is that at the start of the simulation the transverse velocity of the node was given a value equal to the spin speed multiplied by the offset. This starting condition is similar to what would occur to a node if the rod was already spinning, but it does not include the centripetal acceleration and the corresponding deflection of the rod. However this starting condition enabled the final steady condition to be reached quicker than if the nodes had initially been stationary.

The result gave confidence in the ability of the program to simulate a spinning flexible rod, but more evidence was required to confirm that the gyroscopic torques were included correctly, and that the complex pressure forces and shot band forces were being simulated. This was done by comparison with a well validated spinning rigid shot.

A model of an actual shot was composed using both the rigid shot simulation and a two piece flexible shot simulation. Each shot therefore had the same total mass, inertias, position of the centre of gravity, and contact geometry with the bore. Each shot had the same band geometry and elastic properties, including clearance on the front band. They were subjected to the same pressure forces, and each included a slightly angled driving band. The longitudinal principal axis of the shot was also offset slightly from the centre of the driving and centring bands. In practice, if no flexing occurs, these two models should give the same results. Simulations were therefore made, and repeated with the modulus of elasticity increased progressively to a factor of 100. Various parts of the results were examined, including the bending of the flexible shot.

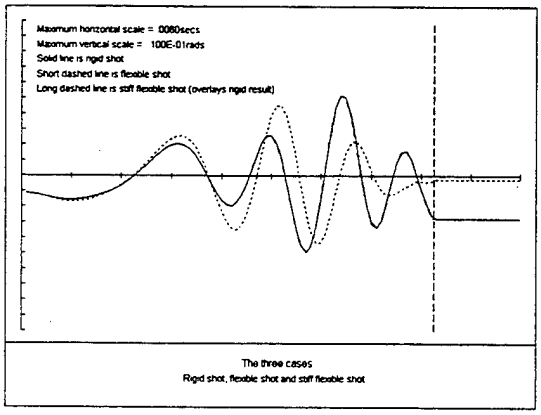

Figure 4. Shot pitch angle.

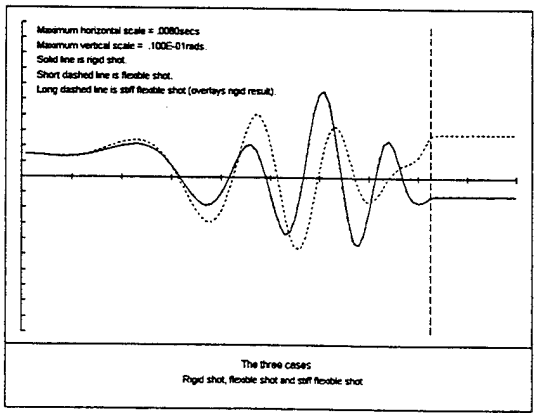

Figure 5. Shot yaw angle.

Figures 4 and 5 each show three results for the shot pitch and yaw. The first is for the rigid shot, the second is for the flexible shot with the modulus of elasticity increased by a factor 100, and the third is for the flexible shot with the correct modulus of elasticity. The first and second results overlay each other. This showed clearly that, on the flexible shot, the additional gyroscopic effects, plus the band forces and the pressure forces, were being simulated correctly. It should also be noted that to achieve such a good match the stiffness coefficients were recalculated at every time step.

As a further point of validation, the actual bend in the shot was about 1mm at shot exit. This compares with measured values of similar shots taken from photographs just after shot exit.

THE SIGNIFICANCE OF SPIN AND FLEXIBILITY

In previous work with long thin spinning projectiles, such a APFSDS, the shot has been simulated by either a non-spinning flexible model, or a rigid spinning model. The importance of including the dynamics of a spinning projectile is already well known, but it can now be seen that the omission of the bending of the shot can give significant errors in the final predictions of shot launch.

In order to compare results between the rigid and flexible shot simulations, definitions for the flexible shot of bounce and bounce velocity in both y_g and z_g directions, pitch and yaw angles, and pitch and yaw velocities, need to be considered.

The shot bounce in each direction, at each point in time, is defined as the position of the centre of gravity of the shot taking into account the deflected shape of the round. This is found by taking the moments of the mass at each node about the y_g or z_g axes. They are summed, and the result divided by the total shot mass.

The bounce velocities are found by calculating the linear momentum of the mass at each node in the directions y_g and z_g. These are summed for each direction, and the results divided by the total shot mass to give the bounce velocities of the complete shot.

The shot pitch and yaw are calculated by making a straight line least squares fit of the nodal positions. The angle of this line then gives the pitch and yaw values.

The pitch and yaw velocities are found by calculating the total angular momentum about the z_g and y_g axes respectively. These are then divided by the shot inertias about the relevant axes.

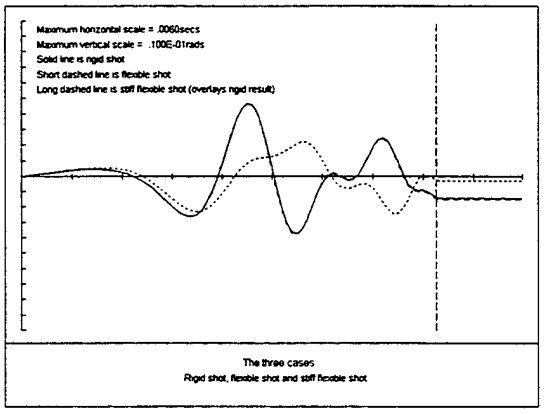

Figure 6. Shot vertical bounce velocity.

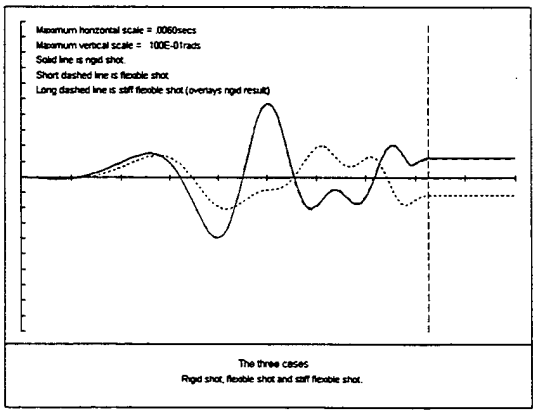

Figure 7. Shot horizontal bounce velocity.

Using the shot described above, which was simulated with the flexible and rigid models, Figures 4 and 5 show the shot pitch and yaw, and Figures 6 and 7 show the shot bounce velocities. It may be noted that Figures 6 and 7 also show the result of the flexible shot with the modulus of elasticity increased by a factor 100, but this overlays the rigid shot result as described above. It may also be noted that a straight barrel was used in the simulation. The important point shown in these figures is that the results of the flexible shot (with the correct modulus of elasticity) are very different from the rigid shot results. This shows that the inclusion of the flexibility of the shot may have an important effect on the overall dynamics and launch characteristics.

CONCLUSIONS

Spin has successfully been incorporated into the simulation of a flexible shot. The results show that the model can simulate shaft whirl, and that the gyroscopic forces, pressure forces and band forces are simulated correctly.

Comparisons between a spinning rigid shot model and the spinning flexible shot model show that the flexibility can have a significant effect on the overall dynamics of the shot, and hence the launch characteristics.

REFERENCES

1. D. N. Bulman. Simulation of Gun Dynamics to Improve Accuracy and Consistency. 15th International Symposium on Ballistics, Israel, 21-24 May 1995.
2. SIMBAD (Simulation of Barrel Dynamics) User Manual (June 1998), Danby Engineering Ltd, High Gill House, Low Row, Richmond, N. Yorks, DL11 6NE, UK. Tel/Fax +44 (0) 1 748 886345/886014.
3. SIMVED (Simulation of Vehicle Dynamics) User Manual (July 1998), Danby Engineering Ltd, High Gill House, Low Row, Richmond, N. Yorks, DL11 6NE, UK. Tel/Fax +44 (0) 1 748 886345/886014..
4. T. F. Erline. Dynamic Analysis of a Puller Sabot Concept. 7th US Symposium on Gun Dynamics, Newport, Rhode Island, 11-13 May 1993.
5. D. N. Bulman. The In-bore Bending Dynamics of Long Rod Projectiles. 13th International Symposium on Ballistics, Stockholm, 1-3 June 1992.
6. S Wilkerson, D. A. Hopkins, B Held. Techniques for Modeling Bullet Exit Conditions Predicted by Transient Finite Element Models. 8th US Symposium on Gun Dynamics, Newport, Rhode Island, 14-16 May 1996.
7. D. A Rabern, K. A. Bannester. Finite Elements Models to Predict the Structural Response of 120mm Sabot/Rods During Launch. 6th. US Army Symposium on Gun Dynamics, Tamiment, Pennsylvania, 15-17 May 1990.
8. D. N. Bulman. A comparison of theoretical jump for rifled and non rifled barrels. 5th US Army Symposium on Gun Dynamics, Rensselaerville NY, 23-25 Sept 87.
9. D. N. Bulman, J. B. Hoyle. An experimental Validation of the SIMBAD Gun Dynamics simulation Package for Flexble Saboted Long Rod Projectiles. 7th US Symposium on Gun Dynamics, Newport, Rhode Island, 11-13 May 1993.
10. G. Barker. An Experimental Investigation into In-bore Yaw in a Rifled Barrel using the RMCS Air Powered Gun. 5th. US Army Symposium on Gun Dynamics, Rensselaerville, NY. 23-25 September 1987.
11. P.W.Fuller. Measurement of Yaw In-bore. 5th International Symposium on Ballistics. Toulouse, 1980.

BIOGRAPHY

Professor Bulman was Professor of Dynamics and Head of Land Systems at the Royal Military College of Science, UK until March 1997. He now works full time developing programs for special dynamic problems, mainly in the defence industry. He has worked in the field of Gun Dynamics since 1976, and also Vehicle Dynamics since 1973. He has lectured extensively in these subjects, and been involved in large research contracts to produce and validate codes for Gun Dynamics Analysis. He is the principal author of the commercial code SIMBAD, which is in use in 14 countries throughout the world. He has also produced codes for vehicle ride and motion analysis, including special codes for active suspension systems.

SIMULATION OF SHOT IMPACTS FOR THE M1A1 TANK GUN

RONALD GAST, STEVEN MORRIS,
Benet Laboratories Watervliet Arsenal, Watervliet NY 12189
MARK COSTELLO
Oregon State University, Corvallis OR 97331

ABSTRACT

Never has the need for simulation in design of components been more acute. Today's business environment requires innovative thinking in product development, especially for the 'big ticket' ordnance items such as main battle tanks and armament. The manufacturing cost of these items and related components prohibits the use of the classical method of product development which includes initial design, prototype manufacture, system testing and redesign. The answer lies in the use of virtual performance simulation to assess a system's response before any hardware is manufactured. Up front costs are greatly reduced since the system components reside in virtual space allowing for rapid electronic design changes and optimization by simulation rather than iterative testing of costly hardware.

One must not be overly enamored by the power and function of the simulation tools. They are just mathematical models written by mere mortals, the execution of which closely mimic nature but do not actually reproduce it. Ultimately, these simulations need to be validated before one becomes comfortable in their use. There are various ways to validate a simulation code. First, one may use dedicated and controlled tests void of extraneous noise to establish relational characteristics among a few test variables. The results may then be directly compared to simulations and validation is achieved when the output closely matches the test data. The second method involves comparing simulated results to inherently noisy field generated test data. The best one may expect to achieve from this type of validation is trends in the responses relative to variations in the system parameters.

It is the purpose of this report to validate a coupled simulation package for the accuracy assessment of large caliber weapons. The simulation packages include SIMBAD a finite element gun dynamics code and BOOM a projectile flight dynamics code. These two models have been coupled such that the output of SIMBAD is the input to BOOM. Simulated results will be compared to field generated accuracy firings for M1A1 tank thus method two validation will be used to assess the worth of this endeavor.

INTRODUCTION

Never has the need for simulation in design of systems been more acute. Today's financial/philosophical environment requires innovative thinking in the business of product development, especially for the 'big ticket' ordnance items such as main battle tanks and armament. The manufacturing cost of these items and related components prohibits the use of the classical method of product development. This method which is an iterative process includes initial design, prototype manufacture, system testing and redesign. As a result considerable time and money is invested for manufacturing and testing of prototype components. We need to rethink the use of this loop if we are to remain competitive and reduce the cost of development. The answer lies in the use of a new class of electronic computational product development functions, namely; virtual performance simulation (VPS), validation by component testing (VCT), and scale model manufacture by stereo lithographic fabrication (STL). By using these methods, prototype manufacture and physical testing phases are minimized and replaced by STL and VPS. Costs are greatly reduced since the system components reside in virtual space allowing for rapid electronic design changes and performance ratings by simulation rather than physical testing. In the end hardware must eventually be manufactured and tested, however, this may be done after a

considerable number of 'excursions' through VPS and STL.

At the heart of VPS resides various modeling and simulation programs some which are legacy codes developed by system designers others are commercial codes which may have been modified for specific uses. In any event all are used for design evaluation. Ultimately, these models and simulations need validation to achieve a level of comfort in their use. There are various ways to validate a simulation code. First, one may use dedicated and controlled tests void of extraneous noise to establish relational characteristics among a few test variables. The results may then be compared to simulations produced using the same range of independent (design) variables and validation is achieved when the output response of the two (test and model) nearly produce the same results. The second method involves the use of field generated data to compare with results of simulations. The field data may contain extraneous 'noise' as well as unknown or unmeasurable system features which affect the system's response. The best one may expect to achieve from this type of validation is trends in the responses relative to variations in the system parameters. This is a type differential analysis and is more prevalent for modeling full operational systems such as fielded ordnance weapons. As the controllable design variables are changed, results yield response trends rather than accurate reproduction of the system's performance.

It is the purpose of this report to validate a coupled simulation package for accuracy assessment of a fielded tank weapon, namely, the M1A1 tank and its main armament the M256 120mm cannon. Since the data to be used has been generated during field firings of the weapon, the second method of validation applies. The importance of simulating the accuracy of this weapon lies in the current trend of establishing gun jump corrections factors. The 'fleet zero' method is used and basically corrections for entire fleet are determined by firing accuracy tests using only a few tanks and gun tubes. Refiring the tank after each retubing is considered too costly and has been abandoned. However, test results for this system reveal that shotfall patterns are strongly a function of the individual gun tubes. Every gun tube that has been manufactured has its own signature regarding its dynamic response during firing and more importantly the impartation of the projectile kinematic state upon exit from the muzzle. To confirm this, factual evidence will be developed later in this report. It seems reasonable that if accurate simulations of gun accuracy could predict the shotfall patterns of individual gun tubes, then jump correction adjustments could be applied to the 'fleet zero' correction. This should be the ultimate goal of all gun dynamic studies.

DYNAMIC INDEXING OF GUN TUBES AND TEST RESULTS

The M256 Cannon has characteristics which cause transverse gun vibrations during firing. One of these is due to the offset breech (about 1.25 inch below centerline of bore). As the gun recoils, this offset mass produces an inertia couple which transmits a vibration wave along the tube's axis overtaking the projectile and disturbing the muzzle before shot exit. Also, as the projectile travels along the bore, interactive loads develop between tube and projectile causing additional vibrations of both. Upon exit the intended direction of the round has been compromised. The effect could be mitigated as ARL suggests [1] by specifying a characteristic bore profile which minimize the vibratory nature of projectile/tube/offset mass interaction. Based upon dynamic analysis, a tube possessing this 'optimum' profile would vibrate in such an manner as to provide a relatively straight path (in a global sense) for the projectile to follow. This would minimize side loadings and projectile cross-axis deflections rendering a benign entrance into free flight void of any asymmetric kinematic excitations. The profile which minimizes this side loading was termed the 'optimum profile'. The method of implementing this feature is called dynamic indexing of the tube (DIT).

Characteristics of the DIT Profile

The 'optimum profile' is dependent upon both projectile and charge temperature; the HEAT round has its own 'optimum profile' as well as another for the KE round. Since the KE round is considered critical the 'optimum profile' is assumed to mean optimum for the KE round. The profile has the following characteristics. In the vertical plane the 'optimum profile' resembles a sine wave having a wavelength about 25% greater than the tube length and a magnitude of about 0.015 inches (in). In the horizontal plane the optimum profile is a negative sine wave of a wavelength equal to the tube length and a magnitude of about 0.002 in. It was not suggested that tubes be manufactured to this profile but rather orient their top vertical centerlines such that the bore profiles (horizontal & vertical) best matched the optimums. A least squares technique and a computer algorithm was incorporated into the manufacturing process. Normally, the standard method of tube indexing (STD) is to orient the top vertical centerline of the gun such that the plane of greatest bending

is vertical and the tube's muzzle points up. This method tends to minimize curvature due to normal gravity droop when cannon is mounted in its vehicle.

Conduction of the Dynamic Indexed Tube Test

In attempt to verify the DIT claim, an extensive test was performed during the early 1990s [2]. A considerable number of new M256 gun tubes were specifically manufactured for the test. Of these a number were dynamically indexed whereas the rest were indexed according to the standard method. The cannons were mounted on M1A1 vehicles and accuracy tests performed. Both HEAT and KE rounds conditioned to various temperatures were used in the test. Each tube fired three (3) rounds using each round type and condition temperature. The centers of impact (COI) and target impact dispersion (TID) were the primary data reported. The reference report contains all the data.

For the study to be reported herein, a portion of the unclassified data will be used. The goal is not to verify dynamic indexing but rather an attempt to validate a dynamic, kinematic and accuracy simulation of the M1A1 fielded weapon's system for a representative sample of M256 gun tubes. It is felt that the profile characteristic of each tube (either indexed to the optimum or standard method) has an effect upon the projectile's 'ride' down the bore and its subsequent jump upon disengagement. One round type conditioned to ambient temperature was chosen for the modelling. Rounds of this type were fired through ten (10) gun tubes. Five (5) were dynamically indexed (DIT) whereas the remaining were of standard index (STD). Profile data was received from Watervliet Arsenal's Quality Assurance Branch and used to establish the 'best' polynomial fit for each tube. The fitting process will be explained later in this report.

Results of the Dynamic Indexed Tube Test

On figure 1 the average COI values for the ten tubes are presented. On the chart the inverted triangular symbols refer to the DIT tubes while the upright triangular symbols refer to the STD tubes. With the exception of one flier for the DIT group the remaining four responses seem to reside in close proximity on the plot, whereas the five from the STD group reside at a different location. The basic idea of dynamic indexing is to reduce the tube to tube variation in impact location and dispersion. But as is concluded in the report [2] neither has the dispersion been significantly reduced nor has the impact location remained constant. However, as the COI data indicates, the DIT tubes brought the impact points closer to the point of aim which is at the crosshairs. Additionally, the DIT tubes were not manufactured to the 'optimum profile' rather the tubes' natural profile was best aligned to the optimum. (There is also some controversy as to the processing sequence after the index plane was found.)

The idea of dynamic indexing versus standard indexing, profile samples, and partial results of a DIT test have been presented in this section. In the next section the gun dynamics and exterior flight simulation models will be discussed and relevant data pertaining to their use will be developed.

DESCRIPTION OF ANALYSIS MODELS

Two analytical computer codes have been used to determine the trajectory of a projectile's flight path, namely; SIMBAD for in bore dynamics and BOOM for free external flight to the target.

Simulation of Barrel Dynamics (SIMBAD) Gun Vibration Model

Dr. David Bulman developed the SIMBAD model in Great Britain while he was a faculty member at the Royal Military College of Science. It is a quick running finite element code, which employs beam elements for the gun tube and a variety of options for modeling the projectile, mount and cradle. It was recently purchased by Benet (in source code form) and has been used exclusively for gun dynamics modeling. Dr. Bulman has continually added functionality to the code enhancing Benet Lab's capability to perform gun dynamics studies for experimental purposes or within the design loop of a gun development program.

The gun tube is defined using either the Euler-Bernoulli or Timoshenko formulation. The projectile and sabot may have its own finite element representation or simply a solid shot coupled to the tube through elastic driving bands. The mount and cradle may also be modeled in finite elements or represented simply using a lumped spring and mass. A direct fixed

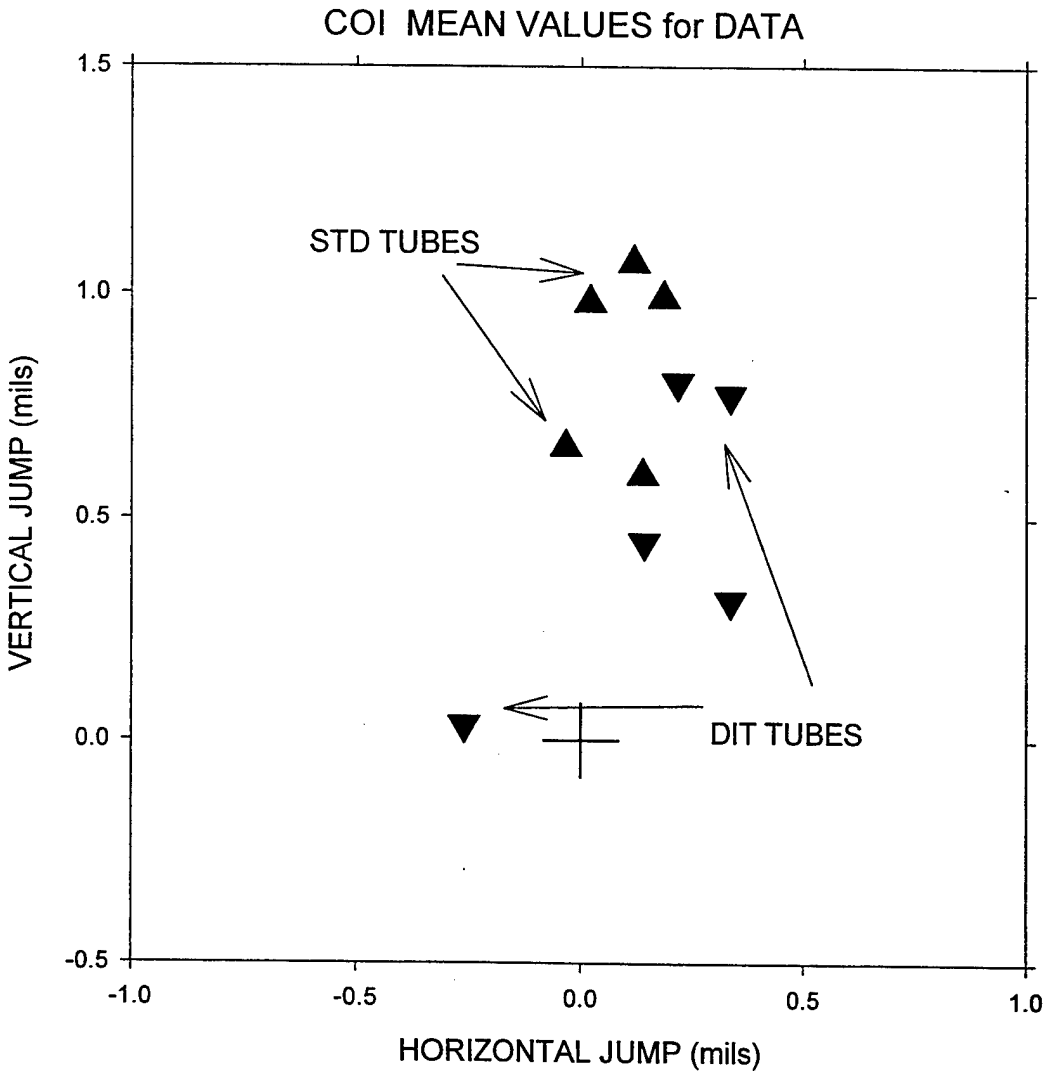

Figure 1 Average Centers of Impact for Select Tubes in DIT Test

time step integration method is employed to solve the system of differential equations. A partial list of SIMBAD applications are:

- Evaluation of optimum dimensions for a gun tube to improve accuracy;
- Examination of the effect of offset masses on weapon performance;
- Examination of the effect that gun mounting parameters have on accuracy, specifically:
  - > wheelbase and clearance;
  - > trunnion position with respect to gun center of gravity;
  - > recoil brake and recuperator location and performance;
- Analysis of the effect that tube straightness has upon accuracy;
- Determination of the effect of that dimensional tolerance of the round has upon accuracy;

The program runs either interactively or through batch files of user defined inputs. For the study conducted herein the tube will be defined using a 40 element Euler beam model and 41 nodes. The centerline profiles for the ten gun tubes used in this study have been determined using statistical methods to be described in the next section. The mount is simulated using non-linear elastic supports to the cradle, which is considered ground. The projectile and sabot are both modeled using 7 finite elements with an additional mass for the penetrator's tail fin. The sabot and gun tube are coupled at two points through linear stiffness elements using data from a static test performed in the early 1990's. A simplified sabot decompression model developed at Benet Labs further perturbs the projectile's exit kinematics. It is based upon conservation of energy, in which the asymmetric compression of the penetrator / sabot interface is converted to transverse rotational energy imparted to the penetrator, thus modifying the pitch and yaw rates at exit. This level of detail is considered sufficient for our needs.

BOOM - A 6 Degree of Freedom Exterior Ballistics Code

Dr. Mark Costello developed the BOOM code while he was a faculty member at the US Military Academy. It is a rigid body dynamics / kinematics computer code used to predict the external flight path of ordnance projectiles. Benet Labs acquired the source code from the author in 1996. Dr. Costello has transferred to Oregon State University in early 1998, however, he continues to upgrade the code increasing its functionality and performance. Validation studies using full scale gun systems have been performed at the Army Research Lab and Aberbeen Proving Ground.

The projectile is described with six rigid body degrees of freedom comprised of three body inertial position coordinates as well as three Euler angle body attitudes. Body frame coordinate system is defined with respect to the earth's inertial reference frame. The dynamics equations are written in body frame coordinates. Dynamics and kinematics values may be expressed in either coordinate system through a series of matrix transform equations, which transfer values from one system to the other. The projectile's inertia matrix may be fully populated (i.e. 9 values) if the center of mass is offset from it's geometric center. Externally applied forces and moments due to aerodynamic lift, drag, and gravity drive the projectile along its flight path. The aerodynamic coefficients are geometry specific and obtained empirically through flight test experiments.

Integration of SIMBAD and BOOM

An interface routine employing matrix equations was developed in which projectile kinematic values from SIMBAD exit conditions were transferred into the coordinate system used in BOOM. It proved to be a bit of a challenge since the author's of both codes resided on different continents. However, it was eventually accomplished thus assuring seamless passing of data from SIMBAD to BOOM.

For the studies conducted in this program the projectile was completely balanced and the atmospheric condition was standard with no wind. Reiterating, our studies are to be of a comparative nature, therefore, much of the code's functionality was not needed.

CONDUCTION OF THE ANALYSIS

The ultimate goal of this study is to decide if the coupling of two simulation codes for predicting in bore gun dynamics and the projectile's flight trajectory is reliable for predicting shot impact location. The means by which this may be established is to model the test conditions of the individual shots and compare the predicted shot impact locations with the test results. To accomplish this the values of many system parameters are required as input to the models. With the exception of the relevant dimensions of the gun tubes used in the test many of remaining parameters were neither measured nor recorded. To deal with this problem, parametric methods of analysis will be used. Nominal values for those unknown parameters considered to be important will be selected and incremented within a reasonable range with simulations being conducted for every combination of parameters. Thus a distribution of shot impact locations for a given gun tube will be generated. Computed and test results can then be compared on the basis of both mean value and standard deviation. In the following paragraphs the relevant system parameters and the rationale for the selection of their range of values will be discussed.

Bore Centerline Profile Estimation

It is a well known fact that the condition of the gun tube's centerline profile affects the in bore vibrational response of both the tube and round [3], as well as the mean impact location and dispersion of the shots fired during an accuracy test [2]. Therefore, in a modeling sense an accurate method of determining the 'correct' bore profile is important. Theoretically speaking it is not the bore profile that is important but rather the curvature of the path (i.e. 2nd derivative of profile) that the projectile must traverse as it progresses downbore. The analytical effect of this has been pointed out by this author and several others [4,5]. The gun tubes used in this test were inspected by Watervliet Arsenal personnel using normal production inspection methods. Bore profile measurements were taken using the mechanical procedure in place at that time (circa 1989). The inspection interval along the tube was approximately 0.75 feet for a total of 23 measurement stations. Profile measurements were subject to an error of approximately 0.00118 inch due to the nature of the measurement system.

The goal is to use this data for the generation of a representative 'smooth' profile which possesses the necessary curvature information to best calculate the interactive forces between the accelerating projectile and gun tube. The means of achieving this is to generate a polynomial fit of the data using a least squares technique. For analysis purposes, the profile is approximated using the functional fit which employs a spacing interval that is much finer than that of the raw data. This 'data' is stored in a tabular file which is used by SIMBAD to set the initial locations of the structure's nodes prior to executing in-bore gun dynamics calculations.

The statistical problem becomes one of deciding what order of polynomial to use for representing the data. Figure 2 contains a schematic of the rationale involved in the fitting process. Shown on this figure are generic measurement data, error bars and the types of fit which may be applied. On the uppermost graph the data with error bars and a high order polynomial fit is represented. In this fit the functional polynomial is made to pass through each reported data point. Since the data contains measurement errors at each station this fit is overly restrictive in that we assume that each point is truly representative of the actual condition of the profile. Conversely, on the middle graph the opposite is true. The fit here is too loose in that most of the function values fall outside of the error bar range. The bottom graph shows a fit that is appropriate for the data and errors shown. The fitted function falls within the error bars, however, it does not pass through each point but rather meanders within error bars sometimes above and sometimes below the measured values.

The statistical method used to determine the proper order of the polynomial fit (selected from Borse [6]) involves computing the Chi-squared statistic as shown on figure 3. The Chi-squared statistic is the summation over all data points of the ratio of the difference between the measured and calculated values squared divided by the square of the measurement error. This resulting summation is compared with the degrees of freedom (dof) used for analysis. This is difference between the number of data points and fit parameters (i.e. one more than the order of fit). If the statistic is much larger than the dof a poor fit results. If much less than the fit is too constrained. The statistic and dof must be nearly the same for the fit to be suitable.

A straightforward method for determining the polynomial order does not exist, rather an iterative process must be employed as follows. Assume an order for the polynomial, generate the fit using least squares, calculate the Chi-squared

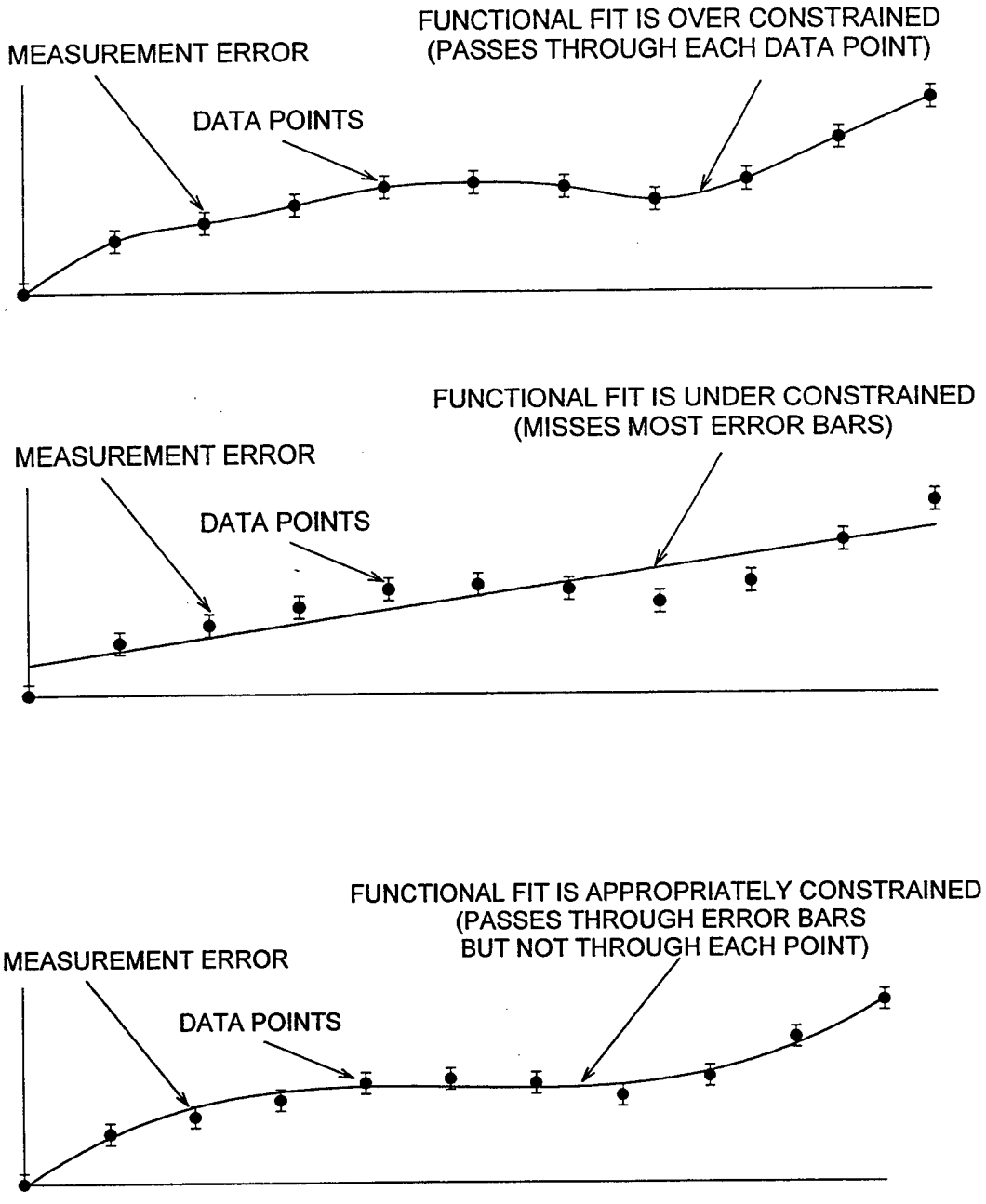

Figure 2. Curve Fitting Process for Data Possessing Errors in Measurement

$$\chi^2 = \sum_{i=1}^{N} \frac{[y(x_i) - y_i]^2}{[\Delta y_i]^2}$$

$$\chi^2 = \begin{array}{l} \gg (N - g) \rightarrow \textit{poor fit} \\ \approx (N - g) \rightarrow \textit{adequate fit} \\ \ll (N - g) \rightarrow \textit{constrained fit} \end{array}$$

N = Number of data points
g = Number of fit parameters

Figure 3. Chi-square Method for Fitting Data with Measurement Error

statistic, and compare with the dof. This process continues until the fit criteria is achieved. This method was used for generating the profile for each gun tube in the analysis. The profile data, calculated fit and curvature derived from the second derivative of the fit for all ten tubes is shown on figures 4a to 4j for the vertical plane and on figures 5a to 5j for the horizontal plane.

On figures 4a to 4e, the vertical profile data, functional fits and curvatures as well as the orders of fit for the 5 DIT tubes are shown. The profile characteristics are quite similar. All 5 tubes tend to point down at the muzzle. Tube #4098 has the greatest deviation of 0.020 inches occurring over the last 50 inches of travel. Tube #4104 has the same amount of deviation, however, it is spread over 100 inches of travel. The remaining 3 tubes have deviations of lesser magnitude. The order of fit specified on the graphs represents the order of the approximating polynomial used to represent the data. For the DIT tubes the curvature in the vertical plane tends to decrease towards the muzzle. The magnitudes near the muzzle, however, are somewhat different. For tube #4098 the value is $-40x10^{-6}$ [1/inch], whereas for #4106 muzzle curvature is only $10x10^{-6}$[1/inch]. The muzzle curvature for the remaining three tubes fall between these values.

The vertical profile data, functional fits, and curvature for the five STD tubes are shown on figures 4f to 4j. These are similar in that the muzzle end of each points up. Tube #4992 has the greatest profile deviation of -0.024 inches which occurs over the last 60 inches of travel. The orders of fit range from 3 to 5. Curvature values are somewhat unique. For tubes #4988 and #4996 curvature tends to begin at $-40x10^{-6}$ [1/inch], grow to slightly above 0, and finally end up at 0 to $-5x10^{-6}$ [1/inch] at the muzzle. Tube #4990 has a curvature which is nearly a mirror image of the tubes #4988 and #4996, whereas the curvature for tubes #4992 and #4994 are very close to 0 for the entire length.

Profile data, fits and curvature values in the horizontal plane for the DIT tubes are shown on figures 5a to 5e. As indicated on the plots the orders of fit range from 2 to 5. Tubes #4100 and #4106 possess the greatest deviation of around 0.012 inches midpoint along the tube. Tube #4104 is nearly straight. Curvature signatures have no similarity. Tube #4104 has nearly 0 curvature, whereas tube #4106 has a curvature signature which bows down and achieves a value of $40x10^{-6}$ [1/inch] at the muzzle. The curvature for tube #4098 is nearly a mirror image of that of #4106. Curvatures for the remaining tubes in this group are within these bounds.

For the STD tubes, the horizontal profile data, fits, and curvatures are shown on figures 5f to 5j. Due to the indexing technique used for these tubes, the horizontal plane possesses nearly zero profile deviation. Hence, all tubes with the exception of #4990 contain curvature responses of less than $10x10^{-6}$ [1/inch]. The curvature response for #4990 begins at $-40x10^{-6}$[1/inch] increases to 0 for about 75 inches and then increases to $20x10^{-6}$[1/inch] at the muzzle. It is anticipated that very little projectile/tube interaction will occur for these tubes.

Projectile Specifications

Kinetic energy trainer rounds were used in this test, a schematic of which is shown on figure 6. It is a multiple piece construction employing a three petal aluminum sabot, aluminum tail fin and low alloy steel penetrator. The nominal dimensions on the round's engineering drawings were consulted to generate the finite element analysis (fea) model for both components. Even though the sabot is flexible, SIMBAD needs explicit specifications for the force/penetration data at the contacting surfaces between sabot bore riders and tube inner diameter at both the front and rear contact points. Lyon [7] conducted stiffness tests for this round and has provided experimental data for both locations. As indicated in his report, the stiffness is non-linear for both areas. The material resistance is small during initial sabot deflection then gradually increases as deflection becomes greater. This, of course is quite understandable since the interaction between the sabot and tube is like a Hertzian contact situation. Resistance is light during initial penetration and builds rapidly thereafter. A second characteristic of this round is that due to its construction (three symmetrical petals of 120° included angle) the assembly stiffness is a function of the location around the sabot's periphery. For example, if the projectile is oriented such that the load is applied to the circumferential center of a petal, its stiffness is different than if the load were applied at the joint between two petals. The stiffness range around the periphery has a 15% variation from the maximum stiffness value.

Gun Mount Specifications

The most elusive modeling parameter in this gun system are the clearances and stiffness between the recoiling cannon

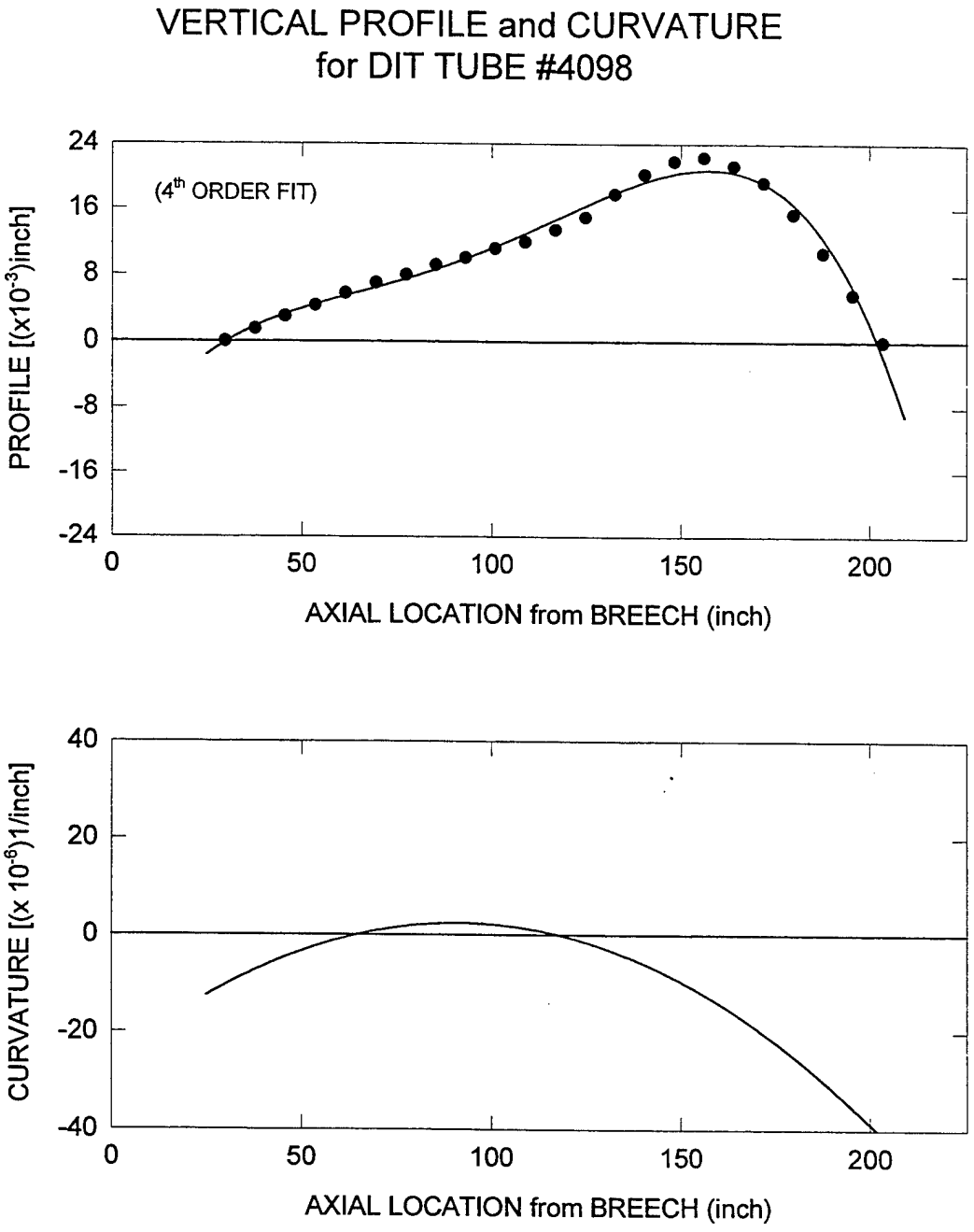

Figure 4a. Vertical Profile and Curvature for Tube # 4098

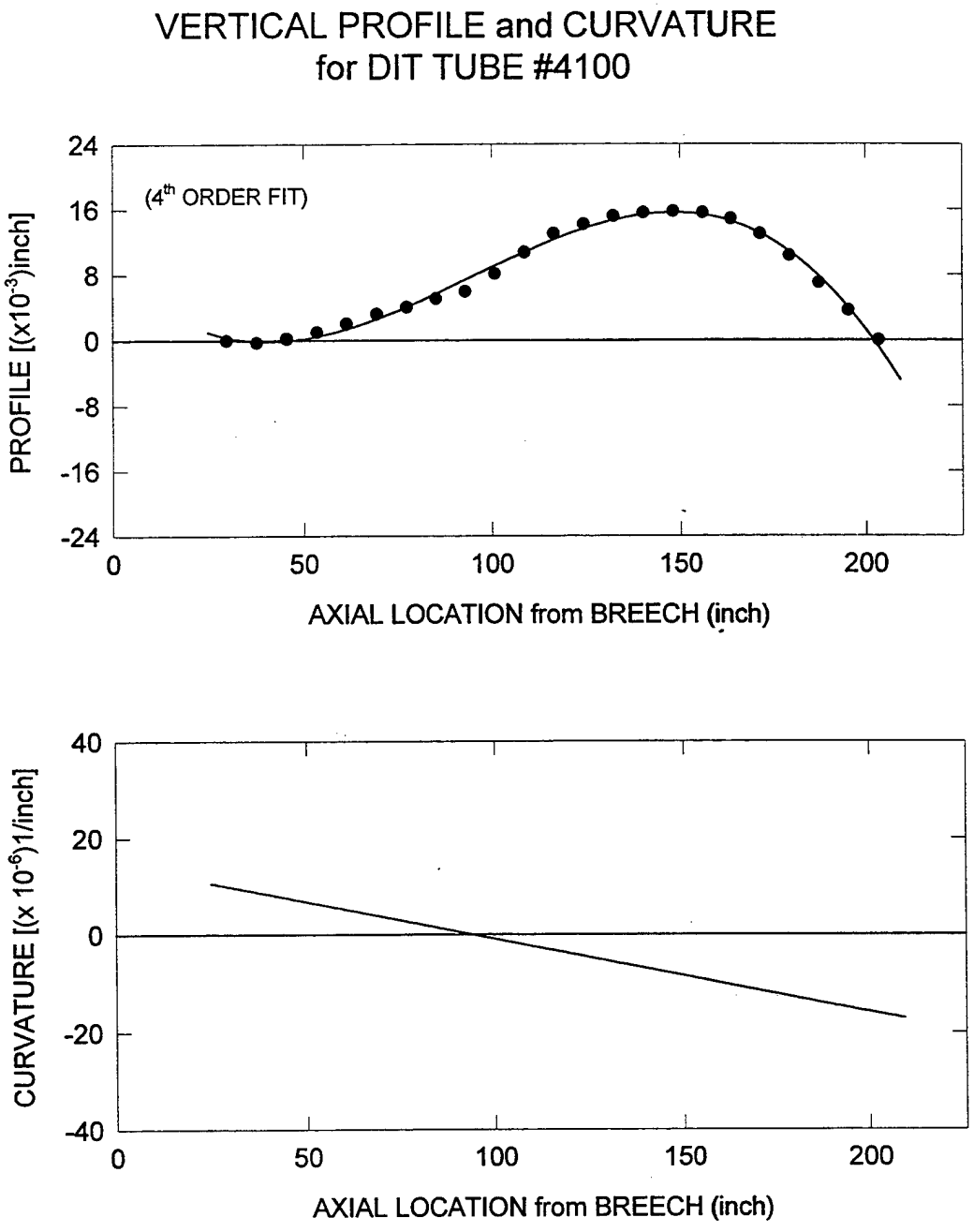

Figure 4b. Vertical Profile and Curvature for Tube #4100

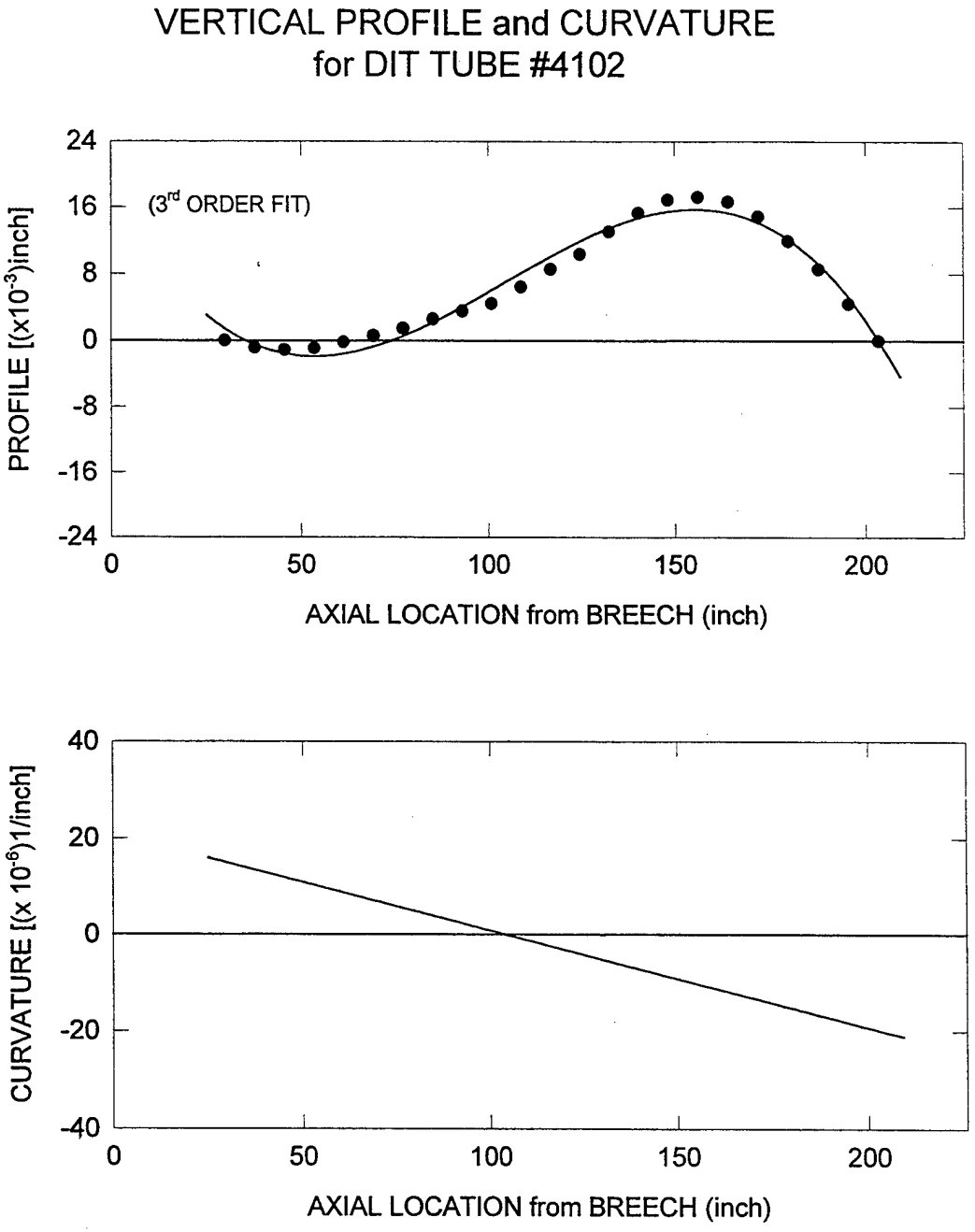

Figure 4c. Vertical Profile and Curvature for Tube #4102

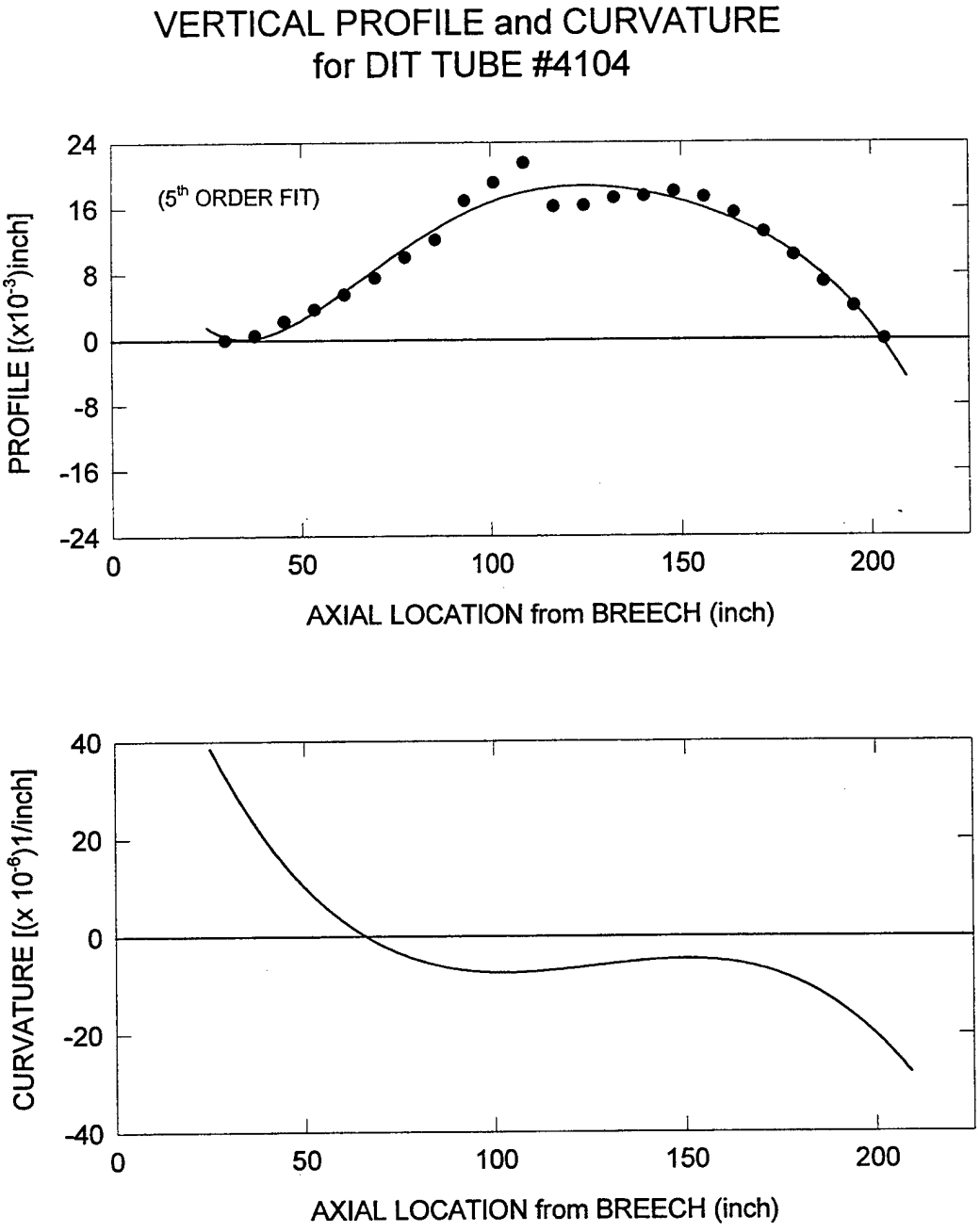

Figure 4d. Vertical Profile and Curvature for Tube #4104

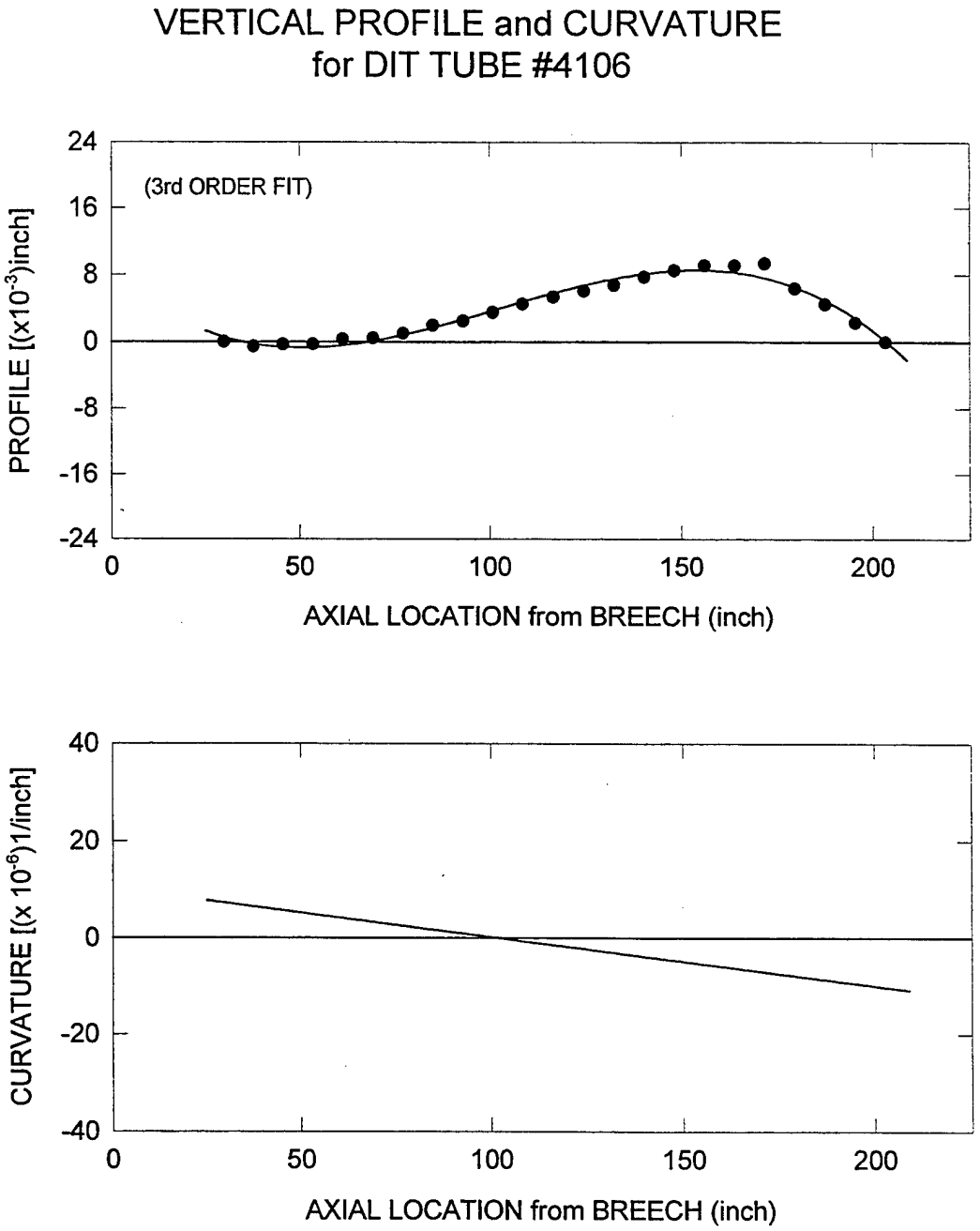

Figure 4e. Vertical Profile and Curvature for Tube #4106

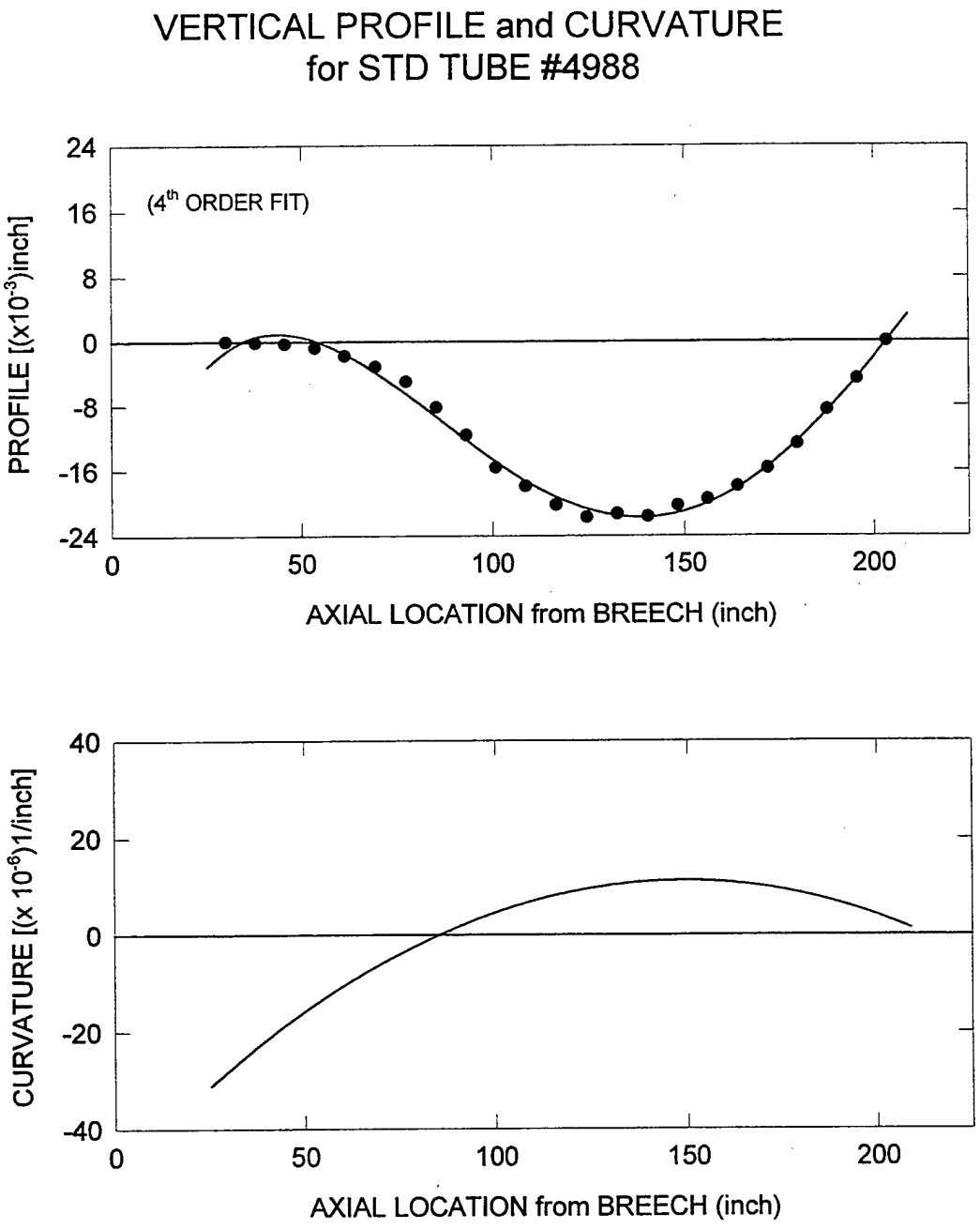

Figure 4f. Vertical Profile and Curvature for Tube #4988

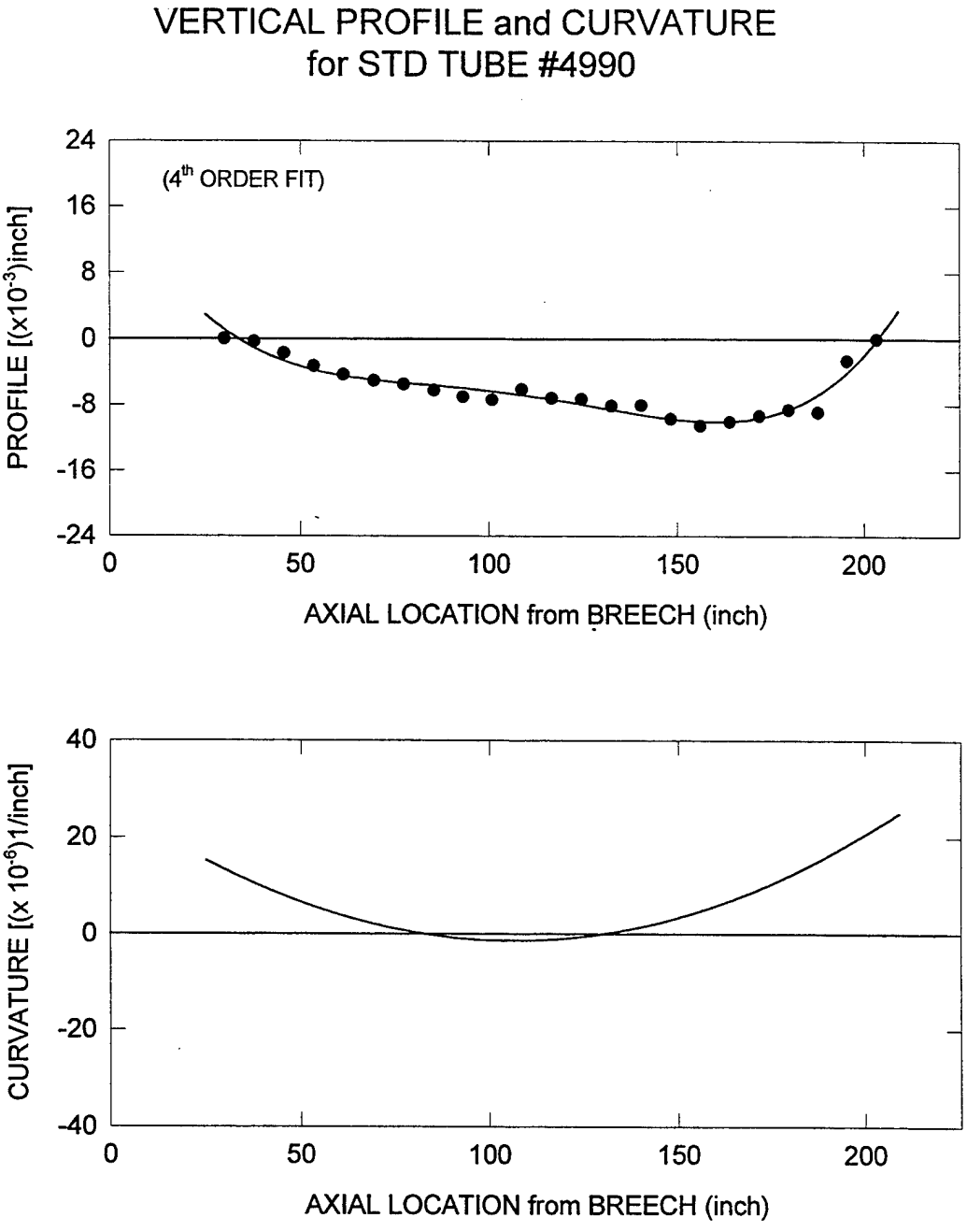

Figure 4g. Vertical Profile and Curvature for Tube #4990

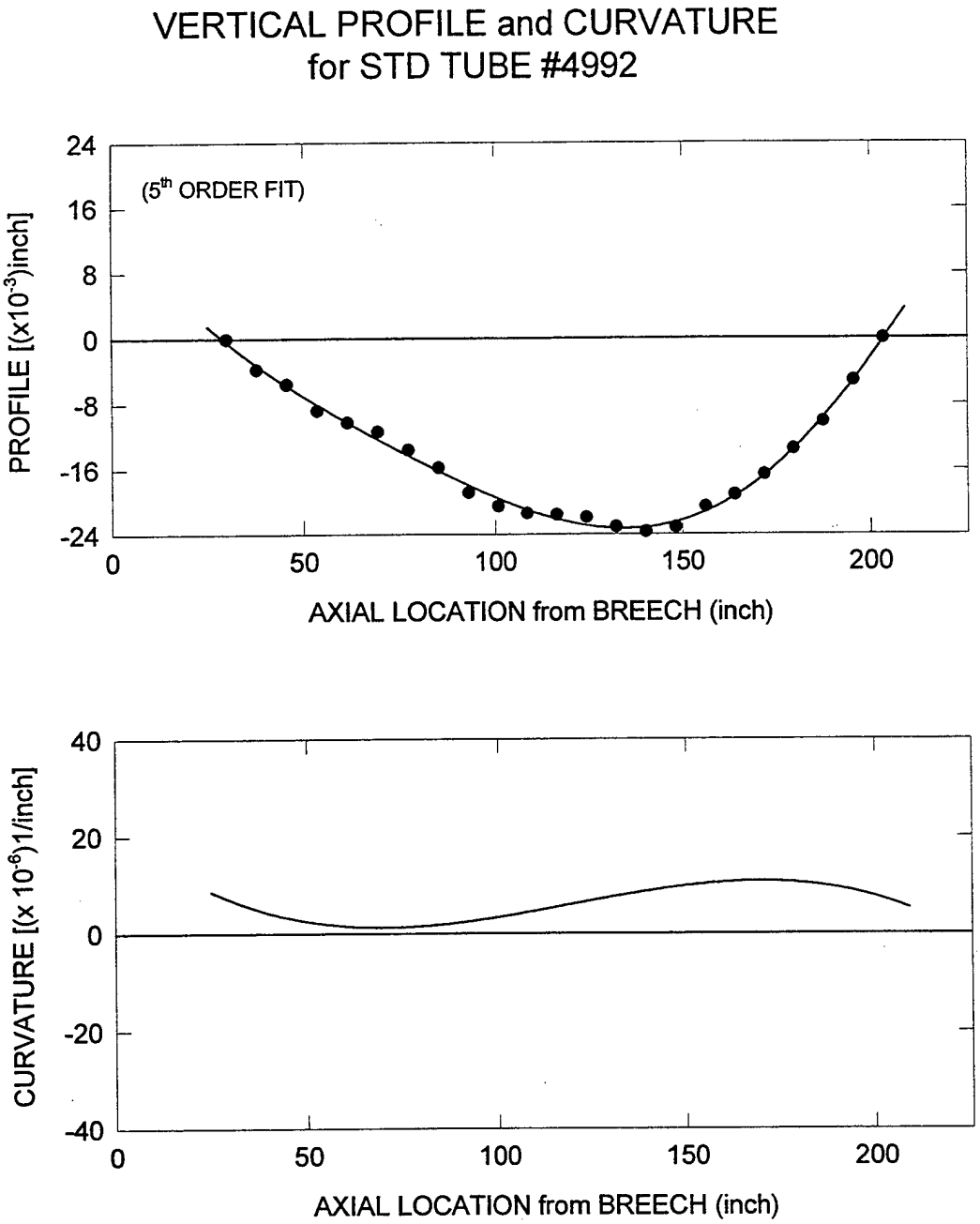

Figure 4h. Vertical Profile and Curvature for Tube #4992

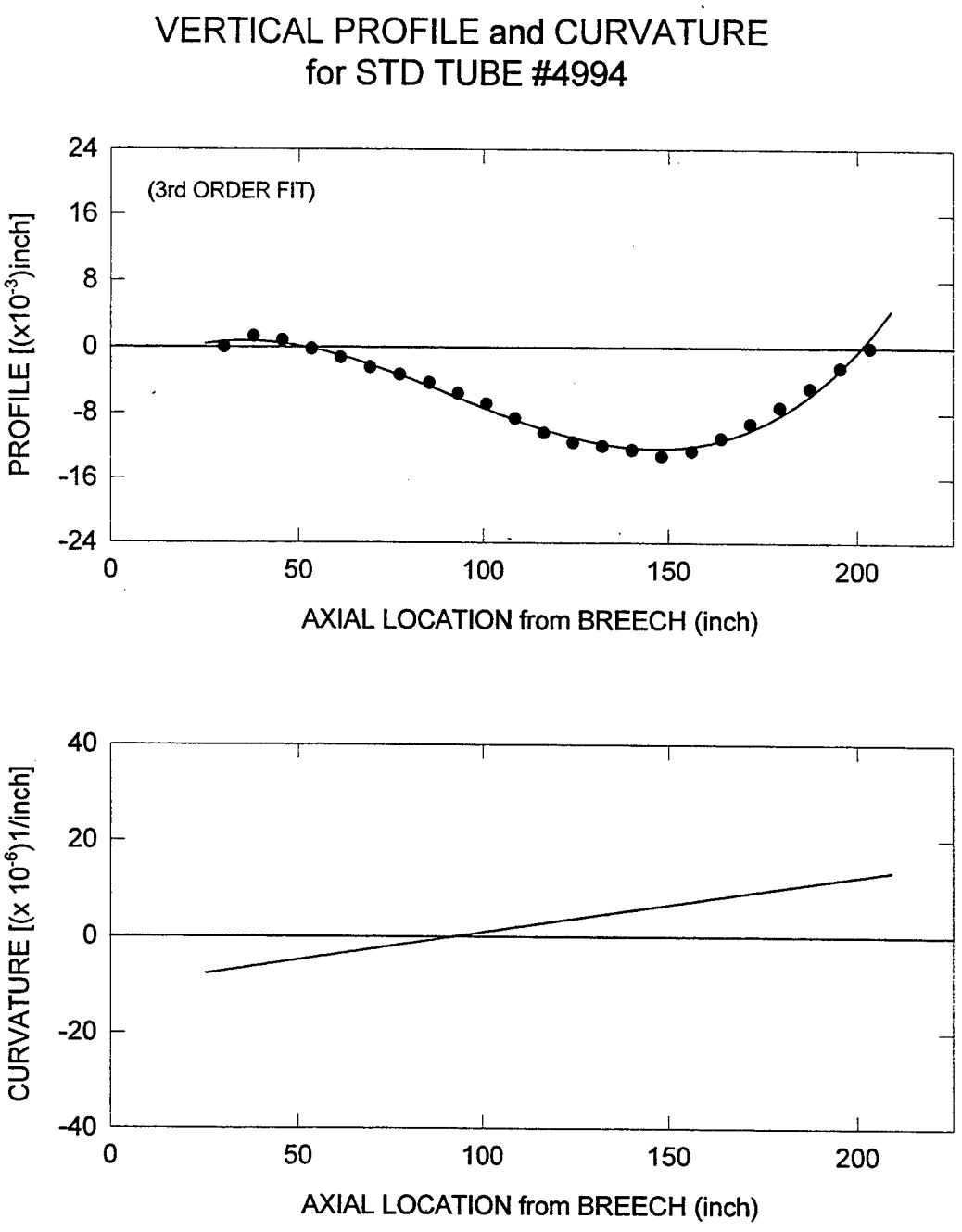

Figure 4i. Vertical Profile and Curvature for Tube #4994

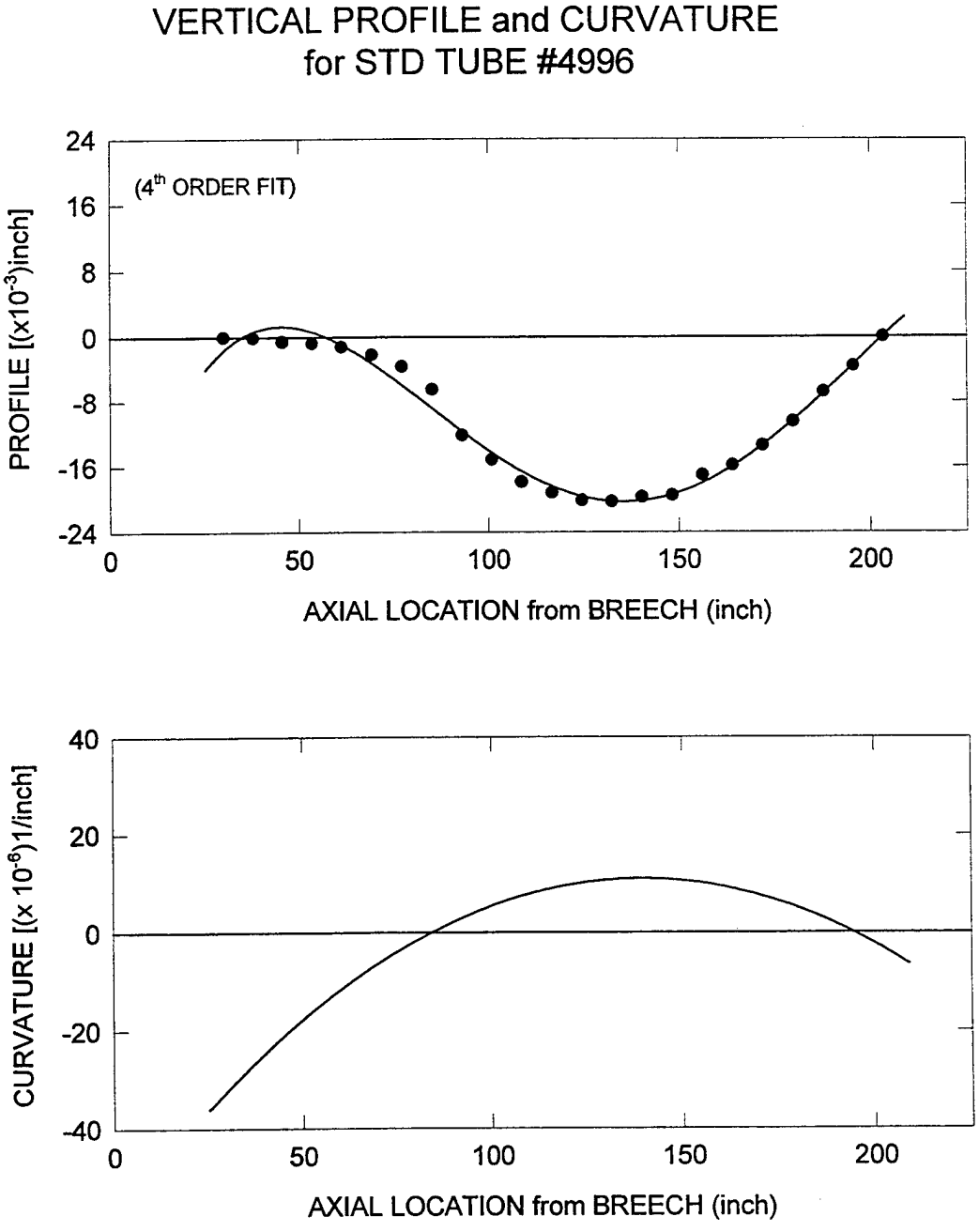

Figure 4j. Vertical Profile and Curvature for Tube #4996

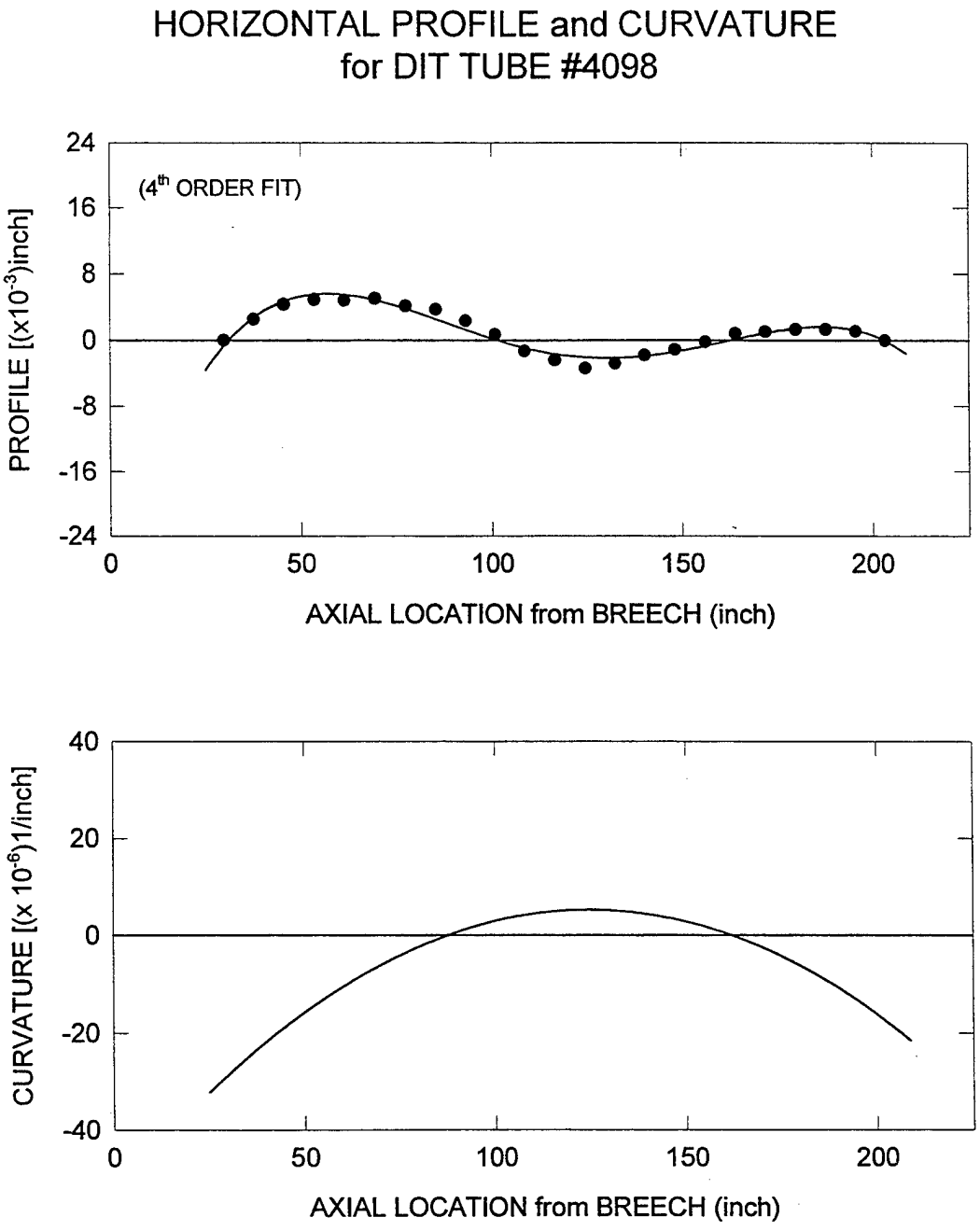

Figure 5a. Horizontal Profile and Curvature for Tube #4098

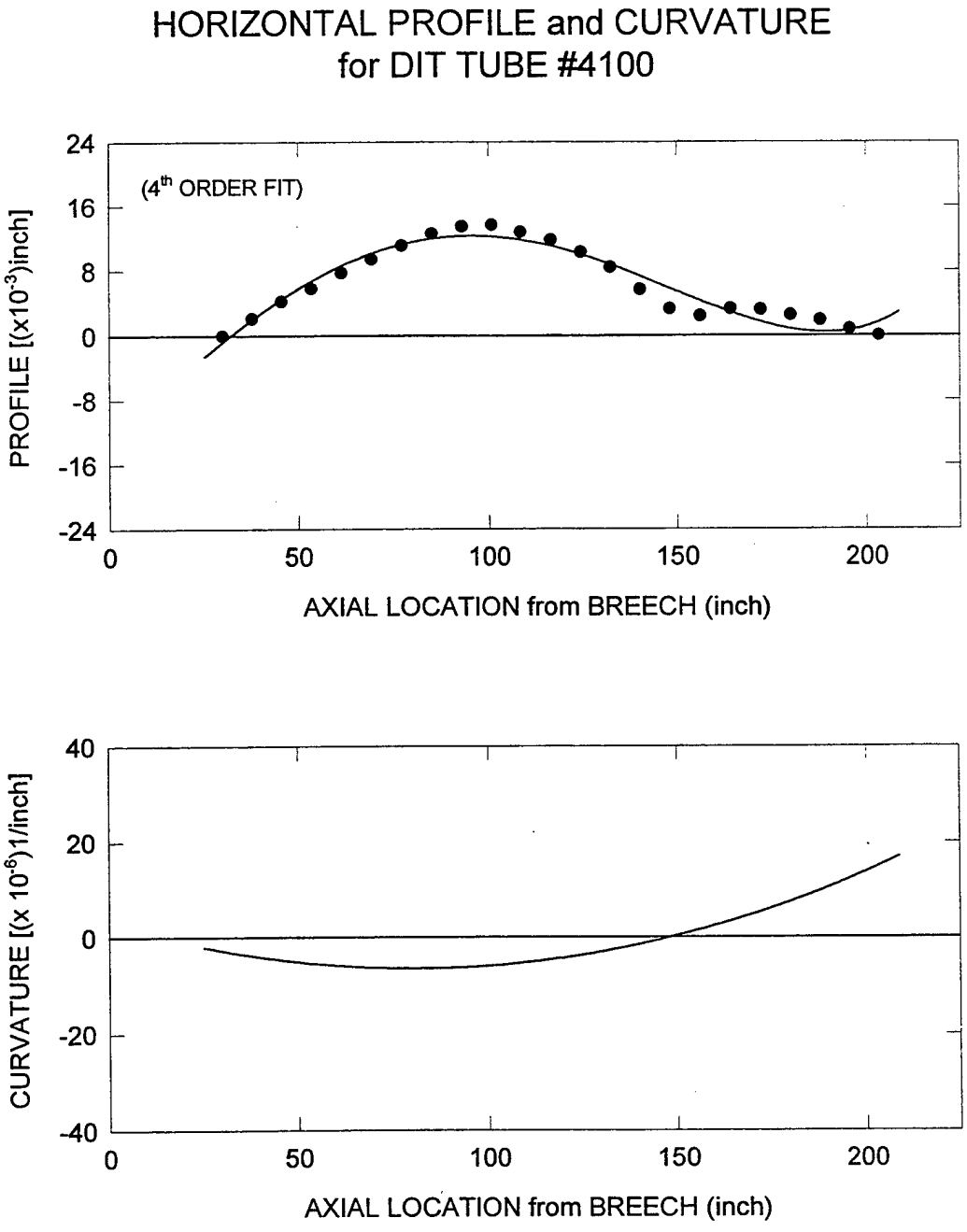

Figure 5b. Horizontal Profile and Curvature for Tube #4100

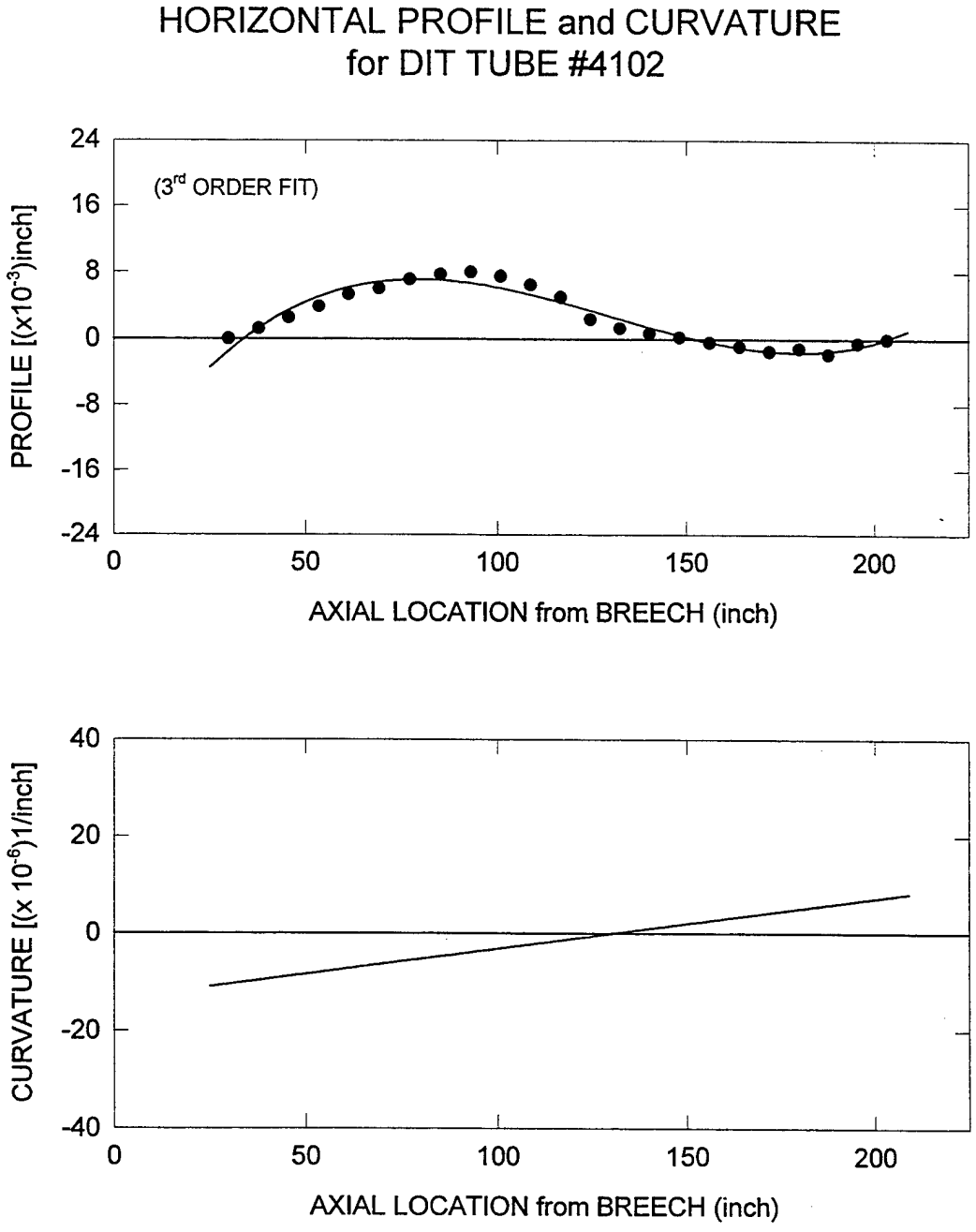

Figure 5c. Horizontal Profile and Curvature for Tube #4102

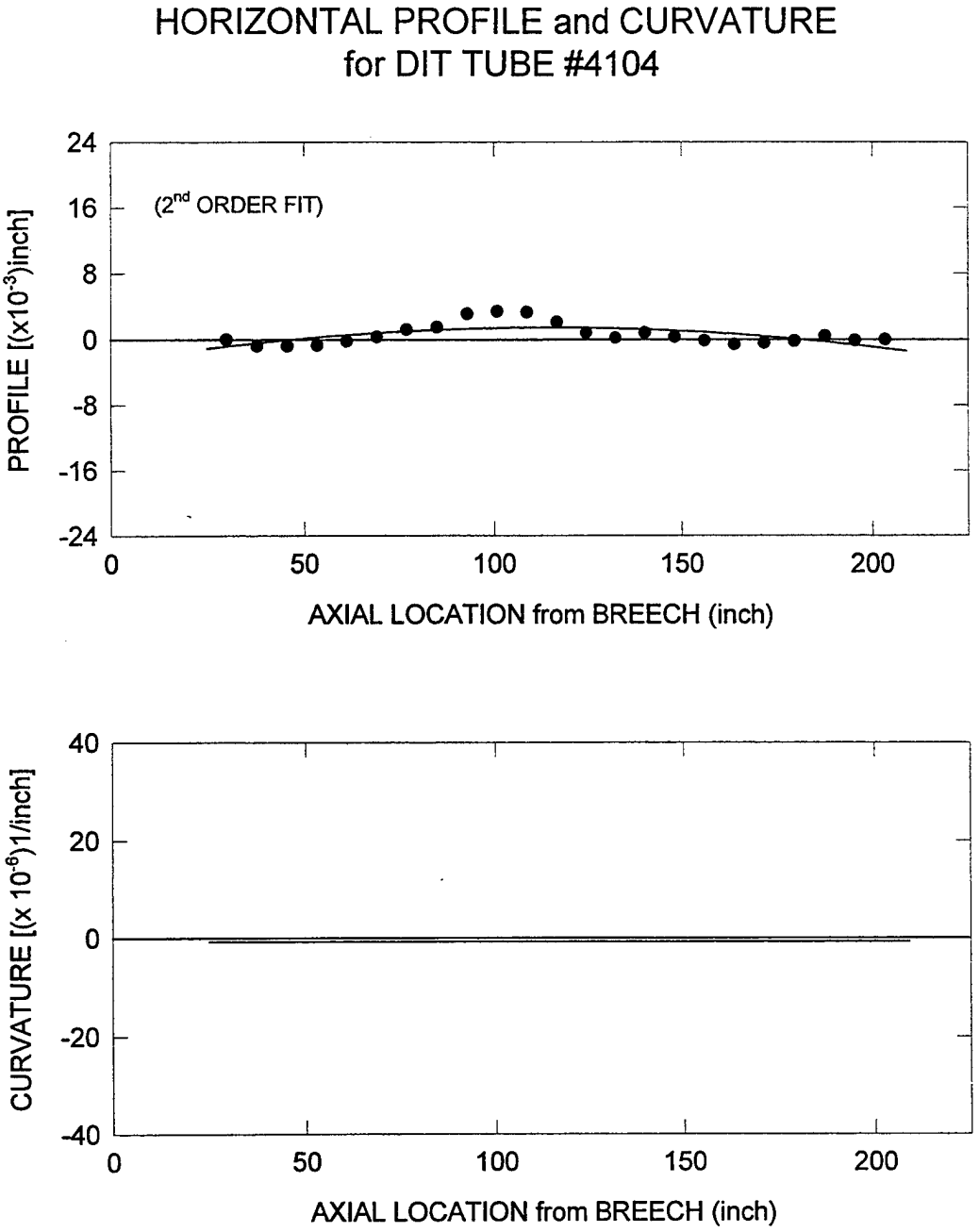

Figure 5d. Horizontal Profile and Curvature for Tube #4104

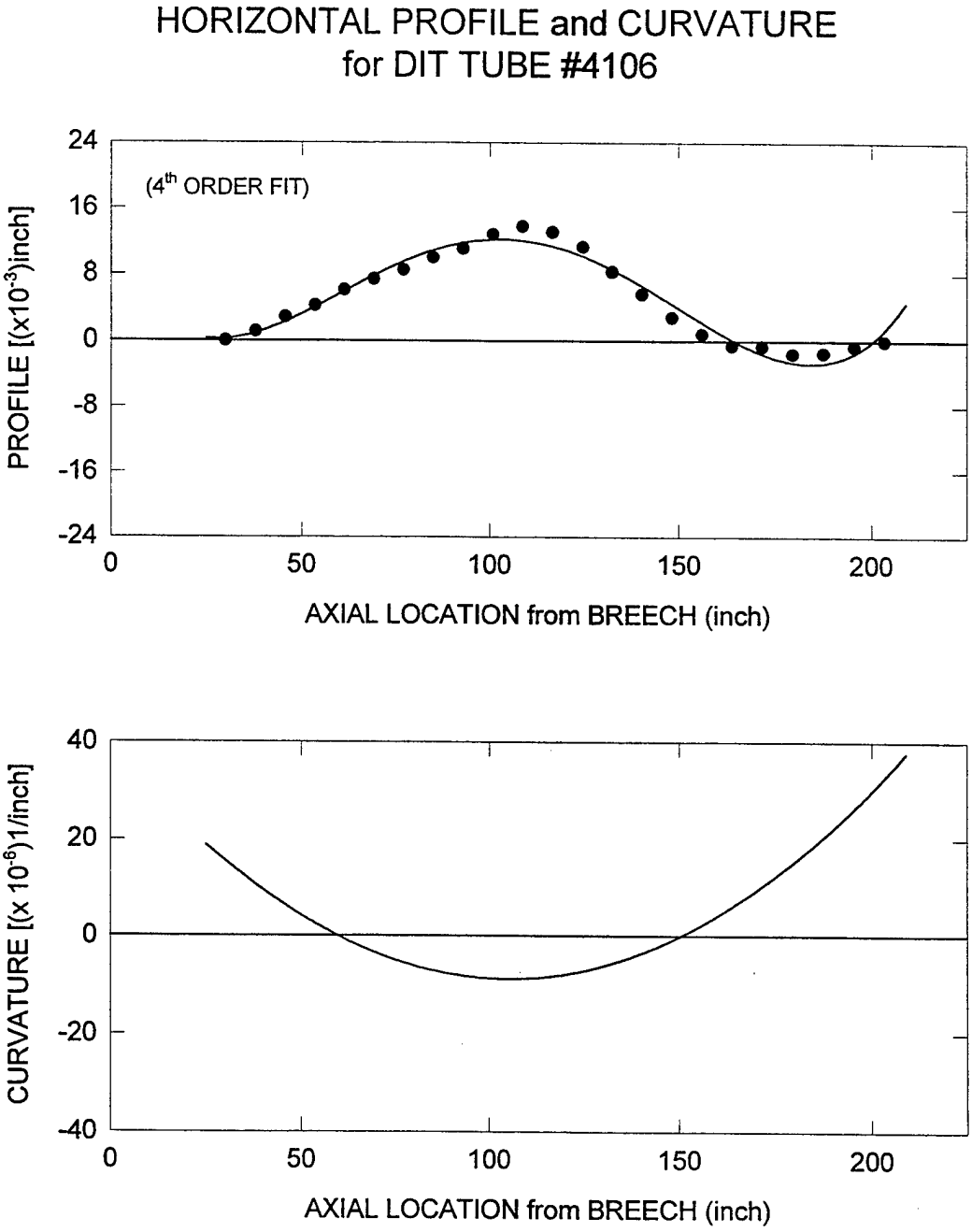

Figure 5e. Horizontal Profile and Curvature for Tube #4106

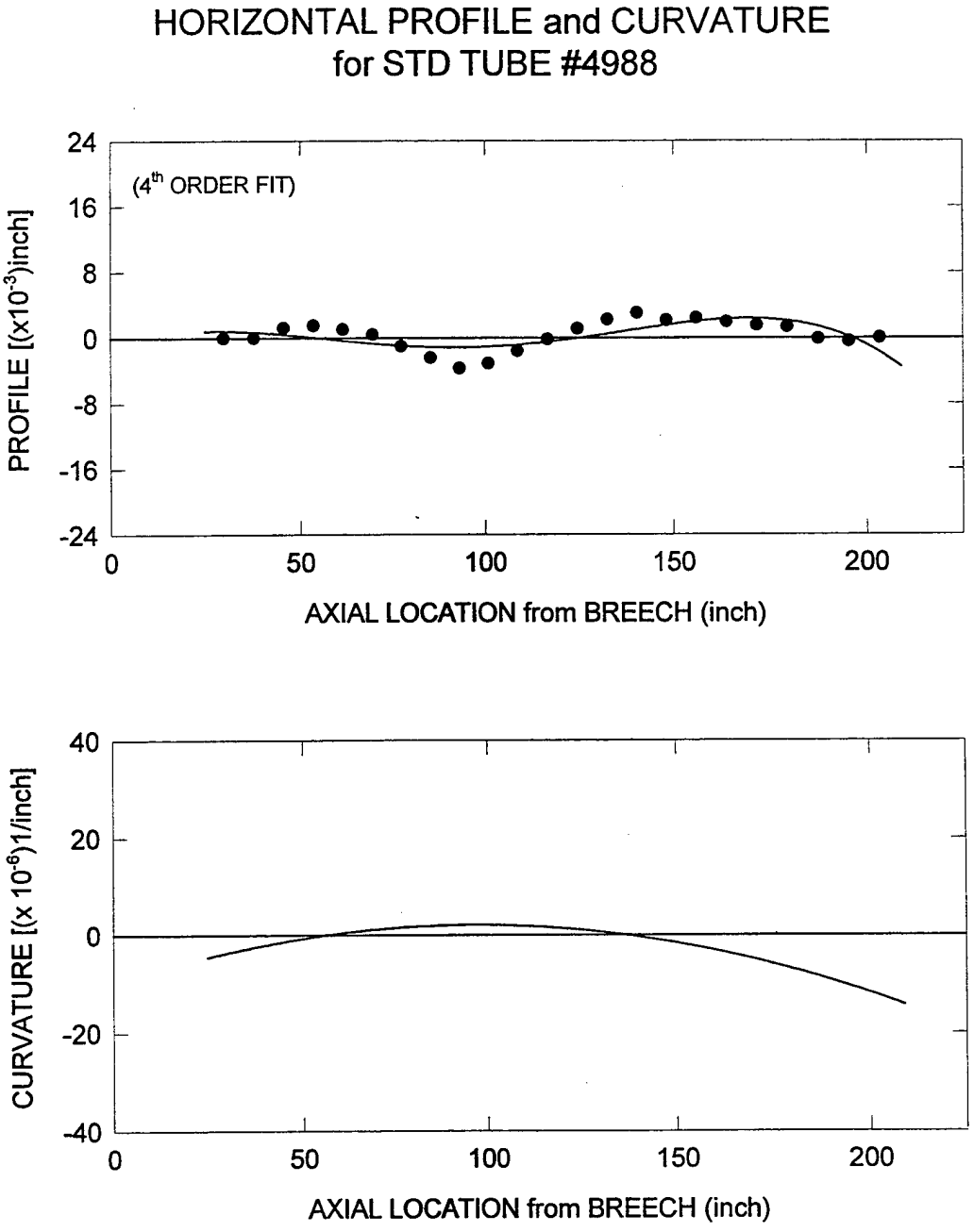

Figure 5f. Horizontal Profile and Curvature for Tube #4988

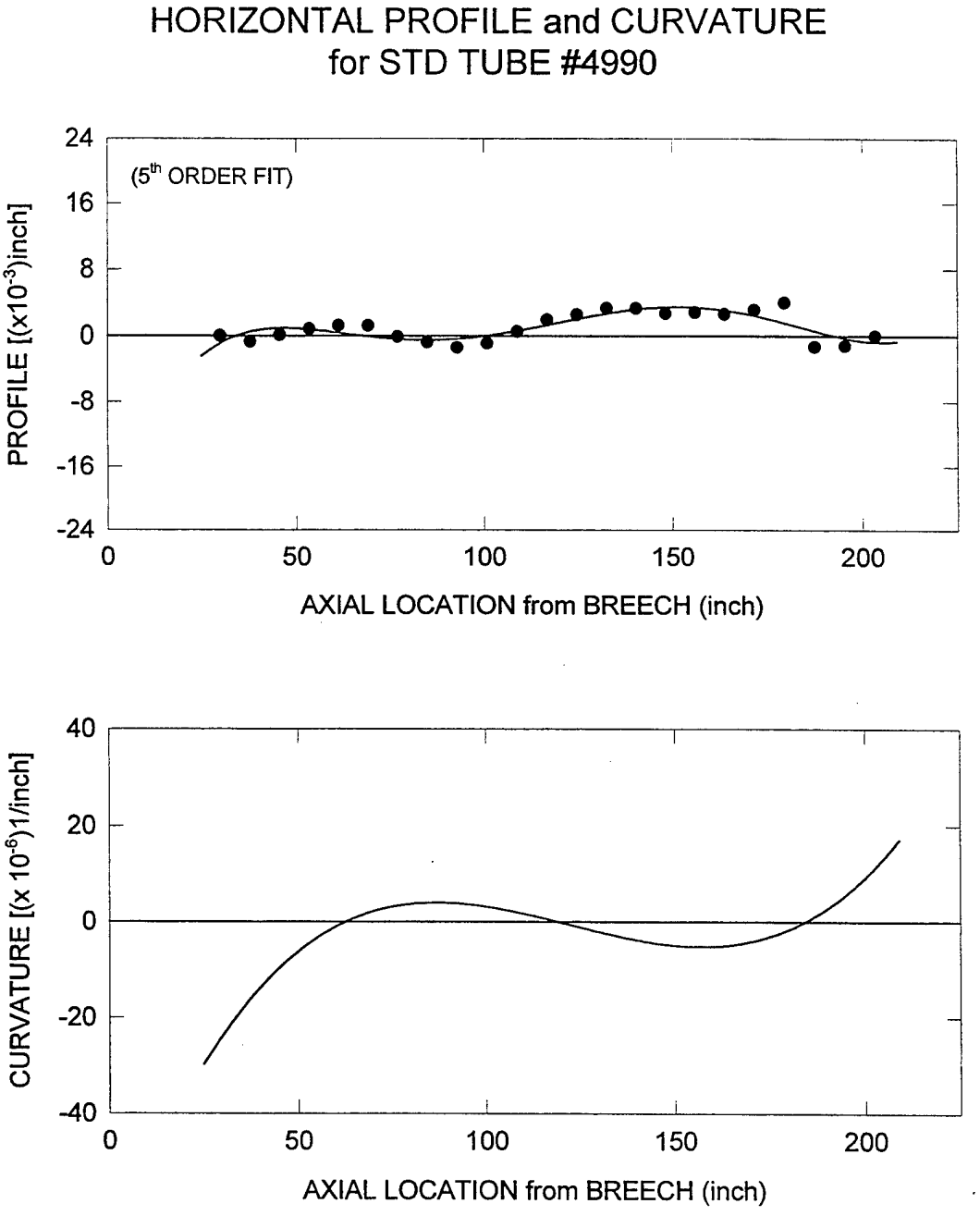

Figure 5g. Horizontal Profile and Curvature for Tube #4990

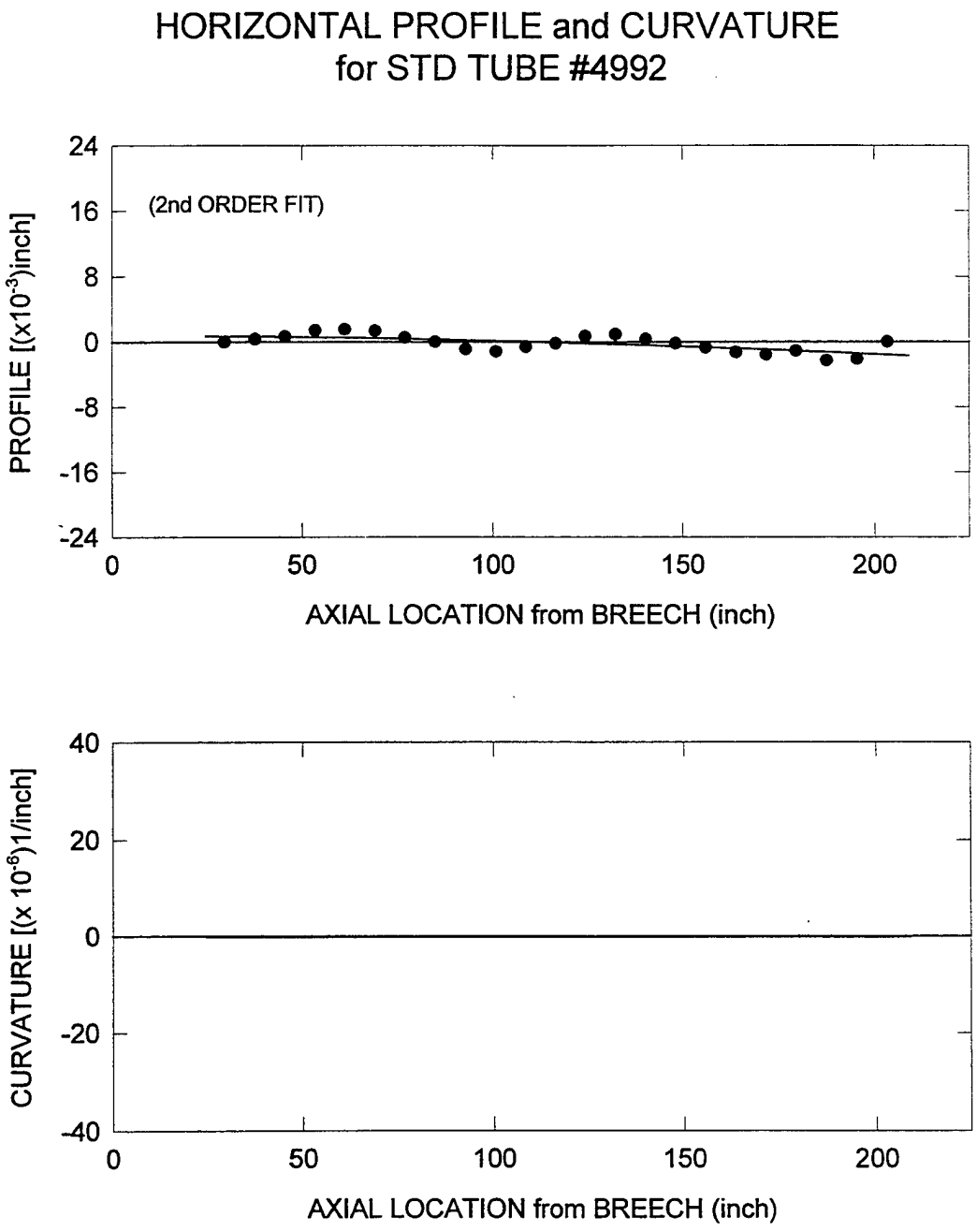

Figure 5h. Horizontal Profile and Curvature for Tube #4992

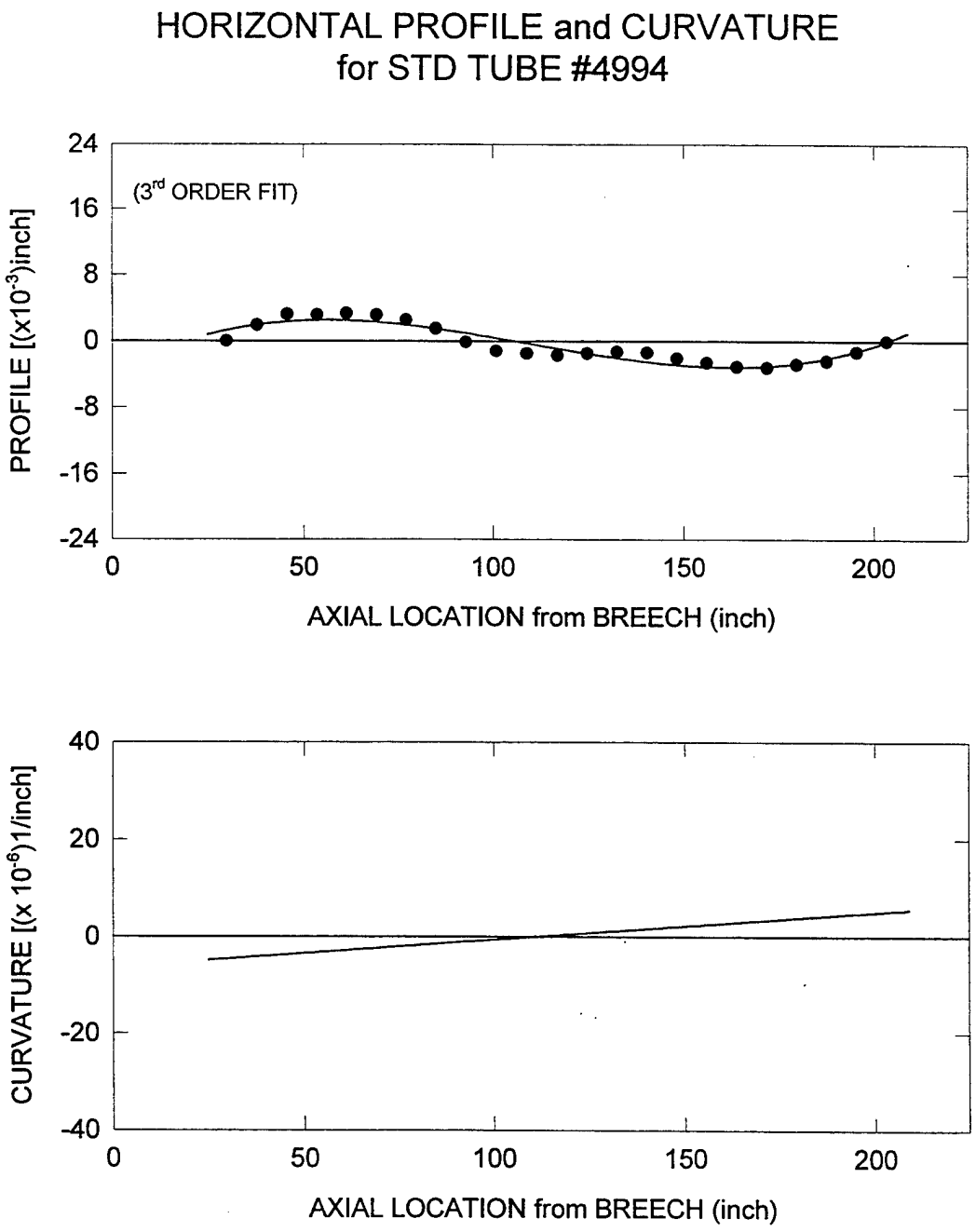

Figure 5i. Horizontal Profile and Curvature for Tube #4994

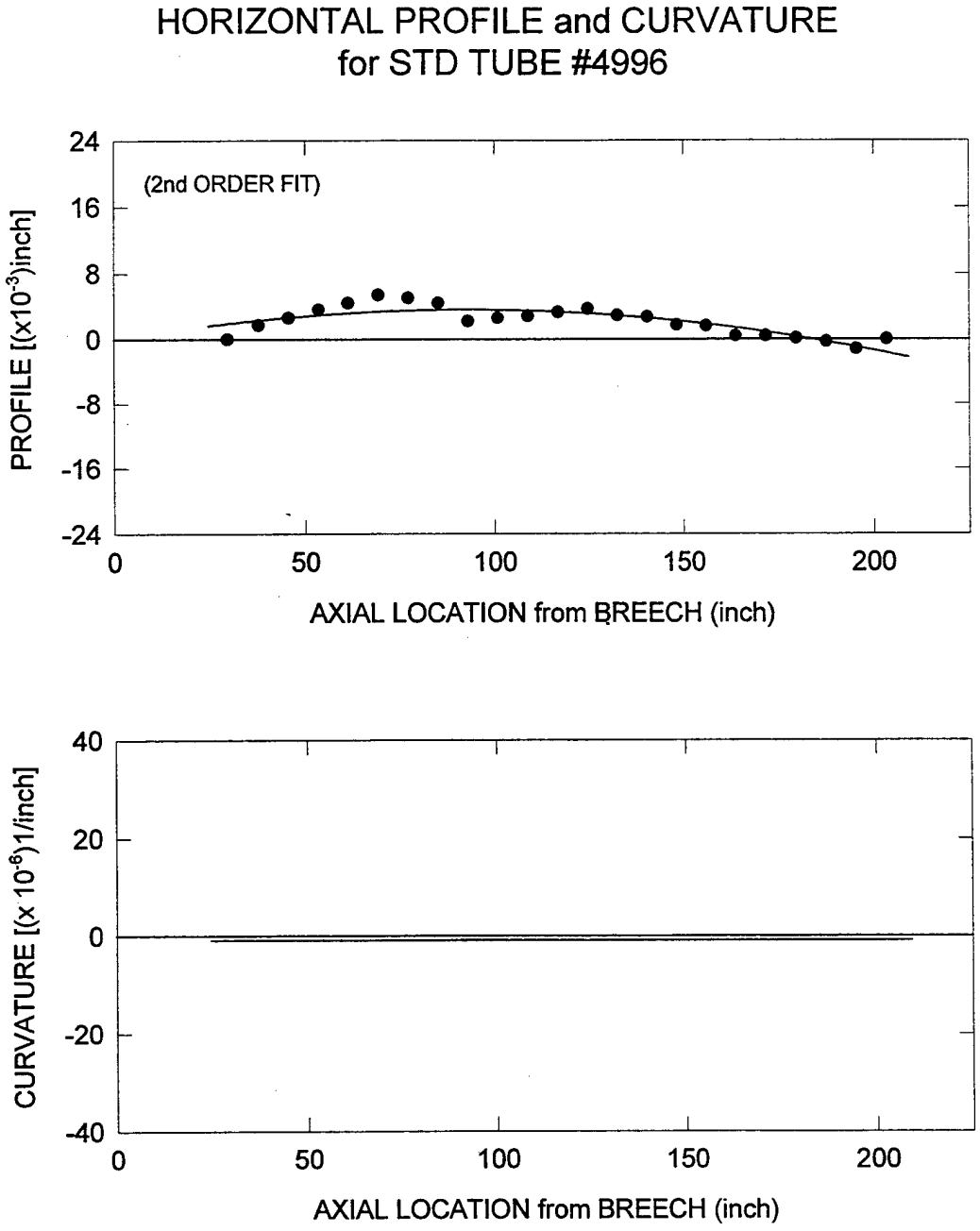

Figure 5j. Horizontal Profile and Curvature for Tube #4996

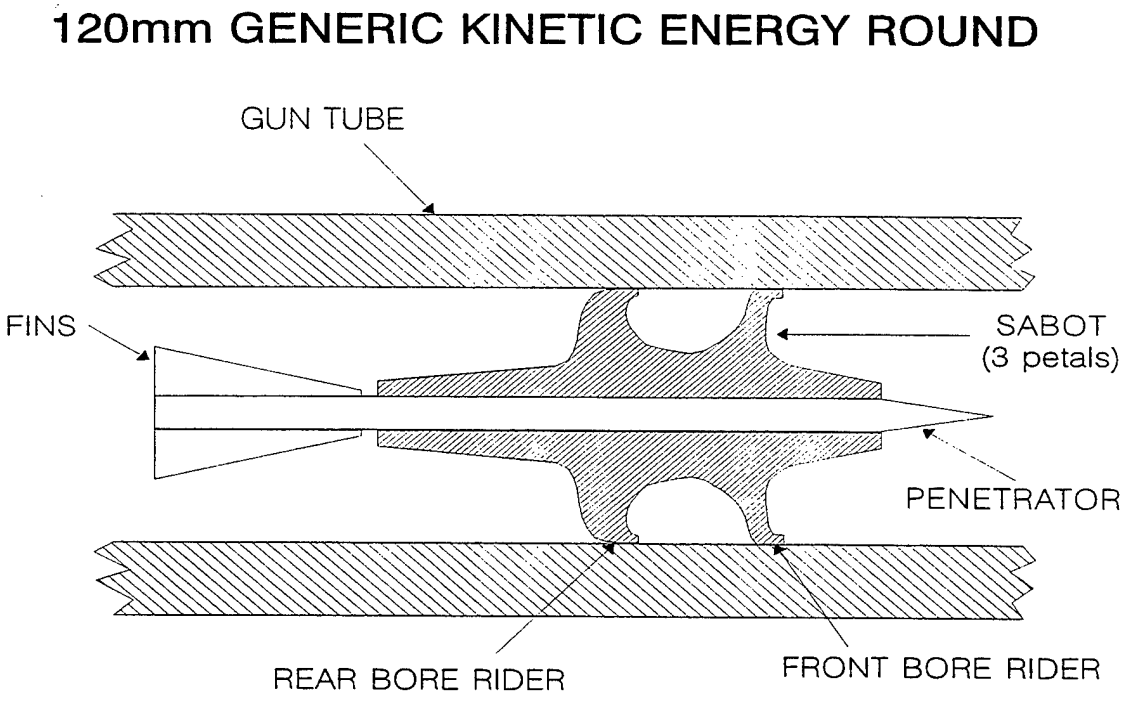

Figure 6. Schematic of Kinetic Energy Round in Gun Bore

and its stationary mount. As with the projectile to tube interface, the tube to mount interface must be explicitly defined. The mounting specifications will be characterized by non-linear spring elements applied at the gun's mounting locations. The function representing this relationship need not be linear nor continuous.

A schematic of the major components involved in the mounting of the gun are shown on figure 7. Points A and B are seal locations within which the recoil fluid resides. These are also considered the cannon's mounting points for vibrational analysis. The spring located in this chamber compresses between the piston head and rear surface of the cradle during recoil. It provides the necessary energy to return the cannon to its in battery position. All components except the cradle are subject to recoil motion and the major level of transverse vibration. The adaptor which has an internal profile closely matching the gun tube's outer profile is held in place by the bearing which drives the adaptor inward thus engaging the tube's outer surface. The king nut which is threaded to the outer surface of the tube provides the clamping force to maintain the bearing/adaptor assembly to the tube. The thrust nut is the link which marries together all of the recoiling components. It has an internal thread which engages a mating thread on the outer diameter of the bearing. When tightened the load pulls the cannon and piston forward through the bearing, king nut, tube and breech threads. The cradle is assumed to be grounded along the face at the shoulder located just forward of the fluid and spring chamber. Examine feature C in the figure. This represents the forward end of the rotor and is considered to be ground with respect to the vibrating cannon.

By examining the relevant component drawings the range of clearances between recoiling and stationary parts in the assembly are 0.005 to 0.010 inches at point A and 0.001 to 0.011 inches at point B. When the cannon is within the clearance its transverse motion will be unopposed by any external loads except its own inertia. However, when the king nut is tightened to its preload specification, the clearance between recoiling and non-recoiling components decreases considerably. Wilkerson has measured these clearance values and has determined that at most 0.002 inches is realizable at either location [8].

To determine the structural resistance during contact a twofold approach was employed. Since the cradle is assumed to be 'grounded' along its mid axial location (see feature C in figure 4), both the breech and the muzzle end resemble short cantilever beams. Stiffness values for this type of structure are well documented in textbooks on deformable materials and for this mount's dimensions the stiffness value would be on the order of several million pounds per inch. A stiffness value of this magnitude is grossly inaccurate yielding an extremely 'stiff' mathematical system along with all of its numerical difficulties. Therefore, an alternate type of response namely Hertzian contact was developed and applied in series with the beam model. Hertzian contact deals with the local microscopic levels of deformation and contact stress between elastic components of various geometries. Consult Roark and Young [9] for details and applications of this method. Unlike the beam model whose stiffness is constant regardless of the level of deformation, the interface stiffness in the Hertzian model begins at zero and rapidly rises in a non-linear fashion for increasing penetration of one material into the other. By employing these two models in series a slightly non-linear load-deflection distribution was determined.

Ballistic Data

The ballistic performance of a particular round is usually recorded during a test in the form of peak propellant gas pressure and muzzle velocity. Variations in these values from shot to shot are not uncommon. For this test, such data was not retained, therefore, a nominal distribution for gas pressure generated from a ballistic simulation will be used in this study.

Aiming of the Weapon

Whenever an accuracy test is performed aiming of the weapon becomes an issue. Super elevation is a term which addresses the amount of elevation loss that a projectile endures as it traverses downrange. It is the amount of additional rotational elevation which must be applied to the weapon (after the muzzle has been aimed at the cross hairs of the target) for the projectile to arrive at the proper impact location under the influence of gravity drop. This is a function of target range and although tank weapons are used for direct fire applications it still must be considered. In addition, since every gun tube has its own specific bore centerline profile which is additive to gravity droop the amount of total elevation will be different from tube to tube. To determine the total elevation (and in fact azimuthal rotation) the

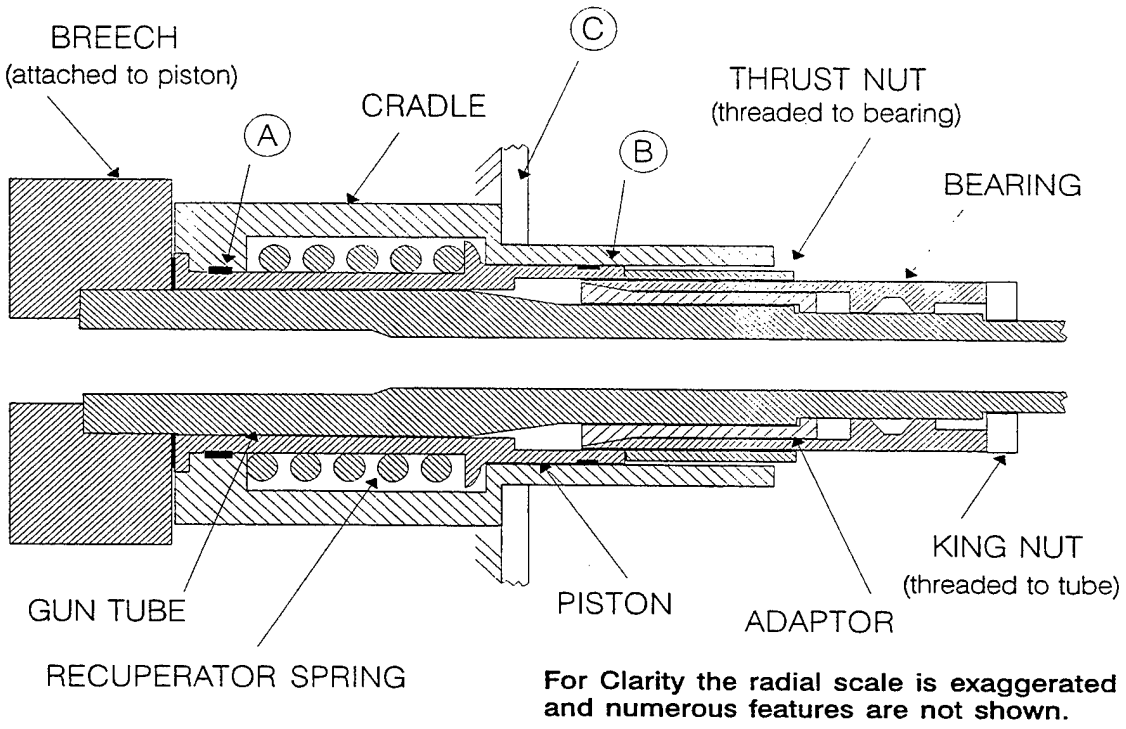

Figure 7. Schematic of M1A1 Gun Mount and Cannon

individual slopes (both horizontal and vertical) of the tubes' muzzle ends will be used. These slopes were determined by calculating the average slope of the secants connecting the last three nodes of the gun tube. The nodal locations from the SIMBAD model of each gun tube in its gravity drooped state will be used for these calculations. Correctly prescribing these values is important to the BOOM code since projectile orientation with respect to gravity is a dominant load during free flight of the round. This parameter was set for each tube in the study and was not varied to induce any dispersion causing effects.

Values for the Uncertain Analysis Parameters

By using the methods, assumptions, and data as indicated, the nominal values and ranges for the uncertain parameters have been determined.

The nominal values are:

Peak Ballistic Pressure:	53,400 pounds/ square inch
Mount Clearance:	0.001 inches
Average Stiffness of Mount:	5.0×10^6 pounds/inch
Rear Bore Rider Stiffness:	513.0×10^3 pounds/inch
Front Bore Rider Stiffness:	236.0×10^3 pounds/inch

The range of values are:

Ballistics pressure:	±2.5%
Mount Clearance:	0.000 - 0.002 inches
Mount Stiffness:	±5%
Bore Rider Stiffness:	±5%

A total of 54 different input files have been generated and applied to each gun tube. With 10 gun tubes in the analysis a grand total of 540 computer runs have been generated, the output of which will be reported in the next section.

RESULTS OF ANALYSIS

The results for each tube will be presented as target impact plots of the firing data, projectile jump at exit from SIMBAD analysis and impact location from BOOM projectile flight analysis in conjunction with SIMBAD exit conditions. The impact scale will be angular with a range of 2.0 mils. The data will be in the form of the three circles (one for the data, one for projectile jump at exit from SIMBAD and one for target impact from BOOM flight simulation) the center of which represents the location of the mean value for each result. The diameter of the circle represents the 1 sigma circular dispersion band based upon a statistical analysis of the results. Presenting in this manner lends itself to a concise and multifaceted comparison between the data and the results. In addition, the horizontal and vertical bore profile data and fit for each gun tube will be shown and discussed in conjunction with the test and analysis results. Figures 9a - 9f contain this information.

Results for the five DIT indexed tubes are shown on figures 8a - 8e. As noted previously, the vertical and horizontal shapes of the bore profile for these tubes are quite similar. In the vertical plane the muzzle points down with a fairly large bow whereas the horizontal profile resembles a low amplitude sine wave the muzzle of which sometimes points left and sometimes right. The calculated values for data and analysis shown on the right chart indicate the relative placement of the results with respect to the aim point (cross hairs). In four of the five cases for the DIT tubes, the results from the BOOM analysis shows better correlation with data (at least in terms of mean values) than the SIMBAD exit conditions. The only exception is tube number 4098 for which the SIMBAD exit conditions are closer to actual impact data than those for BOOM. Circular dispersion calculations from SIMBAD range from 0.041 to 0.054 mils, whereas for BOOM they are 0.060 to 0.071 mils. The range for dispersion in the data is 0.070 to 0.199 mils. We must note that only three shots were fired in the test (in some cases only two were reported), therefore, the small sample size may not be representative of actual dispersion.

Results for the five STD indexed tubes are shown of figures 8f - 8j. Since the top vertical centerline of these tubes were oriented such that the plane of maximum bending was vertical the shapes for all five are very similar. The muzzle end points vertically upward with very little curvature in the horizontal plane. For all five cases the mean values for the impact locations from the BOOM calculations were closer to the data than those for SIMBAD exit conditions. Circular

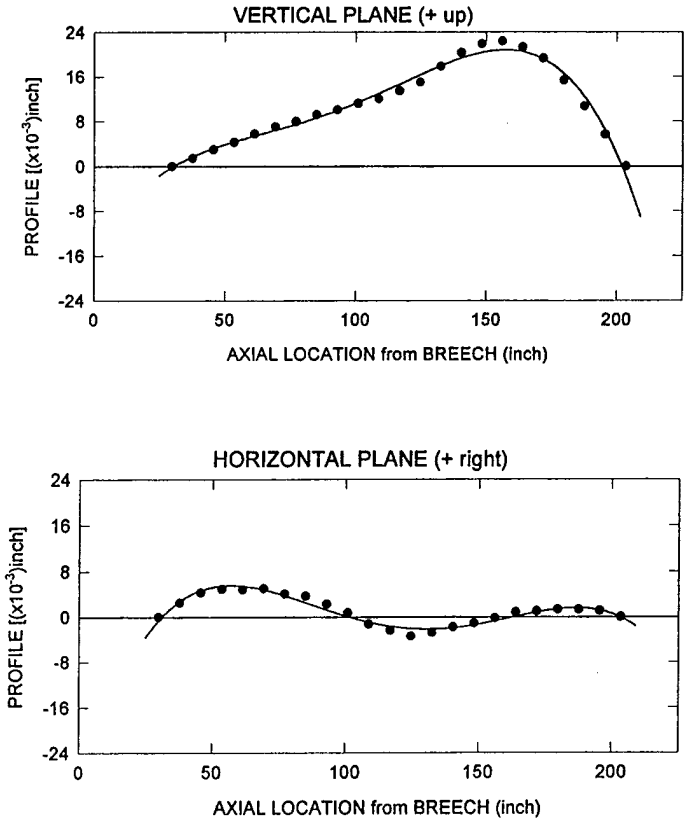

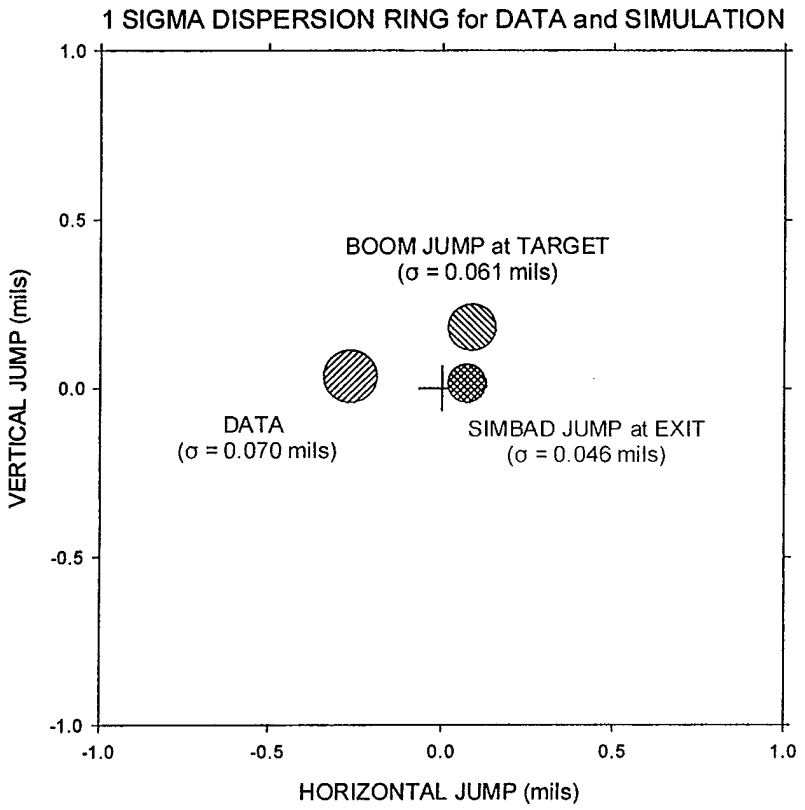

Figure 8a. Comparison of Results for Tube #4098

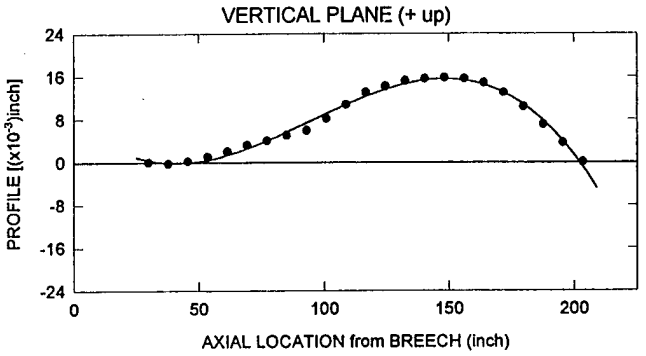

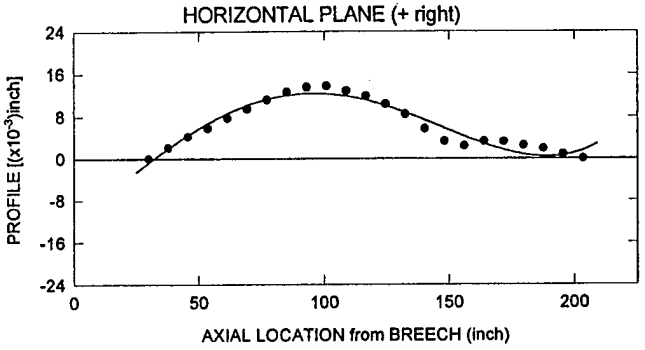

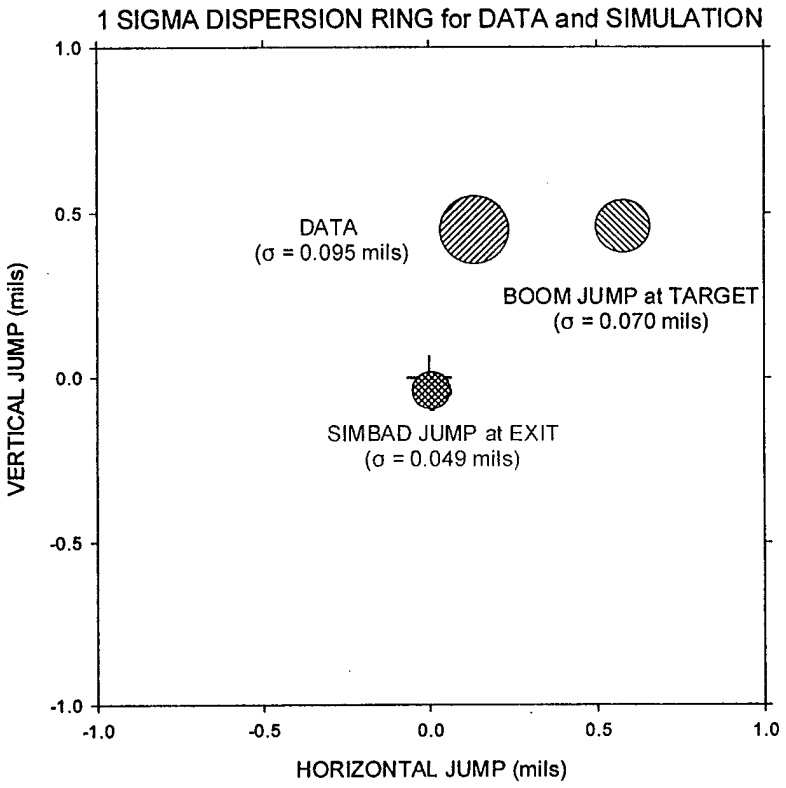

Figure 8b. Comparison of Results for Tube #4100

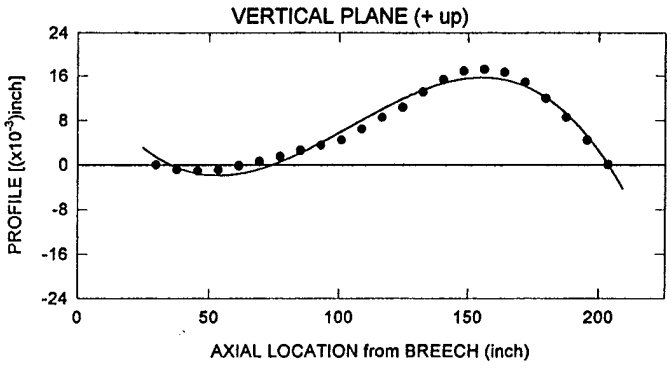

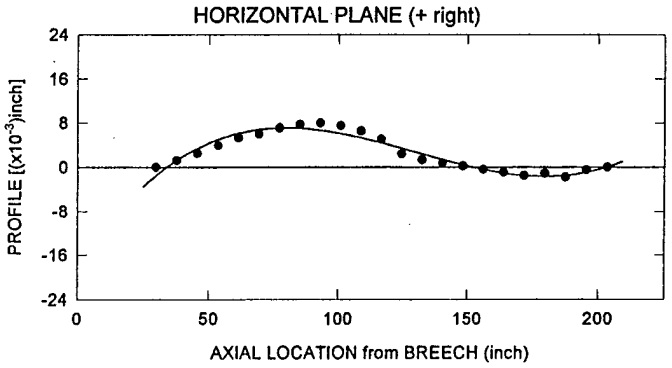

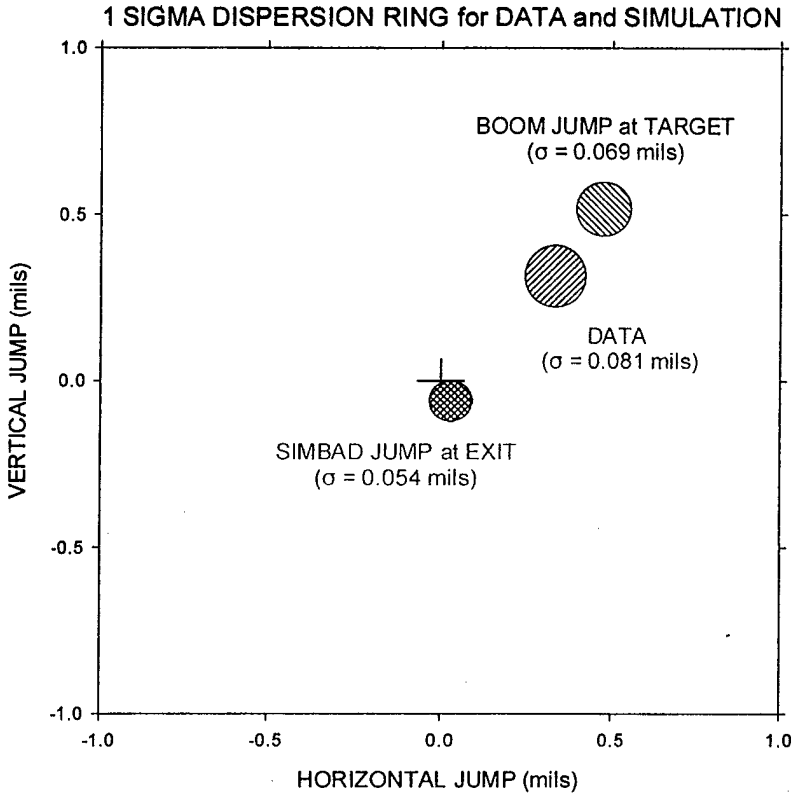

Figure 8c. Comparison of Results for Tube #4102

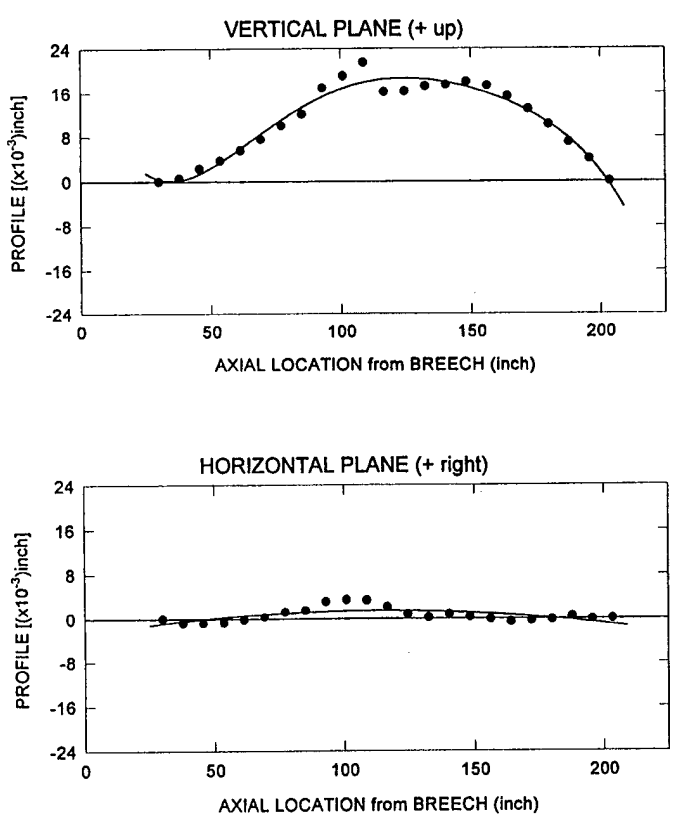

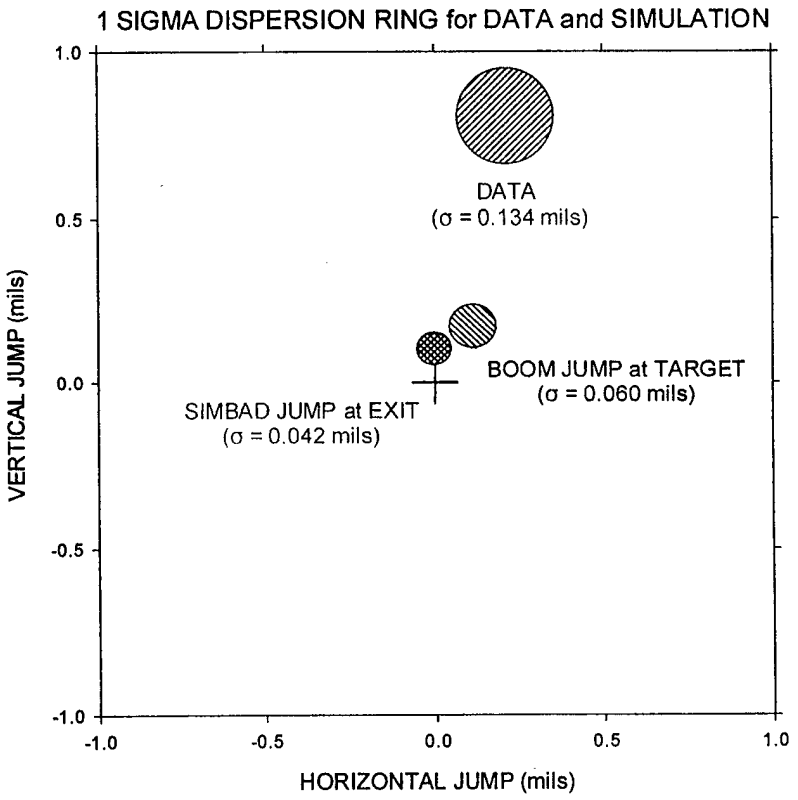

Figure 8d. Comparison of Results for Tube #4104

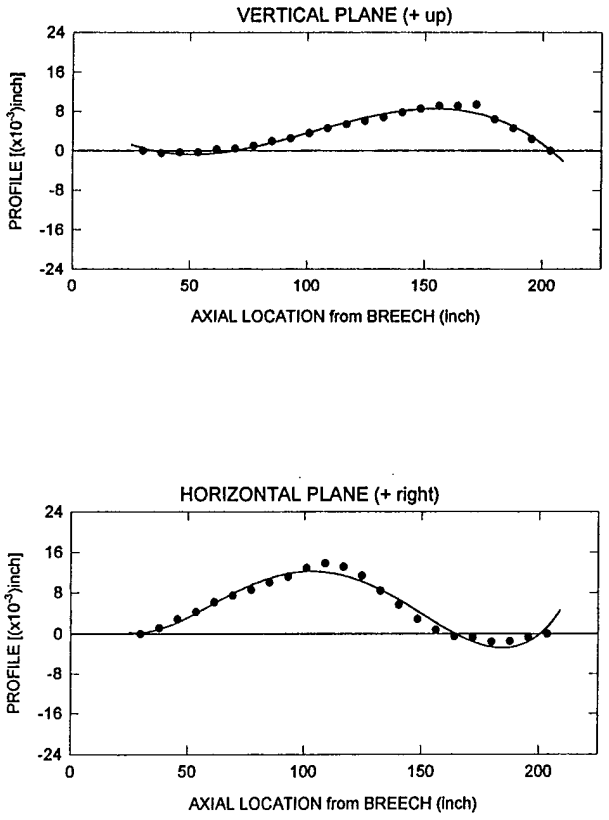

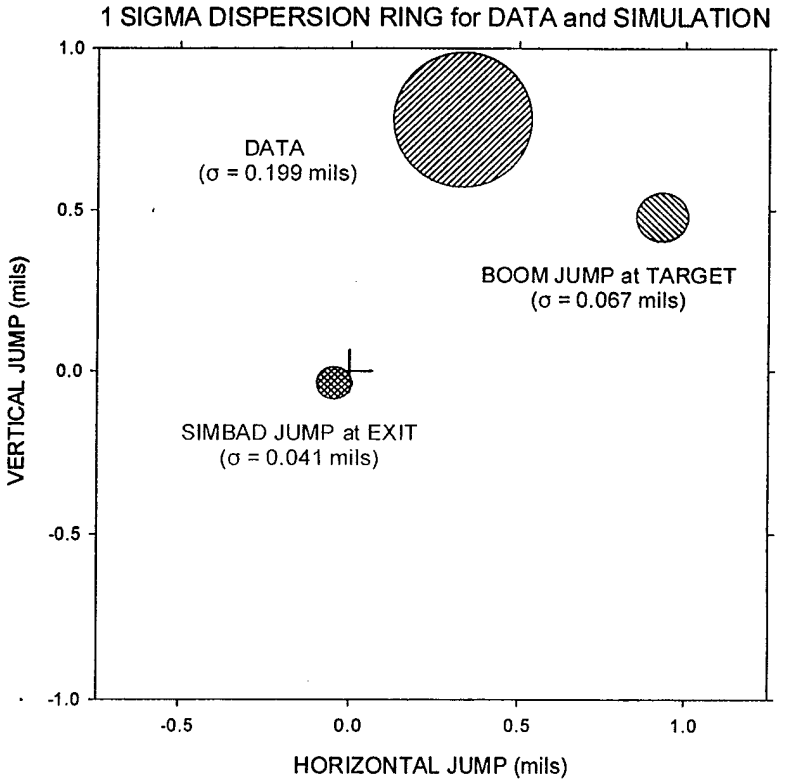

Figure 8e. Comparison of Results for Tube #4106

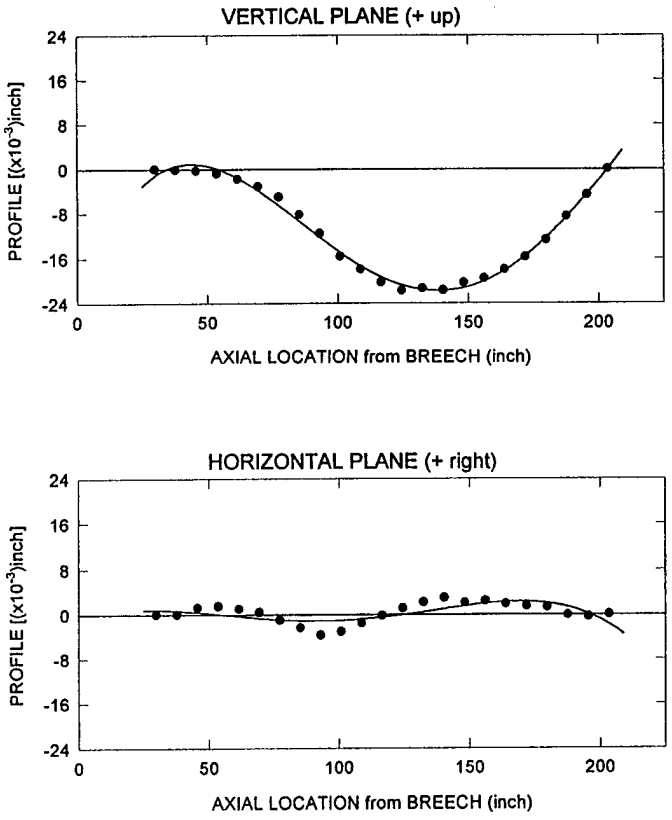

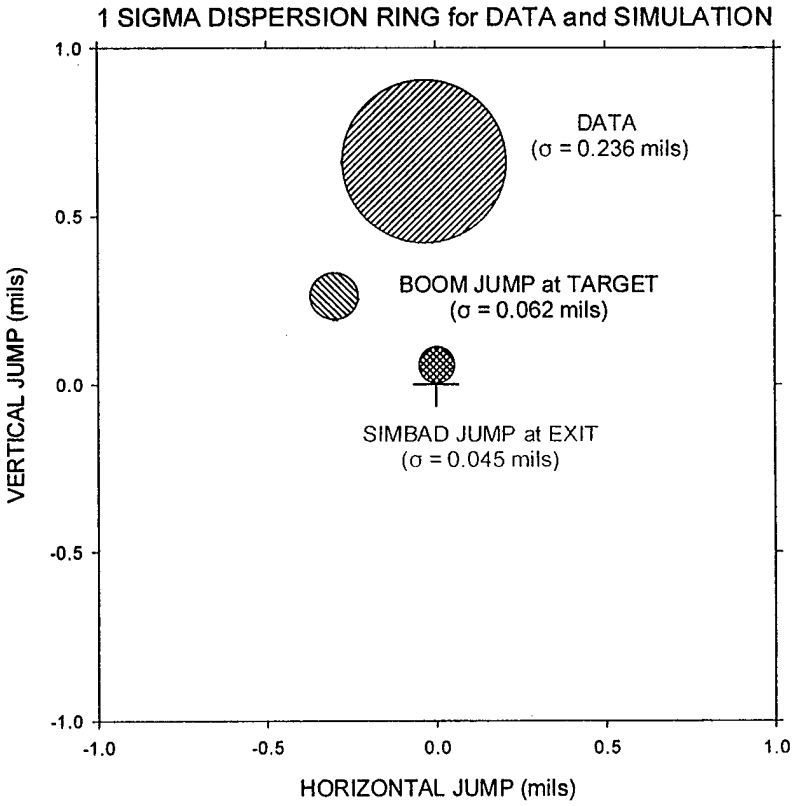

Figure 8f. Comparison of Results for Tube #4988

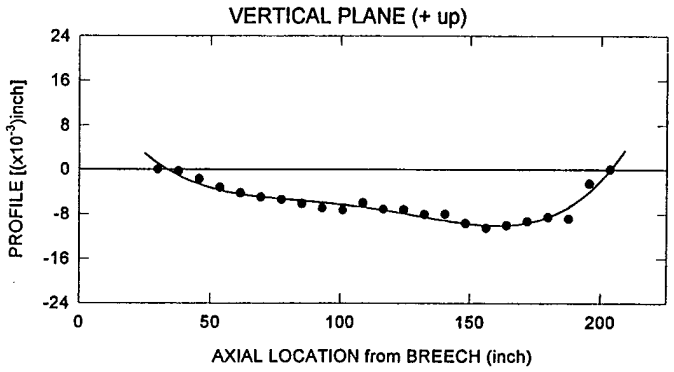

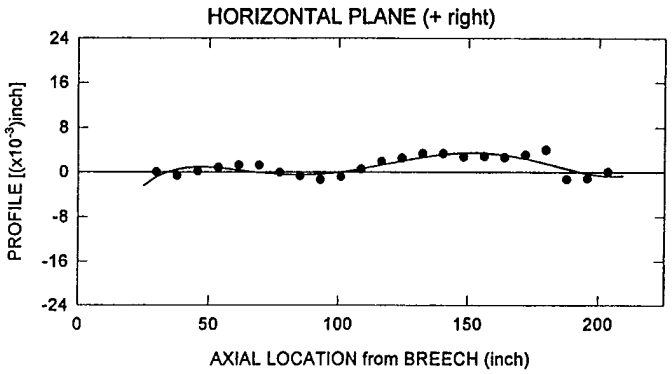

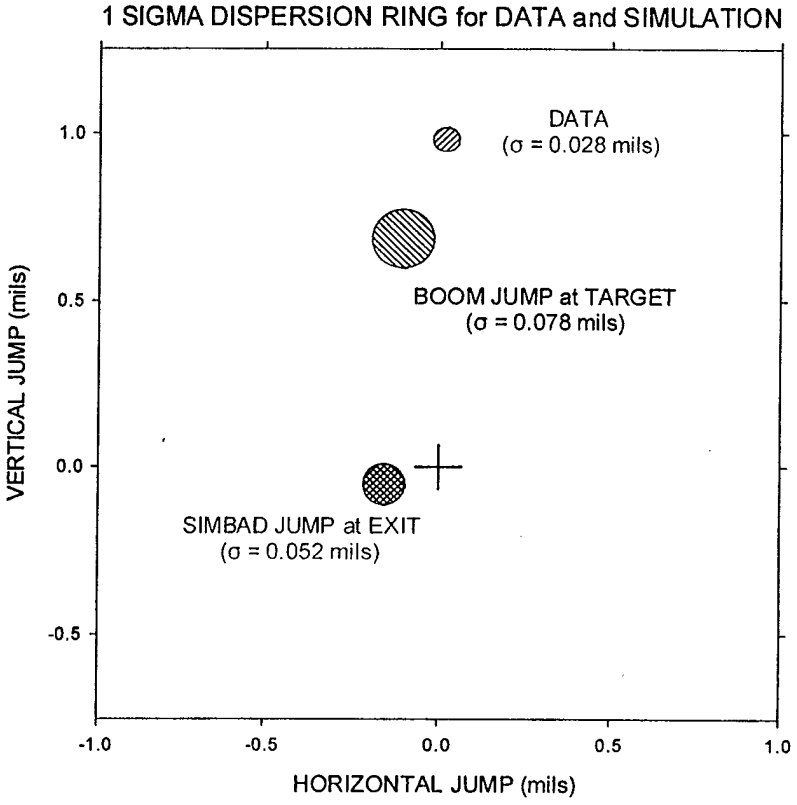

Figure 8g. Comparison of Results for Tube #4990

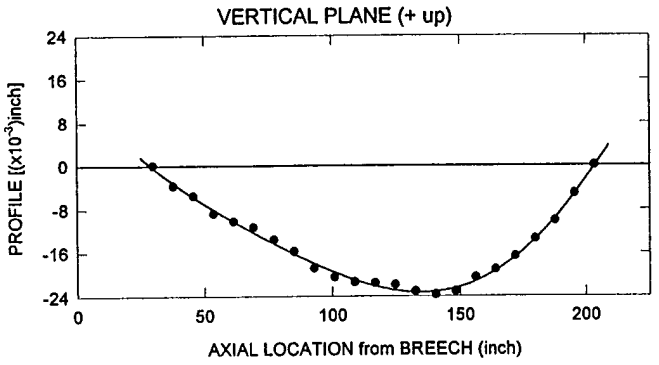

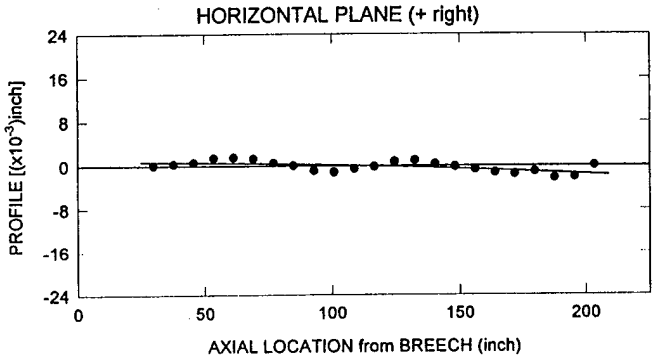

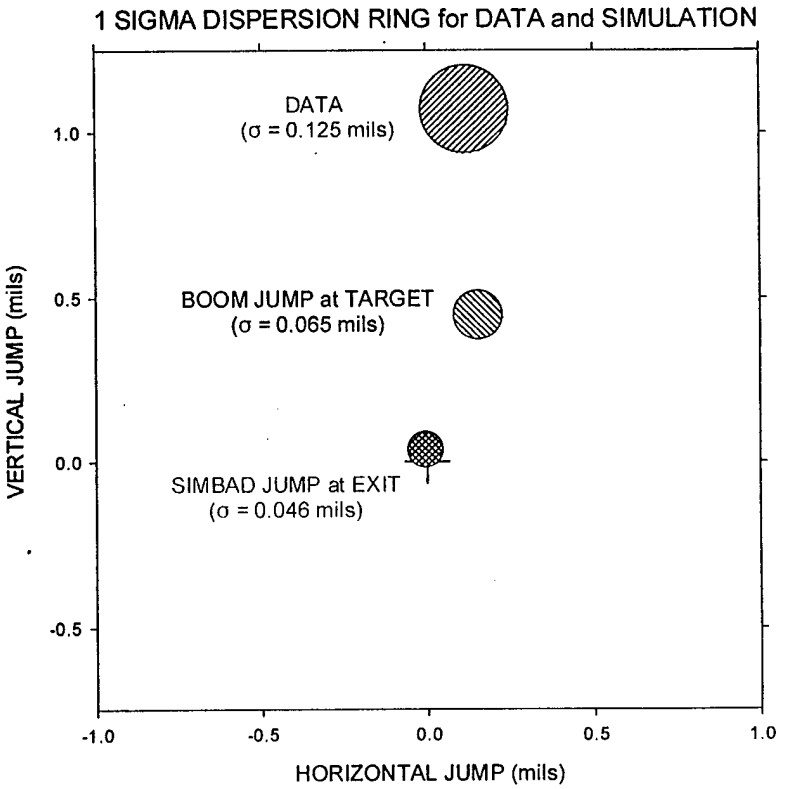

Figure 8h. Comparison of Results for Tube #4992

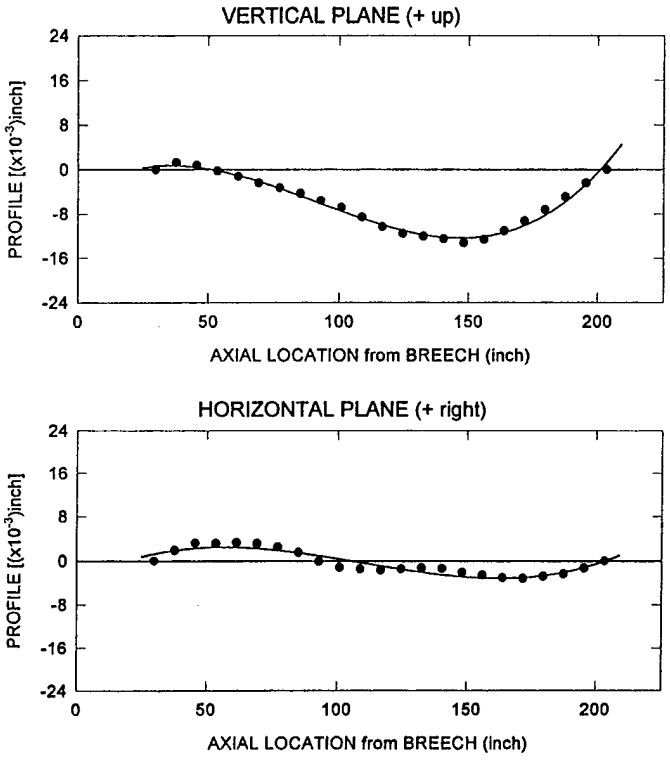

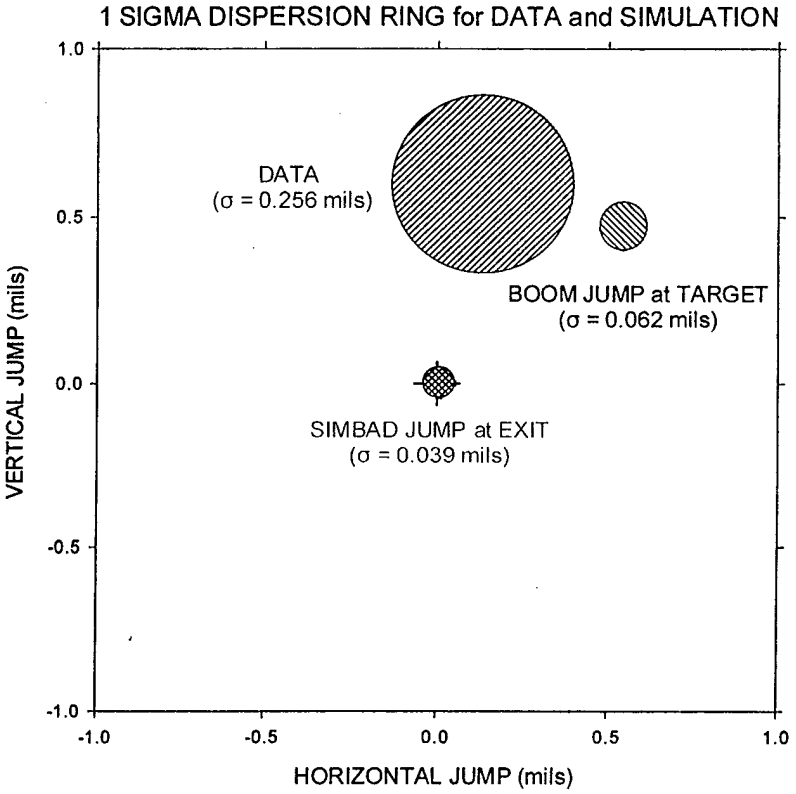

Figure 8i. Comparison of Results for Tube #4994

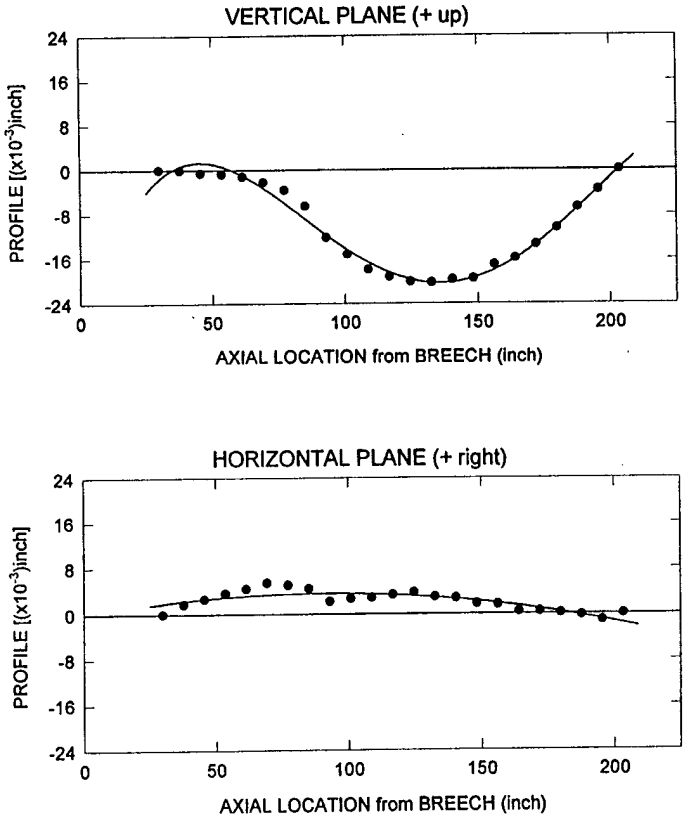

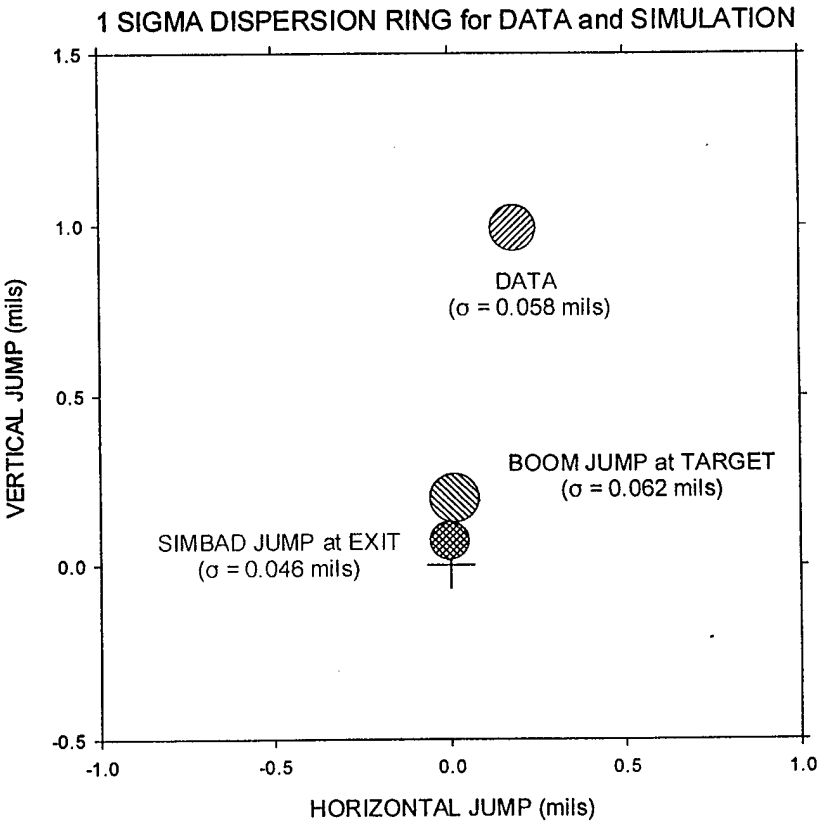

Figure 8j. Comparison of Results for Tube #4996

dispersion calculations from SIMBAD range from 0.039 to 0.052 mils, whereas for BOOM they are 0.058 to 0.078 mils. The range for dispersion in the data is 0.028 to 0.256 mils.

An overall view of the analytical results for projectile jump is shown on figure 9. The leftmost chart contains the mean jump values as indicated from SIMBAD's calculation of the projectile's exit condition. The rightmost chart contains the mean values of the projectile's impact point from the BOOM analysis. The impact window is 2.0 mils by 2.0 mils. The SIMBAD results predict very little perturbation since the mean jump values for all ten tubes are clustered around the cross hairs. However, the same cannot be said for the BOOM results. The mean values for projectile impact from BOOM analysis are scattered about with none near the aim point. Recalling from figure 1, the data values for impact locations are widely scattered as well.

A much better way of comparing the worth of these analytical results is to plot the differential jump mean values on an impact plot. Figure 10 contains this information. A differential jump in the mean is defined as the difference between the mean jump results from firing data and analysis. The leftmost chart contains these values using the SIMBAD analysis whereas the rightmost chart contains the same using BOOM. If either model was a perfect predictor then all differential values would be at the cross hairs. As expected this is not the case. Since SIMBAD's raw jump values did not produce very much perturbation in the projectile's exit condition, the differential values from SIMBAD very nearly replicate the firing data. SIMBAD's differential values for nine of the ten tubes reside well above and to the right of the cross hairs with the lone value just left of it. A one sigma deviation ring plotted about the axis indicates the dispersion in this differential data. For the SIMBAD results its value is 0.758 mils. On the rightmost chart the differential jump mean values for the BOOM analysis are shown. The deviation ring using this analysis is 0.532 mils. A 30 percent improvement in simulation accuracy in predicting the mean jump values for a series of test shots over the SIMBAD results.

RECOMMENDATIONS AND CONCLUSIONS

The topics of gun dynamics modeling, bore profile estimates, projectile flight trajectory modeling, probabilistic analysis, and an integrated approach to estimating shot accuracy and dispersion have been cited in this report. This section contains discussions of the analysis in which the above topics have been included and conclusions based upon the findings from these analysis. The main points of the report will again be discussed in light of their relevance to the topics.

The first point concerns the relevance that bore profile and curvature has upon tube acceptability through the use of gun dynamics and projectile flight trajectory analysis. It is impossible to manufacture perfectly straight gun tubes due to the their slenderness ratios and propensity to warp during manufacture. Current design specifications restrict the amount of profile deviation between measurement points and along the total length of the tube. The real culprit in regard to dynamic excitation is not profile straightness but rather local curvature. A gun tube may pass profile inspection but it may possess high degrees of curvature along its entire length. A projectile forced to ride along this 'bumpy path' will most certainly cause self-induced vibration and vibration to the tube as well.

Bore profile data for the ten tubes used in the test was presented along with a method of determining a correct functional fit of the data points using the Chi-Square statistic. Parameters of this method includes both the number of inspection points and the accuracy of the inspection readings. By twice differentiating the profile fitting function tube curvature is calculated. This tube parameter which was different for each tube proved to be critical in the overall analysis. The mean jump values for each gun tube were different much like that of the data. The intent of the DIT test was to verify a tube indexing method which enhances accuracy. Results from studying a portion of the data indicates a definite migration of shot impact locations dependent upon the indexing method.

It may be concluded that a better method of specifying bore straightness based upon local and overall curvature needs to be developed. Possibly, the same type of algorithm to calculate profile and curvature used in this analysis may be incorporated in the inspection loop during tube manufacture. Curvature calculations may be reported as well as profile data with an acceptance criterion based upon curvature.

The second point involves the complexity of the models. The SIMBAD gun dynamics model is an fem type analysis

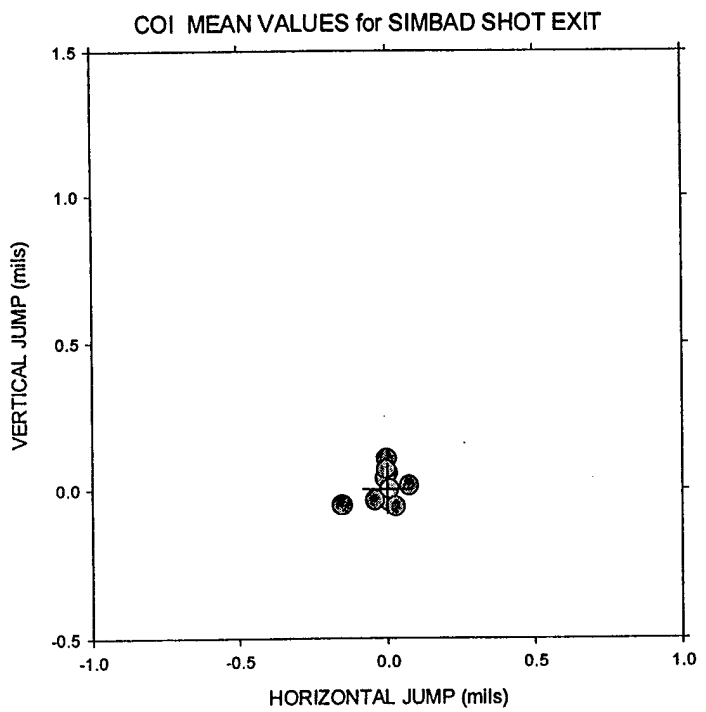

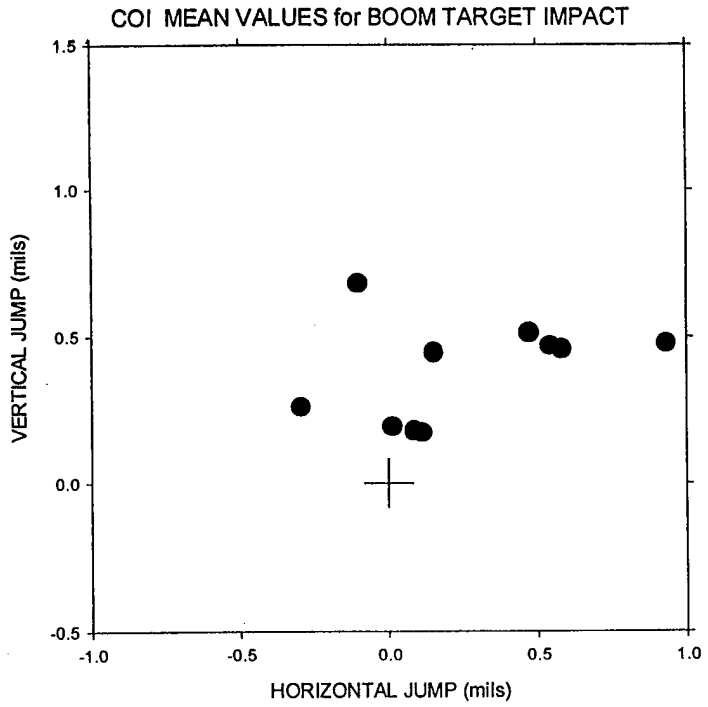

Figure 9. Comparison of Calculated Impact Mean Values Results of Both Models for All Tubes

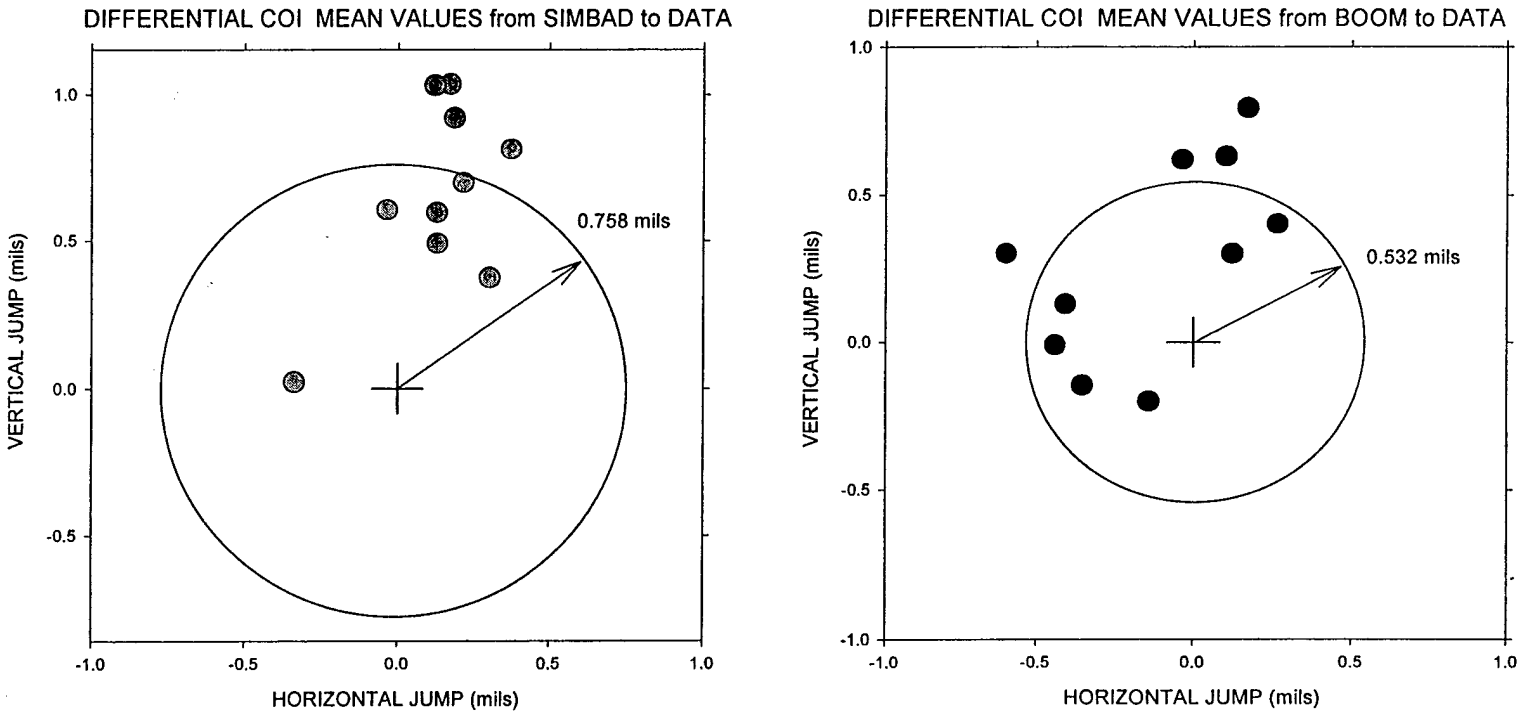

Figure 10. Comparison of Differential Results for Impact Mean Values for All Tubes

in which the structure is defined using beam finite elements. (Either the Euler-Bernoulli or Timoshenko formulation may be specified.) The calculation burden using this type of element is small compared to full three dimensional (3D) elements. The degrees of freedom are on the order of hundreds instead of thousands for the 3D models. The BOOM external flight model assumes that the projectile is a rigid body possessing only six degrees of freedom. Again this minimizes the computational burden in predicting flight trajectories to the target. Although neither model is extremely complex it seems to contain enough of the physics of the problem to be quite beneficial in predicting shotfall patterns and dispersions. Additionally, due to its computational speed the time per run is small. Anyone versed in the use of these models may conduct studies involving 250 to 300 runs per day. This is beneficial when simulation is needed in a design environment to assess critical design parameters and determine sensitivities.

The third point involves the physics that was absent from these analyses. Since the test results was conducted on a round comprised of a long rod penetrator, a flexible projectile was used in the SIMBAD model. The current version of SIMBAD does not support gravity on this type of round, moreover, the direction cosines of the penetrator at projectile exit are not calculated. The BOOM analysis uses direction cosines as initial conditions and the off diagonal terms seem to be quite important in predicting flight trajectories. For the analysis conduct herein the direction cosine matrix was assumed to be a diagonal matrix of ones. The environmental conditions at the test site were unknown, therefore, standard atmosphere and no wind was used in the BOOM analysis. Sensitivities to these parameters were not determined nor used in the dispersion studies. The stiffness response of the sabot's bore riders to the gun tube were based upon a static test conducted at ARL. Benet Labs has funded a more detailed fem for this round using both pressure and acceleration as driving forces. This should improve the sabot/tube interface force/penetration values, the results of which may be applied to subsequent SIMBAD analysis.

The overall purpose of this analysis was to validate a coupled simulation package for predicting the impact location of test data fired from the M1A1 weapon. This has been (to the authors' knowledge) the first system analysis of a coupled gun dynamics and projectile flight simulation codes. The integration of both was not trivial due to the idiosyncracies of each, namely, their dissimilar coordinate systems. At first, the lack of critical data was thought to be a shortcoming, however, after much 'legwork' and shrewd engineering analysis this proved not to be the case. This data was determined and applied to the modeling effort the results of which showed very good correlation with field generated test results. This proves that simulation for accuracy from breech to target is achievable using moderately complex models in the hands of expert weapons' analysts. It is my recommendation that further study including more rounds and more gun tubes is warranted with the intent of gaining improved accuracy (albeit slight) across the full family of rounds for M1A2 tank or any other large caliber weapon in the US Army's inventory.

REFERENCES

1. Schmidt, E., "A Method for Indexing Tank Cannon," BRL IMR 912, Ballistics Research Laboratory, Aberdeen Proving Ground, MD, 1988.

2. Webb, D., Thomas, J., Carter, R., "M1A1 Tank DIT Experiment: Analysis and Results," BRL-MR3962, US Army Lab Command, Aberdeen Proving Ground, MD, 1992.

3. Gast, R., "Curvature-Induced Motion of 60mm Guns, Phase 1: Test Results," ARDEC Tech Report ARCCB-TR-92048, Benet Labs, Watervliet, NY, 1992.

4. Gast, R., "Curvature-Induced Motion of 60mm Guns, Phase 2: Modeling," ARDEC Tech Report ARCCB-TR-94002, Benet Labs, Watervliet, NY, 1994.

5. Simkins, T., "Transverse Response of Gun Tubes to Curvature-Induced Load Functions," *Proceedings of the Second US Army Symposium on Gun Dynamics*, ARLCB-SP-78013, Benet Labs, Watervliet, NY, 1978 pp I-66 to I-77.

6. Borse, G., *Fortran 77 and Numerical Methods for Engineers*, PWS-Kent Publishing Co. Boston, MA 1985, pp 469-471.

7. Lyon, D. "Radial Stiffness Measurements of 120mm Tank Projectiles," ARL-TR-392, Army Research Laboratory, Aberdeen Proving Ground, MD, 1994

8. Wilkerson, S., Army Research Lab Aberdeen, MD, & Gast, R. Benet Labs Watervliet NY, private conversation, 1995.

Crusader Platform Stability and Active Gun Pointing Response Analysis

Gregory S. Johnson and Rickie L. Stuva
United Defense, L.P.
Armament Systems Division
4800 East River Road
Minneapolis, MN 55421
(612) 572-6593

The Crusader Self-Propelled Howitzer under development for the U.S. Army is being designed for higher rates of fire, longer range, and greater mobility than previous ground based systems. Although intended as primarily an indirect-fire field artillery weapon firing from an emplaced position, these requirements have dictated a gun system with active stabilization, subject to repeated large firing shocks and on-board disturbances from automated ammunition loader mechanisms. In this study, a simulation coupling the pointing servo control of a flexible cannon with a multibody representation of tracked vehicle suspension and ammunition loader dynamics is described. Pointing control response to gun firing and disturbance transients is evaluated, along with overall vehicle motion, hydropneumatic suspension damping performance, and loading of the gun drive structures.

This paper has been submitted to the 9th U.S. Army Gun Dynamics Symposium for consideration as a work in progress. It was previously presented on October 14, 1998 at the 69th Shock and Vibration Symposium held in St. Paul, Minnesota.

INTRODUCTION

The Crusader Self-Propelled Howitzer (SPH) is a high mobility, 155 mm field artillery system currently under development for the U.S. Army. An illustration of the prototype configuration is provided in Figure 1. It is intended primarily to engage targets beyond line-of-sight, firing from a stationary position out to ranges of up to 40 km. Accuracy requirements at these ranges have constrained gun pointing errors to a relatively small allocation. Conventional artillery has been able to meet similar error allocations via precision pointing systems which are typically unstabilized. However, other Crusader requirements challenge the ability of a passive system to meet the pointing accuracies required. Mobility capability needed to keep up with the rest of the U.S. Army maneuver force requires the use of a relatively soft hydropneumatic tracked suspension optimized for ride quality. Survivability time lines necessary to meet "shoot and scoot" tactics have also precluded the use of spades or other platform stabilizing devices which reduce vehicle reactions during gun firing, but add deployment and stowage time. In addition, a high 10 to 12 rounds per minute sustained firing rate requires on-board automated ammunition handling equipment moving with sufficient momentum to disturb the vehicle from static equilibrium. To meet these somewhat conflicting requirements for the Crusader SPH, a gun pointing control system is being developed which inertially stabilizes the cannon throughout the loading and firing sequence.

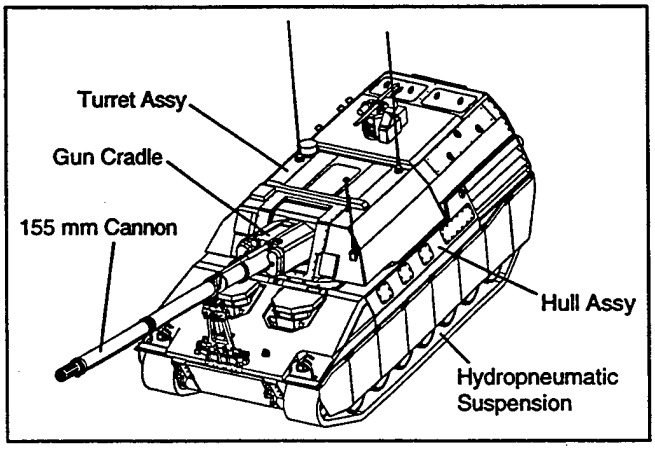

Figure 1 Crusader SPH Prototype

Because vehicle platform disturbance is a significant factor on gun pointing performance, a high fidelity closed loop SPH gun pointing control model with coupled tracked suspension dynamics was created. The primary goal of

this model was to study the interaction between gun pointing and vehicle motion, and provide analytical verification of the pointing servo control laws prior to hardware testing. Important uses for this model have included study of closed loop vehicle and gun pointing response to gun firing and ammunition handling disturbance transients, actuator and cannon support structure dynamic loading characteristics, suspension damping effects on gun pointing, and dynamic space claim definition of the inertially stabilized cannon assembly. Intended future uses will include verification of real-time simulation models, as well as providing a basis for comparison with system test results.

Initial modeling efforts to be presented in this study focused on a two dimensional pitch-plane model of the Elevation Gun Pointing Control System (GPCS), for two reasons. First, the pitch-plane model was to be used as a starting point for a full three dimensional model, proving out the analytical method before attempting the more difficult task of coupling elevation and traverse dynamics with six degree-of-freedom hull motion. Second, the error allocation for gun elevation is more stringent than the allocation given for traverse error because errors at the target are more sensitive to range than deflection. The elevation loop is therefore more critical to overall gun pointing accuracy. Also, gun pointing elevation ranges from -3 to 75 deg for the Crusader SPH, while the traverse angle is limited to +/- 20 deg, with most firings occurring near centerline. While roll motion will couple in to the elevation loop and will need to be considered in the full three dimensional model (currently in-process at United Defense), pitch motion of the vehicle has the most significant impact on gun pointing, and was therefore considered first.

The modeling technique used builds on three main submodels, originally developed for related Crusader analysis activities. A control algorithm development model of the elevation servo control laws, elevation drive actuator dynamics, and sensor characteristics resided in MATRIXx, a control simulation tool from Integrated Systems, Inc. (ISI). Gun tube and cradle structural flexure were represented using beam elements in an MSC/NASTRAN finite element model. Modal analysis allowed these important structural dynamics to be imported to the MATRIXx model via normalized equations of motion, capturing flexure at the cannon muzzle, cradle trunnion, and sensor mounting points. Dynamic response of the SPH suspension was developed originally for an open loop, rigid body firing stability simulation using the Dynamic Analysis and Design System (DADS) tool from Computer Aided Design Systems, Inc. (CADSI). The DADS Track Superelement tracked vehicle suspension module was used to capture the non-linear stiffness and damping characteristics of the SPH suspension units, as well as track compliance and track-soil constitutive effects. An enhanced version of the commercial track superelement, developed by McCullough and discussed in companion paper [1], allowed capture of track tensioning effects unique to Crusader along with improved track shear stiction modeling. Both effects were important for predicting gun firing response of the stationary SPH. Hull and turret structure were left in the DADS model as rigid bodies for this analysis. Coupling between the MATRIXx gun pointing model and the DADS suspension model was then accomplished via the DADS/Plant software tool, also from CADSI, which allowed the vehicle dynamics to be included as an integral part of the servo control "plant" dynamics representation. Figure 2 illustrates the interconnection between the submodels.

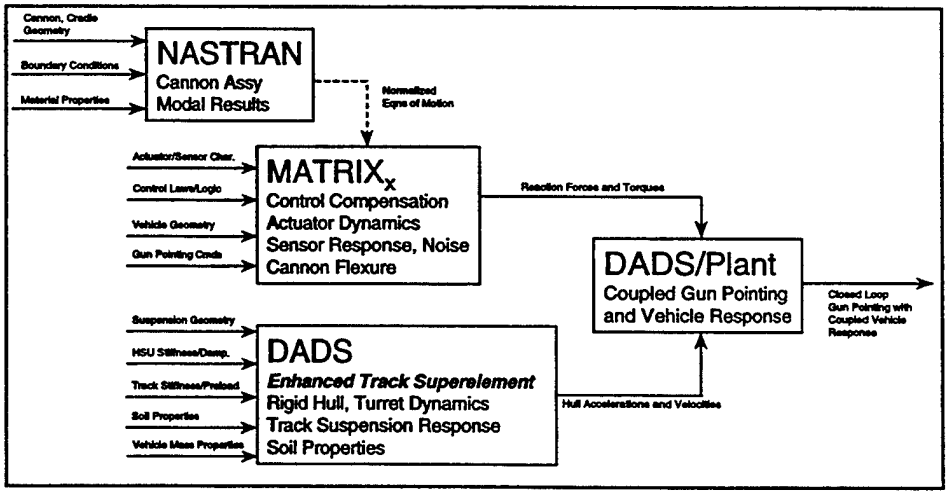

Figure 2 SPH Platform Stability Model Data Flow Diagram

MODEL DEVELOPMENT

Gun firing response of the Crusader SPH involves a complex reaction between suspension, soil, structure, and servo control. A free body diagram of the SPH during gun firing is shown in Figure 3. As indicated, gun recoil resistance forces are transmitted to the vehicle trunnion along the line of the gun bore axis. For on-centerline firings

at 0 deg traverse, the vehicle reaction is a combination of primarily vehicle pitch angular motion, vertical translation (heave), and longitudinal translation (surge). Vehicle weight along with suspension normal and shear reactions from the supporting soil are the remaining external forces acting on the SPH during and after the gun firing transient. Gun pointing motion and internal disturbances from ammunition handling mechanisms will also produce small transients to the vehicle response. Ballistic "gun jump" due to the interaction between projectile and gun tube was not modeled for this analysis, and was assumed to be sufficiently damped so as not to significantly affect gun pointing prior to subsequent firings. Effects of gun jump on precision accuracy during the shot are currently analyzed in a separate gun tube dynamics model.

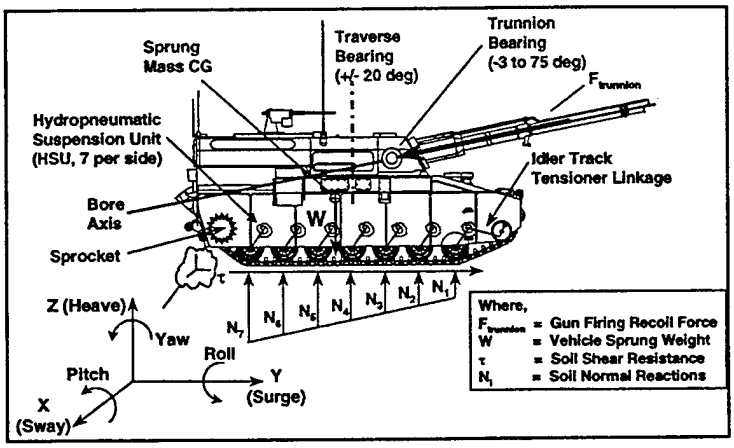

Figure 3 SPH Gun Firing Free Body Diagram

Vehicle and Suspension Dynamics

The tracked suspension being developed for Crusader is a passive, trailing road arm design common to modern high mobility military vehicles. However, instead of using conventional torsion bars and shock absorbers, the Crusader road arms will instead be self-contained hydropneumatic suspension units, or HSU's. Settling response of the vehicle is determined mainly by the stiffness and damping characteristics of the HSU's, and to a lesser extent by track tension and supporting soil characteristics. The stiffness and damping properties of the prototype Crusader suspension are shown in Figures 4 and 5. Note that both have significant non-linearities due to the hydropneumatic design. The spring rates mimic "hardening springs", with increasing rate as the road wheel load is increased, reflecting the pneumatic characteristics of the unit. Although non-linear, an estimate of the suspension natural frequencies for pitch and heave of the vehicle were estimated by linearizing about the static equilibrium position. Because the active pointing system is expected to reject vehicle disturbances, the suspension natural frequency estimate provided a lower bound constraint for the servo control bandwidth.

As shown in Figure 5, the damping characteristics are driven by orifice damping initially, with a velocity-squared dependent "rise rate", reflecting the hydraulic characteristics of the unit. Note that the rise rate is much steeper in jounce (upward road wheel displacement relative to vehicle) than in rebound (downward road wheel displacement relative to vehicle), due to differences in effective orifice area. The rise rate has been set to provide optimal ride characteristics. Although optimal for ride, the rise rate setting and velocity squared properties of the orifice damping mean that the HSU's will provide lower effective damping rates for small road arm velocities. This characteristic is less optimal for vehicle settling near equilibrium and increases susceptibility of suspension response

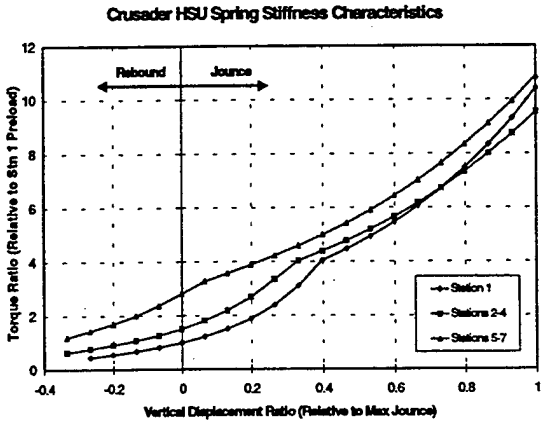

Figure 4 HSU Stiffness Characteristics

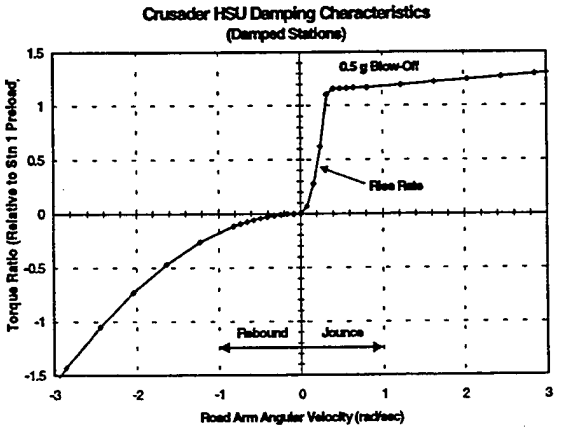

Figure 5 HSU Damping Characteristics

to on-board disturbance, both of which are influenced by low velocity damping. Note that HSU Stations 3, 4, and 5 (not shown in Figure 5) are considered undamped, with only slight damping in both rebound and jounce.

Another unique characteristic of the HSU jounce damping is the "blow-off" level, also shown in Figure 5. At a specific internal HSU chamber pressure, a poppet valve is set to open or "blow-off", causing flow to bypass the damping orifice and greatly increase the effective flow restriction area. This is realized as a corner in the damping curve, with the damping torque becoming relatively constant or slowly increasing for road arm velocities greater than the blow-off velocity. For analysis and design purposes, the blow-off level is identified as a factor of the static preload pressure, or "g's". As in the rise rate case, the blow-off level has been set analytically (at 0.5 g's) to provide optimal ride characteristics. Both stiffness and damping characteristics were modeled as look-up curves in the DADS track superelement model, applying the reaction torque between hull and road arm as a function of road arm angular displacement and velocity. The non-linearities, particularly in damping, have a significant impact on vehicle response and settling after gun firing.

Suspension dynamics of the stationary vehicle during gun firing are also dependent on the supporting soil and track tension. As indicated in Figure 3, shear resistance and normal reactions of the soil are present, which will affect how much of the vehicle reaction energy is transmitted between vehicle angular motion and translational sliding. In the DADS model, the normal pressure is computed using Bekker's [2] soil pressure-sinkage relationship, while the shear stress is modeled using the Baladi and Rohani [3] approximation for shear-slip, from the following:

$$\text{Normal:}\quad P=\left(\frac{k_c}{W}+k_\phi\right)z^n \quad (1) \qquad \text{Shear:}\quad \tau=\frac{G\tau_m\Delta}{\tau_m+G|\Delta|} \quad (2) \qquad \text{where,}\quad \tau_m \cong C+P\tan\phi \quad (3)$$

In Eq. (1), the bearing pressure, P, is a function of the soil sinkage, z, and a constant track width, W. Empirically determined soil constants also exist in the form of a soil cohesiveness coefficient, k_c, internal soil friction coefficient, k_ϕ, and n, the pressure-sinkage coefficient. Because the combat loaded SPH is in the 50 to 60 metric tonne range, firm soil factors where used. Per Bekker's previous findings [2], large values of k_ϕ were assumed to approximate soil compaction.

The shear stress existing between the track and soil, τ, is a function of both the shear slip displacement, Δ, and the shear strength of the soil, τ_m, calculated using the relation in Eq. (3). Constant soil properties for the initial shear modulus G, cohesiveness soil strength C, and angle of internal friction ϕ are again empirically determined constant coefficients. Note that the shear strength is a function of the normal pressure. As modeled in Eqs. (2) and (3), shear resistance between track and soil ramps up and eventually saturates at a maximum value as a function of the shear displacement. Vehicle slipping and the amount of energy transferred between slipping and pitching will therefore depend on this development of the shear resistance, and is a main reason for using the DADS track superelement for modeling emplaced firing dynamics of the Crusader SPH.

The normal pressure and shear stress in Eqs. (1) and (2), are transferred to the track and road wheels, both at the segments of track directly underneath the wheels (N_i in Figure 3), and also through bridging effects between the wheels. See references [4] and [5] for further details regarding the track-soil interaction, and other aspects of the track superelement implementation. It is worth noting that in the commercial version of the DADS track superelement, a numerical inefficiency in the shear - track tension computation for the stationary firing response caused problems in the DADS/Plant implementation by creating convergence errors during the MATRIXx integration. The enhanced version discussed in [1] improves the shear model, allowing its use for stationary vehicle modeling. Because of the sensitivity of the vehicle firing reaction to ground shear, and the difficulty in estimating empirical coefficients for compacted soil, this portion of the model is likely one of the largest sources of error for modeling stationary firing. Improving this model and obtaining soil properties which accurately reflect the soil response for the emplaced SPH are an on-going area of study at United Defense.

Track tension as well has a significant effect on the response dynamics due to the idler track tensioner linkage, also diagrammed in Figure 3. Track tension can drop dramatically as the vehicle goes into jounce from gun firing or mobility maneuvers, increasing the chances of track throw. The tensioning linkage seeks to maintain tension in jounce, by connecting the first HSU station to the idler which is free to rotate about a pivot. As the first station deflects in jounce, it rotates the idler outward, engaging the track and increasing overall track tension. Therefore, as the vehicle heaves, track tension is maintained or increased instead of unloading, while also effectively stiffening the first HSU. This effect is not part of the commercial track superelement model, but was included as part of the enhanced model discussed in [1].

Structural Flexure

Structural resonances will have a significant impact on the gun pointing dynamics and control response for the Crusader SPH, particularly due to a relatively long cannon length needed to meet the 40 km range requirement. In order to initially predict which structural modes will significantly impact pointing, an MSC/NASTRAN beam element model of the cannon with supporting cradle structure was developed. A modal analysis was then performed to obtain the cannon assembly modes and mode shapes. The first three modes (one rigid body, two elastic) which are significant for the cannon response in elevation are shown in Figure 6. Note that corresponding transverse elastic modes exist at approximately the same modal frequencies, but were ignored for the elevation plane description. Because the actuator compliance and reflected motor inertia of the elevation gun drives are modeled separately, the cannon assembly boundary conditions were established as "free-free" with a rotational pin constraint at the gun trunnions, allowing a single rigid body mode representing the gun elevation displacement ($F_0 = 0$, as shown). The other cannon modal frequencies are shown as factors of the first elastic mode (F_1) produced when the cannon structure is coupled with the actuator compliance modeled in MATRIXx.

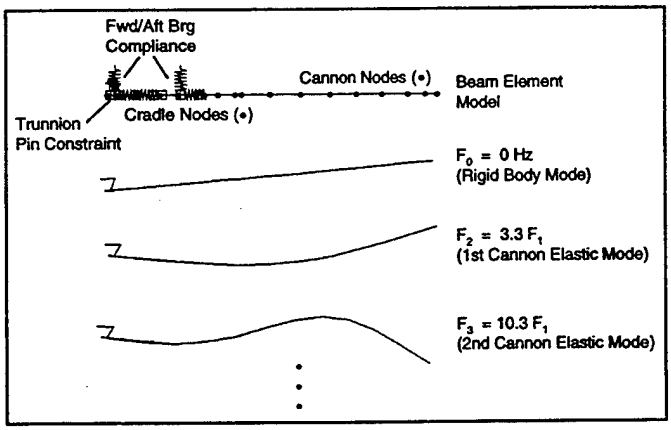

Figure 6 Cannon Assy Modeshapes (Elevation Plane Only)

To include these structural modes in the MATRIXx servo control model, equations of motion describing the rigid and elastic response of the cannon assembly were assembled. Using the procedure described by Meirovitch [6] and others, the equations of motion for the continuous structure can be approximated as

$$[m]\{\ddot{q}(t)\}+[c]\{\dot{q}(t)\}+[k]\{q(t)\}=\{Q(t)\} \tag{4}$$

where {q(t)} is the generalized coordinate vector defining the position of each of the nodes in the finite element model (in physical coordinates), [m], [c], and [k] are the inertia, damping, and stiffness matrices, respectively, and {Q(t)} is the vector of time dependent generalized forces acting on the structure. Next, the eigenvector matrix [u] (normalized with respect to inertia), and the diagonal eigenvalue matrix [ω^2] were obtained from the finite element modal analysis, truncated at the first six modes to capture only the response frequencies of interest through 115 Hz. By transforming the generalized coordinates into principal coordinates via {q(t)} = [u]{η(t)}, substituting into Eq. (4), and then premultiplying by $[u]^T$, the decoupled, normalized equations of motion were realized as

$$\{\ddot{\eta}\}+[2\zeta\omega]\{\dot{\eta}\}+[\omega^2]\{\eta\}=[u]^T\{Q(t)\} \tag{5}$$

where [2ζw] is a diagonal matrix, assuming only structural damping between nodes. For the cannon assembly, ζ was set to a constant 2% of critical damping, based on log decrement correlation with hammer tests performed on similar gun systems. Eq. (5) was then implemented in the MATRIXx model for the node locations corresponding to the trunnion, inertial reference unit (IRU) sensor mounting location, and muzzle. Control and reaction forces at the trunnion were input using the transformation term on the right hand side of Eq. (5). After solving for and integrating the principal coordinates, the generalized coordinate displacements at the three locations were derived using the coordinate transformation equation above.

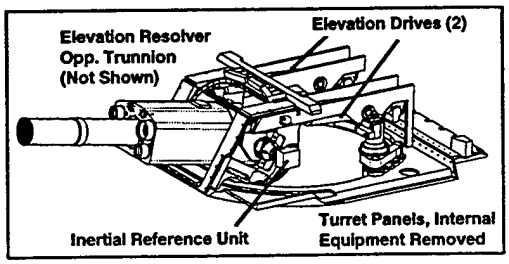

Figure 7 SPH Gun Drives

Gun pointing in elevation is accomplished by two electric drive linear actuators, attached between the gun mount cradle structure and beams on the turret roof, as shown in Figure 7. Compliance of the drives and mounting structure was approximated by estimating the actuator, gun cradle attachment lug (not included in the cannon

finite element model), and turret beam structural compliances via static finite element analysis. An effective drive stiffness was then calculated assuming that the connected components act in series. When used to couple the motor inertia and the flexible cradle and gun tube, the effective drive stiffness added an additional flexure mode, as discussed previously. This new first elastic mode, F_1, was characterized by near rigid body motion of the cannon assembly, primarily flexing the actuator and mounting structure. In order to keep the gun pointing system stable, the servo control laws will need to roll off or attenuate the control response sufficiently near the structural resonance frequencies. Thus, mode F_1 provided the upper bound frequency constraint for the servo control bandwidth.

Gun Pointing Servo Control

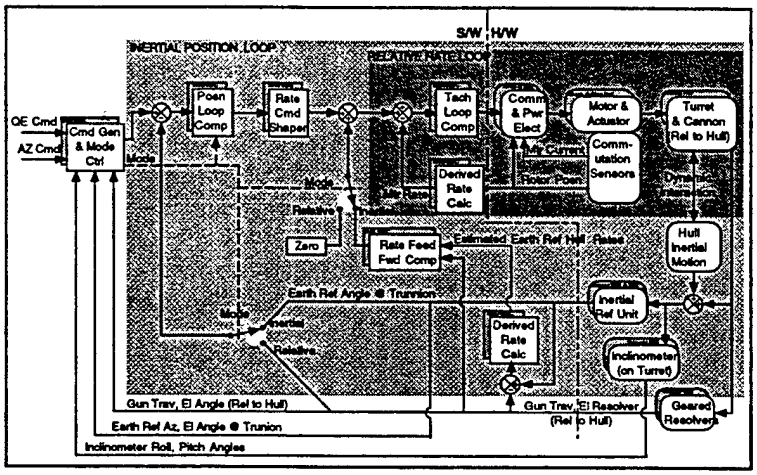

Figure 8 Gun Pointing Control System With Strong Stabilization

Active inertial stabilization for gun pointing is achieved using a method known as "Strong Stabilization" developed by Oslon [7], and first realized in a fielded system by Bigley and Schupan [8]. In this implementation , an outer position loop attempts to decouple the gun from vehicle motion disturbances using angular position feedback from the Inertial Reference Unit (IRU) while an inner rate loop is closed by deriving an estimated motor shaft angular rate from the motor commutation resolver. Without additional inputs, however, this inner relative rate loop provides no inertial stabilization. Since the bandwidth of the outer inertial position loop is limited by the system structural resonances, the position loop alone cannot provide sufficient rejection of the hull suspension motion to meet inertial pointing error requirements. An additional "Strong Stabilization" signal is needed to allow the higher bandwidth inner rate loop to provide additional disturbance rejection. This signal is derived by using the IRU data and elevation position resolver mounted on the gun trunnions to estimate hull angular rates. Estimated hull angular rates are then fed forward as an additional motor rate command which cancels the vehicle motion and keeps the gun orientation stabilized in inertial space despite platform disturbance transients. MATRIXx was used to create a high fidelity model of both the control system and actuator hardware which included: the discrete command shaper and controller; electro-mechanical drive actuators with motor inertia, gear reduction, effective stiffness, equilibration, friction, and brakes; gun mount and tube structural flexure with rotor shield stiction; and sensor measurement dynamics. A block diagram illustrating the Crusader GPCS is provided in Figure 8.

As discussed in the previous two sections, the control system must provide enough bandwidth to reject pointing disturbances due to motion of the platform at frequencies up through the suspension modes, while also attenuating control response sufficiently to not excite the elastic modes starting at F_1. Figure 9 presents a Bode plot

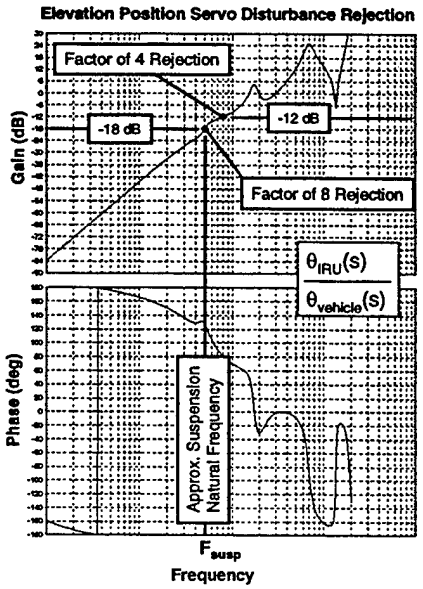

Figure 9 Disturbance Rejection

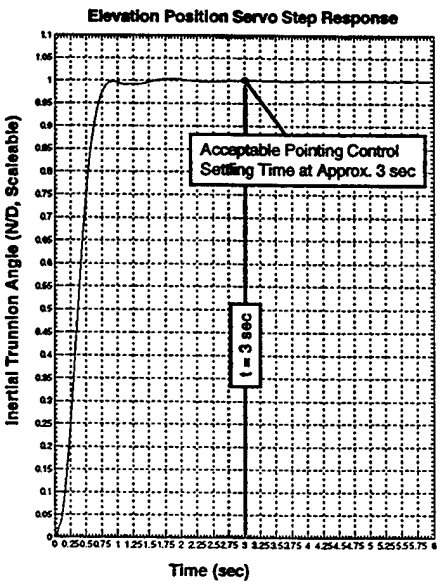

Figure 10 Unit Step Response

of the elevation stabilization error magnitude and phase for a linearized version of the Elevation GPCS, as measured at the Inertial Reference Unit (θ_{IRU}), due to vehicle pitch angular motion ($\theta_{vehicle}$). Hull response was approximated using a single degree of freedom transfer function, tuned to the pitch suspension natural frequency (F_{susp}) with low damping assumed. Note that the suspension pitch mode is close enough to the first elastic mode of the structure ($F_{susp} \cong 0.3F_1$) to influence control gain shaping. As shown, approximately a factor of 8 or more reduction (-18 dB) could theoretically be expected for suspension disturbances using the Strong Stabilization technique. Since relatively small changes in parameters could shift the gain curve, a conservative factor of 4 (-12 dB) was assumed to account for unmodelled dynamics and modeling error. Combined with the step response shown in Figure 10, an acceptable level of vehicle damping was defined which would attenuate vehicle response sufficiently to meet rate of fire requirements. The damping required was then allocated to the suspension design in the form of allowable settling time, amplitude, and frequency thresholds after gun firing shock which would ensure sufficient HSU damping levels.

Coupled Response

Servo control stability and performance was verified under more realistic simulation conditions by using DADS/Plant software to couple the MATRIX GPCS model with the non-linear suspension dynamics of the enhanced DADS track superelement. In the combined model, the track superelement replaces the simplified linear hull motion portion of the "plant" dynamics MATRIXx model (the "Hull Inertial Motion" block in Figure 8). Reaction forces and torques at the trunnion due to drive forces, gun firing recoil force, and acceleration of the cannon assembly were input to the DADS model, which then computed the resulting hull and turret motion for use in the control simulation. With the cannon structural normalized equations of motion embedded in the MATRIXx model as described, coupling between the gun pointing servocontrol, cannon and drive flexure, and suspension dynamics was achieved.

Ammunition handling disturbances were also modeled through DADS/Plant. The most significant source of vehicle disturbance was expected to come from a load arm structure, which transfers propellant and projectiles from magazines to the cannon. The load arm is mounted on centerline with the gun trunnion, and swings from a propellant conveyor near the turret roof to a projectile shuttle at the floor of the hull, and back to the cannon. All motions are in the same plane as gun elevation, with rotational accelerations large enough to provide significant gun pointing disturbance. For the DADS/Plant model, the load arm inertia was modeled in DADS as a rigid body suspended on a revolute joint at the trunnion. A simple proportional velocity control loop in MATRIXx was then used to drive the load arm dynamics with a given velocity profile. Vehicle and gun pointing response with and without load arm disturbance could then be studied to determine the impacts of ammunition handling disturbances on platform stability.

SIMULATION RESULTS

Simulation prediction of the closed loop Crusader SPH Elevation GPCS performance with coupled vehicle motion under different pointing, firing, and disturbance conditions has been performed. To date, the DADS/Plant model has been used for several analyses of closed loop response, including: GPCS response on a stationary suspension, performance verification during gun firing shock at various propellant zones and elevations; vehicle settling and pointing sensitivity to varying suspension damping and track tension settings; definition of gun drive, cradle, and turret mounting limit and fatigue loads after exposure to gun shock; and GPCS performance with load arm disturbance. Preliminary analytical verification of the Elevation GPCS was accomplished by comparing simulated servo error to a representative elevation pointing error allocation for the scenarios studied. Examples of important results from these simulations are presented here for review.

Simulation results of servo control response to severe gun pointing commands on the stationary vehicle are presented in Figure 11. In this scenario, a 444 mil (25 deg) quadrant elevation (QE) step command was followed immediately by a doublet tuned to excite the suspension pitch natural frequency F_{susp}. As indicated in the hull pitch response, there was significant coupling between gun pointing and the suspension, both in the transient created initially by the step response of the GPCS, as well as the pitch resonance created by the doublet command. Pitch amplitude of the vehicle during the doublet reached close to 10 mils. The servo control response indicated by the angle of the cannon bore at the trunnion and the inertial pointing error RMS (measured by the IRU mounted on the trunnion) was stable and well-behaved, despite the suspension motion. During the pitch resonance, the GPCS tracked the command smoothly. Immediately afterward, the pointing error was quickly reduced below the error allocation, despite the remaining vehicle motion. This result indicated that the Elevation GPCS should be capable of

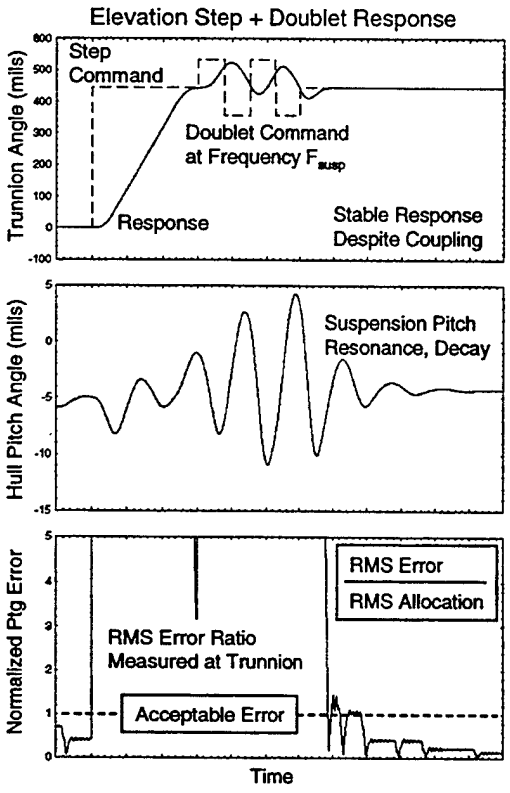

Figure 11 Step and Doublet Response

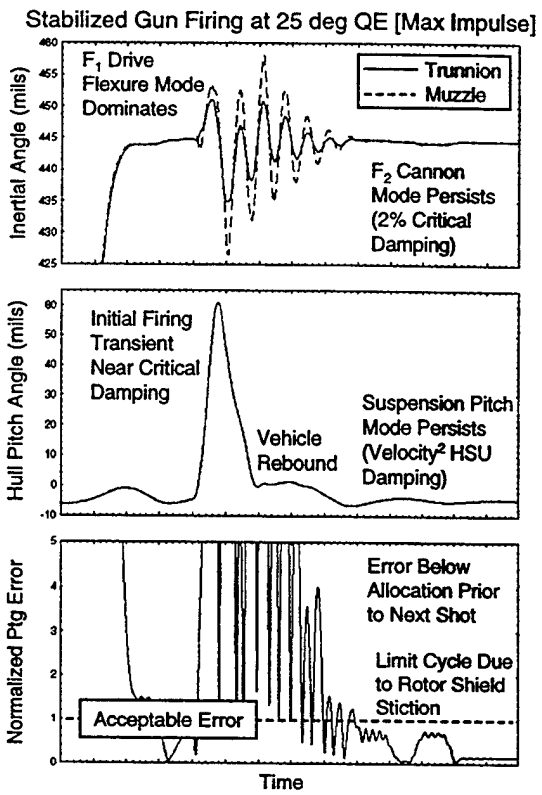

Figure 12 Closed Loop Gun Firing Response

decoupling the cannon motion from the suspension dynamics sufficiently to respond to new gun laying commands, despite vehicle platform disturbance.

Closed loop response to gun firing shock under varying cannon elevations and propellant zone conditions has been studied extensively using the DADS/Plant model. A representative simulation prediction of the vehicle and GPCS response to a maximum impulse gun firing shock at 444 mils (25 deg) QE is presented in Figure 12. As indicated by the hull pitch response, the initial gun firing transient was quickly damped by the suspension, with a secondary smaller transient which persisted. This was primarily due to the non-linearities of the HSU damping, as some or all of the damped road arms exceed their blow-off velocities during the main transient, but then quickly decrease to low velocity and low damping torque corresponding to the velocity-squared portion of the orifice damping (see Figure 5 for reference). Track tensioning effects are evident by the sudden pitch deceleration during vehicle rebound as the idler compensation effectively stiffens the first HSU station.

As expected from the suspension damping behavior, sensitivity studies have shown that changes to the HSU blow-off setting have a primary effect on the magnitude of the initial vehicle reaction, indicated here as an example result in Figure 13. However, it only has a secondary effect on the final settling of the vehicle. Other studies have indicated that varying the jounce damping rise rate of the HSU has a more significant effect, since the lower velocity damping levels are increased. The amount of vehicle sliding with changes in zone and elevation have also had a noticeable non-linear effect on vehicle settling time, perhaps due to changes in the onset of shear saturation. The effects of soil shear on vehicle settling are difficult to predict and will require more study during system test.

As in the step/doublet response, the active stabilization attempts to decouple the cannon motion from the vehicle to keep the pointing orientation fixed in inertial space throughout the firing transient. Although not completely decoupled, the peak inertial cannon motion response amplitude shown in Figure 12 was kept under 10 mils (0.6 deg) amplitude while the vehicle displaced over 60 mils (3.4 deg). Gun pointing error was quickly reduced to within the error allocation well before the subsequent firing, despite a limit cycle caused by

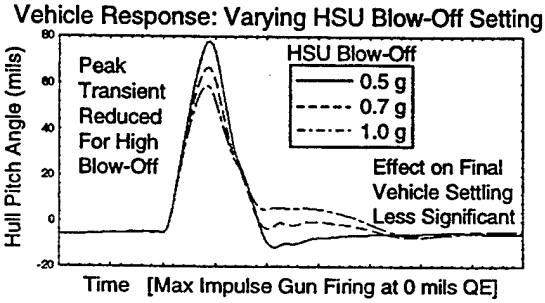

Figure 13 Sensitivity to HSU Blow-Off

stiction between the turret and a seal on the rotor shield covering of the gun mount. The stick-slip at this interface has enough torque to cause a deadband response during fine gun pointing, which was estimated in the MATRIXx model.

Induced tube flexure due to the vehicle reaction and servo response was indicated by the difference between the muzzle and trunnion angles. Resonance of the first elastic mode was evident in the cannon angular response. Although difficult to see in Figure 12, the second elastic mode was also evident, persisting longer than the lower mode due to only 2% critical structural damping. The amplitude was also significantly lower. However, note that the tube motion does not include transients due to the ballistics of the projectile or cannon recoil. Those effects will add to the cannon vibration, but are currently assumed to be a secondary effect on the pointing control error due to their smaller amplitude compared to the response of the first elastic mode. The higher modes were not a factor for the closed loop response.

The structural resonance excited by the gun firing shock illustrates the importance of including the drive compliance and servo control in the firing response simulation. Figure 14 shows a comparison of the elevation drive axial load predicted by a rigid body model, an open loop (drive brakes applied) model with structural compliance, and the full closed loop response model. The case shown corresponds to the maximum impulse, 444 mil gun firing scenario, with actuator loads produced by vehicle pitch and translational accelerations. As indicated, the applied recoil force excited the first elastic mode in the compliant models, creating a higher amplitude response with increased number of cycles compared to the rigid body model. The increased shock response is due to the applied recoil force, which approximates a half-sine shock pulse containing a frequency component close enough to the elastic mode to produce amplification. Active stabilization serves to reduce the peak response. For the lower elevations, the initial peak load was reduced significantly, but the presence of the rebound and track tensioning effects tended to sustain the resonance as indicated in Figure 14. For higher gun elevations which do not experience a pitch rebound as large as the case shown, the peak amplitude was reduced along with the number of significant loading cycles on the drive actuator and gun mount and turret attachments. Thus, compliance and active stabilization both have a significant impact on the fatigue of these structures.

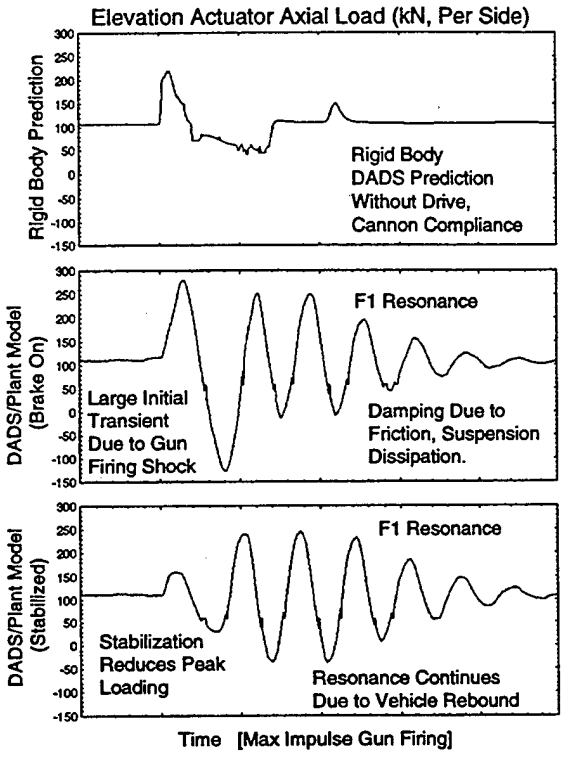

Figure 14 Actuator Loads: Model Comparison

Closed loop response to platform disturbance sources has also been studied to determine their potential impact on the firing timeline. The main pointing disturbances will most likely come from on-board ammunition handling equipment, with the most significant component being the load arm mechanism discussed previously. A representative simulation prediction of the vehicle and GPCS response to a severe load sequence with the gun at 0 mils is presented in Figure 15. As indicated by the load arm motion, the load arm initially swings from a down position at the shuttle (located near the hull floor) up through 90 deg to the breech

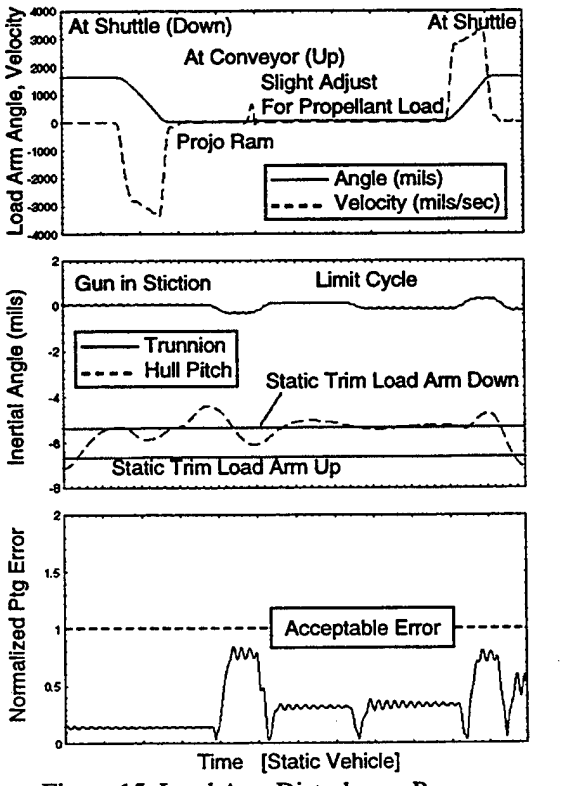

Figure 15 Load Arm Disturbance Response

and propellant conveyor position. A slight adjustment of a few degrees is required after the projectile is rammed to load propellant, and then the load arm swings back to the shuttle position just prior to the next gun firing command.

The effect of the load arm motion is slight, but produces enough disturbance to the vehicle static pitch (or trim) angle to require active stabilization to maintain accurate gun pointing. As shown, the trim angle of the vehicle changes significantly due just to the effective change in vehicle center of mass from one load arm position to the other. Changing the momentum of the load arm during the rotate sequence was then enough to cause transient vehicle pitch motion about these two trim positions, requiring the GPCS to correct the inertial gun pointing angle. However, as shown by the pointing error response, the GPCS provides sufficient bandwidth to reject the load arm disturbance, keeping the RMS error value within the pointing error allocation.

CONCLUSIONS

The simulation model described in this study was used to investigate the effects of gun firing and on-board ammunition handling disturbance transients on gun pointing control laws currently under development for the Crusader Self-Propelled Howitzer. By coupling existing models of the servo control system, structural flexure, and tracked suspension dynamics, initial prediction of pointing control and overall vehicle performance was performed. The effects of the non-linear hydropneumatic suspension characteristics were studied, while the importance of modeling track-ground shear and track tensioner effects for stationary gun firing response prediction was indicated. Modeling the closed loop control along with drive and cannon compliance was also shown to be necessary to accurately predict dynamic loading of the actuators and cannon support structures. With the incorporation of these and other detailed modeling features, the platform stability simulation has been used as a design verification tool prior to hardware testing. Analytical improvements that are currently underway include moving to a full three dimensional model with coupled traverse pointing control, and adding a finite element representation of the remainder of the turret structure. By adding capability incrementally and verifying through test, it is hoped that the platform stability model will continue to be a valuable tool for predicting closed loop gun pointing and vehicle response for Crusader and other future artillery vehicles.

ACKNOWLEDGEMENT

Michael McCullough and Ashok Khubchandani at UDLP/GSD in San Jose, CA assisted in the implementation of the enhanced track superelement model. Thomas Williams and Jeffrey Ireland at UDLP/ASD in Minneapolis, MN assisted in the implementation of the cannon finite element model. Both efforts were key to this analysis.

REFERENCES

[1] McCullough, M.K., "Shock Prediction in Military Tracked Vehicles", *Proceedings of the 69th Shock and Vibration Symposium*, Shock and Vibration Information Analysis Center, to appear, 1998.

[2] Bekker, M.G., *Introduction to Terrain-Vehicle Systems*, University of Michigan Press, Ann Arbor, MI, 1969.

[3] Baladi, G.Y. and Rohani, B., "A Terrain-Vehicle Interaction Model For Analysis of Steering Performance", Technical Report No. GL-79-6, U.S. Army Waterways Experiment Station, Vicksburg, MS, 1979.

[4] McCullough, M.K., and Haug, E.J., "Dynamics of High Mobility Track Vehicles", ASME Design Engineering Technical Conference, Cincinnati, Ohio, 1985.

[5] "DADS Track Superelement User's Manual", Computer Aided Design Software, Inc., Coralville, IA, 1994.

[6] Meirovitch, L., *Elements of Vibration Analysis*, 2nd Edition, McGraw-Hill Inc., 1986

[7] Oslon, A.R., "Shipboard Stabilization of Large Antennas", *American Society of Mechanical Engineers* Paper No. 65-WA/AUT-8, 1965.

[8] Bigley, W.J., and Schupan, F., "Wideband Base Motion Isolation Control For a Mobile Platform", *Proceedings of the 1987 American Control Conference*, American Automatic Control Council, 1987.

The Effect of a Hard Bend in Gun Barrel Centerline

Thomas F. Erline
US Army Research Laboratory
Attn: AMSRL-WM-BC
Aberdeen Proving Ground, MD 21005-5066

A naval cannon was analyzed with the Little RASCAL gun dynamics program to predict shot exit conditions for the US Navy. There appeared to be a manufacturing bend in the barrel's vertical plane. The Little RASCAL program makes modeling hypothetical cases easy. It was simple to modify the vertical centerline and quickly re-analyze. This paper compares the projectile and barrel interacting forces with and without the effects of the sharp bend. More importantly, a small sine wave preceding the bend in the centerline presents itself as a detrimental factor by amplifying the lateral forces.

INTRODUCTION

This paper considers a number of hypothetical cases where the centerline of a gun barrel changes from what the author considers as bent to an unbent state. All other parameters remain the same. In the process of analyzing these hypothetical cases, a concern came up as to why the magnitude of the lateral forces were not diminished by a significant amount It was found that a small sine wave initiates high oscillatory lateral forces. This study, which can be considered a simple functional analysis with the Little RASCAL gun dynamics code [1] operating on a change in the centerline and presenting the resultant barrel-projectile interaction forces as the range, will indicate that a small sine wave in a centerline drives lateral forces more than a single bend in a centerline

The basis of the analysis starts with the simulated firing of the Mk64 projectile from the U.S. Navy's new 5 inch 62 caliber gun mount, the EX45 Mod4 [2]. A prototype 62 caliber barrel (serial number 17448) was mated to the EX45 Mod4 gun mount, and was recently range tested. This was a major milestone for development as part of the Naval Surface Fire Support (NSFS) Program.

The U.S. Army Research Laboratory (ARL) Little RASCAL gun and projectile dynamics simulation program was used to model this gun system's lateral dynamics and provide the shot exit conditions when fired at service charge. This work was sponsored by the Naval Surface Warfare Center Dahlgren Division (NSWCDD)[3].

BACKGROUND

The objectives of the NSFS program require that 5-inch naval guns provide fire support from greater off-shore distances and hit targets at an increased range with increased lethality. The key elements satisfying these objectives are an upgrade to the existing 5"/54 Mk45 Mod2 gun mount and the development of the rocket assisted projectiles(RAP).

NSFS modifications to the Mk45 gun system include structural enhancements to increase the allowable chamber pressure and ballistic impulse, replacement of the 54-caliber barrel with a 62-caliber

barrel, and development of an adaptive digital control system that supports a new Gun Computing System (GCS) and RAP interface requirements. These modifications plus development of certain RAPs will allow the gun system to support engagement ranges of up to 63 nautical miles for certain RAP rounds and potentially up to 21 nautical miles with future ballistic projectiles. Figure 1 illustrates the components of the EX45 Mod4 gun mount.

The 5"/62 EX45 Mod4 gun mount is being developed for the U.S. Navy by the Armament Systems Division of United Defense, LP. The original work supports a recent firing test at NSWCDD Dalgren, Va.

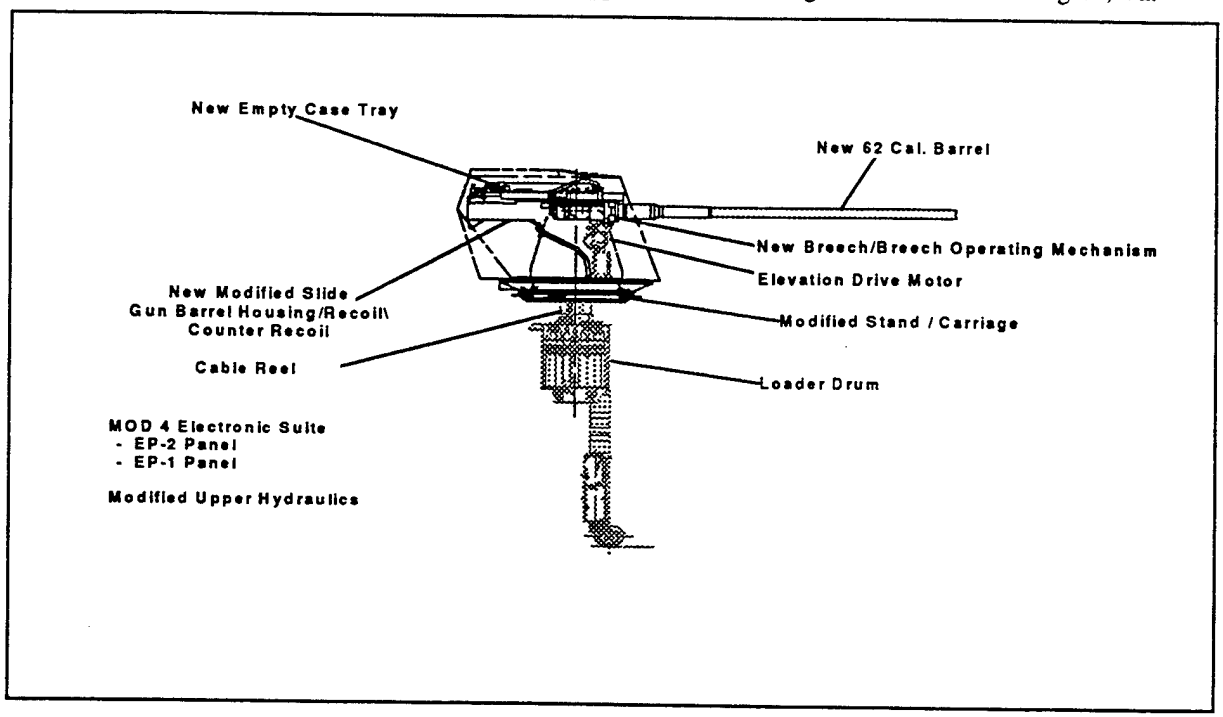

Figure 1. The EX45 Mod4 Gun Mount.

APPROACH

The Little RASCAL gun and projectile dynamics program was chosen for this effort because it can produce reasonable results in a timely manner. Gun dynamics predictions of barrel motion made by Little RASCAL have been shown to agree quite well with experimental results over a wide range of gun system sizes and types [4].

In addition, the 5"/54 Mk45 Mod2 had been previously modeled [5] using the Little RASCAL code, and only minor changes to the gun mount and gun barrel data were required to accurately model the Mod4 gun mount. The gun system information input required includes the geometry and mass description of the gun barrel and breech along with breech center-of-gravity (CG) offsets, trunnion and elevation support locations, and their equivalent spring constants. Information concerning the dimensional mass properties of the 5"/62 gun barrel along with the information necessary to describe the Mod4 gun mount configuration were supplied by United Defense, LP [2].

The final gun system data requirement is a description of the variations in the gun barrel centerline. (The standard centerline definition is the deviation of bore center off a straight line starting at the center of the forcing cone directed to the center of the muzzle. Presently, however, for observational purposes the ARL has been reorienting the centerline so that the support positions used at measurement time define the straight line axis. This configuration allows the observer to see the wanderings of the centerline after the support up to the muzzle.) The centerline of the prototype 62 caliber barrel, S/N17448, displayed in Figure 2, was

supported at 4800mm and 7000mm from the muzzle and was measured by the Aberdeen Test Center personnel at Dalhgren, VA. [5]. Only the vertical component of the centerline is displayed because this is the plane where the perceived hard pressed bend is evident. In Figure 2, the solid line indicates the vertical centerline (CL) with out gravity droop, the dashed line shows the CL with droop, and the line with "x" symbols shows the simple droop from the indicated supports.

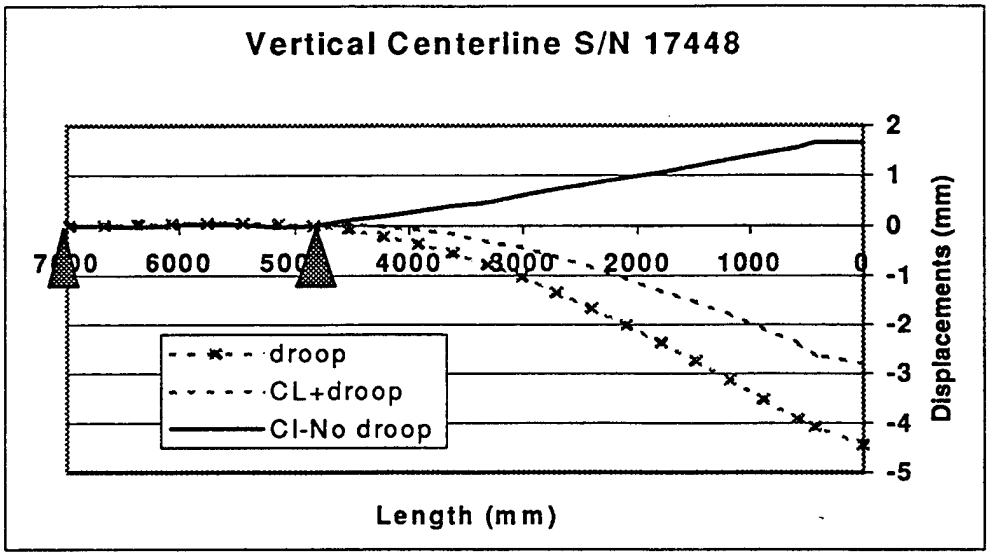

Figure 2. The Prototype 5"/62 Barrel S/N 17448 Vertical Centerline.

MODELING

The Little RASCAL gun and projectile dynamics program is a dynamic displacements code employing a direct structural dynamics analysis approach to the simulation of firing a projectile from a gun. The program is capable of simulating the inertial loading conditions brought about by the projectile interacting with the barrel in a plane as it accelerates the length of the gun tube. The tracking of the inertial loading in-bore allows the program to predict initial launch conditions of the projectile at shot exit. In addition, projectile and gun flexural response can be observed.

Both the gun system and the projectile are modeled using a series of equally spaced cylindrical elements. Nodes are centered and assigned equivalent mass and stiffness values based on standard engineering formulas. Inertial forces and flexural forces are calculated using this simplified description. Flexure at each node is approximated by a second-order finite difference method, which allows the bending forces to be computed. Transverse nodal accelerations caused by these forces are integrated with respect to time to obtain transverse nodal velocities and integrated again to obtain lateral node displacements. Loads induced by pressure effects, mounting conditions, breech CG offset, and the projectile's interaction with the barrel forces are taken into account. This algorithm does not emulate true balloting as the projectile is modeled in the bore without gaps and is forced to follow the dynamically changing centerline. The last assumption, the barrel is always considered as a smoothbore.

The gun system, which includes the breech, barrel, and two gun supports, and the projectile system are two separate models. They are accounted for individually as finite structural systems, except for a variational algorithm that handles their interaction. The interaction of the projectile with the barrel occurs through contact points. The two contact points defined on the projectile are usually positioned where they occur geometrically. The two projectile contact point positions on the barrel are dynamic and change as the projectile traverses the bore. The gun system model and the projectile model are two separate, flexible

entities, with each projectile contact point requiring a user-supplied spring constant. The spring constants serve to define the interface loads between the projectile model and the gun model. There is an algorithm within the program that adjusts the time step to ensure the last projectile spring contact interacts with the node that represents the muzzle of the gun.

Gun Model

Gun system information input includes the geometry and mass description of the gun barrel and breech along with breech CG offsets, trunnion and elevation support locations, and their equivalent spring constants. The breech assembly of the EX45 Mod4 has a weight of 3521 pounds (1598 kg). The axial location of the breech CG is 17.2 inch (436.9 mm) from the rear face of the breech (RFB) and the breech CG with the breech block in the firing position is offset 0.216-inch (5.49 mm) vertically and -0.107 inch (-2.72 mm) horizontally. The trunnion supports are located 22.75 inch (577.8 mm) forward of the rear face of the breech assembly and were assigned a spring constant of 3,200,000 pounds per inch (5.6e+8 N/m). The effective elevation support of the gun assembly is located 55.68 inch (1406.3 mm) forward of the rear breech face and was assigned a spring constant of 135,800 pounds per inch (23.8e+6 N/m). The values for the spring constants of the trunnions and elevation support were supplied by United Defense, LP and were derived from a finite element model used to analyze the gun structure under shipboard shock and vibrations.

Projectile Model

The projectile used in the firing tests is the standard Mk64 high explosive round. This short wheelbase, stiff projectile, shown in Figure 3 body was modeled previously [5]. The major properties of the Mk64 are: length 26.082 inches (662.5 mm), weight 68.70 pounds(31.61 kg), center of gravity 16.560 inches from nose(420.6 mm). The required spring parameters are: forward contact,13.46 inches from nose (342.0 mm), forward spring 1.185e6 lbs/in (2.08e8 N/m), aft contact 22.480 inches from nose (571.0 mm), aft spring 1.125e6 lbs/in (1.97e8 N/m).

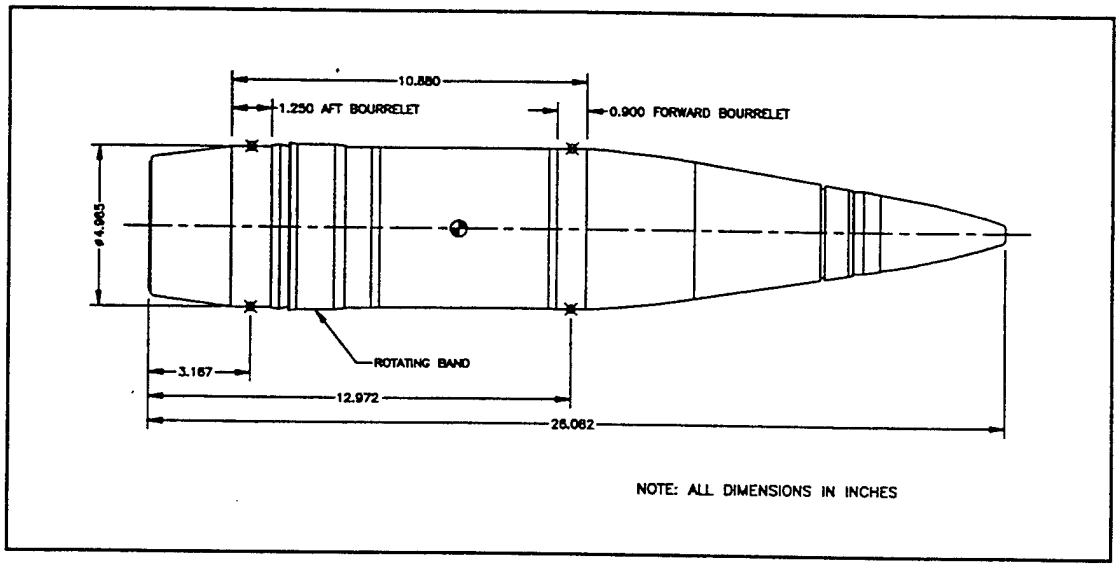

Figure 3. Mk64 A 5-Inch Projectile

HYPOTHETICAL CASES, DISCUSSIONS AND RESULTS

Major cannon producing plants, such as Louisville for the US Navy, routinely practice pressing or bending cannon barrels in the manufacturing process. After the last major pressing operation at Louisville, the barrel is rotated about the axis to find the muzzle high point, then the barrel is indexed up. The evidence of what appears to be a hard bend just before the support point of 4800mm from the muzzle can be noted in Figure 2 but is best observed in Figure 4 where the vertical CL is displayed minus gravity.

The first set of hypothetical cases start with the original vertical CL with gravity noted in Figure 2, and a modified CL called "low-slope" where the hard bend is removed. By constructing a straight line from the support to the muzzle and storing the differences, the remainder of the centerline can be re-constructed anywhere. In this case, noted in Figure 4, the "low-slope" line positions the muzzle at zero displacement The last CL to consider for this first set is the simple droop case also noted in Figure 2.

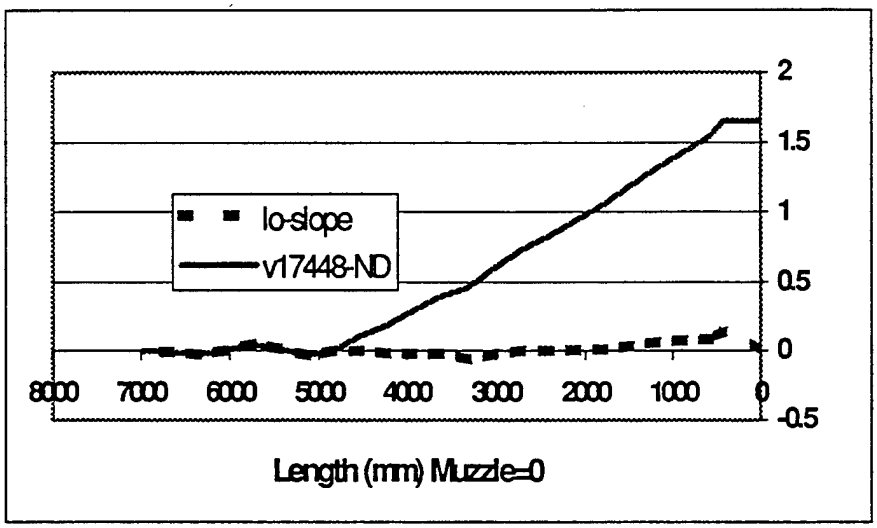

Figure 4. Gravity Free Comparison of Original CL and Modified Low Slope CL.

For simplicity only the projectile front contact forces will be observed throughout this paper. Since the forces are shown in the time domain, note that the projectile front contact reaches the bend at 7.4 ms after shot start When the barrel/ projectile forces are observed in Figure 5, there is a reduction in the magnitude for the two CLs other than original CL. However, the force response for the low slope case is not significantly lower than the original case. There was an expectation of greater magnitude drop in the lateral force in the low slope case. Since the The forces seen for droop only CL are the lowest lateral loads, and could probably represent a best case scenario because this CL is a smooth curve.

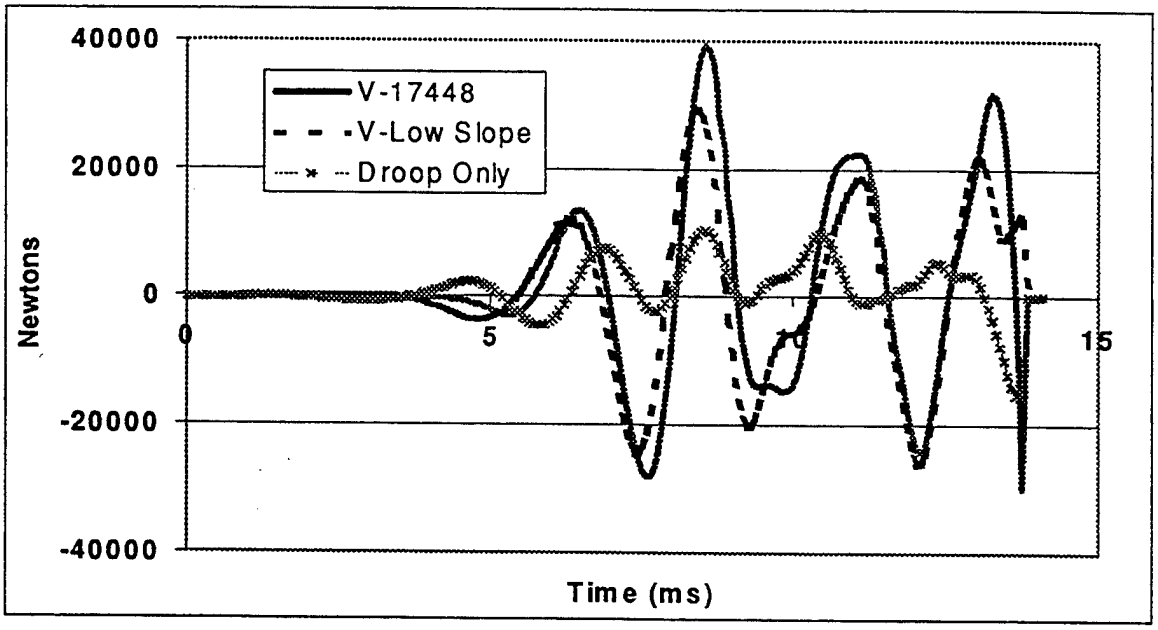

Figure 5. Interaction Forces for Original, Droop Only, and the Low Slope CLs.

The CL's of Figure 2 are displayed again in Figure 6 with scales changed to show a close up of the first 2.5 meters of projectile travel. In Figure 6, note that the CL has a small sine wave of only 0.1 mm peak-to-peak. This small sine wave causes the first 7.4 ms of lateral forces.

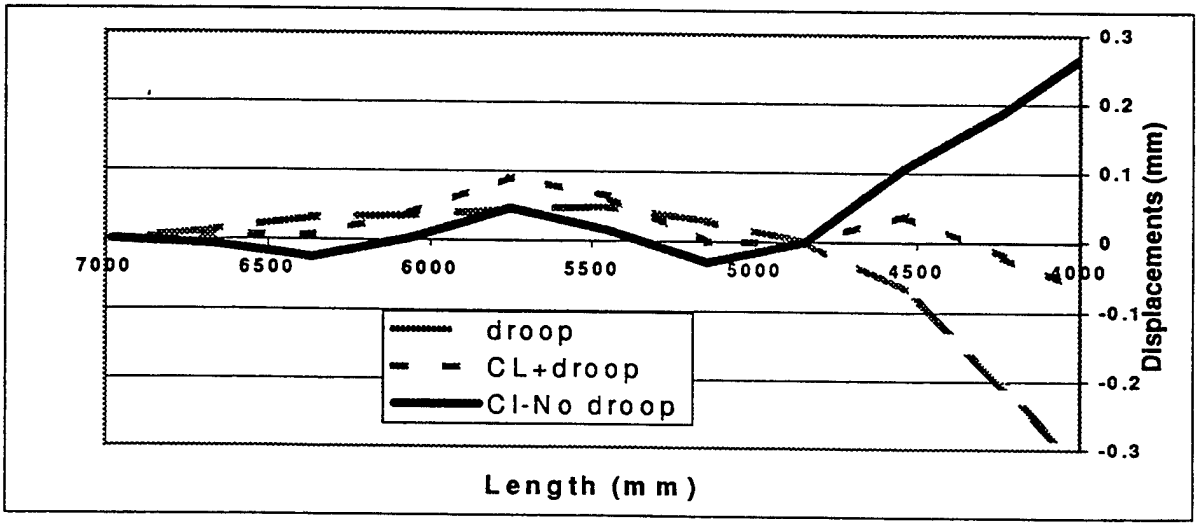

Figure 6. Small Sine Wave Is Evident in First 2.5 Meters of Projectile Travel.

To determine the magnitude of force due to the bend, a hypothetical case is made up where the first 2.2 meters of the CL without gravity is zeroed. Thus, with gravity applied to this hypothetical CL, the first 2.2 meters of the projectile travel follows the droop curve before the front contact meets the bend point.

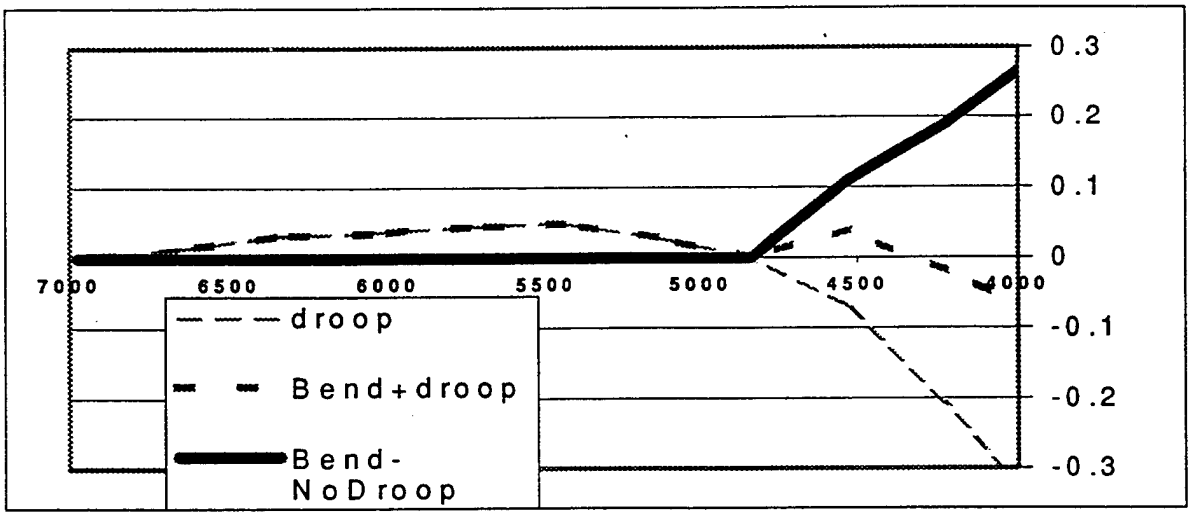

Figure 7. Remove the Small Sine Wave and Isolate the Bend.

In Figure 8 the barrel-projectile interaction forces are shown in a gravity field for the three cases, the original CL, the simple droop CL, and the isolated bend CL. In this example, the forces of the isolated bend case follows the droop case until the bend is encountered, then the peaks fall significantly in comparison to the original forces. Since the forces noted for the original CL are on the order of two times higher than the isolated bend case, the small sine preceding the bend is amplifying the force response.

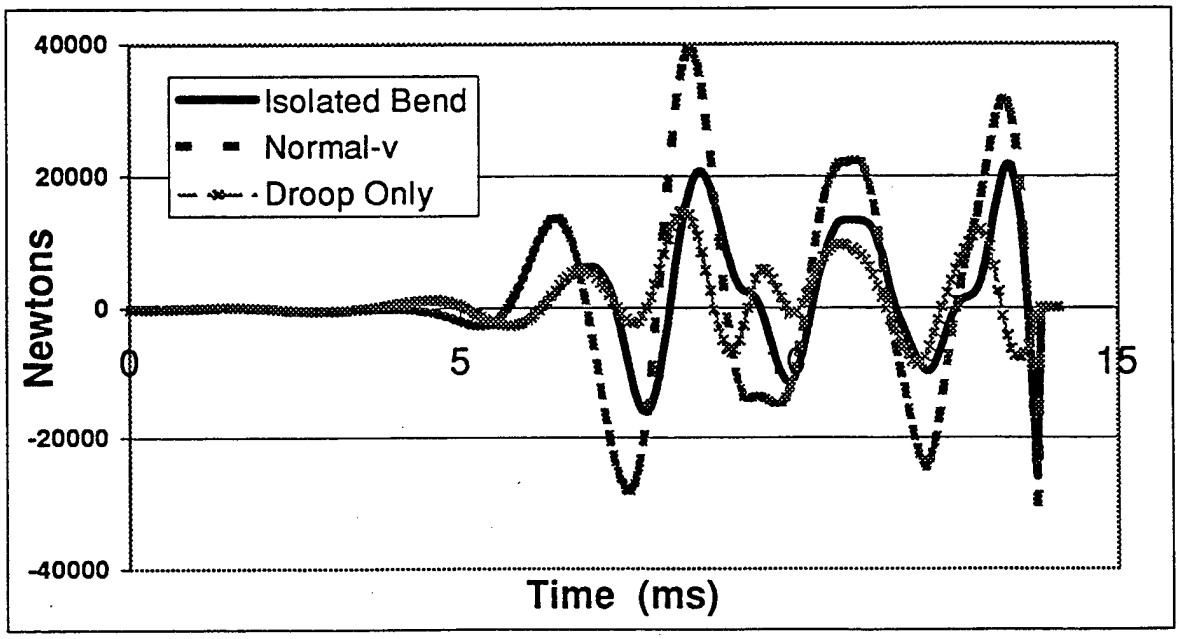

Figure 8. Compare the Isolated Bend Forces to the Original Forces and Droop Forces.

Finally, eliminating the force response due to gravity droop, the following hypothetical cases are compared in a gravity free field: the isolated bend CL (noted in Figure 7), the original CL (Figure 4), and the low slope CL (Figure 4). The forces for these cases, shown in Figure 9, are most interesting because the two curves that contain the small sine way (the original CL and the low slope CL) have their forces almost entirely overlap each other.

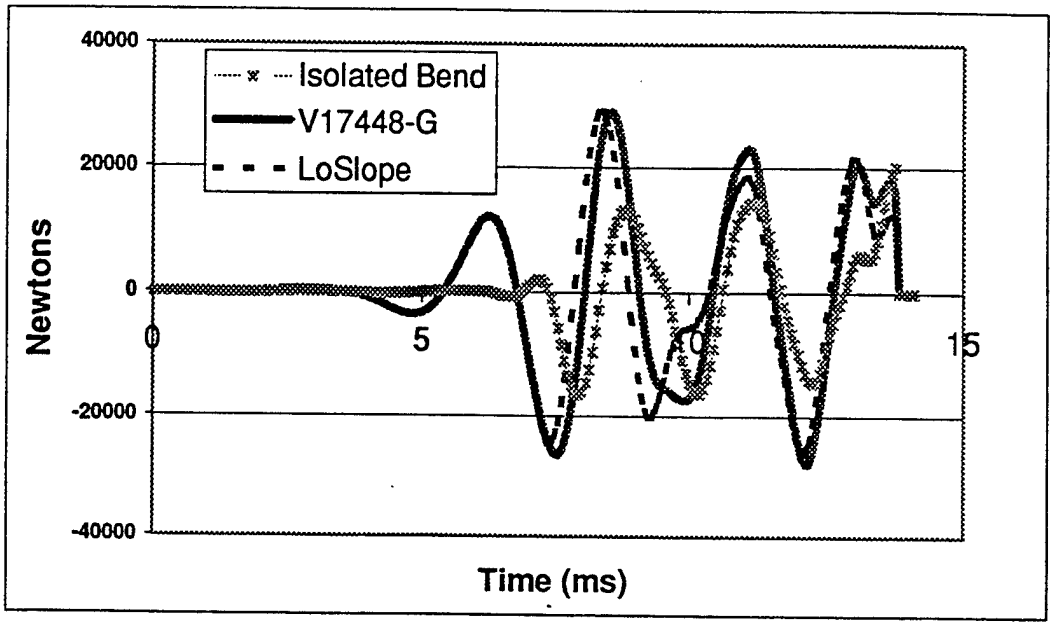

Figure 9. Gravity Free Comparison: The Isolated Bend Forces to the Original Forces and Low Slope Forces

CONCLUSIONS

After analyzing the prototype 62 caliber naval cannon (serial numbered 17448) with the Little RASCAL gun dynamics program, this author was intrigued by the possibility of removing what appeared as a hard bend in the vertical component of the barrel centerline. Using hypothetical cases, for removing the bend and removing what was originally believed to be an insignificant small sine wave preceding the bend, to examine the barrel-projectile interacting forces, this author concludes that:

1) a single isolated bend in a gun barrel centerline is not conducive to generating large lateral loads, but
2) a small sine wave in a gun barrel centerline can significantly amplify lateral loads.

The Little RASCAL program is an ideal vehicle for running hypothetical cases. Since the Little RASCAL is only a first order type of analysis code, the caveats are many: no gaps, no balloting, no spin, etc. Give the same simulations to higher order programs, and this author believes the trends will be the same, only that higher order codes will show higher frequencies and higher loads.

REFERENCES

1. Erline, T. F., M. D. Kregel, and M. Pantano. "Gun and Projectile Flexural Dynamics Modeled by the Little RASCAL - A User's Manual." BRL-TR-3122, U.S. Army Ballistic Research Laboratory, Aberdeen Proving Ground, MD, July 1990.

2. Fischer, L. Private communications. United Defense, LP, Minneapolis, MN, April 1998.

3. Bowen R., and R. D. Cooper. Private communications. U. S. Naval Surface Warfare Center Dahlgren Division, Dalgren, VA, April 1998.

4. Erline, T. F., and M. D. Kregel. "Modeling Gun Dynamics with Dominant Loads." BRL-MR-3683, U.S. Army Ballistic Research Laboratory, Aberdeen Proving Ground, MD, July 1988.

5. Erline, T. F., and L. L. Fischer. "First Order Dynamic Tools for Rapid Assessment of Small Changes to Major Gun and Projectile Dynamic Parameters." Proceedings of the Eighth U.S. Army Symposium On Gun Dynamics, ARCCB-SP-96032, May 1996.

6. Marrs, T., Private communications. Aberdeen Test Center, Aberdeen Proving Ground, MD, August 1998.

EXPERIMENTAL INVESTIGATION ON THE DEVELOPMENT OF THE 120 MM ALUMINUM MORTAR BASEPLATE

Carlos Gutierrez and Dr. Mario Rivera
Benet Laboratories
Close Combat Armaments Center
Watervliet, NY 12189-4050

ABSTRACT

The 120 mm Mortar aluminum cast baseplate concept was introduced as an effort to reduce weight penalty and manufacturing costs. The following investigation deals with the results of some dynamics firing test on a prototype under typical field conditions. The paper analyzes and discusses the dynamics measurement in relation to firing configuration and baseplate geometry. Although, there was catastrophic structural failure there are some encouraging stability findings. The investigation includes a failure mode analysis, presented relative to the dynamic measurements. The paper includes some recommendations concerning material parameters in-particular: it considers issues relative to fracture toughness and yield strength. There is also some information concerning the modeling of baseplate soil mechanics boundary conditions in order to improve computer modeling for future baseplate developments.

INTRODUCTION

The 120-mm mortar is an infantry area fire weapon. It is simply constructed, light, versatile, accurate, and it is capable of delivering a large volume of fire quickly to any given target within its range. A decisive and deadly punch can be delivered to the enemy in a short period of time. Lightness and ease of emplacement of the mortar are features most desired by the soldiers.

The ground mount version utilizes a baseplate that supports the breech-end of the weapon to the ground. It is the baseplate that carries the recoil forces and transmits them to the ground. It is, therefore, essential to have a rugged, durable component that will withstand the high shock load of firing. Recently, there is considerable interest to include the following features in the future manufacture of baseplates:

WEIGHT SAVINGS: Lightweight of the weapon is essential to the solder as he is already burdened with heavy items to carry from one place to another. The promise of a new and lighter baseplate is appealing from the standpoint of portability. The cast aluminum baseplate would decrease the overall weight of the current system.

POTENTIAL MANUFACTURING COST SAVINGS: The cast aluminum one piece baseplate would simplify manufacturing by eliminating long lead-time for materials procurement and simplifying inspection procedures.

IMPROVED STABILITY CONSIDERATION: Stability of the weapon is a most important feature. Stability depends to a greater extent on the geometry of the baseplate. The cast aluminum baseplate offers the versatility of choosing the geometry most favorable for stability without sacrificing strength.

IMPROVED CORROSION RESISTANCE FACTORS: Corrosion in armament systems is a serious problem. Aluminum offers tremendous advantage over its steel counterparts. A simple coat of camouflage paint may be the only additional application.

CONSTRUCTION: The construction of the baseplate is one piece cast aluminum. A hipping process was applied in order to improve material properties. The aluminum baseplate relative to the 120mm mortar was based on the mortar baseplate which is made out of forged aluminum alloy this configuration was taken as a starting design, and was scaled up by 130% to come up with the dimensions for M120 mortar baseplate. A solid model was created on Pro-Engineer, and a drawing was created, using the predictions by the Finite element modeling: ANSI's one of the alloys considered was: Aluminum A206 cast alloy.

The first FEA iteration results showed that aluminum casting provided better strength due to higher deflections than steel. Also, from the unit weight restrictions (not to exceed 130#) point of view it was decided to proceed further with aluminum alloy. The following estimated unit weights of the machined and rough castings were found:

Estimated Weights Summary

	Aluminum Alloy (1^{st} Iteration)	**Aluminum Alloy (2^{nd} Iteration)**
Volume of machined part	823.64 $in.^3$	852 $in.^3$
Est. Wt. Of the machined part	83.19#	86.00#
Est. Wt. Of as-cast part	84.78#	87.2#

The final recommendations of the computer simulation Fracture Mechanics calculations led to the following conclusions:

1. The defect size taken for the calculations is as-cast discontinuities. The recommendation is to process the castings through hot isostatic pressing (HIPPING) AT 300 DEGREE C AND 15,000 PSI PRESSURE. The research indicates up to 200% increase in the ultimate tensile strength in case of 0.75" thick A206 sand casting. Also, the research indicates a decrease in the discontinuities as a result of HIPPING (refer to Annex V for the reference article copy).

2. The fracture mechanics data (Paris's constants, stress concentration factor, etc.) used in the fatigue life prediction are for A356 alloy, which has inferior strength and ductility compared to alloy A206.

3. FEA boundary conditions for the soil is mimicked by the use of a spring in the corner. However, in reality the solid is in intimate contact with the baseplate for the entire bottom face. Therefore the analysis has accounted for this behavior.

FIRING TEST PERFORMED AT APG

The 120mm Cast Baseplate was subjected to a firing test on Aug 5, 1997 at the Aberdeen Test Center (ATC). The test baseplate was instrumented with 20 strain gages, in the following locations: (see Figure 1), and gages numbers 1-4 were mounted on the bottom of the plate, gages number 5-12 were mounted as single gages around the top of the outer ring and gages number 13-20 were mounted in pairs on the top on inner cone. The rationale adhered to in selecting gage location was based on optimal location provided by previous experiences with standard baseplate firing tests and also by following recommendations advanced on similar computer predictions.

RESULTS OF THE TESTS

1. There is a large variation in the value of the maximum strain because the test used several different Charges and Quadrant Elevations (QE) which produces changes in both the magnitude and direction of the load vector.

2. Since the baseplate was seated once and all the test rounds were in the same soil there was not any contribution to the test results due to different solid types. The soil type that was selected was a soil which is typical for these type of tests.

3. Within a five round group of the same QE and Charge there is a strong variation in strain because the solid structure and configuration under the placement tends to change, with each round giving a somewhat different support for the next round.

4. The strong variation in the recorded strains for the last group of readings gives an indication of a highly probable existence of a growing crack, since the plate seems to becoming more and more compliant. This crack resulted in a gross and catastrophic failure on round 25.

5. The data for any particular round shows substantial vibration content which is adequately damped. This speaks well for the overall geometry of the baseplate and its effectiveness to bite into the soil. This relates well, also, to the degree of damping provided by the specific soil conditions. Strong vibrations are particularly evident on the first seating round (S1) because there is little or no contact with the soil before the shot.

6. Gages 3 and 4 clearly show the highest strains as they are near the strongest stress concentration, which is also seen and predicted on the original analysis.

7. It appears that the gages which are symmetrically located frequently show different results than anticipated, especially towards the end of the test. This is additional indication of the presence of cracks or severe internal discontinuities.

8. The peak strains given in Table 4 are sufficient for most engineering purposes and are typical of what was measured in previous tests with different plates. Maximum strains are of the order of 3,500 microinches per inch giving tensile stresses of the order of 90-100 Kpsi and beyond (some yielding may be taking place here).

The strains were measured using standard 120-ohm electrical resistance gages supplied by Micro-measurement Inc. They were all connected as single gages and individually recorded as digital data at a rate of 200,000 data points per second for 0.486395 second (97,279 points). The zero time was set using an optical sensor to detect the muzzle flash at shot ejection with .0768 seconds of data saved before this time. This gave a long baseline before the shot and substantial time after to check for damage to the gage and drift.

Typical strain time variation is also provided in Figures 2.

DATA ANALYSIS

The strain levels are consistent and quite typical for this kind of baseplate firing tests. Strains are high in the central portions with somewhat lower values in the periphery and outer edges of the baseplate. The amount of vibration is consistent with the nature of the shock loading, without any resonant behavior (probably due to the damping effect of the soil). The strong difference in symmetric strain results is an indication of the presence of a large active crack progressing at substantial growth rate. From judging of the strain changes it appears that the onset of the crack is somewhat between rounds 11 and 13. The strain time behavior is normal and is an indication that the baseplate is being damped as expected. No resonant structural activity can be inferred from the data.

GENERAL OBSERVATION ON FIRING STABILITY

One of the criteria of baseplate effectiveness is its ability to remain stationary as much as possible, in fact, one of the classical ways to view a mortar baseplate is to view it as an earth works moving device.

During the firing tests, all the personnel present were favorably impressed by the dynamical stability of the baseplate. The geometry and mass distribution seem to contribute to the proper stability derivatives in pitching, rolling and yawing. There was not any indication of looseness when the test was terminated. The technical staff did not have any difficulty in removing the baseplate from the soil. It was properly implanted and not too deep into the soil. The implanted depth when the test was terminated was a few inches from the level ground.

FAILURE ANALYSIS OF PROTOTYPE CAST ALUMINUM BASEPLATE

OBJECTIVE

The primary purpose of the failure analysis was to determine the case of the failure of this prototype 120-mm mortar aluminum baseplate. Also, this analysis was conducted to characterize the material aspects of the casting.

PROCEDURE

This investigation was performed in accordance with the following procedures:

1. Visual examination and macro photography
2. Stereoscopic examination of fracture surface
3. Chemical analysis
4. Mechanical property evaluation
5. Microstructural examination
6. Fractographic examination by Scanning Electron Microscopy (SEM), and Energy Dispersive Spectroscopy (EDS) on sections of the fracture surface.

RESULTS

VISUAL EXAMINATION AND MACRO PHOTOGRAPHY

Macro Photographs were taken of the two halves of the baseplate after the crack was pressed open. (See Figures 2,3) More than half of the fracture surface was covered with what appeared to be a dark corrosion product. However, after examining the fracture surface under a stereomicroscope, this discoloration proved to be some form of foreign residue coating the surface. The fracture surface had no markings (i.e. crack path) on it to indicate the origin of the crack. In fact, the outermost ends of the cracks were observed to be completely separated form the rest of crack. There were at least three separate cracks involved in the failure process.

As shown in figure 4, one half of the fractured baseplate was sectioned for further examination. Subsequently, the fracture surface(s) were separated from the bulk material. Mechanical property and chemical analysis specimens were removed from the surrounding material. Metallographic samples were removed from both the vicinity of the fracture surface and from the surrounding material.

STEREOSCOPIC EXAMINATION

The fracture surfaces were examined under the stereoscope at magnifications between 4.5x- 81x. On most of the fracture surface, in varying degrees, was a dark translucent coating of a foreign residue, This coating was especially prominent in deep recesses, where it appeared to have "pooled". No evidence of pre-existing flaws, cracks, or material defects and no other foreign material (besides the previously mentioned coating) were found on the fracture surfaces. The fracture surface in selected regions was cleaned using cellular acetate replicas to lift off deposited material/casting (the residue). The fracture mode displayed an intergranular appearance, plainly visible at the low magnifications of the stereoscope.

CHEMICAL ANALYSIS

Chemical Analysis was performed on a piece removed from the material surrounding the fracture surface. The elemental analyses were performed on a direct reading emission spectrometer. The results, compared with the required specifications, are listed in Table 1. Two elements exceeded the required range in an analysis, chromium (Cr) and iron (Fe). However, these deviations were small, on the order of 0.05%, and both were in range for the other analysis.

TABLE 1: CHEMICAL ANALYSIS (WT. %)

Sample	Cu	Mn	Mg	Ti	Fe	Si	Cr	Zn	Al
1st Sample	4.4	0.30	0.30	0.20	0.2	**	0.05	<0.01	Bal. Rem.
2nd Sample	4.1	0.32	0.24	0.20	<0.1	0.07	0.1	<0.01	Bal. Rem.
Required	4.2-5.0	0.20-0.50	0.15-0.35	0.15 0.30	0.15 max	0.10 max	0.05 max	0.010 max	Bal. Rem.

***Note: The original chemical analysis had an unusually high Si values, upon investigation a Si contaminant was found in the system and removed.*

MECHANICAL PROPERTY EVALUATION

Material for mechanical property specimens was removed from the baseplate as shown in figure 4. From this material, four standard ASTM tensile bars and four charpy v-notch specimens were prepared. The results of the mechanical testing of these specimens are listed in Table 2, along with the expected properties.

TABLE 2: TEST RESULTS FOR MECHANICAL PROPERTIES

	Specimen 1	Specimen 2	Specimen 3	Specimen 4	Nominal Published Values
UTS (psi)	invalid	Invalid	48,000	47,200	60,000
YS (0.2%) (psi)	Invalid	Invalid	45,200	44,500	50,000
Elongation (%)	Invalid	Invalid	2.1%	2.1%	12%
RA (%)	Invalid	Invalid	3.3%	2.7%	26%
Charpy V notch (ft-lbs)	3.5	3.25	3.0	3.5	6-8

The mechanical property results failed to meet the expected properties for this material (nominal) in all cases. The A206 cast aluminum from this baseplate possesses low strength; it failed in our tests at a stress lower than that at which it should start to yield. It was brittle; possessing only 1/10th of the elongation and 1/6th the reduction area listed for this alloy. Finally, this alloy shows very low toughness; using only half the nominal expected charpy impact values.

TABLE 3: HARDNESS VALUES (HRB) IN ROCKWELL B SCALE

Reading #	Macro Hardness Reading from Charpy bar surface	Micro Hardness Reading from near fracture surface	Micro Hardness Reading from bulk material
1	56.8	71	67
2	63.0	62	65
3	70.9	72.5	67
4	64.5	68.5	58
5	58.7	63	61.5
6	67.2	58	60
7	72.3	64	58
8	67.7	61.5	58
9			61
10			59.5
11			60
12			71

There appears to be agreement between the macro and micro hardness readings. The same range for the hardness values was found in both the bulk material and next to the fracture surface. However, the random and wide range over which the readings fall, makes drawing clear conclusions difficult.

MICROSTRUCTURAL EXAMINATION

Metallographic samples were taken from, respectively, the fracture surface and a piece of baseplate several inches from the fracture surface. These samples were examined, in the polished condition, for the inclusion content of the material. Both samples were found, to have long lathe-like and long irregular shaped inclusions, as well as small elongated or irregular shaped apparent inclusions. (See Figure 5). There was also extensive shrinkage porosity found dispersed throughout all of the samples, but especially in the vicinity of the fracture surface. (See Figure 6). These specimens were subsequently etched with Kalling's and Keller's etchants, and the microstructure examined. This extensive porosity was located in the grain boundaries and can be described as inter-connected and intergranular shrinkage porosity. After etching it was observed that the "inclusions" were almost entirely located in the grain boundaries. In addition, a fine precipitate could be observed. (See Figure 7). In all cases, the microstructure was an extremely large grained, single phase with a fine precipitate distributed throughout. The grain size was determined to be ASTM No. 1-2, with the preponderance of the measurements in the vicinity of ASTM No. 1.

FRACTOGRAPHIC EXAMINATION

Selected regions of the fracture surface were examined in the Scanning Electron Microscope (SEM) to determine the failure mode on a microscopic level. The fracture surface was examined both before and after cleaning with acetate replicas. Before cleaning, the fracture topography was obscured by the foreign residue, although an intergranular failure mode appeared to be present. The results are shown in figures 8 & 9. The cleaned fracture surface was examined as well and clearly shows an intergranular fracture mode, indicating a brittle, low energy failure process. This observation is completely consistent with the metallographic mechanical property results.

An Energy Dispersive X-ray Spectroscopic (EDS) analysis was performed on the fracture surface before cleaning. EDS was also performed on the acetate replicas removed from the fracture surfaces. However the electron beam appears to have penetrated the foreign residue. (See Figure 10). The inclusions/segregated material in the grain boundaries were examined by Energy Dispersive X-ray Spectroscopy (EDS) to determine their relative chemical composition. This technique can not provide a quantitative chemical analysis, but does provide qualitative information on the elements present. Comparing these results with that of the baseplate material found within the grains, i.e. the matrix, the segregated material was found to be copper rich.

CONCLUSIONS

The 120-mm Aluminum mortar baseplate had almost completed cracking into two pieces. There were three distinctly separate cracks. The fracture surface had an intergranular appearance at the macro level of examination. (The failure mode was confirmed in the SEM as intergranular fracture.) No evidence of pre-existing flaws or material defects was found.

The strength properties were 10 to 20% lower than expected and the % RA and elongation were 80 to 40% lower than expected. The charpy values were less than half of the values expected.

Massive interconnected, intergranular shrinkage porosity, which would have made the material susceptible to intergranular failure, was found dispersed through all the metallographic samples. In addition, a copper richmaterial segregated into the grain boundaries, originally identified as irregular shaped inclusions, was observed. The material was found to have an extremely large grained, single phase with a dispersed fine precipitate. This large grain size, which was determined to be ASTM No. 1 to 2, is detrimental to the material performance.

The 120 mm Aluminum mortar baseplate shows adequate dampening characteristics in regard to the effectiveness to bite into the soil. This speaks well for the overall geometry of the baseplate

The geometry and mass distribution seem to produce a very effective and stable baseplate. Both placement and retrieval are highly acceptable.

Weight savings as compared with the steel baseplate are considerable, about 2 1/2 times lighter, than steel.

TABLE 4: PEAK STRAIN READINGS

Strain Gage Data for the 120 mm Cast Aluminum Baseplate Test conducted at U.S. Army Aberdeen Test Center Aberdeen Proving Grounds Maryland

Gage	1-R	2-C	3-C	4-C	5-R	6-A	7-C	8-A	9-R	10-A	11-C	12-A	13-R	14-C	15-R	16-C	17-R	18-C	19-R	20-C
Rd																				
S1	78	-482	653	977	39	-324	101	-129	-70	-245	157	-151	87	266	76	159	167	173	203	76
S2	52	-353	469	790	119	-160	99	-95	-67	-93	96	-118	81	284	102	118	134	117	127	106
S3	50	-462	790	1169	233	-377	146	-114	-71	-124	216	-345	55	484	150	197	147	187	100	320
T1	187	-941	1286	2377	303	-427	182	-218	-69	-215	395	-448	71	1100	256	379	219	408	213	411
T2	173	-916	1561	2204	186	-335	209	-198	-95	-254	452	-285	99	875	324	372	230	336	240	281
T3	165	-989	1548	2152	197	-307	255	-225	-101	-262	457	-166	158	802	336	417	241	309	285	253
T4	160	-969	1664	2344	226	-307	305	-212	-93	-204	472	-	238	785	332	445	320	400	260	318
T5	182	-1030	1655	2320	248	-225	326	-224	-93	-230	444	-	238	702	318	416	388	438	190	467
T6	85	-712	1108	1409	282	-539	345	-170	-147	-302	460	-	287	446	326	220	302	406	181	452
T7	78	-1308	2039	2112	216	-645	427	-545	-243	-255	289	-	264	492	301	274	146	472	182	433
T8	78	-1943	3237	3701	148	-641	345	-647	-242	-481	269	-	288	382	173	359	71	502	145	302
T9	305	-2640	3887	3868	109	-686	358	-927	-553	-507	216	-	303	354	140	304	92	502	92	220
T10	47	-2613	3908	3798	104	-689	381	-968	-542	-501	228	-	314	340	146	234	103	465	92	204
T11	300	-3415	-	-	216	-853	355	-1227	-343	-683	266	-	292	274	255	572	287	521	210	225
T12	356	-3200	-	-	121	-880	327	-1207	-575	-637	252	-	291	227	196	560	201	512	135	145
T13	176	-3190	-	-	121	-893	307	-1218	-583	-656	262	-	264	226	214	601	218	528	151	142
T14	177	-3095	-	-	106	-900	275	-1218	-580	-677	270	-	248	256	218	607	213	520	157	132
T15	196	-3193	-	-	127	-930	271	-1251	-585	-703	290	-	257	268	231	632	227	551	169	147
T16	121	-3108	-	-	103	-867	413	-1063	-482	-521	398	-	468	696	388	157	316	677	378	244
T17	127	-2946	-	-	124	-753	481	-1020	-339	-419	406	-	669	788	452	284	763	957	367	346
T18	204	-2670	-	-	133	-634	538	-1030	-284	-349	262	-	832	872	481	346	1045	1185	261	432
T19	183	-2613	-	-	130	-617	589	-1044	-268	-347	211	-	950	927	512	394	1129	1271	231	422
T20	269	-2841	-	-	158	-637	716	-1160	-243	-342	203	-	1043	990	575	440	1353	1479	238	450
T21	-	-3307	-	-	165	-814	462	-1318	-359	-487	130	-	1002	901	359	248	1034	1436	158	479
T22	-	-3003	-	-	176	-773	460	-1404	-306	-466	128	-	996	740	490	-	957	1306	206	570
T23	-	-2429	-	-	196	-774	428	-1469	-275	-394	176	-	977	501	888	-	703	695	264	936
T24	-	-1671	-	-	207	-714	336	-1176	-336	-425	355	-	636	313	849	112	478	376	320	842
T25	-	-1126	-	-	174	-556	180	-592	-378	-390	617	-	554	210	688	1030	325	323	307	807

"Virtual Proving Ground"

presented by

Rick Cozby
Acting Chief, Simulation and Technology Division
Headquarters
US Army Test and Evaluation Command

Tuesday, November 17, 1998
9th US Army Gun Dynamics Symposium
McLean, VA

TECOM

U.S. Army Test & Evaluation Command

THE VIRTUAL PROVING GROUND

An Acquisition Streamlining Initiative

Richard S. Cozby
Acting Chief,
Simulation & Technology Div.
HQ, U.S. Army Test & Evaluation Command

AGENDA

- What is TECOM?
- The Virtual Proving Ground
- Leveraging VPG for Training

What is TECOM?

U.S. Army Test & Evaluation Command

- **Developmental Tester for Army Systems in all Environments**
- **System Safety Verifier**
- **Test Technology Developer**
- **Manager of 4 Installations and 10 Test Centers/Sites in 7 States and Panama**
  - *Land* — *4 million acres (35% of the Army's Land)*
  - *Buildings* — *5,461*
  - *Family housing* — *2,653 units*
  - *Roads* — *2,923 miles*
- **Approximately 1800 tests per year (73% Customer Reimbursed)**
- **6027 Civilians + 523 Military + 3530 Contractor Workyears**
- **Army Materiel Command Acquisition Center**

(Estimated FY98 year-end data)

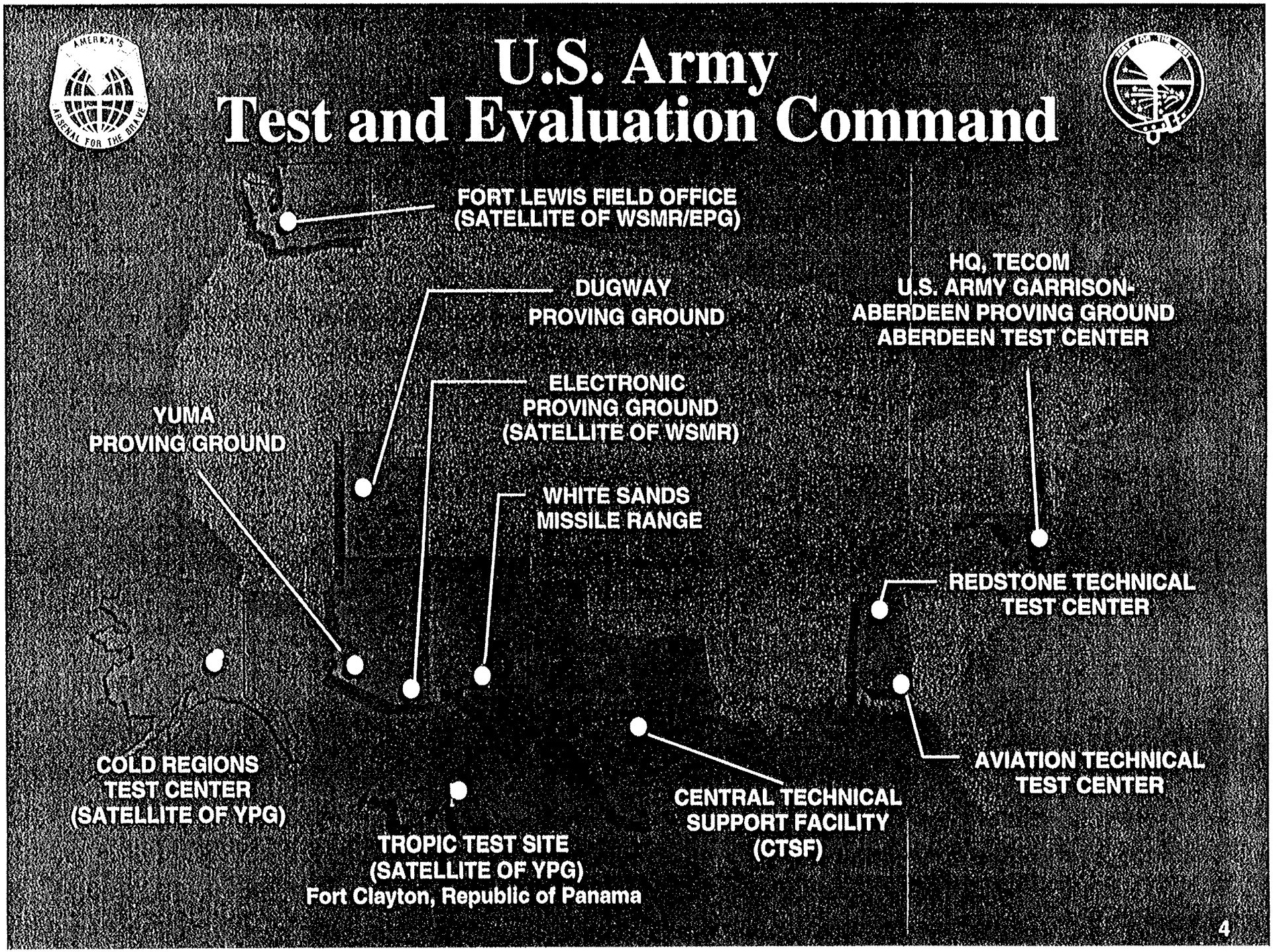
U.S. Army
Test and Evaluation Command
FORT LEWIS FIELD OFFICE
(SATELLITE OF WSMR/EPG)
DUGWAY
PROVING GROUND
ELECTRONIC
PROVING GROUND
(SATELLITE OF WSMR)
YUMA
PROVING GROUND
WHITE SANDS
MISSILE RANGE
HQ, TECOM
U.S. ARMY GARRISON-
ABERDEEN PROVING GROUND
ABERDEEN TEST CENTER
REDSTONE TECHNICAL
TEST CENTER
AVIATION TECHNICAL
TEST CENTER
COLD REGIONS
TEST CENTER
(SATELLITE OF YPG)
TROPIC TEST SITE
(SATELLITE OF YPG)
Fort Clayton, Republic of Panama
CENTRAL TECHNICAL
SUPPORT FACILITY
(CTSF)
4

Test Center Missions

WHITE SANDS MISSILE RANGE
WSMR

Air Defense
Smart Weapons
Space Systems

ELECTRONIC PROVING GROUND
EPG

C4I
EW
Navigation
Systems

AVIATION TECHNICAL TEST CENTER
ATTC

Aircraft
Aviation
Systems

ABERDEEN TEST CENTER
ATC

Ground Systems
Clothing/Pers/
Gen Equip
Lethality/
Vulnerability

DUGWAY PROVING GROUND
DPG

Chemical
Biological
Smoke

REDSTONE TECHNICAL TEST CENTER
RTTC

Small Rockets/
Missiles

YUMA PROVING GROUND
YPG

Desert Env Test
Artillery
Aircraft Armaments
Air Delivery

COLD REGIONS TEST CENTER
CRTC

Arctic Env Test

TROPIC TEST SITE
TTC

Tropic Env Test

TECOM Test Workload Versus Resources

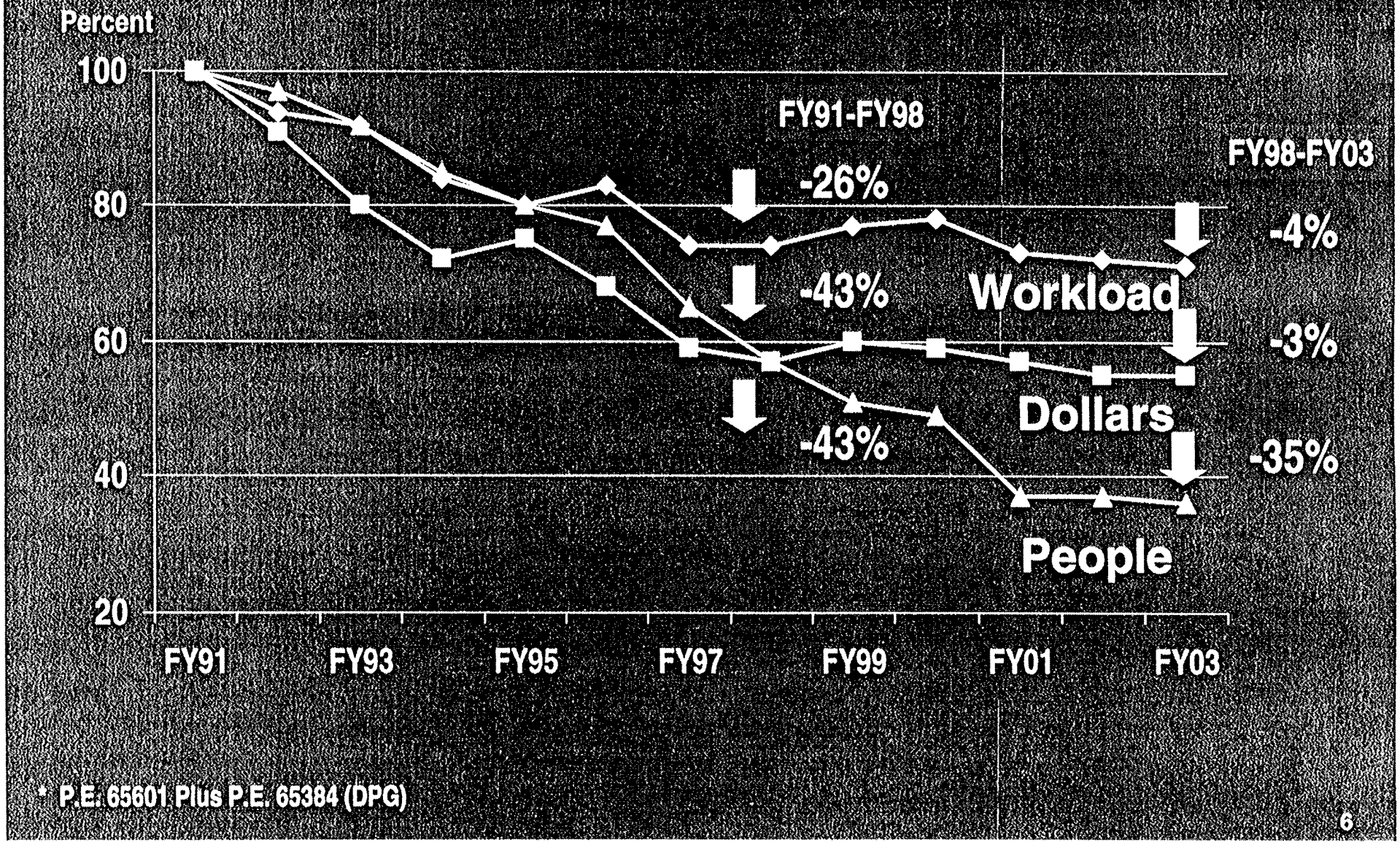

* P.E. 65601 Plus P.E. 65384 (DPG)

Virtual Proving Ground

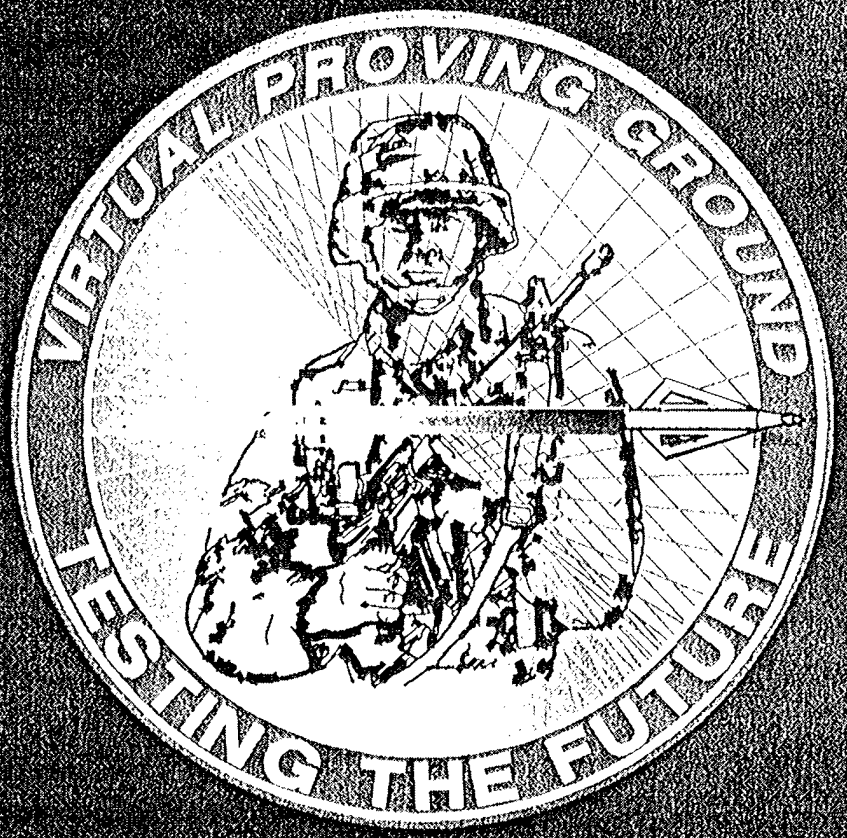

Virtual Proving Ground
Why We're Doing It

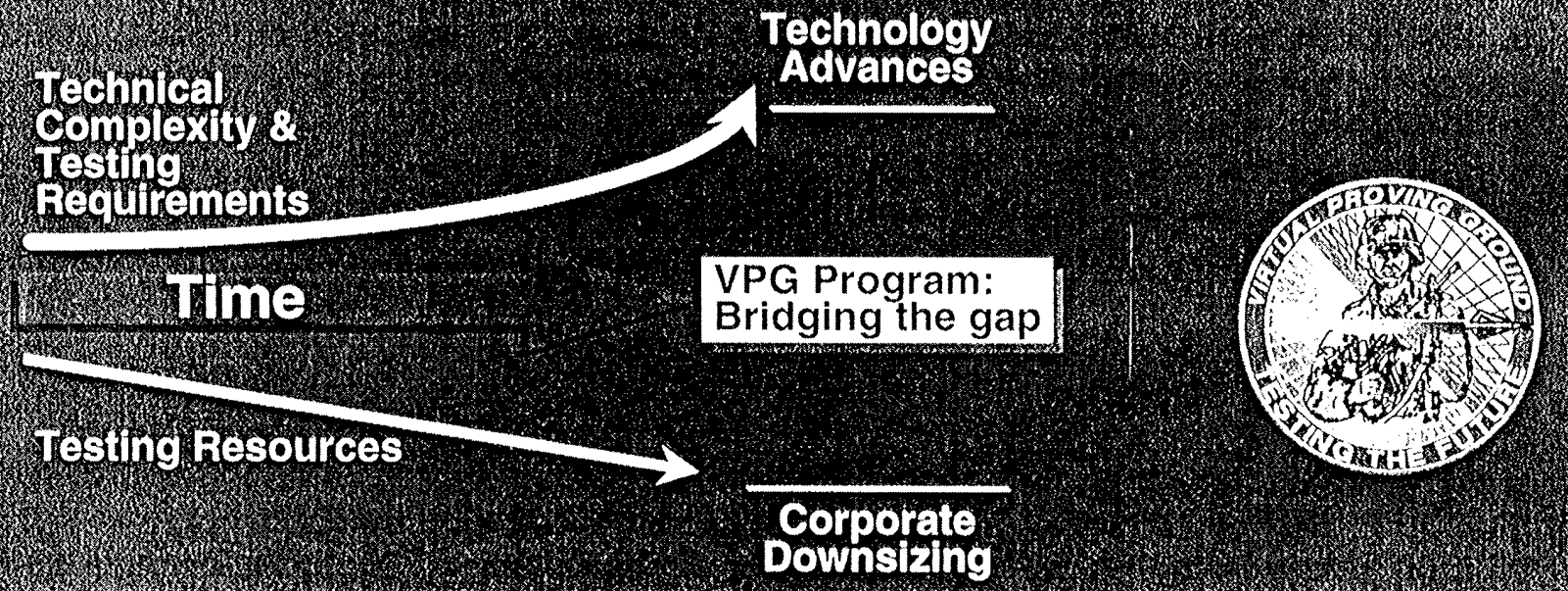

- Comply w/DoD directives expanding use of modeling & simulation
- Implement OSD Simulation, Test & Evaluation Process Guidelines

Virtual Proving Ground Vision

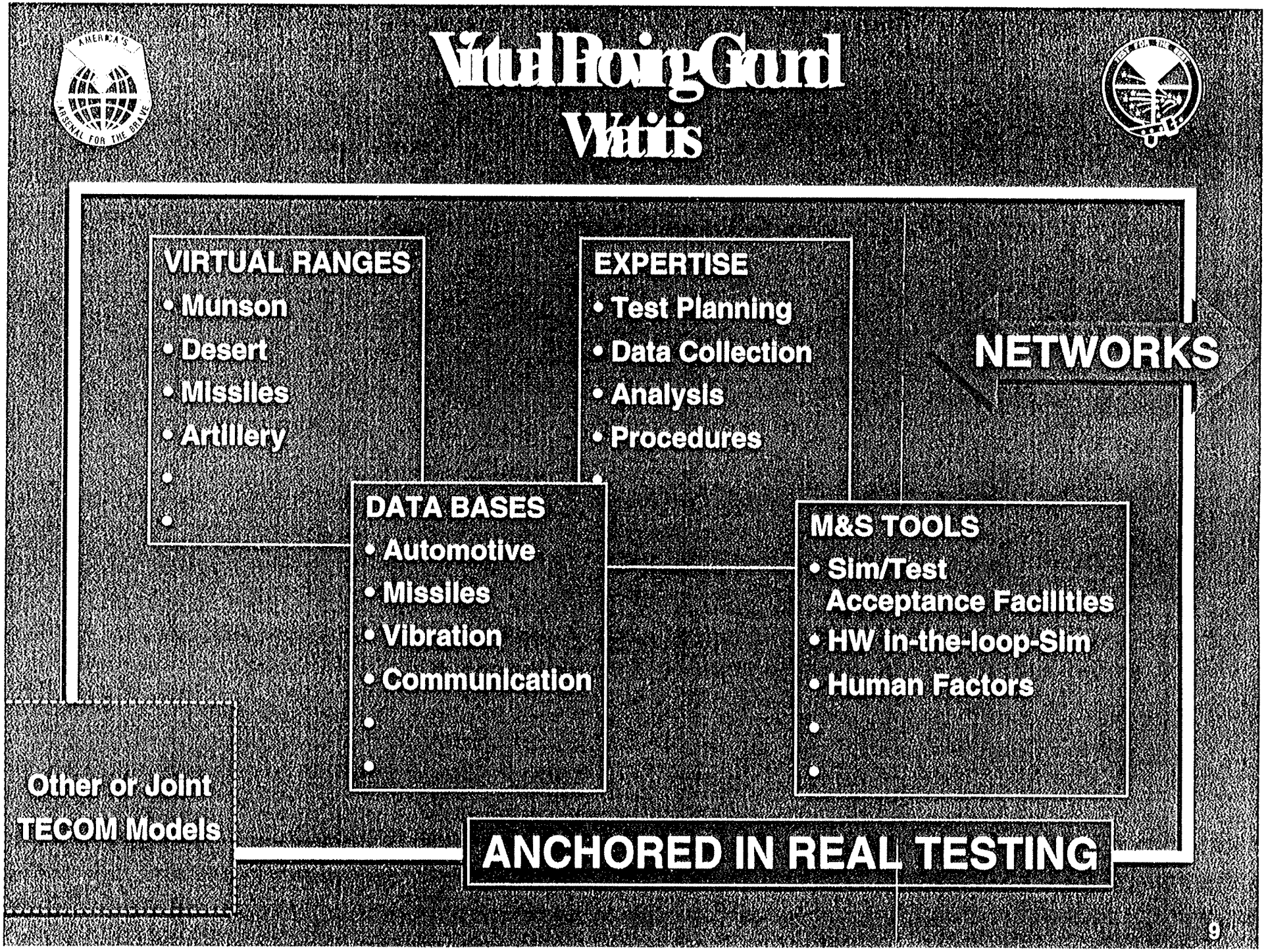

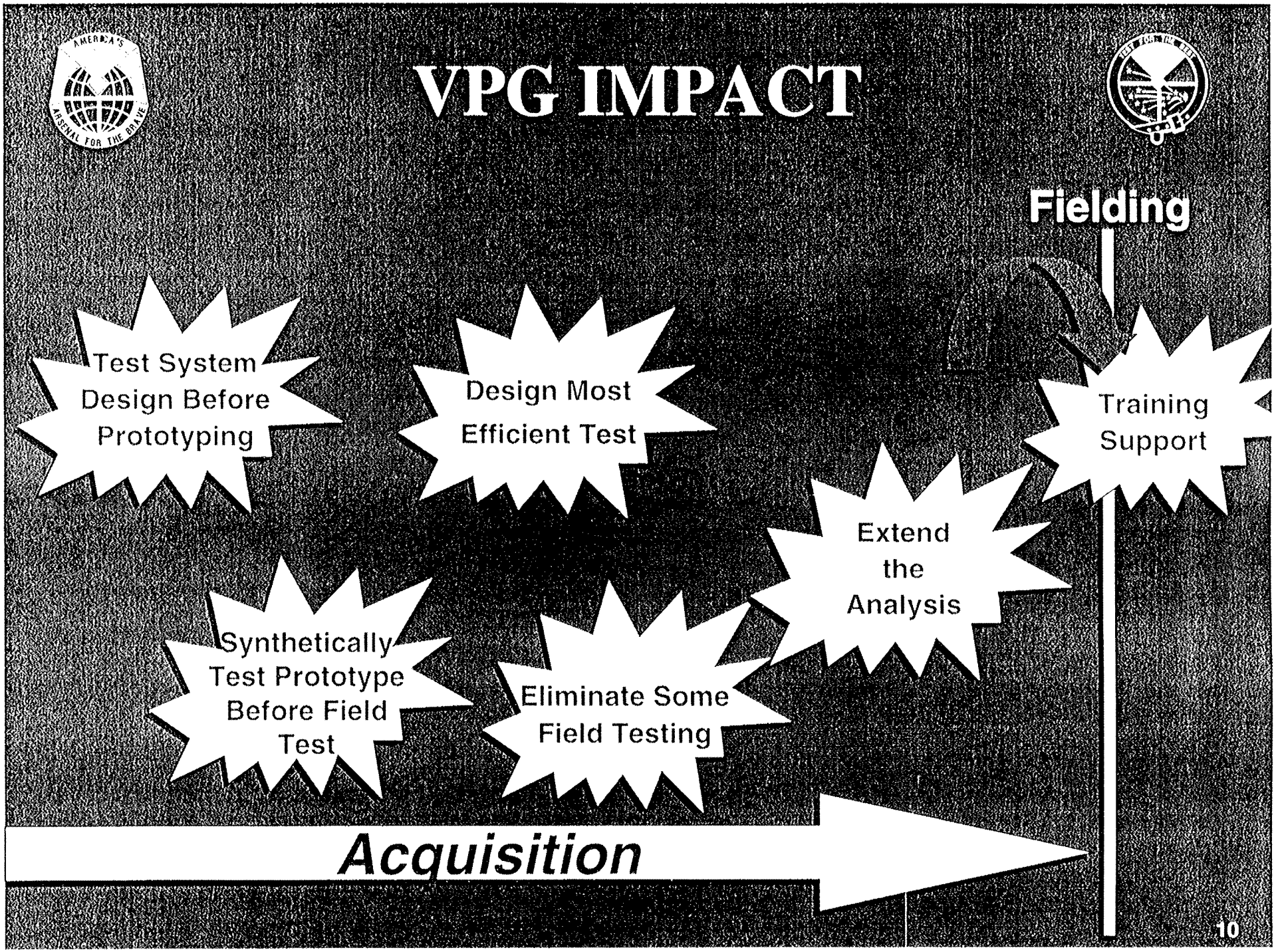
VPG IMPACT
Fielding
Test System Design Before Prototyping
Design Most Efficient Test
Training Support
Extend the Analysis
Synthetically Test Prototype Before Field Test
Eliminate Some Field Testing
Acquisition
10

Cost Avoidance

~$67M / Year Cost Avoidance

Avoidance to date:
~$160M/over POM: $495M
Investment to date:
~ $94M/over POM: $100M

TEST ITEM STIMULATOR/ TEST CONTROL CENTER

$1M IN, $ 6M/YR SAVED

SIMULATION / TEST ACCEPTANCE FACILITY

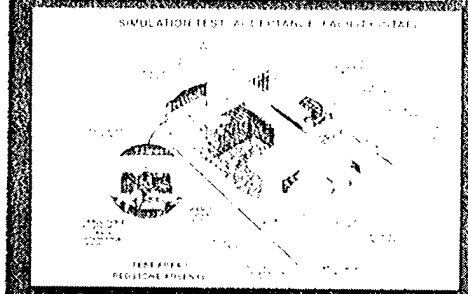

$6M IN, $8M/YR SAVED

Soldiers

Missiles

AERIAL CABLE RANGE

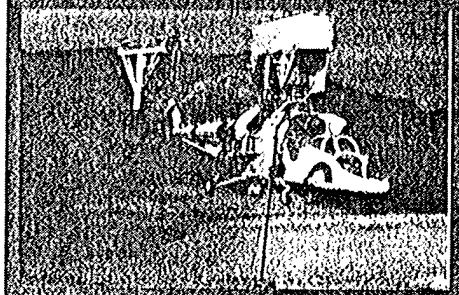

$36M IN, $20M/YR SAVED

FEWER
"THINGS" NEEDED...

Targets

Instrumentation

Rounds

DYNAMIC INFRARED SCENE PROJECTOR

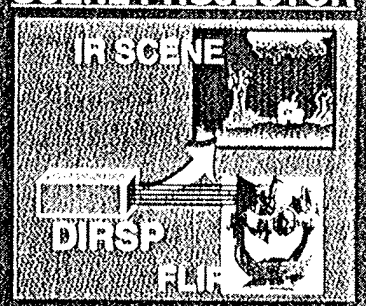

$12M IN, $4M / YR SAVED (PROJ)

SMART MUNITIONS TEST SUITE

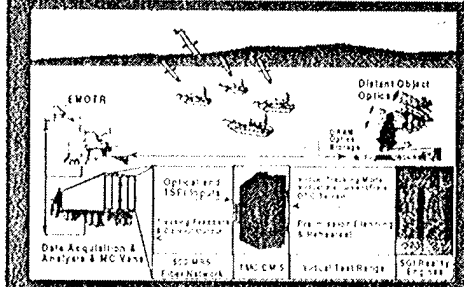

$39M IN, $2M/YR SAVED

FIRING IMPULSE SIMULATOR

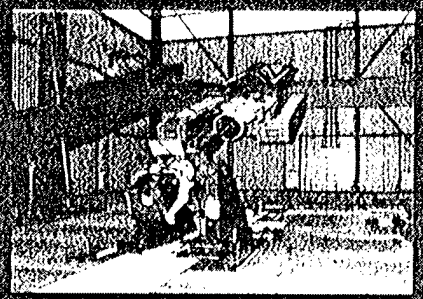

$7M IN, $22M/YR SAVED

FIRE CONTROL TEST COMPLEX

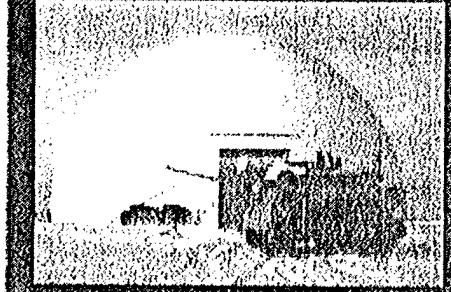

$5M IN, $5M/YR SAVED

VPG Cost Benefits

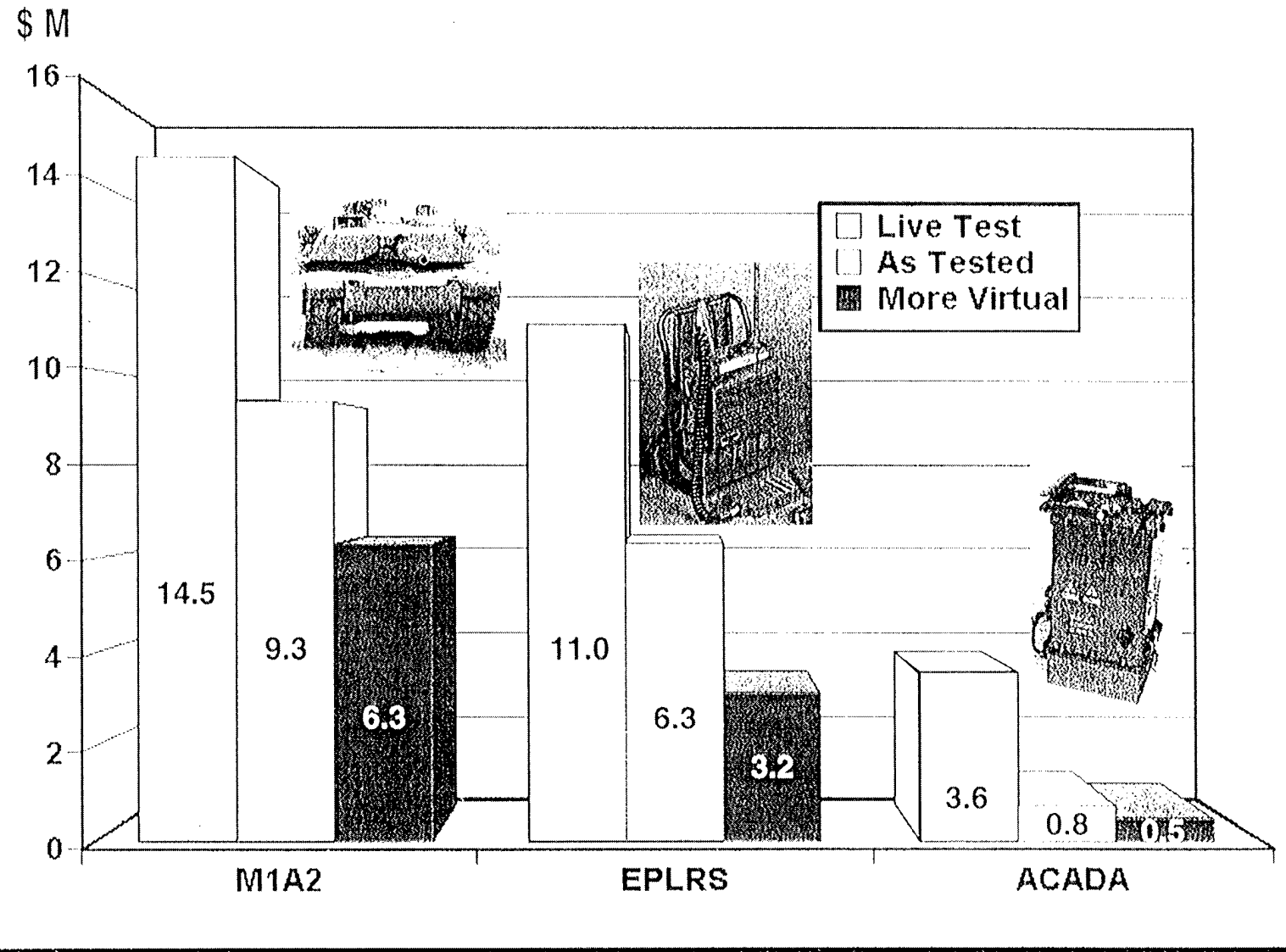

VPG Schedule Benefits

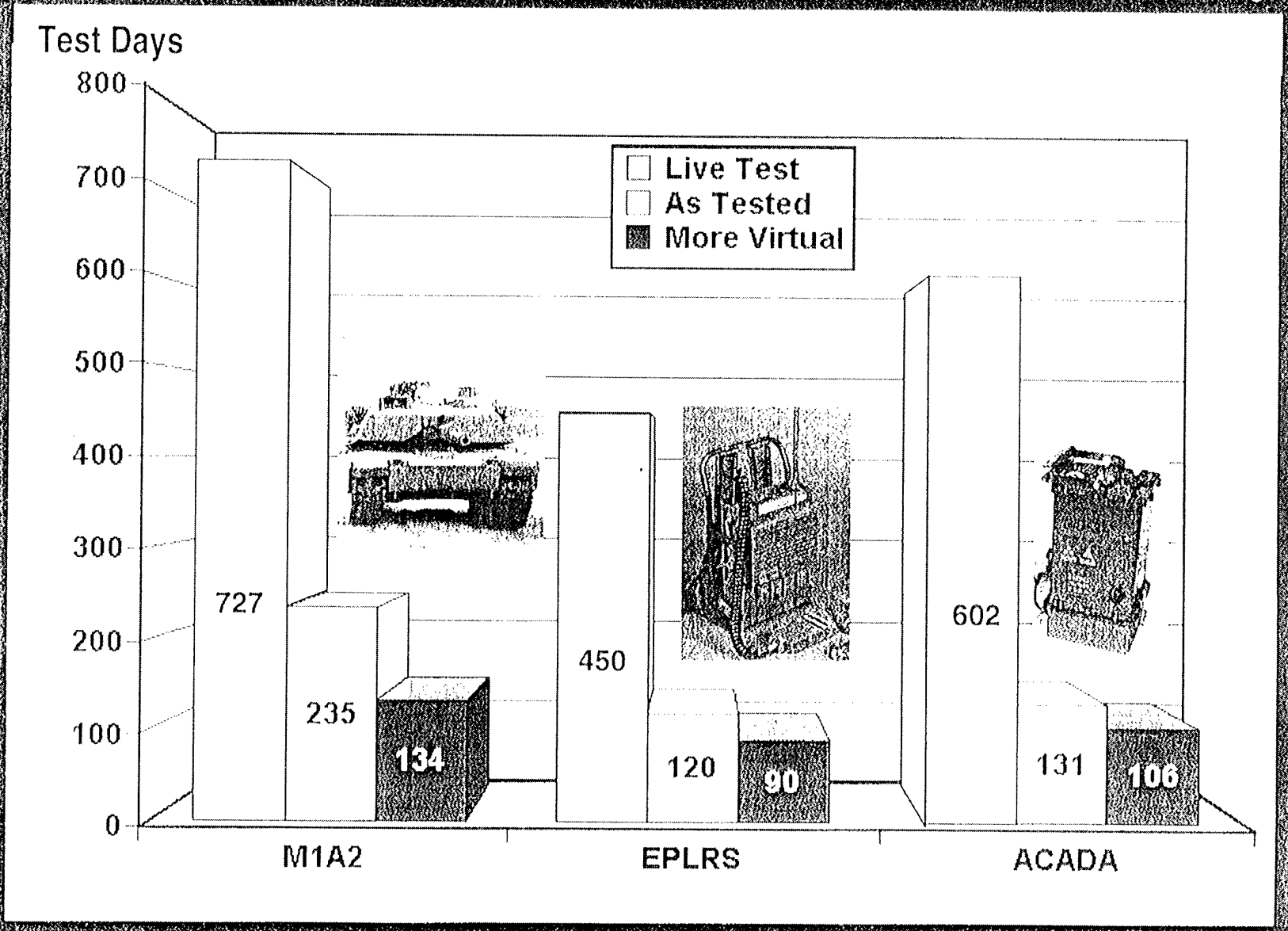

Joint Services Lightweight Integrated Suit Technology

Supported $6 Cost Avoidance Per Suit
$1.2M Annual Production Cost Avoidance
X 1,000,000 suits (Army & USMC)
= $6M Production Cost Avoidance

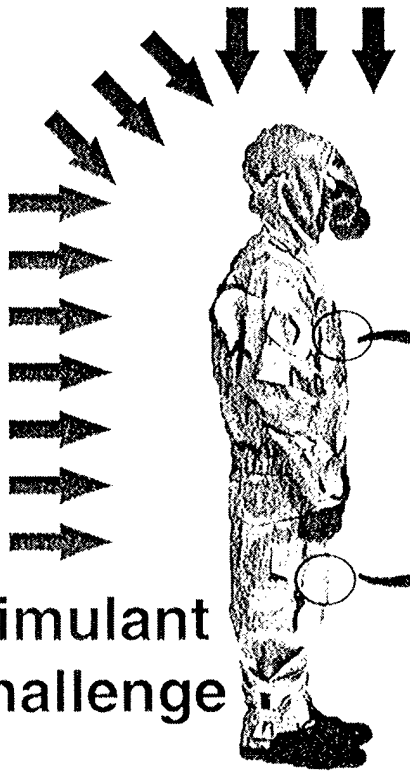

Simulant Challenge

Sampling Patches

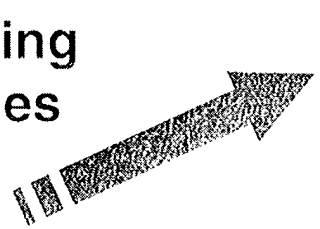

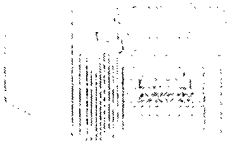

Survey Samples

Refine Design

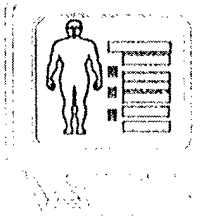

Model Physiological Response

Man-in-Simulant Test

CHEMICAL AGENT DETECTOR TESTING

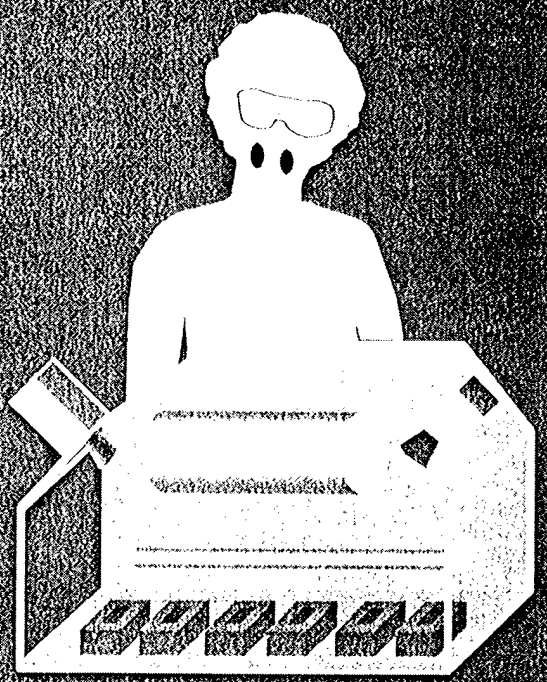

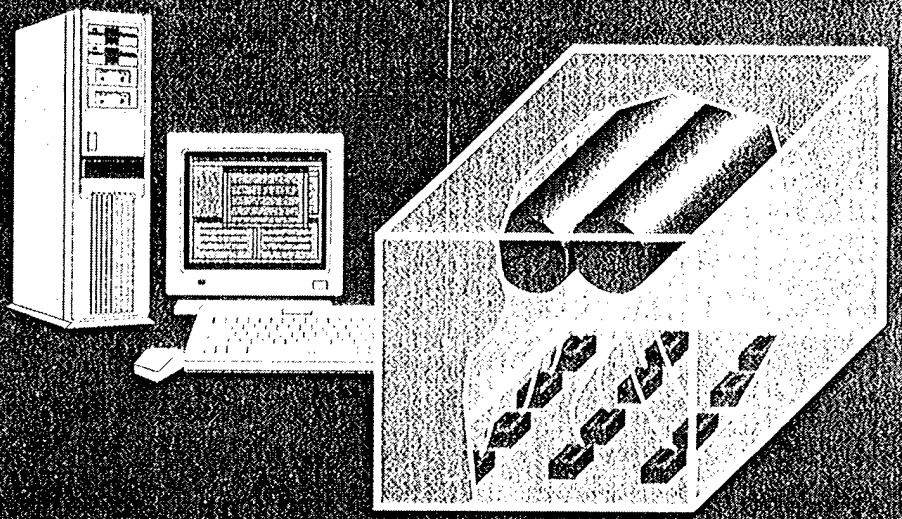

From:

- Manual Operation
- Video Data Collection

To:

- Automated Operation/Data Collection
- Better Control of Environment
- More Capacity
- Wider Range of Test Conditions
- Real-Time Monitoring of Performance

Flight Test Simulation Station

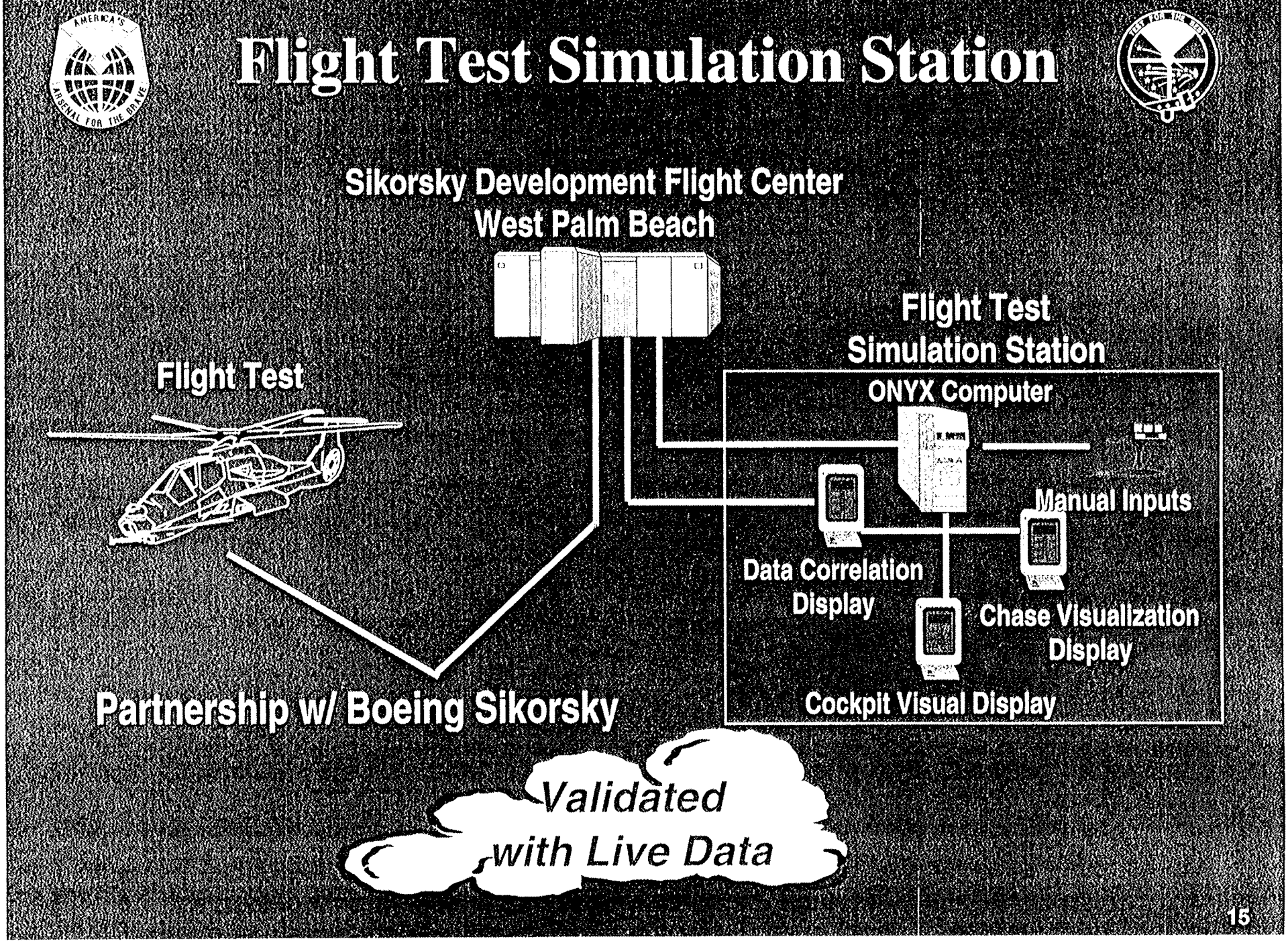

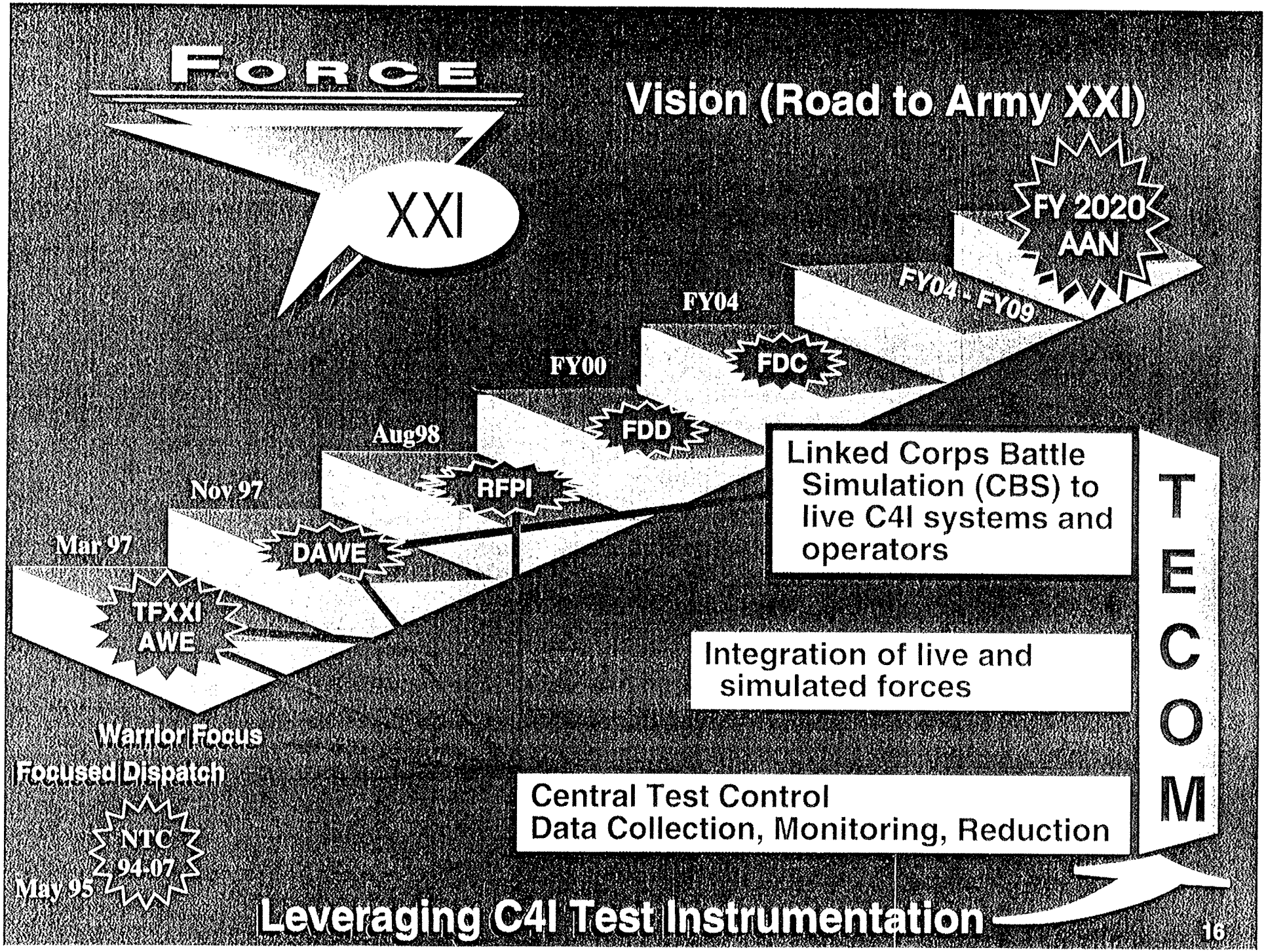
FORCE XXI
Vision (Road to Army XXI)
FY 2020 AAN
FY04 - FY09
FY04
FDC
FY00
FDD
Aug98
RFPI
Nov 97
DAWE
Mar 97
TFXXI AWE
Warrior Focus
Focused Dispatch
NTC 94-07
May 95
Linked Corps Battle Simulation (CBS) to live C4I systems and operators
Integration of live and simulated forces
Central Test Control
Data Collection, Monitoring, Reduction
TECOM
Leveraging C4I Test Instrumentation

Combat Synthetic Test & Training Assessment Range (CSTTAR)

Constructive Wraparound...

Entities (JANUS Simulation & Instrumented Live)

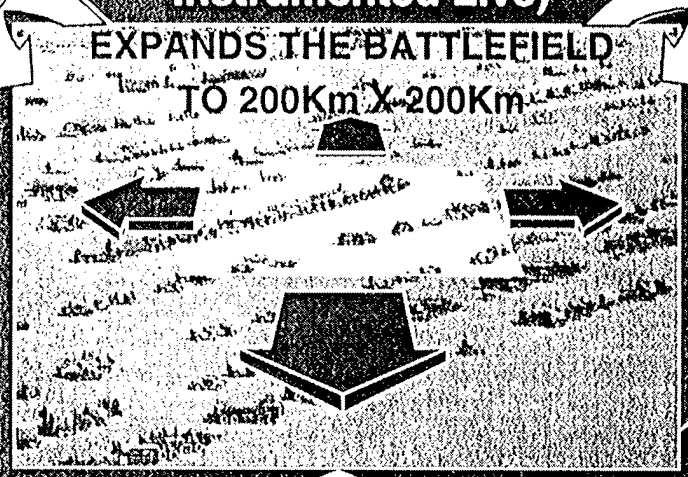

D I S

Virtual Seamless

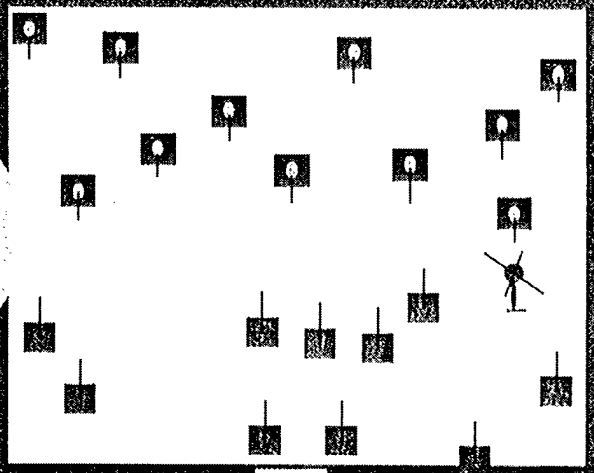

UAV / JSTARS

ASAS

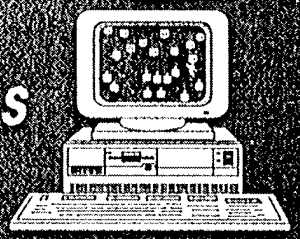

System Simulators

Rapid Force Projection Initiative

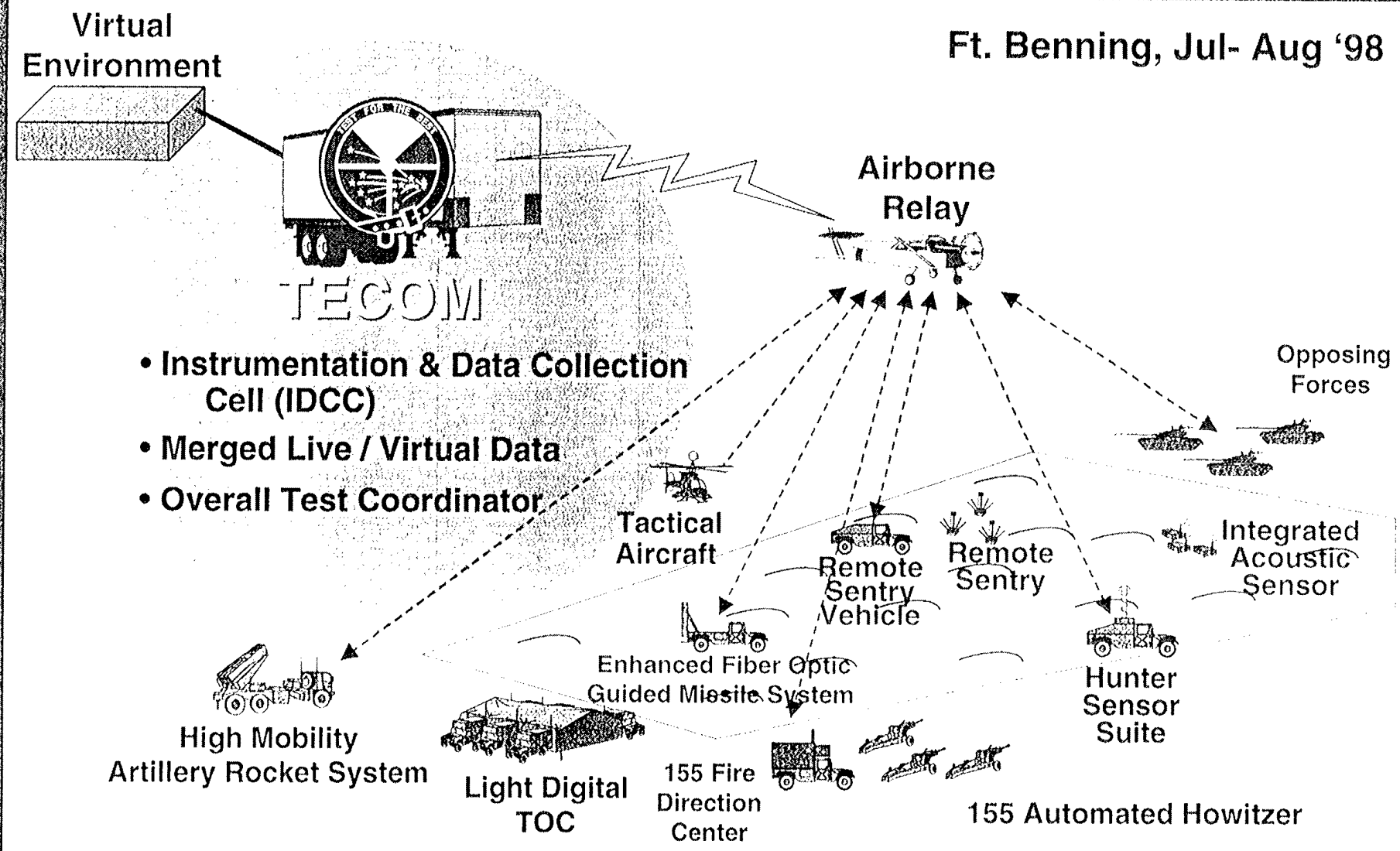

FIRING IMPULSE SIMULATOR

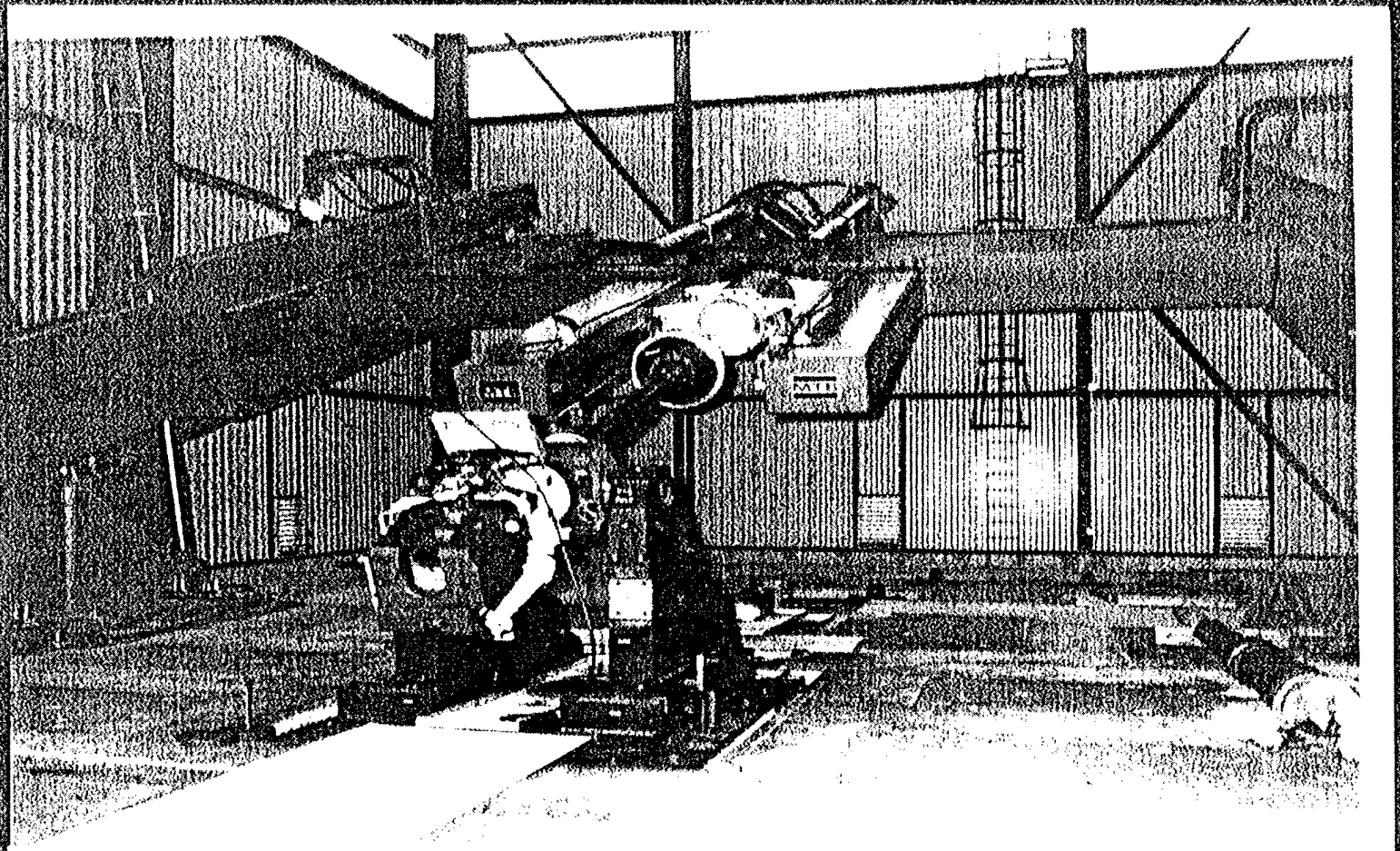

- DELIVERS APPROXIMATELY 3 MILLION POUNDS OF FORCE
- REPLICATES ACTUAL FIRING WITHOUT AMMUNITION, NOISE, TOXIC FUMES, BLAST OVERPRESSURES, AND RANGE CLEAN-UP

Low Cost Competent Munitions Modeling Project

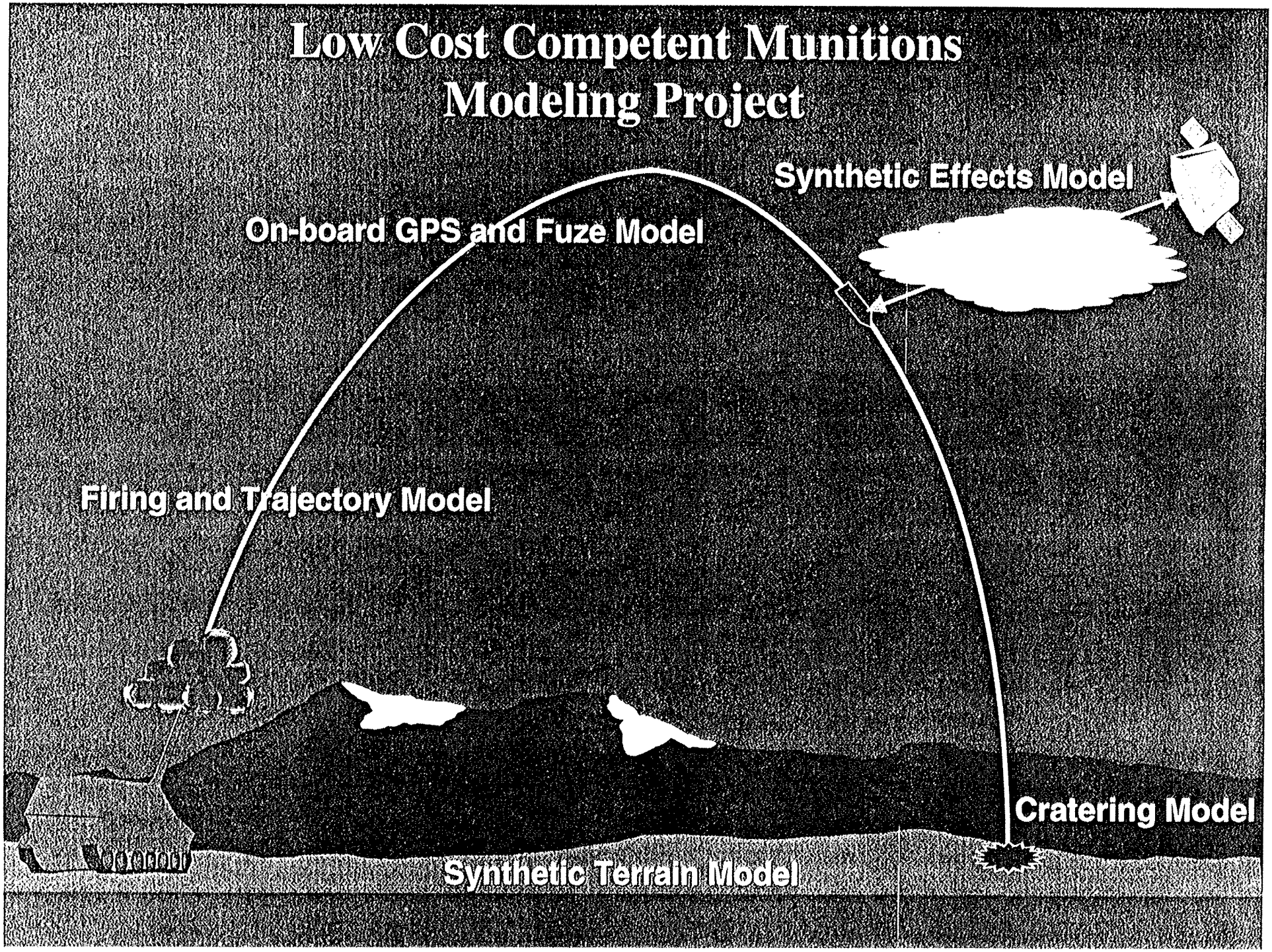

SHOCK & VIBRATION MODELS

CRUSADER AND HARDENED SUBMINIATURE TELEMETRY

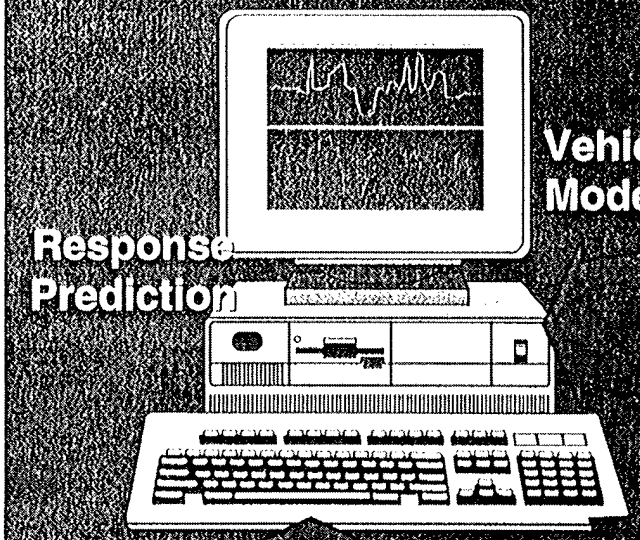

Response Prediction

Vehicle Models

(SPH) SELF-PROPELLED HOWITZER

(RSV) RESUPPLY VEHICLE

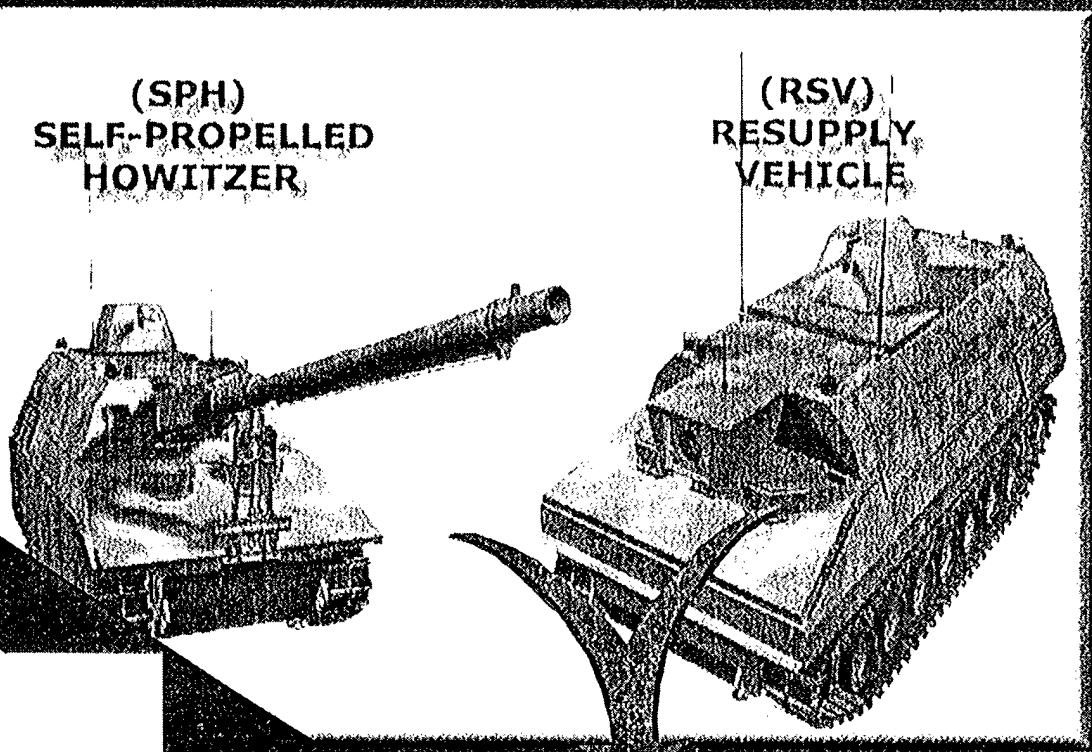

Virtual Instrumentation

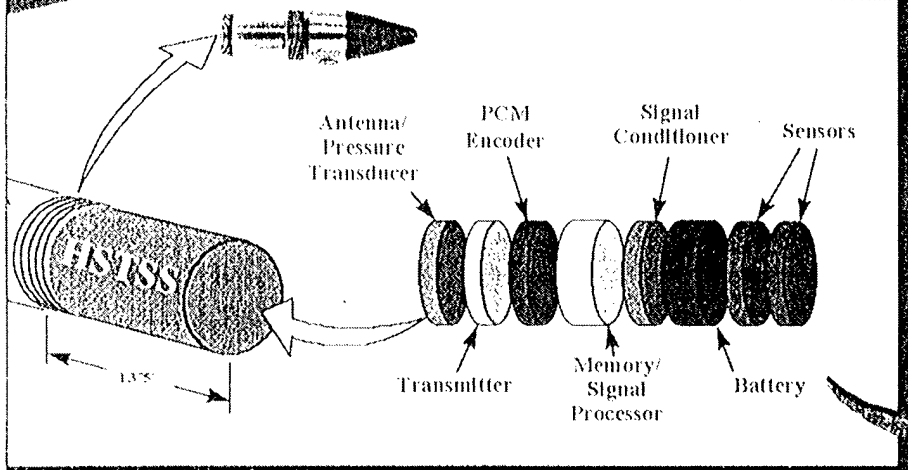

Ground Truth Data

Advanced InfraRed Simulator

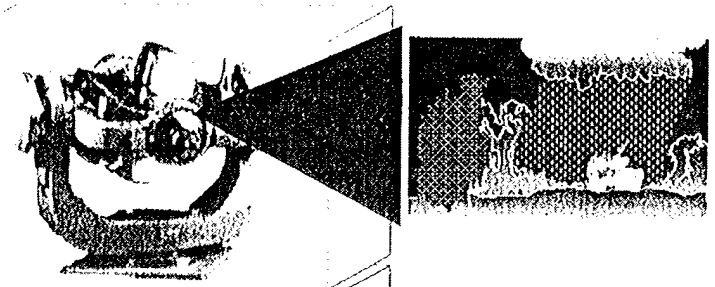

TV Viewing Monitor

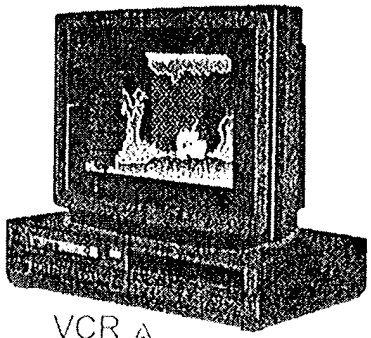

VCR

Analog Video

Live TOW Gunner

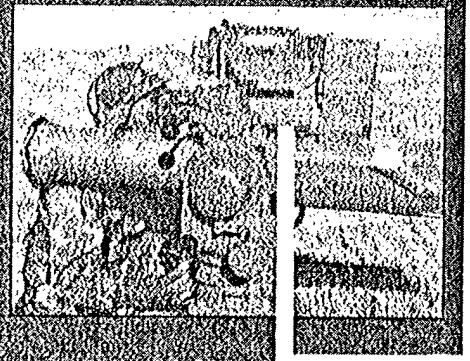

Traversing Unit

Scene Generator

Position Sensors

Scene Generator Electronics

Umbilical

RS-232 and SCSI

CD-ROM

Contains:
- Backgrounds
- Targets
- Missile Signatures

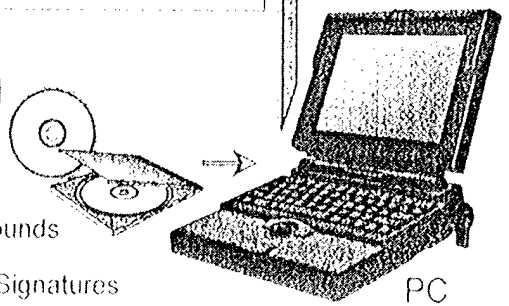

PC Notebook

Fire Control Subsystem

QV - Quantitative Visualization

RT - QV Info_sources

NRT - QV Info

Video | MET | Survey | GPVIS | etc. ••• | GIS

Context Filter INFO OUT | Context Filter INFO OUT | Context Filter INFO OUT | Context Filter INFO OUT | Context Filter INFO OUT

Information Network

Information Presentation ("Thin Clients")

* Qualitative
* Quantitative
* User Specific
* Real Time
* Platform Independent

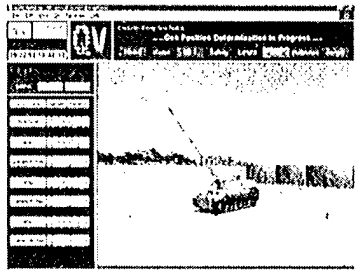

ODBC/SQL | RTI

COTS Data Bases | HLA Federates

RT, NRT - QV Clients

RT, NRT - DB, M&S

GPVIS - Master Controller

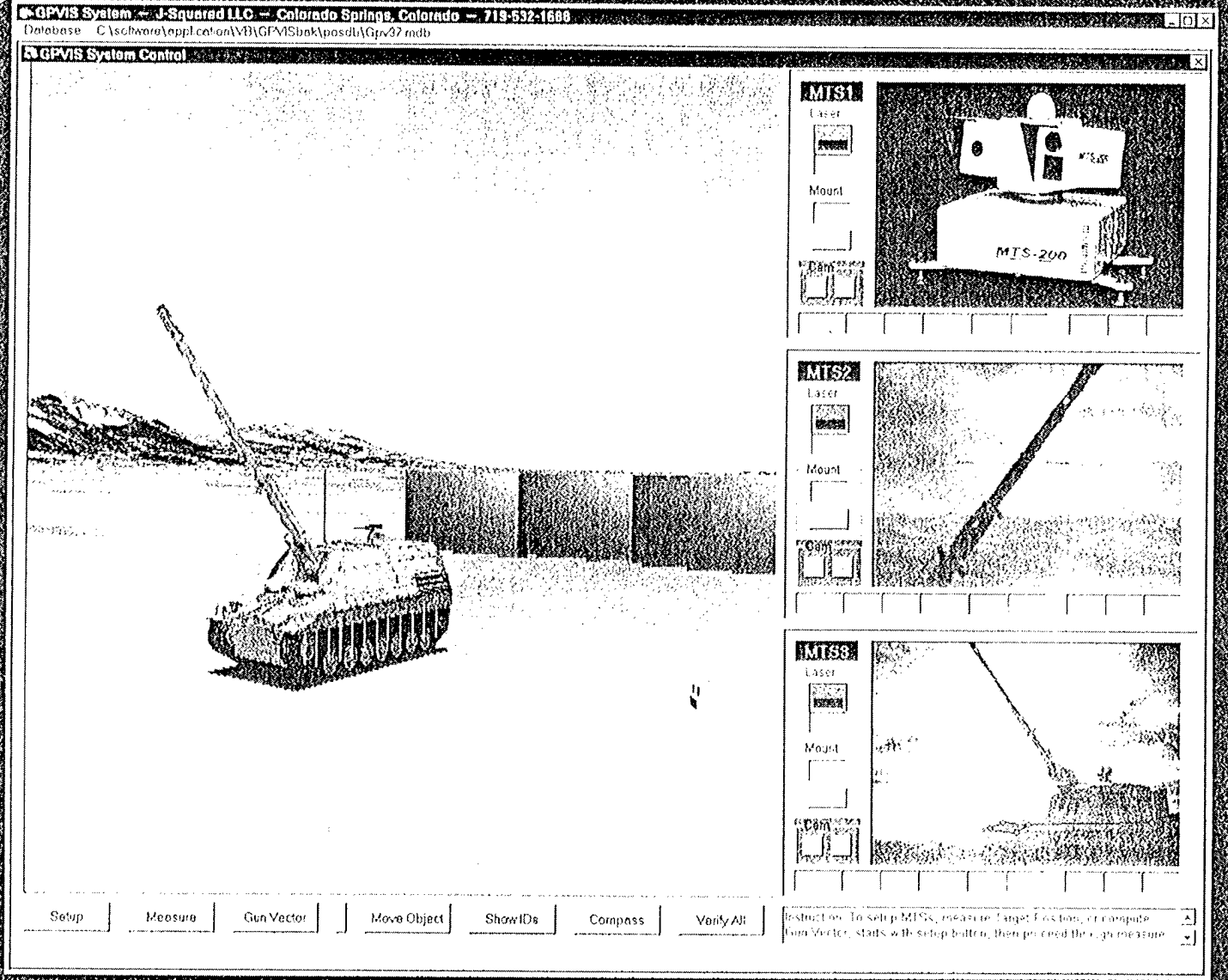

Range Support Operation Example

Gun Position Operation:
- Boresight
  - Obtain Aim Point
    - >*point* > End Game MTSs
- Super-Elevation
  - Obtain flight path
    - >*point* > Midcourse MTSs
- Chassis Orientation
  - Firing Dynamics

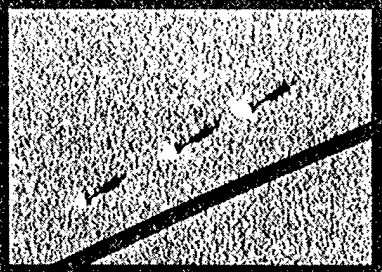

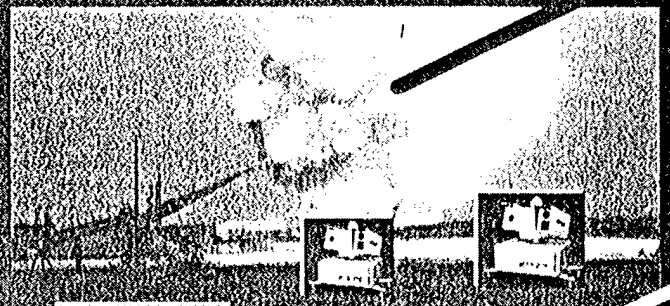

MET

End Game Position:
- High-Speed Photography
- Virtual Target Scoring
- Hard Target Scoring/Effects
- Weapon Vector Scoring

Standard Network Support

Midcourse Position:
- High-Speed Photography >> Ballistic Analysis
- Virtual Target Scoring

LAN & WAN Architectures with ATM & Ethernet (TCP/IP) Support

How To Reach Us

Address:

U. S. Army Test & Evaluation Command
314 Longs Corner Road
ATTN: AMSTE-TM-O
Aberdeen Proving Ground, MD 21005-5055

Phone:

410-278-1417

E-mail:

tmo@tec1.apg.army.mil

TECOM On-Line:

http://www.tecom.army.mil


Bottom Line
TEST TECHNOLOGY GETS GOOD STUFF FOR OUR SOLDIERS...
...with Confidence!
27

"Precision Fire Technology"

presented by

Peter Plostins
Chief, Aerodynamics Branch
Ballistics and Weapons Concepts Division
Weapons and Materials Research Directorate
US Army Research Laboratory

Wednesday, November 18, 1998
9th US Army Gun Dynamics Symposium
McLean, VA

OUTLINE

- BACKGROUND
- DIRECT FIRE JUMP AND DISPERSION MODEL
  - GUN DYNAMICS
  - TRANSITIONAL BALLISTICS
  - FREE FLIGHT AERODYNAMICS
- SIMULATION, MODELING AND EXPERIMENTAL METHODS
- SUMMARY

ACCURACY PROBLEM

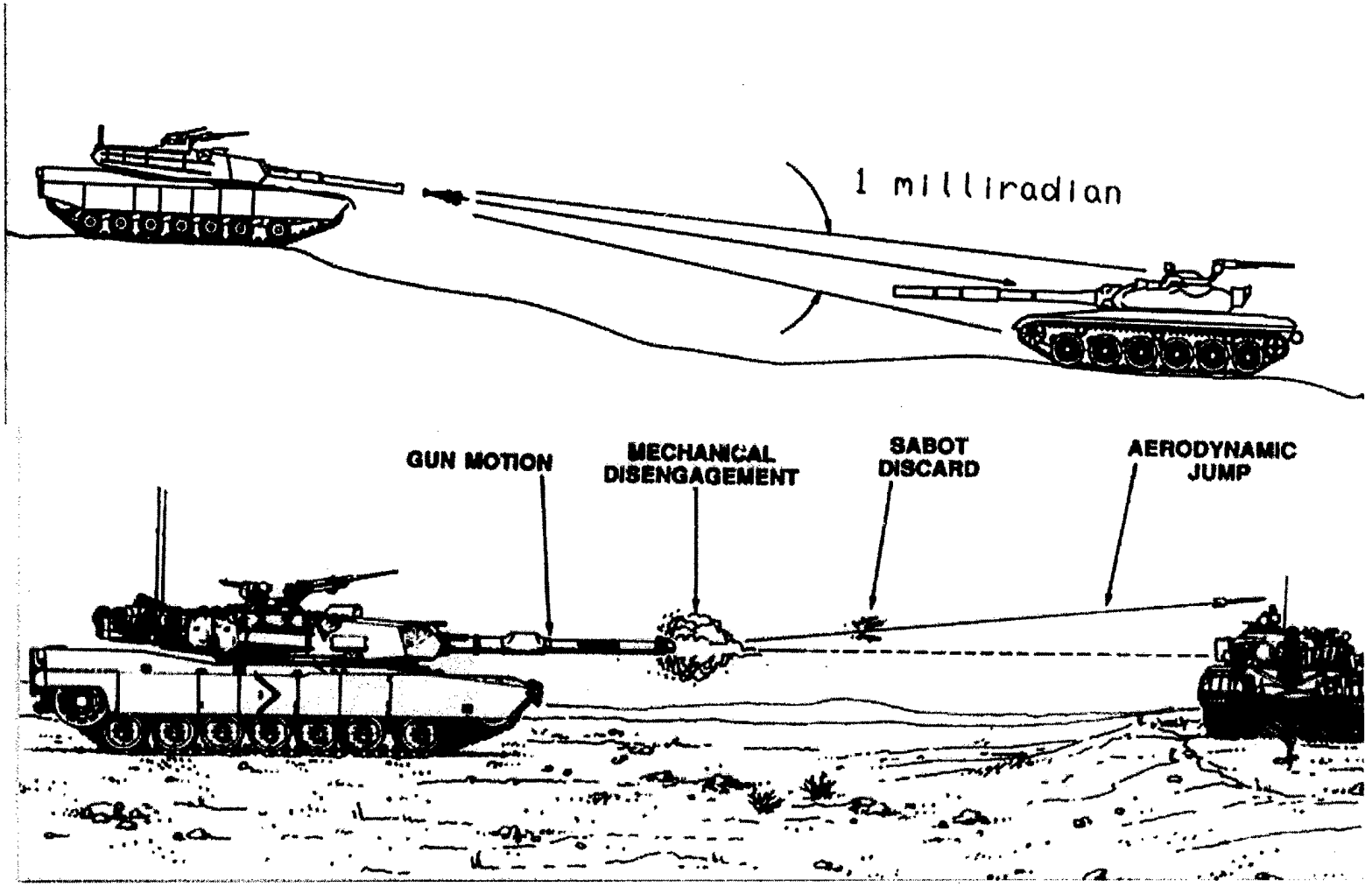

PROJECTILE JUMP 3-D SCHEMATIC

WEAPONS and MATERIALS RESEARCH
DIRECTORATE
Ballistics and Weapons Concepts Division

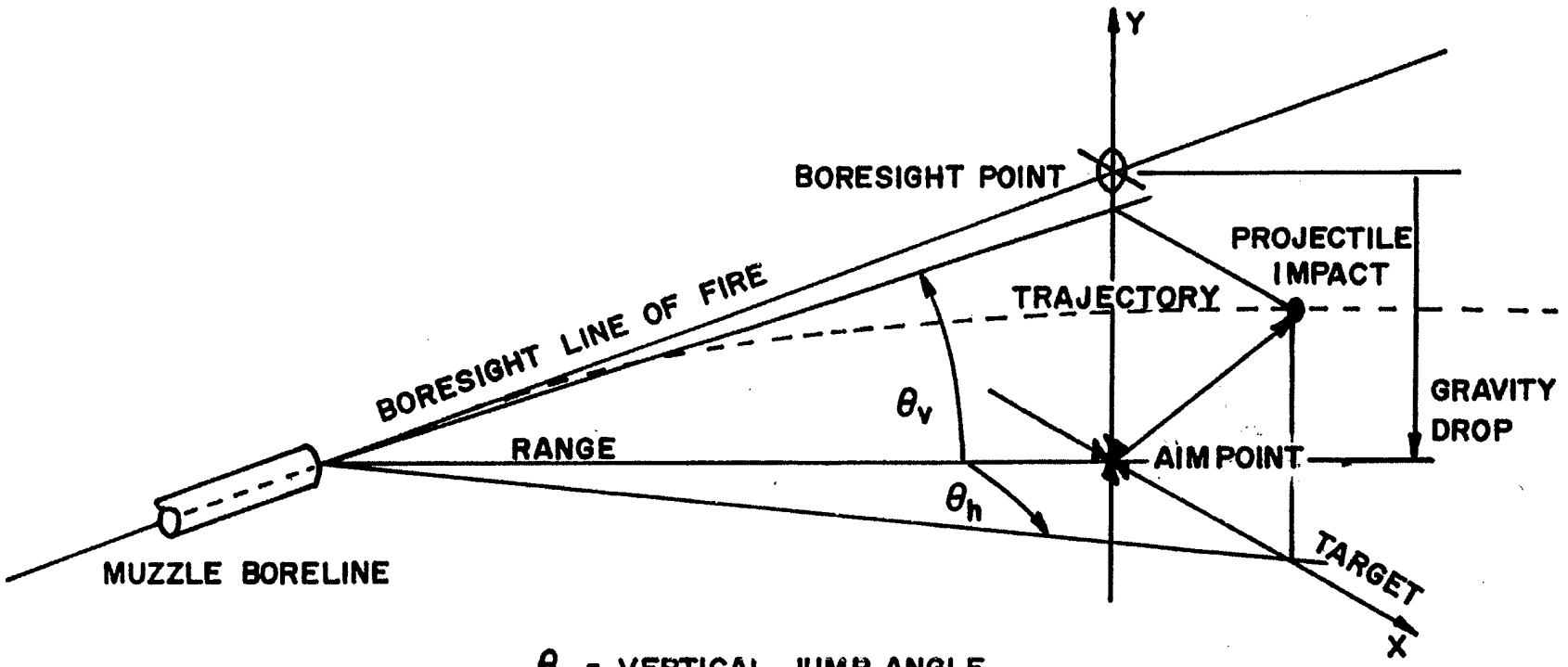

θ_v = VERTICAL JUMP ANGLE

θ_h = HORIZONTAL JUMP ANGLE

JUMP MODEL

WEAPONS and MATERIALS RESEARCH
DIRECTORATE
Ballistics and Weapons Concepts Division

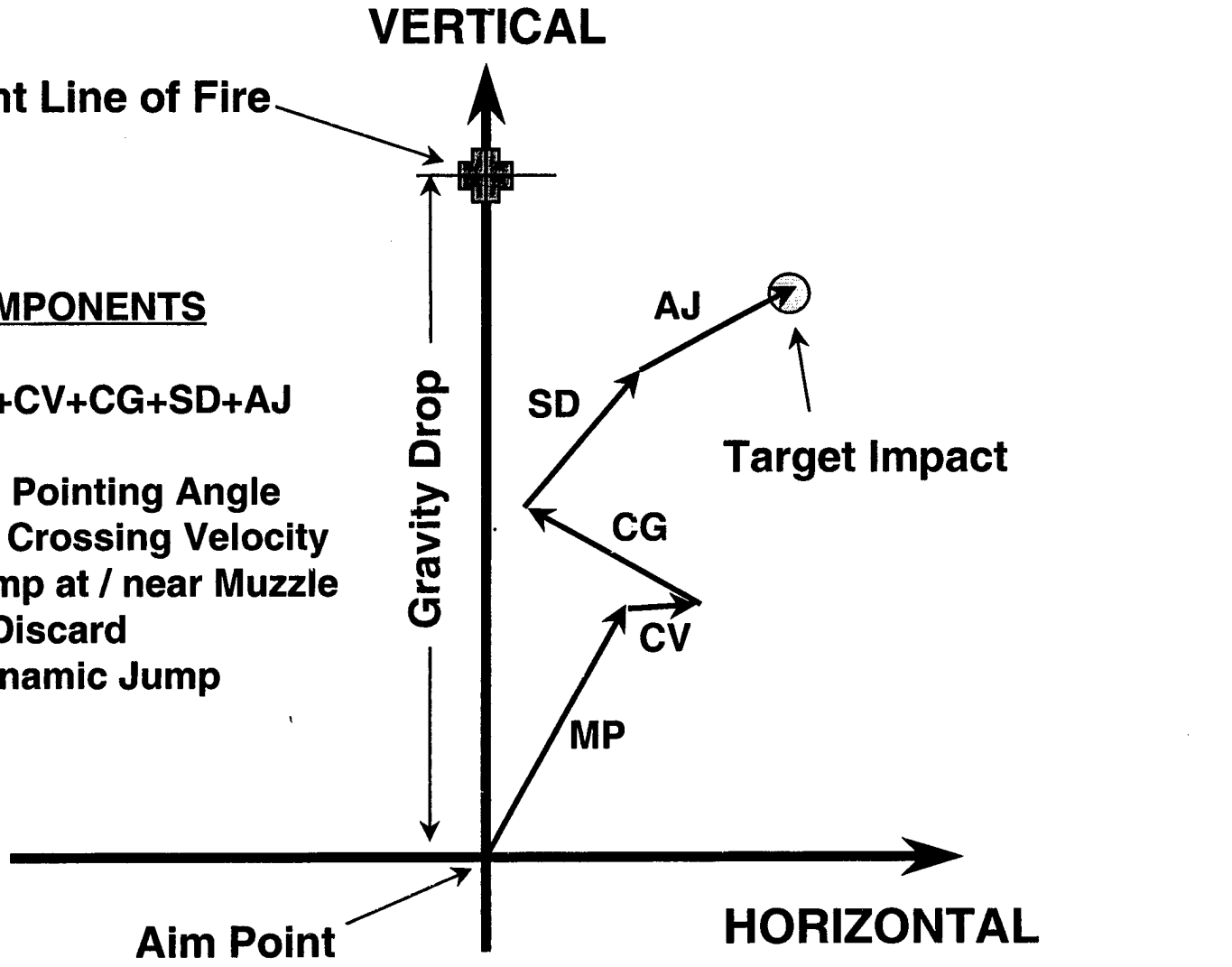

JUMP COMPONENTS

JUMP = MP+CV+CG+SD+AJ

MP - Muzzle Pointing Angle
CV - Muzzle Crossing Velocity
CG - CG Jump at / near Muzzle
SD - Sabot Discard
AJ - Aerodynamic Jump

DISPERSION MODEL

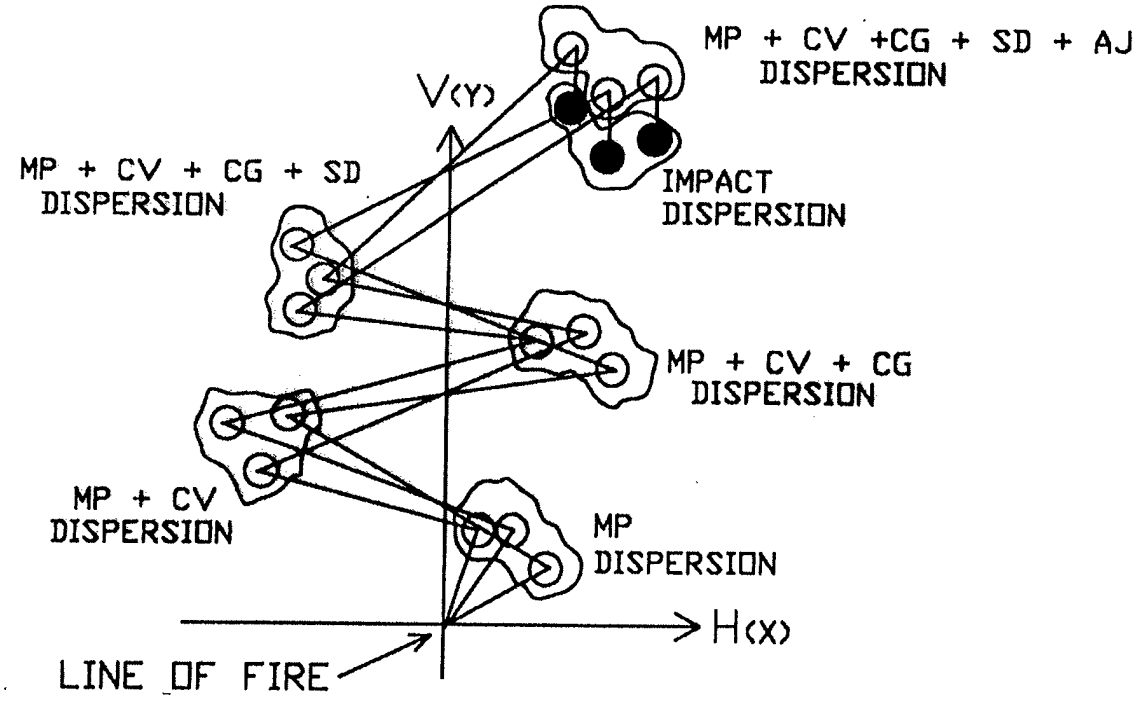

$$DISPERSION = MP + CV + CG + SD + AJ + GD + CORRELATIONS$$

$$\sigma^2 = \sigma_{mp}^2 + \sigma_{cv}^2 + \sigma_{cg}^2 + \sigma_{sd}^2 + \sigma_{aj}^2 + \sigma_{gd}^2 + 2\sigma_{cgaj}$$

GUN SYSTEM DYNAMICS

WEAPONS and MATERIALS RESEARCH
DIRECTORATE
Ballistics and Weapons Concepts Division

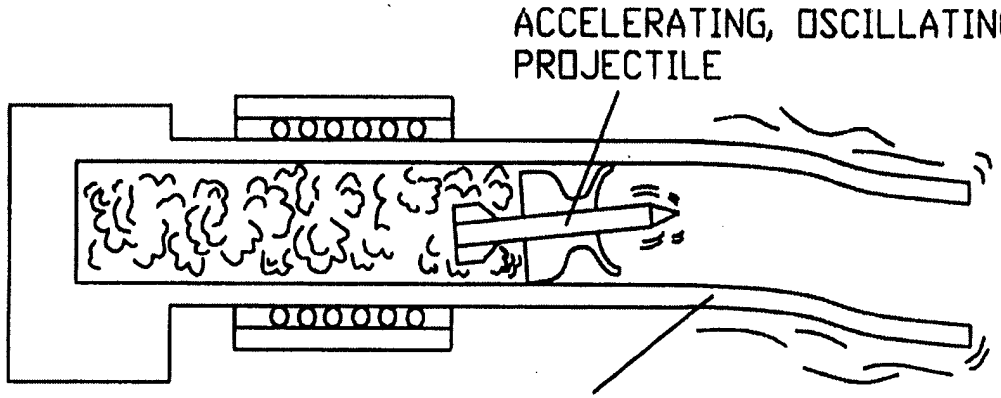

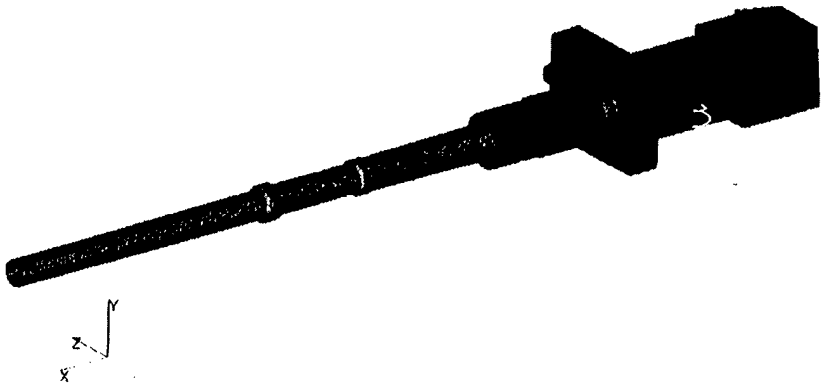

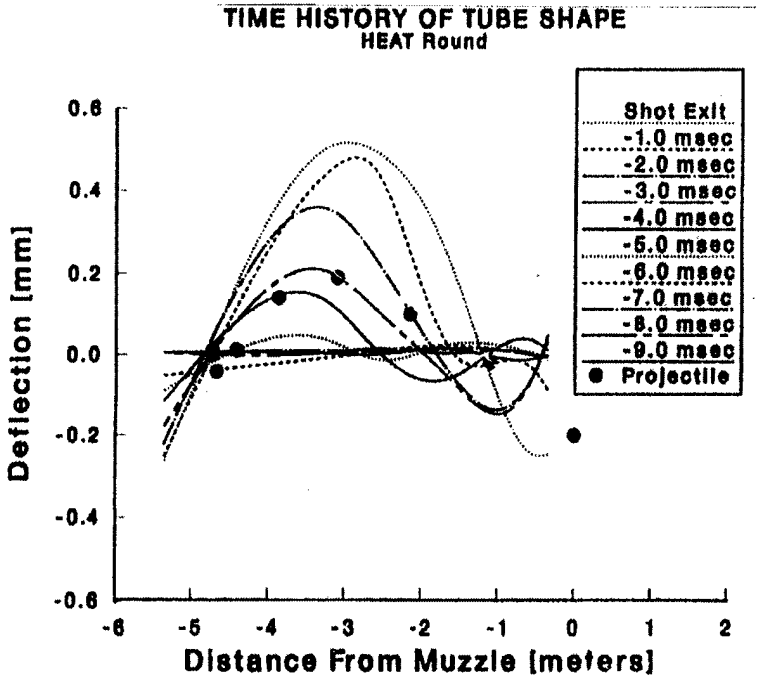

INTERIOR BALLISTIC DISTURBANCE

WEAPONS and MATERIALS RESEARCH
DIRECTORATE
Ballistics and Weapons Concepts Division

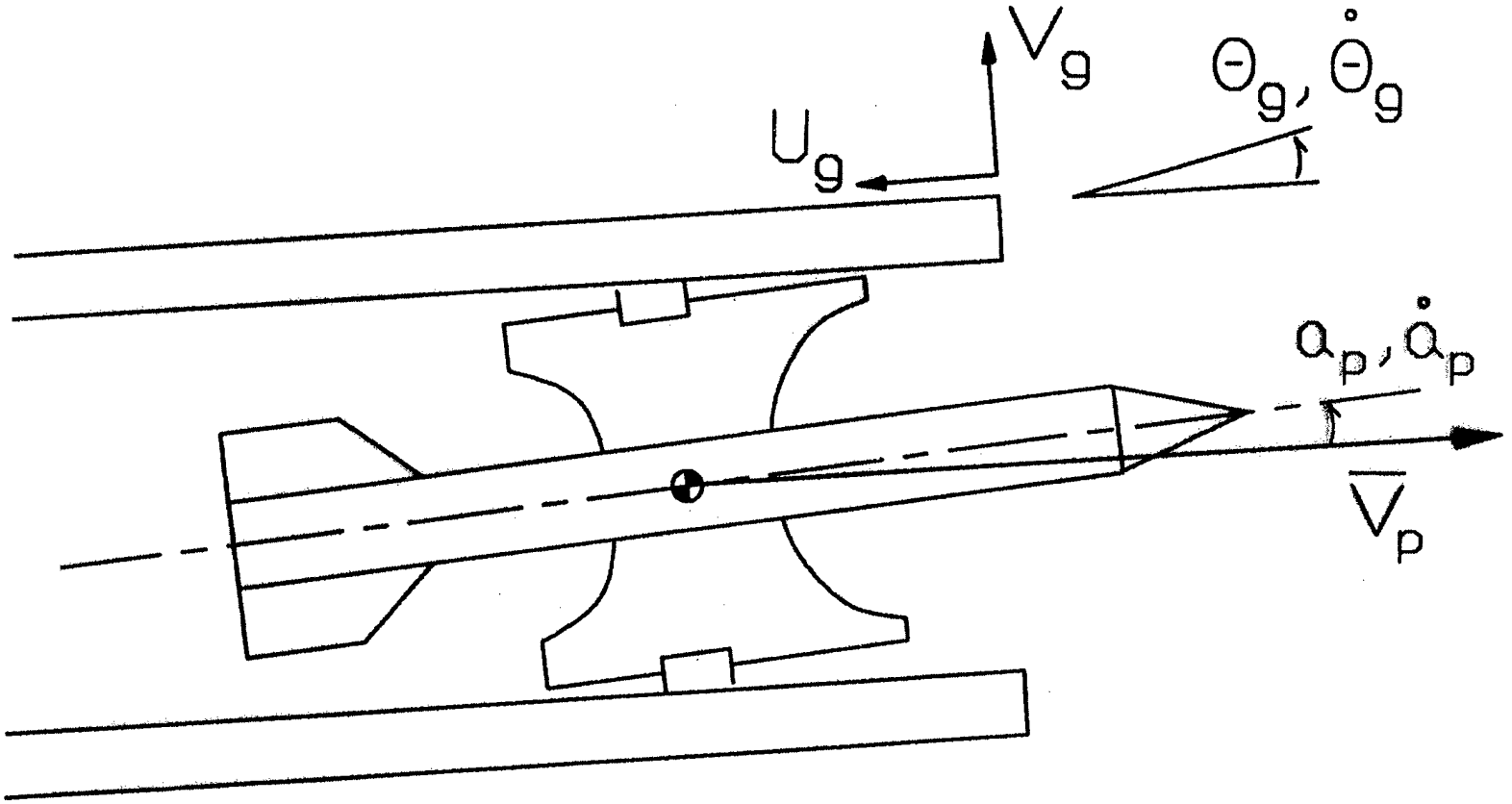

PROJECTILE DYNAMIC STATE AT THE MUZZLE

INBORE STRUCTURAL DYNAMICS MODELING

WEAPONS and MATERIALS RESEARCH
DIRECTORATE
Ballistics and Weapons Concepts Division

- Structural Modeling of the inbore balloting allows the optimization of the inbore response
- The dynamics of the projectile at shot exit are a parameter in the launch accuracy
- The complete 6 DOF dynamic state of the projectile can be evaluated

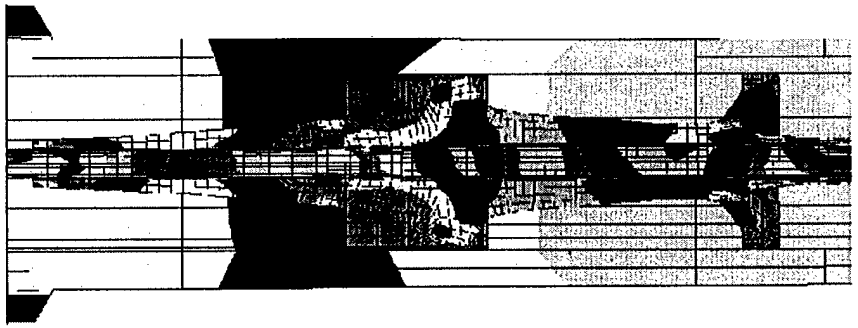

M829A1 Stress and Displacement Dynamic Simulation

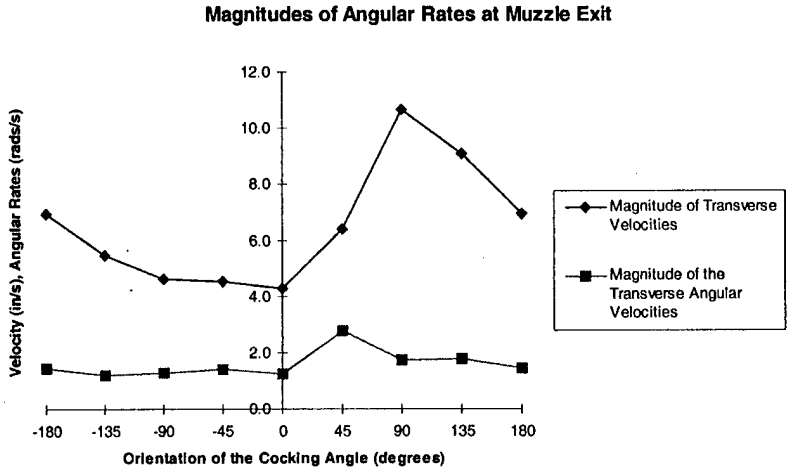

Muzzle Exit Parameter Optimization

GUN MUZZLE MOTION

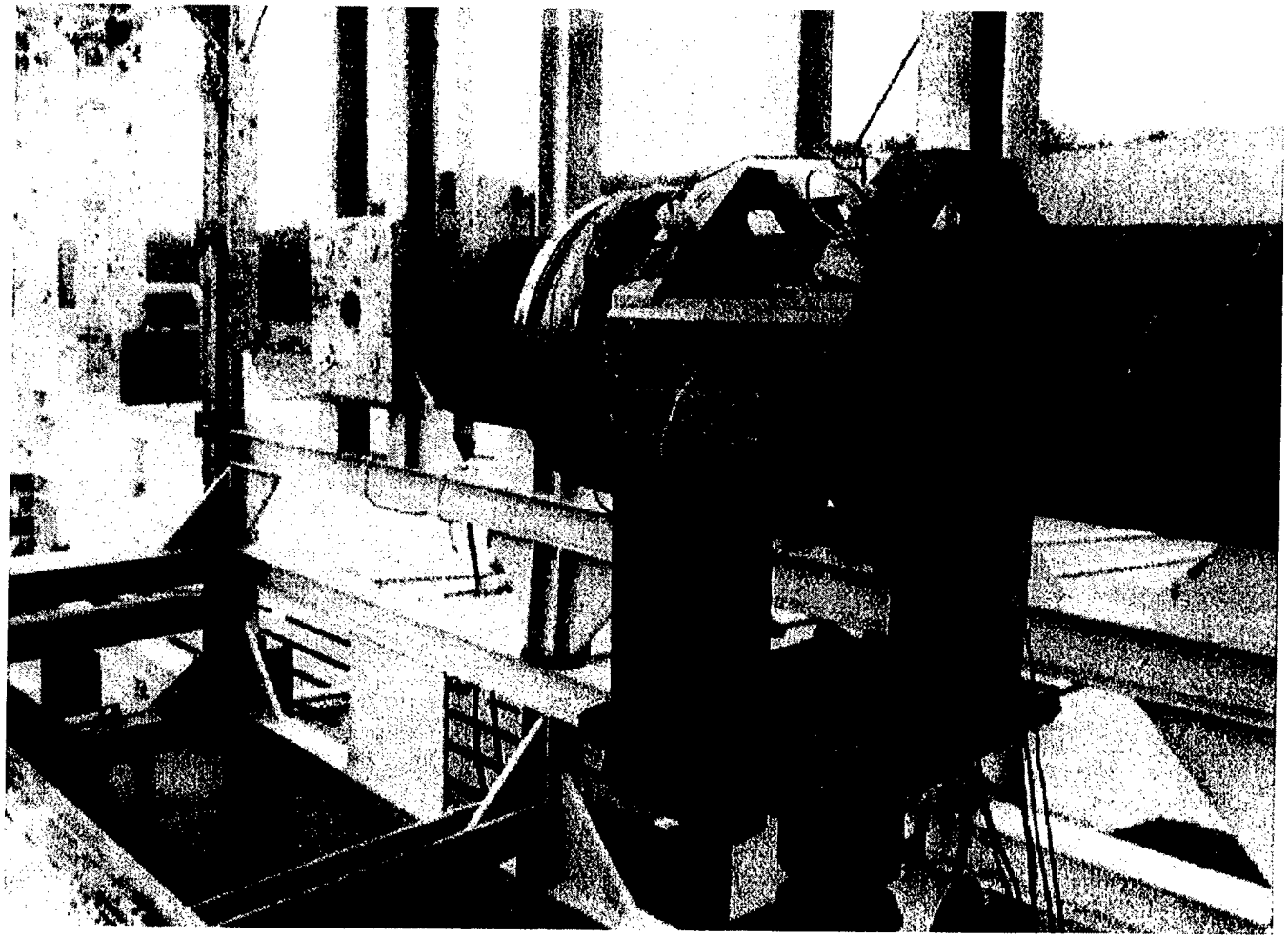

JUMP TEST RESULTS

WEAPONS and MATERIALS RESEARCH
DIRECTORATE
Ballistics and Weapons Concepts Division

Muzzle Pointing Angle
Horizontal Component (Azimuth)

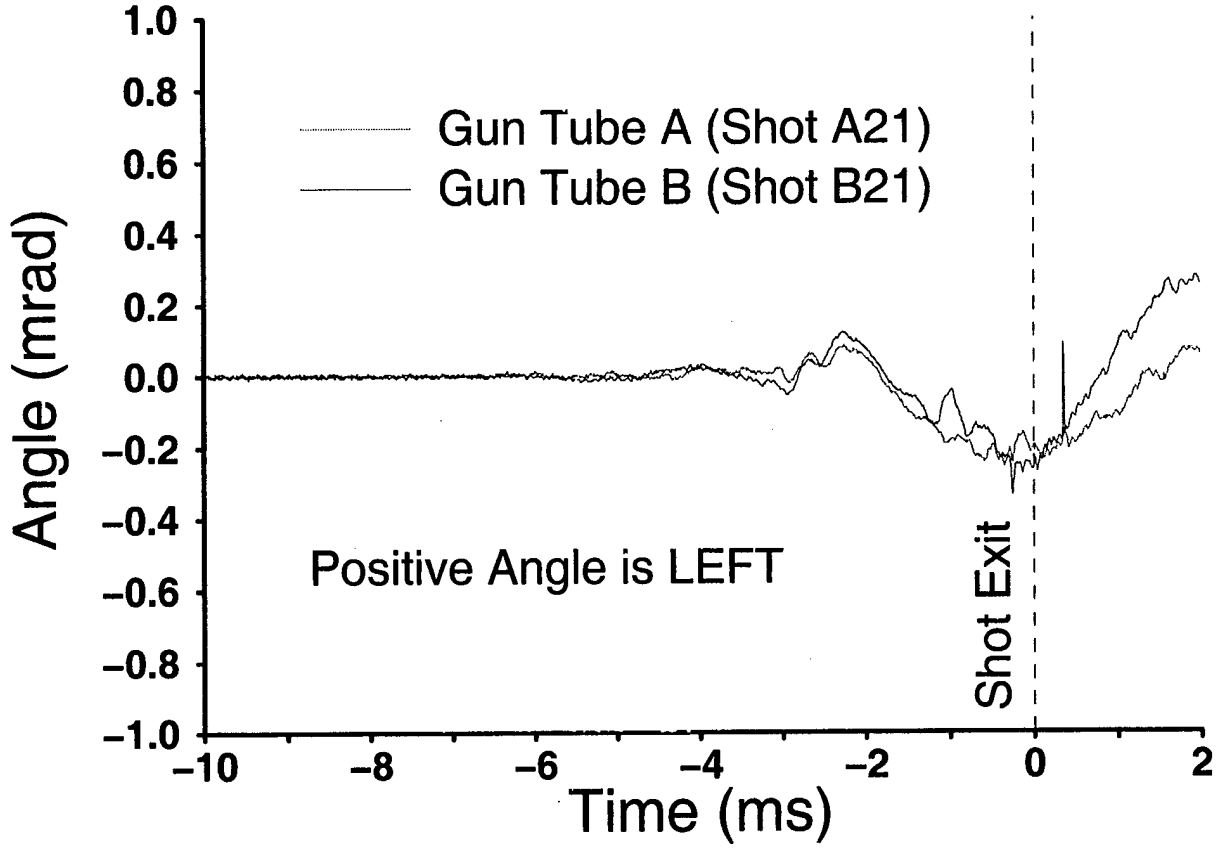

JUMP TEST RESULTS

WEAPONS and MATERIALS RESEARCH DIRECTORATE
Ballistics and Weapons Concepts Division

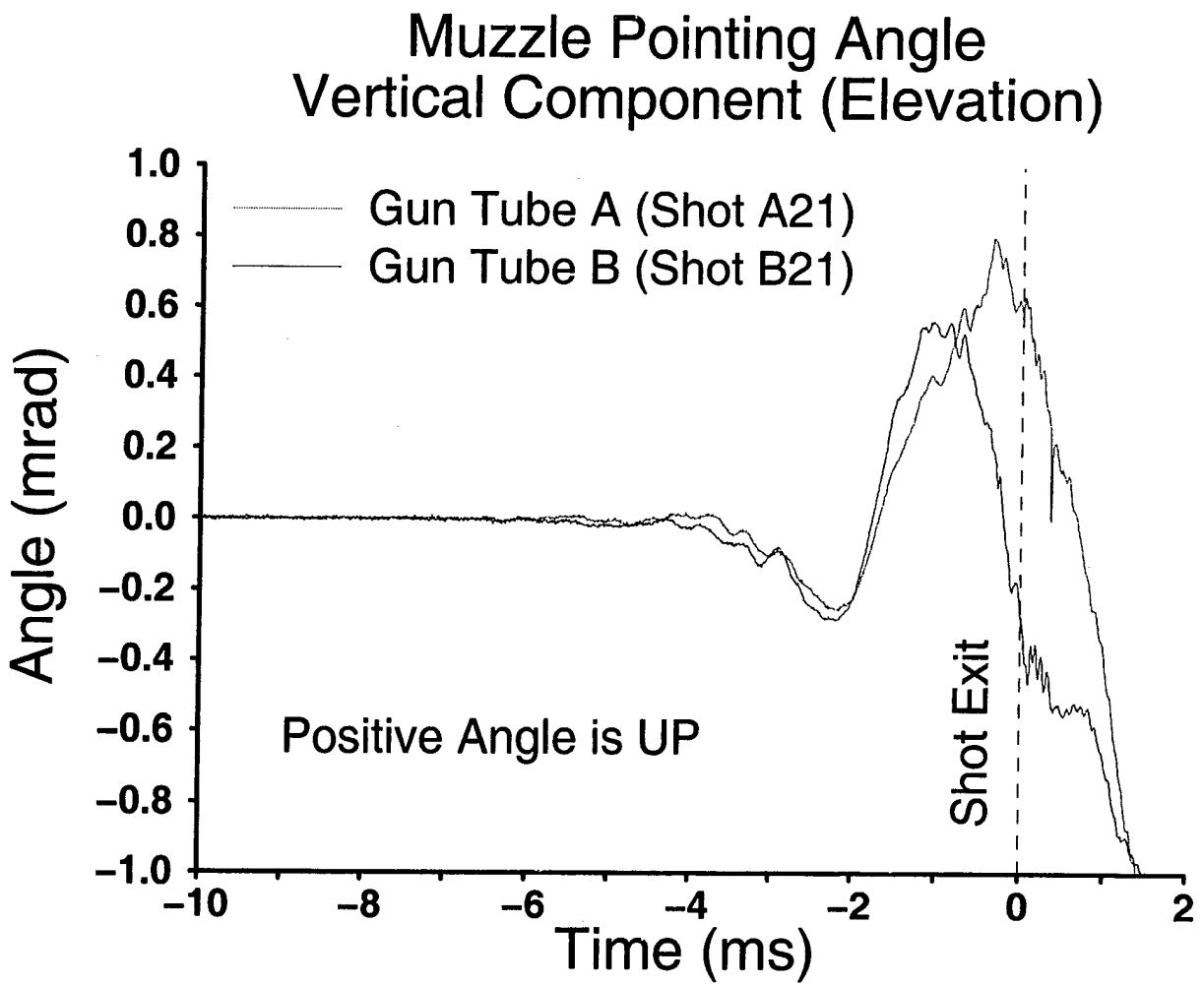

TUBE COMPARISON

WEAPONS and MATERIALS RESEARCH
DIRECTORATE
Ballistics and Weapons Concepts Division

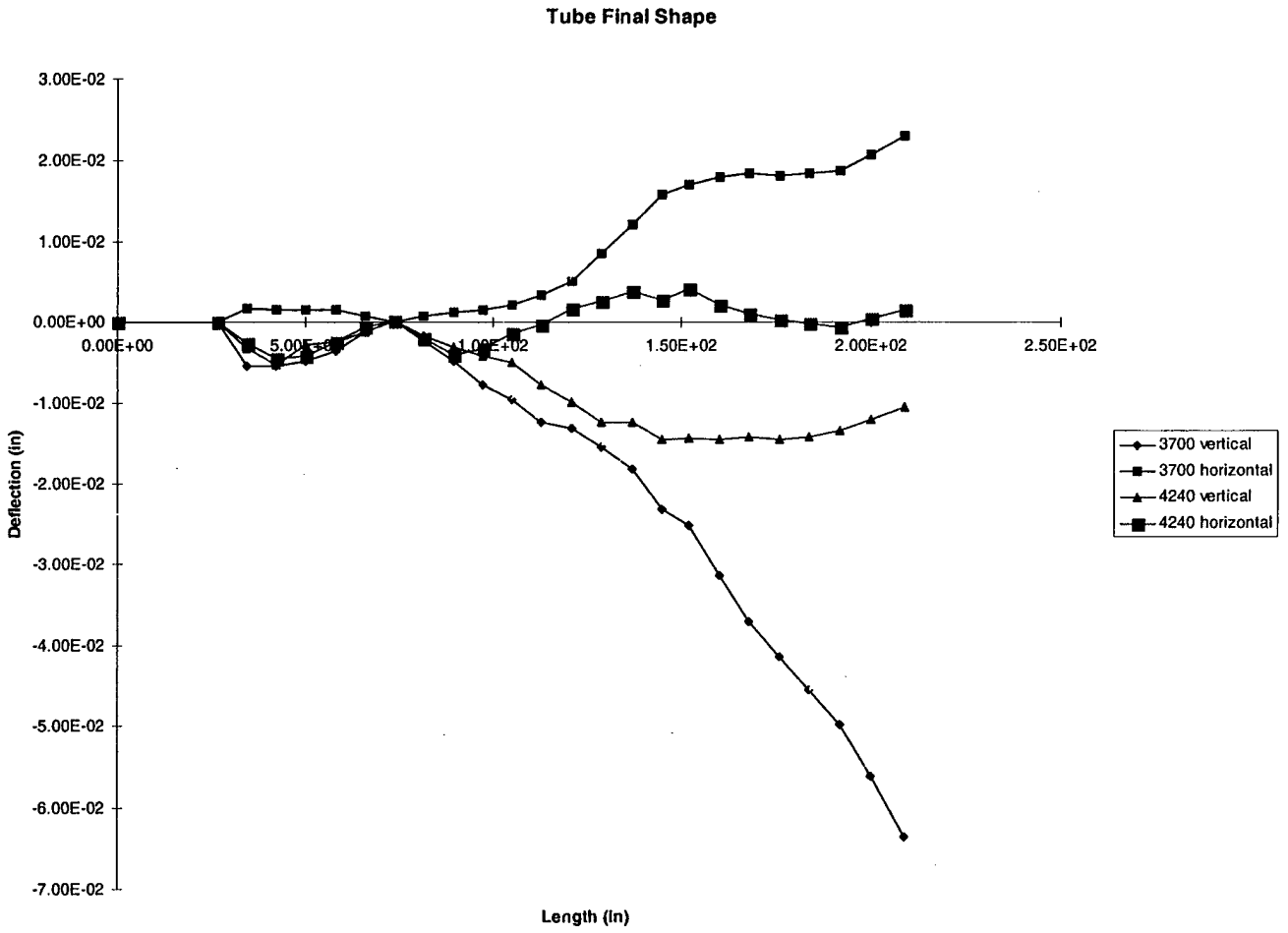

TUBE COMPARISON

Tube Centerline Comparison

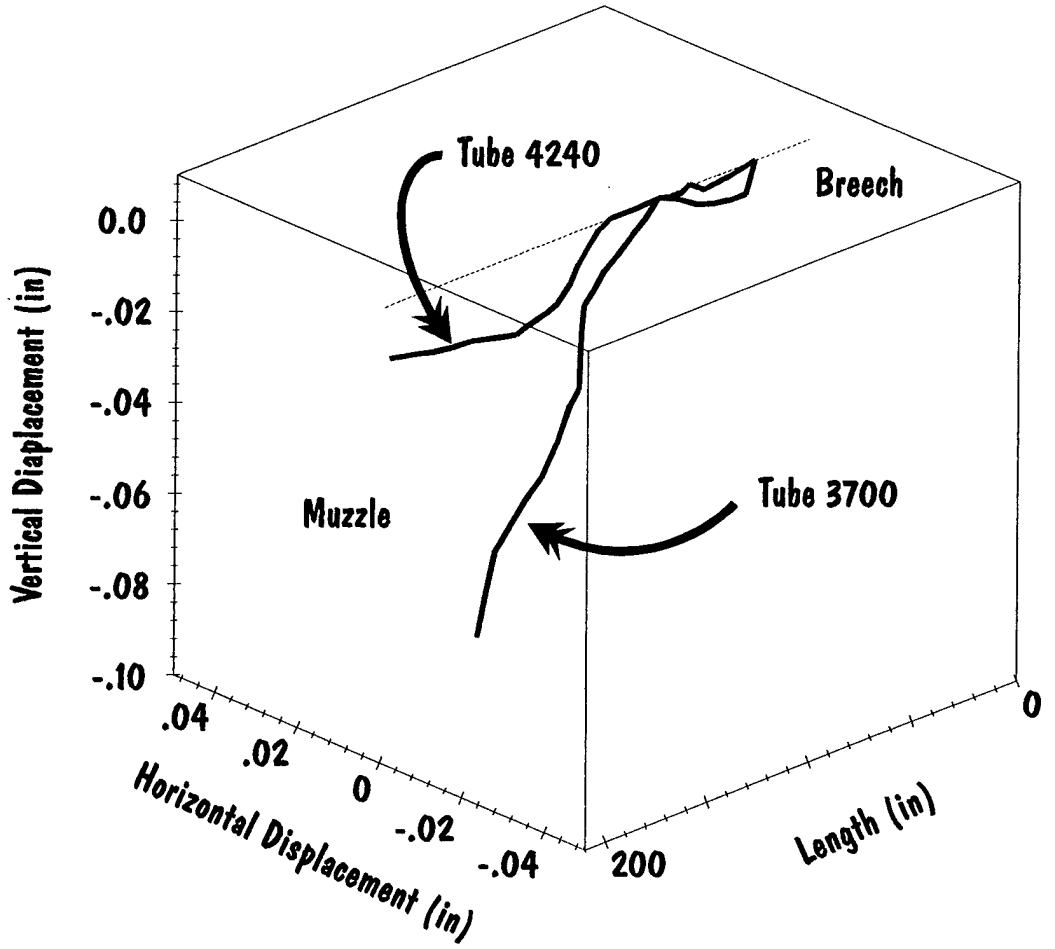

Projectile Angular Rate at Launch Looking Downrange

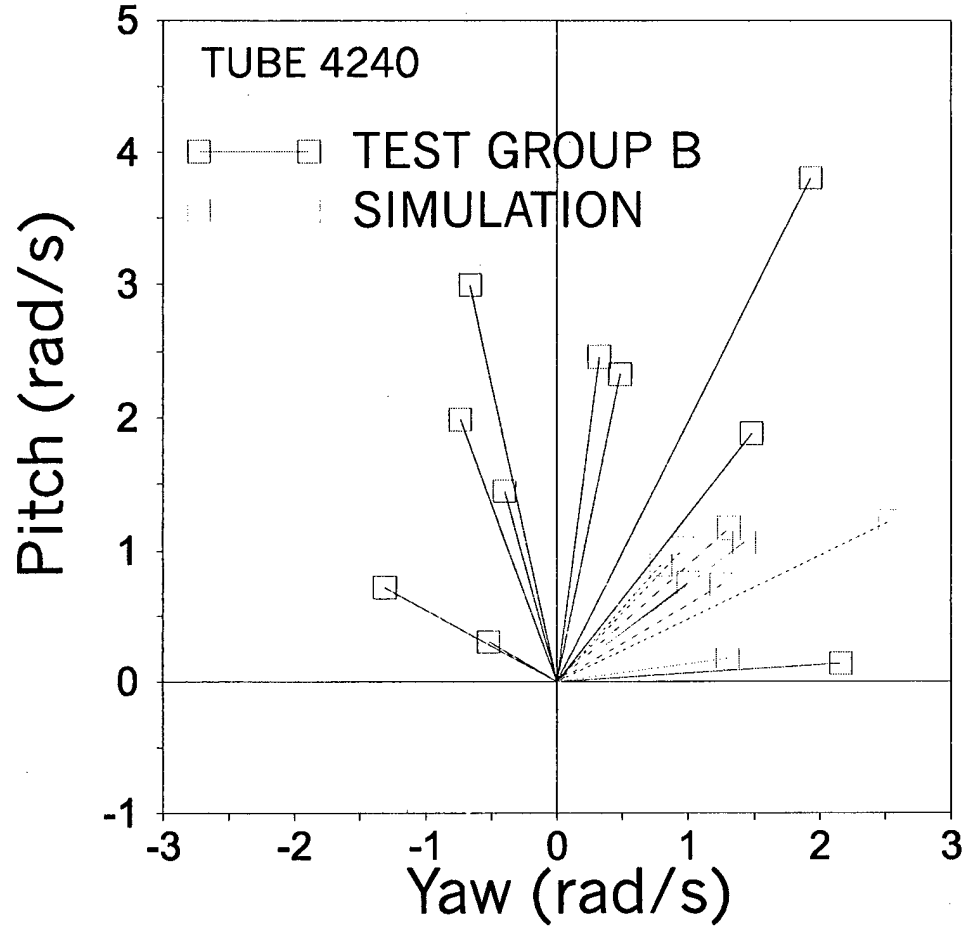

GUN THERMAL MANAGEMENT

WEAPONS and MATERIALS RESEARCH DIRECTORATE
Ballistics and Weapons Concepts Division

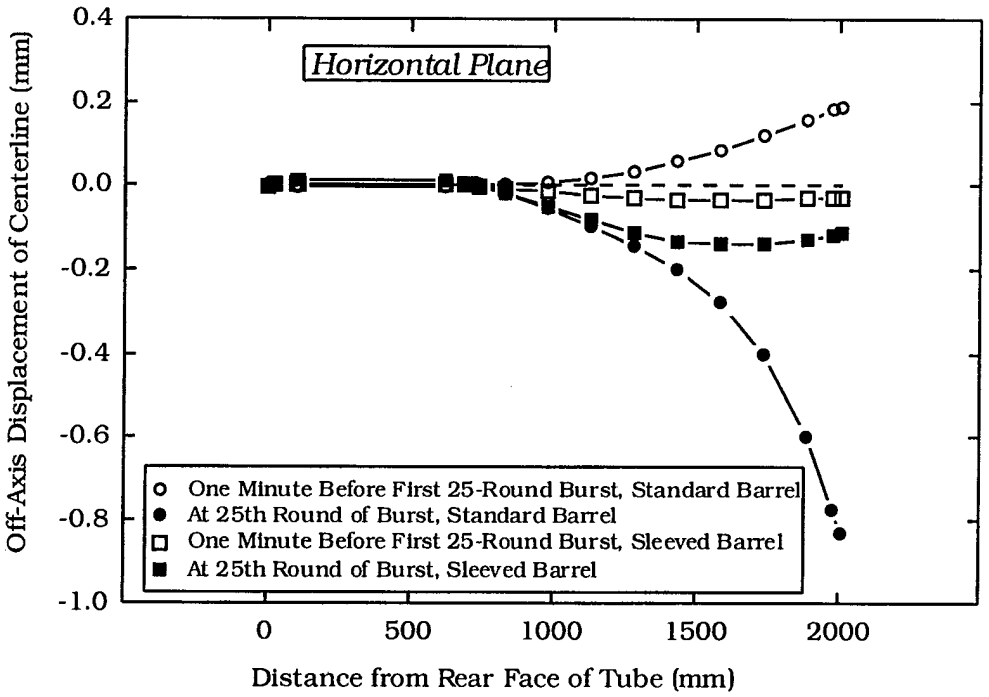

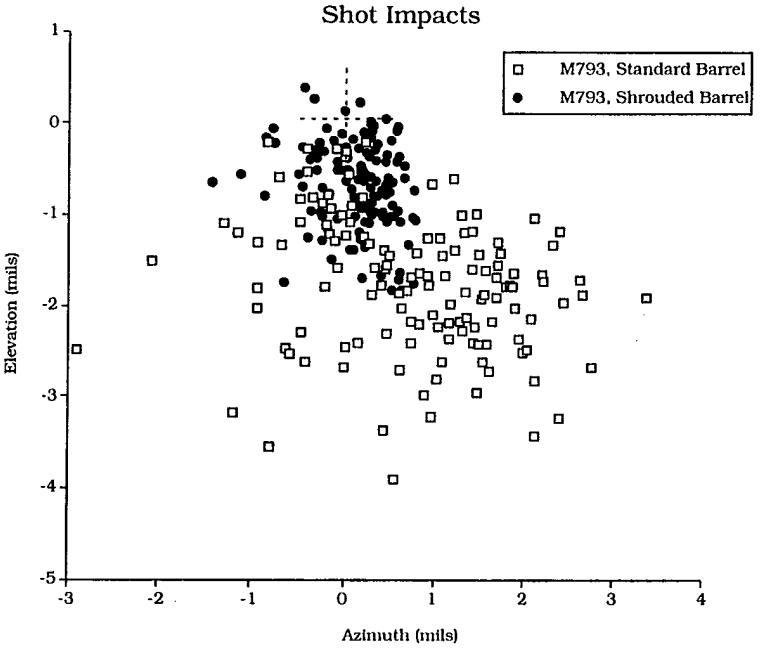

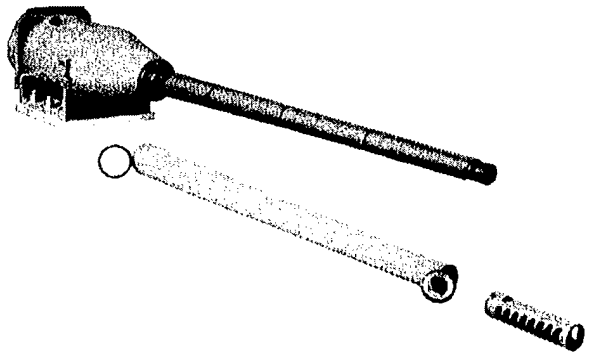

PLASMA SPRAYED SHROUD

TRANSITIONAL BALLISTICS

WEAPONS and MATERIALS RESEARCH
DIRECTORATE
Ballistics and Weapons Concepts Division

- SABOTS CARRY THE PROJECTILE OUT OF THE BORE
- DISCARDED TO achieve A LOW DRAG FLIGHT CONFIGURATION
- ASYMMETRIC MECHANICAL INTERACTIONS OCCUR DURING SEPARATION
- ASYMMETRIC GAS DYNAMIC INTERACTIONS OCCUR DURING SEPARATION
- PROJECTILE LINEAR AND ANGULAR MOTION DISTURBED PRIOR TO ENTRY INTO FREE FLIGHT

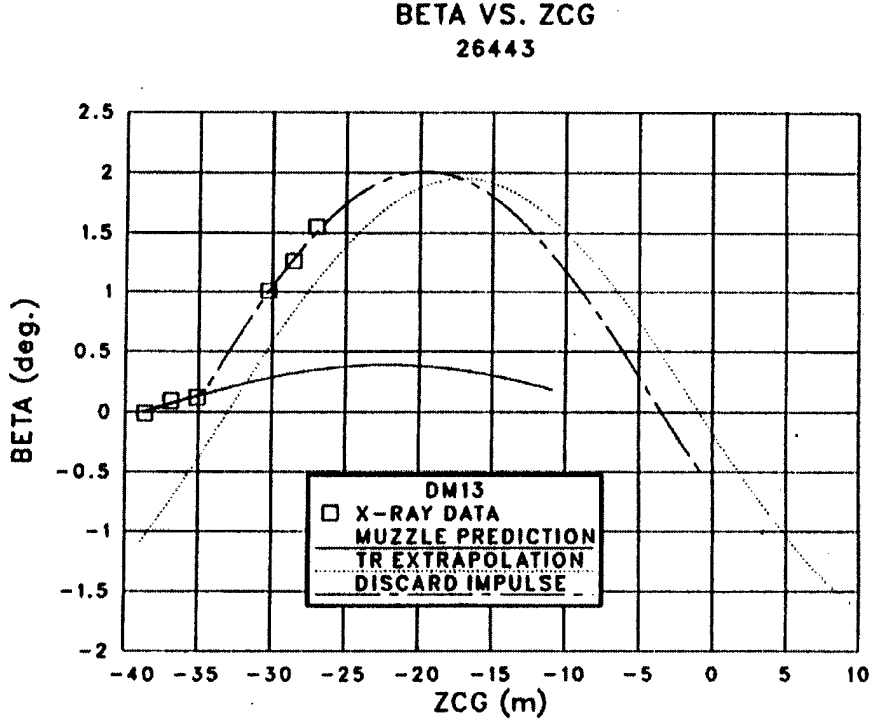

PRECISION FIRE
EXPERIMENTAL TESTING

WEAPONS and MATERIALS RESEARCH
DIRECTORATE
Ballistics and Weapons Concepts Division

JUMP TEST SET-UP

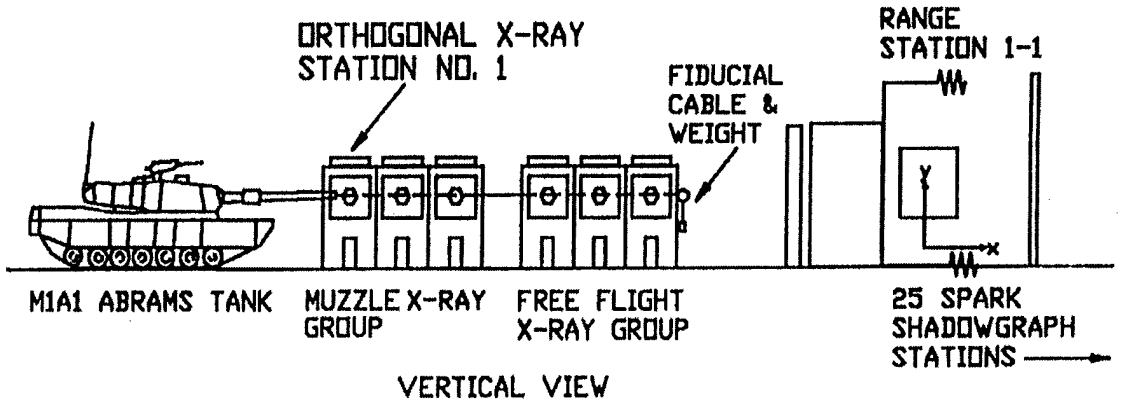

TRANSONIC RANGE FACILITY

- 25 ORTHOGONAL SPARK SHADOWGRAPH STATIONS
- 60 MM to 205 MM CAPABILITY
- 230 M OF INSTRUMENTED LENGTH
- EXTRACTS COMPLETE CONFIGURATION AERODYNAMICS
- LARGEST AND MOST COMPLETE AEROBALLISTIC FACILITY IN THE WORLD

AERODYNAMICS RANGE FACILITY

- 37 ORTHOGONAL SPARK SHADOWGRAPH STATIONS
- 5 MM to 40 MM CAPABILITY
- 100 M OF INSTRUMENTED LENGTH
- DIRECT IMAGE ON FILM
- EXTRACTS COMPLETE CONFIGURATION AERODYNAMICS
- ASME NATIONAL HISTORIC LANDMARK

JUMP TEST SET-UP

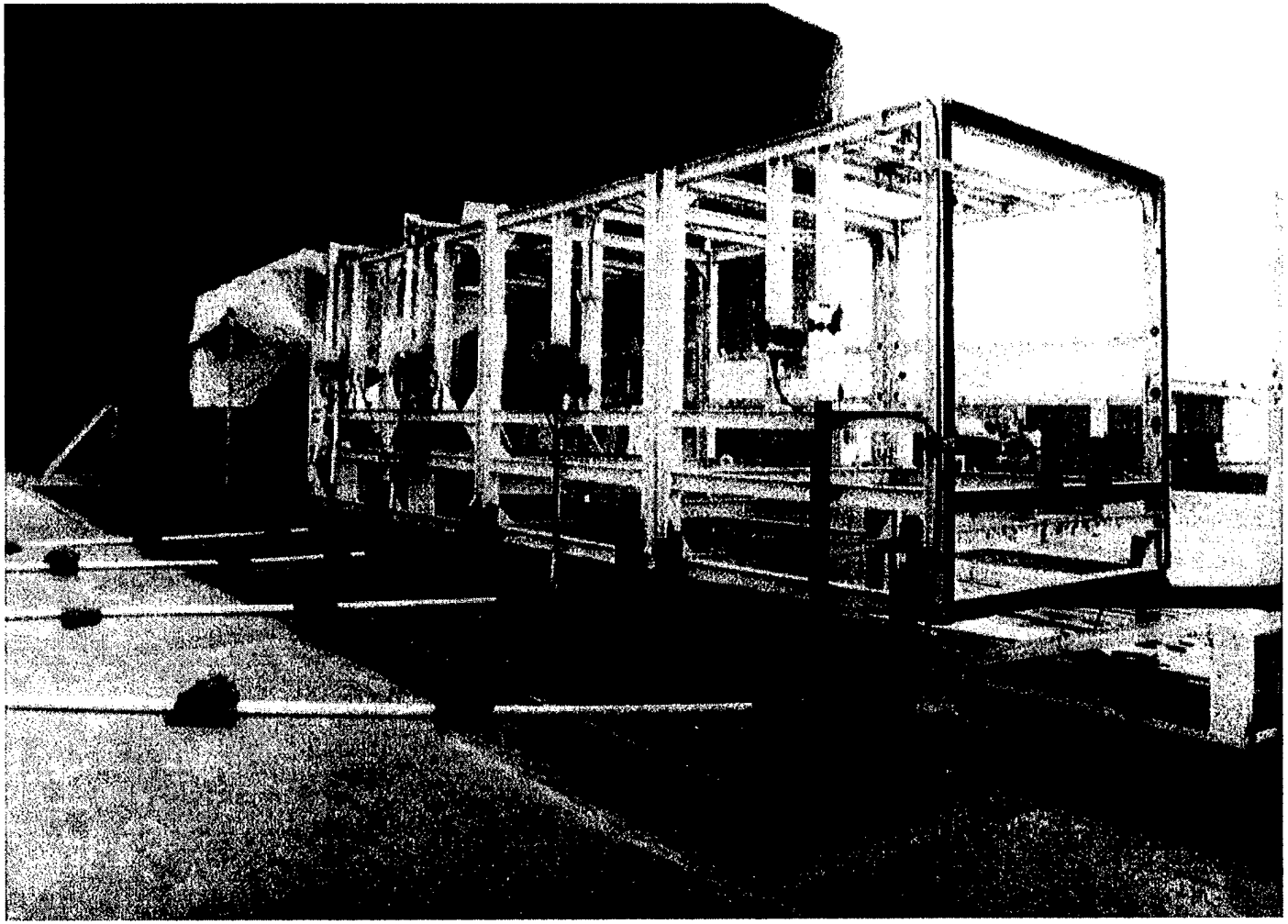

JUMP TEST RESULTS

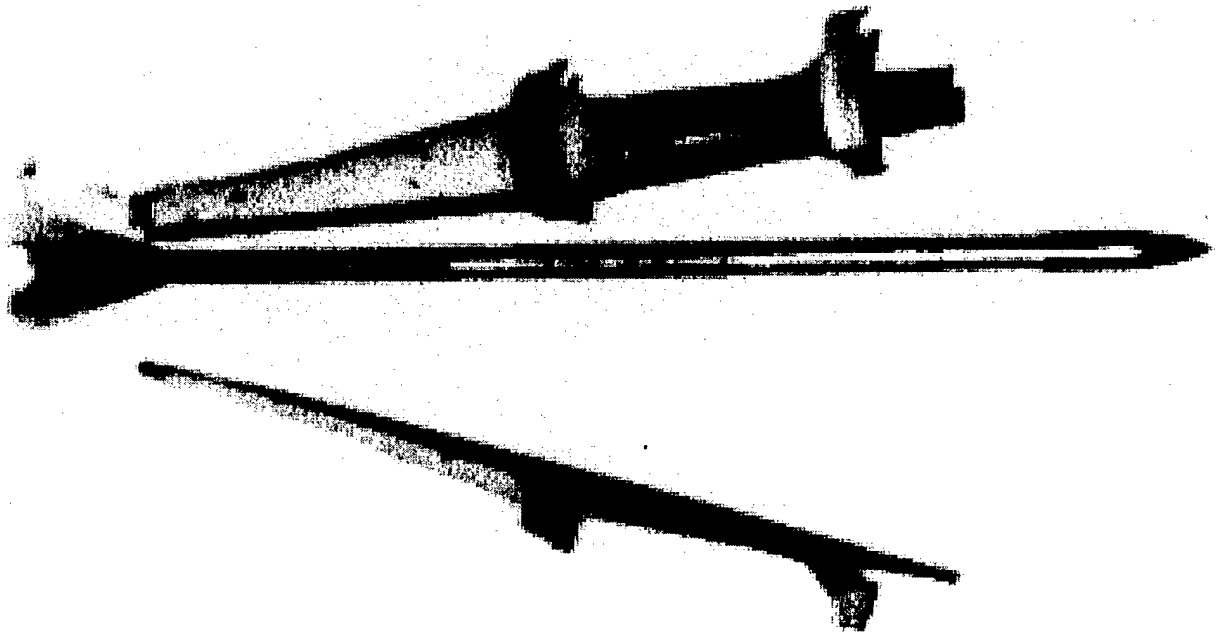

STRUCTURAL DYNAMIC MODELING OF DISCARD

WEAPONS and MATERIALS RESEARCH
DIRECTORATE
Ballistics and Weapons Concepts Division

- Modeling computes interactions between the sabot, obturator and sealing cuff
- Interactions and disturbances between the penetrator and the sabot separation can be determined

Seal Deformation During Sabot Discard

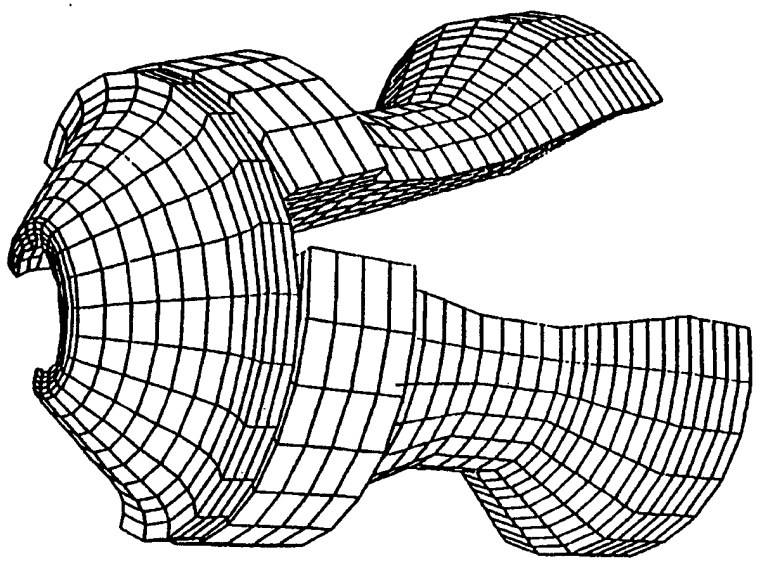

TIME = .24000E-02

DISCARD OF AN EM SABOT ARMATURE

WEAPONS and MATERIALS RESEARCH DIRECTORATE
Ballistics and Weapons Concepts Division

Downrange X-rays from Jump Test (Shot 12)

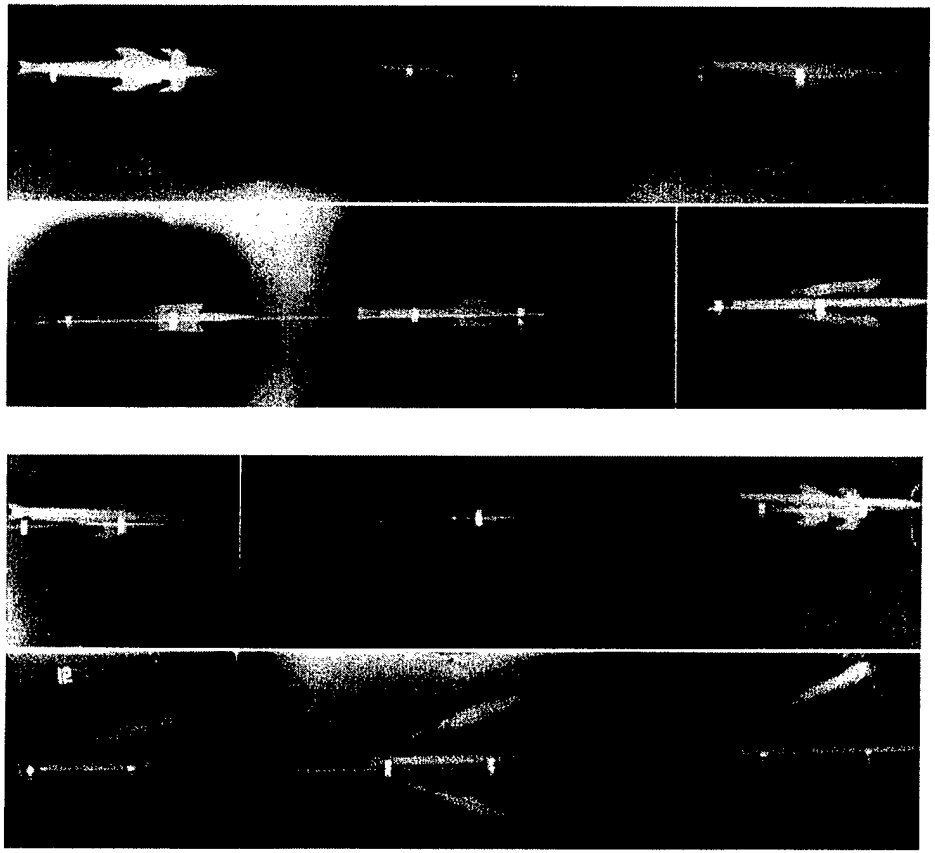

36-22

* *Dimensions are in meters from the muzzle*

Results from Experiment and Model

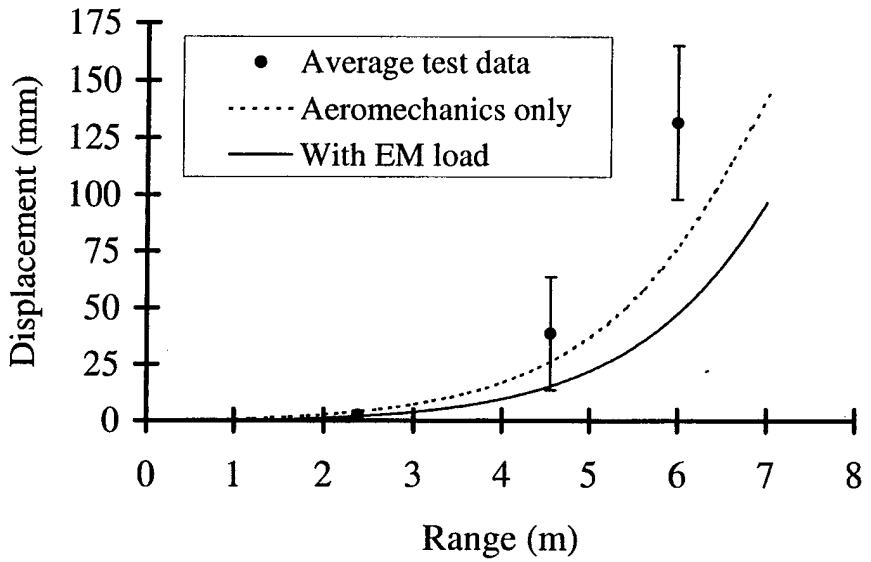

Sabot petal lateral displacement

CURRENT FLOW MODELING OF AN EM SABOT ARMATURE

WEAPONS and MATERIALS RESEARCH DIRECTORATE
Ballistics and Weapons Concepts Division

Calculated Current Streamlines - CCEMG

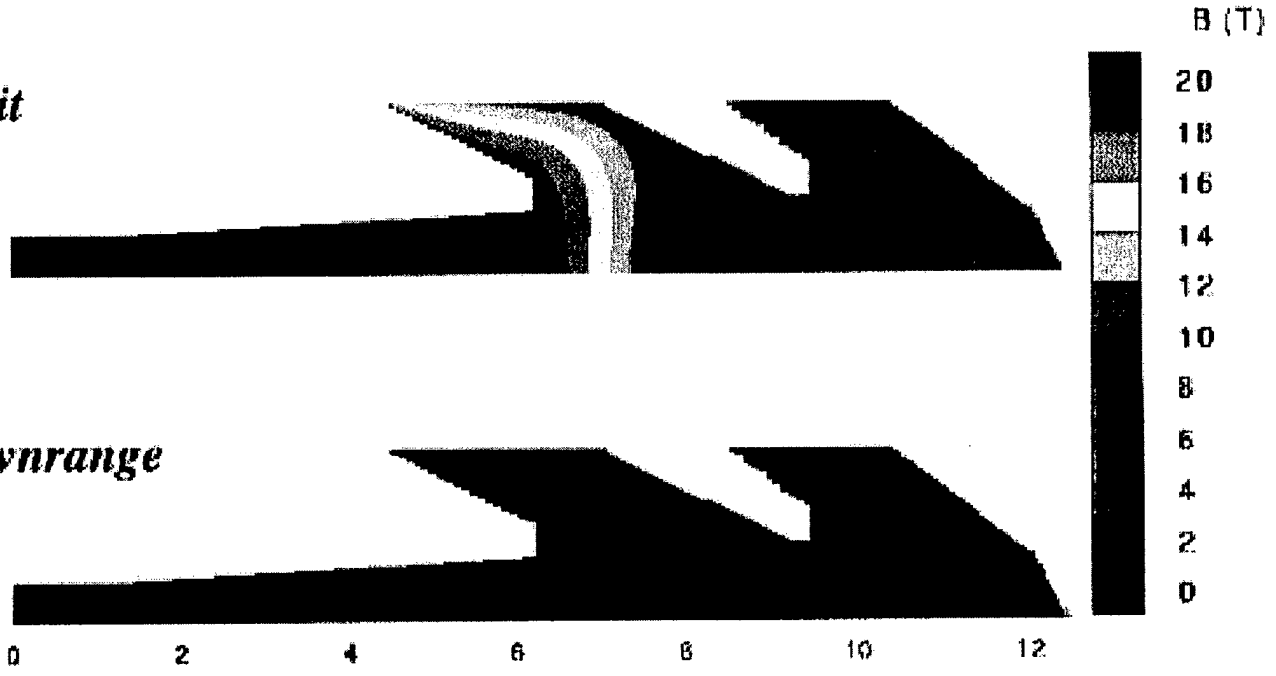

MODELING VS. EXPERIMENT
EM SABOT ARMATURE

WEAPONS and MATERIALS RESEARCH
DIRECTORATE
Ballistics and Weapons Concepts Division

Comparison of calculated heat transport and flash x-ray image

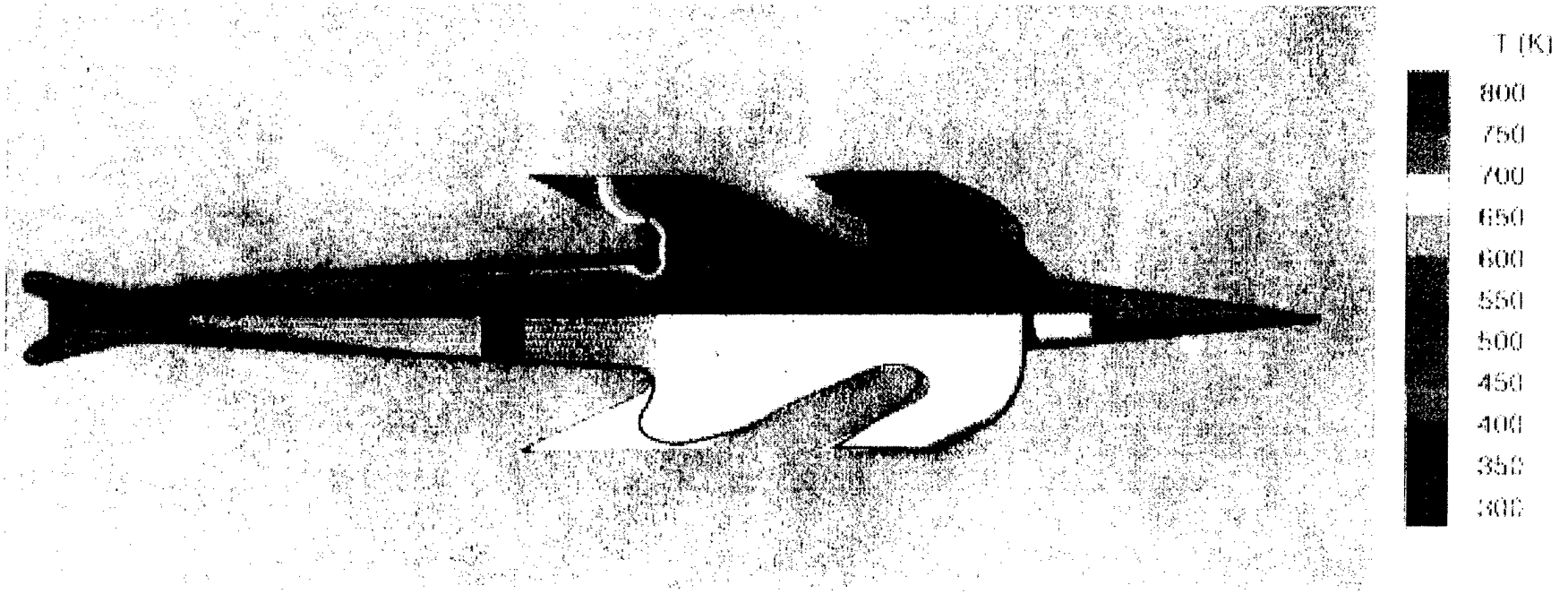

CCEMG Shot 39

1.8 km/s, 0.8 MA

COMPUTATIONAL MODELING OF SABOT DISCARD

WEAPONS and MATERIALS RESEARCH
DIRECTORATE
Ballistics and Weapons Concepts Division

PRESSURE CONTOURS

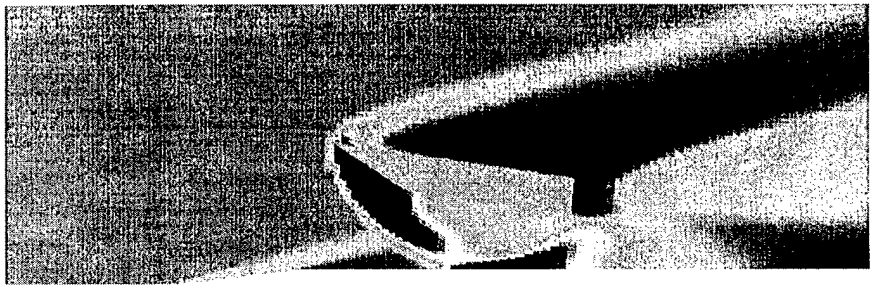

SABOT PETAL AT 10 DEGREES ANGLE OF ATTACK

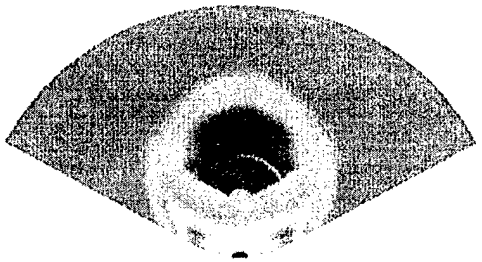

CROSS SECTION OF THE PRESSURE DISTRIBUTION

COMPLEX 3D CFD MODELING OF SABOT FLOW FIELDS

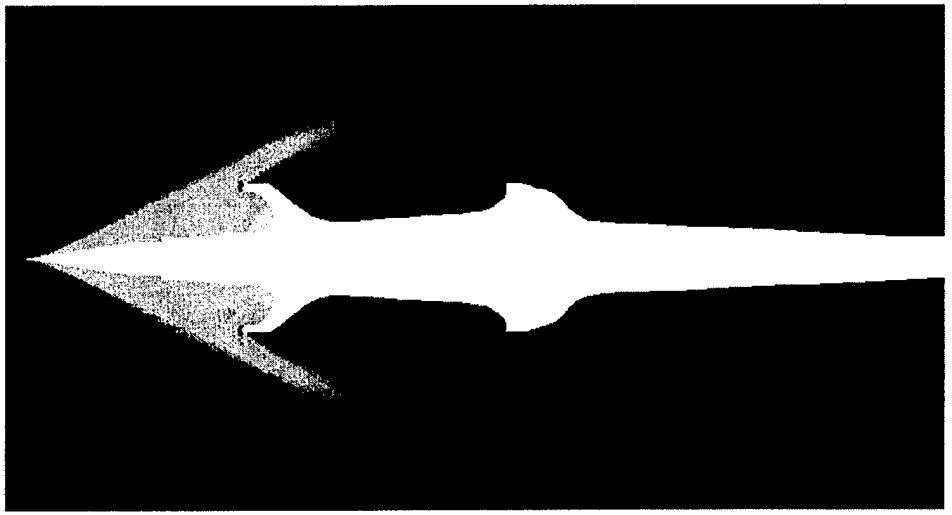

INITIAL FRONT CUP PRESSURE LOADING

SHADOWGRAPH OF A MACH 5 PENETRATOR

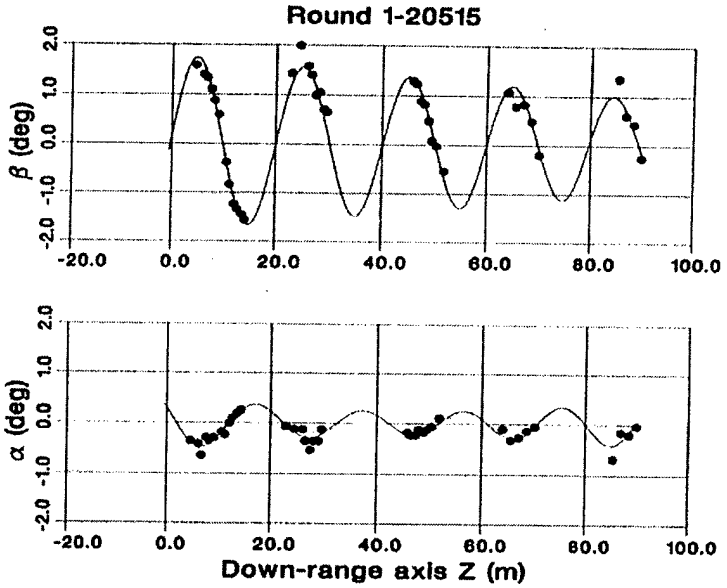

DENSITY CONTOURS
M829 - MACH 5

WEAPONS and MATERIALS RESEARCH
DIRECTORATE
Ballistics and Weapons Concepts Division

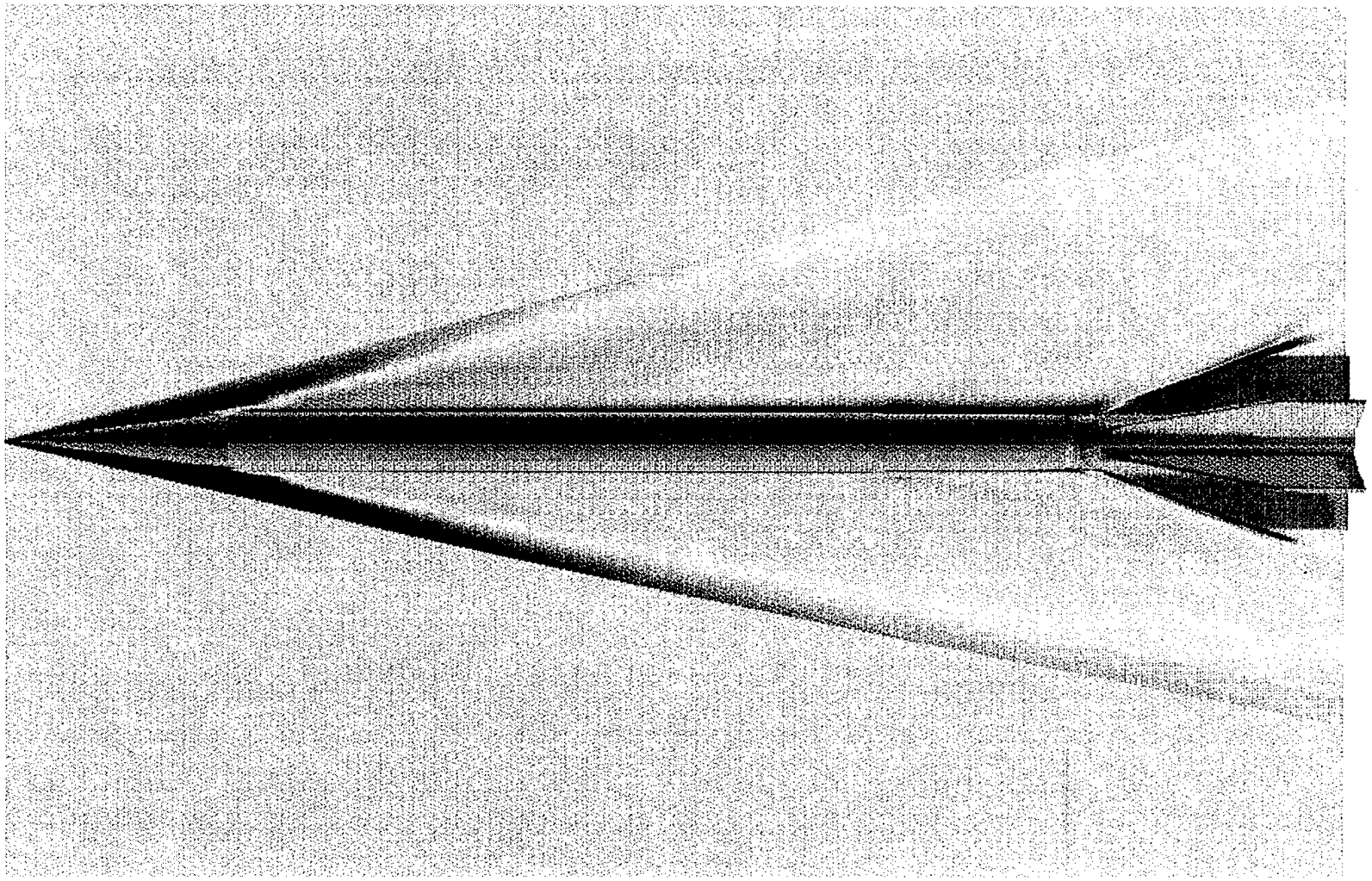

SABOT-REAR, BASELINE, AND SABOT-FORWARD CONFIGURATIONS

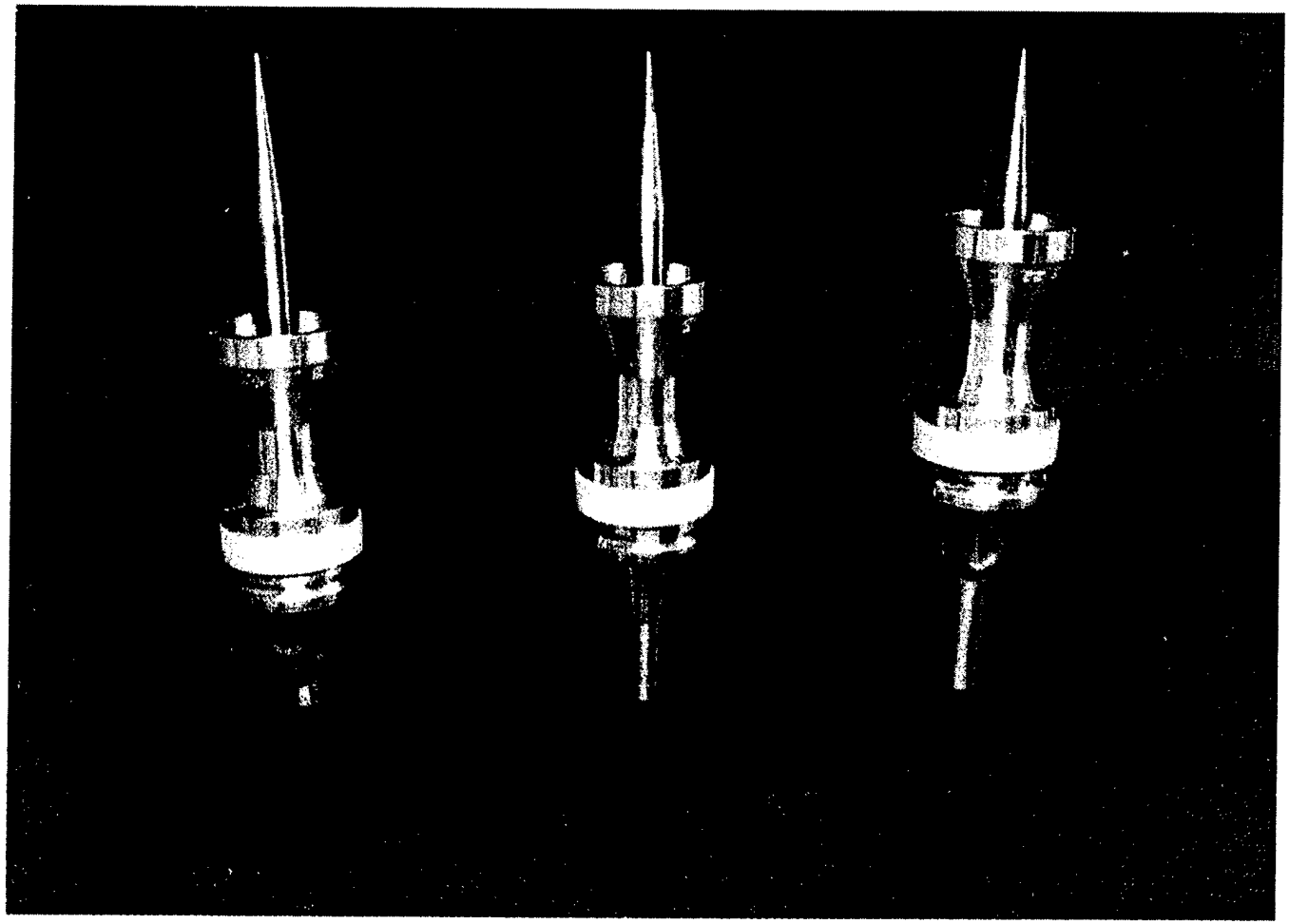

PITCHING MOMENT COEFFICIENT VERSUS MACH NUMBER - M829

WEAPONS and MATERIALS RESEARCH
DIRECTORATE
Ballistics and Weapons Concepts Division

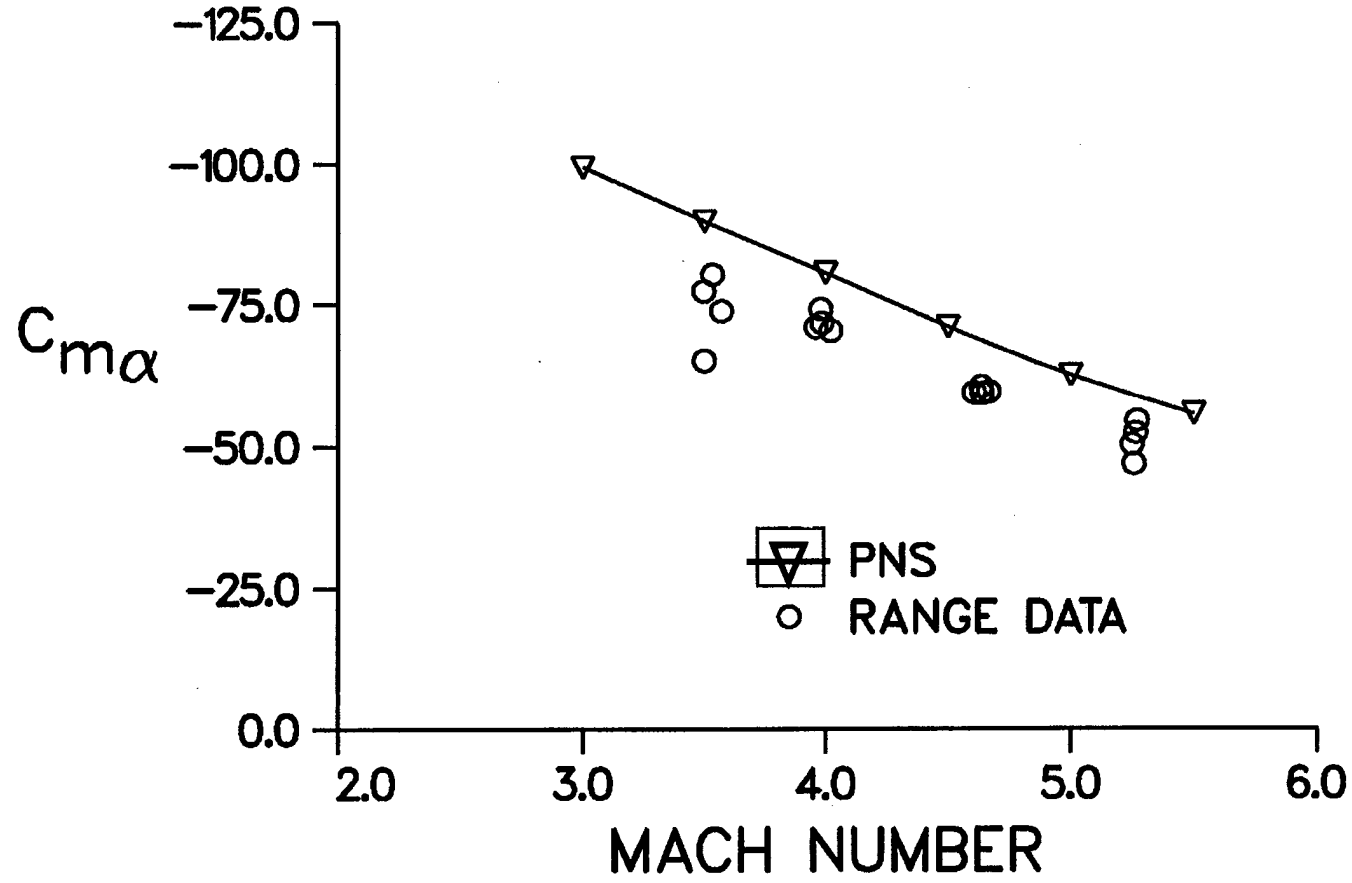

COMPUTATIONAL MODELING OF HEAT TRANSFER

WEAPONS and MATERIALS RESEARCH DIRECTORATE
Ballistics and Weapons Concepts Division

3D PARABOLIZED NAVIER STOKES COMPUTATION OF THE SURFACE TEMPERATURE DISTRIBUTION AT 2 km/s ON AN EM LAUNCHED TITANIUM ALLOY FIN SET

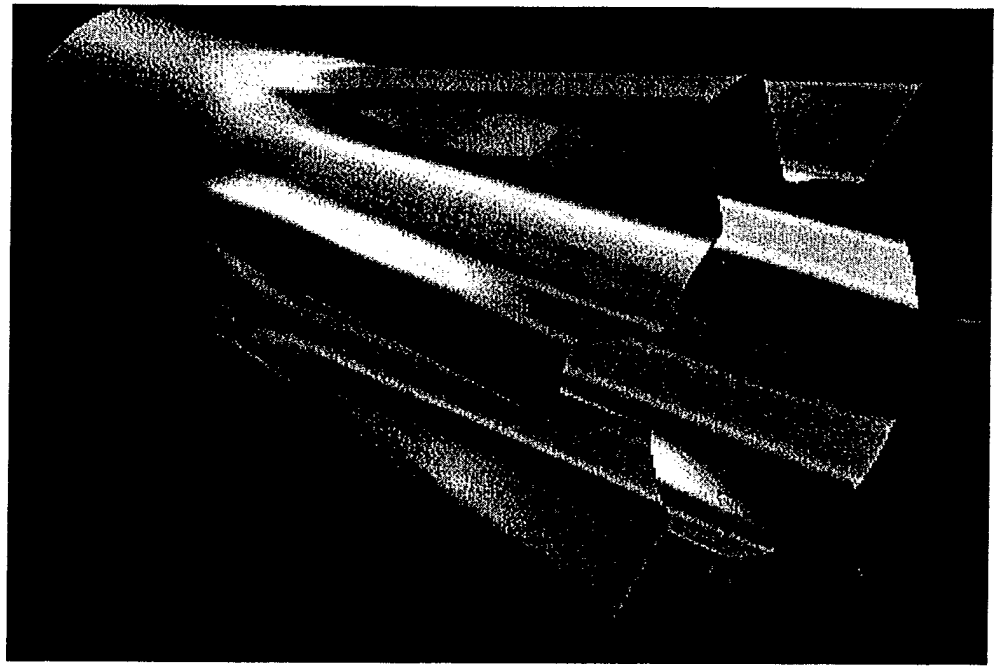

JUMP MODEL

WEAPONS and MATERIALS RESEARCH
DIRECTORATE
Ballistics and Weapons Concepts Division

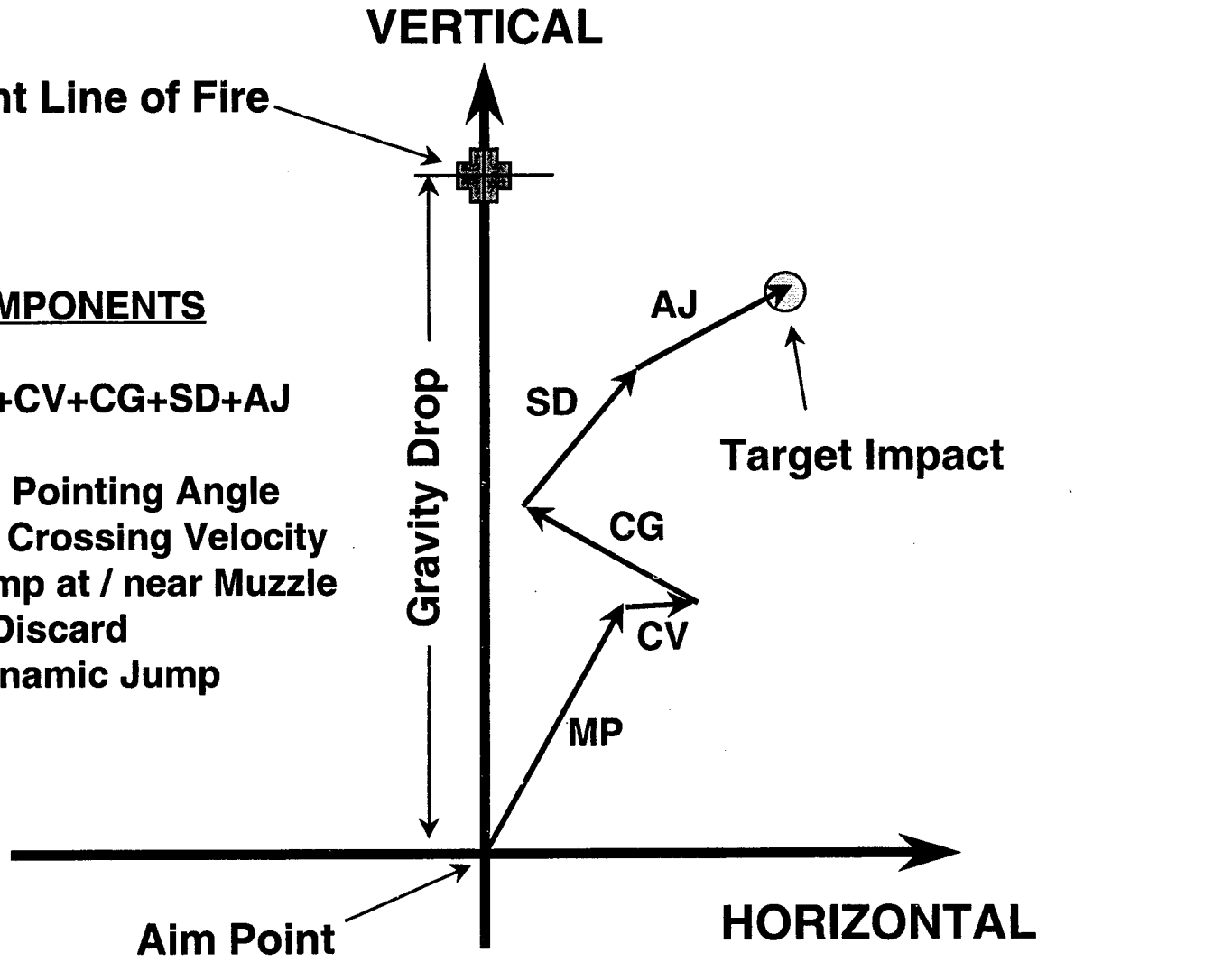

SYSTEM PERFORMANCE CLOSURE DIAGRAM

WEAPONS and MATERIALS RESEARCH
DIRECTORATE
Ballistics and Weapons Concepts Division

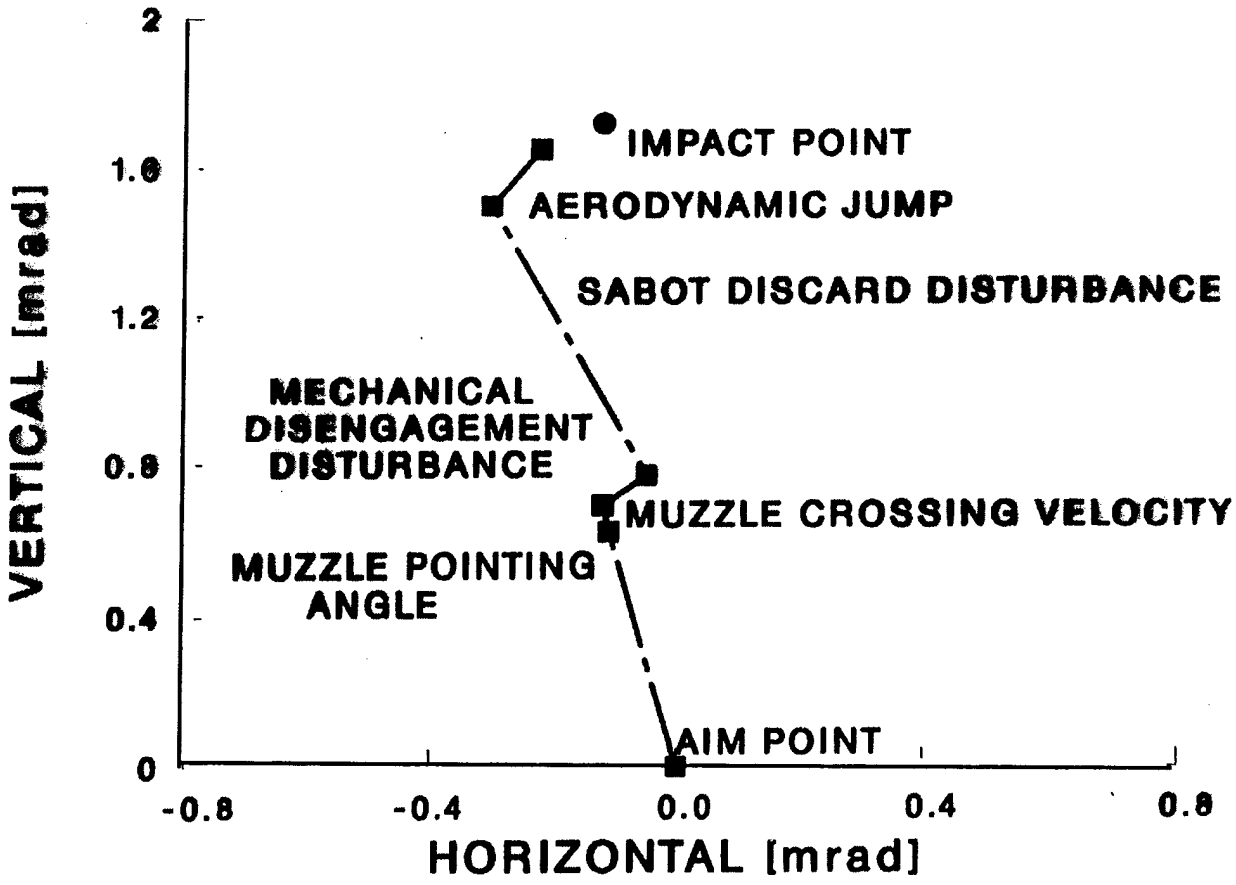

25-mm XM881
Muzzle Pointing Angle

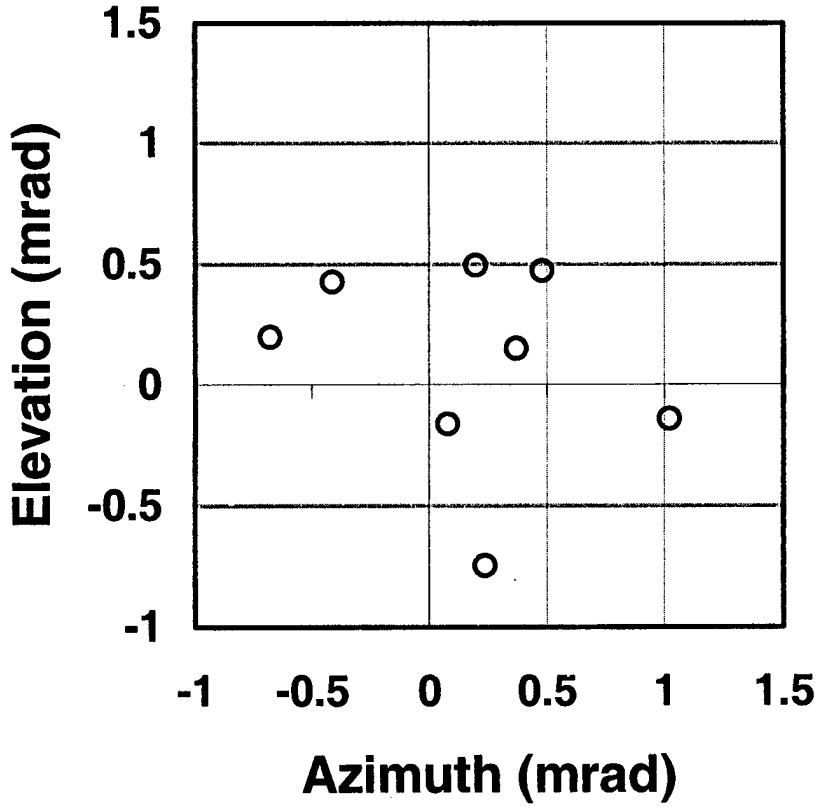

JUMP VECTORS

WEAPONS and MATERIALS RESEARCH
DIRECTORATE
Ballistics and Weapons Concepts Division

25-mm XM881
Muzzle Crossing Velocity

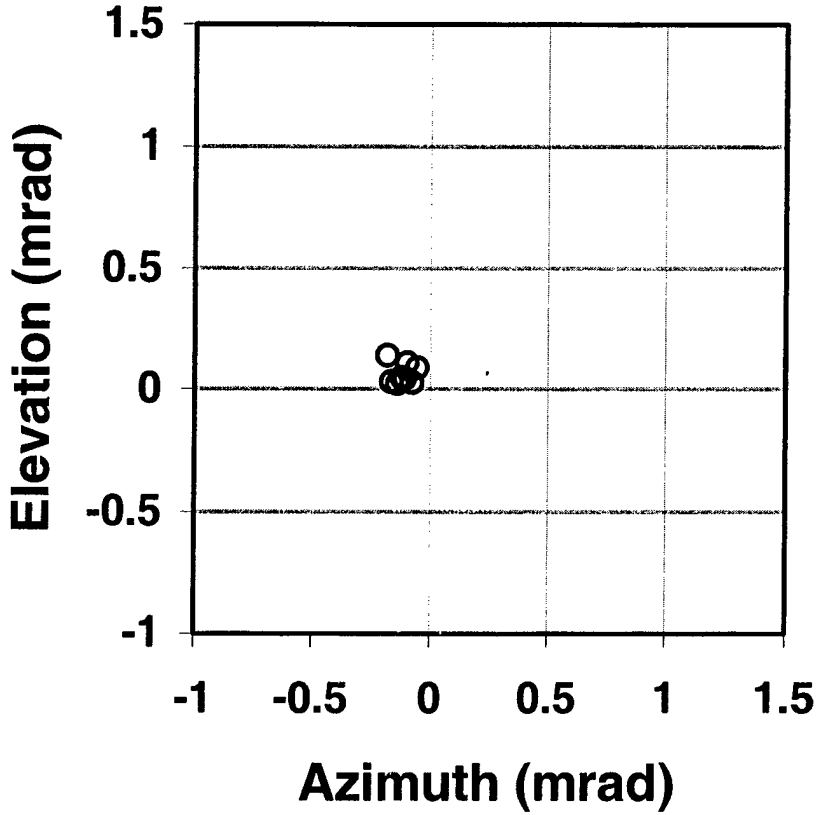

25-mm XM881
Center of Gravity Jump

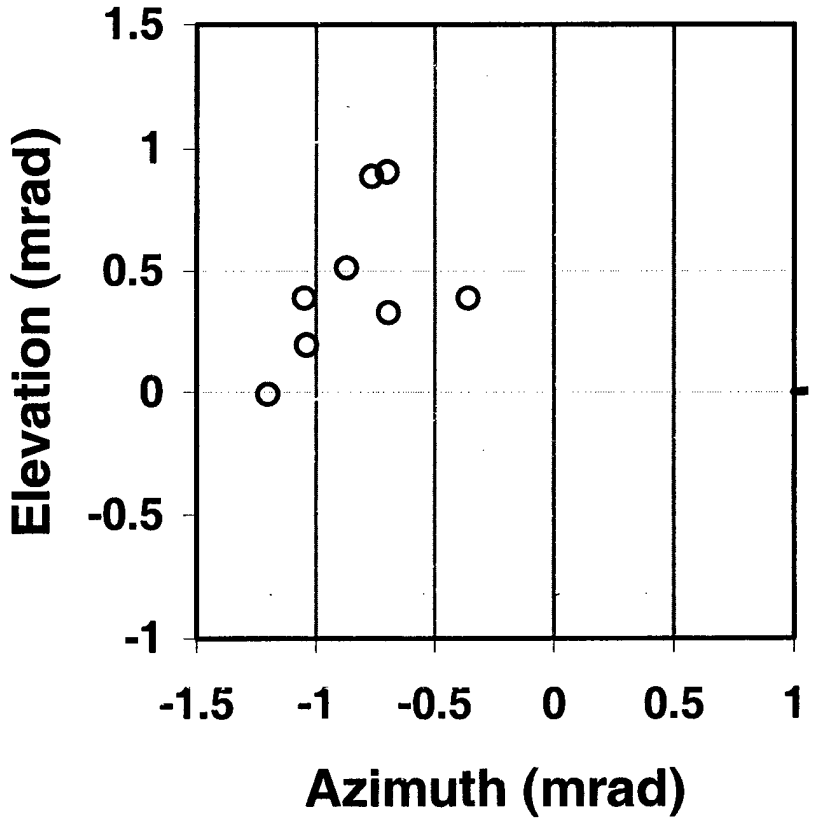

36-35

JUMP VECTORS

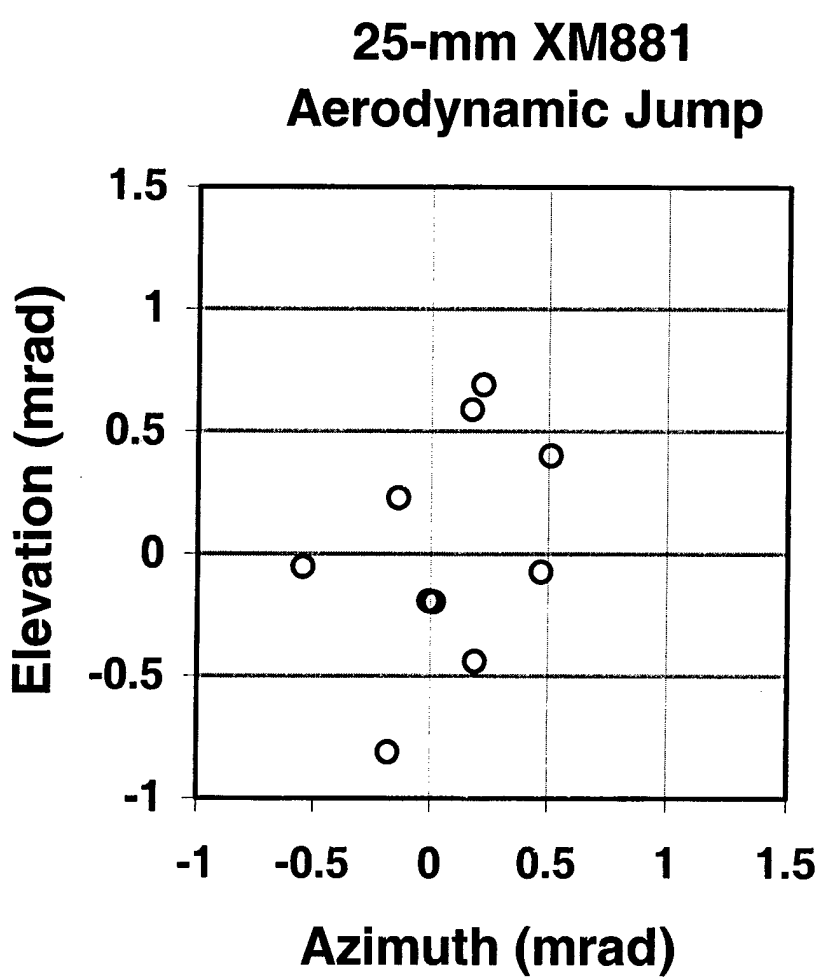

JUMP VECTORS

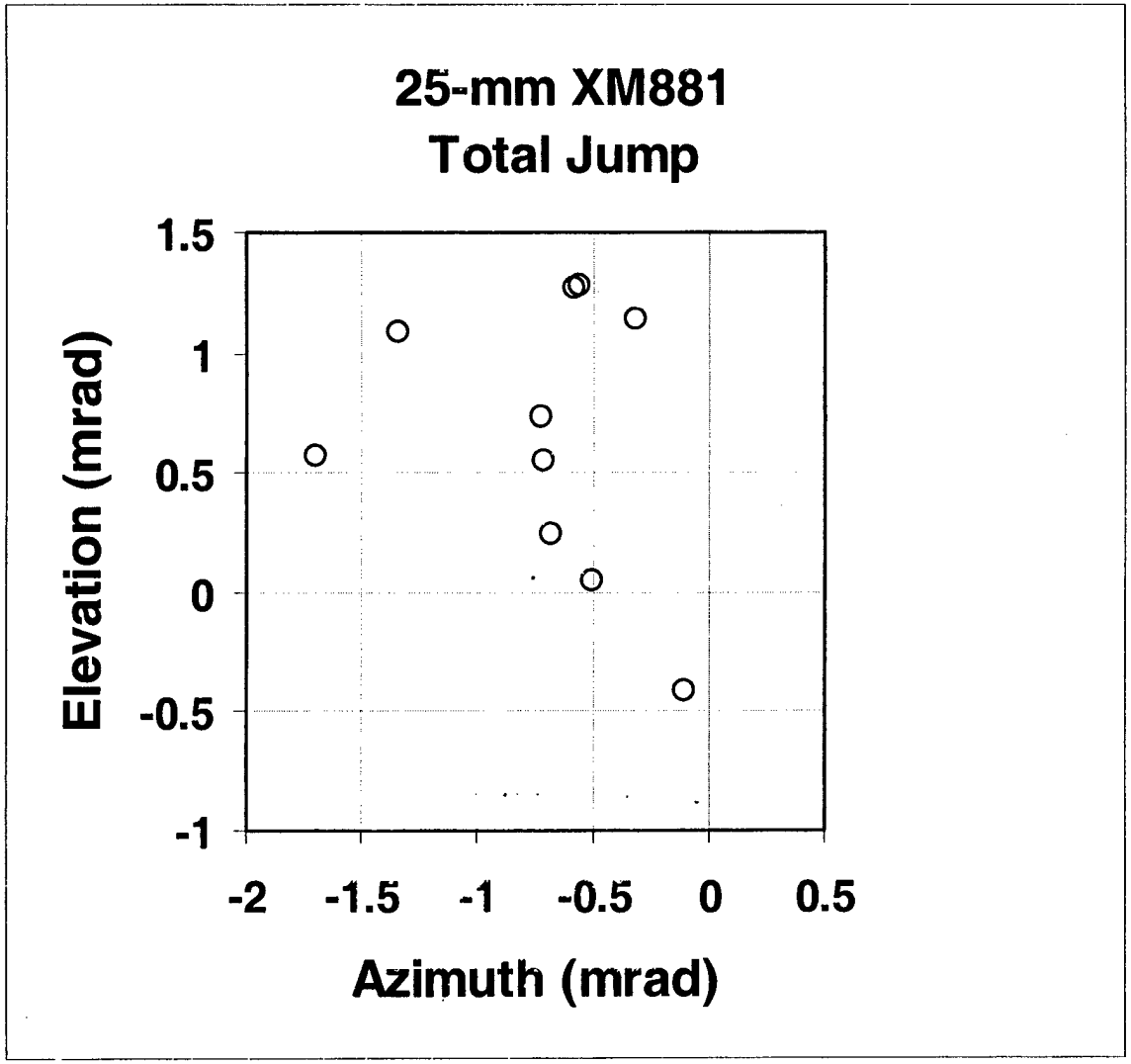

DISPERSION MODEL

WEAPONS and MATERIALS RESEARCH
DIRECTORATE
Ballistics and Weapons Concepts Division

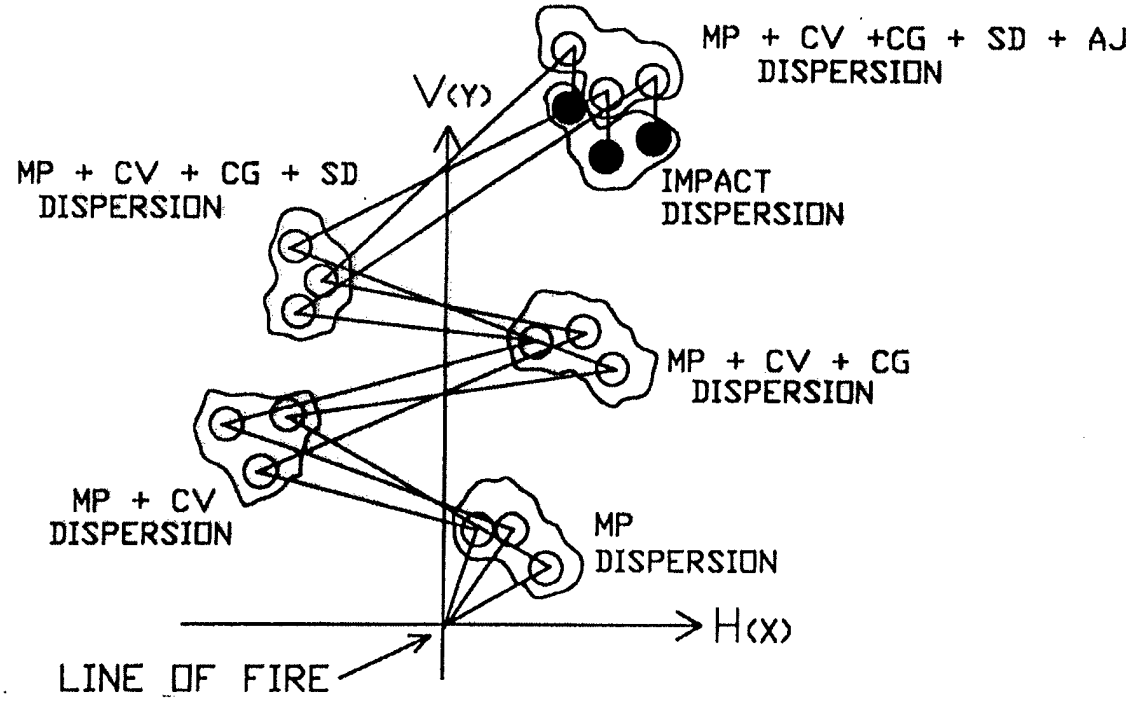

$$DISPERSION = MP + CV + CG + SD + AJ + GD + CORRELATIONS$$

$$\sigma^2 = \sigma_{mp}^2 + \sigma_{cv}^2 + \sigma_{cg}^2 + \sigma_{sd}^2 + \sigma_{aj}^2 + \sigma_{gd}^2 + 2\sigma_{cgaj}$$

JUMP VECTOR ANALYSIS

WEAPONS and MATERIALS RESEARCH
DIRECTORATE
Ballistics and Weapons Concepts Division

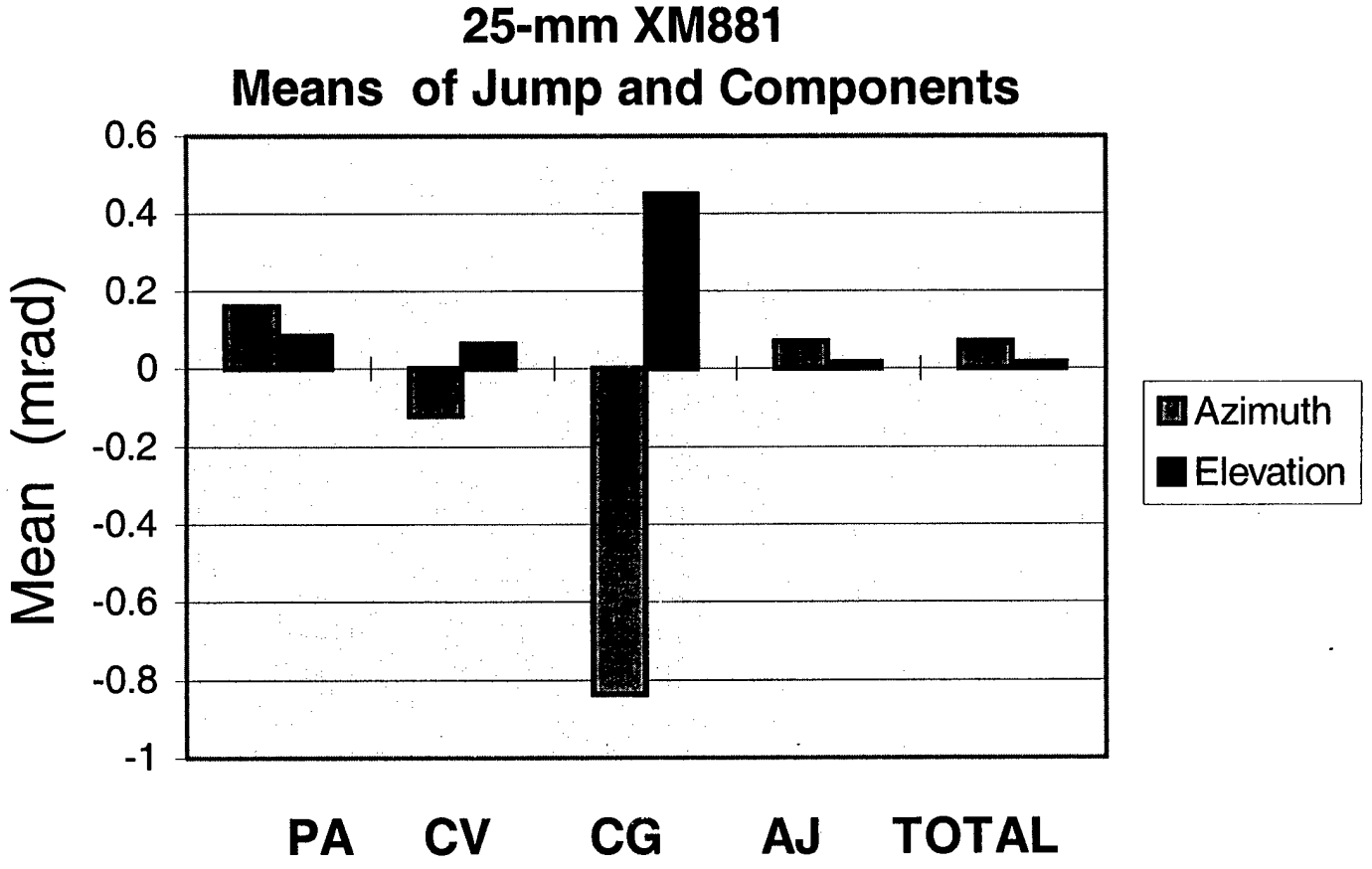

JUMP VECTOR ANALYSIS

WEAPONS and MATERIALS RESEARCH
DIRECTORATE
Ballistics and Weapons Concepts Division

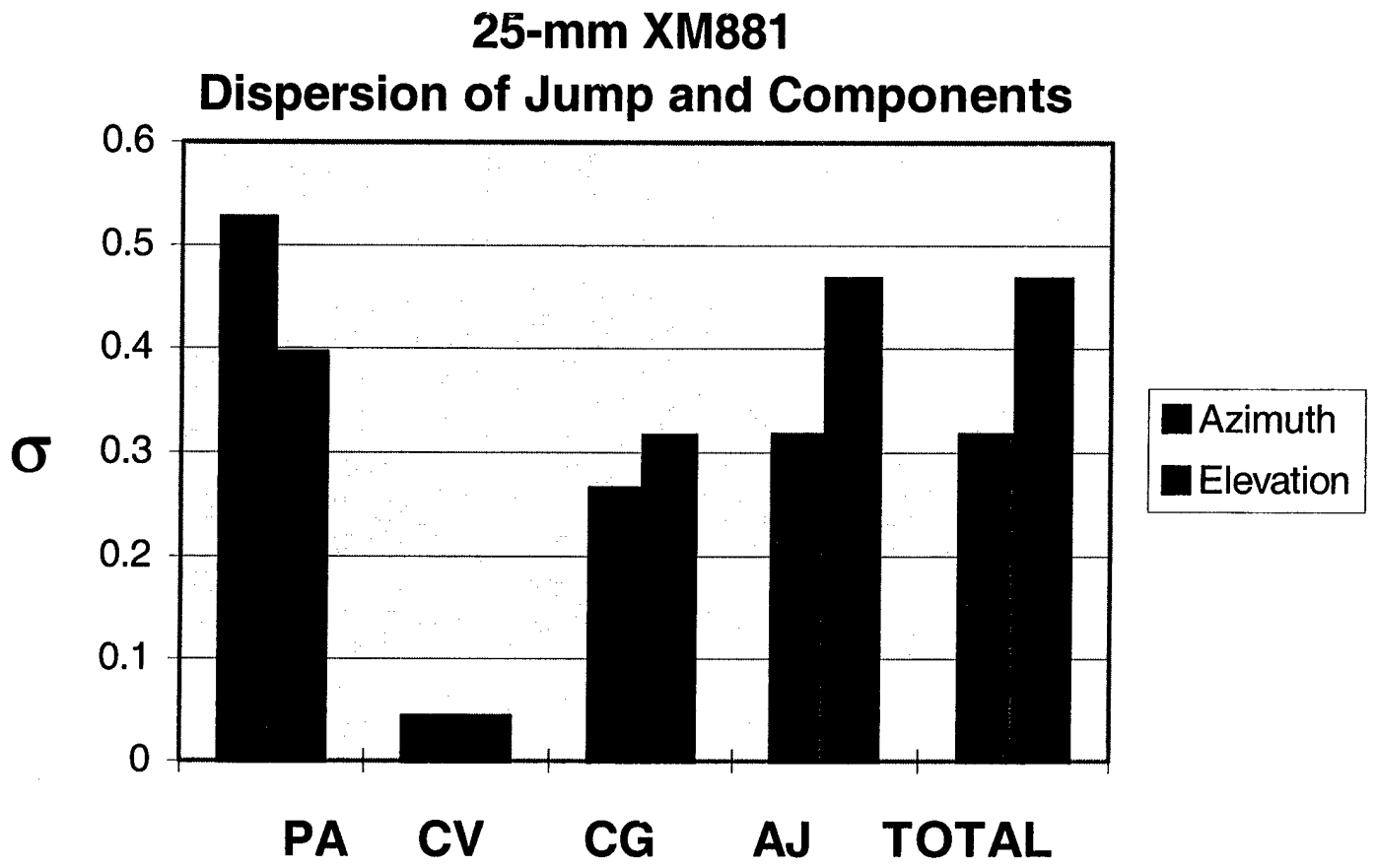

JUMP CORRELATION EFFECT SCHEMATIC

WEAPONS and MATERIALS RESEARCH
DIRECTORATE
Ballistics and Weapons Concepts Division

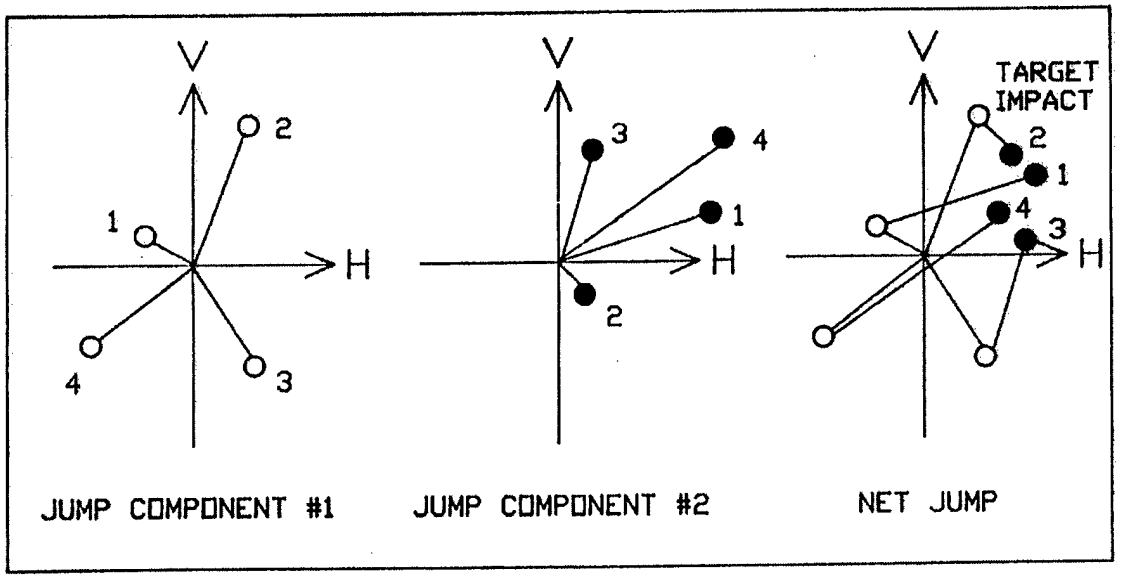

DISPERSION MODEL - TWO CORRELATED COMPONENTS

$$DISPERSION = COMPONENT_1 + COMPONENT_2 + CORRELATION_{12}$$

$$\sigma^2 = \sigma_1^2 + \sigma_2^2 + 2\sigma_{12}$$

NON LINEAR COUPLING IN DISPERSION

WEAPONS and MATERIALS RESEARCH DIRECTORATE
Ballistics and Weapons Concepts Division

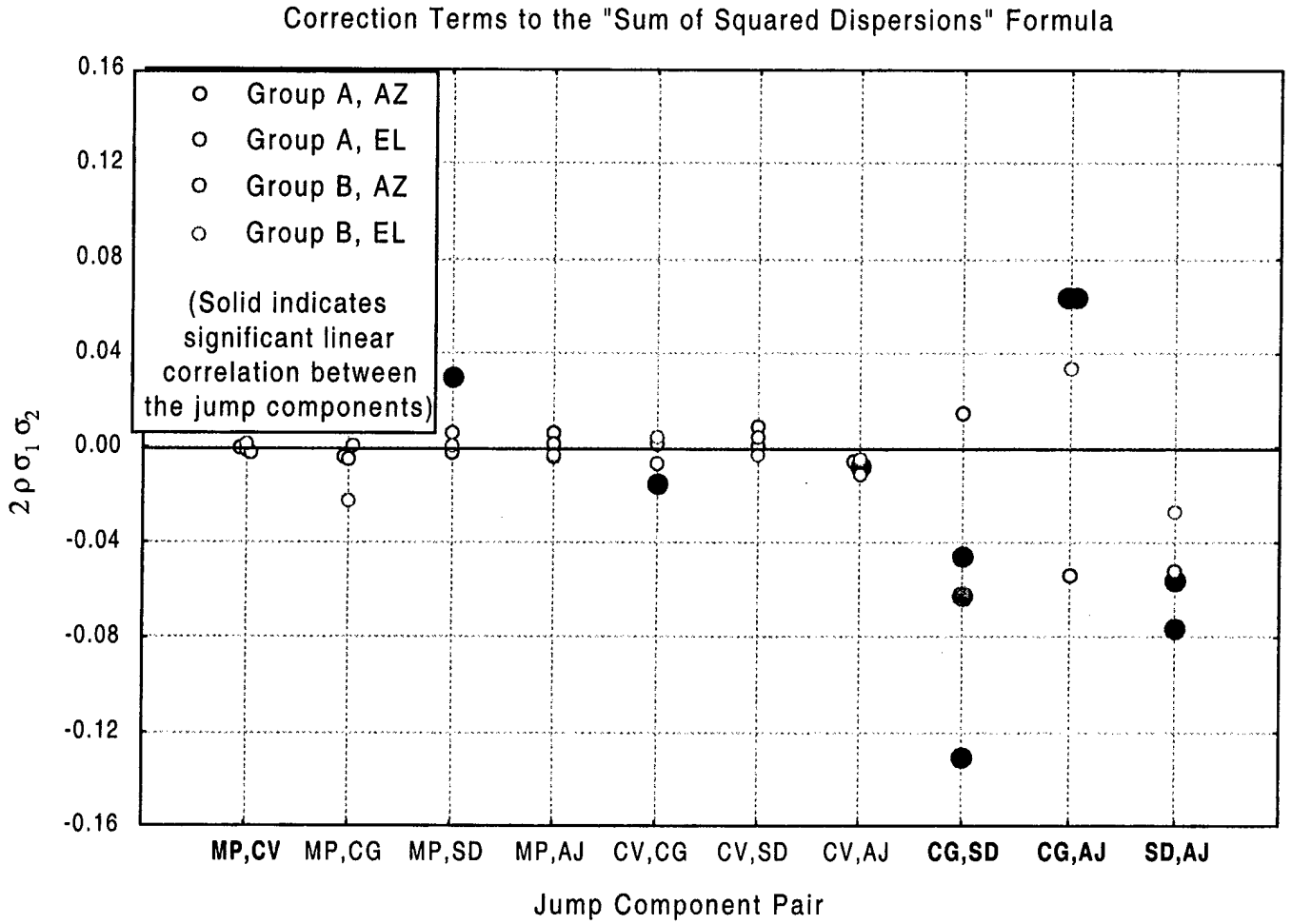

SUMMARY

- SIGNIFICANT PROGRESS HAS BEEN ACHIEVED IN THE UNDERSTANDING OF DIRECT FIRE ACCURACY
- ADVANCED MODELING, SIMULATION AND EXPERIMENTAL TECHNOLOGIES ARE AVAILABLE
- THE ACCURACY PROBLEM CAN ONLY BE ADDRESSED AS A SYSTEM
- IT IS STILL A COMPLEX NON-LINEAR MULTI-DISCIPLINARY PROBLEM
- GUN AND AMMUNITION SYSTEM OPTIMIZATION IS AS ALWAYS A DIFFICULT ENGINEERING PROBLEM

DISTRIBUTION LIST FOR
SPECIAL PUBLICATION ARCCB-SP-99015

NO. OF
COPIES

EXTERNAL DISTRIBUTION:

DEFENSE TECHNICAL INFO CENTER
ATTN: DTIC-OCA (ACQUISITIONS) 2
8725 JOHN J. KINGMAN RD
STE 0944
FT. BELVOIR, VA 22060-6218

COMMANDER
U.S. ARMY ARDEC
ATTN: AMSTA-AR-WEL-TL, BLDG. 59 2
PICATINNY ARSENAL, NJ 07806-5000

INTERNAL DISTRIBUTION:

TECHNICAL LIBRARY
ATTN: AMSTA-AR-CCB-O 2

TECHNICAL PUBLICATIONS & EDITING SECTION
ATTN: AMSTA-AR-CCB-O 2

ERIC KATHE
TECHNOLOGY DIVISION
ATTN: AMSTA-AR-CCB-TC 40